# 2018

# QCD
# and
# High Energy Interactions

## Sponsored by

- CNRS (Centre National de la Recherche Scientifique)
- CEA (Commissariat à l'Énergie Atomique et aux Énergies Alternatives)
- FNRS (Fond National de la Recherche Scientifique)
- BSP (Belgian Science Policy)

**53$^{rd}$ Rencontres de Moriond**
La Thuile, Aosta Valley, Italy - March 17 - 24, 2018

**2018 QCD and High Energy Interactions**



ISBN : 979-10-96879-06-9

**Proceedings of the 53$^{rd}$ RENCONTRES DE MORIOND**

*QCD and High Energy Interactions*

*La Thuile, Aosta Valley, Italy* *March 17-24, 2018*

# 2018

# QCD
# and
# High Energy Interactions

**edited by**

**Étienne Augé**

**Jacques Dumarchez**

**and**

**Jean Trân Thanh Vân**

The $53^{rd}$ Rencontres de Moriond

## 2018 QCD and High Energy Interactions

## was organized by

Étienne Augé (LAL, Orsay)
Jacques Dumarchez (LPNHE, Paris)

## with the active collaboration of:

- E. Berger (A.N.L. Argonne)
- S. Bethke (M.P.I. Munich)
- A. Capella (L.P.T. Orsay)
- A. Czarnecki (U. Alberta)
- D. Denegri (C.E.A. Saclay)
- N. Glover (Durham)
- B. Klima (Fermilab)
- N. Mahmoudi (University of Lyon)
- L. McLerran (Brookhaven Nat. Lab.)
- B. Pietrzyk (L.A.P.P. Annecy)
- L. Schoeffel (CEA - IRFU/SPP - Saclay)
- Chung-I Tan (Brown University)
- J. Trân Thanh Vân (L.P.T. Orsay)
- U. Wiedemann (CERN)

# 2018 RENCONTRES DE MORIOND

The $53^{rd}$ Rencontres de Moriond were held in La Thuile, Valle d'Aosta, Italy.

The first meeting took place at Moriond in the French Alps in 1966. There, experimental as well as theoretical physicists not only shared their scientific preoccupations, but also the household chores. The participants in the first meeting were mainly french physicists interested in electromagnetic interactions. In subsequent years, a session on high energy strong interactions was added.

The main purpose of these meetings is to discuss recent developments in contemporary physics and also to promote effective collaboration between experimentalists and theorists in the field of elementary particle physics. By bringing together a relatively small number of participants, the meeting helps develop better human relations as well as more thorough and detailed discussion of the contributions.

Our wish to develop and to experiment with new channels of communication and dialogue, which was the driving force behind the original Moriond meetings, led us to organize a parallel meeting of biologists on Cell Differentiation (1980) and to create the Moriond Astrophysics Meeting (1981). In the same spirit, we started a new series on Condensed Matter physics in January 1994. Meetings between biologists, astrophysicists, condensed matter physicists and high energy physicists are organized to study how the progress in one field can lead to new developments in the others. We trust that these conferences and lively discussions will lead to new analytical methods and new mathematical languages.

The $53^{rd}$ Rencontres de Moriond in 2018 comprised three physics sessions:

- March 10 - 17: "Electroweak Interactions and Unified Theories"
- March 17 - 24: "QCD and High Energy Hadronic Interactions"
- March 17 - 24: "Cosmology"

We thank the organizers of the $53^{rd}$ Rencontres de Moriond:

- A. Abada, E. Armengaud, J. Conrad, P. Fayet, J.-M. Frère, P. Hernandez, L. Iconomidou-Fayard, P. Janot, M. Knecht, J. P. Lees, S. Loucatos, F. Montanet, J. Orloff, A. Pich, S. Pokorski, V. Tisserand and D. Wood for the "Electroweak Interactions and Unified Theories" session,
- E. Augé, E. Berger, S. Bethke, A. Capella, A. Czarnecki, D. Denegri, N. Glover, B. Klima, N. Mahmoudi, L. McLerran, B. Pietrzyk, L. Schoeffel, Chung-I Tan, J. Trân Thanh Vân and U. Wiedemann for the "QCD and High Energy Hadronic Interactions" session,
- P. Astier, C. Burgess, K. Ganga, Y. Giraud-Héraud, J.-M. Le Goff, H. McCracken, O. Perdereau and F. Vernizzi for the "Cosmology" session

and the conference secretariat and technical staff:

V. de Sá-Varanda and C. Bareille, I. Cossin, G. Dreneau, F. Legrand, G. Perrin and S. Zappino

We are also grateful to Giorgio Palmucci, Mimmo De Pisa, Cipriano Deiana, Francesco Quinto, Laura Basile and the Planibel Hotel staff who contributed through their hospitality and cooperation to the well-being of the participants, enabling them to work in a relaxed atmosphere.

The Rencontres were sponsored by the Centre National de la Recherche Scientifique, the Commissariat à l'Energie Atomique (CEA-Irfu), the Fonds de la Recherche Scientifique (FRS-FNRS) and the Belgium Science Policy. We would like to express our thanks for their encouraging support.

It is our sincere hope that a fruitful exchange and an efficient collaboration between the physicists and the astrophysicists will arise from these Rencontres as from previous ones.

E. Augé, J. Dumarchez and J. Trân Thanh Vân

# Table of Contents

## 6. New Phenomena



## 7. PDF



## 8. QCD

## 9. Heavy Ion



## 10. Electroweak Physics



## 11. Closing

# 1.
# Higgs

# CMS HIGGS BOSON RESULTS

MICHAŁ BLUJ on behalf of the CMS Collaboration
*National Centre for Nuclear Research, Warsaw, Poland*

In this report we review recent Higgs boson results obtained with pp collisions at $\sqrt{s} = 13\,\text{TeV}$ recorded by the CMS detector in 2016 for an integrated luminosity of $35.9\,\text{fb}^{-1}$. The 2016 data allowed the observation of the $\text{H} \to \tau\tau$ and $\text{H} \to \text{WW}$ decays with high significance. We also present a combined measurement based on a full set of CMS analyses performed with 2016 data. These results are compatible with the standard model predictions with precision of several measurements exceeding results from combination of ATLAS and CMS data collected in 2011 and 2012.

## 1 Introduction

After the discovery of a new standard-model-like Higgs boson announced by the ATLAS and CMS collaborations in July 2012 [1,2,3] it became essential to establish the nature of this new boson, i.e. observe its production and decay modes with high significance, measure its couplings to standard model (SM) particles, etc. This objective is achieved by a set exclusive analyses sensitive to different production processes and decays of the Higgs boson which are then combined to extract its properties in the most precise way. In this report we focus on recent results acquired using pp collisions at $\sqrt{s} = 13\,\text{TeV}$ with an integrated luminosity of $35.9\,\text{fb}^{-1}$ recorded by the CMS detector [4] in 2016. We present results obtained with the $\text{H} \to \tau\tau$ and $\text{H} \to \text{WW} \to \ell\nu\ell\nu$ ($\ell = \text{e}, \mu$) channels, and through a combination of all CMS Higgs boson measurements with data collected in 2016, while recent results on final states with hadronic signatures, the $\text{H} \to \text{bb}$ decay and ttH production, are discussed elsewhere [5].

## 2 Observation of the $\text{H} \to \tau\tau$ decay

The $\text{H} \to \tau\tau$ channel, with a relatively high branching fraction of 6.3%, is the fermionic decay mode to which LHC experiments are most sensitive. The CMS search for the $\text{H} \to \tau\tau$ channel is based on an event classification to enhance the impact of events produced in the VBF process, but also in the gluon fusion process with additional jets, which increases the signal-to-background ratio. The $\text{H} \to \tau\tau$ analysis employs an estimate of a full $\tau\tau$ invariant mass, $\text{m}_{\tau\tau}$ with resolution of 15–20%. It is calculated using a likelihood based method taking as input the kinematics of the visible decay products and $p_{\text{T}}^{\text{miss}}$. The signal is extracted from two-dimensional distributions where one dimension is defined by $\text{m}_{\tau\tau}$ and other by a category dependent variable as mass of the tagging jets system, $\text{m}_{\text{jj}}$, in the VBF category [6] as shown in Fig. 1 (left). An observed excess of events above background only hypothesis provides an observation of the $\text{H} \to \tau\tau$ decay with a significance of 4.9 standard deviations, $\sigma$, with 2016 data, and $5.9\sigma$ when combined with previous results with 2011 and 2012 data [7]. The ratio of the measured signal yield to the SM expectation, a signal strength, $\mu$, amounts to $1.09^{+0.27}_{-0.26}$ and agrees across categories as shown in Fig. 1 (right).

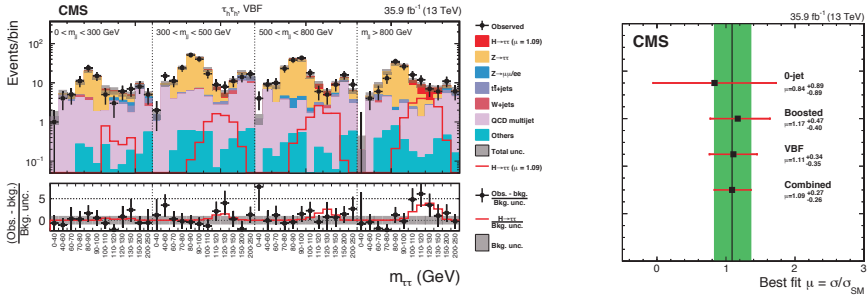


Figure 1 – Left: Distribution of the $\tau\tau$ mass, $m_{\tau\tau}$, in bins of the tagging jets mass, $m_{jj}$, for the VBF category of the $\tau_h\tau_h$ decay channel. The background histograms are stacked, while the signal is shown both as a stacked filled histogram and an open overlaid histogram. The gray band stands for the systematic uncertainties. Right: The H → $\tau\tau$ signal strength per an analysis category and combined. Plots from ref. [6].

## 3 Measurements with the H → WW → $\ell\nu\ell\nu$ process

The H → WW → $\ell\nu\ell\nu$ process is an important tool in probing the Higgs boson couplings as, thanks to large branching fraction ($\mathcal{B}$(H → WW) ≈ 22%) and relatively low background rates, it is sensitive to almost all Higgs boson production mechanisms. The CMS analysis with 2016 collision data [8] categorises events basing on the number of leptons and number of associated jets. The events are further devised based on the lepton flavour and charge composition to create categories with different signal-to-background ratios. It gives in a total of about 30 signal categories sensitive to the ggH, VBF, WH, and ZH production modes. The signal is extracted using distributions of signal sensitive variables depending on the category, e.g. the mass of the lepton pair, $m_{\ell\ell}$, and the transverse mass of the leptons and $p_T^{miss}$ system, $m_T$. The signal strength per an analysis category and a production mode is shown in Fig. 2 left and right, respectively. The measured combined signal strength equals to $\mu = 1.28^{+0.18}_{-0.17}$.

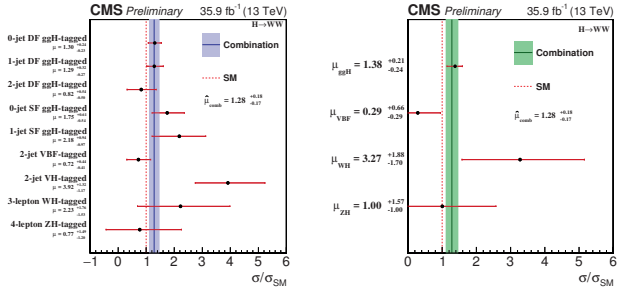


Figure 2 – Signal strength corresponding to the analysis categories (left) and the main Higgs boson production mechanisms (right) measured with the H → WW → $\ell\nu\ell\nu$ decay channel. The vertical continuous line represents the combined signal strength of $\mu = 1.28^{+0.18}_{-0.17}$, while the filled area shows the 68% confidence intervals. Plots from ref. [8].

## 4 Combined measurements

The individual Higgs boson analyses at LHC measure directly only signal yields [a] for a given combination of production and decay modes. However, the production and decay rates, and then

[a] More precisely the ratios of signal yields to the SM expectations, i.e. signal strengths are measured.

individual couplings can be determined separately with a combination of individual analyses to exploit different correlations between production and decay modes to which the analyses (event categories within them) are sensitive. It requires a set of basic theory assumptions which are discussed elsewhere [9].

The CMS Collaboration performed common combined measurements exploiting all analyses based on 13 TeV data collected in 2016 [10]. Production and decay signal strengths obtained with the combined analysis are shown in Fig. 3 (left and middle), all in agreement with the SM expectations. Results of the combined coupling measurement are summarised in Fig. 3 (right) and are in all cases consistent with expectations for the SM Higgs boson. Sensitivity of $\mu_{ggH}$ and $\mu_{ttH}$ measurements with 2016 data exceeds sensitivity of their counterparts from combination of 2011 and 2012 data collected by both ATLAS and CMS detectors [11] by approximately 30% and 50%, respectively. The combined CMS measurement is also used to constrain a set of benchmark

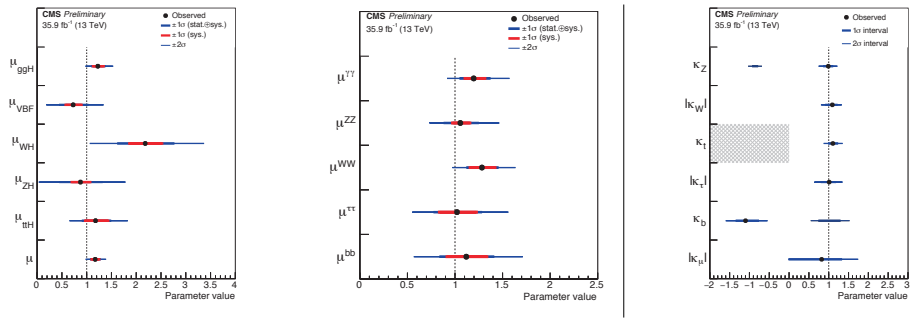


Figure 3 – Signal strength per production mode (left) and per decay mode (middle) from the combined fit. The last point in the per production mode plot indicates the result of the combined signal strength $\mu = 1.17^{+0.10}_{-0.10}$. Right: Measured values of coupling strength scaling factors $\kappa$ with $\mathcal{B}_{BSM} = 0$, and the gg → H and H → $\gamma\gamma$ loops resolved in terms of remaining coupling strength scaling factors. Plots from ref. [10].

models extending the Higgs sector: two-Higgs-doublet models (2HDM) [12] and the constrained supersymmetric model hMSSM [13]. Figure 4 shows the constraints in the two-dimensional parameter space describing studied models: $\cos(\beta-\alpha) - \tan\beta$ for different benchmark 2HDM: Type I (left) and Type II (middle), and $m_A - \tan\beta$ for the hMSSM (right). Non-excluded regions of the parameter space correspond to presence of a SM-like Higgs boson. These indirect constraints are complementary to ones from direct searches, e.g. using the H → $\tau\tau$ decay channel [14].

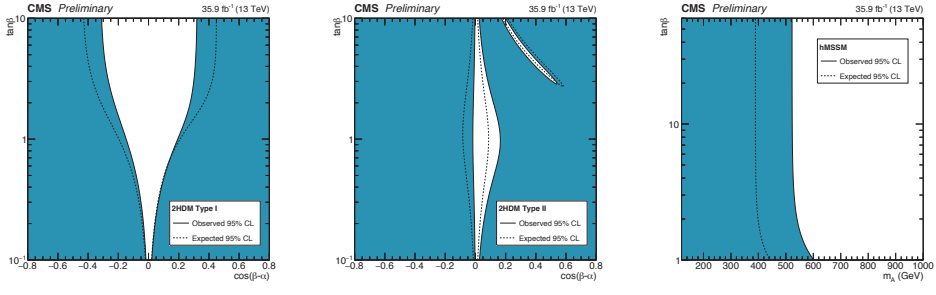


Figure 4 – Constraints in the $\cos(\beta-\alpha) - \tan\beta$ plane for the Type I 2HDM (left) and Type II 2HDM (middle), and in the $m_A - \tan\beta$ plane for the hMSSM (right). The white regions, bounded by the solid lines, represent the regions of the parameter space which are allowed at the 95% confidence level, given the data observed, while the dashed lines indicate the boundaries of the allowed regions expected for the SM Higgs boson. Plots from ref. [10].

## 5 Summary

The CMS Collaboration performed a number of studies on the Higgs boson properties using $35.9\,\text{fb}^{-1}$ of pp collision data recorded in 2016. The studies provide observation of the $\text{H} \to \tau\tau$ decay, per production mode measurements with the $\text{H} \to \text{WW} \to \ell\nu\ell\nu$ process, and combined measurements of multiple production and decay rates and couplings of the Higgs boson. The precision of the combined measurements surpass those from ATLAS and CMS combination of 2011 and 2012 data for ggH and ttH production rates. These measurements are also used to constrain models of the extended Higgs sector complementing direct searches.


## Acknowledgments

We would like to thank the organizers for making the 53rd Rencontres de Moriond a true success. This contribution is supported by National Science Centre (Poland) grant no. 2014/13/B/ST2/02543.


## References


1. G. Aad et al. Observation of a new particle in the search for the Standard Model Higgs boson with the ATLAS detector at the LHC. *Phys. Lett.*, B716:1, 2012.
2. S. Chatrchyan et al. Observation of a new boson at a mass of 125 GeV with the CMS experiment at the LHC. *Phys. Lett.*, B716:30, 2012.
3. S. Chatrchyan et al. Observation of a new boson with mass near 125 GeV in pp collisions at $\sqrt{s} = 7$ and 8 TeV. *JHEP*, 06:081, 2013.
4. S. Chatrchyan et al. The CMS experiment at the CERN LHC. *JINST*, 3:S08004, 2008.
5. M. Schroeder. Higgs physics with hadronic signatures at ATLAS and CMS. *These proceedings*, 2018.
6. A. M. Sirunyan et al. Observation of the Higgs boson decay to a pair of $\tau$ leptons with the CMS detector. *Phys. Lett.*, B779:283, 2018.
7. S. Chatrchyan et al. Evidence for the 125 GeV Higgs boson decaying to a pair of $\tau$ leptons. *JHEP*, 05:104, 2014.
8. CMS Collaboration. Measurements of properties of the Higgs boson decaying to a W boson pair in pp collisions at $\sqrt{s} = 13$ TeV. CMS Physics Analysis Summary CMS-PAS-HIG-16-042, 2018. https://cds.cern.ch/record/2308255.
9. J. R. Andersen et al. Handbook of LHC Higgs Cross Sections: 3. Higgs Properties. 2013.
10. CMS Collaboration. Combined measurements of the Higgs boson's couplings at $\sqrt{s} = 13$ TeV. CMS Physics Analysis Summary CMS-PAS-HIG-17-031, 2018. https://cds.cern.ch/record/2308127.
11. G. Aad et al. Measurements of the Higgs boson production and decay rates and constraints on its couplings from a combined ATLAS and CMS analysis of the LHC pp collision data at $\sqrt{s} = 7$ and 8 TeV. *JHEP*, 08:045, 2016.
12. G. C. Branco et al. Theory and phenomenology of two-Higgs-doublet models. *Phys. Rept.*, 516:1, 2012.
13. A. Djouadi et al. The post-Higgs MSSM scenario: Habemus MSSM? *Eur. Phys. J.*, C73:2650, 2013.
14. A. M. Sirunyan et al. Search for additional neutral MSSM Higgs bosons in the $\tau\tau$ final state in proton-proton collisions at $\sqrt{s} = 13$ TeV. *Submitted to JHEP*, 2018. arXiv:1803.06553.

# Higgs Physics with Hadronic Signatures at ATLAS and CMS

Matthias Schröder on behalf of the ATLAS and CMS Collaborations
*Institute of Experimental Particle Physics at the Karlsruhe Institute of Technology (KIT)*

The precise measurement of the properties of the Higgs boson is of paramount interest in order to verify the standard model nature of the Higgs sector or discover new physics. Crucial information is obtained from investigation of hadronic final states, which offer, for example, a direct probe of the couplings to top or bottom quarks. In this article, latest results of Higgs boson measurements with hadronic signatures by ATLAS and CMS at the LHC are reviewed.

## 1 Introduction

The analysis of hadronic final states offers a unique tool to assess many of the Higgs boson properties, such as its interaction with quarks, which in the standard model (SM) is a Yukawa-type coupling with a strength proportional to the quark mass. At the same time, hadronic final states are very challenging at the LHC, e.g. due to the typically large multijet background and the relatively poor jet energy resolution, which has lead to the development of sophisticated analysis methods relying e.g. on multivariate (MVA) and boosted techniques.

In this article, latest results of Higgs boson measurements with hadronic signatures by the ATLAS and CMS experiments [1,2] are reviewed. The analyses have been performed with up to $36\,\mathrm{fb}^{-1}$ of proton-proton (pp) collision data collected at a centre-of-mass energy of $\sqrt{s} = 13\,\mathrm{TeV}$.

## 2 Final states with bottom quarks

The bottom quark-antiquark ($\mathrm{b\bar{b}}$) final state is particularly interesting from an experimental point of view because it is the most abundant decay of the SM Higgs boson (branching ratio $\mathcal{B}(\mathrm{H} \to \mathrm{b\bar{b}}) = 58\%$), leading to a relatively large production rate. Furthermore, b quark jets (b jets) can be identified (b tagged) in the detector, exploiting the characteristic properties of B meson decays. ATLAS and CMS have developed dedicated b-tagging algorithms, which achieve typical efficiencies of 60–70 % at a 1 % misidentification rate for light-flavour (LF) quark jets.

### *2.1 Measurement of the bottom-Higgs Yukawa coupling*

The Higgs boson decay into $\mathrm{b\bar{b}}$ allows direct access to the bottom-Higgs Yukawa coupling $y_\mathrm{b}$. Experimentally the best channel is the associated production of a Higgs boson with a recoiling vector boson V (W or Z) that decays leptonically and can be identified to reduce the orders of magnitude larger QCD-multijet background. Both ATLAS and CMS target the $\mathrm{Z} \to ll/\nu\nu$ and the $\mathrm{W} \to l\nu$ channels ($l$ being an electron or a muon) and follow similar analysis strategies [3,4].

Events are categorised by the lepton multiplicity and the transverse momentum $p_\mathrm{T}$ of the reconstructed V boson, as well as the jet multiplicity in case of ATLAS, and are further selected requiring the presence of two central b-tagged jets forming the $\mathrm{H} \to \mathrm{b\bar{b}}$ candidate. A dedicated jet energy calibration is applied to improve the resolution of the invariant mass $m_{\mathrm{b\bar{b}}}$ of the

two b-jet candidates. Final sensitivity is achieved with boosted decision trees (BDTs) that are trained in each category and combine the information of several discriminating variables such as $m_{\mathrm{b\bar{b}}}$ or b-tagging information in order to separate signal from SM background. The BDT output distribution of the expected background, which is dominated by V + jets and top quark-antiquark pair ($\mathrm{t\bar{t}}$) production, is modelled using simulation. The signal together with the background normalisation are extracted from a simultaneous fit of the BDT output distributions to the data across all categories. These include also additional control-region categories that are enhanced in different background processes and help to constrain the uncertainties, which are dominated by b-tagging and signal-modelling uncertainties.

ATLAS and CMS obtain signal strengths $\mu = \sigma/\sigma_{\mathrm{SM}}$ of the measured cross section $\sigma$ relative to the SM expectation of $1.20^{+0.42}_{-0.36}$ and $1.2^{+0.4}_{-0.4}$, respectively. In combination with results from the LHC Run-I at $\sqrt{s} = 7\,\mathrm{TeV}$ and 8 TeV, evidence for VH($\mathrm{b\bar{b}}$) production with observed (expected) significances of 3.6 (4.0) and 3.8 (3.8) standard deviations, respectively, is found.

CMS also targets for the first time events where the Higgs boson is produced via gluon-gluon fusion (ggF) to benefit from the large cross section of this channel that amounts to 87 % of the total Higgs boson production rate [5]. The QCD-multijet background is addressed by considering exclusively the regime where the Higgs boson is highly boosted, such that the two b jets are merged into one jet, and recoils against a high-$p_{\mathrm{T}}$ jet from initial-state radiation, leading to an effective dijet topology. The remaining multijet background is estimated from a control region in data with fewer b-tagged jets. An observed (expected) upper limit at the 95 % confidence level (CL) on $\sigma(\mathrm{pp} \to \mathrm{H}) \times \mathcal{B}(\mathrm{H} \to \mathrm{b\bar{b}})$ of 5.8 (3.3) times the SM expectation is obtained.

### *2.2 Measurement of the top-Higgs Yukawa coupling*

The $\mathrm{t\bar{t}}$-associated production of a Higgs boson ($\mathrm{t\bar{t}H}$ production) is the best direct probe of the top-Higgs Yukawa coupling $y_{\mathrm{t}}$ with minimal model dependence. The small SM $\mathrm{t\bar{t}H}$ cross-section of approximately 0.5 pb at $\sqrt{s} = 13\,\mathrm{TeV}$ poses a major challenge, and searches in the $\mathrm{H} \to \mathrm{b\bar{b}}$ final state benefit from the large branching ratio. The jet-energy resolution and the huge combinatorial uncertainty in the event reconstruction limit further the sensitivity and require heavy use of MVA methods to combine the information of several discriminating variables.

Both ATLAS and CMS have performed searches for $\mathrm{t\bar{t}H}(\mathrm{b\bar{b}})$ production [6,7,8]. In the leptonic decay channels of the $\mathrm{t\bar{t}}$ system, events are selected requiring the presence of two or one isolated leptons and are further categorised by the jet multiplicity and b-tagging or MVA-classifier output information. The SM background consists almost entirely of $\mathrm{t\bar{t}}$ + jets events. It is modelled using simulation, but especially the $\mathrm{t\bar{t}}$ + heavy-flavour jet processes are difficult to model, and the associated uncertainties limit the overall sensitivity. The background composition varies between the categories. This is exploited in the final fit to the data, which is performed simultaneously across all categories to extract the signal and constrain the uncertainties.

At ATLAS, a two-staged BDT approach is followed in the signal-enriched categories. A reconstruction BDT is trained to assign the jets to the final-state partons, which allows construction of additional separating variables. They are used together with reconstruction-independent variables as input to a classification BDT that separates signal from background events. In addition, dedicated techniques are applied to reconstruct events in which the Higgs boson and the hadronically decaying top quark are boosted. No classification is performed in the signal-depleted categories, but they provide important additional constraints on the background uncertainties.

At CMS, in the dilepton channel, a classification BDT is constructed per category. Depending on the category, events are further separated into sub-categories with low and high BDT-output, and the output of a matrix-element-method (MEM) is used as final discriminant in each sub-category. In the single-lepton channel, in a novel approach, artificial neural networks (NN) are employed that perform a multi-classification of an event as either signal or any of five different $\mathrm{t\bar{t}}$ + jets background processes. Events are sub-categorised by the most-probable process, and the corresponding NN classifier output is used as final discriminant.

Combining the information in the leptonic channels, ATLAS and CMS measure an excess of events above the background-only hypothesis with observed (expected) significances of 1.4 (1.6) and 1.6 (2.2) standard deviations, respectively (Fig. 1). The corresponding best-fit signal strengths are $\mu = 0.84^{+0.64}_{-0.61}$ and $\mu = 0.72^{+0.45}_{-0.45}$, respectively, compatible with the SM expectation.

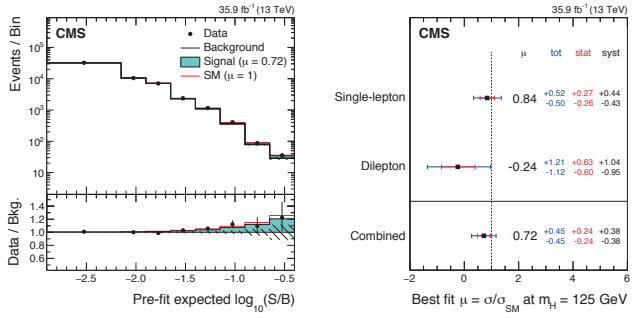


Figure 1 – Final discriminant distribution, reordered by the pre-fit expected signal-to-background ratio (left), and best-fit signal strength (right) in the CMS search for $t\bar{t}H(b\bar{b})$ production in the leptonic channels [7].

CMS has also analysed the all-jets final state of the $t\bar{t}$ system. Events are categorised by the jet and b-tagged jet multiplicity, and the MEM output is used as final discriminant. QCD-multijet events are suppressed using a dedicated quark-gluon jet discriminant, but the remaining QCD events still compose the dominant background, which is modelled from control regions in data. The obtained signal strength is $\mu = 0.9^{+1.5}_{-1.5}$.

### *2.3 Search for Higgs pair production*

In the SM, Higgs pair (HH) production can occur via a three-Higgs-boson vertex and thus provides experimental access to the Higgs boson self-coupling, i.e. allows probing the shape of the Higgs potential after electroweak-symmetry breaking. At the LHC, HH production occurs predominantly via ggF, and there is destructive interference with a top-quark-loop induced channel, resulting in a tiny production cross-section of 33.5 fb at 13 TeV. This is far below the current sensitivity. However, various models of new physics beyond the SM (BSM) predict significantly enhanced non-resonant HH production or resonant HH production. Therefore, HH searches are an important tool to discover BSM physics and to develop the experimental methods for an eventual measurement of SM HH production.

Both ATLAS and CMS have performed searches targeting different combinations of the two involved Higgs boson decays, including $b\bar{b}b\bar{b}$, $b\bar{b}\gamma\gamma$, and $b\bar{b}\tau\tau$, which rely on $H \to b\bar{b}$ in at least one of the two decays to exploit the large branching ratio. For example, a new search by ATLAS in the $b\bar{b}b\bar{b}$ final state [9] sets an observed (expected) 95 % CL upper limit on the non-resonant SM HH production of 13 (21) times the SM expectation. The results are also interpreted as upper limits on HH resonant production in the mass range up to 3 TeV. In general, the different final states complement each other in sensitivity, covering a resonance-mass range up to 4 TeV [10].

## 3 Final states with charm and light-flavour quarks

The Higgs boson coupling to charm (c) and LF (q) quarks is very challenging to measure at the LHC: the couplings are expected to be small, and the $c\bar{c}$ and $q\bar{q}$ final states are overwhelmed by QCD-multijet events. ATLAS has explored new approaches to probe these couplings [11,12].

A search is performed for associated ZH production with $Z \to ll$ and $H \to c\bar{c}$ targeting $y_c$, where again the presence of the leptonically decaying Z boson helps to identify the events above

the multijet background. Further sensitivity is achieved by two dedicated c tagging discriminants that separate c jets against b jets or LF jets. A resonance-search is performed in $m_{c\bar{c}}$, to which the dominant background contribution arises from Z + jets events, which is modelled from simulation. An observed (expected) 95 % CL upper limit on $\sigma(pp \to ZH) \times \mathcal{B}(H \to c\bar{c})$ of 110 (150) times the SM expectation is obtained.

The Higgs boson coupling to LF quarks can be probed in decays to a $\phi$ or $\rho$ meson and a photon $\gamma$. Predominantly, these decays proceed via an intermediate $H \to \gamma\gamma$ decay where one photon decays further to $q\bar{q}$, but there is a small contribution to the amplitude from direct $H \to q\bar{q}$ decays which interferes destructively. Thus, measurement of the $H \to \phi\gamma/\rho\gamma$ decay rate allows probing $y_q$. A resonance search is performed in $m_{\phi\gamma}/m_{\rho\gamma}$, reconstructed from $\pi^+\pi^-/K^+K^-\gamma$ candidates (Fig. 2). The background is modelled from data, generating pseudocandidate events by sampling the relevant quantities from distributions measured in control regions. Observed 95 % CL upper limits on $\mathcal{B}(H \to \phi\gamma/\rho\gamma)$ of 208/52 times the SM expectation are obtained.

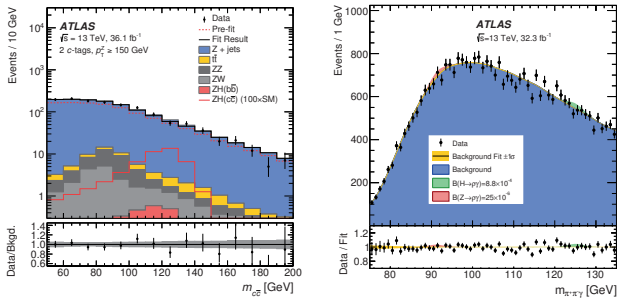


Figure 2 – Observed and predicted distributions of $m_{c\bar{c}}$ in the search for ZH($c\bar{c}$) production (left) [11] and of $m_{\pi^+\pi^-\gamma}$ in the search for $H \to \phi\gamma$ (right) [12].

## 4 Summary

The ATLAS and CMS experiments at the LHC have performed a rich variety of searches in hadronic final states, obtaining crucial information on the properties of the Higgs boson. Sophisticated analysis techniques have been developed to control the challenging SM backgrounds.


## Acknowledgements

I gratefully acknowledge the financial support by the German Federal Ministry of Education and Research.


## References


1. ATLAS Collaboration, *JINST* **3** (2008) S08003.
2. CMS Collaboration, *JINST* **3** (2008) S08004.
3. ATLAS Collaboration, *JHEP* **24** (2017) 1712.
4. CMS Collaboration, *Phys. Lett. B* **780** (2018) 501.
5. CMS Collaboration, *Phys. Rev. Lett.* **120** (2018) 071802.
6. ATLAS Collaboration, *Phys. Rev. D* **97** (2018) 072016
7. CMS Collaboration, CMS-HIG-17-026 (2018), subm. to *JHEP*.
8. CMS Collaboration, CMS-HIG-17-022 (2018), subm. to *JHEP*.
9. ATLAS Collaboration, ATLAS-EXOT-2016-31 (2018), subm. to *JHEP*.
10. CMS Collaboration, CMS Higgs PAG Summary Plots
11. ATLAS Collaboration, ATLAS-HIGG-2017-01 (2018), subm. to *Phys. Rev. Lett.*.
12. ATLAS Collaboration, ATLAS-HIGG-2016-13 (2017), subm. to *JHEP*.

# SM HIGGS PRODUCTION AND DECAY AT THE LHC

M. SPIRA
*Paul Scherrer Institut, CH–5232 Villigen PSI, Switzerland*

The recent discovery of the Higgs boson at the LHC marked the completion of the Standard Model of strong and electroweak interactions. I will summarize the theoretical ingredients involved in the production and decay processes at the LHC that allowed for a quite concise picture of the properties of the discovered resonance. These theoretical calculations are a crucial contribution to the discrimination of the SM from BSM scenarios at the LHC, too.

## 1 Introduction

The discovery of a Standard-Model-like Higgs boson at the LHC [1] completed the theory of electroweak and strong interactions. The measured Higgs mass of $(125.09 \pm 0.24)$ GeV [2] ranges at the order of the weak scale. The existence of the Higgs boson [3] allows the SM particles to be weakly interacting up to high-energy scales. This, however, is only possible for particular Higgs-boson couplings to all other particles so that with the knowledge of the Higgs-boson mass all its properties are uniquely fixed. The massive gauge bosons and fermions acquire mass through their interaction with the Higgs field that develops a finite vacuum expectation value in its ground state. The minimal model requires the introduction of one isospin doublet of the Higgs field and leads after spontaneous symmetry breaking to the existence of one scalar Higgs boson.

## 2 Higgs Boson Decays

The determination of the branching ratios of Higgs-boson decays necessitate the inclusion of the available higher-order corrections [4] and a sophisticated estimate of the theoretical and parametric uncertainties. The parametric uncertainties are dominated by the uncertainties in the top, bottom and charm quark masses as well as the strong coupling $\alpha_s$. We have used the $\overline{\rm MS}$ masses for the bottom and charm quark [5], $\overline{m}_b(\overline{m}_b) = (4.18 \pm 0.03)$ GeV and $\overline{m}_c(3\ {\rm GeV}) = (0.986 \pm 0.026)$ GeV, and the top quark pole mass $m_t = (172.5 \pm 1)$ GeV according to the conventions of the LHC Higgs Cross Section WG (HXSWG) [5]. The $\overline{\rm MS}$ bottom and charm masses are evolved from the input scale to the scale of the decay process with 4-loop accuracy in QCD. The strong coupling $\alpha_s$ is fixed by the input value at the $Z$-boson mass scale, $\alpha_s(M_Z) = 0.118 \pm 0.0015$.

Table 1: Estimated theoretical uncertainties from missing higher orders and the perturbative orders (QCD/elw.) of the results included in the analysis

| Partial Width | QCD | Electroweak | Total | on-shell Higgs |
|---|---|---|---|---|
| $H \to b\bar{b}/c\bar{c}$ | $\sim 0.2\%$ | $\sim 0.5\%$ | $\sim 0.5\%$ | N$^4$LO / NLO |
| $H \to \tau^+\tau^-/\mu^+\mu^-$ | — | $\sim 0.5\%$ | $\sim 0.5\%$ | — / NLO |
| $H \to gg$ | $\sim 3\%$ | $\sim 1\%$ | $\sim 3\%$ | N$^3$LO / NLO |
| $H \to \gamma\gamma$ | $< 1\%$ | $< 1\%$ | $\sim 1\%$ | NLO / NLO |
| $H \to Z\gamma$ | $< 1\%$ | $\sim 5\%$ | $\sim 5\%$ | LO / LO |
| $H \to WW/ZZ \to 4f$ | $< 0.5\%$ | $\sim 0.5\%$ | $\sim 0.5\%$ | NLO |

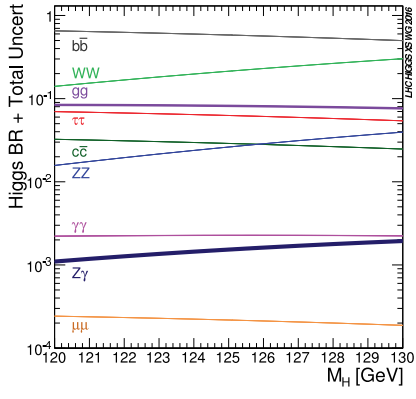


Figure 1 – Higgs boson branching ratios and their uncertainties for Higgs masses around 125 GeV. From Ref. [5].

The total parametric uncertainty for each branching ratio has been derived from a quadratic sum of the individual impacts of the input parameters on the decay modes.

The theoretical uncertainties from missing higher orders in the perturbative expansion are summarized in Table 1 for the individual partial decay processes along with the perturbative orders of the included QCD/elw. corrections [4]. In order to be conservative the total parametric uncertainties are added linearly to the theoretical uncertainties. The final result for the branching ratios is shown in Fig. 1 for the leading Higgs decay modes with branching ratio larger than $10^{-4}$ for the Higgs-mass range between 120 and 130 GeV. They have been obtained with Prophecy4F [6] for the decays $H \to WW, ZZ$ and Hdecay [7] for the other decay modes. The bands represent the total uncertainties of the individual branching ratios. For a Higgs mass $M_H = 125$ GeV the total uncertainty of the leading decay mode $H \to b\bar{b}$ amounts to less than 2%, since the bulk of it cancels out within the branching ratio. The uncertainty of $\Gamma(H \to b\bar{b})$, however, generates a significant increase of the uncertainties for the subleading decay modes. The total uncertainties of $BR(H \to WW/ZZ)$ and $BR(H \to \tau^+\tau^-/\mu^+\mu^-)$ amount to $\sim 2\%$, while the uncertainties of $BR(H \to gg)$ and $BR(H \to c\bar{c})$ range at $\sim 6-7\%$, of $BR(H \to \gamma\gamma)$ at $\sim 3\%$ and of $BR(H \to Z\gamma)$ at $\sim 7\%$. The total decay width of $\sim 4.1$ MeV can be predicted with $\sim 2\%$ total uncertainty.

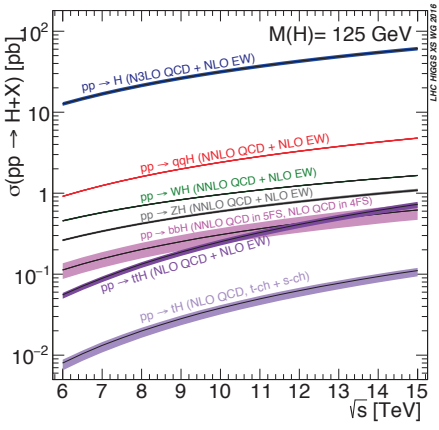


Figure 2 – Higgs boson production cross sections as a function of the c.m. energy at the LHC for a Higgs mass $M_H = 125$ GeV including the most up-to-date higher-order corrections as indicated at the shown cross section bands. The size of the bands reflects the total estimated theoretical uncertainties. From Ref. [5].

## 3 Higgs Boson Production

The dominant Higgs production channel at the LHC is gluon fusion. While the NLO result is known exactly [8] the QCD corrections beyond NLO are known in the heavy-top-quark limit [9,10] that, however, provides a reliable approximation for the inclusive cross section. The next sizeable Higgs production mode is provided by vector-boson fusion. The QCD and elw. corrections are known at NLO exactly, while QCD corrections are known up to N$^3$LO within the structure-function approach [11]. Higgs-strahlung off $W/Z$ bosons is known at NLO elw. and NNLO QCD [12]. Finally Higgs bremsstrahlung off top quarks is known at NLO QCD and elw. [13].

All Higgs boson production cross sections have been updated with the known higher-order corrections and the most recent parton density functions, i.e. the PDF4LHC15 sets [14], where NLO densities have been used consistently for NLO predictions and NNLO densities for NNLO predictions. Using the same values of the input parameters as for the branching ratios discussed before and their uncertainties a rigorous analysis has been performed to derive a sophisticated prediction of the central cross section values and their uncertainties. The results are shown in Fig. 2 as a function of the c.m. energy at the LHC for a Higgs mass $M_H = 125$ GeV. The size of the coloured bands represents the individual sums of the theoretical and parametric uncertainties. All production cross sections with results beyond NLO in QCD exhibit a small residual uncertainty in the few-per-cent range. Only the cross sections for $t\bar{t}H$, $b\bar{b}H$ and $tH$ production develop larger uncertainties. The theoretical and parametric uncertainties of each production process have been added in quadrature. The gluon-fusion cross sections can be predicted with a total (Gaussian) uncertainty of about 5%, the vector-boson-fusion and $WH$ Higgs-strahlung channels with less than 3% uncertainty and the $ZH$ Higgs-strahlung channel with about 4% uncertainty due to the novel loop contributions from $gg \to ZH$. The uncertainties of $t\bar{t}H$ production amount to about $10 - 15\%$, for $s$- and $t$-channel $tH$ production to about $15 - 20\%$ and for $b\bar{b}H$ production to about $20 - 25\%$.

## References


1. G. Aad *et al.* [ATLAS Collaboration], Phys. Lett. **B716** (2012) 1; S. Chatrchyan *et al.* [CMS Collaboration], Phys. Lett. **B716** (2012) 30.
2. G. Aad *et al.* [ATLAS and CMS Collaborations], JHEP **1608** (2016) 045.

3. P. W. Higgs, Phys. Lett. **12** (1964) 132, Phys. Rev. Lett. **13** (1964) 508 and Phys. Rev. **145** (1966) 1156; F. Englert and R. Brout, Phys. Rev. Lett. **13** (1964) 321; G. S. Guralnik, C. R. Hagen and T. W. Kibble, Phys. Rev. Lett. **13** (1964) 585; T. W. B. Kibble, Phys. Rev. **155** (1967) 1554.
4. M. Spira, Prog. Part. Nucl. Phys. **95** (2017) 98 and references therein.
5. D. de Florian *et al.* [LHC Higgs Cross Section Working Group Collaboration], arXiv:1610.07922 [hep-ph].
6. A. Bredenstein, A. Denner, S. Dittmaier and M. M. Weber, Phys. Rev. **D74** (2006) 013004 and JHEP **0702** (2007) 080.
7. A. Djouadi, J. Kalinowski and M. Spira, Comput. Phys. Commun. **108** (1998) 56; A. Djouadi, J. Kalinowski, M. Mühlleitner and M. Spira, arXiv:1801.09506 [hep-ph].
8. A. Djouadi, M. Spira and P. M. Zerwas, Phys. Lett. **B264** (1991) 440; S. Dawson, Nucl. Phys. **B359** (1991) 283; D. Graudenz, M. Spira and P. M. Zerwas, Phys. Rev. Lett. **70** (1993) 1372; M. Spira, A. Djouadi, D. Graudenz and P. M. Zerwas, Nucl. Phys. **B453** (1995) 17; S. Actis, G. Passarino, C. Sturm and S. Uccirati, Phys. Lett. **B670** (2008) 12 and Nucl. Phys. **B811** (2009) 182. C. Anastasiou, S. Bucherer and Z. Kunszt, JHEP **0910** (2009) 068;
9. S. Catani, D. de Florian and M. Grazzini, JHEP **0105** (2001) 025; R. V. Harlander and W. B. Kilgore, Phys. Rev. D **64** (2001) 013015 and Phys. Rev. Lett. **88** (2002) 201801; C. Anastasiou and K. Melnikov, Nucl. Phys. B **646** (2002) 220; V. Ravindran, J. Smith and W. L. van Neerven, Nucl. Phys. B **665** (2003) 325; S. Marzani, R. D. Ball, V. Del Duca, S. Forte and A. Vicini, Nucl. Phys. B **800** (2008) 127.
10. T. Gehrmann, M. Jaquier, E. W. N. Glover and A. Koukoutsakis, JHEP **1202** (2012) 056; C. Anastasiou, C. Duhr, F. Dulat and B. Mistlberger, JHEP **1307** (2013) 003; C. Anastasiou, C. Duhr, F. Dulat, F. Herzog and B. Mistlberger, JHEP **1312** (2013) 088; W. B. Kilgore, Phys. Rev. D **89** (2014) 7, 073008; Y. Li, A. von Manteuffel, R. M. Schabinger and H. X. Zhu, Phys. Rev. D **90** (2014) 5, 053006; C. Anastasiou, C. Duhr, F. Dulat, E. Furlan, T. Gehrmann, F. Herzog and B. Mistlberger, JHEP **1503** (2015) 091; C. Anastasiou, C. Duhr, F. Dulat, F. Herzog and B. Mistlberger, Phys. Rev. Lett. **114** (2015) 21, 212001; C. Anastasiou, C. Duhr, F. Dulat, E. Furlan, T. Gehrmann, F. Herzog, A. Lazopoulos and B. Mistlberger, JHEP **1605** (2016) 058; B. Mistlberger, arXiv:1802.00833 [hep-ph].
11. T. Han, G. Valencia and S. Willenbrock, Phys. Rev. Lett. **69** (1992) 3274; T. Figy, C. Oleari and D. Zeppenfeld, Phys. Rev. **D68** (2003) 073005; T. Figy and D. Zeppenfeld, Phys. Lett. **B591** (2004) 297; E. L. Berger and J. M. Campbell, Phys. Rev. **D70** (2004) 073011; M. Ciccolini, A. Denner and S. Dittmaier, Phys. Rev. Lett. **99** (2007) 161803 and Phys. Rev. **D77** (2008) 013002; P. Bolzoni, F. Maltoni, S. O. Moch and M. Zaro, Phys. Rev. Lett. **105** (2010) 011801 and Phys. Rev. **D85** (2012) 035002; M. Cacciari, F. A. Dreyer, A. Karlberg, G. P. Salam and G. Zanderighi, Phys. Rev. Lett. **115** (2015) no.8, 082002; F. A. Dreyer and A. Karlberg, Phys. Rev. Lett. **117** (2016) no.7, 072001.
12. T. Han and S. Willenbrock, Phys. Lett. **B273** (1991) 167; M. L. Ciccolini, S. Dittmaier and M. Krämer, Phys. Rev. **D68** (2003) 073003; A. Denner, S. Dittmaier, S. Kallweit and A. Mück, JHEP **1203** (2012) 075; O. Brein, A. Djouadi and R. Harlander, Phys. Lett. **B579** (2004) 149; G. Ferrera, M. Grazzini and F. Tramontano, JHEP **1404** (2014) 039 and Phys. Lett. **B740** (2015) 51.
13. W. Beenakker et al., Phys. Rev. Lett. **87** (2001) 201805 and Nucl. Phys. **B653** (2003) 151; L. Reina and S. Dawson, Phys. Rev. Lett. **87** (2001) 201804; S. Dawson, L. H. Orr, L. Reina, and D. Wackeroth, Phys. Rev. **D67** (2003) 071503; Y. Zhang, W. G. Ma, R. Y. Zhang, C. Chen and L. Guo, Phys. Lett. B **738** (2014) 1; S. Frixione, V. Hirschi, D. Pagani, H. S. Shao and M. Zaro, JHEP **1409** (2014) 065 and JHEP **1506** (2015) 184.
14. J. Butterworth *et al.*, J. Phys. **G43** (2016) 023001.

# Better Higgs Measurements through Information Geometry

Johann Brehmer, Kyle Cranmer
*Center for Cosmology & Particle Physics and Center for Data Science, New York University, USA*

**Felix Kling**, Tim M.P. Tait
*Department of Physics and Astronomy, University of California, Irvine, USA*

Tilman Plehn
*Institut für Theoretische Physik, Universität Heidelberg, Germany*

Measuring the properties of the Higgs boson is one of the most important missions for Run 2 of the LHC. These measurements can be understood and optimized with intuitive and powerful tools from information geometry. The central object is the Fisher information matrix. It allows us to define the maximum precision with which theory parameters can be measured in a given experiment. We calculate the information on dimension-six operators in different Higgs signatures. We demonstrate how information geometry lets us improve event selections, determine the most powerful observables, and compare the power of multivariate techniques to traditional histogram-based analyses. In particular, we systematically analyze which LHC signatures offer dedicated $CP$ measurements in the Higgs-gauge sector, and discuss the nature of the information they provide.

## 1 Introduction

After its experimental discovery, the Higgs boson and its properties became one of the most important laboratories to search for physics beyond the Standard Model. In upcoming years, the LHC will accumulate large and complex sets of data, which will allow us to probe and constrain high-dimensional theory spaces. One example is the space of Wilson coefficients an effective field theory (EFT). Conventional rate or histogram based analysis techniques are transparent and reproducible tools for LHC measurements, but suffer from limited performance. This is why many LHC analyses rely on more sophisticated multivariate techniques, such as machine learning or the matrix element method.

Information geometry allows us to compute the maximum sensitivity of LHC data to theory in a transparent way. To demonstrate our approach, we investigate $CP$-violation in the Higgs-gauge coupling. We first review $CP$-sensitive observables at the LHC in Sec. 2, introduce our Fisher information approach in Sec. 3 and present results in Sec. 4.

## 2 CP-Violation in the Higgs-gauge Sector

We evaluate the effect of $CP$-odd operators on the three most promising LHC Higgs signatures: WBF Higgs production, associated $ZH$ production, and Higgs decays to four leptons. From Fig. 1 (left) it is clear that these three processes are governed by the same hard process and hence probe the same coupling. We use the SM EFT framework with $\mathcal{L} = \mathcal{L}_{\text{SM}} + f_i \mathcal{O}_i / \Lambda^2$ and

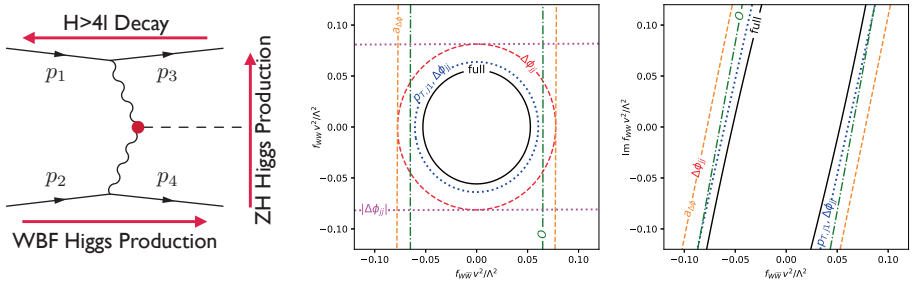


Figure 1 – Left: Feynman diagram for WBF Higgs production, $ZH$ production and Higgs decay $H \to 4\ell$. Center/Right: $1\sigma$ contours for WBF Higgs production with $H \to \tau\tau$ using the information in the fully differential cross section (solid black) and information in histograms of kinematic distributions (colored). See text for explanation.

include the following dim-6 operators for the Higgs-gauge interactions

$$\mathcal{O}_W = i\frac{g}{2}(D^\mu\phi)^\dagger\sigma^k(D^\nu\phi)W^k_{\mu\nu} \quad \mathcal{O}_{WW} = -\frac{g^2}{4}(\phi^\dagger\phi)W_{\mu\nu}W^{\mu\nu} \quad \mathcal{O}_{W\widetilde{W}} = -\frac{g^2}{4}(\phi^\dagger\phi)W_{\mu\nu}\widetilde{W}^{\mu\nu} \quad (1)$$

The goal is to measure the model parameters, with particular emphasize on the $CP$-violating Wilson coefficient $f_{W\widetilde{W}}$.

Since it is not possible to determine the initial or final states spins in these processes, all observables must be constructed as functions of the 4-momenta. The hard process is described by four independent 4-momenta $p_i$, which allow us to construct ten scalar products $(p_i \cdot p_j)$ which are $P$-even by definition. It is possible to construct two $C$-odd observables, but it turns out that their sensitivity to Higgs $CP$ is very limited since it relies on the presence of an additional strong phase. Additionally we can construct one $P$-odd observable

$$O \sim \epsilon_{\alpha\beta\gamma\delta}\, p_1^\alpha p_2^\beta p_3^\gamma p_4^\delta\, \text{sign}[(p_1 - p_2) \cdot (p_3 - p_4)]. \quad (2)$$

The sign factor removes the labeling ambiguity for both initial state partons and final state jets and ensures that the observable is $C$-even. This observable can be related to the angular differences $\Delta\phi_{jj}$ in WBF production [3], $\Delta\phi_{\ell\ell}$ in $ZH$ production [4] and $\Phi$ in Higgs decays [5]. Note that the $CP$ sensitivity is encoded in the sign of these observables, as defined by Eq.(2).

At this stage one might ask why the WBF process can be sensitive to Higgs $CP$ violation, given that we do not measure the charge of the final state jets and that parity is already violated by the weak boson couplings. Indeed, $\Delta\phi_{jj}$ is not a genuine $CP$-odd observable. However it has been shown [2] that it is genuine $\hat{T}$-odd at the LHC, where $\hat{T}$ is the naive-time reversal. Under the assumption that re-scattering effects are negligible, a non-zero expectation value of a genuine $\hat{T}$-odd observable is evidence for $CP$ violation. Re-scattering effects correspond to absorptive, complex-valued loop contributions, for instance an imaginary part in the propagator of an intermediate on-shell particle. Such re-scattering effects are expected to be small in the SM, making $\Delta\phi_{jj}$ a probe for $CP$-violation.

## 3 Information Geometry

We briefly review the basics of information geometry applied to Higgs physics at the LHC [1,2]. Let us consider a given theory which is parametrized by a set of true but unknown model parameters $\theta_0$. In the case of the SM EFT these would be the Wilson coefficients of the dim-6 operators. The outcome of the experiment is then described by the probability distribution function (pdf) $f(x|\theta_0)$. Here $x$ denotes the data characterized by kinematic observables describing an event at the LHC. A measurement process then uses the data to calculate an estimator $\hat{\theta}(x)$ for the

theory parameters. The precision of the measurement is described by the covariance matrix $\text{cov}(\hat{\theta}|\theta_0)$.

The question we would like to answer is: how well could we measure a given set theory parameter. According to the Cramer-Rao [6,7] bound this is precisely given in terms of the Fisher information $I$ which defines a lower bound for the covariance matrix, $\text{cov}(\hat{\theta}|\theta_0) \geq I^{-1}(\theta_0)$. The Fisher information therefore encodes the maximum sensitivity of observables $x$ to model parameters $\theta$ for a given experiment. It is defined as the expectation value of the second derivative of the pdf with respect to the theory parameters at a theory point

$$I_{ij}(\theta_0) = -E\left[\frac{\partial^2 \log f(x|\theta)}{\partial\theta_i\,\partial\theta_j}\middle|\theta_0\right] = \sum_{\text{events}}\sum_k I_{ij}^k(\theta_0), \quad \text{with} \quad I_{ij}^k(\theta_0) = \frac{L}{\sigma_k(\theta)}\frac{\partial\sigma_k(\theta)}{\partial\theta_i}\frac{\partial\sigma_k(\theta)}{\partial\theta_j}\bigg|_{\theta_0}. \tag{3}$$

We use the MadFisher [1] algorithm to calculate the Fisher information using Monte-Carlo simulations. It sums the Fisher information of individual events, with event weights $\sigma_k(\theta)$, generated by MadMax [8,9], as shown at the end of Eq.(3). The Fisher information has desirable properties: it is additive for different experiments and phase space regions, invariant under the reparametrization of observables $x$, and covariant under the under a reparametrization of theory parameters $\theta$. Note that the Fisher information by construction is a symmetric and positive definite rank-two tensor and defines a Riemannian metric on the model space. This allows us to define a distance measure on the theory space. This distance between two parameter two points corresponds to the significance with which one point can maximally be excluded if the other one is true [1].

## 4 Probing Higgs CP with Information Geometry

The maximum precision to measure theory parameters is encoded in the total Fisher information which includes all phase space information. As example we present the Fisher information matrix evaluated at the SM for the WBF process at 13 TeV LHC with $L = 100$ fb$^{-1}$:

$$I_{ij}(\mathbf{0}) = \begin{pmatrix} 715 & -191 & 1 & 0 \\ -191 & 321 & -1 & 0 \\ 1 & -1 & 359 & -81 \\ 0 & 0 & -81 & 23 \end{pmatrix} \begin{matrix} f_W \\ f_{WW} \\ f_{W\widetilde{W}} \\ \text{Im}f_{WW} \end{matrix} \tag{4}$$

A large entry in the Fisher matrix implies that the measurement is particularly sensitive to a given model parameter combination. The entries correspond to the $CP$-conserving operators $f_W$, $f_{WW}$, the $CP$-violating operator $f_{W\widetilde{W}}$, and $\text{Im}f_{WW}$ which models the re-scattering. We can directly see that the measurement is sensitive to both $CP$-conserving and $CP$-violating operators (green entries), with large mixing between the $f_W$ and $f_{WW}$ (blue). There is no correlation between $f_W, f_{WW}$ and $f_{W\widetilde{W}}$ (red), indicating that $CP$-even physics cannot mimic $CP$-violation. However, re-scattering effects are able to mimic $CP$-violation (orange).

Additionally, we can define the information in histograms of distributions in one or two variables by replacing the sum over events in Eq.(3) with a sum over bins of the histogram. This allows us to compare the sensitivity of histogram-based analysis with the full sensitivity. In Fig. 1 we show the corresponding $1\sigma$ contours for pairs of Wilson coefficients, with all other coefficients set to zero, for the WBF $H \to \tau\tau$ channel at 13 TeV LHC with $L = 100$ fb$^{-1}$. In the left panel, we see that the magnitude of the angular difference $|\Delta\phi_{jj}|$ (magenta) is only sensitive to $CP$-conversing physics while the asymmetry in $a_{\Delta\phi_{jj}}$ (orange) is a clear indicator of $CP$ violation. The signed angular difference $\Delta\phi_{jj}$ (red) is sensitive to both $CP$-conserving and $CP$-violating operators and its sensitivity can be enhanced when supplemented with the leading $p_{T,j}$ (blue), reflecting the fact that the effects of dimension-six operators are enhanced at higher momentum transfer. The information in the fully differential cross section is shown in black. Note that in the presence of re-scattering, represented by $\text{Im}f_{WW}$ in the right panel

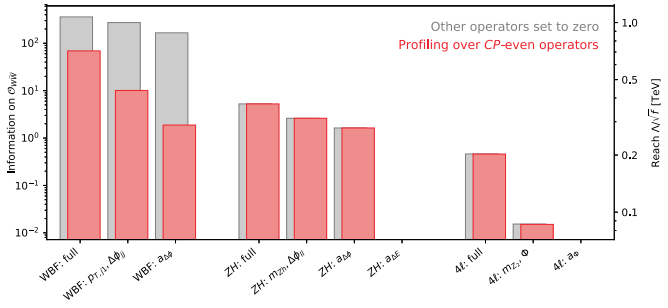


Figure 2 – Comparison of the sensitivity of different channels and observables at the LHC with $L = 100$ fb$^1$ to the $CP$-violating Wilson coefficient $f_{W\widetilde{W}}$.

of Fig. 1, an almost blind direction in parameter space arises and none of the WBF observables can unambiguously prove $CP$ violation.

We can use the total information and information in distributions to quantitatively compare the performance of histogram-based analyses with the full multivariate analysis. This is illustrated in Fig. 2, where we show the information of the WBF $H \to \tau\tau$, the $ZH$ and the $H \to 4\ell$ channels on the $CP$-violating operator $\mathcal{O}_{W\widetilde{W}}$. The grey bars show the sensitivity assuming that all other considered operators are zero, translated into the new physics reach on the right axis. First, Higgs production channels WBF and $ZH$ have significantly higher sensitivity to $\mathcal{O}_{W\widetilde{W}}$ than the Higgs decay $H \to 4\ell$. This is due to the larger momentum flow through the Higgs vertex and the larger rate. Second, the WBF channel requires additional understanding on the nature and size of re-scattering, even though in realistic models the re-scattering effects are expected to be small. In contrast, the $ZH$ channel with its genuine $CP$-odd observable $\Delta\phi_{\ell\ell}$ is unaffected by re-scattering. Last, the asymmetries $a_{\Delta\phi}$ reflect the $CP$-information, while being theoretically clean and not sensitive to any $CP$-even Wilson coefficients. However, the reach of these asymmetries is significantly below the optimal reach. Combining the $CP$-sensitive observables $\Delta\phi$ with information pertaining to the momentum transfer further or even better performing a full multivariate analysis significantly increases the sensitivity.

## Acknowledgments

FK would like to thank the organizers of the Moriond QCD 2018 for giving the opportunity to present this result and for their support through the Moriond 2018 QCD grant. This work is supported in part by the NSF under Grant PHY-1620638, ACI-1450310 and PHY-1505463, the DFG Forschergruppe *New Physics at the LHC* (FOR 2239) and the Moore-Sloan Data Science Environment at NYU.

## References

1. J. Brehmer, K. Cranmer, F. Kling and T. Plehn, *Phys. Rev.* D **95**, 073002 (2017).
2. J. Brehmer, F. Kling, T. Plehn and T. M. P. Tait, arXiv:1712.02350.
3. V. Hankele, G. Klamke, D. Zeppenfeld and T. Figy, *Phys. Rev.* D **74**, 095001 (2006).
4. N. D. Christensen, T. Han and Y. Li, *Phys. Lett.* B **693**, 28 (2010).
5. S. Bolognesi *et al*, *Phys. Rev.* D **86**, 095031 (2012).
6. H. Cramér, Princeton University Press (1946).
7. R. C. Rao, Bull. Calcutta Math. Soc. **37**, 81 (1945);
8. T. Plehn, P. Schichtel and D. Wiegand, *Phys. Rev.* D **89**, 054002 (2014).
9. F. Kling, T. Plehn and P. Schichtel, *Phys. Rev.* D **95**, 035026 (2017).

# PRECISION CALCULATIONS FOR h → WW/ZZ → 4 FERMIONS IN THE THDM WITH PROPHECY4F

Lukas Altenkamp[1], Stefan Dittmaier[1], Heidi Rzehak[2]
[1] *Albert-Ludwigs-Universität Freiburg, Physikalisches Institut, 79104 Freiburg, Germany*
[2] *University of Southern Denmark, CP³-Origins, Campusvej 55, DK-5230 Odense M, Denmark*

We present the next-to-leading-order calculation of the partial decay widths of the light CP-even Higgs boson decaying into four fermions in the Two-Higgs-Doublet Model. Four different renormalization schemes are applied in the calculation, which is implemented into the analysis tool PROPHECY4F. Some sample results on the h→ 4 fermions decay width illustrate how the corrections reduce the dependence on the renormalization scale and the choice of the scheme.

## 1 Introduction

The Higgs-boson decay to four fermions, $\mathrm{h} \to \mathrm{WW/ZZ} \to 4f$, is one of the best studied Higgs decay channels, in particular the decay into four charged leptons, which delivers a very clean experimental signal and plays an important role in the Higgs mass measurement. Improving the accuracy of the measurements requires, at the same time, improving theoretical predictions not only of the Standard Model (SM), but also of possible extensions of the SM to the same level of precision. Hence higher-order corrections need to be taken into account. We present the calculation [1,2] of the Higgs-boson decay to four fermions in the Two-Higgs-Doublet Model (THDM) at next-to-leading order (NLO) including electroweak (EW) as well as QCD corrections. Many SM extensions with non-minimal Higgs sectors contain a second Higgs doublet, and a general THDM can be a low-energy effective theory for these models. In the following, we will restrict the calculation to a THDM with the specific assumptions described below.

## 2 The Two-Higgs-Doublet Model and its renormalization

The Higgs potential $V$ of the THDM is assumed to be

$$\begin{aligned} V = {} & m_{11}^2 \Phi_1^\dagger \Phi_1 + m_{22}^2 \Phi_2^\dagger \Phi_2 - m_{12}^2 (\Phi_1^\dagger \Phi_2 + \Phi_2^\dagger \Phi_1) + \tfrac{1}{2}\lambda_1 (\Phi_1^\dagger \Phi_1)^2 + \tfrac{1}{2}\lambda_2 (\Phi_2^\dagger \Phi_2)^2 \\ & + \lambda_3 (\Phi_1^\dagger \Phi_1)(\Phi_2^\dagger \Phi_2) + \lambda_4 (\Phi_1^\dagger \Phi_2)(\Phi_2^\dagger \Phi_1) + \tfrac{1}{2}\lambda_5 \left[ (\Phi_1^\dagger \Phi_2)^2 + (\Phi_2^\dagger \Phi_1)^2 \right], \end{aligned} \tag{1}$$

where $\Phi_1$, $\Phi_2$ are the two Higgs doublets, $m_{11}^2$, $m_{12}^2$, $m_{22}^2$ the mass parameters, and $\lambda_1, \ldots, \lambda_5$ the quartic Higgs couplings. The symmetry of the Higgs potential under $\Phi_1 \to -\Phi_1$ is only softly broken by non-vanishing values of $m_{12}^2$ [3,4]. In addition, we assume CP-conservation so that all parameters in the Higgs potential are real. The two Higgs doublets can be decomposed as

$$\Phi_1 = \begin{pmatrix} \phi_1^+ \\ (\eta_1 + i\chi_1 + v_1)/\sqrt{2} \end{pmatrix}, \qquad \Phi_2 = \begin{pmatrix} \phi_2^+ \\ (\eta_2 + i\chi_2 + v_2)/\sqrt{2} \end{pmatrix}, \tag{2}$$

where $v_1$, $v_2$ are the Higgs vacuum expectation values and $\phi_1^+, \phi_2^+$, $\eta_1, \eta_2$, $\chi_1, \chi_2$ the charged, the neutral CP-even, and the neutral CP-odd fields, respectively. The fields with the same quantum

numbers can mix, and the resulting mass eigenstates correspond to two CP-even Higgs bosons, $h$ and $H$, where $h$ denotes the lighter CP-even Higgs boson, one CP-odd Higgs boson $A_0$, two charged Higgs bosons $H^\pm$, and a neutral and two charged Goldstone bosons, $G_0$ and $G^\pm$.

We replace the original set of parameters of the Higgs and gauge sector $m_{11}^2$, $m_{22}^2$, $m_{12}^2$, $\lambda_1$, $\lambda_2$, $\lambda_4$, $v_1$, $v_2$, $g_1$, $g_2$, $\lambda_3$, $\lambda_5$ with $g_1$ and $g_2$ being the $U(1)$ and the $SU(2)$ gauge couplings, respectively, by $t_h$, $t_H$, $M_h$, $M_H$, $M_{A_0}$, $M_{H^+}$, $M_W$, $M_Z$, $e$, $\beta$, $\alpha$ (or $\lambda_3$), $\lambda_5$ with $t_h$ and $t_H$ being the tadpole parameters. The masses of the CP-even, CP-odd, and charged Higgs bosons are $M_h$, $M_H$, $M_{A_0}$, $M_{H^+}$, the masses of the $W$ and the $Z$ boson are $M_W$ and $M_Z$. The electric unit charge is denoted by $e$. The parameter $\beta$ is defined via the ratio of the two Higgs vacuum expectation values, $\tan\beta = \frac{v_2}{v_1}$. In our different renormalization schemes [a], we use either the quartic coupling $\lambda_3$ or the mixing angle of the CP-even Higgs bosons $\alpha$ as an input.

In all four renormalization schemes (see Ref. [1] for details), the Higgs- as well as the gauge-boson masses are chosen on-shell, and the electric charge is defined via the ee$\gamma$ vertex in the Thomson limit. The angles $\alpha$, $\beta$ (or $\lambda_3$ instead of $\alpha$) and the coupling $\lambda_5$ are treated as $\overline{\rm MS}$ parameters. The various renormalization schemes differ in the treatment of tadpole contributions:

- Variant 1: The renormalized tadpole parameters $t_\phi^{\rm ren}$ with $\phi = h, H$ vanish. The corresponding counterterm $\delta t_\phi$ is chosen in such a way that explicit one-loop tadpole contributions are canceled. However, this treatment introduces gauge dependences in the relation between bare parameters [9,10], and, hence, also in the relation between renormalized parameters and physical predictions.
- Variant 2: Following a procedure proposed by Fleischer and Jegerlehner (FJ) [13], the bare tadpole parameters $t_\phi^{\rm bare}$ vanish. Gauge dependences in the relation between bare parameters and in the relation between the renormalized parameters and physical predictions do not occur. The inclusion of explicit tadpole contributions can, e.g., be avoided using the same set-up as in the "$t_\phi^{\rm ren} = 0$"-variant if appropriate finite contributions in the $\overline{\rm MS}$ counterterms of $\alpha$ and $\beta$ are taken into account.

The following four different renormalization schemes are applied: [1]

- $\overline{\rm MS}(\lambda_3)$ scheme: $\lambda_3$ and $\beta$ are independent parameters and fixed in the $\overline{\rm MS}$ scheme, and the renormalized tadpole parameters vanish. The mixing angle $\alpha$ can be calculated from $\lambda_3$ and the other independent parameters using tree-level relations. The relation between independent parameters and predicted observables do not depend on a gauge parameter within the class of $R_\xi$ gauges at NLO, since $\lambda_3$ is a basic coupling in the Higgs potential and thus does not introduce gauge dependences, and since the $\overline{\rm MS}$ renormalization of $\beta$ is gauge-parameter independent in $R_\xi$ gauges at NLO [9,10].
- $\overline{\rm MS}(\alpha)$ scheme: This scheme coincides with the $\overline{\rm MS}(\lambda_3)$ scheme except that now $\alpha$ is chosen as independent parameter instead of $\lambda_3$. This scheme suffers from some gauge dependence in the relation between renormalized parameters and predicted observables. Hence, for a meaningful comparison with data, all predictions using this renormalization scheme should be performed in the same gauge. We use the 't Hooft–Feynman gauge.
- FJ($\alpha$) scheme: $\alpha$ and $\beta$ are independent parameters, and the tadpoles are treated following the gauge-independent FJ prescription, $t_\phi^{\rm bare} = 0$. Similar schemes are also described in Refs. [9,10], however, the treatment of $m_{12}^2$ and $\lambda_5$ differs.
- FJ($\lambda_3$) scheme: $\beta$ and $\lambda_3$ are independent parameters, as in the $\overline{\rm MS}(\lambda_3)$ scheme, but the bare tadpole parameters are chosen to vanish.

The parameters $\alpha$, $\beta$, and the Higgs-quartic-coupling parameter $\lambda_5$ depend on a renormalization scale $\mu_{\rm r}$ in all four schemes. The $\mu_{\rm r}$ dependence of $\alpha$, $\beta$, and $\lambda_5$ is calculated by solving the renormalization group equations in the four different renormalization schemes.[1]

[a] Further renormalization schemes of the THDM are discussed in Refs. [5,6,7,8,9,10,11,12].

## 3 Outline of the calculation

The computer program PROPHECY4F[14,15] provides a "**PROP**er description of the **H**iggs d**EC**a**Y** into **4 F**ermions" and calculates observables for the decay process h→WW/ZZ→4$f$ at NLO EW+QCD in the SM. We have extended PROPHECY4F implementing the corresponding decay of the light, neutral CP-even Higgs boson of the THDM in such a way that the features of PROPHECY4F and its applicability basically remain the same. We have performed two independent calculations and implementations, as described in Refs.[1,2] in detail:

- For one calculation, we have used a model file generated by `FeynRules`[16], and for the other one an inhouse model file. The amplitudes for the virtual corrections have been generated with two different versions of `FeynArts`[17,18] and algebraically reduced with `FormCalc`[19,20] in the first calculation and with inhouse Mathematica routines in the second calculation.
- Masses of final-state fermions are neglected, but masses are taken into account in closed fermion loops. Hence, the contribution of diagrams with a closed fermion loop coupling to the Higgs boson does not vanish. We have implemented four different THDM types (Type 1, Type 2, "flipped", "lepton-specific") that differ in how the down-type quarks and charged leptons couple to the two Higgs doublets. Since the up-type quarks couple always in the same manner in all of the four types of THDM and since the dominating contribution originates from the top-quark loop, the differences between the types are negligible.
- Infrared divergences are treated applying dipole subtraction[21,22,23].
- The $W$ and $Z$ resonances are treated in the complex-mass scheme as decribed in Ref.[24]. The evaluation of loop integrals is performed with the `Collier` library[25].

## 4 Numerical results for the partial decay width for h → WW/ZZ → 4$f$

In this section, we show some sample results for the partial decay width $\Gamma^{\mathrm{h}\to 4f}_{\mathrm{THDM}}$ for h → WW/ZZ → 4$f$ for a scenario (scenario A) inspired by Ref.[26] for the Type 1 THDM:

$$M_h = 125 \text{ GeV}, \quad M_H = 300 \text{ GeV}, \quad M_{A_0} = M_{H^+} = 460 \text{ GeV}, \quad \lambda_5 = -1.9, \quad \tan\beta = 2. \quad (3)$$

Within our calculation, we choose the central renormalization scale as the average mass of all scalar degrees of freedom, $\mu_0 = (M_h + M_H + M_{A_0} + 2M_{H^+})/5$.

In Fig. 1, the renormalization scale dependence of $\Gamma^{\mathrm{h}\to 4f}_{\mathrm{THDM}}$, which is obtained by summing over all partial widths of the h boson with massless 4$f$ final states, is shown. We fix $\cos(\beta-\alpha) = c_{\beta-\alpha} = 0.1$ (scenario Aa). Each plot corresponds to the input parameters given in one of the four renormalization schemes. The dashed curves represent the leading-order (LO) results, however, it should be noted that the input parameters have been converted to the respective scheme denoted by the different line colours. Hence, the strict LO result is only represented by the line corresponding to the input scheme, i.e. for example, in the left plot, the strict LO curve is given by the dark blue $\overline{\mathrm{MS}}(\alpha)$ line. The differences between the dashed lines at the scale $\mu_0$ are only due to conversion effects, while at the other scales also the different running behaviour of the $\overline{\mathrm{MS}}$ parameters in the different schemes plays a role. Note that it is important to specify not only the parameter values of a certain scenario, but also the renormalization scheme, in which these parameters are to be interpreted. The solid lines show the NLO result including only the EW corrections. A clear plateau around the central renormalization scale $\mu_0$ is visible, and there is a clear reduction on the scale dependence going from LO to NLO.

A detailed discussion of further results, including also more delicate THDM scenarios, can be found in Refs.[1,2]. The extended version of PROPHECY4F, which covers a SM extension with a singlet scalar as well[27], will be available from its hepforge webpage[b] soon.

[b] `http://prophecy4f.hepforge.org/index.html`

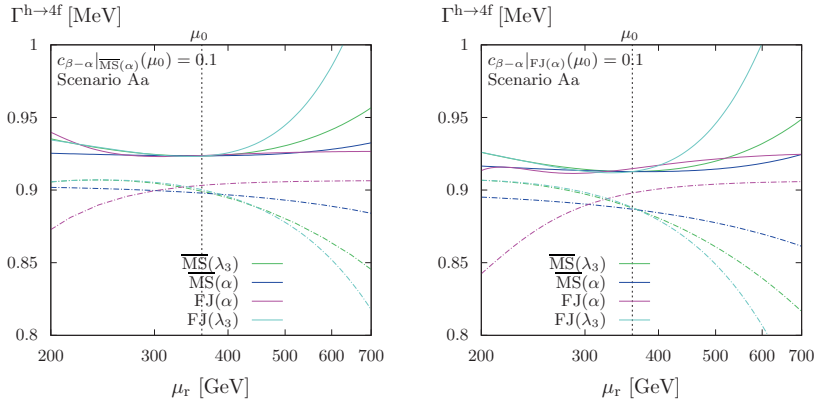


Figure 1 – The renormalization scale dependence of $\Gamma^{h\to 4f}_{\rm THDM}$ for two of the four different input schemes: $\overline{\rm MS}(\alpha)$ (left) and FJ($\alpha$) (right). In each plot, the parameters are converted to the other schemes, $\overline{\rm MS}(\lambda_3)$ (green), $\overline{\rm MS}(\alpha)$ (blue), FJ($\alpha$) (magenta), and FJ($\lambda_3$) (turquoise). The solid lines include NLO EW corrections, the dashed ones show the LO result. The figure is taken from Ref. [2].


## Acknowledgement

SD thanks the organizers of *Rencontres de Moriond* for an interesting and enjoyable conference.


## References


1. L. Altenkamp, S. Dittmaier, H. Rzehak, JHEP **09**, 134 (2017), 1704.02645.
2. L. Altenkamp, S. Dittmaier, H. Rzehak, JHEP **03**, 110 (2018), 1710.07598.
3. J. F. Gunion et al., *The Higgs Hunter's Guide* (Westview, 1900).
4. J. F. Gunion, H. E. Haber, Phys. Rev. **D72**, 095002 (2005), hep-ph/0506227.
5. R. Santos, A. Barroso, Phys. Rev. **D56**, 5366 (1997), hep-ph/9701257.
6. S. Kanemura et al., Phys. Rev. **D70**, 115002 (2004), hep-ph/0408364.
7. D. Lopez-Val, J. Sola, Phys. Rev. **D81**, 033003 (2010), 0908.2898.
8. C. Degrande, Comput. Phys. Commun. **197**, 239 (2015), 1406.3030.
9. M. Krause et al., JHEP **09**, 143 (2016), 1605.04853.
10. A. Denner et al., JHEP **09**, 115 (2016), 1607.07352.
11. M. Krause et al., Phys. Rev. **D95**, 075019 (2017), 1609.04185.
12. A. Denner, J.-N. Lang, S. Uccirati, JHEP **07**, 087 (2017), 1705.06053.
13. J. Fleischer, F. Jegerlehner, Phys. Rev. **D23**, 2001 (1981).
14. A. Bredenstein et al., Phys. Rev. **D74**, 013004 (2006), hep-ph/0604011.
15. A. Bredenstein et al., JHEP **02**, 080 (2007), hep-ph/0611234.
16. N. D. Christensen, C. Duhr, Comput. Phys. Commun. **180**, 1614 (2009), 0806.4194.
17. J. Küblbeck, M. Böhm, A. Denner, Comput. Phys. Commun. **60**, 165 (1990).
18. T. Hahn, Comput. Phys. Commun. **140**, 418 (2001), hep-ph/0012260.
19. T. Hahn, M. Perez-Victoria, Comput. Phys. Commun. **118**, 153 (1999), hep-ph/9807565.
20. T. Hahn, Nucl. Phys. Proc. Suppl. **89**, 231 (2000), hep-ph/0005029.
21. S. Catani, M. H. Seymour, Nucl. Phys. **B485**, 291 (1997), hep-ph/9605323.
22. S. Dittmaier, Nucl. Phys. **B565**, 69 (2000), hep-ph/9904440.
23. S. Dittmaier, A. Kabelschacht, T. Kasprzik, Nucl. Phys. **B800**, 146 (2008), 0802.1405.
24. A. Denner et al., Nucl. Phys. **B724**, 247 (2005), hep-ph/0505042, [Erratum: Nucl. Phys.B854,504(2012)].
25. A. Denner, S. Dittmaier, L. Hofer, Comput. Phys. Commun. **212**, 220 (2017), 1604.06792.
26. H. E. Haber, O. Stål, Eur. Phys. J. **C75**, 491 (2015), 1507.04281.
27. L. Altenkamp, M. Boggia, S. Dittmaier, 1801.07291, to appear in JHEP.

# 2.
# Higgs & Top

# H+jet production at NLO including full top-quark mass dependence

M. Kerner
*Max-Planck-Institut für Physik, Föhringer Ring 6, 80805 München, Germany*

We present predictions for gluon-fusion Higgs boson production in association with one jet at next-to-leading order QCD. The calculation is performed retaining the full dependence on the top-quark mass. The two-loop integrals appearing in the virtual corrections are calculated numerically using the program SecDec. We study the Higgs boson transverse momentum distribution and compare our predictions with approximated results.

## 1 Introduction

One of the major goals of the physics program at the LHC is the detailed study of the properties of the Higgs boson. To achieve this, accurate theoretical predictions of the various production and decay channels of the Higgs boson are required. For the dominant production mechanism, gluon fusion via a top-quark loop, most theoretical predictions are obtained in an effective field theory approach, called HEFT in the following, where the top-quark loop is integrated out by considering the limit $m_t \to \infty$. However, this approximation is only valid if the top-quark mass is much larger than all other scales of the process. While this is the case for inclusive Higgs production, one can expect that the top-quark mass effects are more important for the transverse momentum distribution of the Higgs boson, when $p_{t,\mathrm{H}} \gtrsim m_{\mathrm{T}}$.

Here we present the results of Ref. [1], where the next-to-leading (NLO) QCD predictions for H$+jet$ production retaining the full top-quark mass dependence have been calculated. While this process is known to NNLO in the HEFT approach [2,3,4,5], beyond the leading order [6,7] only approximated results of the top-quark mass effects have been known previously. To improve the HEFT predictions, expansions in $1/m_{\mathrm{T}}^2$ have been calculated [8,9] and combined with the exact Born and real radiation contributions [10]. Recently also an expansion valid in the high-$p_{t,\mathrm{H}}$ region, where $m_{\mathrm{H}}$ and $m_{\mathrm{T}}$ are considered small, has been obtained [11] and combined with the exact Born and real radiation [12,13]. Furthermore, contributions of a bottom quark-loop are known [14,15,16,17].

The most challenging part of calculating the full NLO corrections for H$+jet$ production are the virtual contributions, which involve two-loop four-point integrals with internal masses. So far, only the planar integrals are known analytically [18] and the analytic continuation of these integrals from the Euclidean to the physical region is not straightforward. We therefore evaluate all integrals numerically. In the following we give a brief description of our computational method and present phenomenological results.

## 2 Computational Method

In our calculation of the NLO corrections to H$+jet$ production, we have separated the implementation of the virtual corrections from all other parts, which we implemented in the POWHEG-BOX-V2 framework [19], taking advantage of the existing H$+jet$ NLO calculation in

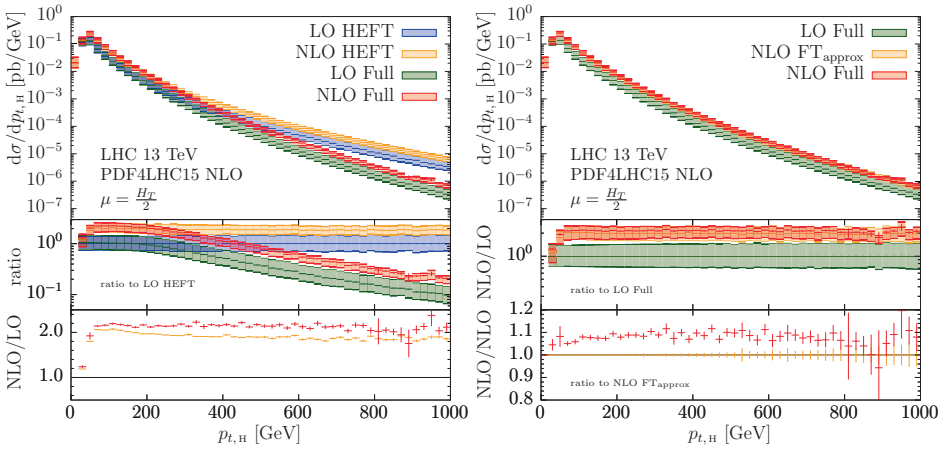


Figure 1 – Higgs boson transverse momentum distribution at LO and NLO in QCD. The results with full top-mass dependence are compared to the HEFT (left) and $FT_{approx}$ (right). The small panels show ratios of these results.

the HEFT approach [20,21]. The LO matrix elements with full top-mass dependence are based on Ref. [7], and the real radiation contributions have been generated with GoSam [22,23]. The libraries Ninja [24,25,26] and OneLoop [27] are used to perform the tensor reduction and for evaluating the scalar one-loop integrals, respectively. The contribution of the virtual corrections, described in the following, are added to the other contributions at the histogram level.

The implementation of the virtual contributions closely follows the method of Refs. [28,29]. We generated all two-loop diagrams with the program Qgraf [30] and we expressed the amplitude in terms of a form-factor decomposition. Using a customized version of Reduze [31], we reduced the contributing loop integrals to a set of master integrals. To facilitate the reduction, we have fixed the ratio $m_H^2/m_T^2 = 12/23$ in this step. We chose a quasi-finite basis of master integrals [32], which is advantageous for the numerical evaluation of the loop integrals. All integrals are calculated numerically with the program SecDec [33,34], using a quasi-Monte Carlo algorithm [35,36,37] for performing the integration. While this method allows us to obtain the full NLO result, the numerical integrations are computationally intensive. We therefore plan to include our results in a grid interpolation framework, which will then allow for a fast evaluation of the virtual contributions and will be included in the POWHEG-BOX framework.

## 3 Results

We present results for H+*jet* production at the LHC at a center-of-mass energy of 13 TeV. Jets are defined using the anti-kt algorithm with $R = 0.4$ and $p_{t,j} > 30\,\text{GeV}$. We use $\overline{\text{MS}}$ renormalization with 5 light quarks and choose the default renormalization and factorization scale $\mu_F = \mu_R = H_T/2$, with $H_T = \sqrt{m_H^2 + p_{t,H}^2} + \sum_i |p_{t,i}|$. Scale uncertainties are estimated by the usual 7-point variation. The PDF4LHC15_nlo [38,39,40,41] parton distributions are used via the LHAPDF [42] interface. The masses of the Higgs boson and top quark are set to $m_H = 125\,\text{GeV}$ and $m_T = m_H\sqrt{23/12} \approx 173.055\,\text{GeV}$.

In Table 1 we list the total cross sections in the full theory, as well as in the HEFT and $FT_{approx}$ approximations, where the latter one includes the full top-mass dependence in the LO and real radiation contributions, while the virtual corrections are evaluated in the HEFT and rescaled by the ratio $B_{full}/B_{HEFT}$ of the LO matrix elements in the full theory and HEFT. We find that the top-mass effects increase the NLO cross section by 9%(6%) relative to the NLO

Table 1: Total cross section of H+*jet* production with the input parameters given in the text. Results with full top-mass dependence, as well as the two approximated results HEFT and $\mathrm{FT}_{\mathrm{approx}}$ are shown.

| THEORY | LO [pb] | NLO [pb] |
|---|---|---|
| HEFT: | $\sigma_{\mathrm{LO}} = 8.22^{+3.17}_{-2.15}$ | $\sigma_{\mathrm{NLO}} = 14.63^{+3.30}_{-2.54}$ |
| $\mathrm{FT}_{\mathrm{approx}}$: | $\sigma_{\mathrm{LO}} = 8.57^{+3.31}_{-2.24}$ | $\sigma_{\mathrm{NLO}} = 15.07^{+2.89}_{-2.54}$ |
| Full: | $\sigma_{\mathrm{LO}} = 8.57^{+3.31}_{-2.24}$ | $\sigma_{\mathrm{NLO}} = 15.99^{+1.60}_{-3.71}$ |

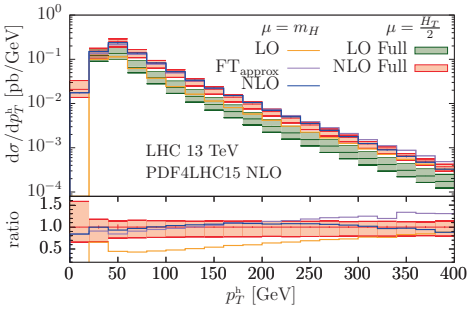


Figure 2 – Transverse momentum spectrum of the Higgs boson using different choices of the renormalization and factorization scale. The lower panel shows the ratio to the NLO result with $\mu = H_T/2$.

HEFT ($\mathrm{FT}_{\mathrm{approx}}$) result.

The dependence of the cross section on the Higgs boson transverse momentum, $p_{t,\mathrm{H}}$, is shown in Figure 1. A comparison of the full theory and HEFT result, given in the left plot, shows significant deviations of the two predictions, which can be attributed to a different scaling behavior of the amplitudes at large $p_{t,\mathrm{H}}$ [43,44]. Despite these large differences, both results lead to K-factors of similar size. However, while the K-factor is nearly constant in the full theory, it slightly decrease in the HEFT. The plot on the right-hand side shows a comparison with the $\mathrm{FT}_{\mathrm{approx}}$ result, which leads to results similar to the full theory. Taking the full top-mass dependence of the virtual contributions into account leads to an increase of about 8% over a large range of the transverse momentum, with slightly smaller corrections at low $p_{t,\mathrm{H}}$.

Finally, in Figure 2 we compare our results with the cross section evaluated using a fixed scale $\mu_R = \mu_F = m_{\mathrm{H}}$. We see that, taking the full top-mass dependence into account, both NLO results are in good agreement within the scale variation band. However using a fixed scale alters the shape of the LO prediction, therefore leading to a highly phase-space dependent K-factor, which decreases from 2.1 at 50 GeV to 1.0 at 400 GeV. Furthermore, we obtain an enhancement in the tail of the $\mathrm{FT}_{\mathrm{approx}}$ result, which shows that retaining the full top-mass dependence leads to an improved cancellation of the scale dependence of the NLO cross section.

## 4 Conclusion

We have presented a calculation of the NLO QCD corrections to H+*jet* production, retaining the full dependence on the top-quark mass. Since many of the two-loop integrals appearing in the virtual corrections are not known analytically, we have evaluated all integrals numerically with the program SECDEC. We plan to provide our results of the virtual contribution in form of a grid interpolation framework, which will allow for a fast evaluation of these contributions without the need of numerical integrations.

The top-mass effects increase the total cross section by 9% with respect to the HEFT result, but significantly reduce the cross section in the high $p_{t,\mathrm{H}}$ region. We also compared our results with an approximation $\mathrm{FT}_{\mathrm{approx}}$, which reproduces the correct shape of the $p_t$-distribution, leading to differences of less than 10% with respect to the full result in the whole $p_t$-range considered. We have also presented results using a fixed scale $\mu_R = \mu_F = m_H$, where we obtain a large phase-space dependence of the K-factor and larger top-quark mass effects, which are required to obtain good agreement with the NLO result using a dynamical scale.

**Acknowledgments**

I want to thank S. Jones and G. Luisoni for the very good collaboration and for comments on these proceedings.

**References**

1. S. P. Jones, M. Kerner, and G. Luisoni, Phys. Rev. Lett. **120**, 162001 (2018).
2. R. Boughezal, et al., JHEP **06**, 072 (2013).
3. X. Chen, et al., Phys. Lett. **B740**, 147 (2015).
4. R. Boughezal, et al., Phys. Rev. Lett. **115**, 082003 (2015a).
5. R. Boughezal, et al., Phys. Lett. **B748**, 5 (2015b).
6. R. K. Ellis, et al., Nucl. Phys. **B297**, 221 (1988).
7. U. Baur and E. W. N. Glover, Nucl. Phys. **B339**, 38 (1990).
8. R. V. Harlander, et al., JHEP **08**, 139 (2012).
9. T. Neumann and M. Wiesemann, JHEP **11**, 150 (2014).
10. T. Neumann and C. Williams, Phys. Rev. **D95**, 014004 (2017).
11. K. Kudashkin, K. Melnikov, and C. Wever (2017), arXiv:1712.06549.
12. J. M. Lindert, et al. (2018), arXiv:1801.08226.
13. T. Neumann (2018), arXiv:1802.02981.
14. R. Mueller and D. G. Öztürk, JHEP **08**, 055 (2016).
15. K. Melnikov, L. Tancredi, and C. Wever, JHEP **11**, 104 (2016).
16. K. Melnikov, L. Tancredi, and C. Wever, Phys. Rev. **D95**, 054012 (2017).
17. J. M. Lindert, et al., Phys. Rev. Lett. **118**, 252002 (2017).
18. R. Bonciani, et al., JHEP **12**, 096 (2016).
19. S. Alioli, et al., JHEP **06**, 043 (2010).
20. J. M. Campbell, R. K. Ellis, and C. Williams, Phys. Rev. **D81**, 074023 (2010).
21. J. M. Campbell, et al., JHEP **07**, 092 (2012).
22. G. Cullen, et al., Eur. Phys. J. **C72**, 1889 (2012).
23. G. Cullen et al., Eur. Phys. J. **C74**, 3001 (2014).
24. P. Mastrolia et al., JHEP **06**, 095 (2012), [Erratum: JHEP11,128(2012)].
25. H. van Deurzen, et al., JHEP **03**, 115 (2014).
26. T. Peraro, Comput. Phys. Commun. **185**, 2771 (2014).
27. A. van Hameren, Comput.Phys.Commun. **182**, 2427 (2011).
28. S. Borowka, et al., Phys. Rev. Lett. **117**, 012001 (2016a), [Erratum: Phys. Rev. Lett.117,no.7,079901(2016)].
29. S. Borowka, et al., JHEP **10**, 107 (2016b).
30. P. Nogueira, J.Comput.Phys. **105**, 279 (1993).
31. A. von Manteuffel and C. Studerus (2012), arXiv:1201.4330.
32. A. von Manteuffel, E. Panzer, and R. M. Schabinger, JHEP **02**, 120 (2015).
33. S. Borowka, et al., Comput. Phys. Commun. **196**, 470 (2015).
34. S. Borowka, et al., Comput. Phys. Commun. **222**, 313 (2018).
35. Z. Li, et al., Chinese Physics C **40, No. 3**, 033103 (2016).
36. J. Dick, F. Y. Kuo, and I. H. Sloan, Acta Numerica **22**, 133 (2013).
37. D. Nuyens and R. Cools, Mathematics of Computation **75**, 903 (2006).
38. J. Butterworth et al., J. Phys. **G43**, 023001 (2016).
39. S. Dulat, et al., Phys. Rev. **D93**, 033006 (2016).
40. L. A. Harland-Lang, et al., Eur. Phys. J. **C75**, 204 (2015).
41. R. D. Ball et al. (NNPDF), JHEP **04**, 040 (2015).
42. A. Buckley, et al., Eur. Phys. J. **C75**, 132 (2015).
43. S. Forte and C. Muselli, JHEP **03**, 122 (2016).
44. F. Caola, et al., JHEP **08**, 150 (2016).

# Recent Top quark results from the Tevatron

Boris Tuchming
(for the CDF and D0 Collaborations)
*Irfu/DPhp, CEA Saclay,*
*91191 Gif-Sur-Yvette, France*

We present recent measurements on top quark physics obtained at the Fermilab Tevatron $p\bar{p}$ collider by the CDF and D0 collaborations. We discuss the measurements of the top quark mass using direct and indirect methods of extraction, the forward-backward production asymmetries, and the top quark polarization.

## 1 Introduction

During the Run II (2001-2011) of the Tevatron $p\bar{p}$ collider at $\sqrt{s} = 1.96$ TeV, approximately 10 fb$^{-1}$ of data has been recorded in the D0 and CDF experiments, allowing to precisely study the top quark properties from $p\bar{p} \to t\bar{t}$ processes. In the following, we summarize latest legacy results obtained either by D0 or CDF, or by combining experimental data from both experiments. In a first part we present measurements of the top quark mass, obtained either directly, or indirectly from the cross-section measurements. We then present the combination of forward-backward production asymmetries, and we conclude with the latest measurement of the top quark polarization obtained at CDF using dilepton events.

## 2 Top quark mass

The top quark with a mass of $\simeq 175$ GeV is the heaviest known fundamental particle of the Standard Model (SM). Precise measurements of its mass are inputs for consistency checks of the SM and could also determine whether the electroweak vacuum is unstable, metastable, or stable [1].

### *2.1 D0 combination*

D0 has recently produced its legacy combined result regarding direct measurements of the top quark mass [2]. The combination is based on measurements in the lepton+jets and dilepton channels, using all the data collected in Run I (1992–1996) and Run II (2001–2011),

corresponding to integrated luminosities of 0.1 fb$^{-1}$ and 9.7 fb$^{-1}$, respectively. The combined mass, calculated with the "best linear unbiased estimate" (BLUE) method, is $m_t = 174.95 \pm 0.40$ (stat) $\pm 0.64$ (syst) $= 174.95 \pm 0.75$ GeV, which has a 0.43% relative uncertainty. This accuracy is much better than what had been anticipated at the beginning of Run II. The dominant uncertainty sources are the statistical uncertainty, the jet energy scale (JES) uncertainty arising from the lepton+jets calibration (0.41 GeV, also of statistical origin), and the signal modeling (0.35 GeV).

### *2.2 Tevatron combination*

The combined Tevatron top quark mass [3] is based on the most recent published measurements from both D0 and CDF. All uncertainties and their correlations are accounted for using the BLUE method. As for the D0 measurement, the dominant sources of uncertainty are the statistical uncertainty, the JES uncertainty arising from the lepton+jets calibration (0.31 GeV), and the signal modeling (0.36 GeV). The combined mass is $m_t = 174.30 \pm 0.35$ (stat) $\pm 0.54$ (syst) GeV, which has a 0.37% relative uncertainty. The summary of Tevatron measurements is shown in Fig. 1.

### *2.3 Indirect extraction of the pole mass from cross section*

A first measurement by D0 exploits the dependence of the theoretical prediction of the inclusive $t\bar{t}$ cross section as a function of the top quark pole mass [4]. The inclusive cross section is measured using the full Run II dataset. The top quark mass is extracted accounting for the dependence of the measurement as a function of the mass due to acceptance effects and using the next-to-next-to-leading-order (NNLO) cross-section calculation of top++ [5]. D0 achieves a 1.9% precision: $m_t = 172.8 \pm 1.1$ (theory)$^{+3.3}_{-3.1}$ (experimental) GeV.

More recently, D0 performs another extraction using its measured differential $t\bar{t}$ cross section [6] as a function of sensitive kinematic variables: the mass of the $t\bar{t}$ system ($m(t\bar{t})$) and the transverse momentum of the top quarks ($p_T(t/\bar{t})$). The mass is extracted from a fit of either the NLO or the NNLO cross section [7] to the unfolded D0 data. The mass is extracted with different factorization and renormalization scales and different PDF to obtain the theory uncertainty. The measurement using NNLO calculations is $m_t = 169.1 \pm 1.1$ (theory) $\pm 2.2$ (experimental) GeV which achieves a 1.5% accuracy [8] and represents a 25% improvement over the measurement using the inclusive cross-section, thus demonstrating the power of the method.

## 3 Forward-backward production asymmetries

The SM predicts a small positive forward-backward asymmetry in the $p\bar{p} \to t\bar{t}$ production due to both strong (QCD) and electroweak (EW) quantum effects: the (anti)top quarks tend to go in the same direction as the incoming (anti)protons. When the first measurements were performed at Tevatron Run II, large departures from SM expectations were observed which brought a lot of excitement [9,10,11,12] as potential indication of new physics beyond the SM. Since then, the theory prediction has been improved by including higher order QCD and EW corrections [13], and both CDF and D0 have completed their asymmetry measurement program using dilepton and lepton+jets channels in the full Run II dataset. They now provide the combination of their measurements obtained with the BLUE method, accounting for all uncertainties and their correlations [14].

The combinations are performed for the three inclusive asymmetries, $A_{\rm FB}^{t\bar{t}} = \frac{N(\Delta y_{t\bar{t}}>0)-N(\Delta y_{t\bar{t}}<0)}{N(\Delta y_{t\bar{t}}>0)+N(\Delta y_{t\bar{t}}<0)}$, $A_{\rm FB}^{\ell} = \frac{N_\ell(q\times\eta>0)-N_\ell(q\times\eta<0)}{N_\ell(q\times\eta>0)+N_\ell(q\times\eta<0)}$, and $A_{\rm FB}^{\ell\ell} = \frac{N(\Delta\eta>0)-N(\Delta\eta<0)}{N(\Delta\eta>0)+N(\Delta\eta<0)}$, based either on the reconstructed rapidities of the top and antitop ($\Delta y = y_t - y_{\bar{t}}$) or on the lepton pseudorapidities ($\eta$), or on the difference between lepton pseudorapidities for dilepton channels ($\Delta\eta = \eta_{\ell^+} - \eta_{\ell^-}$). Here, each $N$ represents a number of events corrected for acceptance and efficiency effects. The combination

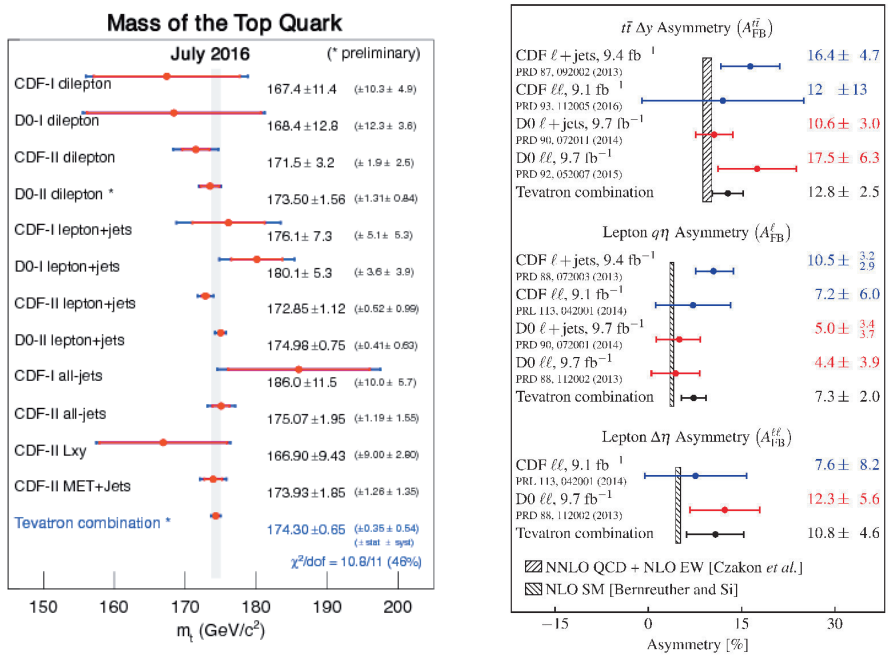


Figure 1 – Summary of Tevatron top quark mass (left) and $p\bar{p} \to t\bar{t}$ forward-backward asymmetry (right) measurements and their combinations.

of differential measurements of $A_{\rm FB}^{t\bar{t}}$ is also performed as a function of $\Delta y$ and of the $t\bar{t}$ mass ($m(t\bar{t})$). As the different measurements are dominated by the uncorrelated statistical uncertainties, the overall correlations are small, at the level of 10%, mainly due to signal modeling uncertainty. However, large correlation effects due to data unfolding have to be properly taken into account for the differential combinations.

In Fig. 1 we summarize the combined inclusive measurements for the three asymmetries. The differential asymmetries are shown in Fig. 2, where linear fits are used to model the combined asymmetries. All combined differential and inclusive asymmetries are compatible within 1.3–1.6 standard deviation of the NNLO QCD + NLO EW predictions of the SM.

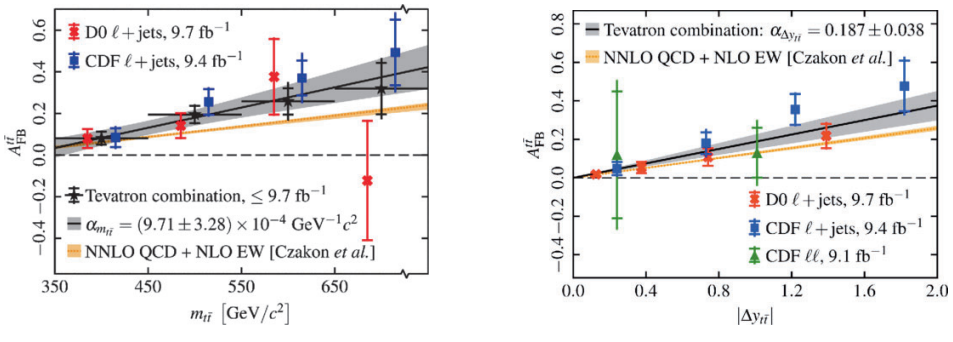


Figure 2 – Differential forward-backward asymmetry as a function of $m(t\bar{t})$ and $\Delta y$.

## 4 Top quark polarization

CDF has recently released a new measurement of top quark polarization using dilepton events[15]. This measurement is performed in the "transverse" and "helicity" basis, where the main axes are, in the $t\bar{t}$ zero momentum frame, the axis perpendicular to the production (top,beam) plane, and the $t\bar{t}$ axis, respectively. This new measurement completes previous measurements at D0 in the dilepton channel (beam basis)[16] and lepton+jets channel (beam, transverse, and helicity bases)[17]. The observables are given by the lepton angles ($\theta^{\pm}$) relative to the reference axis, where the reconstructed lepton directions are obtained after successively boosting the leptons in the $t\bar{t}$ rest frame and in the parent top quark rest frame. The differential angular distribution for $\ell^+$ and $\ell^-$ follows the relation $\frac{1}{\sigma}\frac{d^2\sigma}{d\cos\theta^+ d\cos\theta^-} = \frac{1}{4}(1+\alpha^+P^+\cos\theta^+ + \alpha^-P^-\cos\theta^- - C\cos\theta^+\cos\theta^-)$, where $\alpha$ is the spin analyzing power of the particle ($\simeq 0.99$ within the SM), $P^{\pm}$ is the polarization, and $C$ is the spin correlation. CDF measures the polarization using two-dimensional templates in $(\cos\theta^+, \cos\theta^-)$, considering two scenarios, one with CP conservation ($\alpha^+P^+ = \alpha^-P^-$), and the other one with maximal CP violation ($\alpha^+P^+ = -\alpha^-P^-$). The results are $\alpha P^{\rm CPC}_{\rm helicity} = -0.130\,^{+0.114}_{-0.109}\,({\rm stat}) \pm 0.111\,({\rm syst})$, $\alpha P^{\rm CPV}_{\rm helicity} = -0.046 \pm 0.123\,({\rm stat}) \pm 0.040\,({\rm syst})$, $\alpha P^{\rm CPC}_{\rm transverse} = -0.077 \pm 0.177\,({\rm stat}) \pm 0.098\,({\rm syst})$, and $\alpha P^{\rm CPV}_{\rm transverse} = -0.111\,^{+0.114}_{-0.109}\,({\rm stat})\,^{+0.055}_{-0.056}\,({\rm syst})$. The results as well as the previous D0 results are compatible with the SM which predicts polarization below the percent level in all bases.

## 5 Conclusion

The realm of top quark physics has been pioneered at Tevatron since the top quark discovery in 1995. The Tevatron is still producing competitive results in the finalization of its legacy measurements. The mass of the top quark is measured with a 0.37% accuracy by combining D0 and CDF. D0 also performs and indirect extraction of the pole mass with a 1.5% accuracy. The $t\bar{t}$ differential and inclusive forward-backward asymmetries are in agreement with the Standard Model. Finally, Tevatron also measures the top quark polarization in agreement with the Standard Model.

## References


1. G. Degrassi, S. Di Vita, J. Elias-Miro, J. R. Espinosa, G. F. Giudice, G. Isidori, and A. Strumia, JHEP **08**, 098 (2012).
2. V. M. Abazov *et al.* (D0 Collaboration), Phys. Rev. D **95**, 112004 (2017).
3. Tevatron Electroweak Working Group (CDF and D0 Collaborations), arXiv:1608.01881.
4. V. M. Abazov *et al.* (D0 Collaboration), Phys. Rev. D **94**, 092004 (2016).
5. M. Czakon and A. Mitov, Comput. Phys. Commun. **1852930** (2014).
6. V. M. Abazov *et al.* (D0 Collaboration), Phys. Rev. D **90**, no. 9, 092006 (2014).
7. M. Czakon, P. Fiedler, D. Heymes and A. Mitov, JHEP **1605**, 034 (2016).
8. The D0 Collaboration, D0 Note **6473-CONF** (Sept. 2016).
9. V. M. Abazov *et al.* (D0 Collaboration), Phys. Rev. Lett. **100**, 142002 (2008).
10. T. Aaltonen *et al.* (CDF Collaboration), Phys. Rev. Lett. **101**, 202001 (2008).
11. T. Aaltonen *et al.* (CDF Collaboration), Phys. Rev. D **83**, 112003 (2011).
12. V. M. Abazov *et al.*(D0 Collaboration), Phys. Rev. D **84**, 112005 (2011).
13. M. Czakon, P. Fiedler, and A. Mitov, Phys. Rev. Lett. **115**, 052001 (2015).
14. T. A. Aaltonen *et al.* (CDF and D0 Collaborations), Phys. Rev. Lett. **120**, 042001 (2018).
15. The CDF Collaboration, CDF Note **1132** (Mar. 2018).
16. V. M. Abazov *et al.* (D0 Collaboration), Phys. Rev. D **92**, 052007 (2015).
17. V. M. Abazov *et al.* (D0 Collaboration), Phys. Rev. D **95**, 011101 (2017).

# $t\bar{t}X$ Production at ATLAS and CMS

Julian Glatzer on behalf of the ATLAS and CMS Collaborations
*Institut de Física d'Altes Energies (IFAE), The Barcelona Institute of Science and Technology, Barcelona, Spain*

Recent measurements of top quark pair production in association with $W$-bosons, $Z$-bosons and photons are reported together with a measurement of $t\bar{t}t\bar{t}$ production. The measurements were performed by the ATLAS and CMS collaborations and are based on proton–proton collisions with $\sqrt{s} = 13\,\text{TeV}$ and $8\,\text{TeV}$ at the LHC. The results are compared to Standard Model (SM) theory predictions. The measurements of these rare SM processes provide tests of QCD predictions and serve as a probe for the presence of new physics at the same time.

## 1 Introduction

The cross sections for the production of a top quark pair in association with massive vector bosons, photons or a second top quark pair are several magnitudes smaller than the cross section for the production of $t\bar{t}$. Due to the large centre-of-mass energy and the high number of collisions at the Large Hadron Collider (LHC), they can be measured by the ATLAS[1] and CMS[2] experiments. The measurements of these rare SM processes provide tests of QCD predictions and constrain important background to other measurements (e.g. $t\bar{t}H$ production) and searches. The measurements serve as a probe for the presence of new physics such as vector-like quarks ($t\bar{t}V$), exotic quarks with $q = -4/3$ ($t\bar{t}\gamma$) or gluino pair production ($t\bar{t}t\bar{t}$).

## 2 $t\bar{t}W$ and $t\bar{t}Z$ Production at 13 TeV

Both ATLAS [3] and CMS [4] published simultaneous measurements of the $t\bar{t}W$ and $t\bar{t}Z$ cross section using 13 TeV collision data. The analyses simultaneously measure the $t\bar{t}W$ and $t\bar{t}Z$ cross sections using a likelihood function based on the expected and observed number of events in control and signal regions that either primarily target $t\bar{t}W$ or $t\bar{t}Z$ production.

The signal regions for both measurements are defined based on the number of leptons, jet and $b$-jets, however also object charge and kinematic information are employed. For $t\bar{t}W$ CMS uses 20 signal regions with two same-sign leptons (ee, $\mu\mu$, $e\mu$). ATLAS uses one same-sign di-muon signal region and a region with three leptons of which the mass of each pair is not consistent with the $Z$-boson mass. For $t\bar{t}Z$ production both CMS and ATLAS employ signal

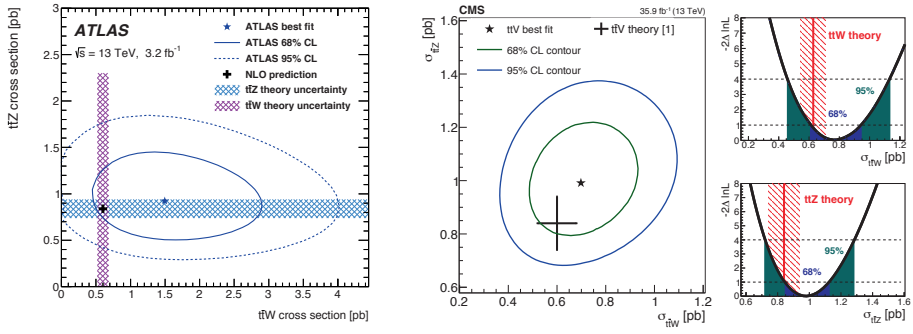


Figure 1 – The result of the simultaneous fit to the $t\bar{t}Z$ and $t\bar{t}W$ cross sections along with the 68% and 95% confidence level (CL) contours for the ATLAS (left) [3] and CMS (right) [4] measurements. The shaded areas correspond to the theoretical uncertainties. The right panel presents the individual measured cross sections along with the 68% and 95% CL intervals and the theory prediction for the CMS measurement.

regions with three and four leptons and different number of jets and $b$-jets. For at least one pair of leptons a mass consistent with the mass of the $Z$ boson is required.

The most important backgrounds from processes including top quarks or di-boson production are estimated using simulation. For the ATLAS measurement the normalisation of the $WZ$ and $ZZ$ process is determined in control regions. The non-prompt lepton background is estimated from data by both experiments. For CMS and the ATLAS 3-lepton channels the background is extrapolated from a region with a looser lepton definition using scale factors from a data control region. For the ATLAS 4-lepton channels simulated event data is corrected using data-driven scale factors. The background from electrons with misidentified charge in the CMS same-charge $ee$ channel is estimated with simulation-based corrections to opposite-charge $ee$ events.

Based on a profile likelihood fit in nine signal and two control regions and $3.2\,\text{fb}^{-1}$ of collision data the ATLAS experiment measures

$$\sigma(t\bar{t}Z) = 0.92 \pm 0.29(\text{stat.}) \pm 0.10(\text{syst.})\,\text{pb} \quad (1)$$

$$\sigma(t\bar{t}W) = 1.50 \pm 0.72(\text{stat.}) \pm 0.33(\text{syst.})\,\text{pb} \quad (2)$$

with a significance of $3.9\sigma$ ($3.4\sigma$ SM expectation) for $t\bar{t}Z$ and $2.2\sigma$ ($1.1\sigma$ SM expectation) for $t\bar{t}W$ production. The systematic uncertainty is dominated by the uncertainties on reconstructed objects for $t\bar{t}Z$ and the uncertainty on the background with non-prompt leptons and misidentified charge of leptons for $t\bar{t}W$ production.

The CMS experiment measures

$$\sigma(t\bar{t}Z) = 0.99\,^{+0.09}_{-0.08}(\text{stat.})\,^{+0.12}_{-0.10}(\text{syst.})\,\text{pb} \quad (3)$$

$$\sigma(t\bar{t}W) = 0.77\,^{+0.12}_{-0.11}(\text{stat.})\,^{+0.13}_{-0.12}(\text{syst.})\,\text{pb} \quad (4)$$

based on a profile likelihood fit in 31 signal and control regions and $35.9\,\text{fb}^{-1}$ of data. A $> 5\sigma$ ($> 5\sigma$ SM expectation) significance for $t\bar{t}Z$ and a significance of $5.3\sigma$ ($4.5\sigma$ SM expectation) for $t\bar{t}W$ production is obtained and the uncertainties are dominated by object uncertainties, such as $b$-jet, trigger and lepton uncertainties. Both measurements are consistent with the SM expectation as shown in Figure 1. The CMS experiment additionally published limits on effective field theory Wilson coefficients for operators that influence the $t\bar{t}Z$ and $t\bar{t}W$ cross sections.

## 3 $t\bar{t}t\bar{t}$ Production at 13 TeV

A search for four top quark production is performed by CMS [5] ($35.9\,\text{fb}^{-1}$) and ATLAS [6] ($36.1\,\text{fb}^{-1}$) using 13 TeV collision data. While the CMS search is interpreted as a search for

SM $t\bar{t}t\bar{t}$ production, the ATLAS analysis targets new physics in the same final state. The CMS search is performed in eight search regions that are defined based on the lepton, jet and $b$-jet multiplicities. For the estimation of the background yields, simulated events are used for the $t\bar{t}W$, $t\bar{t}Z$ and $t\bar{t}H$ processes. For the production of $t\bar{t}$ in association with vector bosons the normalisation is determined in a control region. The yield for events with non-prompt leptons is determined from data using an orthogonal control region with a looser lepton selection.

A cross section for four top quark production of $16.2^{+13.8}_{-11.4}$ fb (SM expectation 9.1 fb) is measured with a significance of $1.6\sigma$. As the four top quark cross section has contributions from virtual Higgs bosons the cross-section measurement can be used to constrain the top quark Yukawa coupling $y_t$. Based on Figure 2 an observed 95% CL limit of $\left|y_t/y_t^{\mathrm{SM}}\right| < 2.1$, where $y_t^{\mathrm{SM}}$ is the SM top quark Yukawa coupling, is derived.

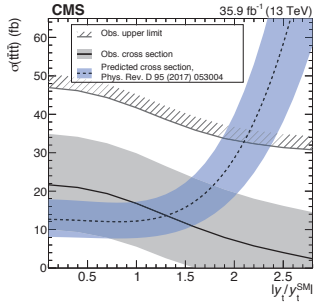


Figure 2 – The predicted SM value of $\sigma(t\bar{t}t\bar{t})$ as a function of $\left|y_t/y_t^{\mathrm{SM}}\right|$ (dashed line), compared with the observed value of $\sigma(t\bar{t}t\bar{t})$ (solid line), and with the observed 95% CL upper limit (hatched line) [5].

## 4 $t\bar{t}\gamma$ Production at 8 TeV

A measurement of the $t\bar{t}\gamma$ cross section was performed by both the ATLAS [7] and the CMS experiment [8] with 20.2 fb$^{-1}$ and 19.7 fb$^{-1}$ of 8 TeV collision data, respectively. The analyses are based on a $t\bar{t}$ $\ell$+jets and $\gamma$ selection (CMS: $\ell$, $\geq 3$ jets, $\gamma$, ATLAS: $\ell$, $\geq 4$ jets, $\geq 1$ $b$-jet, $\gamma$).

The main backgrounds are from non top quark processes with prompt photons ($W\gamma$, $Z\gamma$), $t\bar{t}$ with non-prompt photons and $Z \to ee$, where one electron is misidentified as a photon. For both experiments the normalisation of the $Z \to ee$ background is determined from a fit to the $e\gamma$ mass. For the CMS experiment the normalisation of the $t\bar{t}$ background is determined from a fit of the photon charged-hadron isolation and the normalisation of the non top quark background from a fit of the mass of three jets with highest $\sum p_T$. The $t\bar{t}\gamma$ cross section is obtained from a likelihood fit based on expected and observed number of events. The CMS experiment measured fiducial and total cross sections as well as the ratio to the total $t\bar{t}$ cross section. The measurement has an uncertainty of 21%, which is dominated by the statistical uncertainty of the likelihood fit. The results are consistent with the SM expectation and post-fit photon $p_T$ and $\eta$ distributions are shown in Figure 3.

For the ATLAS analysis the normalisation of the background with prompt photons is fixed to the expectation and the $t\bar{t}\gamma$ cross section is determined from a template fit of the photon isolation, where both the $t\bar{t}\gamma$ cross section and the normalisation of the top quark background are free parameters. The ATLAS measurement of the fiducial $t\bar{t}\gamma$ cross section is consistent with the SM prediction and has a total uncertainty 13% (5.1% statistical uncertainty). The uncertainty is dominated by the uncertainties from the background top quark and non-prompt photon background estimates. The differential cross section measurement is shown in Figure 3.

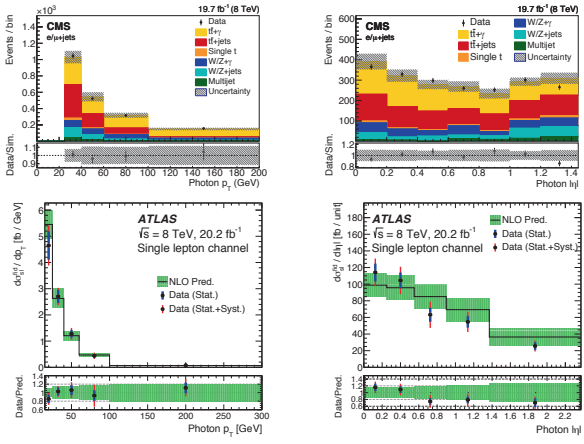


Figure 3 – Distribution of $p_T$ (top left) and $|\eta|$ (top right) of the photon in data and simulation, scaled to the result of the likelihood fit for the CMS experiment [8]. Differential $t\bar{t}\gamma$ cross section in $p_T$ (bottom left) and $|\eta|$ (bottom right) as measured by the ATLAS experiment and the corresponding theoretical predictions [7]. The lower panels show the ratio of the data (top) or the measured differential cross section (bottom) to the corresponding theory predictions.

## 5 Summary

The measurements of $t\bar{t}$ production in association with vector bosons, photons or another $t\bar{t}$ pair provide tests of the SM QCD predictions and obtain sensitivity to a variety of new physics models. The measurement of $t\bar{t}$ production in association with $W$- and $Z$-bosons reached a very interesting precision. The production of $t\bar{t}Z$ was observed with $3.9\sigma$ (ATLAS, 3.2/fb) and $> 5\sigma$ (CMS, 35.9/fb), while the production of $t\bar{t}W$ was observed with $2.2\sigma$ (ATLAS, 3.2/fb) and $5.5\sigma$ (CMS, 35.9/fb). Both measurements are consistent with NLO SM QCD predictions.

Four top quark production was measured with an observed significance of $1.6\sigma$ and constraints on the top quark Yukawa coupling have been derived by CMS. In addition the fiducial cross section of $t\bar{t}\gamma$ production was measured by the ATLAS and CMS experiments and first differential cross-section measurements for photon $p_T$ and $\eta$ have been reported.


## Acknowledgments

The author would like to thank the European Union for the funding from the Horizon 2020 research and innovation programme under the Marie Skodowska-Curie grant agreement No 665919.


## References


1. ATLAS Collaboration, JINST **3**, S08003 (2008)
2. CMS Collaboration, JINST **3**, S08004 (2008)
3. ATLAS Collaboration, Eur. Phys. J. **C77**, 40 (2017)
4. CMS Collaboration, arXiv 1711.02547
5. CMS Collaboration, Eur. Phys. J. **C78**, 140 (2018)
6. ATLAS Collaboration, arXiv 1803.09678
7. ATLAS Collaboration, JHEP **1711**, 086 (2017)
8. CMS Collaboration, JHEP **1710**, 006 (2017)

# Searches with top quarks

J.M. Hogan, on behalf of the ATLAS and CMS collaborations
*Department of Physics & Engineering, Bethel University, St. Paul, MN*

Heavy new physics particles including vector-like quarks, excited quarks, and heavy vector bosons can decay to top quarks alongside other standard model particles. Searches at the CERN LHC in final states with top quarks set strong constraints on the existence of such particles, and measurements of top quark associated production and branching fractions constrain models with flavor-changing neutral currents. No evidence for new physics is seen in these searches, although discovery potential exists for several models.

New physics that couples to top quarks could appear in either their production or decay. Several theories of physics beyond the standard model (SM) predict new particles at the TeV scale that could decay to top quarks. Other models predict anomalous decays of SM top quarks, such as a flavor-changing neutral current decay $t \to uH$.

Top quark production and decay have been studied for over twenty years, providing a well-established set of analysis techniques that are easily adapted to new physics searches. Top quark production is simulated at next-to-leading-order and modeling corrections are derived in the context of top quark property measurements. The significant branching fraction of top quarks to leptons provides a clean event selection handle via electrons or muons, which are reconstructed very reliably in both the ATLAS [1] and CMS [2] detectors at the LHC. For very massive new physics particles, hadronic final states can also be simplified using jet substructure tools to identify the decay products of an entire top quark within one large-radius jet.

This review includes searches for vector-like $T$ and $B$ quarks, excited top quarks, and a heavy $W'$ boson, in final states with top quarks that decay via SM mechanisms. A search for evidence of flavor-changing neutral-current decays is also presented. All results feature 36 fb$^{-1}$ of 13 TeV $pp$ collision data collected by the ATLAS and CMS experiments in 2015 and/or 2016.

## 1 Vector-like quarks

Vector-like quarks (VLQs) have similar properties as SM quarks, with spin 1/2 and electric charge in units of $e/3$. They are set apart by their equal left-handed (LH) and right-handed (RH) coupling to charged currents [3]. Models of new physics motived by "naturalness" arguments often include VLQs as a top quark partner. Potentially divergent quantum corrections to the Higgs boson mass from SM top quark loops could be cancelled by the presence of a top quark partner at the TeV scale.

Both the ATLAS and CMS collaborations search for vector-like $T$ quarks (charge $2e/3$) that decay to $bW$, $tH$, or $tZ$, and for $B$ quarks (charge $-e/3$) that decay to $tW$, $bZ$, or $bH$. Common branching fraction ($\mathcal{B}$) benchmarks are an electroweak singlet with $\mathcal{B}(qW) = 0.5$ and $\mathcal{B}(qZ, qH) = 0.25$, and an electroweak doublet with $\mathcal{B}(qZ, qH) = 0.5$ and $\mathcal{B}(qW) = 0$. If VLQs exist in an electroweak multiplet of more than one new particle, exotically charged VLQs named

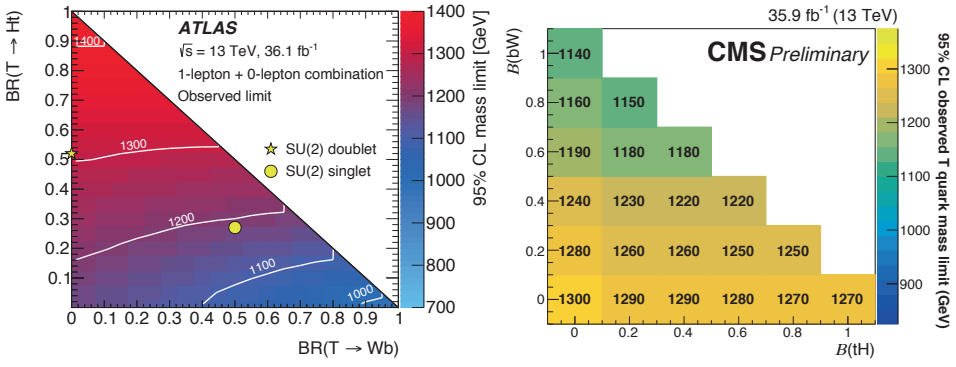


Figure 1 – Observed lower limits on vector-like $T$ quark masses in various branching fraction combinations, from searches by the ATLAS [9] (left) and CMS [10] (right) Collaborations.

$X$ (charge $5e/3$) and $Y$ (charge $-4e/3$) are also possible.

Pair production of $X\overline{X} \to tW^+\bar{t}W^-$ has been excluded for $X$ quark masses below 1.32 TeV by the CMS collaboration. The search is performed in a single-lepton channel [4] and a same-sign (SS) dilepton channel [8]. In the former, top quarks produced with large transverse momentum ($p_{\mathrm{T}}$) that decay hadronically are identified in a large-radius jet using "grooming" algorithms to calculate the mass of the central, high-momentum components more accurately [5,6], and the $N$-subjettiness algorithm [7] to quantify the jet's internal structure. Events are categorized based on the number of "boosted" top quarks. In the SS dilepton channel decays such as $tW^+ \to b\ell^+\nu_\ell\ell^+\nu_\ell$ produce a unique signature that is rare in SM processes.

The ATLAS collaboration has released a new search for pair production of vector-like $T$ quarks in single-lepton and hadronic final states [9]. The focus of the search is using reclustered large-radius jets to reconstruct boosted, hadronically-decaying top quarks and Higgs bosons. Events are categorized according to the numbers of jets, $b$-quark jets, Higgs boson jets, and top quark jets. Both channels are sensitive to $T\overline{T}$ production in event categories with at least two boosted top quark candidates, at least two boosted Higgs boson candidates, or one of each. The hadronic final state requires high missing transverse momentum ($p_{\mathrm{T}}^{\mathrm{miss}}$), the negative vector sum of the $p_{\mathrm{T}}$ of all jets in an event, for sensitivity to $T \to tZ \to t\nu\nu$ decays. This channel has additional sensitivity to $T$ quark production in events with large values of the minimum transverse mass between the $p_{\mathrm{T}}^{\mathrm{miss}}$ and a $b$-quark jet. The search is performed by fitting expected signal and background distributions, dominated by $t\bar{t}$ + heavy flavor jets, to the data in 34 independent search regions. In each search region the scalar sum of the $p_{\mathrm{T}}$ of jets, leptons, and $p_{\mathrm{T}}^{\mathrm{miss}}$ is the input distribution for the fit. No excess over the SM background prediction is observed. This search has particularly strong sensitivity for $T \to tH$ decays, excluding $T$ quark masses below 1.43 TeV (1.34 TeV expected). For the singlet and doublet benchmarks, $T$ quark masses less than 1.19 TeV (1.11 TeV expected) and 1.31 TeV (1.26 TeV expected) are excluded. Figure 1 (left) shows the observed lower limits on the $T$ quark mass.

The CMS collaboration also has new results from a search for pair production of vector-like $T$ and $B$ quarks in three leptonic final states: single-lepton, SS dilepton, and triple lepton [10]. The single-lepton channel has a similar strategy to the previously-mentioned searches: boosted $W$ and Higgs boson decay products are identified in a large-radius jet using groomed mass and $N$-subjettiness. In event categories with a boosted Higgs boson candidate, the scalar sum of the $p_{\mathrm{T}}$ of all physics objects ($S_T$) is used to search for evidence of signal over the simulated backgrounds, predominantly $t\bar{t}$. In categories with only boosted $W$ boson candidates the visible mass of a leptonic top quark decay (or $T \to bW$ decay) is reconstructed as the search distribution. In the SS dilepton and trilepton categories, background from nonprompt lepton production dominates

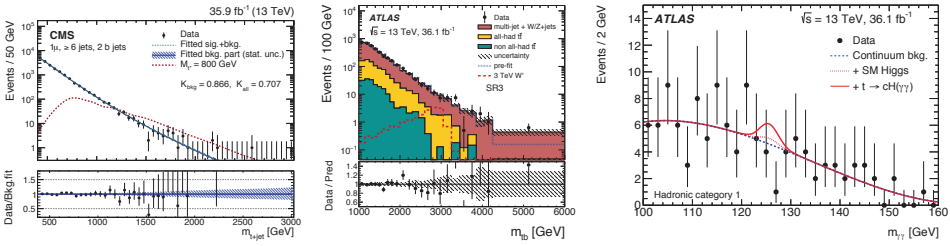


Figure 2 – Distributions of mass observables: $t^* \to tg$ in a $\mu$+jets final state [11] (left), $W' \to tb$ in events with well-identified boosted top quark jets and $b$-quark jets [12] (middle), and $H \to \gamma\gamma$ in events containing $\gamma\gamma$+jet and three-jet combinations consistent with top quark decays [16] (right).

and is estimated from data based on the rates at which prompt and nonprompt leptons pass the chosen identification scheme. Events in these channels are categorized by lepton flavor combinations, using event yields (SS dilepton) or the $S_T$ distribution (trilepton) as the search variable. The trilepton channel has particularly strong sensitivity to $T \to tZ$ decays, which can produce three prompt leptons. No excess of data over the SM prediction is observed in any channel, and a simultaneous fit is performed to data in the three leptonic final states. This search excludes singlet and doublet $T$ quarks with masses below 1.20 TeV (1.16 TeV expected) and 1.28 TeV (1.24 TeV expected). Lower limits on singlet and doublet $B$ quark masses are 1.17 TeV (1.13 TeV expected) and 0.94 TeV (0.92 TeV expected). For $T$ quarks decaying only to $tZ$, masses below 1.30 TeV (1.26 TeV expected) are excluded. Figure 1 (right) shows the observed lower limits on the $T$ quark mass.

## 2 Other massive particle searches

A different type of fermionic heavy quark is predicted in composite top quark models: a spin-3/2 excited top quark, $t^*$. The excited top quark could be the lightest of a spectrum of excited quarks. The $t^*$ decays via a strong interaction to $tg$, producing a typical top quark signature with an additional jet. The CMS collaboration has searched for the $t^*t^* \to t\bar{t}jj$ signature in semileptonic final states [11]. The background to this process is overwhelmingly SM $t\bar{t}$ production with additional jets from initial- or final-state radiation. The sensitive variable in this search is the top quark + jet mass, whose spectrum is shown in Fig. 2 (left). A $t^*$ resonance would appear over the smoothly-falling background distribution. No such excess is observed, and lower limits are set on the mass of the $t^*$, excluding values below 1.2 TeV.

Top quarks can also be produced in decays of $W'$ or $Z'$ bosons, which are featured in many new physics models that predict additional symmetries with new vector currents. These bosons might couple preferentially to third generation particles. The ATLAS collaboration searched for evidence of $W' \to tb$ decays in a hadronic final state that is sensitive to RH $W'$ bosons [12], unlike searches for $W' \to \ell\nu$. In this search boosted top quarks that decay hadronically are identified using a shower deconstruction algorithm that creates a likelihood discriminant for top quark identification based on shower splitting histories [13]. The mass of a $W'$ candidate is constructed by combining a boosted top quark candidate with a small-radius jet that may or may not be identified as a $b$ quark. The background to this search is predominantly multijet events, estimated using a pass/fail ratio technique. The ratio of $W'$ candidates with and without identified $b$-quark jets is calculated in events where the large-radius jet was not identified as a top quark. This ratio is propagated to event categories with top quark jets to estimate the multijet background component. A fit is performed to the mass distribution in three search regions, where no excess above the predicted background is observed. The most sensitive search region mass distribution is shown in Fig. 2 (middle). This search excludes $W'$ boson masses

below 2.9 TeV (LH) and 3.0 TeV (RH). The CMS collaboration obtains complementary results from a search with leptonically decaying top quarks [14], excluding $W'$ boson masses below 2.5 TeV (LH) and 3.4 TeV (RH).

## 3 Flavor-changing neutral currents

The vector-like $T$ quark has flavor-changing neutral current decays to $tZ, tH$, and in certain new physics models the SM top quark may have similar decays. The top quark could decay to an on-shell $Z$ or Higgs boson and a lighter quark, but SM branching fractions for this process are on the order of $10^{-15}$. Most notably, a flavor-violating two-Higgs doublet model could raise this branching fraction by 12 orders of magnitude [15], potentially rendering it observable at the LHC.

The ATLAS collaboration has searched for $t\bar{t} \to bWqH$, with $H \to \gamma\gamma$ and $t \to bW \to bqq'$ or $b\ell\nu$ [16]. Various combinations of three physics objects should yield the mass of the top quark: $\gamma\gamma$+jet, three jets, or $\ell\nu$+jet. In both the hadronic and leptonic final states these top quark candidates are reconstructed, and event categories are formed based on whether one or both candidates' masses lie within optimized windows. An unbinned fit is performed in the $\gamma\gamma$ mass spectrum, using parametric functions for the background and Higgs boson signal, as shown in Fig. 2 (right). No evidence for $H \to \gamma\gamma$ decays is found and upper limits on the branching fractions for $t \to cH$ and $t \to uH$ are set at $2.2 \times 10^{-3}$ and $2.4 \times 10^{-3}$, reaching the level of sensitivity to two-Higgs doublet models.

## 4 Summary

Top quarks are now a common and useful intermediate particle in the decays of predicted massive new physics particles. Precision measurements of top quark associated production and branching fractions are another important search technique. In both of these pathways discovery potential exists with the current LHC dataset, which will only grow in the next several years. So far no excesses have been observed to point toward one of these new physics models. Researchers are already reaching out to new possible signatures, advanced reconstruction methods, and novel analysis techniques to deepen our sensitivity to new physics as luminosity increases come slowly and steadily. Perhaps 140 fb$^{-1}$ of collision data will reveal what 36 fb$^{-1}$ have not.

## References


1. ATLAS Collaboration, *JINST* **3**, S08003 (2008).
2. CMS Collaboration, *JINST* **3**, S08004 (2008).
3. J.A. Aguilar-Saavedra, R. Benbrik, S. Heinemeyer and M. Perez-Victoria, *Phys. Rev.* D **88**, 094010 (2013).
4. CMS Collaboration, CMS-PAS-B2G-17-008 (2017), http://cds.cern.ch/record/2264686.
5. A.J. Larkoski, S. Marzani, G. Soyez, and J. Thaler, *JHEP* **1405**, 146 (2014).
6. S.D. Ellis, C.K. Vermilion, and J.R. Walsh, *Phys. Rev.* D **81**, 094023 (2010).
7. J. Thaler and K. Van Tilburg, *JHEP* **1103**, 015 (2011)
8. CMS Collaboration, CMS-PAS-B2G-16-019 (2016), http://cds.cern.ch/record/2256747.
9. ATLAS Collaboration, arXiv:1803.09678 [hep-ex], submitted to *JHEP*.
10. CMS Collaboration, arXiv:1805.04758 [hep-ex], submitted to *JHEP*.
11. CMS Collaboration, *Phys. Lett.* B **778**, 349 (2018).
12. ATLAS Collaboration, *Phys. Lett.* B **781**, 327 (2018).
13. D.E. Soper and M. Spannowsky, *Phys. Rev.* D **87**, 054012 (2013).
14. CMS Collaboration, *Phys. Lett.* B **777**, 39 (2018).
15. J.A. Aguilar-Saavedra, *Acta Phys. Polon.* B **35**, 2695 (2004).
16. ATLAS Collaboration, *JHEP* **10**, 129 (2017).

# 3.
# Heavy Flavour

# LEPTON NONUNIVERSALITY ANOMALIES & IMPLICATIONS[a]

G.HILLER
*Fakultät Physik, TU Dortmund, Otto-Hahn-Str.4, D-44221 Dortmund, Germany*

We discuss avenues for diagnosing new physics hinted from lepton nonuniversality in rare $b$-decays, and physics implications.

## 1 The situation

We are presently seeing $\sim 2.6\sigma$ hints of new physics (NP) in rare semileptonic $b \to sll$ transitions, indicating lepton nonuniversality (LNU) between electrons and muons in each observable $R_K$ and $R_{K^*}$ [1,2,3] [4]

$$R_H = \frac{\int_{q^2_{\rm min}}^{q^2_{\rm max}} dq^2\, d\mathcal{B}/dq^2(\bar B \to \bar H \mu\mu)}{\int_{q^2_{\rm min}}^{q^2_{\rm max}} dq^2\, d\mathcal{B}/dq^2(\bar B \to \bar H ee)}\,, \quad H = K, K^*, X_s, ... \tag{1}$$

$$R_K^{\rm LHCb} = 0.745^{+0.090}_{-0.074} \pm 0.036\,, \quad R_{K^*}^{\rm LHCb} = 0.69^{+0.11}_{-0.07} \pm 0.05 \tag{2}$$

for the dilepton mass cuts $q^2_{\rm min} = 1.1\,{\rm GeV}^2$ for $R_{K^*}$ and $1\,{\rm GeV}^2$ for $R_K$, and $q^2_{\rm max} = 6\,{\rm GeV}^2$. In lepton-universal models including the SM holds $R_H = 1$ up to tiny corrections of $\mathcal{O}(m_\mu^2/m_b^2)$ despite of the sizable hadronic uncertainties in the individual rates [1]. Electromagnetic corrections [5] [6] are found to not exceed percent level [7]. $R_H - 1$ are clean null tests of the standard model (SM). Previous measurements of $R_{K,K^*}$ by Belle and BaBar are consistent with one. We discuss in section 2 which operators can be responsible for the deviation (2) from universality [8] [9]. In section 3 lepton-specific measurements are emphasized as a means to understand whether the present LNU anomalies are due to physics beyond the standard model (BSM) in electrons, in muons, or in both [10,11], and CP violation is commented on. We discuss side effects from flavor [12] [13] in section 4, which addresses correlations with other sectors, such as charm, or Kaon physics [14,15], as well as lepton flavor violation (LFV), and decays with $\tau$'s, or $\nu$'s. Collider implications and leptoquark signatures related to the $b$-decay anomalies are discussed in section 5 [16,17,18]. We comment on the status of $R_{D,D^*}$ in section 6.

## 2 Model-independent analysis

One employs an effective low energy theory $\mathcal{H}_{\rm eff} = -4\frac{G_F}{\sqrt{2}} V_{tb}V_{ts}^* \sum_i C_i(\mu) O_i(\mu)$ at dimension six

$$\text{V,A operators}\quad \mathcal{O}_9 = [\bar s\gamma_\mu P_L b]\,[\bar\ell\gamma^\mu\ell]\,, \quad \mathcal{O}'_9 = [\bar s\gamma_\mu P_R b]\,[\bar\ell\gamma^\mu\ell]\,, \tag{3}$$

$$\mathcal{O}_{10} = [\bar s\gamma_\mu P_L b]\,[\bar\ell\gamma^\mu\gamma_5\ell]\,, \quad \mathcal{O}'_{10} = [\bar s\gamma_\mu P_R b]\,[\bar\ell\gamma^\mu\gamma_5\ell]\,, \tag{4}$$

$$\text{S,P operators}\quad \mathcal{O}_S = [\bar s P_R b]\,[\bar\ell\ell]\,, \quad \mathcal{O}'_S = [\bar s P_L b]\,[\bar\ell\ell]\,, \tag{5}$$

[a] DO-TH 18/07

$$\mathcal{O}_P = [\bar{s}P_R b]\,[\bar{\ell}\gamma_5\ell]\,, \quad \mathcal{O}'_P = [\bar{s}P_L b]\,[\bar{\ell}\gamma_5\ell]\,, \tag{6}$$

$$\text{tensors } \mathcal{O}_T = [\bar{s}\sigma_{\mu\nu} b]\,[\bar{\ell}\sigma^{\mu\nu}\ell]\,, \quad \mathcal{O}_{T5} = [\bar{s}\sigma_{\mu\nu} b]\,[\bar{\ell}\sigma^{\mu\nu}\gamma_5\ell]\,. \tag{7}$$

This set of semileptonic operators is complete. To discuss LNU one needs to add lepton specific indices $C_i O_i \to C_i^\ell O_i^\ell$, $\ell = e, \mu, \tau$. In the SM, only $O_9, O_{10}$ receive non-negligible and universal contributions, $C_9^{\rm SM} \simeq -C_{10}^{\rm SM} \simeq 4.1$, all other operators are BSM-induced.

To interpret LNU data (2) it is useful to employ the approximation where BSM physics enters the branching ratios linearly, schematically, with amplitude $A = A^{\rm SM} + A^{\rm NP}$,

$$\mathcal{B} = |A|^2 = |A^{\rm SM}|^2 + 2\,{\rm Re}(A^{\rm SM} A^{\rm NP^*}) + |A^{\rm NP}|^2\,, \tag{8}$$

that is, assuming $|C^{\rm NP}| \ll |C^{\rm SM}|$. The complementarity between $R_K$ and $R_{K^*}$ becomes manifest [9]. In fact, it suffices to measure two different (by spin parity of the final hadron) $R_H$ ratios. Then, all others serve as consistency checks, because the Wilson coefficients $C$ and $C'$ enter decay amplitudes in specific combinations dictated by parity and Lorentz invariance

$$\begin{aligned} C + C' \;&:\quad K, K^*_\perp, \dots \\ C - C' \;&:\quad K_0(1430), K^*_{0,\parallel}, \dots \end{aligned} \tag{9}$$

In addition, the $K^*_\perp$ amplitude is subleading at both high and low $q^2$ windows. Here, $C$ and $C'$ refer to V-A and V+A quark currents, respectively, and $0, \parallel, \perp$ refers to longitudinal and transverse parallel and perpendicular transversity, respectively. It follows that[9]

$$R_K \simeq R_\eta \simeq R_{K_1(1270,1400)}, \qquad R_{K^*} \simeq R_\Phi \simeq R_{K_0(1430)}\,, \tag{10}$$

and all $R_H$ are equal if all $C'$ vanish.

Which operators are responsible for the deviation (2) from universality in $R_K, R_{K^*}$? [19]

$${\rm Re}[C_9^{{\rm NP}\mu} - C_{10}^{{\rm NP}\mu} - (\mu \to e)] \sim -1.1 \pm 0.3, \quad {\rm Re}[C_9^{\prime\mu} - C_{10}^{\prime\mu} - (\mu \to e)] \sim 0.1 \pm 0.4\,. \tag{11}$$

The constraint from the $B_s \to \mu\mu$ branching ratio $0 \lesssim {\rm Re}[C_{10}^{{\rm NP}\mu} - C_{10}^{\prime\mu}] \lesssim 0.9$ can be simultaneously satisfied. The measurement of $R_K$ and $R_{K^*}$ identifies the V-A-type operators as the dominant source behind the anomalies. Within leptoquark explanations, this singles out three kinds that can account for (2) at tree level: the scalar triplet leptoquark $S_3$, the vector triplet $V_3$ and the vector singlet $V_1$, whereas the scalar doublet $\tilde{S}_2$ is disfavored as it induces V+A Wilson coefficients. Furthermore, LHCb data allows one to predict [19] $R_{X_s} \simeq 0.73 \pm 0.07$, the LNU ratio for inclusive $B \to X_s \ell\ell$ decays, which can be probed at Belle II.

## 3 Which BSM in electrons, in muons, or in both?

The observation of $R_H < 1$ suggests too few muons, or too many electrons, or a combination thereof. To disentangle this lepton specific measurements are required. Presently much more data is available on $b$-decays to muons than on decays to electrons. Global $b \to s$ fits to Wilson coefficients from $B \to (K, K^*)\mu\mu, B_s \to \mu\mu$ precision studies are presently hinting at NP, too, and can point into the same direction as $R_{K,K^*}$. Therefore, BSM effects in electrons are presently not necessary to account for the data. Analogous studies in $B \to Hee$ are, however, are required for consolidation of this possibility. Early data are already available from Belle [20].

Two main types of explicit BSM models can naturally address LNU at the required level of $\sim 15\%$ on the SM amplitude: $U(1)$ extensions with gauged lepton flavor ($Z'$-models) [21] and leptoquarks [8 18], that can be charged under a flavor symmetry and couple non-universally [13].

Inspection of (8) shows that close to maximal BSM-CP violation switches off SM-NP interference. Together with $R_H < 1$ this requires large NP couplings to electrons as muons would enhance $R_H$. Such large CP phases in the $b \to see$ transition can be searched for with the angular distribution in $B \to K^*ee$, *e.g.* $J_{7,8,9}$ [9]. An explanation of $R_K$ is also possible at $2\sigma$ with (pseudo)-scalar operators, a scenario that can be cross checked with the $B \to Kee$ angular distribution [6 8].

## 4 Side effects from flavor

From a flavor perspective, LNU generically implies LFV[12]. This is obvious for leptoquarks (LQs), which couple with matrix structure $\lambda_{q\ell}$ to quarks $q$ and leptons $\ell$ of three generations each

$$\lambda_{q\ell} = \begin{pmatrix} \lambda_{q_1 e} & \lambda_{q_1 \mu} & \lambda_{q_1 \tau} \\ \lambda_{q_2 e} & \lambda_{q_2 \mu} & \lambda_{q_2 \tau} \\ \lambda_{q_3 e} & \lambda_{q_3 \mu} & \lambda_{q_3 \tau} \end{pmatrix} , \tag{12}$$

and rows=quarks, columns=leptons. Mixing of quark and lepton flavor in one coupling is very different from the SM-Yukawas. The upper left sub-matrix in red indicates the couplings relevant for Kaon and charm physics. Explaining $R_{K,K^*}$ requires [19]

$$\frac{\lambda_{b\mu}\lambda^*_{s\mu} - \lambda_{be}\lambda^*_{se}}{M^2} \simeq \frac{1.1}{(35\,\text{TeV})^2} , \tag{13}$$

where $M$ denotes the LQ mass. In matrix form, where entries with an $'*'$ do not matter,

$$\begin{pmatrix} * & * & * \\ \lambda_{q2e} & \lambda_{q2\mu} & * \\ \lambda_{q3e} & \lambda_{q3\mu} & * \end{pmatrix} + \text{ Occam's razor } (b \to s \text{ fit}) : \begin{pmatrix} * & * & * \\ * & \lambda_{q2\mu} & * \\ * & \lambda_{q3\mu} & * \end{pmatrix} . \tag{14}$$

The latter pattern assumes muon couplings only which is consistent with the global $b \to s$ fit. Viable patterns from flavor models simultaneously explain quark and lepton masses, and CKM and PMNS mixing [13 22]. For instance, models based on $U(1)_{FN} \times A_4$, with $\epsilon, \delta, c_\ell, c_\nu \lesssim 0.2$, give

$$\begin{pmatrix} \rho_d\kappa_e & \rho_d & \rho_d\kappa_\tau \\ \rho\kappa_e & \rho & \rho\kappa_\tau \\ \kappa_e & 1 & \kappa_\tau \end{pmatrix} , \begin{pmatrix} 0 & c_\ell\epsilon^4 & 0 \\ 0 & c_\ell\epsilon^2 & 0 \\ 0 & c_\ell & 0 \end{pmatrix} , \begin{pmatrix} c_\nu\kappa\epsilon^2 & c_\ell\epsilon^4 + c_\nu\kappa\epsilon^2 & c_\nu\kappa\epsilon^2 \\ c_\nu\kappa & c_\ell\epsilon^2 + c_\nu\kappa & c_\nu\kappa \\ c_\ell\delta + c_\nu\kappa\epsilon^2 & c_\ell & c_\ell\delta + c_\nu\kappa\epsilon^2 \end{pmatrix} . \tag{15}$$

LFV and off-diagonal couplings appear generically, as well as electron couplings, or taus. Phenomenological constraints apply [13 22]. LQs which are $SU(2)_L$ triplets couple doublets to doublets, implying BSM effects in $b \to s\nu\nu$ [8] and $b \to c\ell\nu$ [22], see section 6. Predictions for charm decays are given in Table 1 [23]. They depend on the flavor pattern. Here, i): hierarchy, ii) muons only iii) skewed, 1) no kaon bounds 2) kaon bounds apply for $SU(2)_L$-doublet quarks $q_2 = (c, s)$.

Table 1: Branching fractions for the full $q^2$-region (high $q^2$-region) for different classes of leptoquark couplings. Summation of neutrino flavors is understood. "SM-like" denotes a branching ratio which is dominated by resonances or is of similar size as the resonance-induced one. All $c \to ue^+e^-$ branching ratios are "SM-like" in the models considered. See text.

| pattern | $\mathcal{B}(D^+ \to \pi^+\mu\mu)$ | $\mathcal{B}(D^0 \to \mu\mu)$ | $\mathcal{B}(D^+ \to \pi^+e\mu)$ | $\mathcal{B}(D^0 \to \mu e)$ | $\mathcal{B}(D^+ \to \pi^+\nu\bar{\nu})$ |
|---|---|---|---|---|---|
| i) | SM-like | SM-like | $\lesssim 2 \cdot 10^{-13}$ | $\lesssim 7 \cdot 10^{-15}$ | $\lesssim 3 \cdot 10^{-13}$ |
| ii.1) | $\lesssim 7 \cdot 10^{-8}$ $(2 \cdot 10^{-8})$ | $\lesssim 3 \cdot 10^{-9}$ | 0 | 0 | $\lesssim 8 \cdot 10^{-8}$ |
| ii.2) | SM-like | $\lesssim 4 \cdot 10^{-13}$ | 0 | 0 | $\lesssim 4 \cdot 10^{-12}$ |
| iii.1) | SM-like | SM-like | $\lesssim 2 \cdot 10^{-6}$ | $\lesssim 4 \cdot 10^{-8}$ | $\lesssim 2 \cdot 10^{-6}$ |
| iii.2) | SM-like | SM-like | $\lesssim 8 \cdot 10^{-15}$ | $\lesssim 2 \cdot 10^{-16}$ | $\lesssim 9 \cdot 10^{-15}$ |

## 5 Collider implications – leptoquarks!

Producing LQs at the LHC happens through pair production with cross section $\sigma(pp \to \phi^+\phi^-) \propto \alpha_s^2$, recently, *e.g.* [24 25 26]. Single LQ production in association with a lepton $\sigma(pp \to \phi\ell) \propto |\lambda_{q\ell}|^2\alpha_s$ depends on flavor, and is lesser phase space limited than pair production. Links with $b$-anomalies and flavor are manifest via (13)-(15). While $b$-studies are in principle able to determine the columns, the lepton flavor structure of $\lambda_{q\ell}$, theory input is presently required to go on and break

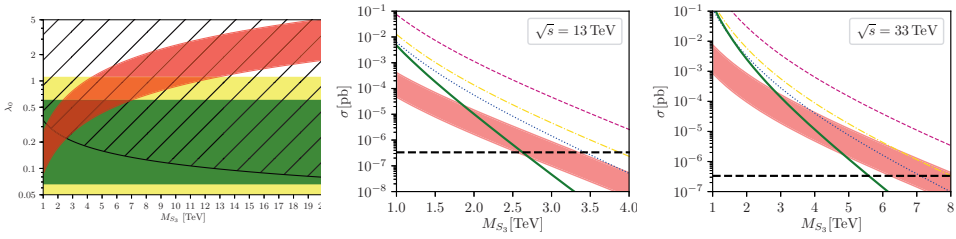


Figure 1 – Red bands: $R_{K,K^*}$ with flavor (16). Plot to the left shows $\lambda_{b\ell}$ vs $M$. Green vertical band gives flavor model prediciton $\lambda_{b\ell} \sim c_\ell$ which points to $M \lesssim 7-8$ TeV. Other plots: Single LQ production cross section for $\sqrt{s} = 13$ TeV and 33 TeV. Magenta, yellow, blue line corresponds to $\lambda_{d\mu} = 1, \lambda_{s\mu} = 1, \lambda_{b\mu} = 1$, respectively. Black dashed line: no-loss reach with 3 ab$^{-1}$. Green curve: pair production (LO Madgraph). Figures from [26].

the ambiguity in the product $\lambda_{b\ell}\lambda^*_{s\ell}$. Quark hierarchies $m_b \gg m_s \gg m_d$, when addressed with a flavor symmetry, imply hierarchies for LQs $\lambda_{s\ell} \sim (m_s/m_b)\,\lambda_{b\ell}$. It follows that third generation quark couplings dominate. Together with (13) one obtains the range from $R_{K,K^*}$ data for $\lambda_{b\ell}$,

$$M/11.6\,\text{TeV} \lesssim \lambda_{\text{b}\ell} \lesssim \text{M}/3.9\,\text{TeV}\,. \tag{16}$$

In figure 1 the single and pair production cross section for the scalar triplet $S_3$ is shown for $\sqrt{s} = 13$ TeV and 33 TeV. One finds that beauty production wins – $bg$-fusion over $dg$- and $sg$-fusion– also at hadronic level despite its PDF suppression if $\lambda_{q\ell}$ follow quark mass hierarchies. Inverted hierarchies $\lambda_{s\ell} > \lambda_{b\ell}$ would be surprising from a symmetry-based flavor perspective and suggest means beyond. Looking for $pp \to \ell\ell^{(\prime)}q$ is therefore very important, yet the vanilla theory channel is $b\ell\ell^{(\prime)}$, or in pair production, $bb\ell\ell^{(\prime)}$, $\ell, \ell' = e, \mu$, also LFV $\ell \neq \ell'$, and $t\ell\nu_{\ell^{(\prime)}}$.

## 6 LNU in charged currents

We briefly comment on the status of LNU in $b \to c\ell\nu$ decays. Input is compiled in table 2 [22].

$$R_{D^{(*)}} = \frac{\mathcal{B}(B \to D^{(*)}\tau\nu_\tau)}{\mathcal{B}(B \to D^{(*)}\ell\nu_\ell)}\,, \qquad \hat{R}_{D^{(*)}} \equiv R_{D^{(*)}}/R^{\text{SM}}_{D^{(*)}}\,, \tag{17}$$

where in the denominator of $R_{D^{(*)}}$ $\ell = \mu$ at LHCb and $\ell = e, \mu$ at Belle and BaBar.

$$\hat{R}^{\text{exp}}_D = 1.35 \pm 0.17\,, \qquad \hat{R}^{\text{exp}}_{D^*} = 1.23 \pm 0.07\,, \qquad \text{(2016)} \tag{18}$$

$$\hat{R}^{\text{exp}}_D = (1.35 \pm 0.17)/(1+x)\,, \qquad \hat{R}^{\text{exp}}_{D^*} = 1.18 \pm 0.07\,, \qquad \text{(NEW)} \tag{19}$$

and $x = 3.6\%$ ($D^0$) and $x = 5.5\%$ ($D^+$) from QED corrections [35], hence $\hat{R}^{\text{exp}}_D = 1.30 \pm 0.16$ and $1.28 \pm 0.16$, respectively [b]. See, *e.g.*,[37 38] for other recent SM predictions of $R_{D^*}$.

In some scenarios, such as LQs $S_3, V_3$ and $V_1$ BSM effects in $R_{K,K^*}$ imply BSM effects in $R_{D,D^*}$, however, due to the large SM contribution in the tree level decays, at a reduced level. Flavor models predict effects up to few percent and around 10 percent in $R_{D^*}$ and $R_D$ [22], respectively, below the present 1 $\sigma$ ranges, (18)-(19).

## 7 Summary

Current data on $R_K, R_{K^*}, R_D, R_{D^*}$ in semileptonic $B$-meson decays hint at violation of lepton-universality, and therefore the breakdown of the SM. The April 2017 release of $R_{K^*}$ by LHCb has

[b] There are two caveats on the QED effects: The dependence on experimental cuts and that the radiative corrections are not for electrons.

Table 2: Experimental results and SM predictions for $R_D^{(*)}$, 'NEW' labels updates since 2016. See text. †Error weighted average; we added statistical and systematical uncertainties in quadrature.

| | | $R_D$ | $R_{D^*}$ |
|---|---|---|---|
| BaBar | [28] | $0.440 \pm 0.058 \pm 0.042$ | $0.332 \pm 0.024 \pm 0.018$ |
| Belle | [29] | $0.375 \pm 0.064 \pm 0.026$ | $0.293 \pm 0.038 \pm 0.015$ |
| Belle | [30] | - | $0.302 \pm 0.030 \pm 0.011$ |
| Belle | [27] | - | $0.270 \pm 0.035^{+0.028}_{-0.025}$ |
| LHCb | [31] | - | $0.336 \pm 0.027 \pm 0.030$ |
| LHCb NEW | [34] | - | $0.286 \pm 0.019 \pm 0.025 \pm 0.021$ |
| average NEW† | | $0.406 \pm 0.050$ | $0.307 \pm 0.015$ |
| SM | | $0.300 \pm 0.008$ [33] | $0.252 \pm 0.003$ [32] |
| SM NEW | | $(0.300 \pm 0.008)(1 + \%)$ [35] | $0.260 \pm 0.008$ [36] |

strengthened the previous hints and allowed to pin down the Dirac structure of the underlying physics to be predominantly of V-A-type. Future data – LNU updates and other observables $R_\Phi, R_{Xs}..., B \to K^{(*)}ee$ – from LHCb and in the nearer future from Belle II are eagerly awaited.

What makes these LNU-anomalies – iff true – so important? They are theoretically clean and intimately linked to flavor: they can give new insights towards the origin of flavor and structure by probing models of flavor. Correspondingly, one should look for imprints in other sectors: $D$, $K$ physics, LFV, including $\mu - e$ conversion and lepton decays.

In addition, new BSM model buildung has been triggered that deserves attention in direct searches at ATLAS and CMS and future colliders. Leptoquarks are flavorful and can be in reach of the LHC, where they can provide complementary information to rare decays, on the couplings $\lambda_{s\ell}, \lambda_{b\ell}$ and masses $M$ separately vs their product (13). Model-independent upper limits on $M$ are at the few $\mathcal{O}(10)$ TeV level, 40, 45 and 20 TeV for $S_3, V_1$ and $V_3$, respectively [19]. The bulk of the parameter space lies outside of the LHC [25 26].

## Acknowledgments

GH is happy to thank the organizers for the opportunity to speak at this wonderful conference, and her collaborators for great collaboration. This work is supported in part by the *Bundesministerium für Bildung und Forschung* (BMBF).

## References

1. G. Hiller and F. Krüger, Phys. Rev. D **69**, 074020 (2004) doi:10.1103/PhysRevD.69.074020 [hep-ph/0310219].
2. R. Aaij *et al.* [LHCb Collaboration], Phys. Rev. Lett. **113** (2014) 151601 [arXiv:1406.6482 [hep-ex]].
3. R. Aaij *et al.* [LHCb Collaboration], JHEP **1708**, 055 (2017) [arXiv:1705.05802 [hep-ex]].
4. J. Albrecht, *these proceedings.*
5. T. Huber, E. Lunghi, M. Misiak and D. Wyler, Nucl. Phys. B **740**, 105 (2006) doi:10.1016/j.nuclphysb.2006.01.037 [hep-ph/0512066].
6. C. Bobeth, G. Hiller and G. Piranishvili, JHEP **0712**, 040 (2007) doi:10.1088/1126-6708/2007/12/040 [arXiv:0709.4174 [hep-ph]].
7. M. Bordone, G. Isidori and A. Pattori, Eur. Phys. J. C **76**, no. 8, 440 (2016) doi:10.1140/epjc/s10052-016-4274-7 [arXiv:1605.07633 [hep-ph]].
8. G. Hiller and M. Schmaltz, Phys. Rev. D **90**, 054014 (2014) doi:10.1103/PhysRevD.90.054014 [arXiv:1408.1627 [hep-ph]].
9. G. Hiller and M. Schmaltz, JHEP **1502**, 055 (2015) doi:10.1007/JHEP02(2015)055 [arXiv:1411.4773 [hep-ph]].

10. R. Fleischer, *these proceedings*.
11. A. Crocombe, *these proceedings*.
12. S. L. Glashow, D. Guadagnoli and K. Lane, Phys. Rev. Lett. **114**, 091801 (2015) doi:10.1103/PhysRevLett.114.091801 [arXiv:1411.0565 [hep-ph]].
13. I. de Medeiros Varzielas and G. Hiller, JHEP **1506**, 072 (2015) doi:10.1007/JHEP06(2015)072 [arXiv:1503.01084 [hep-ph]].
14. A. Iyer, *these proceedings*.
15. G. d'Ambrosio, *these proceedings*.
16. T. You, *these proceedings*.
17. D.M. Morse, *these proceedings*.
18. A. Crivellin, *these proceedings*.
19. G. Hiller and I. Nišandžić, Phys. Rev. D **96**, no. 3, 035003 (2017) doi:10.1103/PhysRevD.96.035003 [arXiv:1704.05444 [hep-ph]].
20. S. Wehle *et al.* [Belle Collaboration], Phys. Rev. Lett. **118**, no. 11, 111801 (2017) doi:10.1103/PhysRevLett.118.111801 [arXiv:1612.05014 [hep-ex]].
21. W. Altmannshofer, S. Gori, M. Pospelov and I. Yavin, Phys. Rev. D **89**, 095033 (2014) doi:10.1103/PhysRevD.89.095033 [arXiv:1403.1269 [hep-ph]].
22. G. Hiller, D. Loose and K. Schönwald, JHEP **1612**, 027 (2016) doi:10.1007/JHEP12(2016)027 [arXiv:1609.08895 [hep-ph]].
23. S. de Boer and G. Hiller, Phys. Rev. D **93**, no. 7, 074001 (2016) doi:10.1103/PhysRevD.93.074001 [arXiv:1510.00311 [hep-ph]].
24. B. Diaz, M. Schmaltz and Y. M. Zhong, JHEP **1710**, 097 (2017) doi:10.1007/JHEP10(2017)097 [arXiv:1706.05033 [hep-ph]].
25. B. C. Allanach, B. Gripaios and T. You, JHEP **1803**, 021 (2018) doi:10.1007/JHEP03(2018)021 [arXiv:1710.06363 [hep-ph]].
26. G. Hiller, D. Loose and I. Nišandžić, Phys. Rev. D 97, 075004 (2018) doi:10.1103/PhysRevD.97.075004 [ arXiv:1801.09399 [hep-ph]].
27. S. Hirose *et al.* [The Belle Collaboration], arXiv:1612.00529 [hep-ex].
28. J. P. Lees *et al.* [BaBar Collaboration], Phys. Rev. Lett. **109**, 101802 (2012) doi:10.1103/PhysRevLett.109.101802 [arXiv:1205.5442 [hep-ex]].
29. M. Huschle *et al.* [Belle Collaboration], Phys. Rev. D **92**, no. 7, 072014 (2015) doi:10.1103/PhysRevD.92.072014 [arXiv:1507.03233 [hep-ex]].
30. Y. Sato *et al.* [Belle Collaboration], arXiv:1607.07923 [hep-ex].
31. R. Aaij *et al.* [LHCb Collaboration], Phys. Rev. Lett. **115**, no. 11, 111803 (2015) Addendum: [Phys. Rev. Lett. **115**, no. 15, 159901 (2015)] doi:10.1103/PhysRevLett.115.159901, 10.1103/PhysRevLett.115.111803 [arXiv:1506.08614 [hep-ex]].
32. S. Fajfer, J. F. Kamenik and I. Nišandžić, Phys. Rev. D **85**, 094025 (2012) doi:10.1103/PhysRevD.85.094025 [arXiv:1203.2654 [hep-ph]].
33. H. Na *et al.* [HPQCD Collaboration], Phys. Rev. D **92**, no. 5, 054510 (2015) Erratum: [Phys. Rev. D **93**, no. 11, 119906 (2016)] doi:10.1103/PhysRevD.93.119906, 10.1103/PhysRevD.92.054510 [arXiv:1505.03925 [hep-lat]].
34. R. Aaij *et al.* [LHCb Collaboration], arXiv:1708.08856 [hep-ex].
35. S. de Boer, T. Kitahara and I. Nišandžić, arXiv:1803.05881 [hep-ph].
36. D. Bigi, P. Gambino and S. Schacht, JHEP **1711**, 061 (2017) doi:10.1007/JHEP11(2017)061 [arXiv:1707.09509 [hep-ph]].
37. F. U. Bernlochner, Z. Ligeti, M. Papucci and D.J. Robinson, Phys. Rev. D **95**, no.11, 115008 (2017) Erratum: [Phys. Rev. D **97**, no. 5, 059902 (2018)] doi:10.1103/PhysRevD.95.115008,10.1103/PhysRevD.97.059902 [arXiv:1703.05330 [hep-ph]].
38. S. Jaiswal, S. Nandi and S. K. Patra, Standard Model predictions of $R(D^{(*)})$," JHEP **1712**, 060 (2017) doi:10.1007/JHEP12(2017)060 [arXiv:1707.09977 [hep-ph]].

# Recent results on heavy quark production at HERA

O. Zenaiev
on behalf of the H1 and ZEUS collaborations
*DESY, Notkestr. 85,*
*Hamburg 22607, Germany*

Measurements of open charm and beauty production cross sections in deep inelastic *ep* scattering at HERA from the H1 and ZEUS Collaborations are combined and reduced cross sections are obtained. The combination method accounts for the correlations of the statistical and systematic uncertainties among the different datasets. Perturbative QCD calculations are compared to the combined data. A next-to-leading order QCD analysis is performed using these data together with the combined inclusive deep inelastic scattering cross sections from HERA. The running charm- and beauty-quark masses are determined.

## 1 Introduction

Measurements of open charm and beauty production in deep inelastic electron–proton scattering (DIS) at HERA provide important input for stringent tests of QCD. This analysis [1] is an extension of the previous H1 and ZEUS combination [2] of charm measurements in DIS [3,4,5,6,7,8,9,10] with new charm and beauty data [11,12,13,14,15,3]. The reduced charm, $\sigma_{\mathrm{red}}^{c\bar{c}}$, and beauty, $\sigma_{\mathrm{red}}^{b\bar{b}}$, cross sections are combined to create one consistent set of charm and beauty cross sections in the kinematic range of photon virtuality $2.5 \leq Q^2 \leq 2000$ GeV$^2$ and Bjorken scaling variable $3 \times 10^{-5} \leq x_{\mathrm{Bj}} \leq 5 \times 10^{-2}$. The data are compared to theoretical predictions obtained in the fixed-flavour-number scheme (FFNS) at next-to-leading order (NLO) QCD and approximate next-to-next-to-leading order (NNLO) using different proton parton distribution functions (PDFs) and used together with the inclusive DIS cross sections from HERA [16] to extract the charm- and beauty-quark masses. The data are also compared to theoretical predictions obtained using the variable-flavour-number scheme (VFNS).

## 2 Input data and combination method

The input data samples [3,4,5,6,7,8,9,10,11,12,13,14,15] used in the combination are listed in Tab. 1. The quantities to be combined are the reduced charm and beauty cross sections, defined as:

$$\sigma_{\mathrm{red}}^{Q\bar{Q}} = \frac{\mathrm{d}^2\sigma^{Q\bar{Q}}}{\mathrm{d}x_{\mathrm{Bj}}\mathrm{d}Q^2} \cdot \frac{x_{\mathrm{Bj}}Q^4}{2\pi\alpha^2\left(1+(1-y)^2\right)}.$$

Here $Q\bar{Q}$ stands for $c\bar{c}$ or $b\bar{b}$ quark-antiquark pairs, and $y$ is the inelasticity. The combined cross sections are determined at common $(x_{\mathrm{Bj}}, Q^2)$ points from the visible cross sections, $\sigma_{\mathrm{vis,bin}}$, defined as the $D$-, $\mu$-, $e$- or jet-production cross sections in a particular kinematic range, using theoretical predictions obtained with HVQDIS, which allows fully differential cross sections to be calculated [17]. The NLO calculations performed with the HVQDIS program are extended

with fragmentation models to provide hadron level cross sections as described elsewhere [2,18]. The updated fragmentation fractions of $c$ quarks into specific charmed hadrons are used [19] and the branching fractions of semi-leptonic decays of heavy-quarks to a muon or electron are taken from the PDG [20].

Table 1: Data sets used in the combination. For each data set the $Q^2$ range, integrated luminosity ($\mathcal{L}$), centre-of-mass energy ($\sqrt{s}$) and the numbers of charm ($N_c$) and beauty ($N_b$) measurements are given.

| Data set | Tagging | $Q^2$ range [GeV$^2$] | $\mathcal{L}$ [pb$^{-1}$] | $\sqrt{s}$ [GeV] | $N_c$ | $N_b$ |
|---|---|---|---|---|---|---|
| 1 H1 VTX [3] | VTX | 5 – 2000 | 245 | 318 | 29 | 12 |
| 2 H1 $D^{*+}$ HERA-I [4] | $D^{*+}$ | 2 – 100 | 47 | 318 | 17 | |
| 3 H1 $D^{*+}$ HERA-II (medium $Q^2$) [5] | $D^{*+}$ | 5 – 100 | 348 | 318 | 25 | |
| 4 H1 $D^{*+}$ HERA-II (high $Q^2$) [6] | $D^{*+}$ | 100 – 1000 | 351 | 318 | 6 | |
| 5 ZEUS $D^{*+}$ 96-97 [7] | $D^{*+}$ | 1 – 200 | 37 | 300 | 21 | |
| 6 ZEUS $D^{*+}$ 98-00 [8] | $D^{*+}$ | 1.5 – 1000 | 82 | 318 | 31 | |
| 7 ZEUS $D^0$ 2005 [9] | $D^0$ | 5 – 1000 | 134 | 318 | 9 | |
| 8 ZEUS $\mu$ 2005 [10] | $\mu$ | 20 – 10000 | 126 | 318 | 8 | 8 |
| 9 ZEUS $D^+$ HERA-II [11] | $D^+$ | 5 – 1000 | 354 | 318 | 14 | |
| 10 ZEUS $D^{*+}$ HERA-II [12] | $D^{*+}$ | 5 – 1000 | 363 | 318 | 31 | |
| 11 ZEUS VTX HERA-II [13] | VTX | 5 – 1000 | 354 | 318 | 18 | 17 |
| 12 ZEUS $e$ HERA-II [14] | $e$ | 10 – 1000 | 363 | 318 | | 9 |
| 13 ZEUS $\mu$ + jet HERA-I [15] | $\mu$ | 2 – 3000 | 114 | 318 | | 11 |

## 3 Combined data and QCD analysis

In total, 209 charm and 57 beauty data points are combined simultaneously to 52 reduced charm and 27 beauty cross-section measurements, respectively. A total $\chi^2$ of 149 for 187 degrees of freedom (dof) is obtained in the combination indicating consistency of input data and conservative estimates of the uncertainties. The individual datasets as well as the results of the combination are shown in Fig. 1.

The combined beauty and charm data are included in a QCD analysis at NLO, performed using xFitter [21], together with the combined HERA inclusive DIS data [16]. The theoretical FFNS predictions for the HERA data are obtained using the OPENQCDRAD programme [22] interfaced in the xFitter framework. The number of active flavours is set to $n_f = 3$ at all scales. The heavy-quark masses are left free in the fit. For the heavy-flavour contributions the scales are set to $\mu_r = \mu_f = \sqrt{Q^2 + 4m_{\rm Q}^2}$. For the light-flavour contributions to the inclusive DIS cross sections, the pQCD scales are set to $\mu_r = \mu_f = Q$. The massless contribution to the longitudinal structure function $F_L$ is calculated to $O(\alpha_s)$. The strong coupling is set to $\alpha_s^{n_f=3}(M_Z) = 0.106$, corresponding to $\alpha_s^{n_f=5}(M_Z) = 0.118$. The $Q^2$ range of the inclusive HERA data is restricted to $Q^2 > Q^2_{\rm min} = 3.5$ GeV$^2$. The $\chi^2$ definition and PDF parameterisation follow the HERAPDF2.0 analysis [16]. The PDF uncertainties are estimated as in the general approach of HERAPDF2.0 [16] in which the experimental, model, and parametrisation uncertainties are taken into account.

The results for the fitted heavy-quark masses extracted are:

$$m_c(m_c) = 1.290^{+0.046}_{-0.041}(\text{exp/fit})^{+0.062}_{-0.014}(\text{model})^{+0.003}_{-0.031}(\text{parameterisation})\ \text{GeV},$$
$$m_b(m_b) = 4.049^{+0.104}_{-0.109}(\text{exp/fit})^{+0.090}_{-0.032}(\text{model})^{+0.001}_{-0.031}(\text{parameterisation})\ \text{GeV}.$$

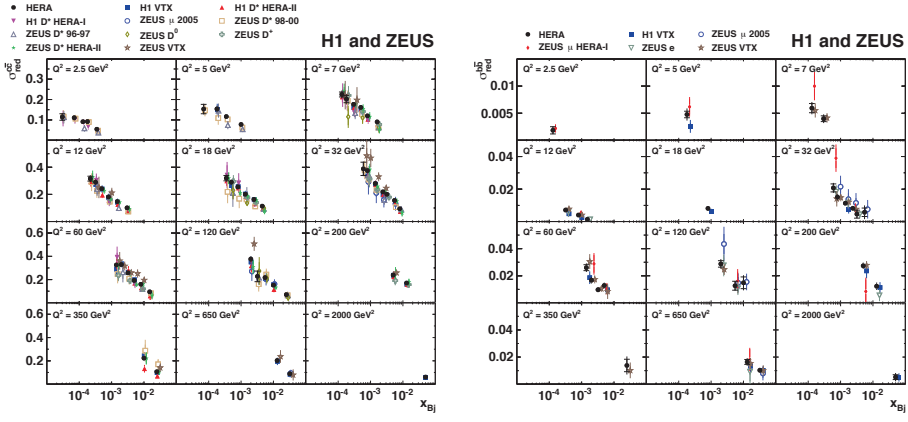


Figure 1 – Combined reduced charm *(left)* and beauty *(right)* cross sections (full circles) as a function of $x_{\mathrm{Bj}}$ for different values of $Q^2$. The inner error bars indicate the uncorrelated part of the uncertainties and the outer error bars represent the total uncertainties. The input measurements are also shown by the different markers. For presentation purposes each individual measurement is shifted in $x_{\mathrm{Bj}}$.

The model uncertainties are dominated by theoretical uncertainties arising from the scale variations. The fit yields $\chi^2/\mathrm{dof} = 1435/1208$. The resulting fit is termed HERAPDF-HQMASS.

The resulting theoretical predictions for the charm data are shown in Fig. 2 *(left)*. The FFNS calculations reasonably describe the charm data, although in the kinematic range where the data are very precise the data show a $x_{\mathrm{Bj}}$ dependence somewhat steeper than predicted by the calculations. This trend is present for the different PDF sets and QCD orders considered [1]. Predictions obtained using the VFNS were also compared to the data; overall, the description is not improved with respect to the FFNS reference calculations [1]. In Fig. 2 (*right*), the ratio of the measured reduced cross sections to the theoretical predictions is shown as a function of $\langle x \rangle$ instead of $x_{\mathrm{Bj}}$, where $\langle x \rangle$ is the geometric mean of the folding variable $x$ calculated at NLO with HVQDIS. A deviation from the reference calculation is evident, showing a steeper slope in $\langle x \rangle$ in the range $0.0005 \lesssim \langle x \rangle \lesssim 0.01$, consistent with being independent of $Q^2$. Due to the larger experimental uncertainties, no conclusion can be drawn for the beauty data.

Since the measured reduced charm cross sections show a stronger $x_{\mathrm{Bj}}$ dependence than obtained in the combined QCD fit of charm and inclusive data, in which the PDFs are dominated by the fit of the inclusive data, a study in which inclusive data with $x_{\mathrm{Bj}} < 0.01$ are excluded from the fit is carried out. A better description of the charm data can be achieved this way, however, the resulting PDFs fail to describe the inclusive data in the excluded $x_{\mathrm{Bj}}$ region [1].

## 4 Summary

Measurements of beauty and charm production cross sections in deep inelastic *ep* scattering by the H1 and ZEUS experiments were combined at the level of reduced cross sections, accounting for their statistical and systematic correlations. The beauty cross sections have been combined for the first time. The data sets were found to be consistent and the combined data have significantly reduced uncertainties. The combined data were compared to perturbative QCD predictions, which are found to describe the data reasonably well. The next-to-leading-order calculations in the fixed-flavour-number scheme provide the best description of the heavy-flavour data. The running charm and beauty masses were extracted in the QCD analysis using the inclusive and new combined charm and beauty HERA data.

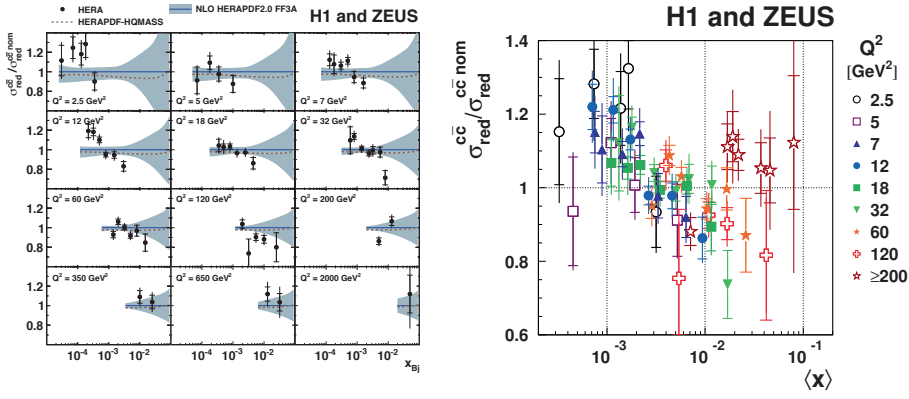


Figure 2 – *(left)* Combined reduced charm cross sections (full circles) as a function of $x_{\mathrm{Bj}}$ for given values of $Q^2$, compared to the NLO QCD FFNS predictions based on HERAPDF-HQMASS (dashed lines) and on HERAPDF2.0 FF3A (solid lines). The shaded bands on the HERAPDF2.0 FF3A predictions show the theory uncertainties obtained by adding PDF, scale and charm-quark mass uncertainties in quadrature. *(right)* Ratio of the combined reduced charm cross sections to the respective NLO FFNS cross-section predictions as a function of the partonic $\langle x \rangle$ for different values of $Q^2$.

## References


1. H. Abramowicz *et al.* [H1 and ZEUS Coll.], arXiv:1804.01019.
2. F. D. Aaron *et al.* [H1 and ZEUS Coll.], Eur. Phys. J. **C73**, 2311 (2013) [arXiv:1211.1182].
3. F. D. Aaron *et al.* [H1 Coll.], Eur. Phys. J. **C65**, 89 (2010) [arXiv:0907.2643].
4. A. Aktas *et al.* [H1 Coll.], Eur. Phys. J. **C51**, 271 (2007) [hep-ex/0701023].
5. F. D. Aaron *et al.* [H1 Coll.], Eur. Phys. J. **C71**, 1769 (2011) [arXiv:1106.1028].
6. F. D. Aaron *et al.* [H1 Coll.], Phys. Lett. **B686**, 91 (2010) [arXiv:0911.3989].
7. J. Breitweg *et al.* [ZEUS Coll.], Eur. Phys. J. **C12**, 35 (2000) [hep-ex/9908012].
8. S. Chekanov *et al.* [ZEUS Coll.], Phys. Rev. **D69**, 012004 (2004) [hep-ex/0308068].
9. S. Chekanov *et al.* [ZEUS Coll.], Eur. Phys. J. **C63**, 171 (2009) [arXiv:0812.3775].
10. S. Chekanov *et al.* [ZEUS Coll.], Eur. Phys. J. **C65**, 65 (2010) [arXiv:0904.3487].
11. H. Abramowicz *et al.* [ZEUS Coll.], JHEP **05**, 023 (2013) [arXiv:1302.5058].
12. H. Abramowicz *et al.* [ZEUS Coll.], JHEP **05**, 097 (2013) [arXiv:1303.6578].
13. H. Abramowicz *et al.* [ZEUS Coll.], JHEP **09**, 127 (2014) [arXiv:1405.6915].
14. H. Abramowicz *et al.* [ZEUS Coll.], Eur. Phys. J. **C71**, 1573 (2011) [arXiv:1101.3692].
15. H. Abramowicz *et al.* [ZEUS Coll.], Eur. Phys. J. **C69**, 347 (2010) [arXiv:1005.3396].
16. H. Abramowicz *et al.* [H1 and ZEUS Coll.], Eur. Phys. J. **C75**, 580 (2015) [arXiv:1506.06042].
17. B. W. Harris and J. Smith, Phys. Rev. **D57**, 2806 (1998) [hep-ph/9706334].
18. P. Nason and C. Oleari, Nucl. Phys. **B565**, 245 (2000) [hep-ph/9903541].
19. M. Lisovyi *et al.*, Eur. Phys. J. **C76**, 397 (2016) [arXiv:1509.01061].
20. C. Patrignani *et al.* [Particle Data Group], Chin. Phys. **C40**, 100001 (2016).
21. S. Alekhin *et al.*, Eur. Phys. J. **C75**, 304 (2015) [arXiv:1410.4412], www.xfitter.org (version 2.0.0).
22. S. Alekhin, J. Blümlein, S. Moch, Phys. Rev. **D86**, 054009 (2012) [arXiv:1202.2281]; I. Bierenbaum, J. Blümlein, S. Klein, Phys. Lett. **B672**, 401 (2009) [arXiv:0901.0669]; S. Alekhin, OPENQCDRAD-1.5, http://www-zeuthen.desy.de/~alekhin/OPENQCDRAD (version 2.1).

# Recent Heavy Flavor Results from the Tevatron

Robert J. Hirosky
for the CDF and D0 Collaborations
*University of Virginia, Department of Physics*
*382 McCormick Rd Charlottesville, VA USA*

This contribution to the 2018 Proceedings of the Rencontres de Moriond QCD Session summarizes a search by the CDF Collaboration for the exotic $X^{\pm}(5568)$ and studies of the $X^{\pm}(5568)$ by the D0 Collaboration. The $X^{\pm}(5568)$ is assumed to decay to the $B_s^0\pi^{\pm}$ final state. The CDF analysis considers the $B_s^0\pi^{\pm}$ invariant mass distribution with $B_s^0 \to J/\psi\phi$ and $\phi \to K^+K^-$. A recent analysis by D0 examines the additional decay channel $B_s^0 \to \mu^{\mp} D_s^{\pm} + any, D_s^{\pm} \to \phi\pi^{\pm}$. Observations in both channels are compared for the D0 data. The CDF analysis does not provide additional evidence for the $X^{\pm}(5568)$ state. Details of the analyses are discussed.

## 1 Introduction

The existence of exotic mesons containing more than one quark-antiquark pair has long been considered possible within the quark model [1,2]. Compared to light-flavored states, those containing heavy quarks can be more recognizable due to the distinctive decay structure of heavy quark hadrons. In fact the unexpected discovery of the exotic $X(3872)$ state by the Belle experiment [3] utilized the channel $B^{\pm} \to K^{\pm}X, X \to \pi^+\pi^- J/\psi$. While this state has been confirmed in numerous experiments, other reported four-quark candidate states have not been able to be confirmed by all experiments. A recent overview of the status of experimental evidence for nonstandard heavy mesons and baryons is available in the references [4].

Many studies of heavy hadrons and exotic states have been reported by the CDF and D0 Experiments using data collected at the Fermilab Tevatron in $p\bar{p}$ collisions at center-of-mass energy $\sqrt{s} = 1.96\,\text{TeV}$. In 2016 the D0 Experiment reported [5] evidence for a new state $X^{\pm}(5568)$ decaying to $B_s^0\pi^{\pm}$, which could be interpreted as a tightly bound diquark-antidiquark pair (eg. [bu][ds], [bd][su], [su][bd], or [sd][bu]). A loosely bound molecular state of B and K mesons may also be considered, but is less favored because of the large mass difference $m_B + m_K - m_{X(5568)}$. This analysis considered the fully hadronic decay $X \to B_s^0\pi^{\pm}$, $B_s^0 \to J/\psi\phi$, and $\phi \to K^+K^-$, as illustrated in Fig. 1a. Results from the D0 analysis are summarized in Fig. 2. The background model includes two components, a combinatorial background which is modeled using sidebands from data (Fig. 2a) and one including genuine $B_s^0$ mesons with a random combination of low momentum charged particles from the primary interaction vertex. The latter is modeled using

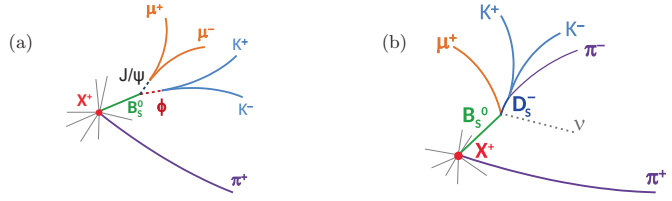


Figure 1 – Illustrations of the decay $X \to B_s^0\pi^\pm$, for (a) the fully hadronic final state considered on both CDF and D0 analyses, $B_s^0 \to J/\psi\phi$ and (b) the semileptonic final state considered by D0, $B_s^0 \to \mu^\mp D_s^\pm + any, D_s^\pm \to \phi\pi^\pm$.

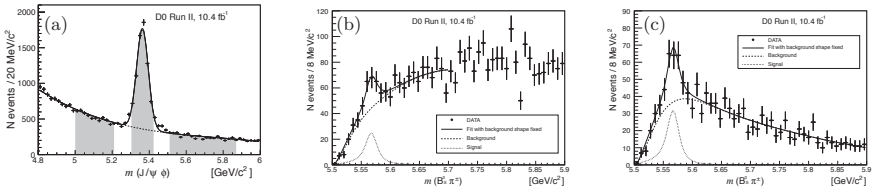


Figure 2 – Summary of D0 analysis of $X^\pm(5568)$ in the hadronc decay channel. The (a) invariant mass of $J/\psi\phi$ candidates for selected events. The shaded regions show the $B_s^0$ signal and sideband regions. The distribution of $m(B_s^0\pi^\pm)$ in data shown with the background distribution for (b) all selected events and (c) after application of a $\Delta R < 0.3$ requirement on the trajectories of the $B_s^0$ and $\pi^\pm$.

Monte Carlo (MC) simulation, tuned to match the $B_s^0$ transverse momentum distribution observed in data. The analysis is performed with and without a topological (cone) cut based on the angular distance between the trajectories of the $B_s^0$ and $\pi^\pm$, $\Delta R = \sqrt{\Delta\eta^2 + \Delta\phi^2} < 0.3$. Including systematic uncertainties and the look-elsewhere effect [6], the $X^\pm(5568)$ state was reported with a significance of $5.1\sigma$ and mass (width) of $5567.8 \pm 2.9^{+0.9}_{-1.9}$ $(21.9 \pm 6.4^{+5.0}_{-2.5})$ MeV/$c$. Subsequent analyses by LHCb [7], CMS [8], and ATLAS [9] Collaborations in proton-proton interactions at $\sqrt{s} = 7$ and 8 TeV do not report evidence for the $X^\pm(5568)$. Similarly, the CDF collaboration also recently reported [10] no evidence $X^\pm(5568)$ using Tevatron data, although with different kinematic coverage than that of Ref. [5]. This result is described below, followed by a summary of the new D0 analysis utilizing an alternative decay channel.

## 2 Search for $X^\pm(5568)$ at CDF

The CDF analysis selects candidate events as follows. A $B_S^0$ sample is constructed by combining $J\psi \to \mu\mu$ candidates with $\phi \to KK$ candidates. A four-track constrained fit requires that the dimuon system is comparable with the $J/\psi$ mass and that the $J\psi\phi$ mass is compatible with that of the $B_s^0$. The decay time of the $B_S^0$ must be inconsistent with prompt production and a momentum cut of $p_T(B_s^0) > 10\,\text{GeV}/c$ is applied. The $B_s^0$ candidates are combined with prompt $\pi^\pm$ candidates and $m(B_s^0\pi^\pm)$ is calculated as $m(J/\psi\phi\pi^\pm) - m(J/\psi\phi) + m_{\text{PDG}}(B_s^0)$, where $m_{\text{PDG}}(B_s^0)$ is the world average reported by the PDG [11]. Figure 3a shows the expected signal shape for the decay of $X^\pm(5568)$ with $p_T(B_s^0) > 10\,\text{GeV}/c$. The acceptance and reconstruction efficiency for the $X^\pm(5568)$ relative to that of $B_s^0$ is reported to be $0.445 \pm 0.27 \pm 0.018$. Backgrounds are modeled using sidebands in the $m(B_s^0\pi^\pm)$ invariant mass distribution, omitting a range $\pm\Gamma_{X(5568)}$ around 5568 MeV. The background is parameterized with a polynomial function as shown in Fig. 3b. A functional form for signal is added for fitting to data. Fit results using both a floating signal amplitude and background-only fit hypothesis are shown in Fig. 3c. The fraction of $B_s^0$ events due to the presence of $X^\pm(5568)$ is found to be $2.3 \pm 1.9\%$, consistent with no presence of signal.

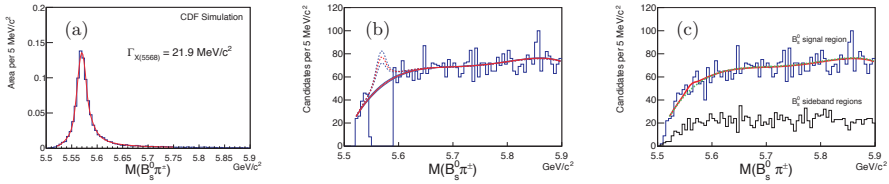


Figure 3 – The (a) expected signal shape for the decay of $X^{\pm}(5568)$ with $p_T(B_s^0) > 10\,\mathrm{GeV}/c$ from CDF simulation. Background (b) parametrization via polynomial function and combination with functional form for signal hypothesis. Fits (c) to the data using a floating signal amplitude and background-only fit hypotheses.

## 3 D0 study of $X^{\pm}(5568)$ with semileptonic decays of the $B_s^0$ meson

D0 also studies the $X^{\pm}(5568)$ using an alternate decay channel, utilizing the semileptonic (SL) decay of the $B_s^0$ meson, $B_s^0 \to \mu^{\mp} D_s^{\pm} + \ any, D_s^{\pm} \to \phi\pi^{\pm}$, where "any" includes the undetected neutrino and possibly a photon or additional hadron(s) produced in the decay. Charge conjugate states are assumed. Compared to the hadronic channel, the SL decay channel has a higher branching fraction, but the resolution is degraded by the presence of the unmeasured neutrino. This effect is reduced by requiring the $\mu^+ D_s^-$ system to have a large invariant mass. The backgrounds in the SL channel are independent of those in the hadronic channel. The data were collected using a combination of single and dimuon triggers. The $D_s^-$ candidates are reconstructed by selecting two opposite sign tracks having an invariant mass consistent with a $\phi$ meson. These are then combined with a third track, assumed to be a pion, which is required to have opposite charge to the muon. The mass of the three tracks is then required to be consistent with a $D_s^-$ meson and must form a vertex that is inconsistent with prompt production. To reconstruct the $B_s^0$ the trajectories of the $D_s^-$ and muon are required to match to a common interaction vertex. Finally, a track representing the pion having $0.5 < p_T < 25\,\mathrm{GeV}/c$ and forming a common vertex with the $B_s^0$ is combined to form $B_s^0\pi^{\pm}$ candidates. A comparable number of selected $B_S^0$ candidates are found in the two channels and the semileptonic decay channel enables an independent study of the $X^{\pm}(5568)$ state. This analysis is described in detail in Ref. [12].

An MC sample for $X^{\pm}(5568)$ signal is processed through the D0 detector simulation. The resulting $m(B_s^0\pi^{\pm})$ distribution is shown in Fig. 4a after selection requirements. Again, two distinct sources of background are considered: (1) reconstructing a $X^{\pm}(5568)$ candidate from the combination of a random charged track with a real $\mu^+$ and $D_s^-$ (2) a combinatorial background where an $X^{\pm}(5568)$ candidate is reconstructed from a spurious $D_s^-$ candidate. The first is modeled using MC samples, the second is modeled using data where the charge of the muon is reversed. The same parameters for $m_X$ and $\Gamma_X$ are used in the fits shown in Fig. 4a for the hadronic and SL samples. For the semileptonic channel alone the fit results are shown in Table 1. The mass and width of the $X^{\pm}(5568)$ for the SL and hadronic channels are consistent within the uncertainties and the observed yields are consistent with coming from a common particle. Combining both channels, the significance of the observed signal is found to be $6.7\sigma$ ($4.7\sigma$) with (without) applying the cone cut and accounting for the LEE and systematic uncertainty.

## 4 Discussion

The D0 hadronic channel analysis measured a yield $\rho$ of $(8.6 \pm 1.9 \pm 1.4)\%$ for the new $X^{\pm}(5568)$ state relative to the $B_s^0$ meson in the kinematic region of the analysis. By comparison CDF sets a limit $\rho < 6.7\%$ at 95% CL. It is interesting to explore possible differences in the kinematic regions explored in the two analyses. The most significant of these are: (1) muon fiducial cuts, $|\eta^{\mu}| < 1.0(2.0)$ for CDF (D0); (2) system boost, $p_T(B_s^0) > 10\,\mathrm{GeV}$ for CDF, while

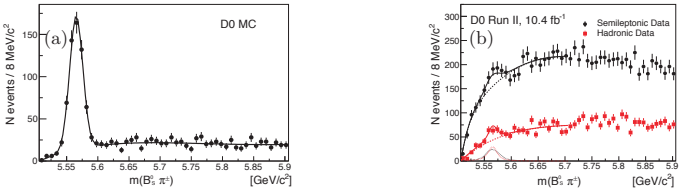


Figure 4 – The (a) invariant mass distribution $m(B_s^0\pi^\pm)$ from MC simulation, where $B_s^0 \to \mu + D_s + any$. The background results from the combination of a random charged track with the $B_s^0$ meson. A comparison (b) of the $m(B_s^0\pi^\pm)$ distribution in data for the hadronic and semileptonic data with the combined fit to both distributions (no cone cut applied). Fits to the background distribution and for signal plus background are shown.

Table 1: Fit results for D0 semileptonic data.

| | Cone Cut | No Cone Cut |
|---|---|---|
| $m_X$, MeV/$c^2$ | $5566.4^{+3.4}_{-2.8}(stat)^{+1.5}_{-0.6}(syst)$ | $5566.7^{+3.6}_{-3.4}(stat)^{+1.0}_{-1.0}(syst)$ |
| $\Gamma_X$, MeV/$c^2$ | $2.0^{+9.5}_{-2.0}(stat)^{+2.8}_{-2.0}(syst)$ | $5566.7^{+9.5}_{-6.0}(stat)^{+1.9}_{-4.6}(syst)$ |
| Local significance | $4.3\,\sigma$ | $4.5\,\sigma$ |

$p_T(B_s^0\pi^\pm) > 10\,\text{GeV}$ for D0; (3) $p_T(\pi^\pm) > 400(500)\,\text{MeV}$ for CDF (D0), (4) analysis performed with multiple topological cuts on the $B_s^0\pi^\pm$ system by D0. Considering these variations, indications are found that the $X^\pm(5568)$ state is preferentially observed in events with one or more forward muons in the D0 data, compared to two central muons (The reader is referred to the conference presentation for additional information.). The D0 signal does not appear to be significantly affected by variations in the system boost. The $B_s^0\pi^\pm$ mass spectrum depends strongly on $p_T(\pi^\pm)$. This affects the background and multiplicity of $X^\pm(5568)$ candidates due to random track combinations. The D0 track reconstruction only provided tracks down to 500 MeV, therefore the effect of lower pion $p_T$ cuts, cannot be tested by both experiments. Finally, the effect of the topological (cone) cut has been extensively studied by D0 and found not to introduce a spurious signal or to significantly modify the observation in the D0 data. While the CDF data show no evidence for the $X^\pm(5568)$ state, this result is only in tension with the D0 measurement at the level of approximately two standard deviations. Because the two experiments employ different selection requirements, a more detailed study of their compatibility requires additional control for variations in the kinematics of the event samples studied.

## References


1. M. Gell-Mann, Phys. Lett. **8**, 214215 (1964).
2. G. Zweig, CERN-TH-401 (1964).
3. S. K. Choi et al. [Belle Collaboration], Phys. Rev. Lett. **91**, 262001 (2003).
4. S. L. Olsen, T. Skwarnicki and D. Zieminska, Rev. Mod. Phys. **90**, no. 1, 015003 (2018).
5. V. M. Abazov et al. [D0 Collaboration], Phys. Rev. Lett. **117**, 022003 (2016).
6. See L. Lyons, Ann. Appl. Stat. 2, 887915 (2008).
7. R. Aaij et al. [LHCb Collaboration], Phys. Rev. Lett. **117**, 152003 (2016), [Addendum: Phys. Rev. Lett. **118**, 109904 (2017)].
8. A. M. Sirunyan *et al.* [CMS Collaboration], Phys. Rev. Lett. **120**, no. 20, 202005 (2018).
9. M. Aaboud *et al.* [ATLAS Collaboration], Phys. Rev. Lett. **120**, no. 20, 202007 (2018).
10. T. A. Aaltonen *et al.* [CDF Collaboration], Phys. Rev. Lett. **120**, no. 20, 202006 (2018).
11. C. Patrignani et al. [Particle Data Group], Chin. Phys. **C40**, 100001 (2016).
12. V. M. Abazov *et al.* [D0 Collaboration], Phys. Rev. D **97**, no. 9, 092004 (2018).

# Heavy Flavour Production and Properties at CMS and ATLAS

A.E. BARTON on behalf of the ATLAS and CMS Collaborations
*Department of Physics, Lancaster University,*
*Lancaster, LA1 4YP, England*

Measurements of heavy flavour properties and production are an important part of the physics program of the ATLAS and CMS experiments at LHC. They can potentially expose physics beyond the standard model, constrain supersymmetry and advance hadron spectroscopy and test QCD. In the past years, the two collaborations have published results in several different fields, such as rare decays, searches for new states, CP and P violation and quarkonia polarisation. In this note, some of the most recent results from ATLAS and CMS are summarised.



## 1 Introduction

ATLAS [1] and CMS [2] are general purpose detectors that measure heavy flavour properties using their inner dectectors, muon spectrometers and electromagnetic calorimeters. Measuring the properties of heavy flavour particles has been part of the $B$ physics program of the ATLAS and CMS experiments since the start of the proton-proton collisions at LHC in 2010. This note presents an overview of recent results obtained using data collected at $\sqrt{s} = 7$ TeV during 2011, $\sqrt{s} = 8$ TeV during 2012 and $\sqrt{s} = 13$ TeV during 2015. Some measurements may constrain new physics scenarios such as supersymmetry or advance $b$ and $c$ hadron spectroscopy and test QCD. The results in CP violation can access physics beyond the standard model.

Most heavy flavour physics events at ATLAS and CMS are selected using single and di-muon triggers. Di-muon triggers select opposite charged muons that exceed a momentum threshold. A vertex quality cut is applied and in some cases a decay length cut. The cuts are adjusted in triggers dedicated to the various analyses under consideration. A representation of the currently collected Run 2 data sets can be seen in Figure 1.

This note contains a small selection of results from a number of analyses, more details can be found in the original references provided.

## 2 Search for a Structure in the $B_s^0\pi^\pm$ Invariant Mass Spectrum

ATLAS and CMS performed an analysis searching for the $X(5568)$ particle for which DØ published evidence of in the $B_s\pi^\pm$ spectrum via the $B_s^0 \to J/\psi\phi$, $J/\psi \to \mu^+\mu^-$, $\phi \to K^+K^-$ decays[3]. DØ also published evidence of the resonance in the semi-leptonic decay $X^\pm(5568) \to B_s^0\pi^\pm$, where $B_s^0 \to \mu^\mp D_s^\pm X$, $D_s^\pm \to \phi\pi^\pm$ [4]. These peaks are visible in Figure 2. ATLAS [5] and CMS [6] have performed searches for the state in their datasets but find no evidence of the state. Consequently, they set limits on the ratio, $\rho_X$, of the cross-section of $X(5568)$ to the cross-section of the $B_s$

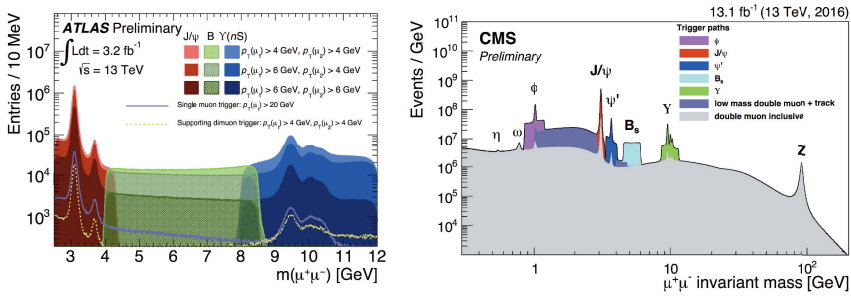


Figure 1 – Di-muon mass spectra showing the collected data under ATLAS (left) and CMS (right) with various trigger configurations[1,2]

meson. The ATLAS values are:

$$\rho_X < 1.5\% \text{ at } 95\% \text{ CL for } p_T(B_s^0) > 10\text{GeV}$$

$$\rho_X < 1.6\% \text{ at } 95\% \text{ CL for } p_T(B_s^0) > 15\text{GeV}$$

The CMS values are:

$$\rho_X < 1.1\% \text{ at } 95\% \text{ CL for } p_T(B_s^0) > 10\text{GeV}$$

$$\rho_X < 1.0\% \text{ at } 95\% \text{ CL for } p_T(B_s^0) > 15\text{GeV}$$

## 3 $B^0 \to K^{*0}\mu^+\mu^-$ Angular Analysis

The $B^0 \to K^{*0}(\to K^+\pi^-)\mu^+\mu^-$ decay proceeds through flavour-changing neutral current exchange. The process can be fully described by the three angles $(\theta_l, \theta_k, \phi)$ and the di-muon invariant mass squared, $q^2$. New physics entering the loop can be detected by analysing the angular distributions of the decay. The angular parameters $P$ and $P'$ observables are less sensitive to theoretical uncertainties at leading order. ATLAS and CMS measured the distributions of the $P_1$ and $P_i'$ angular parameters using $\approx 20$/fb of 8 TeV pp data taken in 2012.

The flavour of the $B^0$ is difficult to determine with high purity, since neither experiment has good particle identification for hadrons. The ATLAS [7] sample is estimated to have a mistag fraction of $\approx 10\%$ as determined from Monte Carlo samples. CMS [8] estimates a mistag fraction of $\approx 14\%$ determined from a data fit. The ATLAS dataset contains 340 events and is fit into three bins. CMS fits 1400 events into seven bins. Both experiments fold the signal PDF using its symmetries to reduce the number of free parameters and improve the fit convergence. ATLAS extracts $P_1$ and $P_i'$ $(i = 4, 5, 6, 8)$ parameters. The S-wave component (non-resonant $K\pi$) is neglected and included as a systematic. CMS extracts $P_1$ and $P_5'$ but includes the S-wave component. A plot from CMS comparing their results to models and other experiments can be seen in figure 3. More distributions can be found in the original papers [7,8].

## 4 Measurement of $b$ hadron lifetimes in $pp$ collisions at $\sqrt{s} = 8$ TeV

CMS measured the lifetimes of the $B^0$, $B_s^0$, $\Lambda_b^0$ and $B_c^+$ hadrons using the decays channels $B^0 \to J/\psi K^{*0}(892)$, $B^0 \to J/\psi K_s^0$, $B_s^0 \to J/\psi\pi^+\pi^-$, $B_s^0 \to J/\psi\phi(1020)$, $\Lambda_b^0 \to J/\psi\Lambda^0$ and $B_c \to J/\psi\pi^+$ using a sample of proton-proton collisions at $\sqrt{s} = 8$ TeV. The results are summarised in table 1.

The precision from each channel is as good as or better than previous measurements in the respective channel. The $B_s^0$ lifetime results are used to obtain the lifetimes of the heavy and

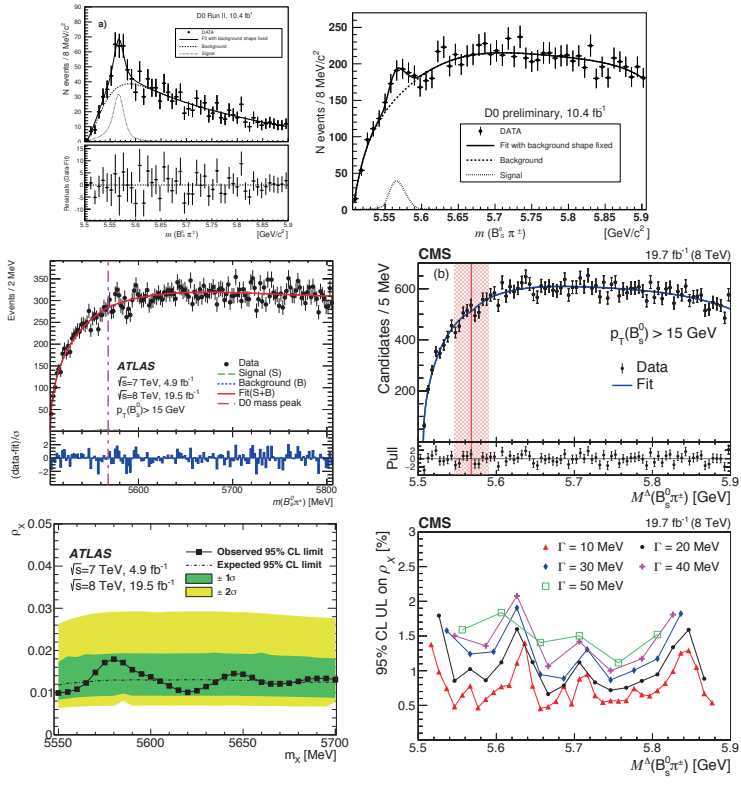


Figure 2 – The top two plots show the evidence of the $X(5568)$ state found by $D\emptyset$ via $B_s^0 \to J/\psi\phi$ and the semi-leptonic decay: $X^\pm(5568) \to B_s^0\pi^\pm$ [3,4]. The middle plots show the $B_s\pi^\pm$ mass spectrum made from the ATLAS [5] (left) and CMS [6] (right) datasets. The bottom plots show the $\rho_X$ limits for the mass spectrum for the ATLAS [5] and CMS [6] datasets respectively.

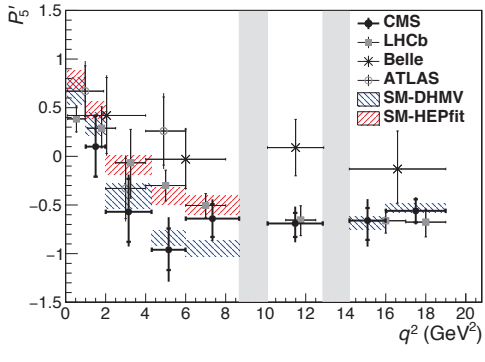


Figure 3 – Measured values of $P_5'$ versus $q^2$ for $B^0 \to K^{*0}\mu^+\mu^-$ compared with theoretical models and other experiments. The statistical uncertainty is shown by the inner vertical bars, while the outer vertical bars give the total uncertainty. The horizontal bars show the bin widths. The vertical shaded regions correspond to the $J/\psi$ and $\psi'$ resonances [8].

Table 1: Summary of the measured lifetimes from CMS [9]

| Channel | Proper decay length ($c\tau$) |
|---|---|
| $B^0 \to J/\psi K^{*0}(892)$ | $453.0 \pm 1.6$ (stat) $\pm 1.5$ (syst) $\mu$m |
| $B^0 \to J/\psi K^0_s$ | $457.8 \pm 2.7$(stat) $\pm 2.7$ (syst)$\mu$m |
| $B^0$ combined | $454.1 \pm 1.4$ (stat) $\pm 1.3$ (syst) $\mu$m |
| $B^0_s \to J/\psi \pi^+\pi^-$ | $502.7 \pm 10.2$ (stat) $\pm 3.2$ (syst) $\mu$m |
| $B^0_s \to J/\psi \phi(1020)$ | $443.9 \pm 2.0$ (stat) $\pm 1.2$ (syst) $\mu$m |
| $\Lambda^0_b \to J/\psi \Lambda^0$ | $442.9 \pm 8.2$ (stat) $\pm 2.7$ (syst) $\mu$m |
| $B_c \to J/\psi \pi^+$ W.R.T. $B^+$ | $162.3 \pm 8.2$ (stat) $\pm 4.7$ (syst) $\pm 0.1(\tau B^+)$ $\mu$m |

light $B^0_s$ mass eigenstates. The precision of the $\Lambda^0_b$ lifetime measurement is also as good as any previous measurement in the $J/\psi\Lambda^0$ channel. The measurement of the $B^+_c$ meson lifetime finds a longer lifetime than measured at the Tevatron experiments [11,12,13], this agrees with results from LHCb [14,15]. All measured lifetimes are compatible with the current world-average values.

## 5 Observation of the decay $Z \to \psi(\ell^+\ell^-)$

CMS [10] made public an observation of the $Z$ boson rare decay to a $\psi$ meson and two oppositely charged same-flavour leptons, $\ell^+\ell^-$, where $\psi$ represents the sum of $J/\psi$ and $\psi(2S) \to J/\psi X$, and $\ell = \mu, e$. The analysis is using a sample of proton-proton collisions at $\sqrt{s} = 13$ TeV with an integrated luminosity of 35.9 fb$^{-1}$. The signal is observed with a significance in excess of 5 standard deviations. Removing contributions from $\psi(2S)$ decays to $J/\psi$, the signal is interpreted as being entirely from $Z \to J/\psi\ell^+\ell^-$, with fiducial branching fraction relative to that of the decay $Z \to \mu^+\mu^-\mu^+\mu^-$ measured to be:

$$\frac{\mathcal{B}(Z \to J/\psi\ell^+\ell^-)}{\mathcal{B}(Z \to \mu^+\mu^-\mu^+\mu^-} = 0.70 \pm 0.18(\text{stat}) \pm 0.05(\text{syst})$$

This result is obtained with the assumption of no $J/\psi$ polarisation. Extreme polarisation scenarios give a variation of the fiducial branching fraction measurement of $(-22$ to $+24)\%$.

## References


1. ATLAS Collaboration, *JINST 3* (2008) S08003
2. CMS Collaboration, *JINST 3* (2008) S08004
3. D$\emptyset$ Collaboration, Phys. Rev. Lett. 117, 022003 (2016)
4. D$\emptyset$ Collaboration, arXiv:1712.10176
5. ATLAS Collaboration, arXiv:1802.01840
6. CMS Collaboration, PRL 120 (2018) 202005
7. ATLAS Collaboration, ATLAS-CONF-2017-023
8. CMS Collaboration, arXiv:1710.02846
9. CMS Collaboration, arXiv:1710.08949
10. CMS Collaboration, CMS-PAS-BPH-16-001
11. CDF Collaboration,Phys. Rev. Lett. 97 (2006) 012002
12. D$\emptyset$ Collaboration, Phys. Rev. Lett. 102 (2009) 092001
13. CDF Collaboration, Phys. Rev. D 87 (2013) 011101
14. LHCb, Eur. Phys. J. C 74 (2014) 2839
15. LHCb, Phys. Lett. B 742 (2015) 29

## Recent LHCb measurements of $CP$ violation and mixing in beauty and charm

G. Tellarini
*Istituto Nazionale Fisica Nucleare, Sezione di Ferrara,*
*via Saragat 1, Ferrara 44100, Italy*

This document reports an ensemble of recent LHCb measurements of $CP$ violation in different $b$-hadron decays. Recent studies of $CP$ violation in the charm sector and of $D^0$-$\bar{D}^0$ mixing are also presented.

The measurements described in the following are performed using the full Run 1 data sample, corresponding to an integrated luminosity of 3fb$^{-1}$ at $\sqrt{s}$= 7 and 8 TeV. Some measurements also exploit a fraction of Run 2 data corresponding to 2 fb$^{-1}$ collected at $\sqrt{s}$=13 TeV.

### 1 $CP$ Violation measurements to determine the Unitary Triangle angle $\gamma$

Precise knowledge of Unitary Triangle (UT) parameters from Standard Model (SM) processes is crucial to highlight possible New Physics (NP) effects in decays where loop topologies contribute. A SM benchmark is the UT angle $\gamma = arg(-\frac{V_{ub}^* V_{ud}}{V_{cb}^* V_{cd}})$, which can be measured in a quite wide ensemble of $B \to Dh$ tree-level decays ($h$=$\pi$,K). Among the UT angles, $\gamma$ is currently the least well measured. The current world average, $\gamma = (73.5^{+4.3}_{-5.0})^\circ$ [2], is the combination of several measurements of different $B^+$, $B^0$ and $B_s^0$ tree-level decays involving the $b \to u$ and $b \to c$ quark transitions from different experiments including LHCb which dominates the average ($\gamma = (76.8^{+5.1}_{-5.7})^\circ$ [3]).

**$CP$ violation in $B^\pm \to D^{(*)}h^\pm$ and $B^\pm \to DK^*$ decays** is related to the UT angle $\gamma$. Recent analyses of $B^\pm \to D^{(*)}h^\pm$ [4] and $B^\pm \to DK^*$ [6] exploit also the 2fb$^{-1}$ of Run 2 and consider additional decay modes with respect to the previous results on Run 1 data [5 7]. The $CP$ violation in the partially-reconstructed decay mode $B^\pm \to D^{(*)}h^\pm$, $D^* \to D\pi^0(\gamma)$ is observed at 4.3$\sigma$ level. In the $B^\pm \to DK^*$ analysis the 4-body $D$ meson decays ($D \to K^\mp\pi^\pm\pi^+\pi^-$, $\pi^-\pi^+\pi^-\pi^+$) are exploited in addition to the 2-body $D$ meson decays.

**$CP$ violation in $B_s^0 \to D_s^\pm K^\mp$** decays is measured by means of a time-dependent analysis [8] of the decay rates

$$\frac{d\Gamma_{B(\overline{B})\to f}(t)}{dt} \propto \frac{e^{-\Gamma_s t}}{2}\left(\cosh\left(\frac{\Delta\Gamma_s}{2}t\right) + A_f^{\Delta\Gamma}\sinh\left(\frac{\Delta\Gamma_s}{2}t\right) \pm C_f\cos\left(\Delta m_s t\right) \mp S_f\sin\left(\Delta m_s t\right)\right) \tag{1}$$

which depend on the $CP$ observables:

$$C_f = \frac{1-r_B^2}{1+r_B^2}, S_{f(\bar{f})} = \pm\frac{2r_B\sin(\delta_B \mp (\gamma - 2\beta_s))}{1+r_B^2}, A_{f(\bar{f})}^{\Delta\Gamma} = \frac{-2r_B\cos(\delta_B \mp (\gamma - 2\beta_s))}{1+r_B^2}, \tag{2}$$

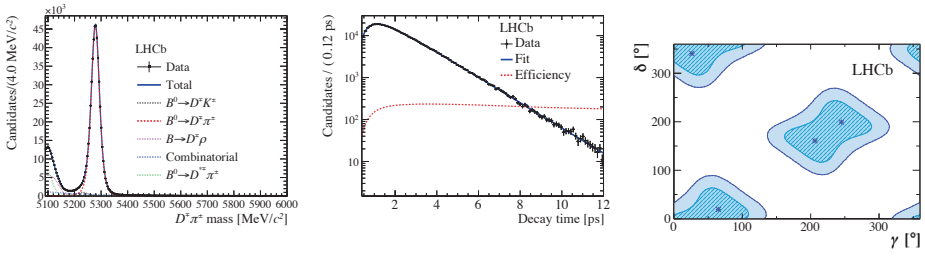


Figure 1 – Left: fit to the $B^0$ invariant mass distribution of selected $B^0 \to D^\mp \pi^\pm$ candidates, including signal and background. Middle: fit to the decay-time distribution of the signal candidates. Right: contour plot for $\delta_B$ and $\gamma$ shown at 39% and 87% CL.

where the dependence on the ratio of magnitudes $r_B$ and the strong phase difference $\delta_B$ of the amplitudes between the $b \to c$ and $b \to u$ transitions, the weak mixing phase $\beta_s$ and the weak phase $\gamma$ is shown. The results are: $C_f = 0.73 \pm 0.14 \pm 0.05$, $A_f^{\Delta\Gamma} = 0.39 \pm 0.28 \pm 0.15$, $A_{\bar{f}}^{\Delta\Gamma} = 0.31 \pm 0.28 \pm 0.15$, $S_f = -0.52 \pm 0.20 \pm 0.07$ and $S_{\bar{f}} = -0.49 \pm 0.20 \pm 0.07$. Assuming the absence of penguin pollution, $-2\beta_s = \phi_s$ and taking the value of $\phi_s$ from the world-average value the physics parameters are obtained: $\gamma = (128\,^{+17}_{-22})^\circ$, $\delta_B = (358\,^{+13}_{-14})^\circ$ and $r_B = 0.37\,^{+0.10}_{-0.09}$ where the values of $\gamma$ and $\delta_B$ are expressed modulo 180°. Evidence for $CP$ violation is seen at the $3.8\sigma$ level.

**$CP$ violation in $B^0 \to D^\mp \pi^\pm$** [9] decays is measured for the first time at a hadron collider. In this decay mode, the sensitivity to the angle $\gamma$ is limited by the small value of $r_B$ ($\sim$0.01) but compensated by the huge statistics already collected in Run 1 and the small background contamination. Since $\Delta\Gamma = 0$, the $CP$ observables are $C_f$, $S_f$ and $S_{\bar{f}}$. In addition second-order terms in $r_B$ are neglected, thus it is assumed $C_f = C_{\bar{f}} = 0$. Figure 1 (left) shows the fit to the $B^0$ invariant mass distribution and (centre) the decay-time fit to the signal candidates. Using as external input $r_B$ [11, 10] and $\beta$ [2] constraints on $\gamma$ and $\delta_B$ are extracted and shown in Fig.1 on the right.

## 2 $CP$ violation in charmless $B^0$ and $B_s^0$ decays

Charmless $B^0$ and $B_s^0$ decays to $CP$ eigenstates receives contributions from tree, penguin and $B_{(s)}^0$ mixing topologies. $CP$ violation measurements in these decays might reveal the presence of NP once compared with SM benchmarks. In particular, under specific assumptions, these decays are sensitive to the weak phase $\gamma$. A time-dependent analysis of $B^0 \to \pi^+\pi^-$, $B_s^0 \to K^+K^-$ and $B_{(s)}^0 \to K^+\pi^-(\pi^+K^-)$ decays is performed [12]. The results exploiting Run 1 data are reported in Tab. 1. The $CP$ observables $C_{\pi\pi}$ and $S_{\pi\pi}$ are the most precise measurements to date from a single experiment. The evidence of $CP$ violation in the $B_s^0 \to K^+K^-$ decay corresponds to $4\sigma$ and supersedes the previous LHCb result [13].

Table 1: $CP$ observables and asymmetries reported for $B^0 \to \pi^+\pi^-$, $B_s^0 \to K^+K^-$ and $B_{(s)}^0 \to K^+\pi^-(\pi^+K^-)$ decays. The measured signal yield ($N_{sig}$) is quoted for each decay.

| Parameter | | $N_{sig}$ | Parameter | | $N_{sig}$ |
|---|---|---|---|---|---|
| $C_{\pi\pi}$ | $-0.34 \pm 0.06 \pm 0.01$ | 28650 ± 230 | $C_{KK}$ | $0.20 \pm 0.06 \pm 0.02$ | 36840 ± 220 |
| $S_{\pi\pi}$ | $-0.63 \pm 0.05 \pm 0.01$ | | $S_{KK}$ | $0.18 \pm 0.06 \pm 0.02$ | |
| $A_{CP}^{B^0 \to K\pi}$ | $-0.084 \pm 0.004 \pm 0.003$ | 94220 ± 340 | $A_{KK}^{\Delta\Gamma}$ | $-0.79 \pm 0.07 \pm 0.10$ | |
| $A_{CP}^{B_s^0 \to \pi K}$ | $0.213 \pm 0.015 \pm 0.007$ | 7030 ± 120 | | | |

## 3 $CP$ violation in $b$-baryons decays

First evidence of $CP$ violation in $b$-baryon decays has been observed at $3.3\sigma$ level by LHCb in $\Lambda_b^0 \to p\pi^-\pi^+\pi^-$ decays[15]. A recent search is performed using $\Lambda_b^0 \to pK^-\pi^+\pi^-$, $\Lambda_b^0 \to pK^-K^+K^-$ and $\Xi_b^0 \to p\pi^+K^-K^+$ decays exploiting the Run 1 data[14]. Triple products of final state particle momenta are used to define the $CP$ and $P$ asymmetries which are measured in the whole and certain phase-space regions. Both approaches return results compatible with the hypotheses of $CP$ and $P$ conservations, as shown in Fig.2.

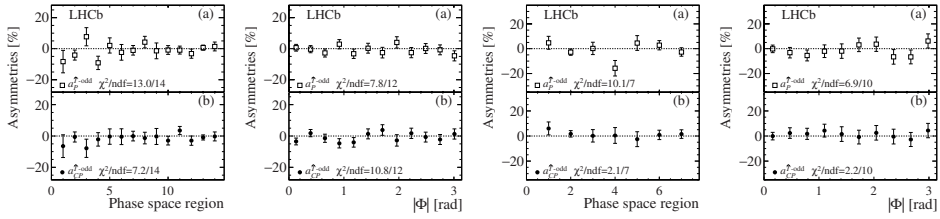


Figure 2 – $CP$ and $P$ asymmetries in different regions of the phase space of (left) $\Lambda_b^0 \to pK^-\pi^+\pi^-$ and (right) $\Lambda_b^0 \to pK^-K^+K^-$ decays.

## 4 $CP$ violation measurement in $B_s^0 \to \phi\phi$ decays

The $B_s^0 \to \phi\phi$ decay is forbidden at tree-level and proceeds by $b \to s\bar{s}s$ penguin transitions. The weak mixing phase $\phi_s^{s\bar{s}s}$ can reveal NP once compared with the $\phi_s^{c\bar{c}s}$ measurement. The results of the time-dependent angular analysis using the Run 1 and Run 2 data [16] give $\phi_s^{s\bar{s}s} = -0.07 \pm 0.13 \pm 0.03$ rad and $|\lambda| = 1.02 \pm 0.05 \pm 0.03$ superseding the previous measurement using data sample collected in Run 1 [17]. No evidence of $CP$ violation is found.

## 5 $CP$ violation measurement in $B^+ \to D_{(s)}^+ \bar{D}^0$ decays

$CP$ violation measurements are also performed using doubly-charmed $B^+ \to D_{(s)}^+ \bar{D}^0$ decay modes, where $\bar{D}^0 \to K^+\pi^-, K^+\pi^-\pi^+\pi^-, D^+ \to K^+K^-\pi^+$ and $D_s^+ \to K^+K^-\pi^+$, [18] using Run 1 data. The $B^+$-$B^-$ asymmetry is measured through the fit to the $\mathrm{m}(D_{(s)}^+\bar{D}^0)$ invariant mass and subtracting the production and detection asymmetries the $CP$ asymmetries are determined: $A_{CP}(B^+ \to D_s^+\bar{D}^0) = (-0.4 \pm 0.5 \pm 0.5)\%$ representing the first measurement in this decay and $A_{CP}(B^+ \to D^+\bar{D}^0) = (2.3 \pm 2.7 \pm 0.4)\%$ representing the most precise measurement to date. In both decays the results are compatible with $CP$ symmetry given the current sensitivity.

## 6 $CP$ violation in the charm sector

**$CP$ violation in $\Lambda_c^+$ three-body decays** So far there is no evidence of $CP$ violation in the charm sector. A recent LHCb analysis exploiting the Run 1 data [19], searches for $CP$ violation measuring the difference of $CP$ asymmetries, $\Delta A_{CP} = A_{CP}^{pKK} - A_{CP}^{p\pi\pi} \approx A_{raw}^{pKK} - A_{raw}^{p\pi\pi}$, between the $\Lambda_c \to pK^-K^+$ and $\Lambda_c \to p\pi^-\pi^+$ decays which is independent on the production and detection asymmetries. The result, $\Delta A_{CP} = (0.30 \pm 0.91 \pm 0.61)\%$, is compatible with the hypothesis of $CP$ symmetry. This analysis represents the first search of $CP$ violation in three-body $\Lambda_c^+$ decays.

**$D^0$ mixing** Using the Run 1 and Run 2 data the $D^0$ mixing parameters $y'$ and $x'^2$ are measured through the fit to the decay-time dependent ratio of $D^0 \to K^+\pi^-$ and $D^0 \to K^-\pi^+$ decays and

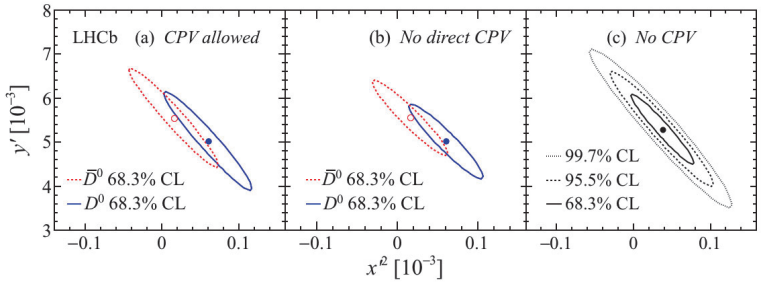


Figure 3 – Mixing parameters fit where the data points are interpreted under three different hypothesis.

of the corresponding charge conjugate decays. The result for the $D^0$ mixing parameters, as shown in Fig.3, are interpreted under three different hypotheses: $CP$ violation allowed, no direct $CP$ violation and no $CP$ violation. The overall picture is compatible with the hypothesis of $CP$ symmetry and this measurement provides the most stringent bounds on the $CP$ violation parameters from a single experiment.

## 7 Summary

The most recent LHCb measurements contributing to improve the knowledge of the UT angle $\gamma$ in tree-level decays are described. Other measurements from LHCb involving loop and baryon decays have been shown. LHCb is also providing new measurements of the $\phi_s$ phase exploiting different $B_s^0$ decays. Concerning the charm sector, LHCb is contributing to the search of $CP$ violation in charm hadron decays and to improve the measurements of the charm mixing parameters.

## References


1. Brod, J. & Zupan, JHEP **01**, 051 (2014).
2. HFLAV Collaboration, arXiv:1612.07233, updates online.
3. LHCb Collaboration, LHCb-CONF-2017-004.
4. LHCb Collaboration, PLB **777**, 16-30 (2018).
5. LHCb Collaboration, PLB **760**, 117 (2016).
6. LHCb Collaboration, JHEP **11**, 156 (2017).
7. LHCb Collaboration, PRD **90**, 112002 (2014).
8. LHCb Collaboration, JHEP **03**, 059 (2018).
9. LHCb Collaboration, arXiv:1805.03448.
10. Babar Collaboration, PRD **78**, 032005 (2008).
11. Belle Collaboration, PRD **82**, 051103 (2010).
12. LHCb Collaboration, LHCb-PAPER-2018-006.
13. LHCb Collaboration, JHEP **10**, 183 (2013).
14. LHCb Collaboration, LHCb-PAPER-2018-001.
15. LHCb Collaboration, NP **13**, 391-396 (2017).
16. LHCb Collaboration, LHCb-CONF-2018-001.
17. LHCb Collaboration, PRD **90**, 052011 (2014)
18. LHCb Collaboration, arXiv:1803.10990.
19. LHCb Collaboration, arXiv:1712.07051.
20. LHCb Collaboration, PRD **97**, 031101 (2018).

# Status and prospects of Belle II at SuperKEKB

I.Komarov on behalf of Belle II collaboration
*Deutsches Elektronen-Synchrotron (DESY),*
*Notkestrasse 85, Hamburg, Germany*

The Belle II experiment at SuperKEKB accelerator has started collecting the first data from $e^+e^-$ collisions. The dataset collected this year will be used for detector studies that will be coupled with physics analyses, such as searches for the dark photon. In 2019, Belle II commissioning will enter the final phase and detector will start data taking with gradually increasing instantaneous luminosity. In this talk, we review some of the key Belle II features and analysis techniques together with their applications. Using the Full Event Interpretation algorithm, by 2021 Belle II will be able to improve world average measurement of $\mathcal{R}(D^{(*)})$ by a factor of 2. Around the same time, high sensitivity to time-dependent $CP$ Violation measurements will allow to improve $b \to qqs$ results by a factor of 2. Belle II has an ambitious programme in $\tau$ physics, aiming to move down the upper limit of the rate of Charged Lepton Flavour Violating $\tau$ decays by an order of magnitude. Belle II has an unique reach for many heavy quarkonia measurements, such as energy scans of $e^+e^-$ collisions at energies above open flavour limit that will reveal the structure of heavy bottomonium-like resonances.

## 1 Belle II experiment at SuperKEKB

The Belle II experiment [1] is a $4\pi$ detector collecting data in $e^+e^-$ collisions produced by the SuperKEKB accelerator located in Tsukuba, Japan. While the SuperKEKB accelerator utilizes the tunnels of its predecessor, the KEKB accelerator, and will reuse some of KEKBs components, it is a new machine otherwise, designed to operate with double the beam current. Focusing magnets of the SuperKEKB will ensure a beam width of $\sim 50$ nm at the point of bunch crossing, which is 20 times smaller than that of KEKB. Higher beam current and more compact interaction region will allow for instantaneous luminosity of $8.0 \times 10^{35}\text{cm}^{-2}\text{s}^{-1}$, 40 times higher than KEKB.

Belle II inherits the design of the Belle detector with major improvements in all of the subsystems. The Belle II interaction point is surrounded by the vertex detector that will provide precise measurements of charged-particle production vertices with a resolution that improves upon that of Belle by a factor of two. The vertex detector is surrounded by the central drift chamber (CDC), which is used for the track reconstruction. The aerogel Cherenkov counters and time-of-propagation counters, in conjunction with the CDC, provide particle identification.

The technology used in Belle II is expected to improve significantly $\pi$ and $K$ separation. Electromagnetic showers are detected by an array of CsI(Tl) crystals located inside the solenoid coil. The outermost layer of the detector is composed of 14 iron layers alternating with scintillators and serves for $K_L$ and $\mu$ detection.

SuperKEKB and Belle II are in the Phase II of commissioning now. The detector is currently recording collisions at $\Upsilon(4S)$ energy and low instantaneous luminosity with the BEAST II detector installed in place of the vertex detector. BEAST II contains a slice of the vertex detector and radiation monitors used in beam background studies [2]. Alongside tuning of the detector and accelerator, Belle II will collect 20fb$^{-1}$ of data. Later this year, BEAST II will be replaced by the vertex detector and Belle II will start Phase III of data taking in 2019.

## 2 Physics at Phase II

The Belle II hardware trigger (L1 trigger) consists of orthogonal trigger lines that generate trigger decisions based on outputs from different subdetector-systems. These lines trigger on a variety of elementary signatures, in particular on high-energy clusters in ECL and back-to-back muon tracks. In Phase III, the outputs of the L1 will be processed by the high-level trigger (HLT) that will be tuned for B-physics. During the Phase II, the lower instantaneous luminosity allows for operations without HLT, that means that a large number of low-multiplicity events will be recorded which will open the path for physically-significant and unique measurements.

### *2.1 Dark Photon*

Cosmological observations suggest the existence of dark matter (DM) [3], but this is yet to be directly observed in laboratories. One of the minimal DM scenario implies that the portal to the DM sector, the dark photon, can be produced directly in $e^+e^-$ collisions together with an initial state radiation photon. Such a process will have very clean signature: single photon in the detector and recoil mass distribution for this process will peak on the mass of the dark photon. The main backgrounds of this measurement are $e^+e^-(\gamma)$ and $\gamma\gamma(\gamma)$ with all particles but a single $\gamma$ escape the detection. These backgrounds can be constrained by a thorough study of ECL blind spots, which will be an important part of the detector commissioning. Search for the single photon at the Phase II will allow reducing the current upper limit on the dark photons strength of kinetic mixing [4] for dark photons below 1 GeV/$c^2$ by a factor of two.

## 3 Physics at Phase III: some of the key techniques, features and measurements

### *3.1 Full event interpretation and $\mathcal{R}(D^{(*)})$*

Belle II is expected to gather 50ab$^{-1}$ of data in $e^+e^-$ collisions by 2025. This dataset will be used for a plethora of measurements covering a vast variety of phenomena, from precise measurements of CKM parameters to direct searches of beyond the Standard Model objects [5]. One of the unique features of the Belle II experiment (with respect to the existing collider experiments) is a possibility of full event interpretation. At Belle II, $B$-mesons are produced in pairs during the decay of the $\Upsilon(4S)$. If one of the $B$-mesons ("tag" meson) decays to the fully-reconstructible final state, and another ("signal" meson) decays to the final state with missing energy, it is possible to constrain the lost momentum using known 4-momentum of initial state and reconstructed 4-momenta:

$$p_{miss} = (p_{beam} - p_{tag} - p_{signal}). \quad (1)$$

Full event interpretation is crucial for analyses of B decays with neutrinos in the final state. The most intriguing analyses of this kind are the measurements of $\mathcal{R}(D)$ and $\mathcal{R}(D^*)$ variables

defined as

$$\mathcal{R}(D^{(*)}) = \frac{\mathcal{B}(B \to D^{(*)}\tau\nu_\tau)}{\mathcal{B}(B \to D^{(*)}l\nu_l)},\ l = e,\ \mu \tag{2}$$

since their current values show $4\sigma$ tension with their SM predictions. Signal ($B \to D^{(*)}\tau\nu_\tau$), normalisation ($B \to D^{(*)}l\nu_l$) and background decay candidates populate different areas in the signal lepton momentum versus invariant mass of the missed energy (squared 4-vector of the missed momentum) phase space. Using a two-dimensional fit of this plane, Belle II will reach current world average precision with only $5\text{ab}^{-1}$ of data.

### *3.2 Time dependent CP violation measurements*

Another strong side of B-factories are measurements of the time dependent $CP$ violation in $B^0$ decays. Here, the tag meson decaying to the flavour eigenstate is partially reconstructed to define a decay vertex. The signal meson is fully reconstructed and the decay time information $\Delta t$ is obtained from the known boost and the distance between the two vertices along the $z$-axis. Reduced boost of the Belle II experiment with respect to its predecessor is compensated by increased vertex resolution, yielding a 20% better $\Delta t$ resolution.

Amplitude of time-dependent $CP$ asymmetry in $b \to ccs$ decays gives direct input to measurements of the CKM angle $\phi_1$, but it is also interesting to measure corrections to the amplitude in penguin-dominated $b \to qqs$, $(q = u, d, s)$ decays. $B \to \eta' K^0$ is a particularly promising channel of this kind since it is has among the strictest QCD predictions $\Delta S^{QCDF} = 0.01 \pm 0.01$ [6] that are far more precise than results of the current measurements $\Delta S^{Data} = -0.05 \pm 0.06$ [7]. Signal decay candidate in this analyses is reconstructed from several final states, most of them containing multiple neutral particles. Due to the low track multiplicity in the event, Belle II can effectively handle such cases (compared to hadron machine experiments). This, together with the good sensitivity to the time-dependent $CP$ violation phenomena, will allow Belle II measurement of $\Delta S$ in $B \to \eta' K^0$ decays with $5\text{ab}^{-1}$ to be twice as precise as the current world average.

### *3.3 $\tau$ at Belle II*

Belle II is not only a B-factory, but also a $\tau$ factory: $e^+e^-$ collisions produce almost equal amounts of prompt $\tau^+\tau^-$ and $b\bar{b}$ pairs, so by the end of data taking Belle II is expected to have recorded 45 billion of $e^+e^- \to \tau^+\tau^-$ events. This dataset will be sufficient to put many world-best constraints on branching fractions of charged lepton flavour violating decays. Belle II will be able to put an upper limit of $Br(\tau \to \mu\gamma)$ to $10^{-9}$, testing several non-SM scenarios by way of this [8, 9].

### *3.4 Out of the resonance*

Most of the time Belle II will collect data from $e^+e^-$ collisions at $\Upsilon(4S)$ energy, but a few percent of the dataset will be collected away from the $4S$ resonance, in its vicinity. Energy scans above $b\bar{b}$ threshold will allow to perform production cross-section measurements for $h_b(nP)\pi\pi$, $\Upsilon(nS)\pi\pi$ and $B^{(*)}_{(s)}\bar{B}^{(*)}_{(s)}$ final states. These cross-sections are crucial to understand the inner structure of bottomonium-like hadrons.

## 4 Conclusion

At 0:38 am (GMT+09:00), April 26, 2018, Belle II has recorded and reconstructed the first hadronic event in $e^+e^-$ collisions (see Figure 1). The data taking with low luminosity will continue until June 2018 and the collected data will be used for beam background studies,

detector calibration and an early physics program. The data taking will resume in 2019 with gradual increase of the instantaneous luminosity and by 2025, Belle II is expected to collect 50ab$^{-1}$ of data in $e^+e^-$ collisions. This dataset will allow for addressing many of the hottest topics in flavour physics and perform a set of unique searches beyond the Standard Model.

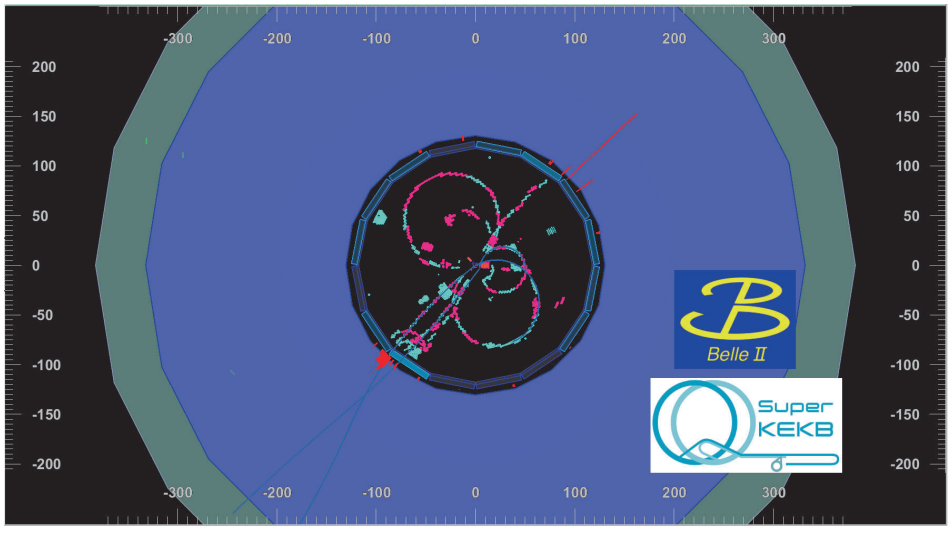


Figure 1 – Event display of the first hadronic event recorded and reconstructed at Belle II

## References


1. T. Abe *et al.*, arXiv:1011.0352.
2. P.M.Lewis *et al.*, arXiv:1802.01366.
3. P.A.R.Ade *et al.*(Planck Collaboration), Astron. Astrophys. **594**, A13 (2016).
4. J.P.Lees on behalf of the BaBar Collaboration, *Phys. Rev. Lett.* **119**, 131804 (2017).
5. E. Kou, P. Urquijo, The Belle II collaboration, and The B2TiP theory community, *In preparation.*
6. M. Beneke,Phys. Lett. **B620**, 143150 (2005).
7. Y. Amhis *et al.* (HFLAV),Eur.Phys.J. **C7712**, 895 (2017).
8. G. Cvetič, C. Dib, C. S. Kim, and J. D. Kim,*Phys. Rev.* D **66**, 034008 (2002).
9. C. Yue, Y. Zhang, L. Liu,Phys.Lett. **B547**, 252-256 (2002).

# Right-handed Currents Searches and Parity Doubling

James Gratrex and Roman Zwicky
*Higgs Centre for Theoretical Physics, School of Physics and Astronomy, University of Edinburgh, Edinburgh EH9 3JZ, Scotland*

The extraction of right-handed currents, beyond the Standard Model, faces theoretical challenges from long-distance contributions. We show that these effects can be controlled by combining, for example, studies of $B \to V(1^-)\gamma$ and $B \to A(1^+)\gamma$ observables. The sum of the long-distance contributions can be extracted without compromise, and the individual pieces follow from a ratio predicted by theory. This leads to significant reduction in the uncertainty of long-distance contributions. The ideas extend to charm decays and the low $q^2$-region of $B \to V\ell\bar{\ell}$, and open the prospect of checking input affecting the angular $B \to K^*\mu\mu$-anomaly.

## 1 Introduction

The Standard Model (SM) is a highly successful, yet peculiar, theory. One of its peculiarities is that the weak interactions are of the V-A type. It is intuitively clear that this leaves traces in the polarisation (or the angular distribution) of weak decays. Such traces would be perfect probes for right-handed currents (RHC) searches were it not for non-perturbative effects of QCD diluting the purity of the signal.

A particularly good setting to test the chirality of interactions is when there is a photon in the final state, as the photon helicity is then in direct correspondence with the handedness of the interaction. In particular, in the limit of no (quark) masses, chirality and handedness are the same. For example, the QED interaction reads $\bar{q}\not{A}q = \bar{q}_L\not{A}q_L + \bar{q}_R\not{A}q_R$. Thus, the reaction $\bar{q}_L + q_L \to \gamma_L$ is an on-shell process where the two half-helicities of the quarks add up to match the $\pm 1$ helicity of the photon (termed left- and right-handed respectively). If the interactions were chiral, $H^{\rm int} \sim \bar{q}_L\not{A}q_L$, then the resulting photon polarisation would always be left-handed. Denoting the amplitude of left- and right-handed photons by $\mathcal{A}_{L,R}$ respectively, this reads $\mathcal{A}_R/\mathcal{A}_L = 0$.

Such transitions are not present in the flavour-changing neutral currents (FCNCs) in the SM. The next best possibility is to couple the photon to two quarks of opposite chirality in a directly gauge-invariant way, at the expense of a quark mass term. This is realised by the so-called electric dipole operator (known as the $O_7^{(\prime)}$-term in the effective Hamiltonian)

$$H^{\rm eff} \supset C_7^{(\prime)} O_7^{(\prime)} \sim m_b(m_s)\bar{s}_{L(R)}\sigma_{\mu\nu}F^{\mu\nu}b_{R(L)} \,, \tag{1}$$

where $F^{\mu\nu}$ is the photon field strength tensor. The concrete appearance of $m_b(m_s)$ can be understood from a spurion analysis [1]. The dimension-six effective Hamiltonian is written as $H^{eff}_{b\to s\gamma/\ell\bar{\ell}} \sim C\bar{s}_L\Gamma b O_r + C'\bar{s}_R\Gamma b O_r$, with flavour-neutral $O_r$ and $C'/C|_{SM} \ll 1$ similar to $C_7'/C_7|_{SM} = m_s/m_b$. This hierarchy, and therefore RHC searches, is affected by the non-perturbative QCD matrix elements

$$\mathcal{A}_{\mathbb{1}(5)} = \langle X_s\gamma^*|\bar{s}(\gamma_5)\Gamma b O_r|B\rangle \,. \tag{2}$$

More concretely, one of the simplest processes testing the helicity is the $B \to V\gamma$ decay, where $V$ is a $J = 1$ vector meson. The amplitude of left- and right-handed polarised photon is then given by

$$\mathcal{A}_{R(L)} \sim C(\mathcal{A}_{\mathbb{1}} \mp \mathcal{A}_{\mathbb{5}}) + C'(\mathcal{A}_{\mathbb{1}} \pm \mathcal{A}_{\mathbb{5}}) \,, \tag{3}$$

making the link between chirality and photon polarisation explicit. In that case, the algebraic relation $\sigma^{\alpha\beta}\gamma_5 = -\frac{i}{2}\epsilon^{\alpha\beta\gamma\delta}\sigma_{\gamma\delta}$, does miracles, $\mathcal{A}_{\mathbb{1}}/\mathcal{A}_{\mathbb{5}}|_{O_7,O_7'} = T_1(0)/T_2(0) = 1$, on the level of the dipole operator as it enforces the form factor relation $T_1(0) = T_2(0)$, see Ref. [2] for example. This then results in

$$\frac{\mathcal{A}_R}{\mathcal{A}_L}\Big|_{O_7,O_7'} = \frac{m_s}{m_b} \equiv \hat{m}_s \ . \tag{4}$$

Beyond the SM (BSM) shifts to $O_7'$, of the form $\hat{m}_s \to \hat{m}_s + \Delta_{\rm RHC}$, are what we refer to as RHC in this context. As hinted at, long-distance (LD) contributions $\epsilon_{L,R}$ dilute the purity of the signal. Schematically,

$$\frac{\mathcal{A}_R}{\mathcal{A}_L}\Big|_{B\to V\gamma} = \frac{\epsilon_R + \hat{m}_s + \Delta_{\rm RHC}}{1+\epsilon_L} \simeq \epsilon_R + \hat{m}_s + \Delta_{\rm RHC} \,, \tag{5}$$

where we have assumed that $\epsilon_L \ll 1$, which computations [3,4,5] and indirect evidence tend to support. Eq. (5) makes it clear that in order to distinguish RHC from LD contributions one needs to be able to predict $\epsilon_R$ (or essentially $\mathcal{A}_{\mathbb{1}} - \mathcal{A}_{\mathbb{5}}$ up to $\mathcal{O}(C'/C)$).

In this work, we advocate a novel approach invoking new observables [6]. At the level of the standard dimension-six $H^{\rm eff}$, $\epsilon_R$ arises through an $\bar{s}_L\Gamma b\,\bar{q}\Gamma' q$-interaction, and is sensitive to the parity quantum number of the $V$-state. Hence, if for every vector state there were a partner of opposite parity then one could discern $\Delta_{\rm RHC}$ from $\epsilon_R$. This is the idea of our work, and we advocate to combine decay channels of nearly-degenerate parity partners.

In the chiral symmetry restoration limit, the following exact relation will be shown to hold:

$$\mathcal{A}_\chi^{B\to V\gamma}(C, C') = \mathcal{A}_\chi^{B\to A\gamma}(-C, C') \,, \tag{6}$$

with $\chi = L, R$, and $A$ an opposite-parity partner of the $V$ meson. This is the solution to our problem, since we are concerned with mixing up $C'$ (i.e. $\Delta_{\rm RHC}$) with LD-effects $\epsilon_R$ induced by $C$-type operators cf. Eq. (3). As we shall see, the problem is then shifted from estimating $\mathcal{A}_{\mathbb{1}} - \mathcal{A}_{\mathbb{5}}$ to estimating

$$\mathbb{R}_{A,V} \equiv \frac{\mathrm{Re}[\epsilon_R^{B\to A\gamma}]}{\mathrm{Re}[\epsilon_R^{B\to V\gamma}]} = 1 + \mathcal{O}(m_q, \langle\bar{q}q\rangle) \,. \tag{7}$$

To some extent it is the operator state correspondence of quantum field theory, expressed by the LSZ formalism, that allows for this shift in perspective. We would like to stress already at this point that the crucial practical question is not the actual value of $\mathbb{R}_{A,V}$, but rather its uncertainty (in the real world), which of course indirectly benefits from the closeness to the symmetry limit.

## 2 Relating axial and vector meson matrix elements in the chiral symmetry limit

It is conceptually beneficial to consider the chiral restoration limit $\{m_q, \langle\bar{q}q\rangle, \dots\} \to 0$, where the axial flavour symmetries are restored: $\mathrm{SU}(N_F)_V \to \mathrm{SU}(N_F)_V \times \mathrm{SU}(N_F)_A \times \mathrm{U}(1)_A$.[a] The relation we are to use is that in the restoration limit the quark propagator in the gluon background field, $S_G^{(q)}(w,z) = \langle w|(\not{D} + im_q)^{-1}|z\rangle$, obeys

$$\gamma_5 S_G^{(q)}(w,z) = -S_G^{(q)}(w,z)\gamma_5 \,, \tag{8}$$

[a] To what extent the $U(1)_A$ is restored due to the axial anomaly is an interesting question, but is not relevant for our purposes. Finite-temperature lattice computations above the chiral phase transition give evidence of $U(1)_A$-restoration [7].

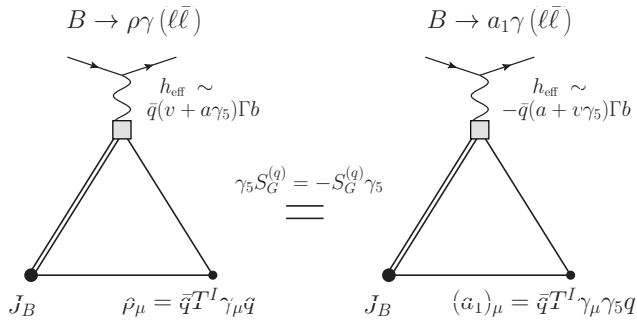


Figure 1 – A diagrammatic interpretation of the procedure outlined in the main text, using the relation Eq. (8). which necessitates the limits $\{m_q, \langle\bar{q}q\rangle, \dots\} \to 0$. The argument only requires that the weak vertex $h_{\rm eff}$ be a local operator, and thus applies to both SD (form-factor) and LD (charm-loop) contributions. Note that the trick applies equally well to annihilation diagrams where the photon is emitted from one of the lines inside the triangle graph in the figure. The schematic correlation functions on the left and right are exactly equal, from where the information on the matrix elements can be assessed.

for which the vanishing of the $\mathrm{SU}(N_F)_A \times \mathrm{U}(1)_A$-violating condensates is a necessary condition, as can be understood from the Banks-Casher relation [6].

The starting point is that any information of the matrix element $\langle V\gamma^*|h_{\rm eff}|B\rangle$, where $\gamma^*$ is a potentially off-shell photon, can be extracted from the correlation function

$$\mathcal{M}^{[V]}_{(v,a)} \equiv \langle 0|\mathcal{T}\{J_B(x)V^I_\mu(y)h_{\rm eff}(0)\}|0\rangle\ , \quad h_{\rm eff} = \bar{q}(v + a\gamma_5)\Gamma b\, O_r\ , \tag{9}$$

by analysing its dispersion relation, as $J_B = \bar{b}\gamma_5 q$ and $V^I_\mu \to \rho(a_1)^I_\mu = \bar{q}\gamma_\mu T^I(\gamma_5)q$ are interpolating operators for the $B$-meson and the vector (axial) mesons respectively. In Eq. (9), $\Gamma$ is a Dirac structure, while $O_r$ stands for the remaining part of the operator. For example, $O_r = \mathbb{1}$ and $O_r = \bar{c}\Gamma' c, \bar{u}\Gamma' u, \dots$ distinguish between short-distance (SD) and LD (e.g. four-quark) operators. Contracting the quark lines and focusing on the $\rho$ meson final state, the matrix element assumes the form

$$\mathcal{M}^{[\rho^0]}_{(v,a)} \sim \int D\mu_G \mathrm{Tr}[(v + a\gamma_5)S^{(b)}_G(0,x)\gamma_5 S^{(d)}_G(x,y)\gamma_\mu S^{(d)}_G(y,0)]\ , \tag{10}$$

where the path-integral measure is given by $D\mu_G = DG_\mu \det(\not{D} + iM_f)e^{iS(G)}$ ($D_\mu = (\partial - igG)_\mu$).

Now comes the main trick. Substituting $\gamma_\mu \to \gamma_\mu(\gamma_5)^2$ and using Eq. (8) leads to an expression, $\mathcal{M}^{[a_1]}_{(a,v)} = -\mathcal{M}^{[\rho^0]}_{(v,a)}$, for which the $a_1$ meson matrix element is the same up to a sign with the variables $a$ and $v$ interchanged (Fig. 1). From this expression, Eq. (6) follows, which is our main formal result. In the last equation it is understood that $V$ and $A$ become degenerate in the chiral restoration limit [6], and are referred to as parity doublers.[b]

## 3 Phenomenological implications

In effect, Eq. (6) means that the ratio Eq. (5), amended to include an axial meson, is then given by

$$\frac{\mathcal{A}_R}{\mathcal{A}_L}\Big|_{B\to V(A)\gamma} = \frac{\epsilon_R \pm (\hat{m}_s + \Delta_{\rm RHC})}{(1 + \epsilon_L)} \simeq \epsilon_R \pm (\hat{m}_s + \Delta_{\rm RHC})\ , \tag{11}$$

[b] Parity doubling has a long history in particle physics [8], and has recently been investigated on the lattice [9,10], with the additional surprise of an emergent symmetry. For a table of relevant opposite parity states, we refer the reader to Tab. 1 in Ref. [6].

which is the equation from which our phenomenological results are derived. Beyond the symmetry limit, the only relevant change to Eq. (11) is that the LD contributions $\epsilon_R, \epsilon_L \to \epsilon_{V(A),R}, \epsilon_{V(A),L}$ are dependent on the final state to a degree that needs to be estimated by analytical methods.

The crucial question for RHC searches is how the hierarchy and the sign change in Eq. (11) can be exploited. Concerning the hierarchy, the rate itself is not promising, since $\Gamma_{\rm tot} \sim |\mathcal{A}_L|^2 + |\mathcal{A}_R|^2$ and the effect of the RHCs might be too small to be seen in experiment. A more promising route is to consider angular distributions, e.g. $B \to V\ell\bar{\ell}$, or time-dependent decay rates in $B \to V\gamma$, as originally proposed by the authors of Ref. [11].

The time-dependent rate of a neutral $B_D$-meson ($D = d, s$), under general and valid assumptions, reads [12]

$$\mathcal{B}(\bar{B}_D[B_D] \to V\gamma) = B_0 e^{-\Gamma_D t}[\mathrm{ch}(\frac{\Delta\Gamma_D}{2}t) - H\,\mathrm{sh}(\frac{\Delta\Gamma_D}{2}t) \mp C\cos(\Delta m_D t) \pm S\sin(\Delta m_D t)]\ , \quad (12)$$

where $\Delta\Gamma_D \equiv \Gamma_D^{(H)} - \Gamma_D^{(L)}$ is the width difference, and $\Delta m_D \equiv m_D^{(H)} - m_D^{(L)}$ the mass difference, of the heavy ($H$) and light ($L$) mass eigenstates. $S$ and $C$ are related to indirect and direct CP violation respectively.[c] The quantities $S$ and $H$ are linear in $\mathcal{A}_R$, and given in terms of the amplitudes by

$$S(H) = 2\mathrm{Im(Re)}\left[\frac{q}{p}(\bar{\mathcal{A}}_L\mathcal{A}_L^* + \bar{\mathcal{A}}_R\mathcal{A}_R^*)\right]\mathcal{N}^{-1}\ , \quad (13)$$

with $\mathcal{N} = |\mathcal{A}_L|^2 + |\bar{\mathcal{A}}_L|^2 + |\mathcal{A}_R|^2 + |\bar{\mathcal{A}}_R|^2$. We choose to illustrate the approach by the mode $B_s \to \phi\gamma$ and $B_s \to f_1(1420)\gamma$, with other modes discussed in Ref. [6], as this mode is not sensitive to CKM factors. The observables $H$ and $S$ are well-approximated by

$$H_{B_s\to\phi(f_1)\gamma} \simeq 2\{\pm(\Delta_R\cos(\phi_R) + \hat{m}_s) - \mathrm{Re}[\epsilon^c_{\phi(f_1),R}]\}\ , \quad S_{B_s\to\phi(f_1)\gamma} \simeq 2\{\pm\Delta_R\sin(\phi_R)\}\ . \quad (14)$$

The vanishing of $S_{B_s\to\phi(f_1)\gamma} \simeq 0$ in the SM comes from the cancelation of all weak phases involved, and this quantity is therefore a null test for weak phases of RHC. From Eq. (14), we obtain the remarkable equation

$$H_{\phi\gamma} + H_{f_1\gamma} \simeq -2\mathrm{Re}[\epsilon^c_{\phi,R} + \epsilon^c_{f_1,R}] = -2\mathrm{Re}[\epsilon^c_{\phi,R}](1 + \mathbb{R}^c_{f_1,\phi})\ , \quad (15)$$

where the SD physics drops out. Its SD-sensitive counterpart is

$$\Delta_R\cos(\phi_{\Delta_R}) = \frac{1}{4}(H_{\phi\gamma} - H_{f_1\gamma}) + \frac{1}{2}\mathrm{Re}[\epsilon^c_{\phi,R} - \epsilon^c_{f_1,R}] - \hat{m}_s\ . \quad (16)$$

In Eq. (15), $\mathbb{R}^i_{A,V} \equiv \mathrm{Re}[\epsilon^i_{A,R}]/\mathrm{Re}[\epsilon^i_{V,R}]$ is the more refined version of Eq. (7), in that it includes the information on the flavour of the four-quark operator from which it derives. The main points are as follows:

- Eq. (15) shows that one can measure the sum of the LD contributions without compromise from RHC or SM SD physics, owing to the previously-mentioned exact form factor relation $T_1(0) = T_2(0)$.
- One can extract the LD parts of the individual modes, entering Eq. (16), by an analytic prediction of $\mathbb{R}^c_{f_1,\phi}$. We again stress that it is not the value (deviation from unity) but the error on $\mathbb{R}^c_{f_1,\phi}$ which is important. By flavour symmetries it is clear that the measurement of a single axial vector meson can reveal valuable information on the size of LD contributions.
- Making the last point more concrete, an error of 20% on $\mathbb{R}^c_{f_1,\phi}$, assuming a perfect measurement, allows us to extract $\mathrm{Re}[\epsilon^c_{\phi,R}]$ to 10%. This is a much-improved situation as compared to an *a priori* computation [13].

[c] $H \equiv \mathcal{A}^{\Delta\Gamma}$ in the Particle Data Group (PDG) notation.

- These methods apply straightforwardly to charm physics [14], and can be extended to $B \to V\ell\bar{\ell}$ at low $q^2$, although this will require taking into account that the exact form-factor relation $T_1(0) = T_2(0)$ no longer holds [2]. In particular, the real and imaginary parts of the angular moment $\mathbb{G}_2^{2,2}$, equivalent to $P_1 = A_T^{(2)}$ and $P_3$ respectively, also exhibit the required linear dependence on the right-handed amplitude [15,16,17]. Measuring the analogues of $\epsilon_R$ in this channel allows to cross-check the LD theory input into the anomalous angular $B \to K^*\mu^+\mu^-$ measurement e.g. $P_5'$ [18,19,20,21].

## 4 Conclusions

In this work, we have advocated that long-distance effects contaminating searches for right-handed currents in $B \to V\gamma(\ell\bar{\ell})$ decays can be controlled by considering the corresponding parity-doubler decay mode $B \to A\gamma(\ell\bar{\ell})$. In the limit where the chiral symmetry is restored, the V-A contributions to the right-handed amplitude come with the opposite sign between these two channels. This can be applied phenomenologically by combining observables, as shown explicitly for example in measurements of time-dependent CP asymmetry in $B_s \to \phi(f_1)\gamma$ in Eqs. (15) and (16), to extract and measure ratios of long-distance contributions. In turn this can lead to a cleaner extraction of Beyond the SM contributions to right-handed currents.

It is again important to stress that the main benefit is not in the prediction of the long-distance ratio itself, but the reduced theoretical uncertainty that results. This is also useful in resolving the current tension between predictions of the size of long-distance charm loop contaminations in exclusive [3,4] and inclusive $B \to X_s\gamma$ decays [22], where the inclusive contamination was estimated to be roughly an order of magnitude larger.

Corrections to the results in this work, applying beyond the symmetry limit, can still be understood systematically by investigating the symmetry relations between vector and axial mesons, such as the parameters entering their light-cone distribution amplitudes [13,23]. This allows the approach we advocate above to be applied in real-world experimental searches, with good prospects at Belle II and LHCb [24,25].


## Acknowledgments

We are grateful to Tadeusz Janowski and Marco Pappagallo for suggestions on the manuscript. RZ wishes to thank the Moriond participants for a pleasant atmosphere, good discussions and atmosphere. JG is supported by an STFC studentship (grant reference ST/K501980/1).


## References


1. G. D'Ambrosio, G.F. Giudice, G. Isidori and A. Strumia, *Minimal flavor violation: an effective field theory approach*, *Nucl. Phys.* B **645**, 155 (2002), hep-ph/0207036.
2. A. Bharucha, D.M. Straub and R. Zwicky, *$B \to V\ell^+\ell^-$ in the Standard Model from light-cone sum rules*, JHEP **08**, 098 (2016), 1503.05534.
3. A. Khodjamirian, G. Stoll and D. Wyler, *Calculation of long distance effects in exclusive weak radiative decays of B meson*, *Phys. Lett.* B **358**, 129 (1995), hep-ph/9506242.
4. P. Ball and R. Zwicky, *Time-dependent CP asymmetry in $B \to K^*\gamma$ as a (quasi) null test of the Standard Model*, *Phys. Lett.* B **642**, 478 (2006), hep-ph/0609037.
5. P. Ball, G.W. Jones and R. Zwicky, *$B \to V\gamma$ beyond QCD factorisation*, *Phys. Rev.* D **75**, 054004 (2007), hep-ph/0612081.
6. J. Gratrex and R. Zwicky, *Parity doubling as a tool for right-handed current searches*, 1804.09006.
7. A. Tomiya *et al.*, *Evidence of effective axial $U(1)$ symmetry restoration at high temperature QCD*, *Phys. Rev.* D **96**, 034509 (2017), 1612.01908. [Addendum: *Phys. Rev.* D **96**,

079902 (2017)].
8. S.S. Afonin, *Parity doubling in particle physics*, *Int. J. Mod. Phys* A **22**, 4537 (2007), 0704.1639.
9. M. Denissenya, L. Ya. Glozman and C.B. Lang, *Isoscalar mesons upon unbreaking of chiral symmetry*, *Phys. Rev.* D **91**, 034505 (2015), 1410.8751.
10. C. Rohrhofer *et al.*, *Approximate degeneracy of $J = 1$ spatial correlators in high temperature QCD*, *Phys. Rev.* D **96**, 094501 (2017), 1707.01881.
11. D. Atwood, M. Gronau and A. Soni, *Mixing induced CP asymmetries in radiative B decays in and beyond the Standard Model*, *Phys. Rev. Lett.* **79**, 185 (1997), hep-ph/9704272.
12. F. Muheim, Y. Xie and R. Zwicky, *Exploiting the width difference in $B_s \to \phi\gamma$*, *Phys. Lett.* B **664**, 174 (2008), 0802.0876.
13. J. Gratrex and R. Zwicky, *Long-distance charm loops in $B \to (V, A)\ell\bar{\ell}$ decays from light-cone sum rules*, in preparation.
14. S. de Boer and G. Hiller, *The photon polarization in radiative D decays, phenomenologically*, *Eur. Phys. J.* C **78**, 188 (2018), 1802.02769.
15. J. Gratrex, M. Hopfer and R. Zwicky, *Generalised helicity formalism, higher moments and the $B \to K_{J_K}(\to K\pi)\bar{\ell}_1\ell_2$ angular distributions*, *Phys. Rev.* D **93**, 054008 (2016), 1506.03970.
16. F. Kruger and J. Matias, *Probing new physics via the transverse amplitudes of $B_0 \to K^{*,0}(K \to \pi^+)\ell^+\ell^-$ at large recoil*, *Phys. Rev.* D **71**, 094009 (2005), hep-ph/0502060.
17. D. Becirevic and E. Schneider, *On transverse asymmetries in $B \to K^* l^+ l^-$*, *Nucl. Phys.* B **854**, 321 (2012), 1106.3283.
18. W. Altmannshofer, C. Niehoff, P. Stangl and D.M. Straub, *Status of the $B \to K^*\mu^+\mu^-$ anomaly after Moriond 2017*, *Eur. Phys. J.* C **77**, 377 (2017), 1703.09819.
19. M. Ciuchini *et al.*, *On flavourful Easter eggs for new physics hunger and lepton flavour universality violation*, *Eur. Phys. J.* C **77**, 688 (2017), 1704.05447.
20. B. Capdevila *et al.*, *Patterns of new physics in $b \to s\ell^+\ell^-$ transitions in the light of recent data*, JHEP **01**, 93 (2018), 1704.05340.
21. A. Arbey, T. Hurth, F, Mahmoudi and S. Neshatpour, *Hadronic and new physics contributions to $B \to K^*\ell^+\ell^-$*, 1806.02791.
22. B. Grinstein, Y. Grossman, Z. Ligeti and D. Pirjol, *The photon polarization in $B \to X\gamma$ in the standard model*, *Phys. Rev.* D **71**, 011504 (2005), hep-ph/0412019.
23. J. Gratrex and R. Zwicky, *Axial and vector meson distribution amplitudes and their symmetries*, in preparation.
24. J. Li *et al.* [Belle Collaboration], *Time-dependent CP asymmetries in $B^0 \to K^0_S\rho^0\gamma$ decays* , *Phys. Rev. Lett.* **101**, 251601 (2008), 0806.1980.
25. R. Aaij *et al.* [LHCb Collaboration], *First observations of the rare decays $B^+ \to K^+\pi^+\pi^-\mu^+\mu^-$ and $B^+ \to \phi K^+\mu^+\mu^-$*, *JHEP* **10**, 064 (2014), 1408.1137.

# 4.
# Heavy Flavour & New Physics

# Rare decays, radiative decays and $b \to s\ell^+\ell^-$ transitions at LHCb

A. Crocombe on behalf of the LHCb collaboration
*Department of Physics, University of Warwick,*
*Coventry CV4 7AL, United Kingdom*

Rare flavour-changing neutral-decays are heavily suppressed within the Standard Model of particle physics. As such, measurements of the properties of these decays are sensitive to the contribution from new particles. A number of tensions have been observed in $b \to s\ell^+\ell^-$ processes with respect to the SM. A summary of recent measurements of leptonic, radiative and rare semileptonic processes by the LHCb collaboration is presented.

## 1 Introduction

Rare decays of $b$-, $c$- and $s$-hadrons that proceed via a flavour-changing neutral-current (FCNC) transition are heavily suppressed within the Standard Model (SM). As such, they provide excellent tools to search for New Physics (NP) effects as any potential NP contribution can be at a similar level to the SM contribution. Indirect searches for NP can be carried out by searching for deviations from SM predictions in the rate or angular distributions of these rare decays.

In these proceedings an overview of recent rare decay results from the LHCb collaboration is presented, highlighting results that currently indicate tensions with the SM predictions and opportunities for future measurements. The majority of results presented make use of the $3\,\text{fb}^{-1}$ data sample collected by LHCb during Run 1 of the LHC.

## 2 Rare leptonic decays

The decays $B^0_{(s)} \to \mu^+\mu^-$ can be used as very powerful probes of the SM as they are heavily suppressed, both due to loop and helicity suppression. The rate of these decays can be precisely predicted to better than 10% [1]. In addition, the experimental signatures of these decays are very clean allowing them to be measured even with small expected branching fractions. A search for the decays is carried out by LHCb [2] making use of the Run 1 dataset and in addition data corresponding to $1.4\,\text{fb}^{-1}$ collected in Run 2. The reconstructed invariant mass distribution of the $B^0_s \to \mu^+\mu^-$ candidates is shown in Fig. 1. This results in the first single experiment observation of the the decay $B^0_s \to \mu^+\mu^-$ at a level of 7.8 standard deviations, with a measured branching fraction of $\mathcal{B}(B^0_s \to \mu^+\mu^-) = (3.0 \pm 0.6^{+0.3}_{-0.2}) \times 10^{-9}$. The effective lifetime [3] of the decay is measured for the first time and found to be $\tau(B^0_s \to \mu^+\mu^-) = 2.04 \pm 0.44 \pm 0.05$ ps. No significant excess of $B^0 \to \mu^+\mu^-$ events is observed and a limit is set on its branching fraction of $\mathcal{B}(B^0 \to \mu^+\mu^-) < 3.4 \times 10^{-10}$ at 95% confidence level. These results are all in agreement with SM predictions [1] and set stringent limits on potential NP models.

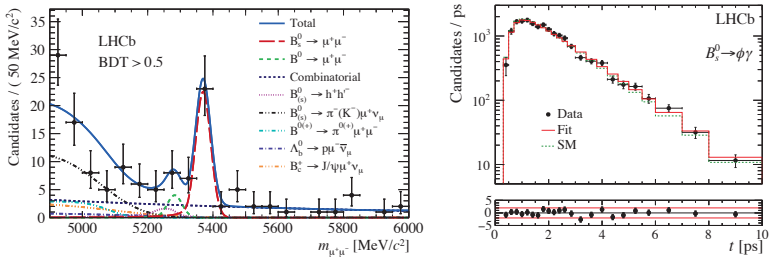


Figure 1 – Invariant mass distribution of $B^0_{(s)} \to \mu^+\mu^-$ candidates and the resulting fit (left) and the decay-time distribution of $B^0_s \to \phi\gamma$ candidates as well as the fitted distribution and SM expectation (right).

## 3 Rare radiative decays

Photons produced in $b \to s\gamma$ transitions are predominantly left-hand polarised in the SM but could have any polarisation in extensions of the SM. The polarisation can be probed through the time dependence of the $B^0_s \to \phi\gamma$ decay. A non-zero value of the parameter $\mathcal{A}^\Delta$ [4], which is related to the difference between left- and right-handed polarised photons, would indicate the presence of NP. A time-dependant analysis of the $B^0_s \to \phi\gamma$ decay mode carried out by LHCb [5] results in a fitted value of $\mathcal{A}^\Delta = -0.98^{+0.46+0.23}_{-0.52-0.20}$. The decay-time distribution and fit result is shown in Fig. 1. This is compatible with the SM expectation [4] within two standard deviations.

## 4 Flavour anomalies in $b \to s\ell^+\ell^-$ transitions

While the results presented above are in agreement with SM predictions, there have been a number of recent results in decays which proceed via $b \to s\ell^+\ell^-$ transitions which are beginning to show tensions with the SM. The differential branching fractions of the $b \to s\ell^+\ell^-$ decays $B^+ \to K^+\mu^+\mu^-$, $B^0 \to K^0\mu^+\mu^-$, $B^+ \to K^{*+}\mu^+\mu^-$ [6], $B^0 \to K^{*0}\mu^+\mu^-$ [7] and $B^0_s \to \phi\mu^+\mu^-$ [8] as measured by LHCb are all systematically lower than SM predictions at low dimuon invariant mass squared ($q^2$). While no individual decay channel shows a significant overall deviation, the measurements all appear to point towards a consistent deviation with respect to SM predictions.

Another set of observables sensitive to NP can be accessed by carrying out an angular analysis. Of particular interest is the analysis of the decay $B^0 \to K^{*0}\mu^+\mu^-$, where measurements of so-called optimised angular observables [9] with reduced theoretical uncertainties are made. The LHCb measurement [10] of the observable $P'_5$ shows tensions with the SM of approximately 3 standard deviations in two bins of $q^2$. Figure 2 shows the result of the analysis as well as results from ATLAS [11], Belle [12] and CMS [13] along with SM predictions [14,15].

While no individual decay mode has yet to unambiguously point to NP, it is possible to carry out a global fit to evaluate a combined significance of all these measurements. By combining the above measurements and including additional results from other experiments and in other decay channels, a number of global fits [16,17,18] favour a best-fit point that is approximately 5 standard deviations from the SM. The best-fit point favours a modification of the vector coupling or a modification of both the vector and axial-vector coupling of the decay.

## 5 $b \to d\ell^+\ell^-$ transitions

Decays which proceed via a $b \to d\ell^+\ell^-$ transition are further suppressed with respect those that proceed via a $b \to s\ell^+\ell^-$ due to the relative CKM factors. As such, similar measurements of the decay properties can in principle be carried out. The $b \to d\ell^+\ell^-$ decays $B^+ \to \pi^+\mu^+\mu^-$ [19]

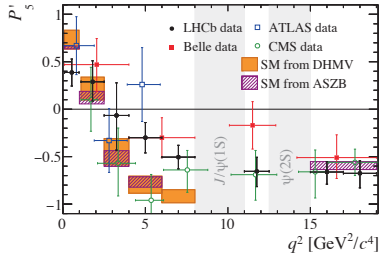


Figure 2 – Measurement of $P'_5$ in bins of $q^2$ from LHCb, ATLAS, Belle and CMS as well as SM predictions.

and $\Lambda_b \to p\pi^-\mu^+\mu^-$ [20] are all observed by LHCb and evidence for $B^0 \to \pi^+\pi^-\mu^+\mu^-$ [21] is also found.

The decay $B^0_s \to \overline{K}^{*0}\mu^+\mu^-$ is the $b \to d\ell^+\ell^-$ partner process to the decay $B^0 \to K^{*0}\mu^+\mu^-$. Along with potential to probe NP, the decay could be used in conjuncture with its partner to make a measurement of the CKM ratio $|V_{td}/V_{ts}|$. LHCb carries out a search for this decay [22] using the Run 1 dataset as well as 1.6 fb$^{-1}$ collected in Run 2. Figure 3 shows the reconstructed invariant mass distribution of the $B^0_s \to \overline{K}^{*0}\mu^+\mu^-$ candidates. The significance of the fitted $B^0_s \to \overline{K}^{*0}\mu^+\mu^-$ is found to be $3.4\sigma$ including systematic uncertainties. This constitutes the first evidence for this decay mode.

The branching fraction of this decay, normalised to the $B^0 \to J/\psi\,\overline{K}^{*0}$ control mode, is measured to be $\mathcal{B}(B^0_s \to \overline{K}^{*0}\mu^+\mu^-) = (2.9 \pm 1.0 \pm 0.2 \pm 0.3) \times 10^{-8}$, where the first uncertainty is statistical, the second systematic and the third due to uncertainties on parameters used for normalisation. This measurement is in agreement with SM predictions [23,24].

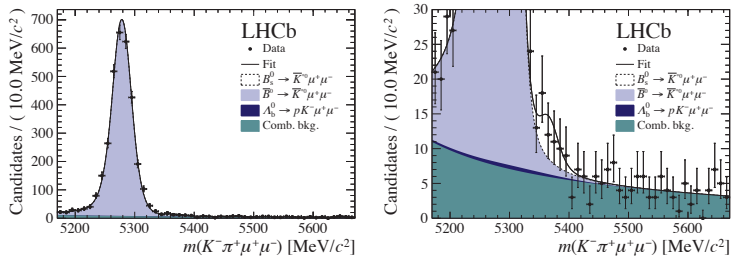


Figure 3 – Invariant mass distribution of $B^0_s \to \overline{K}^{*0}\mu^+\mu^-$ candidates (left) and the same zoomed in on the signal component (right). The result of the fit to the candidates is also shown with components detailed in the legend.

## 6 Rare baryonic decays

LHCb has also recently searched for baryonic FCNC decays, which are largely unexplored as probes of NP. The difference in hadronic physics in these modes allows for independent verification of existing tensions in mesonic modes while the different spin of baryons allows access to more angular observables. Initial searches for these modes will provide the basis for more in-depth analyses in the future.

The decay $\Lambda_c^+ \to p\mu^+\mu^-$ proceeds via a $c \to u\ell^+\ell^-$ transition. It is expected to be heavily suppressed by the GIM mechanism in the SM and have a branching fraction of $\mathcal{O}(10^{-9})$. The LHCb search for this decay [25] sees no significant excess of signal events and a new best limit on the branching fraction is set to $\mathcal{B}(\Lambda_c^+ \to p\mu^+\mu^-) < 9.6 \times 10^{-8}$ at 95% confidence limit.

Finally, the decay $\Sigma^+ \to p\mu^+\mu^-$ is a $s \to d\ell^+\ell^-$ FCNC process. Evidence for this decay has previous been reported by the HyperCP collaboration [26], where all three of the observed candidates have almost the same dimuon invariant mass. Further analysis of this mode is thus of interest to investigate this potential new resonance. LHCb carries out a search [27] for this mode and finds evidence for it at the level of 4 standard deviations. The measured branching fraction is $\mathcal{B}(\Sigma^+ \to p\mu^+\mu^-) = (2.1^{+1.6}_{1.2}) \times 10^{-8}$ and is consistent with SM predictions [28]. However, data are inconsistent with originating from the narrow resonance favoured by Hyper-CP.

## 7 Conclusions

Rare FCNC decays can be used as powerful tools to search for NP physics effects. Already many strong limits have been placed on potential NP models due to measurements made of rare $b$-hadron decay modes. On the other hand, a number of recent results have shown tensions in branching fractions and angular observables in $b \to s\ell^+\ell^-$ transitions with respect to SM predictions, and global fits favour certain NP scenarios at the level of 5 standard deviations.

The majority of these results make use of only the Run 1 LHCb dataset and further investigation of these modes making use of larger datasets will be essential in confirming the presence of these anomalies. In addition, a number of decay modes expanding the range of measurements to other flavour transitions have already started to be analysed. Further investigation of these modes will be very important in determining the flavour structure of any potential NP scenarios.

## References


1. C. Bobeth *et al.*, *Phys. Rev. Lett.* **112**, 101801 (2014).
2. R. Aaij *et al.* [LHCb Collaboration], *Phys. Rev. Lett.* **118**, 191801 (2017).
3. K. De Bruyn *et al.*, *Phys. Rev.* D **86**, 014027 (2012).
4. F. Muheim *et al.*, *Phys. Lett.* B **664**, 174 (2008).
5. R. Aaij *et al.* [LHCb Collaboration], *Phys. Rev. Lett.* **118**, 021801 (2017).
6. R. Aaij *et al.* [LHCb Collaboration], *JHEP* **06**, 133 (2014).
7. R. Aaij *et al.* [LHCb Collaboration], *JHEP* **11**, 047 (2016) Erratum:*JHEP* **04**, 142 (2017).
8. R. Aaij *et al.* [LHCb Collaboration], *JHEP* **09**, 179 (2015).
9. S. Descotes-Genon *et al.*, *JHEP* **01**, 048 (2013).
10. R. Aaij *et al.* [LHCb Collaboration], *JHEP* **02**, 104 (2016).
11. The ATLAS collaboration, ATLAS-CONF-2017-023.
12. S. Wehle *et al.* [Belle Collaboration], *Phys. Rev. Lett.* **118**, 111801 (2017).
13. A.M. Sirunyan *et al.* [CMS Collaboration], *Phys. Lett.* B **781**, 517 (2018).
14. S. Descotes-Genon *et al.*, *JHEP* **12**, 125 (2014).
15. W. Altmannshofer and D.M. Straub, *Eur. Phys. J.* C **75**, 382 (2015).
16. B. Capdevila *et al.*, *JHEP* **01**, 093 (2018).
17. M. Ciuchini *et al.*, *Eur. Phys. J.* C **77**, 688 (2017).
18. L.-S. Geng *et al.*, *Phys. Rev.* D **96**, 093006 (2017).
19. R. Aaij *et al.* [LHCb Collaboration], *JHEP* **10**, 034 (2015).
20. R. Aaij *et al.* [LHCb Collaboration], *JHEP* **04**, 029 (2017).
21. R. Aaij *et al.* [LHCb Collaboration], *Phys. Lett.* B **743**, 46 (2015).
22. R. Aaij *et al.* [LHCb Collaboration], arXiv:1804.07167.
23. R.N. Faustov and V.O. Galkin, *Eur. Phys. J.* C **73**, 2593 (2013).
24. B. Kindra and N. Mahajan, arXiv:1803.05876.
25. R. Aaij *et al.* [LHCb Collaboration], *Phys. Rev.* D **97**, 091101 (2018).
26. H. Park *et al.* [HyperCP Collaboration], *Phys. Rev. Lett.* **94**, 021801 (2005).
27. R. Aaij *et al.* [LHCb Collaboration], arXiv:1712.08606.
28. X.-G. He *et al.*, *Phys. Rev.* D **72**, 074003 (2005).

# NEW PROBES OF NEW PHYSICS WITH LEPTONIC RARE B DECAYS

R. FLEISCHER
*Nikhef, Science Park 105, 1098 XG Amsterdam and Department of Physics and Astronomy, Faculty of Science, Vrije Universiteit Amsterdam, 1081 HV Amsterdam, Netherlands*

Decays of the kind $B^0_{s,d} \to \ell^+\ell^-$ belong to the most favourable processes for probing the flavour structure of the Standard Model, with outstanding sensitivity to new (pseudo)-scalar contributions. While the branching ratio of $B^0_s \to \mu^+\mu^-$ has already been measured at the LHC in the ballpark of the Standard Model expectation, there is still significant room for New-Physics effects. We discuss how these may be revealed in the future super-high precision era of $B$-decay studies by utilising new theoretically clean observables, including CP-violating asymmetries. Another promising decay is $B^0_s \to e^+e^-$, which has received little attention in view of its enormously helicity suppressed Standard Model branching ratio, with the most recent experimental upper bound dating back to 2009. Using the current constraints on New Physics from $B^0_s \to \mu^+\mu^-$ as a guideline, we show that the $B^0_s \to e^+e^-$ branching ratio may be hugely enhanced through new (pseudo)-scalar contributions up to the regime of $B^0_s \to \mu^+\mu^-$.

## 1 Setting the Stage

Within the Standard Model (SM), the leptonic decays $B^0_q \to \ell^+\ell^-$ $(q = s, d)$ receive only loop contributions from penguin and box topologies, and show a helicity suppression which results in branching ratios proportional to $m^2_\ell$, where $m_\ell$ denotes the masses of the final state leptons. Another key feature is the simple situation concerning strong interactions, which are described by a single hadronic parameter, the $B_q$ decay constant $f_{B_q}$. These modes belong to the cleanest rare $B$ decays and offer an outstanding setting to explore the flavour sector of the SM, with high sensitivity to New Physics (NP) contributions. Particularly interesting are new (pseudo)-scalars, which may lift the helicity suppression. In Fig. 1, we show a compilation of experimental information in comparison with the SM picture. So far, only $B^0_s \to \mu^+\mu^-$ has been observed, which was a highlight of LHC run 1. In the case of $B^0_{s,d} \to \tau^+\tau^-$, the helicity suppression is not very effective due to the large $\tau$ mass but the $\tau$ reconstruction makes experimental analyses challenging. Interestingly, the $B_{s,d} \to e^+e^-$ modes, which are extremely helicity suppressed in the SM, have not yet received attention at the LHC.

New observables of the decay $B_s \to \mu^+\mu^-$ were pointed out, which offer interesting probes at the high-precision frontier.[1] In the following, we focus on the constraints for NP effects following from the current $B_s \to \mu^+\mu^-$ data,[2] their implications for the branching ratios of $B^0_{s,d} \to \tau^+\tau^-$, $B^0_{s,d} \to e^+e^-$,[3] and address the impact of new sources of CP violation.[4]

## 2 In Pursuit of New Physics

The theoretical framework is given by effective quantum field theory, where the decays at hand are described by a low-energy effective Hamiltonian.[1] In the SM, only the operator $O_{10} = (\bar{q}\gamma_\mu P_L b)(\bar{\ell}\gamma^\mu\gamma_5\ell)$ contributes with a real Wilson coefficient. In the presence of NP, new four-

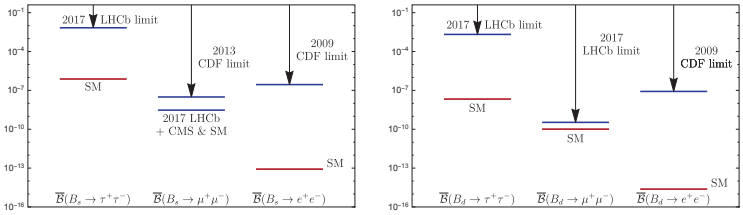


Figure 1 – Overview of experimental information on $B_q \to \ell^+\ell^-$ branching ratios as defined in Eq. (1) and comparison with the corresponding SM predictions.

fermion operators involving (pseudo)-scalar lepton densities may enter. Their effect is described by short-distance coefficients $P^q_{\ell\ell}$ and $S^q_{\ell\ell}$, where the former includes the SM and pseudo-scalar NP effects while the latter originates from new scalars. In the SM, we have $P^q_{\ell\ell} = 1$ and $S^q_{\ell\ell} = 0$.

Due to the presence of $B^0_s$–$\bar{B}^0_s$ mixing and the sizeable $B_s$ decay width difference $\Delta\Gamma_s/\Gamma_s \sim 0.1$, a subtle difference arises between the untagged, time-integrated branching ratio

$$\overline{\mathcal{B}}(B_s \to \mu^+\mu^-) \equiv \frac{1}{2}\int_0^\infty \langle \Gamma(B_s(t) \to \mu^+\mu^-)\rangle \, dt \overset{\text{LHC}}{=} (3.0 \pm 0.5) \times 10^{-9}, \tag{1}$$

measured at the LHC, and theoretical predictions $\mathcal{B}(B_s \to \mu^+\mu^-)$ which usually refer to a setting without the oscillations.[1,5] The conversion involves an observable $\mathcal{A}^{\mu\mu}_{\Delta\Gamma_s}$, which depends on $P_{\mu\mu}$ and $S_{\mu\mu}$ and takes the SM value +1, yielding[3] $\overline{\mathcal{B}}(B_s \to \mu^+\mu^-)_{\text{SM}} = (3.57 \pm 0.16) \times 10^{-9}$. Electromagnetic corrections were recently calculated in Ref. 6 and were found to be tiny. The observable $\mathcal{A}^{\mu\mu}_{\Delta\Gamma_s}$ contains information equivalent to the effective lifetime

$$\tau_{\mu\mu} \equiv \frac{\int_0^\infty t \, \langle \Gamma(B_s(t) \to \mu^+\mu^-)\rangle \, dt}{\int_0^\infty \langle \Gamma(B_s(t) \to \mu^+\mu^-)\rangle \, dt} = [2.04 \pm 0.44(\text{stat}) \pm 0.05(\text{syst})] \, \text{ps} \tag{2}$$

which was measured by the LHCb collaboration for the first time with the value given above.[7]

In order to probe NP effects through the measured $B^0_s \to \mu^+\mu^-$ branching ratio, the quantity

$$\overline{R}^s_{\mu\mu} \equiv \overline{\mathcal{B}}(B_s \to \mu^+\mu^-)/\overline{\mathcal{B}}(B_s \to \mu^+\mu^-)_{\text{SM}} = 0.84 \pm 0.16 \tag{3}$$

plays a central role.[1,2] Assuming real coefficients $P_{\mu\mu}$ and $S_{\mu\mu}$, we obtain the constraints shown in Fig. 2. Interestingly, $\overline{R}^s_{\mu\mu}$ alone does not allow a separation of these contributions and sizeable NP effects could still be present.[3] They could be revealed through a future measurement of $\mathcal{A}^{\mu\mu}_{\Delta\Gamma_s}$. Unfortunately, the current value of $\mathcal{A}^{\mu\mu}_{\Delta\Gamma_s} = 8.24 \pm 10.72$ does not yet have an impact.

Let us now explore implications of these NP constraints for other $B_q \to \ell^+\ell^-$ processes.[3] To this end, we employ a scenario with flavour-universal NP (FUNP) contributions, which is

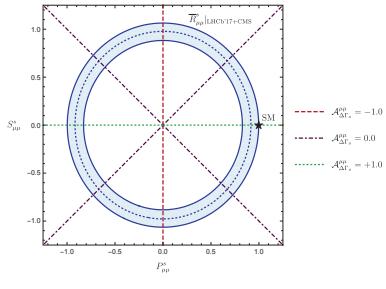


Figure 2 – Constraints in the $P_{\mu\mu}$–$S_{\mu\mu}$ plane following from the LHC data and impact of $\mathcal{A}^{\mu\mu}_{\Delta\Gamma_s}$ (see Ref. 3).

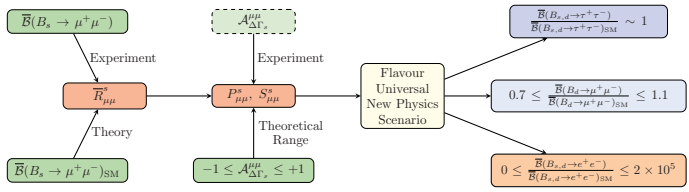


Figure 3 – Flowchart to explore the impact of $B_s \to \mu^+\mu^-$ NP constraints for other $B_{s,d} \to \ell^+\ell^-$ decays.

characterised by the feature that $C_{10}^{\ell\ell(\prime)}$, $C_P^{\ell\ell(\prime)}$, $C_S^{\ell\ell(\prime)}$ do not depend on flavour labels. In Fig. 3, the corresponding strategy is illustrated in a flowchart.

In the case of $B_d^0 \to \mu^+\mu^-$, the ratio

$$\frac{\overline{\mathcal{B}}(B_d \to \mu^+\mu^-)}{\overline{\mathcal{B}}(B_s \to \mu^+\mu^-)} \propto \left[\frac{|P^d_{\mu\mu}|^2 + |S^d_{\mu\mu}|^2}{|P^s_{\mu\mu}|^2 + |S^s_{\mu\mu}|^2}\right] \left(\frac{f_{B_d}}{f_{B_s}}\right)^2 \left|\frac{V_{td}}{V_{ts}}\right|^2 \tag{4}$$

is a particularly interesting quantity, where the ratio of CKM matrix elements can be determined from an analysis of the unitarity triangle. In the FUNP scenario, an essentially linear correlation between the branching ratios arises, with a moderate suppression of $\overline{\mathcal{B}}(B_d \to \mu^+\mu^-)$ with respect to the SM expectation, in analogy to the current LHC data for $B_s \to \mu^+\mu^-$.

Concerning $B_q^0 \to \tau^+\tau^-$ decays, the NP effects are strongly suppressed by the mass ratio $m_\mu/m_\tau \sim 0.06$ in the FUNP scenario, resulting in

$$0.8 \le \overline{R}^s_{\tau\tau} \equiv \overline{\mathcal{B}}(B_s \to \tau^+\tau^-)/\overline{\mathcal{B}}(B_s \to \tau^+\tau^-)_{\rm SM} \le 1.0, \quad 0.995 \le \mathcal{A}^{\tau\tau}_{\Delta\Gamma_s} \le 1.000, \tag{5}$$

with a similar picture for $B_d^0 \to \tau^+\tau^-$. First experimental bounds were obtained by LHCb.[8]

In the case of $B_q^0 \to e^+e^-$, we have a situation complementary to $B_q^0 \to \tau^+\tau^-$ within the FUNP framework, where the NP effects are hugely amplified by the mass ratio $m_\mu/m_e \sim 207$. In this scenario, the (pseudo)-scalar New Physics contributions lift the helicity suppression of the extremely small SM branching ratio, as illustrated in Fig. 4, where the red and green bands describe $P^s_{\mu\mu} < 0$ and $P^s_{\mu\mu} > 0$, respectively. These results correspond to

$$0 \le \overline{R}^s_{ee} \le 1.7 \times 10^5, \quad 0 \le \overline{\mathcal{B}}(B_s \to e^+e^-) \le 1.4 \times 10^{-8}; \tag{6}$$

a similar picture arises for the $B_d \to e^+e^-$ decay, with $0 \le \overline{\mathcal{B}}(B_d \to e^+e^-) \le 4.0 \times 10^{-10}$. The most recent experimental constraints on these modes were obtained by the CDF collaboration: $\overline{\mathcal{B}}(B_s \to e^+e^-) < 2.8 \times 10^{-7}$ and $\overline{\mathcal{B}}(B_d \to e^+e^-) < 8.3 \times 10^{-8}$, and date back to 2009.[9] It would be most interesting to search for these modes at the LHC, where an observation would give an unambiguous signal for physics beyond the SM.

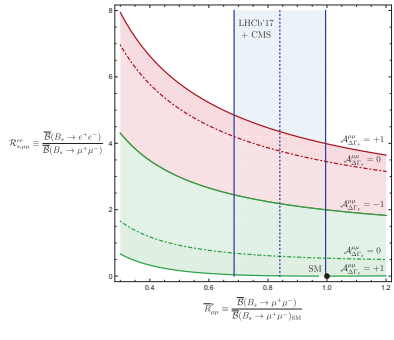


Figure 4 – Correlation between the $B_s \to e^+e^-$ and $B_s \to \mu^+\mu^-$ branching ratios in the FUNP scenario.

## 3 Impact of CP Violation

New sources of CP violation may enter through phases of the short-distance coefficients. In the case of $B_s \to \mu^+\mu^-$ decays, we have the following time-dependent CP asymmetry:[1,2]

$$\frac{\Gamma(B_s^0(t) \to \mu^+_\lambda \mu^-_\lambda) - \Gamma(\bar{B}_s^0(t) \to \mu^+_\lambda \mu^-_\lambda)}{\Gamma(B_s^0(t) \to \mu^+_\lambda \mu^-_\lambda) + \Gamma(\bar{B}_s^0(t) \to \mu^+_\lambda \mu^-_\lambda)} = \frac{\mathcal{C}^\lambda_{\mu\mu}\cos(\Delta M_s t) + \mathcal{S}_{\mu\mu}\sin(\Delta M_s t)}{\cosh(y_s t/\tau_{B_s}) + \mathcal{A}^{\mu\mu}_{\Delta\Gamma_s}\sinh(y_s t/\tau_{B_s})}, \tag{7}$$

where $\lambda$ is the muon helicity and $y_s \equiv \Delta\Gamma_s \tau_{B_s}/2$. The $\mathcal{C}^\lambda_{\mu\mu}$ term cancels in the helicity-averaged rates, and $(\mathcal{C}^\lambda_{\mu\mu})^2 + (\mathcal{S}_{\mu\mu})^2 + (\mathcal{A}^{\mu\mu}_{\Delta\Gamma_s})^2 = 1$. These CP asymmetries were analysed within specific NP models,[2] and a detailed study to probe possible CP-violating phases of $P^s_{\mu\mu} \equiv |P^s_{\mu\mu}| e^{i\varphi^{\mu\mu}_{P_s}}$ and $S^s_{\mu\mu} \equiv |S^s_{\mu\mu}| e^{i\varphi^{\mu\mu}_{S_s}}$ has recently been performed,[4] showing that the CP asymmetries do not offer sufficient information to determine all parameters from the data. However, assuming specific scenarios, much sharper pictures can be obtained. Explorations of CP violation offer valuable insights and are an essential part for revealing the full dynamics of the $B_s^0 \to \mu^+\mu^-$ decays.

## 4 Conclusions

We are moving towards new frontiers with $B_q \to \ell^+\ell^-$ decays. The $B_s^0 \to \mu^+\mu^-$ mode has been observed, and $\Delta\Gamma_s$ provides access to a new – theoretically clean – observable $\mathcal{A}^{\mu\mu}_{\Delta\Gamma_s}$, which should be fully exploited in the future. What are the implications of the $B_s^0 \to \mu^+\mu^-$ measurement for the other $B_{s,d} \to \ell^+\ell^-$ decays? Assuming flavour-universal NP effects, $B_d \to \mu^+\mu^-$ is found to be moderately suppressed with respect to the SM and the NP effects strongly suppressed by $m_\mu/m_\tau \sim 0.06$ in $B_{s,d} \to \tau^+\tau^-$ decays. On the other hand, NP effects could by hugely amplified in this scenario by $m_\mu/m_e \sim 207$ in $B_{s,d} \to e^+e^-$, thereby lifting $\overline{\mathcal{B}}(B_s \to e^+e^-)$ up to the regime of $\overline{\mathcal{B}}(B_s \to \mu^+\mu^-)$, with the exciting possibility that it may be within reach at the LHC. New sources of CP violation may enter $B_q \to \ell^+\ell^-$ decays and offer an interesting playground, both for theorists within specific extensions of the SM and for experimentalists to explore future measurements of the corresponding observables. Decays of the kind $B_q \to \ell^+\ell^-$ offer new degrees of freedom for NP searches at the upcoming LHC upgrade and beyond!


### Acknowledgments

I am very grateful to Gilberto Tetlalmatzi-Xolocotzi, Ruben Jaarsma and Daniela Galárraga Espinosa for our recent collaborations on topics discussed here. This research has been supported by the Netherlands Foundation for Fundamental Research of Matter (FOM) programme 156, "Higgs as Probe and Portal", and by the National Organisation for Scientific Research (NWO).


### References


1. K. De Bruyn, R. Fleischer, R. Knegjens, P. Koppenburg, M. Merk, A. Pellegrino and N. Tuning, Phys. Rev. Lett. **109**, 041801 (2012).
2. A. J. Buras, R. Fleischer, J. Girrbach and R. Knegjens, JHEP **1307**, 77 (2013).
3. R. Fleischer, R. Jaarsma and G. Tetlalmatzi-Xolocotzi, JHEP **1705**, 156 (2017).
4. R. Fleischer, D. Galárraga Espinosa, R. Jaarsma and G. Tetlalmatzi-Xolocotzi, Eur. Phys. J. C **78**, 1 (2018).
5. K. De Bruyn, R. Fleischer, R. Knegjens, P. Koppenburg, M. Merk and N. Tuning, Phys. Rev. D **86**, 014027 (2012).
6. M. Beneke, C. Bobeth and R. Szafron, Phys. Rev. Lett. **120**, 011801 (2018)
7. R. Aaij *et al.* [LHCb Collaboration], Phys. Rev. Lett. **118**, 191801 (2017).
8. R. Aaij *et al.* [LHCb Collaboration], Phys. Rev. Lett. **118**, 251802 (2017).
9. T. Aaltonen *et al.* [CDF Collaboration], Phys. Rev. Lett. **102**, 201801 (2009).

# UTILISING $B \to \pi K$ DECAYS AT THE HIGH-PRECISION FRONTIER

R. FLEISCHER [1,2], R. JAARSMA [1 a], E. MALAMI [1] AND K. K. VOS [3]
[1] *Nikhef, Science Park 105, 1098 XG Amsterdam, Netherlands*
[2] *Department of Physics and Astronomy, Faculty of Science, Vrije Universiteit Amsterdam, 1081 HV Amsterdam, Netherlands*
[3] *Theoretische Physik 1, Naturwissenschaftlich-Technische Fakultät, Universität Siegen, D-57068 Siegen, Germany*

For about twenty years, $B \to \pi K$ decays are in the focus of $B$-decay studies. We show that a correlation between the CP asymmetries of $B^0_d \to \pi^0 K_S$ reveals a tension with the Standard Model. Should it be due to New Physics, a modified electroweak penguin sector provides particularly interesting possibilities. We present a new method to determine the electroweak penguin parameters, which uses an isospin relation and requires only minimal $SU(3)$ input. We apply it to the current data for $B \to \pi K$ decays and discuss the prospects for utilizing CP violation in $B^0_d \to \pi^0 K_S$. The strategy has the exciting potential to establish New Physics in the electroweak penguin sector in the high-precision era of $B$-physics.

## 1 Introduction

Decays of the type $B \to \pi K$ have been in the spotlight for over two decades (see Refs. 1,2 and references therein). This is a particularly interesting class of decays because the leading contributions come from QCD penguin topologies; the tree topologies are suppressed by the CKM matrix element $V_{ub}$. Moreover, electroweak (EW) penguin topologies give contributions at the same level as the tree topologies.

The decay $B^0_d \to \pi^0 K_S$ is the only $B \to \pi K$ channel with a mixing-induced CP asymmetry, which arises from interference between $B^0_d$–$\bar{B}^0_d$ mixing and the decay of $B^0_d$ or $\bar{B}^0_d$ into the $\pi^0 K_S$ final state. Moreover, all $B \to \pi K$ decays may have direct CP violation, arising from interference between penguin and tree contributions. The correlation between the CP asymmetries of the $B^0_d \to \pi^0 K_S$ mode has revealed a discrepancy in the past, which could be explained by a modified EW penguin sector.[2] We provide an up-to-date picture of this correlation, and present a new method to pin down the parameters governing the EW penguin contributions.[3,4]

## 2 The $B \to \pi K$ System

The EW penguin topologies contributing to $B^0_d \to \pi^- K^+$ and $B^+ \to \pi^+ K^0$ are colour-suppressed and play a minor role. On the other hand, the $B^0_d \to \pi^0 K^0$ and $B^+ \to \pi^0 K^+$ channels have also contributions from colour-allowed EW penguin toplogies. These effects are described by the following parameter, which can be calculated using the $SU(3)$ flavour symmetry: [5,1]

$$q e^{i\phi} e^{i\omega} \equiv -\left(\frac{\hat{P}_{EW} + \hat{P}^C_{EW}}{\hat{T} + \hat{C}}\right) \stackrel{\rm SM}{=} \frac{-3}{2\lambda^2 R_b}\left(\frac{C_9 + C_{10}}{C_1 + C_2}\right) R_q = (0.68 \pm 0.05) R_q. \qquad (1)$$

[a] Speaker

Here $\phi(\omega)$ is a CP-violating (CP-conserving) phase, and $\hat{P}_{EW}(\hat{T})$ and $\hat{P}^{\rm C}_{EW}(\hat{C})$ are colour-allowed and colour-suppressed EW penguin (tree) amplitudes, respectively. Note that $\omega$ vanishes in the $SU(3)$ limit, and that its smallness is a model-independent result.[6] Furthermore, $\lambda \equiv |V_{us}| = 0.22$, $R_b$ is a side of the unitarity triangle (UT), the $C_i$ are Wilson coefficients, and $SU(3)$-breaking corrections are parametrized by $R_q = 1.0 \pm 0.3$.

The tree and QCD penguin topologies are described by the hadronic parameters

$$r_{\rm c} e^{i\delta_{\rm c}} \equiv (\hat{T} + \hat{C})/P', \quad r e^{i\delta} \equiv (\hat{T} - \hat{P}_{tu})/P', \tag{2}$$

where $\hat{P}_{tu}$ is the difference between QCD penguin amplitudes with $t$ and $u$ quarks, and $P' \propto P_{tc}$. In order to determine these parameters, we follow Refs. 1,2 and use $B \to \pi\pi$ data, where contributions from EW penguins are tiny, and employ the $SU(3)$ flavour symmetry, yielding: [3,4]

$$r_{\rm c} e^{i\delta_{\rm c}} = (0.17 \pm 0.06) e^{i(1.9 \pm 23.9)^\circ}, \quad r e^{i\delta} = (0.09 \pm 0.03) e^{i(28.6 \pm 21.4)^\circ}. \tag{3}$$

Here, we allowed for non-factorizable $SU(3)$-breaking corrections of 20%. In an analysis of $B_{d,s} \to \pi\pi$, $KK$, $\pi K$ modes we did not find indications of anomalously large non-factorizable $SU(3)$-breaking corrections. [7]

The amplitudes of the $B \to \pi K$ decays satisfy the following isospin relation: [1,2]

$$\sqrt{2} A(B_d^0 \to \pi^0 K^0) + A(B_d^0 \to \pi^- K^+) = \sqrt{2} A(B^+ \to \pi^0 K^+) + A(B^+ \to \pi^+ K^0) \equiv 3 A_{3/2}. \tag{4}$$

Here $3A_{3/2} \equiv 3|A_{3/2}| e^{i\phi_{3/2}}$ is an isospin $I = 3/2$ amplitude, which is given by

$$3A_{3/2} = -(\hat{T} + \hat{C}) e^{i\gamma} + (\hat{P}_{EW} + \hat{P}^{\rm C}_{EW}) = -(\hat{T} + \hat{C}) \left( e^{i\gamma} - q e^{i\phi} e^{i\omega} \right), \tag{5}$$

where $\gamma = (70 \pm 7)^\circ$ is the corresponding UT angle, and $|\hat{T} + \hat{C}|$ can be determined from the $B \to \pi\pi$ system using the following $SU(3)$ relation: [8]

$$|\hat{T} + \hat{C}| = R_{T+C} \, |V_{us}/V_{ud}| \, \sqrt{2} |A(B^+ \to \pi^+ \pi^0)|. \tag{6}$$

The $SU(3)$-breaking effects are given by $R_{T+C} \approx f_K/f_\pi = 1.2 \pm 0.2$, where the central value is obtained in factorization and the uncertainty allows for non-factorizable corrections.

The direct CP asymmetries $A_{\rm CP}^f \equiv \left(|\bar{A}_f|^2 - |A_f|^2\right) / \left(|\bar{A}_f|^2 + |A_f|^2\right)$ are proportional to $r_{\rm (c)} \sin\delta_{\rm (c)} \sin\gamma$, giving values of $\mathcal{O}(10\%)$. Together with the branching ratios they are ingredients of a sum rule,[9] which vanishes in the SM up to corrections of $\mathcal{O}(r^2_{\rm (c)})$.[3,4] The current experimental data [10] are in agreement with the SM pattern.[4] Since the uncertainty of $A_{\rm CP}^{\pi^0 K^0}$ is still large, we use the sum rule to predict this observable: [3,4]

$$A_{\rm CP}^{\pi^0 K^0} = -0.14 \pm 0.03. \tag{7}$$

The mixing-induced CP asymmetry $S_{\rm CP}^f$ enters the time-dependent rate asymmetry as

$$\frac{\Gamma(\bar{B}_d^0(t) \to \pi^0 K_{\rm S}) - \Gamma(B_d^0(t) \to \pi^0 K_{\rm S})}{\Gamma(\bar{B}_d^0(t) \to \pi^0 K_{\rm S}) + \Gamma(B_d^0(t) \to \pi^0 K_{\rm S})} = A_{\rm CP}^{\pi^0 K_{\rm S}} \cos(\Delta M_d t) + S_{\rm CP}^{\pi^0 K_{\rm S}} \sin(\Delta M_d t), \tag{8}$$

where $\Delta M_d$ is the mass difference between the $B_d$ mass eigenstates. We have

$$S_{\rm CP}^{\pi^0 K_{\rm S}} = \sin(\phi_d - \phi_{00}) \sqrt{1 - (A_{\rm CP}^{\pi^0 K_{\rm S}})^2}, \tag{9}$$

where $\phi_d = (43.2 \pm 1.8)^\circ$ is the CP-violating $B_d^0$–$\bar{B}_d^0$ mixing phase.[2] The key quantity is the angle $\phi_{00} \equiv \arg(\bar{\rm A}_{00} {\rm A}_{00}^*)$ between $A_{00} \equiv A(B_d^0 \to \pi^0 K^0)$ and its CP-conjugate $\bar{A}_{00}$, which can be expressed in terms of the hadronic parameters in Eq. 2 as follows: [3,4]

$$\tan\phi_{00} = 2(r\cos\delta - r_{\rm c}\cos\delta_{\rm c}) \sin\gamma + 2 r_{\rm c} \left(\cos\delta_{\rm c} - 2\tilde{a}_{\rm C}/3\right) q \sin\phi + \mathcal{O}(r^2_{\rm (c)}). \tag{10}$$

Here $\tilde{a}_{\rm C} \equiv a_{\rm C} \cos(\Delta_{\rm C} + \delta_{\rm c})$ parametrizes the small colour-suppressed EW penguin contributions.

## 3 Correlation Between the CP Asymmetries of $B_d^0 \to \pi^0 K_S$

We may calculate $\phi_{00}$ using the numerical values in Eqs. 1 and 3. However, the cleanest way to determine this quantity is from the amplitude triangles corresponding to the isospin relation for the neutral decays in Eq. 4, as it requires only minimal $SU(3)$ input and no topologies have to be neglected.[2] From Eq. 9, we can then determine $S_{CP}^{\pi^0 K_S}$ as a function of $A_{CP}^{\pi^0 K_S}$. This yields the correlation shown in the left panel of Fig. 1, which is more constrained than in previous work [2] due to a better determination of $\gamma$. We also show current data [10] and the prediction from the sum rule. We observe a discrepancy between the data and the correlation at the $2\sigma$ level.

In the right panel of Fig. 1, we show a new constraint, obtained from the angle $\phi_\pm \equiv \arg(\bar{A}_\pm A_\pm^*)$ between $A_\pm \equiv A(B_d^0 \to \pi^- K^+)$ and its CP-conjugate $\bar{A}_\pm$. For $\phi = 0°$, which includes the SM, we obtain $\phi_\pm|_{\phi=0} = 2\,r\cos\delta\sin\gamma + \mathcal{O}(r^2) = (8.7 \pm 3.5)°$, where the numerical value follows from Eq. 3. We can also extract this angle from the amplitude triangles. The tension between these two constraints shows that also the correlation itself is not in agreement with the SM. We could obtain a consistent picture in Fig. 1 if the CP asymmetries of $B_d^0 \to \pi^0 K_S$ moved by $\sim 1\sigma$ and $\mathcal{B}r(\pi^0 K^0)$ went down by $\sim 2.5\sigma$. On the other hand, Fig. 1 may also be a hint of NP, where a modified EW penguin sector is a particularly interesting scenario.

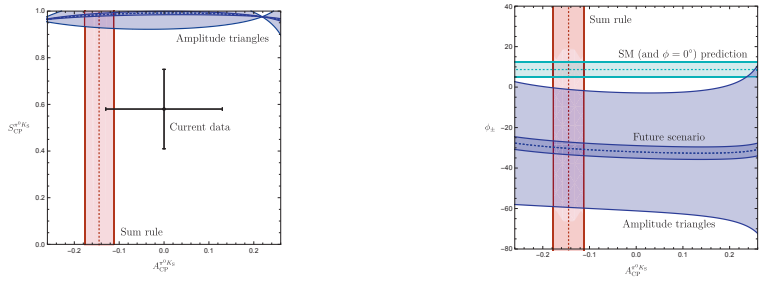


Figure 1 – Correlation between the CP asymmetries of $B_d^0 \to \pi^0 K_S$ (left), and $\phi_\pm$ as a function of $A_{CP}^{\pi^0 K_S}$ (right).

## 4 Determination of the EW Penguin Parameters

The EW penguin parameters $q$ and $\phi$ can also be determined from the isospin relation in Eqs. 4 and 5. Specifically, we can use the amplitude triangles to express these parameters as a function of $3|A_{3/2}|/|\hat{T}+\hat{C}|$, yielding contours in the $\phi$–$q$ plane.[3,4] This method requires only minimal $SU(3)$ input to determine $|\hat{T}+\hat{C}|$ from Eq. 6, and no topologies have to be neglected.

The analysis can be done for both the neutral decays and the charged decays separately. It requires us to fix the relative orientation of the triangles, which we can do through $S_{CP}^{\pi^0 K_S}$ in the case of the neutral decays, and with the angle between $A(B^+ \to \pi^+ K^0)$ and its CP conjugate, which is of $\mathcal{O}(1°)$, for the charged decays. Since the current uncertainty of $S_{CP}^{\pi^0 K_S}$ is still large,[10] we perform the analysis for the charged decays, yielding the contours in the left panel of Fig. 2.

In order to determine the values of $q$ and $\phi$ we need further input. This can be obtained from $S_{CP}^{\pi^0 K_S}$ using the hadronic parameters in Eq. 2. In particular, we can convert a measurement of this observables into a value of $\phi_{00}$, and subsequently obtain a contour in the $\phi$–$q$ plane from Eq. 10. As the strong phases enter only as $\cos\delta_{(c)}$, this expression is very insensitive to variations of these small parameters, thereby having a theoretically favourable structure. Furthermore, the small contributions from colour-suppressed EW penguins can be included through data.[3,4]

In view of the current large uncertainty of $S_{CP}^{\pi^0 K_S}$, we study 3 different scenarios. In the right panel of Fig. 2, we give again the contours from the amplitudes triangles, now assuming perfect measurements and progress on the calculation of $R_{T+C}$.[2] In addition, we show the contours from

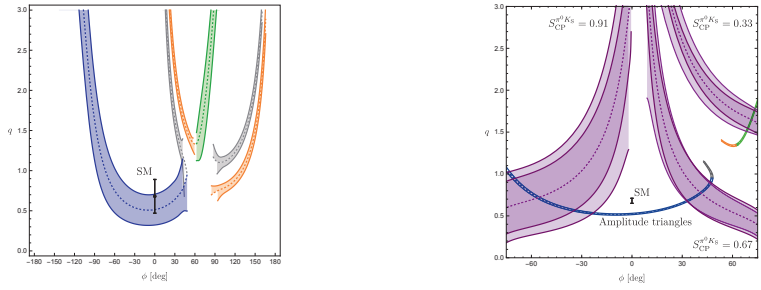


Figure 2 – Contours in the $\phi$–$q$ plane for charged $B \to \pi K$ data following from the isospin relation in Eqs. 4 and 5. The left panel shows current data, whereas the right one corresponds to future scenarios. The purple contours follow from different assumed measurements of $S_{\rm CP}^{\pi^0 K_S}$.

$S_{\rm CP}^{\pi^0 K_S}$, where we assume a precision of $\pm 0.04$ for the CP asymmetries of $B_d^0 \to \pi^0 K_S$ at the end of Belle II,[11] and include 20% non-factorizable $SU(3)$-breaking corrections for the hadronic parameters entering Eq. 10. We give separately the experimental (small bands) and theoretical (wide bands) uncertainties, and observe that we can match the experimental precision with theory. Moreover, we see that $S_{\rm CP}^{\pi^0 K_S}$ provides complementary information on $q$ and $\phi$, allowing the determination of these parameters.

## 5 Conclusions

We have performed a state-of-the-art $B \to \pi K$ analysis, showing that a tension with the SM in the correlation of the $B_d^0 \to \pi^0 K_S$ CP asymmetries has become stronger. In order to clarify this intriguing picture, either data have to move to confirm the SM, or we may have NP, where a modified EW penguin sector provides a particularly interesting scenario. We present a new strategy to determine the EW penguin parameters $q$ and $\phi$, which has the potential to resolve this puzzling situation and reveal new sources of CP violation.


## Acknowledgments

This research has been supported by the Netherlands Organisation for Scientific Research (NWO) and by the Deutsche Forschungsgemeinschaft (DFG), research unit FOR 1873 (QFET).


## References


1. A. J. Buras, R. Fleischer, S. Recksiegel and F. Schwab, *Phys. Rev. Lett.* **92**, 101804 (2004); *Nucl. Phys.* B **697**, 133 (2004).
2. R. Fleischer, S. Jäger, D. Pirjol and J. Zupan, *Phys. Rev.* D **78**, 111501 (2008).
3. R. Fleischer, R. Jaarsma and K. K. Vos, arXiv:1712.02323 [hep-ph].
4. R. Fleischer, R. Jaarsma, E. Malami and K. K. Vos, in preparation.
5. M. Neubert and J. L. Rosner, *Phys. Lett.* B **441**, 403; *Phys. Rev. Lett.* **81**, 5076 (1998).
6. M. Beneke, G. Buchalla, M. Neubert and C. T. Sachrajda, *Nucl. Phys.* B **606**, 245 (2001).
7. R. Fleischer, R. Jaarsma and K. K. Vos, *Phys. Rev.* D **94**, 113014 (2016); *JHEP* **1703**, 055 (2017).
8. M. Gronau, J. L. Rosner and D. London, *Phys. Rev. Lett.* **73**, 21 (1994).
9. M. Gronau, *Phys. Lett.* B **627**, 82 (2005); M. Gronau and J. L. Rosner, *Phys. Rev.* D **74**, 057503 (2006).
10. C. Patrignani *et al.* [Particle Data Group], *Chin. Phys.* C **40**, 100001 (2016 and 2017).
11. T. Abe *et al.* [Belle-II Collaboration], arXiv:1011.0352 [physics.ins-det].

# Lepton Flavour Universality tests with B decays at LHCb

Johannes Albrecht
*Fakultät Physik, TU Dortmund, Germany*

This article discusses tests of lepton flavour universality that are carried out with the LHCb experiment. The experimental situation of $b \to s\ell^+\ell^-$ and $b \to c\ell\nu$ decays is summarised.

## 1 Introduction

In the Standard Model of particle physics (SM), the electroweak gauge bosons $Z^0$ and $W^\pm$ have identical couplings to all three lepton flavours. This prediction is called lepton flavour universality (LFU) and is well tested in tree level decays, e.g. of tau leptons, light mesons or the gauge bosons themselves.[1]

Recent measurements of loop level beauty decays of the type $b \to s\ell^+\ell^-$ and semileptonic beauty decays of the type $b \to c\ell\nu$ have shown tensions with the SM prediction of LFU. The most precise measurements of these quantities, performed by the LHCb collaboration, are summarised in these proceedings. All measurements are based on $3\,\text{fb}^{-1}$ of data collected at $\sqrt{s} = 7\,\text{TeV}$ and $8\,\text{TeV}$.

## 2 Lepton Flavour Universality in $b \to s\ell^+\ell^-$ decays

A very clean test for new physics can be performed by taking ratios of $b \to s\ell^+\ell^-$ decays to different lepton species. At the current experiments, $b \to s\ell^+\ell^-$ decays with electrons and muons in the final state are accessible. If the momentum transfer of the dilepton system is sufficiently above the dilepton mass, uncertainties in the hadronic form factors cancel to a very good approximation, leaving a SM prediction with uncertainties below 1%.[2] In the recent years, the interest in lepton flavour universality tests has increased, mainly driven by two measurements from the LHCb collaboration: the ratio of $B^+ \to K^+\mu^+\mu^-$ to $B^+ \to K^+e^+e^-$, called $R_K$,[3] and the ratio of $B^0 \to K^{*0}\mu^+\mu^-$ to $B^0 \to K^{*0}e^+e^-$, called $R_{K^*}$.[4] The LHCb collaboration uses basically the same strategy for both analyses, that is discussed here for general $b \to s\ell^+\ell^-$

decays with the corresponding hadron named $H$. The LFU testing ratio $R_H$ is then defined as

$$R_H = \frac{\int \frac{d\Gamma(B\to H\mu^+\mu^-)}{dq^2}\, dq^2}{\int \frac{d\Gamma(B\to He^+e^-)}{dq^2}\, dq^2}\,,$$

where the differential decay rate is measured in certain $q^2$ ranges. The $q^2$ ranges corresponding to the $J/\psi$ and $\psi(2S)$ is always excluded from the LFU analysis and is used as control channel. To cancel experimental uncertainties in the absolute efficiencies of the measurements, the ratio $R_H$ is not measured directly, but as double ratio, normalising the non-resonant signal mode to the corresponding high-statistics $J/\psi$ mode. The ratio $R_H$ is then measured as

$$R_H = \frac{\mathcal{B}(B\to H\mu^+\mu^-)}{\mathcal{B}(B\to HJ/\psi(\to\mu^+\mu^-))}\Bigg/\frac{\mathcal{B}(B\to He^+e^-)}{\mathcal{B}(B\to HJ/\psi(\to e^+e^-))}\,.$$

A few comments are in order to explain this experimental strategy: firstly, this method tests for LFU violations in the FCNC decays, it relies on the conservation of LFU in the corresponding resonant decay modes. To test this assumption, the ratio of the resonant channels

$$r(J/\psi) = \frac{B\to K^{(*)}J/\psi(\to\mu^+\mu^-)}{B\to K^{(*)}J/\psi(\to e^+e^-)}\,,$$

is confirmed to agree with LFU conservation. It has to be stressed that this test is a more stringent test than necessary, because it tests the absolute ratio of muon to electron reconstruction, identification and selection efficiencies while in the analyses of $R_H$, only relative efficiencies between non-resonant and resonant channels are required. If the ratio $r(J/\psi)$ is tested in bins of the daughter particle momenta, it can directly test the range of $q^2$ covered in the analysis.

The most precise test of $r(J/\psi)$ has been performed in LHCb's analysis of $R_{K^*}$, it was found to be in agreement with unity with a precision of 4.5%. Compared to the statistical uncertainties of the LFU tests of the order of 10%, this uncertainty is subdominant. For further tests with enlarged datasets, the precision in the determination of efficiencies as cross-checked in $r(J/\psi)$ needs to be studied in more detail.

The experimentally best accessible mode of all $b\to s\ell^+\ell^-$ decays is $B^+\to K^+\ell^+\ell^-$. The LHCb collaboration published a measurement using $3\,\text{fb}^{-1}$ of data.[3] The uncertainty of the measurement is dominated by the statistical uncertainty of the electron channel, with a signal yield of $172^{+20}_{-19}$ events, i.e. the statistical uncertainty is of the order of 12%. Dominant systematic uncertainties are the modelling of the mass shape and the determination of the trigger efficiencies, both accounting for about 3%. The value of $R_K$ is found to be

$$R_K = 0.745^{+0.090}_{-0.074}(\text{stat}) \pm 0.036(\text{syst})\,, \tag{1}$$

which is in tension with the SM prediction[5] of 1.0 with a significance of 2.6 standard deviations ($\sigma$). The BaBar and Belle experiments have also published[6,7] tests of LFU, but their analysed dataset is much smaller than the LHCb dataset and hence the measurement has significantly larger uncertainties. The status of all measurements is summarised in Fig. 1 (left).

The next accessible $b\to s\ell^+\ell^-$ channel is $B^0\to K^{*0}\ell^+\ell^-$, which has been published by the LHCb collaboration with $3\,\text{fb}^{-1}$ with a signal yield of 89 and 111 events in the low and central bin of $q^2$, respectively. Similarly to $R_K$, the measurement is implemented as double ratio with the resonant decay mode. Both $q^2$ bins are found below the SM prediction,

$$R_{K^*} = \begin{cases} 0.66\ ^{+\ 0.11}_{-\ 0.07}\,(\text{stat}) \pm 0.03\,(\text{syst}) & \text{for } 0.045 < q^2 < 1.1\ \text{GeV}^2/c^4\,, \\ 0.69\ ^{+\ 0.11}_{-\ 0.07}\,(\text{stat}) \pm 0.05\,(\text{syst}) & \text{for } 1.1\ \ < q^2 < 6.0\ \text{GeV}^2/c^4\,. \end{cases}$$

The measurement of $R_{K^*}$ is shown in Fig. 1 (right). The significances of the deviation of the SM expectation are 2.1 and 2.4 $\sigma$ for the low and middle $q^2$ bin, respectively. The statistical

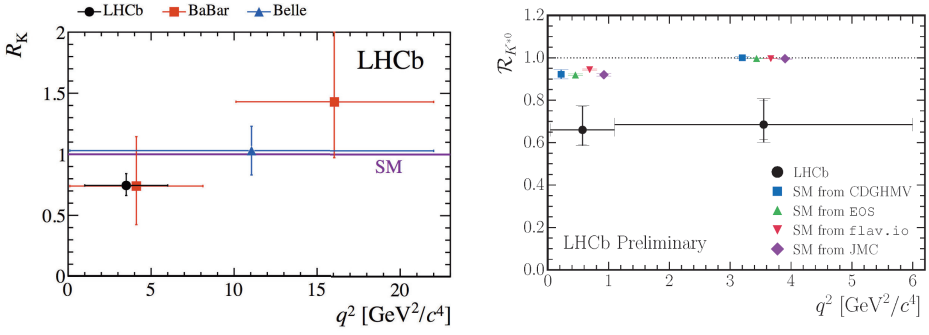


Figure 1 – (left) Summary of the measurements of $R_K$ of the LHCb,[3] BaBar[6] and Belle[7] experiments. The SM prediction is indicated as a line at 1.0. (right) LHCb measurement[4] of $R_{K^*}$, together with several SM predictions.

uncertainty is of the order of 15%, dominant systematic uncertainties are due to data/MC corrections (up to 5%) and background modelling (up to 5%).

The LHCb experiment has already collected a factor three more beauty mesons with respect to the $3\,\text{fb}^{-1}$ that are used for the measurements described above. Therefore, the tensions seen in the $R_K$ and $R_{K^*}$ measurements should get clarified in the foreseeable future. Then, the Belle 2 experiment will start to take data and will be able to further test LFU.

Additionally to the channels discussed above, LFU can be tested in $B_s^0 \to \phi\ell^+\ell^-$ decays, where a first observation of the channel $B_s^0 \to \phi e^+e^-$ should be possible already with $3\,\text{fb}^{-1}$ of LHCb data. Also $B^+ \to K^-\pi^+\pi^-\ell^+\ell^-$ and $\Lambda_b \to \Lambda\ell^+\ell^-$ decays are analysed to test for violation of lepton universality. Combining the already collected large datasets and the analysis of more channels, the question if LFU is conserved in the SM should be conclusively answered in the near future. A quantitative analysis of the future sensitivities to discover LFU is discussed in Ref.[8]

## 3 Lepton Flavour Universality in $b \to c\ell\nu$ decays

Lepton flavour universality can also be tested in semileptonic decays of the type $b \to c\ell\nu$. The observable $R_D^*$ is defined as $R_D^* = \frac{\bar{B}^0 \to D^{*+}\tau^-\bar{\nu}_\tau}{\bar{B}^0 \to D^{*+}\mu^-\bar{\nu}_\mu}$. The SM prediction is calculated to be $R_D^* = 0.252 \pm 0.003$[9], the difference to unity originates in the non-negligible tau-lepton mass. LHCb has also measured[10] $R_D^* = 0.336 \pm 0.027 \pm 0.030$, using the leptonic $\tau^-$ decay mode $\tau^- \to \mu^-\bar{\nu}_\mu\nu_\tau$. The compatibility with the SM prediction is $2.1\sigma$. More recently, LHCb has also measured $R_D^*$ in the hadronic $\tau^-$ decay mode $\tau^- \to \pi^+\pi^-\pi^-(\pi^0)\nu_\tau$, in which the neutral pion is not reconstructed. $R_D^*$ was measured[11] to a value of $0.291 \pm 0.019 \pm 0.026 \pm 0.013$, compatible with the SM prediction at $1.0\sigma$. The experimental situation of the measurements of $R_D^*$ and also the here not discussed $R_D$ is shown in Fig. 2. The combination of both ratios is in tension with the SM with a significance of $4.1\sigma$.[12]

LFU can also be tested in $B_c^+$ decays. LHCb has performed a measurement of the ratio $R_{B_c^+} = \mathcal{B}(B_c^+ \to J/\psi\tau^+\nu_\tau)/\mathcal{B}(B_c^+ \to J/\psi\mu^+\nu_\mu)$, where the $\tau^+$ is reconstructed in the leptonic decay mode.[13] The value found is $R_{B_c^+} = 0.71 \pm 0.17 \pm 0.18$ which is $2.0\sigma$ above the SM prediction. It should be noted that the tensions seen in $R_{B_c^+}$ are in the same direction as the tensions seen in $R_{D^{(*)}}$.

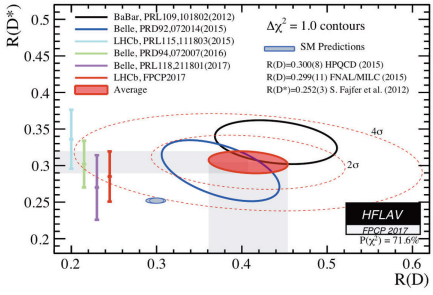


Figure 2 – Summary of the measurements of $R_D$ and $R_D^*$.[12]

## 4 Summary

The recent experimental results testing lepton flavour universality show intriguing tensions. In $b \to s\ell^+\ell^-$ decays, a tension of $4.0\sigma$ is observed, it is even increased if the muonic measurements discussed in Ref.[14] are included. In $b \to c\ell\nu$ decays, a tension with a combined significance of also about $4\sigma$ is seen. Significant theoretical efforts are ongoing to explain both types of anomalies in unified models, a detailed discussion can be found in Refs.[15,16] On the experimental side, the dataset already collected by the LHCb collaboration is about a factor three larger than the dataset analysed here, so interesting updates on the presented measurements can be expected in the near future. Also, the Belle 2 experiment has started to take data and will be able to provide an important cross check of the measurements from the LHCb collaboration.


### Acknowledgments

J. A. gratefully acknowledges support of the Deutsche Forschungsgemeinschaft (DFG, Emmy Noether programme: AL 1639/1-1) and of the European Research Council (ERC Starting Grant: PRECISION 714536).


### References


1. C. Patrignani et al. (PDG), Chin. Phys. C, 40, 100001 (2016) and 2017 update.
2. M. Bordone et al., Eur. Phys. J. C 76 (2016) no.8, 440.
3. R. Aaij et al. [LHCb Collaboration], Phys. Rev. Lett. 113 (2014).
4. R. Aaij et al. [LHCb Collaboration], JHEP 1708 (2017) 055.
5. C. Bobeth, G. Hiller and G. Piranishvili, JHEP 12, 040 (2007).
6. BaBar Collaboration (J. P. Lees et al.), Phys. Rev. D86, 032012 (2012).
7. Belle Collaboration (J. T. Wei et al.), Phys. Rev. Lett. 103, 171801 (2009).
8. J. Albrecht, F. Bernlochner, M. Kenzie, S. Reichert, D. Straub and A. Tully (2017).
9. S. Fajfer et al., Phys. Rev. D 85 (2012) 094025.
10. R. Aaij et al. [LHCb Collaboration], Phys. Rev. Lett. 115 (2015) no.11, 111803 Erratum: [Phys. Rev. Lett. 115 (2015) no.15, 159901].
11. R. Aaij et al. [LHCb Collaboration], Phys. Rev. Lett. 120 (2018) no.17, 171802.
12. HFLAV FPCP 2017
13. R. Aaij et al. [LHCb Collaboration], Phys. Rev. Lett. 120 (2018) no.12, 12180.
14. Andrew Crocombe, *Rare decays at LHCb*, *This proceedings.*
15. Gudrun Hiller, Introductory talk to the Heavy Flavour session, *This proceedings.*
16. Andreas Crivellin, *Explaining the Flavour anomalies with Leptoquarks*, *This proceedings.*

# Explaining the Flavour Anomalies with Leptoquarks

ANDREAS CRIVELLIN
*Paul Scherrer Institut, CH–5232 Villigen PSI, Switzerland*

Several experiments observed deviations from the Standard Model (SM) in the flavour sector: LHCb found a $5\,\sigma$ discrepancy compared to the SM in $b \to s\mu^+\mu^-$ transitions (including hints for lepton flavour universality violation (LFUV) in $R(K)$ and $R(K^*)$). In addition BELLE, BABAR and LHCb founds hints for LFUV in $b \to c\tau\nu$ transitions at the $4\,\sigma$ level. In addition, there is the long-standing discrepancy in the anomalous magnetic moment of the muon with a significance of more than $3\,\sigma$. All these anomalies are related to muons and taus, while the corresponding electron channels seem to be SM like. Interestingly, leptoquarks provide a common solutions to all these hints for LFUV which I discuss in these proceedings.

## 1 Introduction

The discovery the Higgs at the LHC provided the final ingredient of the SM and no direct evidence for physics beyond the SM has been found at the LHC so far. However, there are very intriguing indirect hints for new physics (NP) in the flavor sector, mainly in semileptonic decays of $B$-mesons and the long-lasting discrepancy in the anomalous magnetic moment (AMM) of the muon.

$\boldsymbol{b \to s\ell^+\ell^-}$: Deviations from the SM found by LHCb [1] in the decay $B \to K^*\mu^+\mu^-$ arise mainly in an angular observable called $P_5'$ [2], with a significance of 2–3$\sigma$ depending on assumptions made for the hadronic uncertainties. LHCb has further observed signs for LFUV in $B \to K^{(*)}\ell^+\ell^-$ decays [3] ([4]). Here, the measured ratio branching fraction ratios $R(K^{(*)}) = \frac{\mathrm{Br}[B\to K^{(*)}\mu^+\mu^-]}{\mathrm{Br}[B^{(*)}\to Ke^+e^-]}$ disagree with their theoretically clean SM predictions by $2.6 - 2.8\sigma$ each. Combining these observables with all other available $b \to s$ data, it is found that NP is preferred over the SM by more than $5\sigma$ [5,6]. Here a destructive interference with the SM of the order of 25% is required to account for the data.

$\boldsymbol{b \to c\tau\nu}$: Hints for LFUV in $R(D)$ and $R(D^*)$ were observed first by the BaBar collaboration in 2012 and were confirmed by BELLE and LHCb. Here a combined discrepancy of around $4.0\sigma$ was found [7] and recently LHCb also measured $R(J/\Psi)$ finding consistency. Here, an constructive order 10% effect at the amplitude level is required.

$\boldsymbol{a_\mu}$: The AMM of the muon $a_\mu \equiv (g-2)_\mu/2$, provides another motivation for NP connected to muons. The experimental value of $a_\mu$ is completely dominated by the Brookhaven experiment

E821[8] and is given by $a_\mu^{\rm exp} = (116\,592\,091 \pm 54 \pm 33) \times 10^{-11}$, where the first error is statistical and the second one systematic. This amounts to a discrepancy between the SM and experimental value of more than $3\,\sigma$ (see for example Ref.[9] for a review). Here an effect which is of the order of the electro-weak SM contribution is preferred by the measurement.

## 2 Explanations

Interestingly, all these hints for NP can be explained by leptoquarks, i.e. hypothetical new particles which couple directly quarks to leptons. In fact, there are 10 representations of leptoquarks (5 scalars and 5 vectors) which are invariant under the SM gauge group and couple to SM fermions only[10].

$\boldsymbol{b \to s\ell^+\ell^-}$: Here an explanation with leptoquarks is quite straight forward . There are three representations of LQ with give a good fit to data, in this case a $C_9 = -C_{10}$ pattern. Since the required effect is quite small and arises at tree-level, the bounds from other processes like $b \to s\gamma$, $B_s$ mixing or $b \to s\nu\nu$ are very weak. However, once couplings to electrons are non-zero, correlations with $b \to se\mu$ processes and $\mu \to e\gamma$ arise, implying stringent bounds which differ for the three representations[11].

$\boldsymbol{a_\mu}$: Even though leptoquarks must be quite heavy due to LHC constraints, it is still possible to get the required sizable effect in the AMM since the contribution can be chrially enhanced by a factor $m_t/m_\mu$ compared to the SM[12]. In fact, among the 5 scalar leptoquark representations which are invariant under the SM gauge group, only two can generate such an enhanced effect because they possess couplings to left- and right-handed muons simultaneously: $\Phi_1$ being an $SU(2)_L$ singlet with hypercharge $-2/3$ and $\Phi_2$ being an $SU(2)_L$ doublet with hypercharge $-7/3$. These leptoquarks lead to simultaneous effects in $Z \to \mu^+\mu^-$ couplings which can be measured at future colliders[13] as shown in the left plot of Fig. 1.

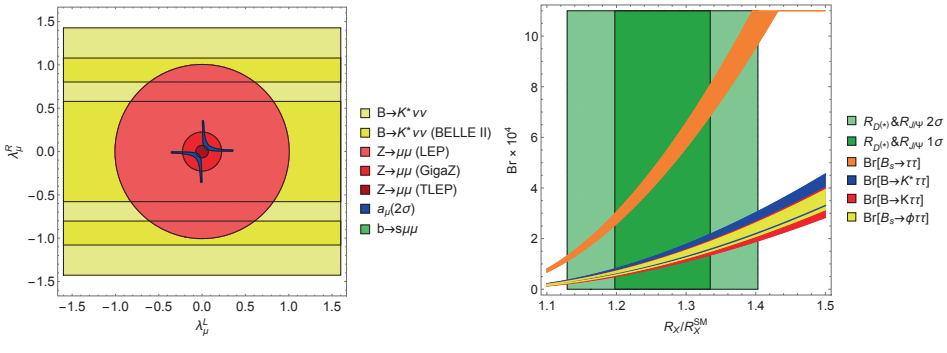


Figure 1 – Left: Allowed regions in the $\lambda_\mu^L$-$\lambda_\mu^R$ plane from current and future experiments for the $SU(2)_L$ singlet leptoquarks $\Phi_1$ with $M = 1\,$TeV. Right: Predictions for $b \to s\tau^+\tau^-$ processes as a function of $R_X/R_X^{\rm SM}$ with $R_X = {\rm Br}[B \to X\tau\nu]/{\rm Br}[B \to X\ell\nu]$ $(X = D, D^*)$ or $R_X = {\rm Br}[B_c \to X\tau\nu]/{\rm Br}[B_c \to X\ell\nu]$ $(X = J/\Psi)$.

$\boldsymbol{B \to D^{(*)}\tau\nu_\tau}$: Leptoquarks can provide a valid explanation here as well (see e.g. [14] for an early account). However, for a single scalar LQ, the coupling structure should be aligned to the bottom quark in order to avoid $b \to s\nu\nu$ bounds and in this case the effect in $R(D)$ and $R(D^*)$ is proportional to the small CKM element $V_{cb}$ and large third generation couplings are required to account for the anomalies. These large third generation couplings lead again to stringent bounds from direct LHC searches[15] and electroweak precision observables[16]. However, LHC bounds from $\tau\tau$ searches and EW precision constraints can be avoided in case of a non-CKM suppressed leptoquark contributions to $R(D)$ and $R(D^*)$. For single scalar leptoquark representations, this leads to unacceptably large effects in $b \to s\nu\nu$ transitions[17]. However, the crucial observation

is that the $SU(2)_L$ singlet $\Phi_1$ and an $SU(2)_L$ triplet $\Phi_3$ both with hypercharge $Y = -2/3$ can contribute with opposite relative sign to $R(D^{(*)})$ than to $b \to s\nu\nu$ processes such that the effect in $R(D^{(*)})$ is doubled while the contributions in $B \to K^{(*)}\nu\nu$ cancel at tree-level [18,19]. Alternatively, one can use the vector-leptoquark $SU(2)$ singlet which automatically avoids effects in $b \to s\nu\nu$ [20]. In both cases, the generic prediction is a huge enhancement of $b \to s\tau\tau$ processes [21] as shown in the right plot of Fig. 1.

## 3 Pati Salam models for the Vector Leptoquark

As explained above, the $SU(2)$ singlet vector leptoquark with hypercharge 2/3 is a natural candidate for a simultaneous explanation of the flavour anomalies [18,20,22,23,24]. Furthermore, it is part of the theoretically very appealing Pati-Salam (PS) model. However, in conventional PS models, the bounds on the breaking scale from $K_L \to \mu e$ and $K \to \pi\mu e$ are so strong (at the PeV scale) [25] that any other observable effect in flavour physics is ruled out. Nonetheless, these bounds can be avoided by introducing vector like fermions and the model can be realized either as a gauge theory with a Higgs mechanism or as a composite model.

**Gauge model:** By supplementing the standard PS model with three generations of vector-like fermions transforming as fundamentals of $SU(4)$ one can avoid the $K_L \to \mu e$ and $K \to \pi\mu e$ bounds [26]. Furthermore, all flavour violation originates from the LQ while also the B-L $Z'$ couples in a flavour diagonal way. However, there are strong LHC bounds on this $Z'$ bosons which require the introduction of additional neutral fermions.

**Pati-Salam broken on a Randall-Sundrum background:** If the PS gauge symmetry is implemented in the 5D Randall-Sundrum (RS) background [27], the mass scale of the Kaluza-Klein (KK) resonances (including the VLQ) can be much lower, i.e. in the few TeV range. The suppression of the lepton flavour violating kaon decays can be achieved by introducing the SM fermions as zero modes of bulk fermions [28] with their couplings to the KK modes determined by their localization along the RS bulk. Since the zero mode localizations are free parameters, one can obtain the required non-trivial flavour structure in order to give interesting effects in $b \to s\mu^+\mu^-$ and $b \to c\tau\nu$ transitions. However, the size of the effects is limited by constraints from $D - \bar{D}$ mixing and sizeable effects in $\tau \to 3\mu$ are predicted [29].

## 4 Conclusions

In these proceedings we reviewed the anomalies in the flavour sector related to charged leptons. Interestingly, all these anomalies involve muons and/or taus while the corresponding electron channels seem to agree with the SM predictions. All these anomalies and can be explained using leptoquarks which are therefore a prime candidate for NP.

## Acknowledgments

A.C. thanks the organizers for the invitation to *Moriond QCD* and for the opportunity to present these results. This work is supported by an Ambizione grant of the Swiss National Science Foundation (PZ00P2_154834).

## References

1. The LHCb Collaboration [LHCb Collaboration], LHCb-CONF-2015-002, CERN-LHCb-CONF-2015-002.
2. S. Descotes-Genon, T. Hurth, J. Matias and J. Virto, JHEP **1305**, 137 (2013) doi:10.1007/JHEP05(2013)137 [arXiv:1303.5794 [hep-ph]].
3. R. Aaij *et al.* [LHCb Collaboration], Phys. Rev. Lett. **113**, 151601 (2014) doi:10.1103/PhysRevLett.113.151601 [arXiv:1406.6482 [hep-ex]].

4. R. Aaij *et al.* [LHCb Collaboration], JHEP **1708**, 055 (2017) doi:10.1007/JHEP08(2017)055 [arXiv:1705.05802 [hep-ex]].
5. B. Capdevila, A. Crivellin, S. Descotes-Genon, J. Matias and J. Virto, JHEP **1801**, 093 (2018) doi:10.1007/JHEP01(2018)093 [arXiv:1704.05340 [hep-ph]].
6. W. Altmannshofer, P. Stangl and D. M. Straub, Phys. Rev. D **96**, no. 5, 055008 (2017) doi:10.1103/PhysRevD.96.055008 [arXiv:1704.05435 [hep-ph]].
7. Y. Amhis *et al.* [HFLAV Collaboration], Eur. Phys. J. C **77**, no. 12, 895 (2017) doi:10.1140/epjc/s10052-017-5058-4 [arXiv:1612.07233 [hep-ex]].
8. G. W. Bennett *et al.* [Muon g-2 Collaboration], Phys. Rev. D **73**, 072003 (2006) doi:10.1103/PhysRevD.73.072003 [hep-ex/0602035].
9. A. Nyffeler, Phys. Rev. D **94**, no. 5, 053006 (2016) doi:10.1103/PhysRevD.94.053006 [arXiv:1602.03398 [hep-ph]].
10. W. Buchmuller, R. Ruckl and D. Wyler, Phys. Lett. B **191**, 442 (1987) Erratum: [Phys. Lett. B **448**, 320 (1999)]. doi:10.1016/S0370-2693(99)00014-3, 10.1016/0370-2693(87)90637-X
11. A. Crivellin, D. Müller, A. Signer and Y. Ulrich, Phys. Rev. D **97**, no. 1, 015019 (2018) doi:10.1103/PhysRevD.97.015019 [arXiv:1706.08511 [hep-ph]].
12. A. Djouadi, T. Kohler, M. Spira and J. Tutas, Z. Phys. C **46**, 679 (1990). doi:10.1007/BF01560270
13. E. Coluccio Leskow, G. D'Ambrosio, A. Crivellin and D. Müller, Phys. Rev. D **95**, no. 5, 055018 (2017) doi:10.1103/PhysRevD.95.055018 [arXiv:1612.06858 [hep-ph]].
14. S. Fajfer, J. F. Kamenik, I. Nisandzic and J. Zupan, Phys. Rev. Lett. **109**, 161801 (2012) doi:10.1103/PhysRevLett.109.161801 [arXiv:1206.1872 [hep-ph]].
15. D. A. Faroughy, A. Greljo and J. F. Kamenik, Phys. Lett. B **764**, 126 (2017) doi:10.1016/j.physletb.2016.11.011 [arXiv:1609.07138 [hep-ph]].
16. F. Feruglio, P. Paradisi and A. Pattori, Phys. Rev. Lett. **118**, no. 1, 011801 (2017) doi:10.1103/PhysRevLett.118.011801 [arXiv:1606.00524 [hep-ph]].
17. X. Q. Li, Y. D. Yang and X. Zhang, JHEP **1608**, 054 (2016) doi:10.1007/JHEP08(2016)054 [arXiv:1605.09308 [hep-ph]].
18. R. Alonso, B. Grinstein and J. Martin Camalich, JHEP **1510**, 184 (2015) doi:10.1007/JHEP10(2015)184 [arXiv:1505.05164 [hep-ph]].
19. A. Crivellin, D. Müller and T. Ota, JHEP **1709**, 040 (2017) doi:10.1007/JHEP09(2017)040 [arXiv:1703.09226 [hep-ph]].
20. L. Calibbi, A. Crivellin and T. Ota, Phys. Rev. Lett. **115**, 181801 (2015) doi:10.1103/PhysRevLett.115.181801 [arXiv:1506.02661 [hep-ph]].
21. B. Capdevila, A. Crivellin, S. Descotes-Genon, L. Hofer and J. Matias, Phys. Rev. Lett. **120**, 181802 (2018) doi:10.1103/PhysRevLett.120.181802 [arXiv:1712.01919 [hep-ph]].
22. R. Barbieri, G. Isidori, A. Pattori and F. Senia, Eur. Phys. J. C **76**, no. 2, 67 (2016) doi:10.1140/epjc/s10052-016-3905-3 [arXiv:1512.01560 [hep-ph]].
23. D. Buttazzo, A. Greljo, G. Isidori and D. Marzocca, JHEP **1711**, 044 (2017) doi:10.1007/JHEP11(2017)044 [arXiv:1706.07808 [hep-ph]].
24. L. Di Luzio, A. Greljo and M. Nardecchia, Phys. Rev. D **96**, no. 11, 115011 (2017) doi:10.1103/PhysRevD.96.115011 [arXiv:1708.08450 [hep-ph]].
25. P. Q. Hung, A. J. Buras and J. D. Bjorken, Phys. Rev. D **25**, 805 (1982). doi:10.1103/PhysRevD.25.805
26. L. Calibbi, A. Crivellin and T. Li, arXiv:1709.00692 [hep-ph].
27. L. Randall and R. Sundrum, Phys. Rev. Lett. **83**, 3370 (1999) doi:10.1103/PhysRevLett.83.3370 [hep-ph/9905221].
28. Y. Grossman and M. Neubert, Phys. Lett. B **474**, 361 (2000) doi:10.1016/S0370-2693(00)00054-X [hep-ph/9912408].
29. M. Blanke and A. Crivellin, arXiv:1801.07256 [hep-ph].

# $B$ anomalies: From warped models to colliders

Abhishek M. Iyer
*INFN Sezione di Napoli,*
*via Cintia, 80126 Napoli Italia*

We address the anomalies in the semi leptonic decays of $B$ mesons in a warped custodial framework. Two possible solutions of lepton non-universality are discussed: A) The muon singlets couple non-universally to NP and B) The non-universality is in the coupling of lepton doublets. Both these scenarios are characterized by different predictions for rare Kaon decays. An essential feature of these solutions is that the electron contribution to the Wilson coefficients (WC) is non-vanishing, thereby offering possibilities of different patterns of solutions. Beginning with a generic $Z'$ model, we demostrate how the observation of the ratio $N_{\mu\mu}/N_{ee}$ can be mapped to a given pattern of WC which satisfy the anomalies.

## 1 Introduction

The observation of lepton flavour universality (LFU) violation in the semi-leptonic decay of $B$ mesons has fueled several new physics (NP) explanations. In the neutral current sector ($b \to sll$ transitions), these observations are parametrized through the measurement of the following ratio [1]:

$$R_K = \left.\frac{\mathcal{B}(B^+ \to K^+\mu^+\mu^-)}{\mathcal{B}(B^+ \to K^+e^+e^-)}\right|_{q^2=1-6\ GeV^2} = 0.745^{+0.090}_{-0.074}\ (stat) \pm 0.036\ (syst) \tag{1}$$

The SM predicts this ratio to be $R_K^{SM} = 1.0003 \pm 0.0001$, implying a $\sim 2.6\ \sigma$ deviation from the SM expectation. Furthermore, this observation was corroborated by the measurement of $R_{K^*} = \frac{\mathcal{B}(B^0 \to K^{*0}\mu^+\mu^-)}{\mathcal{B}(B^0 \to K^{*0}e^+e^-)}$, signaling a $2.4\sigma$ deviation for low $q^2$ and $\sim 2.5\ \sigma$ for medium $q^2$ bins.

In this talk, we will consider their explanation in a Randall Sundrum model with custodial symmetry [2]. This model is characterized by the presence of fermions and gauge bosons in the bulk. On account of this construction, the warped framework admits non-universal coupling of the SM fermions to the KK gauge bosons, thereby offering an explanation to the observed anomalies in the $b \to sll$ sector. Two scenarios of the solutions will be discussed:A) Unorthodox case where non-universality exists in the coupling of lepton singlets to NP and B) Standard scenario where the lepton doublets couple non-universally to NP [3]. An important aspect of this

framework is that the electron coupling to NP is non-vanishing. This results in a possibility where a multi-dimensional (2 or 4) fit to data, (involving both electrons and muons) is possible. With this as a background, we devise a strategy where the information on the extent of electron and muon contribution can be extracted at high $p_T$ hadron experiments. This technique is general for any model with heavy neutral vector bosons. We demonstrate that any differences in the number of di-electrons and di-muons must be due NP effects and not due to experimental uncertainties in their detection.

## 2 $b \to sll$ anomalies

The geometry of the RS model, facilitates differential localization of the fermion fields in the bulk by appropriate choice of bulk mass parameters $c$. This offers an understanding of the hierarchical pattern of the Yukawa couplings. Consequently, the couplings of the fermions to the KK gauge bosons are different thereby leading to the possibility of FCNC at tree level. For the quarks we assume the first two generation couple universally, implying the presence of a $U(2)$ symmetry while the non-universality is due to the third generation couplings. Additionally, we assume that the down type singlets also couple universally. The bulk mass parameters for the third generation quark is chosen to lie in the range $c_{Q_3} \in [0.4, 0.5]$ and $c_{t_R} \in [0, 0.5]$ while the ranges for other fields are chosen to be $c > 0.5$. These numbers, in particular for the down type quarks, are motivated keeping in mind the constraints from $\Delta F = 2$ processes. For the lepton sector we consider the following two scenarios:
**Scenario A:** The non-universality is due the coupling of the muon singlets while the doublets couple universally to NP.
**Scenario B:** In this case the doublets couple non-universally to NP while the coupling of the singlets is assumed to be universal.
In order to describe the observed deviations, we evaluate the NP effects to the Wilson coefficients of the following operators:

$$\mathcal{L} \supset \frac{V_{tb}^* V_{ts} G_F \alpha}{\sqrt{2}\pi} \sum_i C_i \mathcal{O}_i \tag{2}$$

In warped custodial models, there are four additional contributions to tree-level FCNC: $X \in Z_{SM,Z_X,Z_H,\gamma^{(1)}}$. The effective four fermion interactions describing the $b \to sll$ transitions in this case can be written as:

$$\mathcal{L}_{NP} \subset \sum_{X=Z_{SM},Z_H,Z_X,\gamma^{(1)}} X_\mu \left[\alpha_L^{bs}(X)(\bar{s}_L\gamma^\mu b_L) + \alpha_R^{bs}(X)(\bar{s}_R\gamma^\mu b_R) + \bar{l}\left(\alpha_V^l(X)\gamma^\mu - \alpha_A^l(X)\gamma^\mu\gamma^5\right) l\right] \tag{3}$$

where $\alpha_{V,A}^l(X) = \frac{\alpha_L^l(X) \pm \alpha_R^l(X)}{2}$. Matching Eq.3 to the operators in Eq. 2, the Wilson co-efficients for each gauge field $X$ is given as:

$$\begin{aligned}
\Delta C_9 &= -\frac{\sqrt{2}\pi}{M_X^2 G_F \alpha}\alpha_L^{bs}(X)\alpha_V^l(X), \qquad \Delta C_9' = -\frac{\sqrt{2}\pi}{M_X^2 G_F \alpha}\alpha_R^{bs}(X)\alpha_V^l(X) \\
\Delta C_{10} &= \frac{\sqrt{2}\pi}{M_X^2 G_F \alpha}\alpha_L^{bs}(X)\alpha_A^l(X), \quad \Delta C_{10}' = \frac{\sqrt{2}\pi}{M_X^2 G_F \alpha}\alpha_R^{bs}(X)\alpha_A^l(X)
\end{aligned} \tag{4}$$

We work in the mass basis of the up-type quarks such that the rotation matrix $D$ in the down sector corresponds to the $V_{CKM}$. Under the assumption that the down type quark singlets couple universally to NP, $C_{9,10}'$ is zero. We now evaluate the contribution to $C_{9,10}$ for the two scenarios discussed above:
**Scenario A**:The ranges chosen for $c$ parameter scan for the leptons are $c_{\mu_L} = c_L \in [0.45, 0.55]$ and $c_{\mu_R} \in [0.45, 0.55]$. Fig. 1 gives the results of the scan. The scan in this scenario has some interesting features: As shown in the left plot of Fig 1, we find that there exists region in the

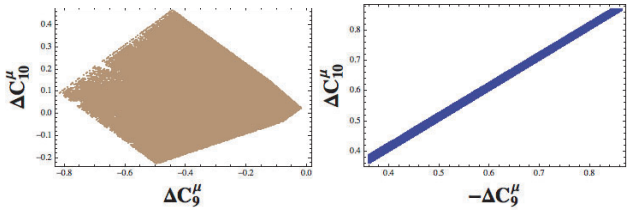


Figure 1 – Scenario **A**: Plots gives the correlation in the $C_9$ and $C_{10}$ parameter plane for both the electron and the muon. We use $M_{KK} = 3\ TeV$

parameter space where $\Delta C_{10}^{\mu}$ is vanishing while $\Delta C_9^{\mu}$ is considerable. This is an artefact of the similar scanning ranges for the doublets and muon singlets and corresponds to the case where $\alpha_L^l(X) = \alpha_R^l(X)$. In such a case, there exist a parameter space where the corresponding electron contributions are also small, thereby reducing the fit to a 1-D case. However, the fits can be obtained just outside the 2 $\sigma$ region. This tight constraint can be relaxed by involving the electrons, thereby making it a 4-D fit to the data.

**Scenario B:** This is the standard scenario, where the electron contributions are typically small. The non-universality in the lepton sector is due to the differential coupling of the muon doublets to NP. Additionally, we allow the coupling of the third generation lepton doublet to also be a free parameter (subject to fitting the tau mass). Right plots of Fig. 1 gives the results of the analysis illustrating the correlation in the $C_{10}^{\mu} - C_9^{\mu}$ plane. The 2-D fit can be reduced to a 1-D fit when $C_{10}^{\mu} = -C_9^{\mu}$.

## 3 Correlating the pattern of solutions to high $p_T$ searches at colliders

The different pattern of solutions to the $B$ anomalies, involving electrons and/or muons can be probed at high energy $p$-$p$ collisions. To begin with, we consider the following neutral current Lagrangian:

$$\mathcal{L}_{eff} = \frac{\lambda_{bs}}{M^2}(\bar{s}\gamma_\mu b)\left[\lambda_e(\bar{e}\gamma^\mu e) + \lambda_\mu(\bar{\mu}\gamma^\mu\mu) + \lambda_\tau(\bar{s}\gamma_\mu b)(\bar{\tau}\gamma^\mu\tau)\right] + \left[\frac{\lambda_b\lambda_\mu}{M^2}(\bar{b}\gamma_\mu b)(\bar{\mu}\gamma^\mu\mu) + \frac{\lambda_c\lambda_\mu}{M^2}(\bar{c}\gamma_\mu c)(\bar{\mu}\gamma^\mu\mu)\right] \tag{5}$$

Given the lagrangian in Eq. 5, the Wilson-coefficients for the $R(K^*)$ anomalies is given as

$$C_9^e = -\frac{\sqrt{2}\pi}{G_F\alpha}\frac{\lambda_{bs}\lambda_e^V}{M^2} \quad C_9^\mu = -\frac{\sqrt{2}\pi}{G_F\alpha}\frac{\lambda_{bs}\lambda_\mu^V}{M^2} \quad C_{10}^e = -\frac{\sqrt{2}\pi}{G_F\alpha}\frac{\lambda_{bs}\lambda_e^{AV}}{M^2} \quad C_{10}^\mu = -\frac{\sqrt{2}\pi}{G_F\alpha}\frac{\lambda_{bs}\lambda_\mu^{AV}}{M^2} \tag{6}$$

where $\lambda^V = \frac{L+R}{2}$ and $\lambda^{AV} = \frac{L-R}{2}$. $L(R)$ is the coupling strength of doublets (singlets) to $Z'$. As an illustration, we assume $L = R$, implying the axial-vector couplings of the leptons to $Z'$ vanish. In this case the ratio of $C_9$ for muons and electrons is simply $\frac{C_\mu^9}{C_e^9} = \frac{\lambda_\mu^V}{\lambda_e^V}$. Notice here that the quark dependence cancels out.

Now consider the production of $Z'$ in $pp$ collisions with its corresponding decays into electrons and muons. The ratio of number di-muons to di-electrons in the $Z'$ mass bin at luminosity $\mathcal{L}$ is simply: $\delta = \frac{\sigma_{Z'}(\lambda_\mu^V)^2\mathcal{L}\epsilon_\mu}{\sigma_{Z'}(\lambda_e^V)^2\mathcal{L}\epsilon_e} = \frac{N_\mu}{N_e}$. As shown in Table. 1, electrons and muons are accompanied by different acceptance efficiencies.

In order to ensure that the measurement of this ratio is purely due to the difference in couplings of the $Z'$ to the leptons, the acceptance efficiencies must be made approximately similar *i.e.* $\epsilon_e \simeq \epsilon_\mu$. This can be achieved by using the electron jet techniques and using the following substructure variables to identify the electron [4]:

A) Hadronic energy fraction: The jets corresponding to the electrons must be associated with

Table 1: Comparison of efficiencies of acceptance for electrons and muons for $m_{Z'} = 3000$ GeV

| | $\epsilon_\mu$ | $\epsilon_e$ |
|---|---|---|
| Simple Isolation($> 1$ leptons) | 59.33 | 39.79 |
| Mass cuts ($> 1000 GeV$) | **58.79** | 39.61 |

very small $H - cal$ deposits. This helps in limiting QCD to a great extent and B) Tracks: The leading jet is associated with exactly one track, while the subleading jet may have 0 or 1 track. The latter condition is useful in accepting events which would otherwise have been rejected by the standard electron identification criteria. Table 1 gives a comparison of the efficiencies when electron jets techniques are employed and we find that the acceptance efficiencies are within $5 - 10\%$ of each other. The continuum SM background has been estimated and is similar for both the electrons and the muons. As a result, any discrepancy in the observation of the ratio can be attributed to the difference in the couplings of the NP to electrons and muons. As shown in the third column of Table 2, this technique can also be extended to tau jets and can be used to extract information on $C_9^\tau$, albeit with lesser accuracy than the leptons. This will have implications for processes like $B \to K^* \tau\tau$

Table 2: Comparison of efficiencies of electron jets and muons for different $m_{Z'}$ masses. A selectrion criteria of the $m_{\mu\mu}$ or $m_{j_0 j_1}$ ($> 1000$) GeV is imposed. For the electron jets the QCD fake rate is $< 1$ in $3 \times 10^5$ events. For $\tau$ jets the QCD fake rate is 0.2%

| $m_{Z'}$ (GeV) | $\epsilon_\mu$ | $\epsilon_e$ (Electron jets) | $\epsilon_\tau$ (tau jets) |
|---|---|---|---|
| 2000 | 71.45 | 64.75 | 31.25 |
| 2500 | 66.35 | 63.06 | 37.28 |
| 3000 | 58.79 | 60.37 | 40.88 |
| 3500 | 51.68 | 59.50 | 43.98 |

## 4 Conclusions

We discussed a warped model with custodial symmetry to address the $B$ anomalies. The pattern of the solutions included contributions to the Wilson coefficients of both the electron and the muon. This provided a natural motivation to look at high $p_T$ experiments which can possibly probe the nature of these solutions. We construct a simple variable $N_{\mu\mu}/N_{ee}$ and demonstrate that this ratio can be mapped to the pattern of WC which satisfy the anomalies


## Acknowledgments

AI were supported in part by MIUR under Project No. 2015P5SBHT and by the INFN research initiative ENP. A.I would also like to thank the organisers of Rencontres de Moriond for the opportunity to present the talk.


## References


1. R. Aaij *et al.* [LHCb Collaboration], Phys. Rev. Lett. **113**, 151601 (2014) doi:10.1103/PhysRevLett.113.151601 [arXiv:1406.6482 [hep-ex]].
2. L. Randall and R. Sundrum, Phys. Rev. Lett. **83**, 3370 (1999) doi:10.1103/PhysRevLett.83.3370 [hep-ph/9905221].
3. G. D'Ambrosio and A. M. Iyer, arXiv:1712.08122 [hep-ph].
4. G. D'Ambrosio, A. M. Iyer et al.;. To appear.

# CAN WE REACH THE SCALE OF NEW PHYSICS BEHIND THE $B$ ANOMALIES? [1] [a]

TEVONG YOU
*DAMTP, University of Cambridge, Wilberforce Road, Cambridge, CB3 0WA, UK;*
*Cavendish Laboratory, University of Cambridge, J.J. Thomson Avenue,*
*Cambridge, CB3 0HE, UK*

Indirect signs of new physics beyond the Standard Model may be appearing in $B \to K^{(*)}\mu^+\mu^-$ decays. If confirmed, the title question will be of paramount importance in determining the strategy for future colliders. We answer it by estimating the sensitivity to minimal, anomaly-compatible $Z'$ and leptoquark models at the high luminosity LHC, 27 TeV HE-LHC, and 100 TeV FCC-hh; this conservative analysis outlines an upper bound on the available parameter space and the conditions for a reasonable guarantee of direct discovery.

## 1 Introduction

Various measurements involving flavour-changing neutral currents in $B \to K^{(*)}\mu^+\mu^-$ decays are in tension with Standard Model (SM) predictions. Taken individually, none are statistically significant enough yet to claim new physics, but collectively they are remarkably consistent with each other: in a global fit, the pull on a Wilson coefficient is over $4\sigma$ away from the SM value. The $B$ anomalies are reviewed elsewhere in these proceedings [2]; it goes without saying that more data and further corroboration by related measurements or independent experiments will be needed to confirm them. Here, let us consider the implications if they are indeed established beyond any reasonable doubt—we will then be in the tantalising position of knowing that fundamentally new physics awaits us at potentially accessible energies. The crucial question is: how accessible exactly? Will a 27 TeV high energy upgrade of the LHC (HE-LHC) be sufficient? Or must we go to 100 TeV as proposed for the FCC-hh? Even then, could the new physics remain just out of reach?

Ideally, we would have a no-lose theorem for going to higher energy, in the same way that at the LHC the Higgs boson or some other discovery was guaranteed to appear below 1 TeV (or, going back further, how massive electroweak gauge bosons were inevitable on the basis of Fermi's theory). Unfortunately, a similar partial wave analysis of the effective operator involved in $b \to s\mu^+\mu^-$ with the required size of new physics places an upper limit on the scale of unitarity violation at $\sim 80$ TeV [3]—beyond the reach of the FCC-hh. Nevertheless, there are still good prospects for discovery given that new physics would typically show up well below the scale of unitarity violation, and other bounds can come into play long before then.

Our strategy [1] is therefore to consider minimal, pessimistic models of $Z'$ and leptoquarks that UV-complete the effective operator at tree level. We make a first quantitative estimate of the sensitivity to these models at the 27 TeV HE-LHC and 100 TeV FCC-hh. The minimal models are naïve in that they include only the couplings necessary to explain the anomalies and

[a] Cavendish-HEP-18/10, DAMTP-2018-18

are pessimistic in the sense that more realistic models will generally (and sometimes necessarily) induce further couplings to other generations of quarks and leptons that would increase their discoverability potential; demonstrating sensitivity to the pessimistic case therefore implies sensitivity to more realistic, model-dependent cases as a corollary. This forms an alternative way of establishing a more conditional "no-lose" theorem (although unlike the unitarity violation limit our bound may still be evaded by even more contrived models).

## 2 Future Collider Sensitivity to $Z'$ and Leptoquarks

We use an approximate method [4] to extrapolate the 95 % CL limits from current searches for $Z'$ and leptoquarks at the LHC to higher luminosities and energies. It assumes that the limit at a particular mass is mainly driven by the number of background events in a narrow width window, so that the same limit will also apply at higher energy and luminosity at the equivalent mass with the same number of background events. There are clearly limitations to this assumption, but this conservative approach is sufficient for an initial order of magnitude estimate.

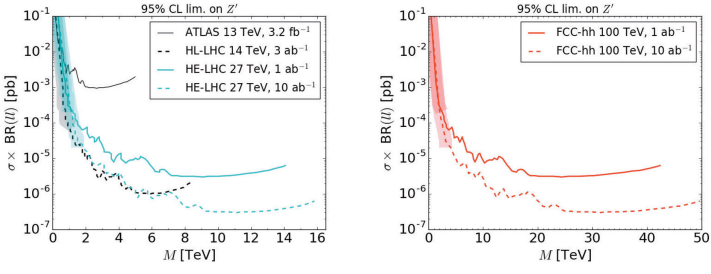


Figure 1 – Projected 95% CL limits on di-muon final states at future colliders described in the legends. The conservative extrapolation method underestimates the actual limit at low masses, as indicated by the shaded region.

We begin with the $Z'$ case. Fig. 1 shows the 95% CL limit on the cross-section times branching ratio (in pb) for the di-muon final state. On the left plot the ATLAS limit for 13 TeV with 3.2 fb$^{-1}$ is denoted by a solid black line, and the limits extrapolated to HL-LHC and HE-LHC are represented by dashed black and cyan lines, respectively. On the right are the corresponding extrapolated limits for FCC-hh in red. The solid (dashed) cyan and red lines are for 1 (10) ab$^{-1}$ of integrated luminosity.

We may now apply these projected limits to our "naïve" $Z'$ model defined by coupling only to $sb$ and $\mu\mu$. As an example, the left plot of Fig. 2 shows dashed blue contours of the cross-section (in units of fb) for $pp \to Z' \to \mu^+\mu^-$ with $M_{Z'} = 1.5$ TeV at the HL-LHC in the plane of the $Z'$ coupling strength, $g_{sb}$ vs $g_{\mu\mu}$. The parameter space compatible with explaining the $B$ anomalies lies along the green band. The 95% CL reach is shaded in blue. We also see that increasing $g_{sb}$ beyond a certain point gives too large a contribution to $B_s - \bar{B}_s$ mixing, shaded in red. The grey region is where the $Z'$ width is larger than 10% of its mass and the narrow width approximation breaks down.

The right plot in Fig. 2 summarises the coverage at the HL-LHC as a function of mass on the horizontal axis, with the vertical axis going along the anomaly-compatible green region for each mass. The colour-coding of the shaded regions are the same as described above, and we see that there is virtually no sensitivity to the large region of available parameter space. The HL-LHC is therefore not guaranteed to find a $Z'$ if it is indeed the source of the anomalies.

However, Fig. 3 shows the corresponding plots for a 100 TeV FCC-hh, with an example $M_{Z'} = 15$ TeV plot on the left and the coverage summary plot on the right. The 27 TeV HE-LHC is also shown in dotted lines for comparison. While the naïve model may still evade

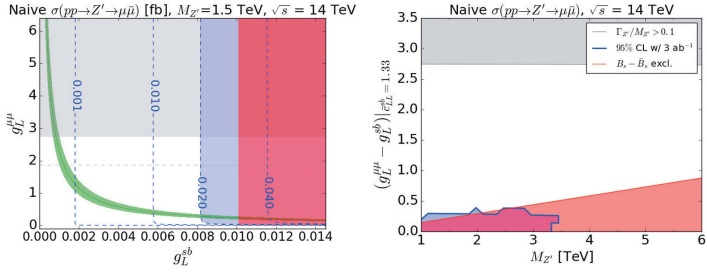


Figure 2 – Parameter space that explains the anomaly (shaded green on the left, whole region on the right) with HL-LHC coverage shown in blue and excluded by $B_s - \bar{B}_s$ mixing in red. The narrow width assumption breaks down in the grey region.

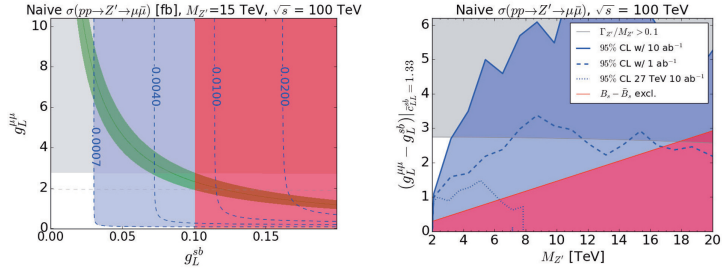


Figure 3 – As in Fig. 2 but for 100 TeV FCC-hh (and 27 TeV HE-LHC in dotted blue on the right).

searches at HE-LHC, there is complete coverage for narrow width $Z'$'s at FCC-hh (we note that the low mass regions are underestimated by the extrapolation method).

We now turn to the case of leptoquarks. The 95% CL limit for the $\mu\mu jj$ final state by CMS at 8 TeV is shown in solid black in the left plot of Fig. 4. The extrapolation to HL-LHC, HE-LHC, and FCC-hh are as described above with the same colour coding. In this case the pair production of scalar leptoquarks is model-independent as it depends only on their coupling to gluons [b]—the cross-section is therefore plotted directly on top of the limit curves, with masses excluded below their intersection. We see that the sensitivity to "naïve" scalar leptoquarks reaches masses around 2.5, 4.5, and 12 TeV for HL-LHC, HE-LHC, and FCC-hh, respectively. However, the lower plot of Fig. 4 shows that anomaly-compatible leptoquarks may have masses up to 40 TeV before being excluded by $B_s - \bar{B}_s$ mixing.

## 3 Conclusion

In lieu of a general no-lose theorem, we may make the following conditional statement:

*If the neutral current B anomalies are due to a narrow width $Z'$ there is a good but not complete sensitivity at the HE-LHC, whereas it is guaranteed to be discovered by the FCC-hh; and if leptoquarks are responsible, then a discovery is only guaranteed for masses below 4.5 and 12 TeV at HE-LHC and FCC-hh respectively.*

The caveat is that "guarantee" is only meant in the sense that it is extremely unlikely (though not impossible) that nature will conspire to hide further the already contrived models considered here. On the contrary, these naïve models are overly pessimistic and difficult to

[b] The vector leptoquark case is more model-dependent but limits are typically stronger for $\mathcal{O}(1)$ couplings. There are also model-dependent single leptoquark production limits [1].

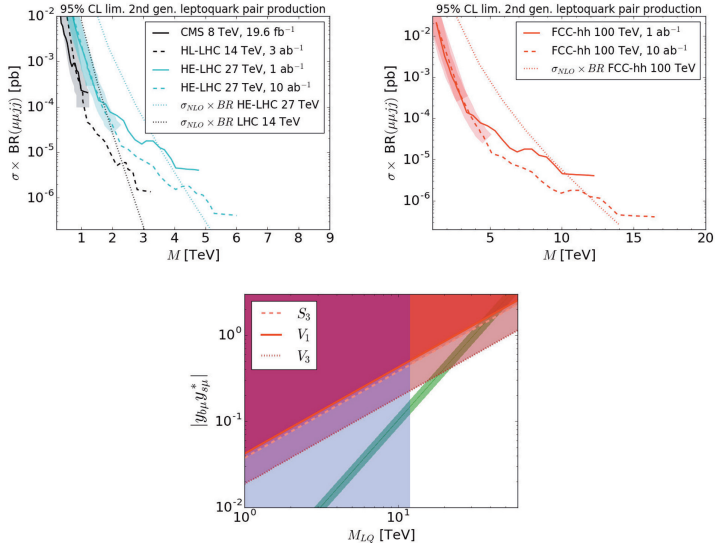


Figure 4 – 95% CL limits as described in Fig. 1 but for leptoquark pair production. The available parameter space compatible with the anomaly in green is displayed on a log-log scale in the bottom plot, with the red region excluded by $B_s - \bar{B}_s$ mixing.

realise consistently[c]: for example, going from gauge to mass eigenstates generally induces further couplings, as in the so-called "$33\mu\mu$" $Z'$ model which already has complete coverage at HE-LHC[1]. The situation for leptoquarks will also be more optimistic.

Further refinements to these estimates can be made, and the sensitivity to more realistic benchmark scenarios can help determine the optimal strategy for targeting new physics. Even if the anomalies vanish, it is interesting to investigate the interplay between direct and indirect searches. On the other hand, should the anomalies be confirmed, it will be the start of a long, but tremendously exciting programme.

## Acknowledgments

I thank Ben Allanach and Ben Gripaios for their collaboration, and the organisers of the Rencontres de Moriond for inviting me to contribute this talk. I am supported by a Research Fellowship from Gonville and Caius College and partially supported by STFC consolidated grant ST/P000681/1.

## References

1. B. C. Allanach, B. Gripaios and T. You, JHEP **1803** (2018) 021 doi:10.1007/JHEP03(2018)021 [arXiv:1710.06363 [hep-ph]].
2. G. Hiller, *these proceedings*.
3. L. Di Luzio and M. Nardecchia, Eur. Phys. J. C **77** (2017) no.8, 536 doi:10.1140/epjc/s10052-017-5118-9 [arXiv:1706.01868 [hep-ph]].
4. A. Thamm, R. Torre and A. Wulzer, JHEP **1507** (2015) 100 doi:10.1007/JHEP07(2015)100 [arXiv:1502.01701 [hep-ph]].

[c] It is, in fact, impossible to have a naïve $Z'$ model without additional couplings.

# 5.
# Heavy Flavour & Spectroscopy

# Charmonium Decays at BESIII

Liang Yan
*Department of Physics, University of Turin and INFN,*
*Via P. Giuria 1, Torino, Italy*

BESIII has collected $1.3 \times 10^9$ $J/\psi$ and $0.5 \times 10^9$ $\psi(3686)$ data. The decay modes of $J/\psi$ and $\psi(3686)$ have been studied directly, including electromagnetic dalitz decay, radiative decay, hadronic decay and rare decay. Based on the largest date samples of $J/\psi$ and $\psi(3686)$, the studies of Charmonium states which could not be produced directly in $e^+e^-$ collision, such as $\chi_{cJ}$, $h_c$ and $\eta_c$, have been performed via $J/\psi$ and $\psi(3686)$ decays.

## 1 Introduction

As a theory of the strong interaction, Quantum Chromodynamics (QCD) has been well tested in the high energy region. However, in the lower energy region, non-perturbative effects are dominant, and theoretical calculations are very complicated. The charmonium states are an ideal laboratory where our understanding of non-perturbative QCD and its interplay with perturbative QCD can be tested in a controlled framework. [1]. Hadronic and electromagnetic transitions between charmonium states and their decays have been measured with the largest data samples collected in BESIII. In this paper, we present the recent charmonium decay results at BESIII.

## 2 $\psi(3686) \to e^+e^-\chi_{cJ}, \chi_{cJ} \to e^+e^-J/\psi$

Electromagnetic (EM) Dalitz decay plays an important role in revealing the structure of hadrons and the interactions betweens photons and hadrons. This decay is widely observed in the light-quark meson sector, but not yet in charmonium decay. The EM Dalitz decays in charmonium transitions have access to the EM transition form factors (TFFs) of these charmonium states. The $q^2$-dependence of charmonium TFFs can provide additional information on the interactions between the charmonium states and the electromagnetic field, where $q^2$ is the square of the invariant mass of the $e^+e^-$ pair, and serve as a sensitive probe to their internal structures. At BESIII, the decays $\psi(3686) \to e^+e^-\chi_{cJ}$ and $\chi_{cJ} \to e^+e^-J/\psi$ are observed for the first time [2]. The measured branching fractions are $\mathcal{B}(\psi(3686) \to e^+e^-\chi_{cJ}) = (11.7 \pm 2.5 \pm 1.0) \times 10^{-4}$, $(8.6 \pm 0.3 \pm 0.6) \times 10^{-4}$, $(6.9 \pm 0.5 \pm 0.6) \times 10^{-4}$ for $J = 0, 1, 2$, and $\mathcal{B}(\chi_{cJ} \to e^+e^-J/\psi) = (1.51 \pm 0.30 \pm 0.13) \times 10^{-4}$, $(3.73 \pm 0.09 \pm 0.25) \times 10^{-3}$, $(2.48 \pm 0.08 \pm 0.16) \times 10^{-3}$ for $J = 0, 1, 2$, respectively. The ratios of the branching fractions $\frac{\mathcal{B}(\psi(3686) \to e^+e^-\chi_{cJ})}{\mathcal{B}(\psi(3686) \to \gamma\chi_{cJ})}$ and $\frac{\mathcal{B}(\chi_{cJ} \to e^+e^-J/\psi)}{\mathcal{B}(\chi_{cJ} \to \gamma J/\psi)}$ are also reported. Also, the $\alpha$ values of helicity angular distributions of the $e^+e^-$ pair are determined for $\psi(3686) \to e^+e^-\chi_{c1,2}$ and $\chi_{c1,2} \to e^+e^-J/\psi$. The measured $q^2$ distributions are consistent with those of the signal MC simulation based on the assumption of a point-like meson [3]. This first observation of the $q^2$-dependent charmounium EM Dalitz transitions can help understand the discrepancy between the experimental measurements and the theoretical predictions of the $\psi(3686) \to \gamma\chi_{cJ}$.

## 3 $\psi(3686) \to \gamma\eta', \gamma\eta$ and $\gamma\pi^0$

The properties of charmonium state radiative decays to a pseudoscalar meson have been predicted by various phenomenological mechanisms. The measurements of $\psi(3686) \to \gamma\eta', \gamma\eta$ and $\gamma\pi^0$ could be helpful to test the different theoretical predictions. The ratio $R_{J/\psi} \equiv \frac{\mathcal{B}(J/\psi\to\gamma\eta)}{\mathcal{B}(J/\psi\to\gamma\eta')}$ has been predicted based on the first-order perturbative QCD calculation, and $R_{\psi(3686)} \equiv \frac{\mathcal{B}(\psi(3686)\to\gamma\eta)}{\mathcal{B}(\psi(3686)\to\gamma\eta')}$ is expected to be approximately equal to $R_{J/\psi}$. The decay rates of $J/\psi$ and $\psi(3686) \to \gamma\pi^0$ are expected to be smaller than those of $J/\psi$ and $\psi(3686) \to \gamma\eta$ or $\gamma\eta'$ as a consequence of suppressed gluon coupling to isovector currents. By analyzing the data sample of $448\times10^6$ $\psi(3686)$ events collected at $\sqrt{s} = 3.686$ GeV with the BESIII detector, we observe clear signals of $\psi(3686)$ decays to $\gamma\eta', \gamma\eta$, and $\gamma\pi^0$ [4]. The ratio of branching fractions of $\psi(3686) \to \gamma\eta$ and $\psi(3686) \to \gamma\eta'$ is calculated to be $R_{\psi(3686)} = (0.66 \pm 0.13 \pm 0.02)\%$. This is about 30 times smaller than the corresponding ratio from $J/\psi$ radiative decays. $R_{J/\psi} = (21.4 \pm 0.9)\%$. And the branching fraction of $\psi(3686) \to \gamma\pi^0$ is measured to be $(0.66 \sim 1.15) \times 10^{-7}$ which is one order larger than the prediction [5].

## 4 $\psi(3686) \to n\bar{n}$ and $p\bar{p}$

The measurements of $\psi(3686) \to n\bar{n}$ and $\psi(3686) \to p\bar{p}$ could be used to determine the relative phase angle between the amplitudes of the strong and electromagnetic interactions. And the relative phase angle has been studied via $J/\psi$ two-body decays to mesons and baryons. All results favor near orthogonality between the two amplitudes. $J/\psi \to p\bar{p}$ and $n\bar{n}$ have been measured by BESIII, and confirm the previously measured orthogonal relative phase angle. But the experimental knowledge of $\psi(3686)$ decays is relatively limited. The angular distributions of final states in $\psi(3686) \to p\bar{p}$ and $n\bar{n}$ decays are also interesting. Due to the Okubo-Zweig-Iizuka (OZI) mechanism, the decays of $J/\psi$ and $\psi(3686)$ to hadrons are mediated via three gluons or a single photon at the leading order. Perturbative QCD predicts the "12% rule", $Q_h = \frac{\mathcal{B}(\psi(3686)\to h)}{\mathcal{B}(J/\psi\to h)} = \frac{\mathcal{B}(\psi(3686)\to\mu^+\mu^-)}{\mathcal{B}(J/\psi\to\mu^+\mu^-)} \approx 12.7\%$. It was first observed to be violated in the decay of $\psi$ into $\rho\pi$ by MARKII, called the "$\rho\pi$ puzzle" . Further precise measurements of $J/\psi$ and $\psi(3686)$ decay to $N\bar{N}$ may provide additional knowledge to help understand the $\rho\pi$ puzzle. By using $1.07 \times 10^8$ $\psi(3686)$ events collected with the BESIII detector, we observe the decay $\psi(3686) \to n\bar{n}$ for the first time and measure $\psi(3686) \to p\bar{p}$ with improved accuracy [6]. The measured branching fractions are $\mathcal{B}(\psi(3686) \to n\bar{n}) = (3.06 \pm 0.06 \pm 0.14) \times 10^{-4}$ and $\mathcal{B}(\psi(3686) \to p\bar{p}) = (3.05 \pm 0.02 \pm 0.12) \times 10^{-4}$. With the hypothesis that the polar angular distributions of the neutron and proton in the center-of-mass system obey $1 + \alpha\cos^2\theta$, we determine the $\alpha$ parameters to be $\alpha_{n\bar{n}} = 0.68 \pm 0.12 \pm 0.11$ and $\alpha_{p\bar{p}} = 1.03 \pm 0.06 \pm 0.03$ for $\psi(3686) \to n\bar{n}$ and $\psi(3686) \to p\bar{p}$, respectively. To compare with the "12% rule", we use our measured branching fractions to obtain $\frac{\mathcal{B}(\psi(3686)\to p\bar{p})}{\mathcal{B}(J/\psi\to p\bar{p})} = (14.4\pm0.6)\%$ and $\frac{\mathcal{B}(\psi(3686)\to n\bar{n})}{\mathcal{B}(J/\psi\to n\bar{n})} = (14.8\pm 1.2)\%$, where $\mathcal{B}(J/\psi \to p\bar{p}) = (2.120 \pm 0.029) \times 10^{-3}$ and $\mathcal{B}(J/\psi \to n\bar{n}) = (2.09 \pm 0.16) \times 10^{-3}$ are the world average results. Both ratios are consistent with the 12% rule.

In the decay of $J/\psi \to n\bar{n}$ and $p\bar{p}$, both the branching fractions and $\alpha$ values are very close between the two decay modes, which is expected if the strong interaction is dominant in $J/\psi \to N\bar{N}$ decay and the relative phase of between the strong and EM amplitudes is close to 90 degrees. In contrast, in $\psi(3686)$ decays the branching fractions are quite close between the two decay modes, but the $\alpha$ values are not, which may imply a more complex mechanism in the decay of $\psi(3686) \to N\bar{N}$.

## 5 $\psi(3686) \to \Lambda_c^+\overline{p}e^+e^- + c.c.$

Flavor changing neutral current (FCNC) transitions of heavy quarkonium are of great interest since they can provide indications for physics beyond the Standard Model (SM). In the

framework of the SM, FCNC transitions are strongly suppressed by the Glashow, Iliopoulos and Maiani (GIM) mechanism . The SM predictions of branching fractions (BFs) for FCNC decays range from $10^{-10}$ to $10^{-14}$ [7,8]. However, some new physics models such as the Topcolor model [9], the minimal supersymmetric SM with R-parity violation [10] and the two Higgs doublet model [11] predict the BFs of the same FCNC decays to be two to three orders of magnitude larger. Furthermore, calculations using a four-quark operator description [12] predict these BFs in the range from $10^{-5}$ to $10^{-6}$, which is within the sensitivity of the BESIII experiment. Any observation of a FCNC decay would be clear evidence for physics beyond the SM. The search of FCNC process $\psi(3686) \to \Lambda_c^+ \overline{p} e^+ e^- + c.c.$ is performed for the first time in BESIII with $448 \times 10^6$ $\psi(3686)$ events [13]. But no signal events are observed and the upper limit on the BF at the 90% C.L. is determined to be $1.6 \times 10^{-6}$. The result is within the expectations of the SM, and no evidence for new physics is found.

## 6 $J/\psi \to \Lambda_c^+ e^- + c.c.$

The Big Bang theory, the prevailing cosmological model for the evolution of the universe, predicts exactly equal numbers of baryons and antibaryons in the dawn epoch. However, the observed baryon number (BN) exceeds the number of antibaryons by a very large ratio, currently estimated at $10^9 \sim 10^{10}$ [14]. To give a reasonable interpretation of the baryon-antibaryon asymmetry, Sakharov proposed three principles [15], the first of which is that BN conservation must be violated. Many proposals predict BN violation within and beyond the SM. In the collider experiments, the CLEO Collaboration searched for very rare processes which violate BN conservation in decays of heavy-flavor mesons. In particular, they suggested to look for the process $D^0 \to \bar{p} + e^+$, which is an inverse process of $p \to \pi^0 e^+$ at the quark level. The upper limit from the CLEO measurement is $10^{-5}$ [16] at 90% Confidence Level (CL), limited by low statistics. Instead, thanks to the huge data sample of $J/\psi$ decays produced at the BESIII experiment, we are able to study the analogous process $J/\psi \to \Lambda_c^+ e^-$ with much higher statistics and therefore better sensitivity. By analyzing $1.3 \times 10^9$ $J/\psi$ events, the decay of $J/\psi \to \Lambda_c^+ e^- + c.c.$ has been investigated for the first time [17]. No signal events have been observed and thus the upper limit on the branching fraction is set to be $6.9 \times 10^{-8}$ at the 90% CL, which is more than two orders of magnitude more strict than that of CLEO's measurement in the analogous process.

## 7 $\chi_{cJ}, h_c$ and $\eta_c$ decays

Thanks to the largest data samples of $J/\psi$ and $\psi(3686)$ collected in BESIII, we could study the charmonium states which are not directly generated from $e^+e^-$ collision, such as $\chi_{cJ}, h_c$ and $\eta_c$.

Contributions of the color octet mechanism (COM) to decays of $P$-wave heavy quarkonia have been proposed for more than two decades, and many theoretical predictions for exclusive $\chi_{cJ}$ decays to baryon anti-baryon pairs have been made. However, there are large differences between predictions and the experimental measurements. By the radiative decays of $\psi(3686) \to \gamma\chi_{cJ}$, the decays $\chi_{c1,2} \to \Sigma^+\bar{\Sigma}^-$ and $\Sigma^0\bar{\Sigma}^0$ are observed for the first time, and the branching fractions for $\chi_{c0} \to \Sigma^+\bar{\Sigma}^-$ and $\Sigma^0\bar{\Sigma}^0$ decays are measured with improved precision. The branching fraction ratios between the charged and neutral modes are consistent with the prediction of isospin symmetry [18].

For charmonium states below the $D\bar{D}$ threshold, the hadronic transitions of the spin-singlet P-wave state $h_c(1^1P_1)$ are one of the best places to test the spin-spin interaction between heavy quarks [19], but they remain the least accessible experimentally because the $h_c(1^1P_1)$ can not be produced resonantly in $e^+e^-$ annihilation or from electric-dipole radiative transitions of the $\psi(3686)$. The $h_c$ is expected to decay to lower-mass charmonia state through hadronic transitions, but this has not been observed yet. In the framework of QCDME, the branching fraction of $h_c \to \pi\pi J/\psi$ (including charged and neutral modes) is predicted to be 2% [20], while it is

predicted to be 0.05% when neglecting the nonlocality in time[21]. An experimental measurement is desirable to distinguish between these calculations. A search for the hadronic transition $h_c \to \pi^+\pi^- J/\psi$ is carried out via $\psi(3686) \to \pi^0 h_c, h_c \to \pi^+\pi^- J/\psi$ [22]. No signal is observed. The upper limit of the product of branching fractions $\mathcal{B}(\psi(3686) \to \pi^0 h_c)\mathcal{B}(h_c \to \pi^+\pi^- J/\psi)$ at the 90% C.L. is determined to be $2.0 \times 10^{-6}$. Using the PDG value for the branching fraction of $\psi(3686) \to \pi^0 h_c$ of $(8.6 \pm 1.3) \times 10^{-4}$, the upper limit on $\mathcal{B}(h_c \to \pi^+\pi^- J/\psi)$ is determined to be $2.4 \times 10^{-3}$, which is the most stringent upper limit to date.

Decays of $\eta_c$ into vector meson pairs have stood as a bewildering puzzle in charmonium physics for a long time. There is a large discrepancy between theoretical predictions and experimental results. To help understand the $\eta_c$ decay mechanism, high precision measurements of the branching fraction are desirable. Using $(223.7 \pm 1.4) \times 10^6$ $J/\psi$ events accumulated with the BESIII detector, we study $\eta_c$ decays to $\phi\phi$ and $\omega\phi$ final states. The branching fraction of $\eta_c \to \phi\phi$ is measured to be $(2.5 \pm 0.3^{+0.3}_{-0.7} \pm 0.6) \times 10^{-3}$. No significant signal for the double Okubo-Zweig-Iizuka suppressed decay of $\eta_c \to \omega\phi$ is observed, and the upper limit on the branching fraction is determined to be $Br(\eta_c \to \omega\phi) < 2.5 \times 10^{-4}$ at the 90% confidence level[23].

## 8 Summary

Thanks to the largest data samples of $J/\psi$ and $\psi(3686)$ which are collected in BESIII experiment, many interesting charmonium decays have been studied, but a few of them are mentioned in this paper. The charmonium states mass region is an ideal place to study the connection of the perturbative and the non-perturbative QCD region. And rare decays could be performed to search for the physics beyond SM. In the future, more exciting results are expected.

## References


1. D. M. Asner *et al.*, *Int. J. Mod. Phys.* A **24**, S1 (2009).
2. M. Ablikim *et al.*, *Phys. Rev. Lett.* **118**, 221802 (2017)
3. A. Faessler, C. Fuchs and M. I. Krivoruchenko, *Phys. Rev.* C **61**, 035206 (2000).
4. M. Abilikim *et al.*, *Phys. Rev.* D **96**, 052003 (2017).
5. Q. Zhao, *Phys. Lett.* B **697**, 52 (2011).
6. M. Ablikim *et al.*, arXiv: hep-ex/1803.02039.
7. M. A. Sanchis-Lonzano, *Z. Phys.* C **62**, 271 (1994).
8. Y. M. Wang *et al.*, *Eur. Phys. J.* C **54**, 107 (2008).
9. C. Hill, *Phys. Lett.* B **345**, 483 (1995).
10. C. S. Aulakh and R. N. Mohapatra, *Phys. Lett.* B **119**, 136 (1982).
11. S. Glashow and S. Weinberg, *Phys. Rev.* D **15**, 1858 (1977).
12. X. Zhang, arXiv: hep-ph/0010105.
13. M. Ablikim *et al.*, arXiv: hep-ex/1802.04057.
14. F. C. Adams and G. Laughlin, *Rev. Mod. Phys.* **69**, 337 (1997).
15. A. D. Sakharov, JETP *Lett.*, **5**, 24 (1967).
16. P. Rubin *et al.* (CLEO Collaboration), *Phys. Rev.* D **79**, , (097101)2009.
17. M. Ablikim *et al.*, arXiv: hep-ex/1803.04789.
18. M. Abilikim *et al.*, *Phys. Rev.* D **97**, 052011 (2018).
19. S. Godfrey, *J. Phys.: Conf. Ser.* **9**, 123 (2005).
20. Y.-P. Kuang, S.-F. Tuan, and T.-M. Yan, *Phys. Rev.* D **37**, 1210 (1988).
21. P. Ko, *Phys. Rev.* D **52**, 1710 (1995).
22. M. Abilikim *et al.*, *Phys. Rev.* D **97**, 052008 (2018).
23. M. Abilikim *et al.*, *Phys. Rev.* D **95**, 052004 (2017).

# Recent studies of charm baryon spectroscopy and decays at Belle

Y. Kato
*Kobayashi-Maskawa Institute, Nagoya University, Nagoya 464-8602, Japan*

In this article, recent studies of charmed baryons by Belle experiment are reported. These includes search for hidden strange pentaquark, first observation of $\Xi_c(2930)^+$, confirmation of excited $\Omega_c^0$ decaying into $\Xi_c K$, and first measurement of the production rate of various charmed baryons. All the studies are performed by full data sample of the Belle experiment.

## 1 Introduction

The charmed baryon is an unique laboratory to study the structure of baryon. As the constituent mass of the charm quark is more than 5 times larger than those of up, down, and strange quarks, the charmed baryon is expected to be a bound state of light di-quark and charm quark. This means charmed baryons are simpler than those composed with up, down, and strange quarks only. Therefore, it is easy to extract the dynamics inside baryons.

The Belle is an asymmetric $e^+e^-$ collider experiment operated mainly at the mass of the excited bottomonium $\Upsilon(4S)$, which decays into $B\bar{B}$ pair with almost 100% branching fraction. Therefore, it is also called as B-factory experiment. In the Belle experiment, charmed baryons are produced mainly in two reactions. One is $e^+e^- \to \gamma^* \to c\bar{c}$ and the other is $B$ meson decay. Belle has collected data sample with an integrated luminosity of around 1 $ab^{-1}$. This huge data set enabled the study of various charmed baryons. In this article, recent results the charmed baryon studies by the Belle collaboration are presented.

## 2 Search for hidden strange pentaquark in the $\Lambda_c^+ \to p\phi\pi^0$

The LHCb collaboration observed two hidden charmed pentaquark states decaying into $J/\psi p$ in the $\Lambda_b^0 \to J/\psi K^- p$ decay [1]. The analogue search for the hidden strangeness pentaquark ($P_s$) can be performed by switching $b$ quark to $c$ quark ($\Lambda_b^0$ to $\Lambda_c^+$) and $c$ quark to $s$ quark ($J/\psi$ to $\phi$). The target decay is $\Lambda_c^+ \to p\phi\pi^0$.

Belle performed this search [2]. No significant signal for the $\Lambda_c^+$ decay is observed and the upper limit of $\mathcal{B}(\Lambda_c^+ \to \phi p\pi^0) < 15.3 \times 10^{-5}$ at 90% confidence level is obtained. Figure 1 shows the $\Lambda_c^+$ yield in each $m(\phi p)$ bin. No significant signal for $P_s$ is observed and upper limit of $\mathcal{B}(\Lambda_c^+ \to P_s^+\pi^0) \times \mathcal{B}(P_s^+ \to \phi p) < 8.3 \times 10^{-5}$ at 90% confidence level is obtained.

## 3 Observation of $\Xi_c(2930)^0$

Evidence of excited state of charmed strange baryon $\Xi_c(2930)$ decaying into $\Lambda_c^+ K^-$ in the decay of $B^- \to K^-\Lambda_c^+\bar{\Lambda}_c^-$ was reported by BaBar collaboration [3]. However, the significance was not quoted in the paper and need further confirmation. Belle performed the same search with improved statistics [4]. Figure 2 shows the $m(\Lambda_c^+ K^-)$ where clear peak corresponds to

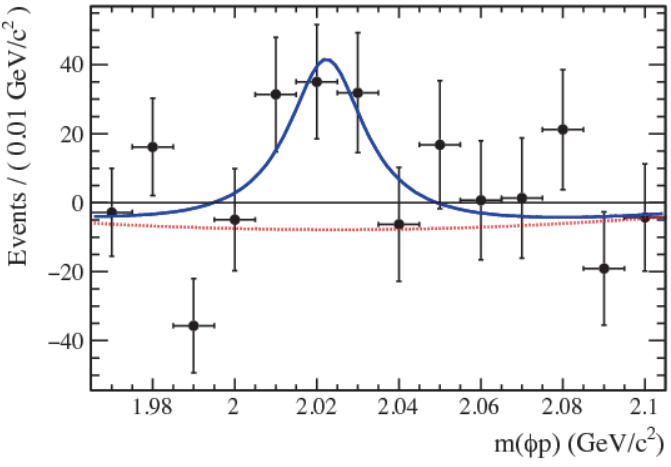


Figure 1 – Observed $m(\phi p)$ distribution in $\Lambda_c^+ \to p\phi\pi^0$ decay with fit line.

$\Xi_c(2930)^0$ can be seen. The statistical significance is $5.1\sigma$. This is the first charmed baryon whose existence is established by using $B$ meson decay. The mass and width are obtained as $[2928.9\pm3.0(\text{stat.})^{+0.9}_{-12.0}(\text{syst.})]$ MeV/$c^2$ and $[19.5\pm8.4(\text{stat.})^{+5.9}_{-7.9}(\text{syst.})]$ MeV, respectively. These are consistent with those measured by BaBar collaboration.

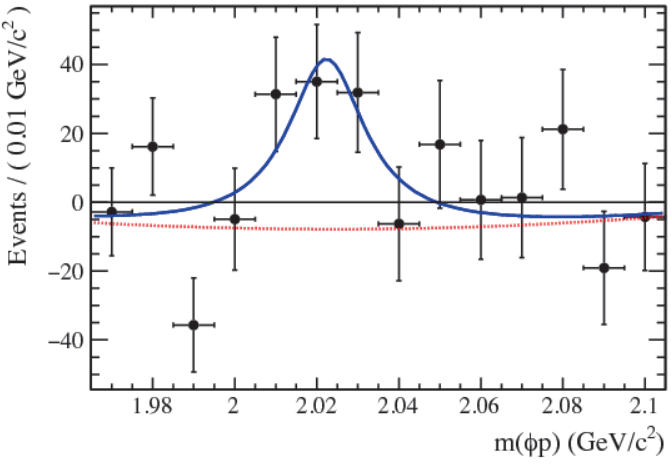


Figure 2 – Observed $m(\Lambda_c^+ K^-)$ distribution in the $B^- \to K^-\Lambda_c^+\bar{\Lambda}_c^-$ decay. with fit result. Box histogram shows the distribution in the sideband of $\Lambda_c^+$.

## 4 Observation of excited $\Omega_c$ in $e^+e^-$ collision

LHCb collaboration observed 5 $\Omega_c$ excited states decaying into $\Xi_c^+ K^-$ [5]. To understand the nature of these excited states, the study with different production mechanism is very useful.

Figure 3 shows the $m(\Xi_c^+ K)$ distribution measured by Belle experiment [6]. The existence of four states: $\Omega_c(3000)$, $\Omega_c(3050)$, $\Omega_c(3066)$, and $\Omega_c(3119)$ are confirmed with significance greater than $3\sigma$. In the fit, the width of each resonance is fixed to those measured by LHCb collaboration. The obtained masses are consistent with those measured by LHCb collaboration.

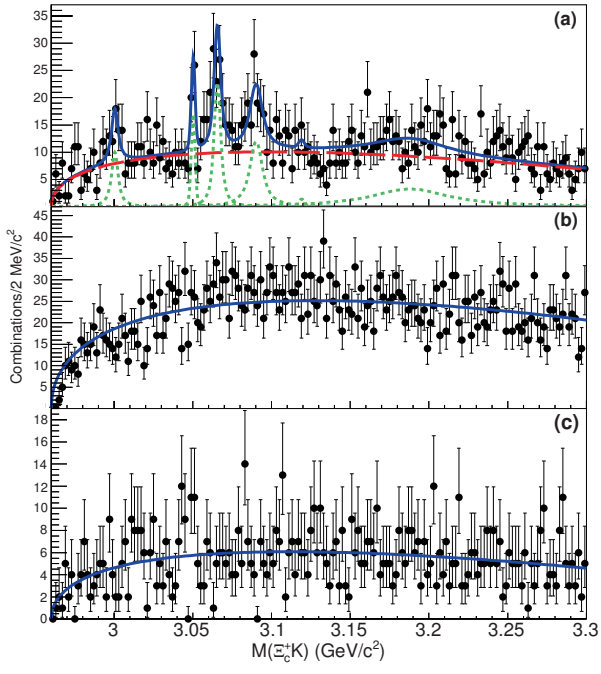


Figure 3 – (a) The $m(\Xi_c^+ K)$ distribution. (b) The wrong sign $m(\Xi_c^+ K^-)$ mass distribution. (c) The mass distribution for the $\Xi_c$ sideband region.

## 5 Production ratio of various charmed baryons and hyperons

It is experimentally known that the production cross section of hadrons divided by the number of spin degree of freedom $2J+1$ (production rate), in the $e^+e^-$ collision lie on the $exp(-\alpha m)$, where $\alpha$ is the slope parameter. Belle performed measurement of production ratio for hyperons and charmed baryons. In the measurement, the contribution of feed down from heavier resonances are subtracted. This is the first measurement of systematic study of the production rate for the charmed baryons. Figure 4 shows the result of production rate for baryons. For the charmed baryons, a factor three suppression of $\Sigma_c$ states relative to $\Lambda_c$ states is observed. This feature is not seen in the hyperons. If charmed baryon production proceeds via diquark anti-diquark pair production, the mass difference of the spin zero diquark ($\Lambda_c^+$) and spin one diquark ($\Sigma_c$) may explain it.

## 6 Summary

Belle is still actively working on the study of charmed baryons after eight years since the end of data taking. The strange pentaquark decaying into $\phi p$ is searched for in the $\Lambda_c^+ \to \phi p \pi^0$, and no

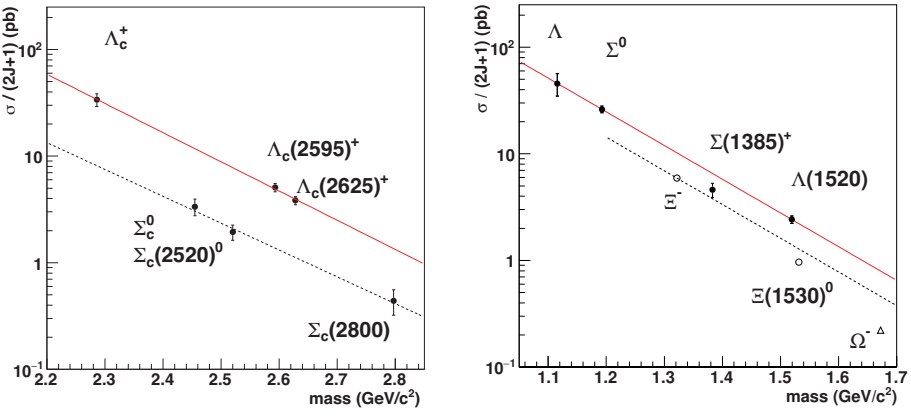


Figure 4 – Cross section divided by number of spin degree of freedom for hyperons (left) and charmed baryons (right).

significant signal is observed. An excited charmed strange baryon $\Xi_c(2930)^+$ is firstly observed in the decay $B^- \to \Lambda_c^+ \bar{\Lambda}_c^- K^-$. Existence of the four of five excited $\Omega_c^0$ reported by LHCb collaboration are confirmed. The production rate of various charmed baryons are measured for the first time. A factor three suppression of $\Sigma_c$ states relative to $\Lambda_c$ states is observed, which suggests diquark structure of the charmed baryons. The upgrade of Belle, Belle II has just started collecting collision data. More exciting results like discovery of new excited state or determination of quantum numbers are expected.

## 7 Acknowledgments

This work is supported by a Grant-in-Aid for Scientific Research (S) "Probing New Physics with Tau-Lepton" (No.26220706) and Grant-in-Aid for Scientific Research on Innovative Areas "Elucidation of New Hadrons with a Variety of Flavors".

## References

1. R. Aaij *et al.* [LHCb Collaboration], Phys. Rev. Lett. **115**, 072001 (2015) doi:10.1103/PhysRevLett.115.072001
2. B. Pal *et al.* [Belle Collaboration], Phys. Rev. D **96**, no. 5, 051102 (2017) doi:10.1103/PhysRevD.96.051102.
3. B. Aubert *et al.* [BaBar Collaboration], Phys. Rev. D **77**, 031101 (2008) doi:10.1103/PhysRevD.77.031101
4. Y. B. Li *et al.* [Belle Collaboration], Eur. Phys. J. C **78**, no. 3, 252 (2018) doi:10.1140/epjc/s10052-018-5720-5.
5. R. Aaij *et al.* [LHCb Collaboration], Phys. Rev. Lett. **118**, no. 18, 182001 (2017) doi:10.1103/PhysRevLett.118.182001
6. J. Yelton *et al.* [Belle Collaboration], Phys. Rev. D **97**, no. 5, 051102 (2018) doi:10.1103/PhysRevD.97.051102
7. M. Niiyama *et al.* [Belle Collaboration], Phys. Rev. D **97**, no. 7, 072005 (2018) doi:10.1103/PhysRevD.97.072005.

# SEARCH FOR DOUBLY HEAVY BARYON VIA WEAK DECAYS

Run-Hui Li[a], Cai-Dian Lu[b]
[a] *School of Physical Science and Technology, Inner Mongolia University, Hohhot 010021, China;*
[b] *Institute of High Energy Physics, YuQuanLu 19B, Beijing 100049, China .*

Using the factorization approach and taking into account the final state interaction, we calculate the two body non-leptonic decays of doubly heavy baryons. After comparing the semileptonic decays and all possible hadronic decay channels, we found some channels with large branching ratios. Taking the detection efficiency into consideration, we suggest $\Xi_{cc}^{++}$ as the first search goal and $\Xi_{cc}^{++} \to \Lambda_c^+ K^- \pi^+ \pi^+$ and $\Xi_{cc}^{++} \to \Xi_c^+ \pi^+$ as the golden discovery channels with $\Lambda_c^+$ reconstructed by $pK^-\pi^+$ and $\Xi_c^+ \to pK^-\pi^+$, respectively.

## 1 Motivation

Doubly or triply heavy flavor baryons with two or three heavy quarks ($b$ or $c$ quark) are predicted by the quark model, whose existence is also allowed by the QCD theory. However, the experimental search of these states is very slow. The first evidence was reported by the SELEX experiment for $\Xi_{cc}^+$ in 2002 [1,2]. However, it has never been confirmed by later experiments with larger data, such as FOCUS [3], BaBar [4] and Belle [5,6]. Utilizing as large as $0.65\,\mathrm{fb}^{-1}$ data, the LHCb collaboration even performed a thorough search in the discovery channel used by SELEX, $\Xi_{cc}^+ \to \Lambda_c^+ K^- \pi^+$, but did not find any significant signal [7]. On the theoretical side, analysis on the production of doubly heavy baryons [8,9] indicates a large possibility of observing $\Xi_{cc}$ at LHC. Therefore searching for the doubly heavy baryons was proposed as an important physical goal by the LHCb collaboration. Although there had been a lot of research on the masses and decay constants of doubly heavy baryons, people knew little about doubly heavy baryon decays. To make the experimental searching more efficient, it became urgent and necessary to study the branching ratios of doubly heavy baryon decays.

As ground states of doubly heavy baryons, they can only decay weakly. There are a huge number of decay channels to study, since there are many hadronic states below their mass scale. After a carful study of all possible decay channels of the doubly heavy baryons, we give suggestions of some golden channels with large branching ratios and all charged final sates for experimental search.[10] Following our suggestions, the LHCb experiment [11] did find the $\Xi_{cc}^{++}$ state through one of our suggested decay channels $\Xi_{cc}^{++} \to \Lambda_c^+ K^- \pi^+ \pi^+$ with $\Lambda_c^+$ reconstructed by $pK^-\pi^+$.

## 2 Theoretical study of doubly heavy baryons decays

Comparing to the doubly heavy baryons with $b$ quark(s), the doubly charm baryons are easier to be observed because their production needs less energy. Under the flavor $SU(3)$ symmetry doubly charm baryons $\Xi_{cc}^{++}$, $\Xi_{cc}^+$ and $\Omega_{cc}^+$ form a spin-$\frac{1}{2}$ and a spin-$\frac{3}{2}$ triplets. The latter triplet will decay to the former one via electromagnetic or strong interactions. As ground states, the spin-$\frac{1}{2}$ triplet can only decay weakly through one of the $c$ quarks.

Lifetime is an important point in the choice of the candidates. On one hand the branching ratios are related directly to the lifetime of the mother particle, on the other hand particles with longer lifetimes will be easier to be identified in experiments. Different theoretical work gives quite different predictions for the lifetimes of doubly charm baryons [12], which makes it hard to judge by the absolute values of lifetimes. Luckily, because of the effect of destructive Pauli interference it is expected that $\tau(\Xi_{cc}^{++}) \gg \tau(\Xi_{cc}^{+}) \sim \tau(\Omega_{cc})$. Their ratio is predicted [12] to be $\mathcal{R}_\tau \equiv \tau_{\Xi_{cc}^{+}}/\tau_{\Xi_{cc}^{++}} = 0.25 \sim 0.37$ with less theoretical uncertainty. Therefore we suggested $\Xi_{cc}^{++}$ as a prior candidate in experimental search. This is contrary to the finding of the SELLEX experiment, who declared the discovering of $\Xi_{cc}^{+}$ instead of $\Xi_{cc}^{++}$.

### *2.1 Semileptonic decays*

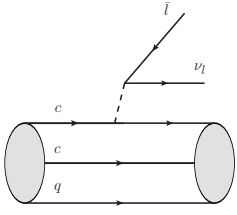


Figure 1 – Semileptonic decay of a doubly charm baryon.

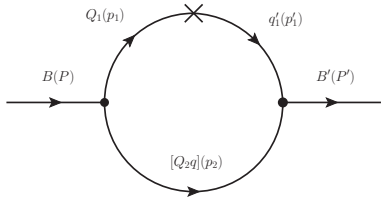


Figure 2 – Baryon to baryon transition depicted by light front quark model in the diquark picture.

On the theoretical side the simplest case is semi-leptonic decays (shown in Fig. 1), whose amplitudes can be factorized safely into a leptonic and a hadronic part. The hadronic part is a baryon to baryon weak transition matrix element, which can be parameterized as

$$\begin{aligned}\langle B'(P',S_z')|(V-A)_\mu|B(P,S_z)\rangle = \quad & \bar{u}(P',S_z')\left[\gamma_\mu f_1(q^2) + i\sigma_{\mu\nu}\tfrac{q^\nu}{M} f_2(q^2) + \tfrac{q_\mu}{M} f_3(q^2)\right] u(P,S_z) \\ & -\bar{u}(P',S_z')\left[\gamma_\mu g_1(q^2) + i\sigma_{\mu\nu}\tfrac{q^\nu}{M} g_2(q^2) + \tfrac{q_\mu}{M} g_3(q^2)\right]\gamma_5 u(P,S_z). \quad (1)\end{aligned}$$

To get the branching ratios, the key task is the calculation of the form factors $f_{1,2,3}(q^2)$ and $g_{1,2,3}(q^2)$ defined in Eq.(1). The first calculation is made in the light front quark model (LFQM) [13]. If one combines the spectators ($c$ and $q$ quarks) in Fig. 1 as a diquark, a baryon to baryon transition is similar to a meson to meson one shown in Fig.2. Since the diquark can be either a spin-0 or spin-1 state, a physical transition is a mixture of these two cases. With the form factors obtained in LFQM, the branching fractions of related semileptonic decays are all calculated.[13] Here we only list the four branching ratios of $\Xi_{cc}^{++}$ semileptonic decays:

$$\begin{aligned}&\mathcal{BR}(\Xi_{cc}^{++} \to \Xi_c^{+} l^{+}\nu_l) = 5.25\times10^{-2},\ \mathcal{BR}(\Xi_{cc}^{++} \to \Xi_c^{\prime+} l^{+}\nu_l) = 5.84\times10^{-2}, \\ &\mathcal{BR}(\Xi_{cc}^{++} \to \Lambda_c^{+} l^{+}\nu_l) = 4.81\times10^{-3},\ \mathcal{BR}(\Xi_{cc}^{++} \to \Sigma_c^{+} l^{+}\nu_l) = 4.38\times10^{-3}, \quad (2)\end{aligned}$$

where the two decays in the first line of Eq. (2) are induced by $c \to s$ transition and those in the second line by $c \to d$ transition. One can see that branching ratios of the two Cabbibo favored decays are at the order of $10^{-2}$ which is about 10 times larger than the Cabbibo suppressed ones. For the sake of particle reconstruction in experiments one needs to take the secondary decays into consideration, which decreases the branching ratios by a factor of $10^{-2}$. As a result, the branching ratios of semi-leptonic decays used in experimental research are expected to be of the order $10^{-4}$. Comparing to non-leptonic decays, whose branching ratios[14] are of the order $10^{-3} \sim 10^{-4}$, the semi-leptonic decays are not competitive. what's more, the largest disadvantage of semi-leptonic decays is the phenomena of missing energy in experiments caused by the neutrinos.

*2.2 Non-leptonic decays*

We first consider the simplest non-leptonic decays: a doubly charm baryon decays into a single charm baryon and a meson. Theoretically non-leptonic charm decays are difficult to deal with. The scale of charm is very special, which is much higher than $\Lambda_{\rm QCD}$ but not high enough for a good heavy quark mass expansion. The non-perturbative QCD plays a major role, which restricts the application of most factorization theories. The factorization assisted topological diagrammatic approach, which works well in charm meson decays to predict the $\Delta A_{\rm cp}$ successfully [15], also does not work here, since there are not enough experimental data. Therefore the doubly charm baryon decays need to be considered from the beginning. The leading order topological diagrams contributions in decays of doubly charm baryon to a single charm baryon and a meson can be classified into the diagrams in Fig. 3.[10]

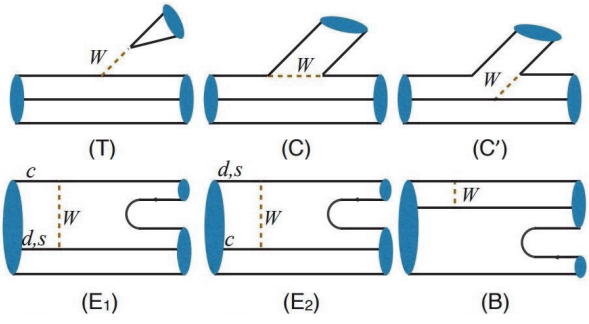


Figure 3 – Topologies of two body nonleptonic decays of doubly charm baryons.

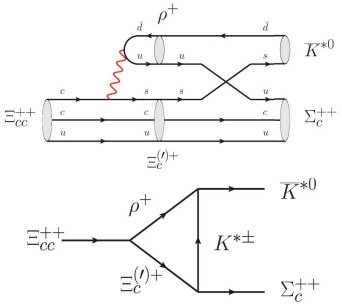


Figure 4 – The rescattering diagram of $\Xi_{cc}^{++} \to \Xi_c^{(\prime)+}\rho^+ \to \Sigma_c^{++}\overline{K}^{*0}$. Shown at quark and hadron level.

From the experience of D meson decays,[15] we notice that the emission diagram (denoted by T) is dominated by the short distance contribution, which can be factorized as production of a meson decay constant and a weak transition of baryon to baryon. With the form factors evaluated in LFQM,[13] this contribution is easy to calculate. Considering the detection efficiency and comparing among the theoretical results, we find that among short distance contribution denominated decays $\Xi_{cc}^{++} \to \Xi_c^+\pi^+$ is the best channel for detection with $\Xi_c^+$ reconstructed by the final state $pK^-\pi^+$. The secondary decay $\Xi_c^+ \to pK^-\pi^+$ is estimated to have a branching ratio of about two percent.[10]

Similar to the D meson decays, long distance contribution is dominating in other diagrams. This part of contribution has never been calculated in the literature and we evaluate it firstly with the rescattering mechanism of the final-state-interaction. The rescattering mechanism is induced by quark exchanges, and it can be calculated as triangle diagrams by using the effective Lagrangian with couplings at hadron level. The depiction of this mechanism is shown in Fig. 4 with the $t$-channel rescattering diagram of $\Xi_{cc}^{++} \to \Xi_c^{(\prime)+}\rho^+ \to \Sigma_c^{++}\overline{K}^{*0}$ as an example. The calculated branching ratios are expected to have large errors because of the uncertain hadronic parameters. In order to reduce ambiguity, we use their ratios instead of branching fractions to draw conclusions. Most of the theoretical uncertainties due to the hadronic parameters canceled in the ratios. Our sample results of ratios of the long distance dominated decays are listed in Table 1.

We find that $\Xi_{cc}^{++} \to \Sigma_c^{++}\overline{K}^{*0}$ decay has the largest branching fraction at the order of several percent. The secondary decays can be $\Sigma_c^{++} \to \Lambda_c^+\pi^+$ and $\overline{K}^{*0} \to K^-\pi^+$. The total 4-body decay is very difficult to calculate precisely, but our estimation shows that $\mathcal{BR}(\Xi_{cc}^{++} \to \Lambda_c^+K^-\pi^+\pi^+)$ can even reach $\mathcal{O}(10\%)$ because of the rich resonant contributions. In detection, $\Lambda_c$ can be reconstructed by $pK^-\pi^+$.

Table 1: Branching fractions of $\Xi_{cc}^{++}$ and $\Xi_{cc}^{+}$ decays with the long-distance contributions, relative to that of $\Xi_{cc}^{++} \to \Sigma_c^{++}(2455)\overline{K}^{*0}$.

| Baryons | Modes | $\mathcal{B}_{\rm LD}$ |
|---|---|---|
| $\Xi_{cc}^{++}(ccu)$ | $\Sigma_c^{++}(2455)\overline{K}^{*0}$ | defined as 1 |
| | $pD^{*+}$ | 0.04 |
| | $pD^{+}$ | 0.0008 |
| $\Xi_{cc}^{+}(ccd)$ | $\Lambda_c^{+}\overline{K}^{*0}$ | $(\mathcal{R}_\tau/0.3)\times 0.22$ |
| | $\Sigma_c^{++}(2455)K^{-}$ | $(\mathcal{R}_\tau/0.3)\times 0.01$ |
| | $\Xi_c^{+}\rho^{0}$ | $(\mathcal{R}_\tau/0.3)\times 0.04$ |
| | $\Lambda D^{+}$ | $(\mathcal{R}_\tau/0.3)\times 0.004$ |
| | $pD^{0}$ | $(\mathcal{R}_\tau/0.3)\times 0.001$ |

## 3 Conclusion

In the purpose of finding out the golden decay channels for experimental search, we systematically analyzed the properties and decays of doubly heavy baryons. Utilizing the form factors of doubly heavy baryon to single heavy baryon weak transition, the branching fractions of the semi-leptonic decays and the two body non-leptonic decays of doubly charm baryons are calculated. We find that $\Xi_{cc}^{++} \to \Lambda_c^{+}K^{-}\pi^{+}\pi^{+}$ with $\Lambda_c \to pK^{-}\pi^{+}$ has the first priority. In 2017, the LHCb collaboration declares the discovery of $\Xi_{cc}^{++}$ via this decay following our suggestions.[11] We also suggest the $\Xi_{cc}^{++} \to \Xi_c^{+}\pi^{+}$ decay with $\Xi_c^{+} \to pK^{-}\pi^{+}$ as a good candidate for experimental search. As for the search of $\Xi_{cc}^{+}$ state, our calculation shows that $\Xi_{cc}^{+} \to \Lambda_c^{+}\overline{K}^{*0}(\to K^{-}\pi^{+})$ is a prior candidate.


### Acknowledgments

We thank F.S. Yu, H.Y. Jiang, W. Wang and Z.X. Zhao for excellent collaboration. This work was partly supported by National Natural Science Foundation of China (Grant Nos. 11521505, 11621131001, 11447009, 11505098, and 11765012), and partly supported by the plan of *Young Creative Talents* under *the Talent of the Prairie* project of Inner Mongolia.


### References


1. M. Mattson *et al.* [SELEX Collaboration], Phys. Rev. Lett. **89**, 112001 (2002).
2. A. Ocherashvili *et al.* [SELEX Collaboration], Phys. Lett. B **628**, 18 (2005).
3. S. P. Ratti, Nucl. Phys. Proc. Suppl. **115**, 33 (2003).
4. B. Aubert *et al.* [BaBar Collaboration], Phys. Rev. D **74**, 011103 (2006).
5. R. Chistov *et al.* [Belle Collaboration], Phys. Rev. Lett. **97**, 162001 (2006).
6. Y. Kato *et al.* [Belle Collaboration], Phys. Rev. D **89**, no. 5, 052003 (2014).
7. R. Aaij *et al.* [LHCb Collaboration], JHEP **1312**, 090 (2013).
8. J. W. Zhang, X. G. Wu, T. Zhong, Y. Yu and Z. Y. Fang, Phys. Rev. D **83**, 034026 (2011).
9. C. H. Chang, C. F. Qiao, J. X. Wang and X. G. Wu, Phys. Rev. D **71**, 074012 (2005).
10. F. S. Yu, H. Y. Jiang, R. H. Li, C. D. Lu, W. Wang and Z. X. Zhao, Chinese Phys. C42 (2018) 051001
11. R. Aaij *et al.* [LHCb Collaboration], Phys. Rev. Lett. **119**, no. 11, 112001 (2017).
12. M. Karliner and J. L. Rosner, Phys. Rev. D **90**, no. 9, 094007 (2014) and references therein
13. W. Wang, F. S. Yu and Z. X. Zhao, Eur. Phys. J. C **77**, 781 (2017).
14. R. H. Li, C. D. Lu, W. Wang, F. S. Yu and Z. T. Zou, Phys. Lett. B **767**, 232 (2017).
15. H. n. Li, C. D. Lu and F. S. Yu, Phys. Rev. D **86**, 036012 (2012).

## Multi-quark state production and hadron correlation in high energy multiproduction processes

LI, Shi-Yuan

The non-relativistic wave function framework is applied to study the production and decay of the exotic hadrons which can be effectively described as bound states of other hadrons. We investigate the production of exotic hadrons in the multi-production processes at high energy hadronic colliders. This study provides crucial information for the measurements of the relevant exotic hadrons. In this factorization framework the amplitude of the production of the ingredient hadrons can be extracted from the hadron production data as well as can be calculated by the event generators. So the relevant hadron correlations are useful information and suggested to studied in experiments to improve the parametrization of the amplitude. Another important topic of hadron correlation is relevant to the reconstruction of some unknown particle by the invariant mass of two particles which are believed as decay product of that particle to be discovered. However, possible correlations from PQCD radiation effects should be investigated and vetoed.

Recently, more and more new exotic hadron states, *e.g.*, the XYZ mesons, have been observed. They are assumed as multiquark states and/or as bound states of other ingredient hadrons in lots of theoretical investigations. Such investigations can be done not only via their decay processes, where the branching ratios and distributions of the decay products can be studied, but also via their production processes (from the decay of the heavier particles or directly from the multiproduction processes). In both cases, the more complex the process is, the more information of inner structure can be drawn. In general, the production processes are more complex.

At the same time, the studies on the production processes also provide the information of the cross section, rapidity and transverse momentum distributions, *etc.*, of the relevant particles on a specific collider, which can help the experimentalists to set the proper triggers and cutoffs for the measurements. A good example is Large hadron Collider (LHC) where various detectors cover a large rapidity range. They can be used to study exotic hadron production in B-decays, as well as direct production in the multiproduction process of high energy hadronic collisions and nuclear collisions. So the distributions mentioned above are crucial for the studies on exotic hadrons with a specific detector at LHC.

Furthermore, the direct production of the exotic hadrons in the multiproduction process of high energy scattering can set a crucial point for the understanding of the hadronization mechanism. Since the exotic hadrons always refer to the states with more than three constituent quarks (here we do not discuss hybrids or glueballs), one of the feasible ways for understanding their production mechanism is to employ the combination model to combine the necessary constituent quarks into the relevant hadron. However, in any hadronization process, as pointed by us, the produced color-singlet (anti)quark system eventually transits to various hadron states (the mesons, baryons and beyond) with the total probability exactly 1:

$$\sum_h |U_{hq}|^2 = \sum_h |\langle h|U|q\rangle|^2 = \langle q|U^+U|q\rangle = 1. \tag{1}$$

Here we introduce the unitary time-evolution operator $U$ to describe the hadronization process. For the quark state $|q\rangle$ and the corresponding hadron state $|h\rangle$, the matrix element $U_{hq} = \langle h|U|q\rangle$ describes the transition amplitude. $U_{hq}$ is determined by (low energy) Chromodynamics (QCD) but beyond the present approach of calculation. This leaves the space for various hadronization models to mimic the transition process. The unitary operator $U$ reflects the fact that there are no free quarks in the final states of any high energy process, *e.g.*, the so-called quark confinement. The introduction of multiquark states sets a challenge for the hadronization models dealing with the transition from color-singlet (anti)quark system to the hadron system.

As a matter of fact from experiments, the production of general mesons and baryons is dominant, *i.e.*,

$$\sum_{h=B,\bar{B},M} |\langle h|U|q\rangle|^2 \sim 1 - \varepsilon, \tag{2}$$

here $B$, $\bar{B}$ and $M$ denote baryon, antibaryon and meson, respectively. If the exotic hadrons are produced, $\varepsilon$ could be a small but non-vanishing value. Since the production rate is proportional to the quark density to the power of constituent quark number in the hadron, in the cases of large number of quarks produced such as those in high energy nuclear collisions, the more constituent quarks a hadron contains, the larger production rate one gets. So to regain the unitarity, one needs the special 'combination function' which reflects the confinement and may be related with the whole system rather than the several quarks to be combined into a specific hadron. Since the present knowledge is not enough to judge how many kinds of multiquark states there are and how they 'share' the total probability of $\varepsilon$, one can not predict the production rate of a specific multiquark state. What we can suspect, though, seems that if there are a lot of kinds of multiquark hadrons, each only shares a small part of the small $\varepsilon$. So the production rate of each is almost vanishing.

However, if one of the exotic states is the bound state of other hadrons, *i.e.*, its production can be taken as from the combination of mesons and/or (anti)baryons, there is generally no straightforward unitarity constraint as above on its production rate. Unlike quarks, hadrons are not confined. They can be either free, or bound with other hadron(s), even lepton(s) (*e.g.*, hydrogen atom). As a matter of fact, in the cases that the number of produced hadrons are large, such as in high energy ion collisions, the familiar hadron bound states, such as deuterons, $\alpha$ particles, *etc.*, have been observed. So it is natural to investigate the productions of the 'hadronic molecule' relevant to exotic states. The measurements and explanations of large production rate of X(3872) and X(5568) are also good examples. Their large production rates lead to insights on the investigation of their structure and production mechanism, especially the colour and spin structures. In this note of talk I would like to address that for the sake of better extracting the binding information of X(3872), the correlation of the ingredient hadron is very important information. On the other hand, the uncertainty of ways of data selection, especially the employment of the cone cut, for the X(5568) reconstruction, can be better understood by studying the correlations in the more clean environment, i.e., $e^+e^-$ annihilation at relevant energy.

For those XYZ states possibly considered as hadronic molecules, we can describe them with the framework of various Non-Relativistic (NR) effective theories, especially the NR wave function method, and concentrate on their inclusive production. The ingredient hadrons in the hadronic molecule are loosely bound, hence the relative momentum between them is fairly small with respective to the hadron mass (almost of the order of charm quark), so the hadronic molecule is in principle a NR system.

Besides the application of the investigation on positronium, the NR wave function is also used for the heavy quarkonium production and decay, generally referred to as the 'color-singlet model'.

The Non-Relativistic Quantum Chromodynamics (NRQCD) implies that the quark pair in color octet could also transfer into a color-singlet hadron, which is referred to as the color-octet

model and used to explain the production rate and transverse momentum of prompt quarkonium in hadronic collisions. But for the case of hadron as basic degree of freedom, there is no problem of color confinement because every object is color-singlet. Hence the relevant complexity is eliminated. If the system of bound hadrons is properly modeled and the NR wave function is obtained, the NR wave function framework can be used for various decay and production processes of hadronic molecules.

This method has been applied to the near threshold enhancements of mass spectra in the $J/\Psi \to \gamma p\overline{p}$ and $J/\Psi \to p\bar{\Lambda}K^-$ channels of the production of bound states X($p\overline{p}$) and X($p\bar{\Lambda}$). In that note, the decay to the corresponding ingredient hadrons is described by an effective Lagrangian. However, for the direct production of the mesons and baryons at high energy hadronic collisions, it is impossible to construct the effective Lagrangian. In Ref. before, we suggested to employ the general event generator to extract the cross section of the ingredient hadrons. In fact, this is one of the advantages of the NR wave function framework. One can expand the amplitude with respective to the relative momentum between the ingredients because it is relatively small. Thus the cross section is factorized. Only the cross section (rather than the amplitude) of the ingredient hadron production is needed, which can be fixed by fitting the correlation data of the relevant hadrons.

In the formulations for the calculation of hadronic molecule production rate in the NR wave function framework, taking $pp$ scattering at LHC, say $pp \to A + B + X \to H(A, B) + X$, as an example, only the NR wave function (and/or its derivatives) at the origin and correspondingly, only the square of the absolute value of the production amplitude (and/or its derivatives) of ingredient hadron A and B, are relevant. This means that the details of the structure of the bound state and the production of the ingredient hadron in all the phase space, are not fully used. So this framework provide the benchmark of the information least sensitive to the models and details of the strong dynamics in the momentum scale of several MeV to several ten MeV. At the same time, if the universality of the wave function is confirmed, the factorization is well established. The free pair cross section $p(p_1)p(p_2) \to A(p_A) + B(p_B) + X$ can be expressed as:

$$\begin{aligned}\frac{1}{N}\frac{dN}{d^3P_H d^3q} \propto \frac{1}{F}\sum\!\!\!\!\!\!\int \prod_{j\neq A,B}\frac{d^3p_j}{(2\pi)^3 2E_j} \\ \times\overline{|\hat{O}|^2}(p_j, P_H = p_A + p_B, q = p_A - p_B) \\ \times(2\pi)^4\delta^{(4)}(P_{intial} - \sum_{j\neq A,B} p_j - p_A - p_B).\end{aligned} \tag{3}$$

Here the average is on various spin states, and the proper initial flux factor $1/F$ and phase space integral are needed. $\hat{O}$ is the amplitude of production of two free ingredient particles (with vanishing relative momentum and proper angular momentum state). It is not possible to be calculated directly with some effective quantum field theory/model when the initial state is (anti) protons and $A$ and $B$ are hadrons or clusters. However, it can be obtained with an event generator such as PYTHIA or equivalently Shandong Quark Combination Model, etc. for the case that $A$ and $B$ are both on shell. It is the advantage that in the above framework we employ, only the on shell case is considered, so that the numerical calculation with event generator is plausible. The quantity of Eq. (3) describes the two hadrons/clusters ($A$ and $B$) correlation in the phase space. For the hadron case, by proper integral on components of $P_H$ and/or $q$, the resulting correlations can be directly compared with data and serve for tuning the parameters.

Since the special physical picture of the non-relativistic framework, it is only valid in the rest frame of the two ingredient particles. One can define the following covariant space-like relative momentum $\hat{q}$ as

$$\hat{q} = (p_A - p_B) - \frac{(p_A - p_B)\cdot(p_A + p_B)}{(p_A + p_B)^2}(p_A + p_B). \tag{4}$$

It is clear that in the rest frame of $A$ and $B$ ($H(A, B)$) where $\vec{p}_A + \vec{p}_B = 0$, $\hat{q} = (0, \vec{k})$ and the

$k = \sqrt{-\hat{q}^2}$ is exactly the absolute value of the 3-relative momentum $|\vec{p}_A - \vec{p}_B|$.

Employing the event generator, one gets

$$\frac{1}{N}\frac{dN}{d^3P_H d^3\hat{q}}, \forall \hat{q}, \tag{5}$$

then extrapolates to the special case $k = 0$. Numerically, one can take an average around $k = 0$ for the above quantity. Then we get, up to the kinematic factors as for the covariant form,

$$\begin{aligned}&\frac{1}{F}\sum\!\!\!\!\!\!\int\prod_{j\neq A,B}\frac{d^3p_j}{(2\pi)^3 2E_j}\overline{|\hat{O}|^2}(p_j, P_H = p_A + p_B, k = 0)\\ &\times(2\pi)^4\delta^{(4)}(P_{intial} - \sum_{j\neq A,B} p_j - P_H).\end{aligned} \tag{6}$$

It is exactly the differential cross section of the bound state $H(A, B)$ divided by $|\Psi(0)|^2$.

There are several very basic facts supporting the extrapolation. First of all, the amplitude and cross section are analytical in phase space. Any practical generator should reproduce this property, and any ultraviolet divergence is not present. Secondly, the study of strong interaction is complex because of the SU(3) non-Abelian interaction, but its simulation has one simplicity: All particles taking part in the strong interactions are massive, which eliminates the infrared singularities.

Based on the above discussion, it is very helpful to study the correlations experimentally.

On the other hand, based on our calculation for two-jet events in electron positron annihilations, it is shown that there is peak around the B-pi invariant mass threshold, so it is crucial to make clear the cut of D0 is reasonable or not. The interested readers are asked to refer to our published or publishing papers.

**Acknowledgments**

This work is supported in part by National Natural Science Foundation of China (grant No. 11775130,11635009), and the Natural Science Foundation of Shandong Province (grant No. ZR2017MA002).

**References**

1. W. Han, S. -Y. Li, Z. -G. Si and Z. -J. Yang, Phys. Lett. B **642**, 62 (2006).
2. Y. Jin, S. -Y. Li, Z. -G. Si, Z. -J. Yang and T. Yao, Phys. Lett. B **727**, 468 (2013).
3. Y. Jin, S. Y. Li, Y. R. Liu, Z. G. Si and T. Yao, Phys. Rev. D **89**, no. 9, 094006 (2014).
4. W. Han, S. -Y. Li, Y. -H. Shang, F. -L. Shao and T. Yao, Phys. Rev. C **80** (2009) 035202.
5. Y. Jin, S. Y. Li, Y. R. Liu, L. Meng, Z. G. Si and X. F. Zhang, Chin. Phys. C **41** (2017) no.8, 083106.
6. Y. Jin, S. Y. Li and S. Q. Li, Phys. Rev. D **94** (2016) no.1, 014023

# EXOTIC INTERPRETATION OF $\Omega_c$ EXCITED STATES

M. PRASZAŁOWICZ
*M. Smoluchowski Institute of Physics, Jagiellonian University,*
*S. Łojasiewicza 11, 30-348 Kraków, Poland*

We use the chiral quark-soliton model to interpret five excited $\Omega_c$ states recently reported by the LHCb collaboration and confirmed by Belle. We briefly recapitulate the model and its application to light baryons. We then show how the model can be extended to the case of baryons with one heavy quark. We test the model against ground state heavy baryons and then examine possible excitations. We argue that it is not possible to accommodate all five $\Omega_c$'s within five parity minus excitations predicetd by the model and propose to interpret two narrowest states split by 70 MeV as pentaquarks belonging to the SU(3) representation $\overline{15}$.

## 1 Chiral Quark Soliton Model ($\chi$QSM)

$\chi$QSM [1] (for review see Ref. [2] and references therein) is based on an old argument by Witten, which says that in the limit of a large number of colors ($N_c \to \infty$), $N_c$ relativistic valence quarks generate chiral mean fields represented by a distortion of a Dirac sea that in turn interacts with the valence quarks themselves. The soliton configuration corresponds to the solution of the Dirac equation for the constituent quarks (with gluons integrated out) in the mean-field approximation, where pseudoscalar mean fields respect so called *hedgehog* symmetry, since it is impossible to construct a pseudoscalar field that changes sign under inversion of coordinates, which would be compatible with the $\mathrm{SU}(3)_{\mathrm{flav}}\times\mathrm{SO}(3)$ space symmetry. This means that neither spin ($\boldsymbol{S}$) nor isospin ($\boldsymbol{T}$) are *good* quantum numbers. Instead a *grand spin* $\boldsymbol{K} = \boldsymbol{S} + \boldsymbol{T}$ is a *good* quantum number.

The ground state configuration corresponds to the fully occupied $K^P = 0^+$ valence level, as shown in Fig. 1.a. Therefore the soliton does not carry definite quantum numbers except for the baryon number resulting from the valence quarks. Spin and isospin appear when the rotations in space and flavor are quantized and the resulting *collective* hamiltonian is analogous to the one of a symmetric top. There are two conditions that the *collective* wave funcions have to satisfy:

- allowed SU(3) representations must contain states with hypercharge $Y' = N_c/3$,
- the isospin $\boldsymbol{T}'$ of the states with $Y' = N_c/3$ couples with the soliton spin $\boldsymbol{J}$ to a singlet: $\boldsymbol{T}' + \boldsymbol{J} = 0$.

As a result, the lowest praity (+) baryons belong to the $\mathrm{SU}(3)_{\mathrm{flavor}}$ octet of spin 1/2 and decuplet of spin 3/2. The first exotic representation is $\overline{\mathbf{10}}$ of spin 1/2 with the lightest state corresponding

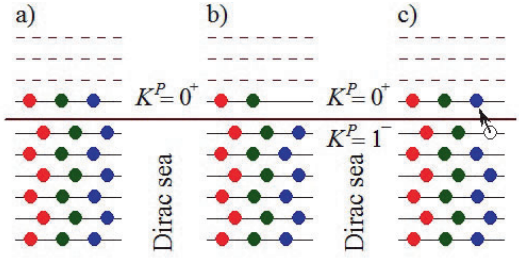


Figure 1 – Schematic pattern of light quark levels in a self-consistent soliton configuration. In the left panel all sea levels are filled and $N_c$ (=3 in the Figure) valence quarks occupy the $K^P = 0^+$ lowest positive energy level. Unoccupied positive energy levels are dpicted by dashed lines. In the middle panel one valence quark has been stripped off, and the soliton has to be supplemented by a heavy quark not shown in the Figure. In the right panel a possible excitation of a sea level quark, conjectured to be $K^P = 1^-$, to the valence level is shown, and again the soliton has to couple to a heavy quark. Strange quark levels that exhibit different filling pattern are not shown.

to the putative $\Theta^+(1540)$ (see *e.g.* Moriond proceedings[4] 2005). The model has been successfully tested in the light baryon sector.

## 2 $\chi$QSM and heavy baryons

Recently wa have proposed [5], following Ref. [6] to generalize the above approach to heavy baryons, by stripping off one valence quark from the $K^P = 0^+$ level, as shown in Fig. 1.b, and replacing it by a heavy quark to neutralize the color. In the large $N_c$ limit both systems: light and heavy baryons are described essentially by the same mean field, and the only difference is now in the quantization condition:

- allowed SU(3) representations must contain states with hypercharge $Y' = (N_c - 1)/3$.

The lowest allowed SU(3) representations are in this case $\overline{\mathbf{3}}$ of spin 0 and to $\mathbf{6}$ of spin 1 shown in Fig. 2.

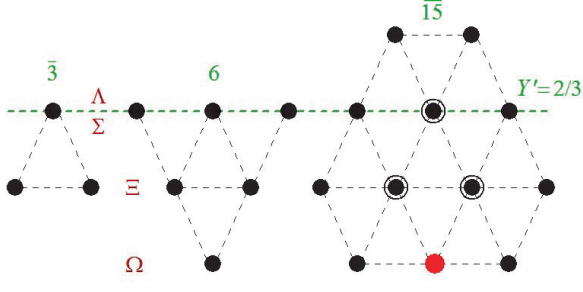


Figure 2 – Rotational band of a soliton with one valence quark stripped off. Soliton spin corresponds to the isospin $T'$ of states on the quantization line $Y' = 2/3$. We show three lowest allowed representations: antitriplet of spin 0, sextet of spin 1 and the lowest exotic representation $\overline{\mathbf{15}}$ of spin 1 or 0. Heavy quark has to be added.

An important feature of this approach is that both $\mathbf{6} - \overline{\mathbf{3}}$ splitting and the splittings inside these multiplets due to the strange quark mass are *predicted* using as an input the light sector spectrum and are in good agreement with experiment [5]. The new ingredient is a hyperfine splitting due to the spin-spin interaction of a soliton and a heavy quark, which can be parametrized phenomenologically. Moeover, the decay widths can be calculated within the same approach, and the results for the charm baryons are shown in Fig. 3.

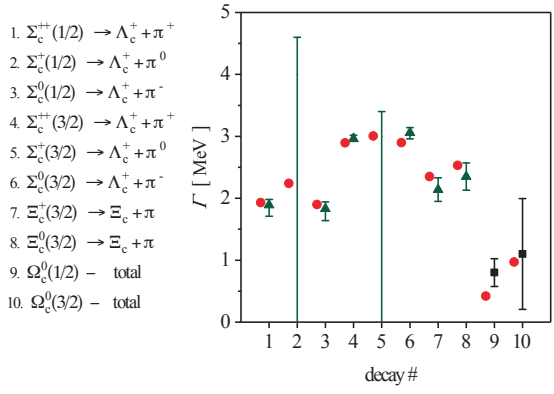


Figure 3 – Decay widths of the charm baryons. Red full circles correspond to our theoretical predictions. Dark green triangles correspond to the experimental data[7] Data for decays 4 – 6 of $\Sigma_c(\mathbf{6}_1, 3/2)$ have been divided by a factor of 5 to fit within the plot area. Widths of two LHCb[8] $\Omega_c$ states that we interpret as pentaquarks are plotted as black full squares with theoretical values shown as red full circles.

## 3 Excitations of heavy baryons

Two possible kinds of excitations are present in the $\chi$QSM. Firstly, higher SU(3) representations, similar to the antidecuplet in the light sector, appear in the rotational band of the soliton of Fig. 1.b. The lowest possible exotic SU(3) representation is $\overline{\mathbf{15}}$ of positive parity and spin 1 ($\overline{\mathbf{15}}$ of spin 0 is heavier) depicted in Fig. 2. Second possibility corresponds to the excitation of the sea quark from the $K^P = 1^-$ sea level to the valence level [6] shown in Fig. 1.b (or alternatively valence quark excitation to the first excited level [a] of $K^P = 1^-$). In this case the parity is negative but the rotational band is the same (see Fig. 2) with, however, different quantization condition:

- the isospin $\boldsymbol{T}'$ of the states with $Y' = (N_c - 1)/3$ couples with the soliton spin $\boldsymbol{J}$ as follows: $\boldsymbol{T}' + \boldsymbol{J} = \boldsymbol{K}$, where $\boldsymbol{K}$ is the grand spin of the excited level.

We have shown that the model describes well the only fully known spectrum of negative parity antitriplets of spin 1/2 and 3/2 [5]. There has been no experimental evidence for the sextet until recent report of five $\Omega_c^0$ states reported by the LHCb [8] and confirmed by BELLE [9]. In the sextet case the above mentioned condition predicts that the soliton spin can be quantized as $J = 0, 1$ and 2. By adding one heavy quark we end up with five possible total spin $S$ excitations: for $J = 0$ $S = 1/2$, for $J = 1$ $S = 1/2$ and 3/2, and for $J = 2$ $S = 3/2$ and 5/2. Although the number of states coincides with the experimental results [8,9], it is not possible to accommodate all five $\Omega_c^0$ states within the constraints imposed by the $\chi$QSM [5]. We have therefore *forced* model constraints (note that in the **6** case we cannot predict the mass splittings, since there is a new parameter in the splitting hamiltonian that corresponds to the transition of Fig. 1.c, which is not known from the light sector), which allows to accommodate only three out of five LHCb states (see black vertical lines in Fig. 4). Two heaviest $\chi$QSM states (green lines in Fig. 4) lie already above the decay threshold to heavy mesons, and it is quite possible that they have very small branching ratio to the $\Xi_c^+ + K^-$ final state analyzed by the LHCb. Two remaining states indicated by dark-blue arrows in Fig. 4, which are hyper fine split by 70 MeV (as the ground state sextets that belong to the same rotational band), can be therefore interpreted as the members of exotic $\overline{\mathbf{15}}$ of positive parity shown as a red dot in Fig. 2. This interpretation

[a] We thank Victor Petrov for pointing out this possibility.

is reinforced by the decay widths, which can be computed in the model. These widths are of the order of 1 MeV and agree with the LHCb measurement (see Fig. 3). Such small widths are in fact expected in the present approach, since the leading $N_c$ terms of the relevant couplings cancel in the non-relativistic limit.

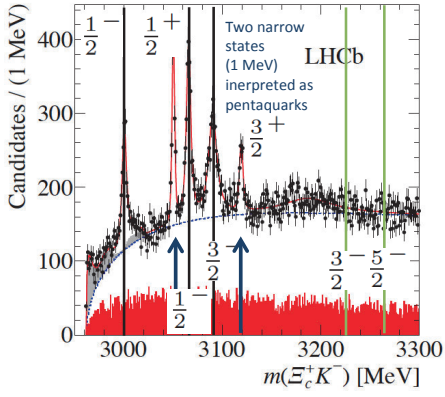


Figure 4 – Spectrum of the $\Omega_c^0$ states (from Ref.[8]) with theoretical predictions of the present model

The simplest way to falsify or to confirm our identification is to search for the *isospin* partners of $\Omega_c^0$ from the $\overline{\mathbf{15}}$. They can be searched in the mass distribution of $\Xi_c^0 + K^-$ or $\Xi_c^+ + \bar{K}^0$: the $\Omega_c^0$'s from the sextet do not decay into these channels. Our model applies also to the bottom sector, and – where the data is available – it describes very well both masses and decay widths.


### Acknowledgments

It is a pleasure to thank my collaborators H.-C. Kim, M.V. Polyakov and G.S. Yang and the organizers of the Rencontres de Moriond for giving me an opportunity to present our work. This work was supported by the Polish NCN grant 2017/27/B/ST2/01314.


### References


1. D. Diakonov, V. Y. Petrov and P. V. Pobylitsa, Nucl. Phys. B **306** (1988) 809.
2. C. V. Christov, A. Blotz, H. C. Kim, P. Pobylitsa, T. Watabe, T. Meissner, E. Ruiz Arriola and K. Goeke, Prog. Part. Nucl. Phys. **37** (1996) 91.
3. E. Witten, Nucl. Phys. B **160** (1979) 57, and **223** (1983) 422, and **223** (1983) 433.
4. M. Praszalowicz in Moriond proceedings 2005, eds. E. Auge and J. Tran Thanh Van.
5. G. S. Yang, H. C. Kim, M. V. Polyakov and M. Praszalowicz, Phys. Rev. D **94** (2016) 071502, and Phys. Rev. D **96** (2017) 094021 Erratum: [Phys. Rev. D **97** (2018) 039901], and H. C. Kim, M. V. Polyakov and M. Praszalowicz, Phys. Rev. D **96** (2017) 014009 Addendum: [Phys. Rev. D **96** (2017) 039902].
6. D. Diakonov, Prog. Theor. Phys. Suppl. **186** (2010) 99.
7. C. Patrignani *et al.* (Particle Data Group), Chin. Phys. C **40** (2016) 100001.
8. R. Aaij *et al.* [LHCb Collaboration], Phys. Rev. Lett. **118** (2017) 182001.
9. J. Yelton *et al.* [Belle Collaboration], Phys. Rev. D **97** (2018) 051102.

# STABLE TETRAQUARKS

CHRIS QUIGG [a]
*Theoretical Physics Department, Fermi National Accelerator Laboratory*
*P.O.Box 500, Batavia, Illinois 60510 USA*

For very heavy quarks, relations derived from heavy-quark symmetry imply novel narrow doubly heavy tetraquark states containing two heavy quarks and two light antiquarks. We predict that double-beauty states will be stable against strong decays, whereas the double-charm states and mixed beauty+charm states will dissociate into pairs of heavy-light mesons. Observing a new double-beauty state through its weak decays would establish the existence of tetraquarks and illuminate the role of heavy color-antitriplet diquarks as hadron constituents.

## 1 Introduction

Since the BELLE collaboration's discovery of the charmonium-associated state $X(3872)$,[1] hadron spectroscopy has been reinvigorated and recast.[2] Many of the newly observed states invite identification with compositions beyond the traditional quark–antiquark meson and three-quark baryon schemes, possibilities foreseen in the foundational quark-model papers.[3] Tetraquark states composed of a heavy quark and antiquark plus a light quark and antiquark have attracted much attention. All the observed candidates fit the form $c\bar{c}q_k\bar{q}_l$, where the light quarks $q$ may be $u, d,$ or $s$. The putative tetraquarks typically have strong decays to $c\bar{c}$ charmonium + light mesons. None is observed significantly below threshold for strong decays into two heavy–light meson states $\bar{c}q_k + c\bar{q}_l$.

Estia Eichten and I have examined the possibility of unconventional tetraquark configurations for which all strong decays are kinematically forbidden.[4] In the heavy-quark limit, stable—hence exceedingly narrow—$Q_iQ_j\bar{q}_k\bar{q}_l$ mesons must exist. To apply this insight, we take into account corrections for finite heavy-quark masses to deduce which tetraquark states containing $b$ or $c$ quarks might be stable. The most promising candidate is a $J^P = 1^+$ isoscalar double-$b$ meson, $\mathcal{T}^{\{bb\}^-}_{[\bar{u}\bar{d}]}$. I will sketch our derivation and results, emphasizing the consequences for experiment, and indicate areas in which experimental and theoretical work can be productive.

[a] Email: quigg@fnal.gov

FERMILAB–CONF–18/099–T

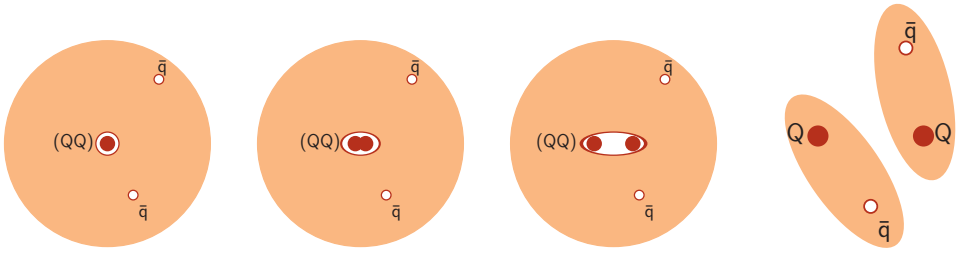


Figure 1 – Schematic evolution of a $Q_iQ_j\bar{q}_k\bar{q}_l$ state as the heavy-quark masses decrease (and the mean separation between the heavy quarks increases) from left to right.

## 2 Heavy-quark symmetry implies stable heavy tetraquark mesons $Q_iQ_j\bar{q}_k\bar{q}_l$

One-gluon-exchange between a pair of color-triplet heavy quarks is attractive for $(QQ)$ in a color-$\bar{\mathbf{3}}$ configuration and repulsive for the color-**6** configuration. The strength of the $\bar{\mathbf{3}}$ attraction is half that of the corresponding $(Q\bar{Q})$ in a color-**1**. This means that in the limit of very heavy quarks, we may idealize the color-antitriplet $(QQ)$ diquark as a stationary, structureless color charge, as depicted in the leftmost panel in Figure 1. We can separate the strong dynamics binding the diquark from the long-range color interaction by which the light antiquarks interact with each other and are bound to the diquark "nucleus."

For sufficiently heavy quarks $Q$, a $Q_iQ_j\bar{q}_k\bar{q}_l$ tetraquark meson is stable against strong decays, as we can show by considering possible decay modes. First, we note that dissociation into two heavy–light mesons is kinematically forbidden. The $\mathcal{Q}$ value for the decay is $\mathcal{Q} \equiv m(Q_iQ_j\bar{q}_k\bar{q}_l) - [m(Q_i\bar{q}_k) + m(Q_j\bar{q}_l)] = \Delta(q_k, q_l) - \frac{1}{2}\left(\frac{2}{3}\alpha_s\right)^2[1 + O(v^2)]\overline{M} + O(1/\overline{M})$, where $\Delta(q_k, q_l)$, the contribution due to light dynamics, becomes independent of the heavy-quark masses, $\overline{M} \equiv (1/m_{Q_i} + 1/m_{Q_j})^{-1}$ is the reduced mass of $Q_i$ and $Q_j$, and $\alpha_s$ is the strong coupling. The velocity-dependent hyperfine corrections, here negligible, are calculable in the nonrelativistic QCD formalism.[5] For large enough values of $\overline{M}$, the middle term on the right-hand side dominates, so the tetraquark is stable against decay into two heavy-light mesons.

What of the other possible decay channel, a doubly heavy baryon plus a light antibaryon, $(Q_iQ_j\bar{q}_k\bar{q}_l) \to (Q_iQ_jq_m) + (\bar{q}_k\bar{q}_l\bar{q}_m)$? For very heavy quarks, the contributions of $Q$ motion and spin to the tetraquark mass are negligible. Since the $(QQ)$ diquark is a color-antitriplet, heavy-quark symmetry tells us that $m(Q_iQ_j\bar{q}_k\bar{q}_l) - m(Q_iQ_jq_m) = m(Q_xq_kq_l) - m(Q_x\bar{q}_m)$. The flavored-baryon–flavored-meson mass difference on the right-hand side has the generic form $\Delta_0 + \Delta_1/M_{Q_x}$. Using the observed mass differences, $m(\Lambda_c) - m(D) = 416.87$ MeV and $m(\Lambda_b) - m(B) = 340.26$ MeV, and choosing effective quark masses $m_c \equiv m(J/\psi)/2 = 1.55$ GeV, $m_b \equiv m(\Upsilon)/2 = 4.73$ GeV, we find $\Delta_1 = 176.6$ MeV$^2$ and $\Delta_0 = 303$ MeV, hence the mass difference in the heavy-quark limit is 303 MeV. The right-hand side is in every case smaller than the mass of the lightest antibaryon, $m(\bar{p}) = 938.27$ MeV, so no decay to a doubly heavy baryon and a light antibaryon is kinematically allowed.

*With no open channels in the heavy-quark limit, stable $Q_iQ_j\bar{q}_k\bar{q}_l$ mesons must exist.* To assess the implications for the real world, we must first test whether it makes sense to idealize the $(QQ)$ diquark as a tiny, structureless, color-antitriplet color source.[b] As the separation between the heavy quarks increases, the light-antiquark cloud screens the $Q_iQ_j$ interaction, altering the $\bar{\mathbf{3}}, \mathbf{6}$ mix, and eventually leading to the division of the $(Q_iQ_j\bar{q}_k\bar{q}_l)$ state into a pair of heavy–light mesons. These changes are indicated in the progression from left to right in Figure 1. Using a half-strength Coulomb+linear quarkonium potential, we verified that the rms core radii are

[b] See Ref. 6 for a thoughtful critical assessment.

small on the expected tetraquark scale: $\langle r^2\rangle^{1/2} = 0.28$ fm $(cc); 0.24$ fm $(bc); 0.19$ fm $(bb)$. This conclusion is supported by exploratory lattice QCD studies.[7]

To ascertain whether stable tetraquark mesons might be observed, we must estimate masses of the candidate configurations. Numerous model calculations exist in the literature,[c] but heavy-quark symmetry makes it possible to compute the $Q_iQ_j\bar{q}_k\bar{q}_l$ tetraquark masses directly, through the relation $m(Q_iQ_j\bar{q}_k\bar{q}_l) - m(Q_iQ_jq_m) = m(Q_xq_kq_l) - m(Q_x\bar{q}_m)$, with due attention to spin configurations and finite-mass corrections that arise from hyperfine interactions and kinetic-energy shifts for the light degrees of freedom.[d] Experiments have determined nearly all the information about heavy baryons and heavy–light mesons needed to evaluate the right-hand side in every case of interest, i.e., for tetraquarks based on $bb, bc,$ and $cc$ diquarks.[e] The doubly heavy baryons have been more elusive: for the moment, the strongest evidence we have is for the $\Xi_{cc}^{++}$ candidate reported by the LHC$b$ experiment at a mass of $3621.40 \pm 0.78$ MeV.[9] With this input, we compute the mass of the lightest $(cc)$ tetraquark as $m(\{cc\}[\bar{u}\bar{d}]) = 3978$ MeV, which lies 102 MeV above the threshold for decay into $D^+D^{*0}$.[f] This would be a $J^P = 1^+$ axial-vector meson, symmetric in $cc$ flavor and antisymmetric in the light antiquark flavors.

In the absence of comprehensive experimental information about the other doubly heavy baryons, we rely for now on model calculations of their masses[11] as inputs to our tetraquark mass calculation. Our results for the lowest-lying levels are given in Table 1. We find two

Table 1: Expectations for ground-state tetraquark masses, in MeV.

| State | $J^P$ | $m(Q_iQ_j\bar{q}_k\bar{q}_l)$ | Example Decay Channel | $\mathcal{Q}$ [MeV] |
|---|---|---|---|---|
| $\{cc\}[\bar{u}\bar{d}]$ | $1^+$ | 3978 | $D^+D^{*0}$ 3876 | 102 |
| $\{cc\}[\bar{q}_k\bar{s}]$ | $1^+$ | 4156 | $D^+D_s^{*+}$ 3977 | 179 |
| $\{cc\}\{\bar{q}_k\bar{q}_l\}$ | $0^+, 1^+, 2^+$ | 4146, 4167, 4210 | $D^+D^0, D^+D^{*0}$ 3734, 3876 | 412, 292, 476 |
| $[bc][\bar{u}\bar{d}]$ | $0^+$ | 7229 | $B^-D^+/B^0D^0$ 7146 | 83 |
| $[bc][\bar{q}_k\bar{s}]$ | $0^+$ | 7406 | $B_sD$ 7236 | 170 |
| $[bc]\{\bar{q}_k\bar{q}_l\}$ | $1^+$ | 7439 | $B^*D/BD^*$ 7190/7290 | 249 |
| $\{bc\}[\bar{u}\bar{d}]$ | $1^+$ | 7272 | $B^*D/BD^*$ 7190/7290 | 82 |
| $\{bc\}[\bar{q}_k\bar{s}]$ | $1^+$ | 7445 | $DB_s^*$ 7282 | 163 |
| $\{bc\}\{\bar{q}_k\bar{q}_l\}$ | $0^+, 1^+, 2^+$ | 7461, 7472, 7493 | $BD/B^*D$ 7146/7190 | 317, 282, 349 |
| $\{bb\}[\bar{u}\bar{d}]$ | $1^+$ | 10482 | $B^-\bar{B}^{*0}$ 10603 | **−121** |
| $\{bb\}[\bar{q}_k\bar{s}]$ | $1^+$ | 10643 | $\bar{B}\bar{B}_s^*/\bar{B}_s\bar{B}^*$ 10695/10691 | **−48** |
| $\{bb\}\{\bar{q}_k\bar{q}_l\}$ | $0^+, 1^+, 2^+$ | 10674, 10681, 10695 | $B^-B^0, B^-B^{*0}$ 10559, 10603 | 115, 78, 136 |

real-world candidates for stable tetraquarks: the axial vector $\{bb\}[\bar{u}\bar{d}]$ meson, $\mathcal{T}_{[\bar{u}\bar{d}]}^{\{bb\}-}$ bound by 121 MeV, and the axial vector $\{bb\}[\bar{u}\bar{s}]$ and $\{bb\}[\bar{d}\bar{s}]$ mesons bound by 48 MeV. Given the provisional doubly heavy baryon masses, we expect all the other $Q_iQ_j\bar{q}_k\bar{q}_l$ tetraquarks to lie at least 78 MeV above the corresponding thresholds for strong decay.[g] We note that exploratory lattice studies also suggest that double-beauty tetraquarks should be stable.[13,14] Promising final states include $\mathcal{T}_{[\bar{u}\bar{d}]}^{\{bb\}}(10482)^- \to \Xi_{bc}^0\bar{p}$, $B^-D^+\pi^-$, and $B^-D^+\ell^-\bar{\nu}$ (which establishes a weak decay), $\mathcal{T}_{[\bar{u}\bar{s}]}^{\{bb\}}(10643)^- \to \Xi_{bc}^0\bar{\Sigma}^-$, $\mathcal{T}_{[\bar{d}\bar{s}]}^{\{bb\}}(10643)^0 \to \Xi_{bc}^0(\bar{\Lambda}, \bar{\Sigma}^0)$, and so on.

If they should lie near enough to threshold, the *unstable* doubly heavy tetraquarks might

[c] A useful compilation appears in Table IX of Ref. 8.

[d] The arithmetic is made explicit in Ref. 4.

[e] The lifetime ($\approx 0.4$ ys) of the top quark is too short to permit the formation of hadrons containing $t$.

[f] An earlier sighting by the SELEX Collaboration[10] of a $\Xi_{cc}^+$ candidate at 3519 MeV would imply $m(\{cc\}[\bar{u}\bar{d}]) =$ 3876 MeV, coincident with the threshold for dissociation into a heavy-light pseudoscalar and heavy-light vector. Signatures for weak decay would include $D^+K^-\ell^+\nu$ and $\Xi_c^+\bar{n}$. The $D^0D^+\gamma$ channel opens at 3734 MeV.

[g] In model calculations, Karliner and Rosner[12] estimate somewhat deeper binding, and so point to additional $bc$ and $cc$ candidates.

be observed in "wrong-sign" (double flavor) combinations bearing $DD, DB,$ or $BB$ quantum numbers. For example, a $J^P = 1^+$ $\mathcal{T}^{\{cc\}}_{[\bar{d}\bar{s}]}(4156)^{++} \to D^+ D_s^{*+}$ resonance would constitute *prima facie evidence* for a non-$q\bar{q}$ level carrying double charge and double charm. This would be a new kind of resonance, for which no attractive force is present at the meson–meson level. Other nearly bound candidates include $1^+$ $\mathcal{T}^{\{bb\}}_{\{\bar{q}_k\bar{q}_l\}}(10681)^{0,-,--}$ ($\mathcal{Q} = +78$ MeV), $1^+$ $\mathcal{T}^{\{bc\}}_{[\bar{u}\bar{d}]}(7272)^0$ ($\mathcal{Q} = +82$ MeV), $0^+$ $\mathcal{T}^{[bc]}_{[\bar{u}\bar{d}]}(7229)^0$ ($\mathcal{Q} = +83$ MeV), and $1^+$ $\mathcal{T}^{\{cc\}}_{[\bar{u}\bar{d}]}(3978)^+$ ($\mathcal{Q} = +102$ MeV).

The production of stable doubly heavy tetraquarks (or their nearly bound counterparts) is undoubtedly a rare event, since it entails—at a start—the production of two heavy quarks and two heavy antiquarks. We have no rate calculation to offer, but note the large yield of $B_c$ mesons in the LHC*b* experiment:[15] $8995 \pm 103$ $B_c \to J/\psi\mu\nu_\mu X$ candidates in 2 fb$^{-1}$ of $pp$ collisions at 8 TeV, and the CMS observation[16] of double-$\Upsilon$ production in 8-TeV $pp$ collisions: $\sigma(pp \to \Upsilon\Upsilon + \text{ anything}) = 68 \pm 15$ pb. These suggest that the Large Hadron Collider experiments should be the first focus of searches for novel tetraquark mesons. The ultimate search instrument might be a future electron–positron Tera-$Z$ factory, for which the branching fractions[17] $Z \to b\bar{b} = 15.12 \pm 0.05\%$ and $Z \to b\bar{b}b\bar{b} = (3.6 \pm 1.3) \times 10^{-4}$ encourage the hope of many events containing multiple heavy quarks.

Two recent investigations go beyond the kinds of arguments I have presented here. Beginning from a situation in which all the constituents are taken to be heavy, so that one-gluon exchange prevails, Czarnecki and collaborators have proposed a figure of merit that governs the color-($\bar{\mathbf{3}}, \mathbf{6}$) admixture in the putative diquark system.[18] They conclude that no stable $QQ\bar{Q}\bar{Q}$ (equal-mass) tetraquarks are to be expected in very-heavy-quark limit, and they find support for the binding of $bb\bar{q}\bar{q}$, in agreement with our conclusions. A generalization allows them to explore how the result depends on $N_c$, the number of colors. A lattice–NRQCD study of the $bb\bar{b}\bar{b}$ system reveals no tetraquark with mass below $\eta_b\eta_b$, $\eta_b\Upsilon$, $\Upsilon\Upsilon$ thresholds in the $J^{PC} = 0^{++}, 1^{+-}, 2^{++}$ channels.[19]

## 3 Some tasks to advance our understanding

*Homework for Experiment.* The most straightforward request is to *look for double-flavor resonances of two heavy–light mesons near threshold.* The ingredients for such searches should already exist in experiments that have reconstructed many $D$, $D_s$, $B$, and $B_s$ mesons. Next, *extend to $\sqrt{s} = 13$ TeV the measurement of representative cross sections for final states containing two heavy quarks and two heavy antiquarks.* Then we need to *discover and determine the masses of doubly-heavy baryons.* These masses are essential "engineering information" for our purposes, as they are needed to implement the heavy-quark–symmetry calculation of tetraquark masses.[h] An important element of the study of doubly heavy baryons is to *resolve the conundrum of the large mass difference between the $\Xi_{cc}^+$ and $\Xi_{cc}^{++}$* candidates reported by SELEX and LHC*b*, respectively. The ultimate experimental goal is to *find stable tetraquarks through their weak decays.*

*Homework for Theory.* An important challenge is to *develop expectations for the production of final states containing $Q_i, \bar{Q}_i, Q_j, \bar{Q}_j$, and eventually for the anticipated stable tetraquarks.* For the stable $Q_iQ_j\bar{q}_k\bar{q}_l$ states we discuss here, *refine lifetime estimates beyond the simplest guess-by-analogy of $\tau \approx 1/3$ ps.* Extend the considerations of Refs. 6, 18 to *understand how color configurations evolve with $QQ$ (and $\bar{q}\bar{q}$) masses.* Continue to explore how diquarks influence hadron spectroscopy, by *analyzing the stability of different body plans in the heavy-quark limit.* A notable example is a possible $(Q_iQ_j)(Q_kQ_l)(Q_mQ_n)$ dibaryon, with $\bar{Q}_p\bar{Q}_q\bar{Q}_r$ color structure.

[h] Doubly heavy baryons are of considerable interest in their own right. A light quark bound to a doubly heavy diquark has much in common—in both color configuration and dynamics—with a heavy–light meson. A further goal is to observe excitations of the diquark core, along with the energy levels of the bound light quark.

## 4 Summary

In the limit of very heavy quarks $Q$, novel narrow doubly heavy tetraquark states must exist. Heavy-quark symmetry relates the doubly heavy tetraquark mass to the masses of a doubly heavy baryon, heavy-light-light baryon, and heavy-light meson. In the future, when we have more complete experimental knowledge of the doubly heavy baryon spectrum, the heavy-quark–symmetry relations should provide the most reliable predictions of doubly heavy tetraquark masses. Our current mass estimates—which must rely on plausible model inputs for the doubly heavy baryon masses—lead us to expect that the lightest $J^P = 1^+$ $\{bb\}[\bar{u}\bar{d}]$, $\{bb\}[\bar{u}\bar{s}]$, and $\{bb\}[\bar{d}\bar{s}]$ states should be exceedingly narrow, decaying only through the charged-current weak interaction. The observation of these novel tetraquark mesons would herald a new form of stable matter, in which the doubly heavy color-$\bar{\mathbf{3}}$ ($Q_iQ_j$) diquark is a basic building block. Unstable $Q_iQ_j\bar{q}_k\bar{q}_l$ tetraquarks with small $\mathcal{Q}$-values may be observable as resonant pairs of heavy-light mesons in channels with double flavor: $DD, DB, BB$.


### Acknowledgments

Je souhaite dire un très grand merci aux gentils organisateurs, à nos amies sauvetrices du secretariat, au personnel du Planibel, à Kim et Van, et à tous les fondateurs des Rencontres de Moriond. I am grateful to the Delta Institute for Theoretical Physics and Nikhef, the National Institute for Subatomic Physics, for generous hospitality in Amsterdam, where this note was prepared. I thank Estia Eichten for collaboration on the work reported here. This manuscript has been authored by Fermi Research Alliance, LLC under Contract No. DE-AC02-07CH11359 with the U.S. Department of Energy, Office of Science, Office of High Energy Physics.


### References


1. S. K. Choi *et al.* [Belle], Phys. Rev. Lett. **91** (2003) 262001 [hep-ex/0309032].
2. The extensive literature may be traced from the recent review by S. L. Olsen, T. Skwarnicki, and D. Zieminska, Rev. Mod. Phys. **90** (2018) 015003 [arXiv:1708.04012].
3. G. Zweig, CERN-TH-401 (1964); CERN-TH-412 (1964). M. Gell-Mann, Phys. Lett. **8** (1964) 214.
4. E. J. Eichten and C. Quigg, Phys. Rev. Lett. **119** (2017) 202002 [arXiv:1707.09575]. For a very early indication that such states could arise, see J.-P. Ader, J.-M. Richard and P. Taxil, Phys. Rev. D **25** (1982) 2370.
5. W. E. Caswell and G. P. Lepage, Phys. Lett. **167B** (1986) 437.
6. J.-M. Richard, A. Valcarce, & J. Vijande, Phys. Rev. C **97** (2018) 035211 [arXiv:1803.06155].
7. A. Peters *et al.*, PoS LATTICE **2015** (2016) 095 [arXiv:1508.00343].
8. S. Q. Luo *et al.*, Eur. Phys. J. C **77** (2017) 709 [arXiv:1707.01180].
9. R. Aaij *et al.* [LHC*b*], Phys. Rev. Lett. **119** (2017) 112001 [arXiv:1707.01621].
10. M. Mattson *et al.* [SELEX], Phys. Rev. Lett. **89** (2002) 112001 [hep-ex/0208014].
11. M. Karliner and J. L. Rosner, Phys. Rev. D **90** (2014) 094007 [arXiv:1408.5877].
12. M. Karliner and J. L. Rosner, Phys. Rev. Lett. **119** (2017) 202001 [arXiv:1707.07666].
13. P. Bicudo *et al.*, Phys. Rev. D **93** (2016) 034501 [arXiv:1510.03441].
14. A. Francis *et al.*, Phys. Rev. Lett. **118** (2017) 142001 [arXiv:1607.05214].
15. R. Aaij *et al.* [LHC*b* Collaboration], Eur. Phys. J. C **74** (2014) 2839 [arXiv:1401.6932].
16. V. Khachatryan *et al.* [CMS Collaboration], JHEP **1705** (2017) 013 [arXiv:1610.07095].
17. C. Patrignani *et al.* [Particle Data Group], Chin. Phys. C **40** (2016) 100001.
18. A. Czarnecki, B. Leng, & M. B. Voloshin, Phys. Lett. B **778** (2018) 233 [arXiv:1708.04594].
19. C. Hughes, E. Eichten, & C. T. H. Davies, Phys. Rev. D **97** (2018) 054505 [arXiv:1710.03236].

# 6.
# New Phenomena

# Searches for exotic Higgs bosons with the ATLAS and CMS experiments

A. Raspereza
*DESY, Notkestrasse 85,*
*Hamburg D-22607, Germany*

This note presents searches for a light pseudoscalar boson produced in decays of the 125 GeV Higgs boson, and for a doubly charged Higgs boson, performed by the ATLAS and CMS collaborations using run-2 LHC data collected at a center-of-mass energy of 13 TeV.

The discovery of the scalar particle with a mass near 125 GeV, denoted in the following $H$, by the CMS and ATLAS Collaborations [1,2] has opened a new era in particle physics. Following this discovery a comprehensive physics program is underway to investigate the properties of the $H$ boson and explore mechanism of electroweak symmetry breaking. Measurements, performed so far, indicate that, at the current level of precision, the new state is compatible with the Standard Model (SM) Higgs boson [3]. However it is well possible that the new boson is the first observed member of the extended Higgs sector predicted by theories beyond the SM (BSM). Searches for additional Higgs bosons at the LHC focus primarily on general two Higgs Doublet models (2HDM) and Minimal Supersymmetric Standard Model (MSSM). A large variety of well-motivated theories exist, which predict Higgs sector richer than that of 2HDM. Particular interest is attracted by models, where two Higgs doublets are extended by one additional singlet complex field, which doesn't couple to fermions and gauge bosons and interacts only with itself and Higgs doublets. The Higgs sector of these models, denoted in the following 2HD+1S, features seven physical states: three CP-even bosons, two CP-odd bosons, and two charged bosons. Such Higgs sector is realized, for example, in the Next-to-Minimal Supersymmetric Standard model (NMSSM) [4,5]. In the 2HD+1S models the $H$ boson can be identified with the lightest or next-to-lightest CP-even state. The experimental searches, discussed in this note, address specific scenario, in which the lightest pseudoscalar boson ($a$) has large singlet component, and therefore its couplings to the SM particles are significantly reduced. For this reason analyses, probing conventional production modes of $a$, such as gluon-gluon fusion or b-quark associated production, have limited sensitivity to the expected signal in this scenario. The $a$ boson is nonetheless potentially accessible through the $H \to aa$ decay and can be identified via its decay into a pair of down-type fermions, $a \to \mu^+\mu^-, \tau^+\tau^-, b\bar{b}$. The Higgs-Brout-Englert mechanism predicts proportionality of fermionic couplings of $a$ to the fermion mass. The decay rates of $a$ into fermions in the 2HD+1S models also depend on the way Higgs doublets couple to fermions and on parameter $\tan\beta$ - the ratio of vacuum expectation values of two Higgs doublets. Detailed description of various 2HD+1S models can be found, for example, in Reference [6].

The CMS Collaboration has carried out search for the $H \to aa$ decay, exploiting final states with two muons and two $\tau$ leptons, $aa \to (\mu^+\mu^-)(\tau^+\tau^-)$ [8], as well as two $\tau$ leptons and two b-quarks, $aa \to (\tau^+\tau^-)(b\bar{b})$ [9]. The analyses have been performed on 36 fb$^{-1}$ of run-2 data collected at $\sqrt{s} = 13$ TeV. The event selection in both analyses targets inclusive production of $H$ with dominant contribution from the gluon-gluon fusion process. Searches cover the range of

the $a$ boson mass, $m_a$, between 15 GeV and half the mass of the $H$ boson and use conventional isolation techniques to select muons, electrons and $\tau$ leptons. At very low masses ($m_a < 15$ GeV) decay products of $a$ bosons are expected to be highly collimated and overlap, making analyses, targeting isolated leptons, insensitive to the $H \to aa$ signal.

In the study of the $(\mu^+\mu^-)(\tau^+\tau^-)$ final state four decay modes of $\tau$ pairs are considered: $\tau_e\tau_h$, $\tau_\mu\tau_h$, $\tau_e\tau_\mu$ and $\tau_h\tau_h$. Here $\tau_e(\tau_\mu)$ denotes leptonic decay of $\tau$ into electron (muon), and $\tau_h$ - hadronic decay of $\tau$. The reconstruction of $\tau_h$ is done for the 1-prong, 1-prong+$\pi^0$'s and 3-prong decay channels. Details of the $\tau_h$ reconstruction techniques at CMS can be found in Reference [7]. A large background suppression is obtained by requiring the visible invariant mass of four leptons to be less than certain threshold, optimized separately for each channel. Because of neutrinos, the visible invariant mass is expected to peak below 125 GeV for the signal, whereas major background processes populate region above 125 GeV. The signal is extracted from the unbinned maximum likelihood fit to the reconstructed mass spectrum of the $a \to \mu\mu$ candidate in all analyzed channels with superposition of analytical functions for the resonant signal and smooth background contributions. No evidence of signal was found. The search results have been translated into an upper 95% confidence level (CL) limit on the quantity $\frac{\sigma}{\sigma_{SM}}\mathcal{B}(H \to aa \to \mu\mu\tau\tau)$ as a function of $m_a$. In this expression $\sigma_{SM}$ denotes inclusive production cross section of $H$ in the SM, $\sigma$ is the actual cross section, and $\mathcal{B}(H \to aa \to \mu\mu\tau\tau)$ is the branching fraction of the $H \to aa \to (\mu^+\mu^-)(\tau^+\tau^-)$ decay. The upper limit on the branching fraction ranges from $1.2 \times 10^{-4}$ at $m_a = 60$ GeV to $4.7 \times 10^{-4}$ at $m_a = 47$ GeV under assumption that $H$ is produced at the LHC with the rate predicted by the SM.

In the study of the $(\tau^+\tau^-)(b\bar{b})$ final state three decay channels of $\tau\tau$ have been employed: $\tau_\mu\tau_h$, $\tau_e\tau_h$ and $\tau_e\tau_\mu$. Despite its large branching fraction, the $\tau_h\tau_h$ channel is not considered in the search. The triggers, recording events with hadronic decay signatures of $\tau$ lepton, have $p_{\mathrm{T}}$ thresholds ($p_{\mathrm{T}}$ stands for transverse momentum) significantly higher than typical visible transverse momentum of reconstructed $\tau_h$ in the cascade decays $H \to aa$, $a \to \tau\tau$, leading to negligible signal acceptance in the $\tau_h\tau_h$ decay mode after the trigger requirement. Events are selected if they have a pair of oppositely charged $\tau$ candidates. Additionally event is required to have at least one b-quark jet reconstructed within the CMS tracker acceptance of $|\eta| < 2.4$ ($\eta$ denotes pseudorapidity), and having $p_{\mathrm{T}} > 20$ GeV. In majority of cases the sub-leading b-quark jet in signal events is too soft to be reliably reconstructed or produced outside the tracker acceptance, where b-tagging algorithm, exploiting decay length information, cannot be applied. To enhance sensitivity of the search the final selected sample is split into several categories depending on the value of the visible invariant mass of $\tau$ decay products and b-quark jet, $m^{vis}_{\tau\tau b}$. Thresholds, defining event categories, are optimized individually for each $\tau\tau$ decay channel. Because of neutrinos from $\tau$ decays and missing b-quark jet, the signal concentrates in the region $m^{vis}_{\tau\tau b} < 125$ GeV and is well separated from background processes characterized by higher values of $m^{vis}_{\tau\tau b}$. The signal-to-background ratio is therefore higher for categories with lower values of $m^{vis}_{\tau\tau b}$. The signal is extracted from the binned maximum likelihood fit to the reconstructed spectra of the visible invariant mass of the di-tau system, $m^{vis}_{\tau\tau}$, in all studied di-tau decay channels and all event categories defined by $m^{vis}_{\tau\tau b}$. Figure 1 (left) shows the $m^{vis}_{\tau\tau}$ spectrum in the most sensitive channel, corresponding to the $\tau_\mu\tau_h$ decay mode with $m^{vis}_{\tau\tau b} < 75$ GeV. The search has found no signal and upper 95% CL limits have been set on $\frac{\sigma}{\sigma_{SM}}\mathcal{B}(H \to aa \to \tau\tau bb)$. Assuming the SM production rates for $H$, the analysis sets upper limit on the branching fraction in the range from about 3.5% at $m_a = 35$ GeV to 12% at $m_a = 15$ GeV.

Figure 1 (right) demonstrates complementarity of various CMS searches for the $H \to aa$ signal performed on run-1 and run-2 data. Plot shows an upper limit on the quantity $\frac{\sigma}{\sigma_{SM}}\mathcal{B}(H \to aa)$ as a function of $m_a$. As a representative example the 2HD+1S model of type-III is chosen, where one of the Higgs doublets couples to quarks and another to charged leptons. The $\tan\beta$ value is set to 5. In the chosen scenario the $a$ boson couplings to leptons are enhanced and limits on $\mathcal{B}(H \to aa)$ well below 100% can be set over the entire probed range of $m_a$, assuming the

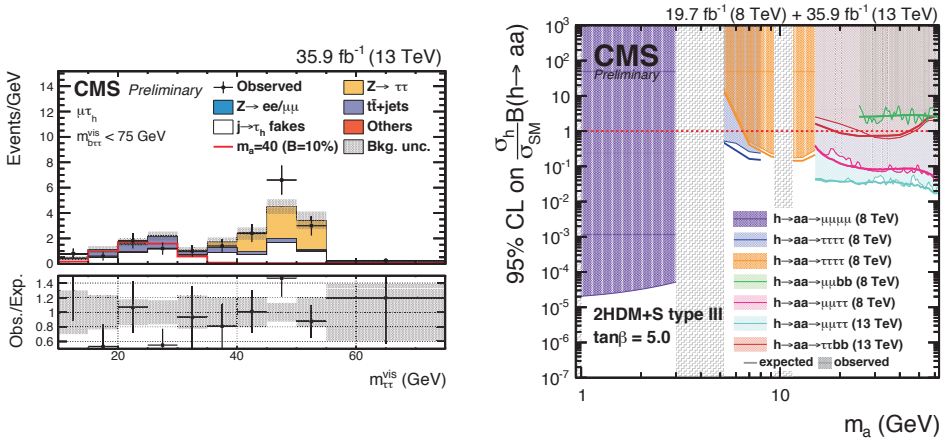


Figure 1 – Left: The $m_{\tau\tau}^{vis}$ distribution in the $\tau_\mu\tau_h$ channel with $m_{\tau\tau b}^{vis} < 75$ of the CMS search for $H \to aa \to (\tau^+\tau^-)(b\bar{b})$. Right: Upper limit on $\frac{\sigma}{\sigma_{SM}}\mathcal{B}(H \to aa)$ as a function of $m_a$ from various CMS analyses performed on run-1 and run-2 datasets. The interpretation is done within the 2HD+1S model of type-III with $\tan\beta = 5$.

SM production rates for $H$.

The $H \to aa \to 4\mu$ decay mode provides the cleanest channel to search for very light pseudoscalar boson. The sensitivity of this channel gets however reduced at $m_a > 2m_\tau$ ($m_\tau$ is the $\tau$ lepton mass), since decay of $a$ into heavier $\tau$ lepton becomes kinematically allowed and supplants the $a \to \mu\mu$ decay. In the 2HD+1S models predicting the same dependence of $a$ couplings to down-type fermions on $\tan\beta$, further reduction of $\mathcal{B}(a \to \mu\mu)$ occurs at $m_a > 2m_b$ ($m_b$ is the mass of b-quark) for the benefit of the $a \to b\bar{b}$ decay.

Using run-2 dataset collected at $\sqrt{s} = 13$ TeV, the ATLAS Collaboration has performed search for the $H \to aa \to 4\mu$ signal, covering mass range 1 GeV $\leq m_a \leq$ 15 GeV [10]. The analysis selects events compatible with the hypothesis of the production of two identical particles, decaying to $\mu^+\mu^-$. Events are rejected if invariant mass of any $\mu^+\mu^-$ pair is compatible with $J/\Psi$, $\Upsilon$ or $Z$ resonances. Finally invariant mass of four muons is required to be compatible within the detector resolution with the mass of $H$. The signal is extracted from the distribution of the averaged mass of two reconstructed $a \to \mu^+\mu^-$ candidates. No data events have been selected into the final sample, and the expected background yield amounts to $0.4 \pm 0.1$ events. Figure 2 (left) presents results of the search in terms of an upper limit on $\frac{\sigma}{\sigma_{SM}}\mathcal{B}(H \to aa)$ as a function of $m_a$ for the 2HDM+1S model of type-II with $\tan\beta$=5. This type of 2HD+1S models corresponds to the Higgs sector of the NMSSM and postulates that one Higgs doublet couples to up-type fermions and another - to down-type fermions. Within this benchmark scenario, an upper limit on $\mathcal{B}(H \to aa)$ is set below $10^{-3}$ at $m_a < 2m_\tau$ and ranges from about 20 to 50% at $2m_\tau < m_a < 2m_b$ for the SM production rate of $H$. At $m_a > 2m_b$ the upper limit is greater than 1, i.e. analysis has no sensitivity to the benchmark model in that mass range.

Another interesting class of BSM theories consists of Higgs triplet models, which predict doubly charged physical state, $H^{\pm\pm}$. One example is given by Left-Right Symmetric (LRS) models [11,12]. Doubly charged Higgs bosons can couple to either left-handed or right-handed fermions. In LRS models two cases are distinguished and denoted $H_L^{\pm\pm}$ and $H_R^{\pm\pm}$. The ALTAS Collaboration has performed search on 36 fb$^{-1}$ of run-2 data for a pair produced doubly charged Higgs bosons [13]. The analysis targeted decays into same sign lepton pairs, $H^{\pm\pm} \to e^\pm e^\pm, e^\pm\mu^\pm, \mu^\pm\mu^\pm$ that dominate at low values of the Higgs triplet vacuum expectation value. The search has higher sensitivity to the $H_L^{\pm\pm}$ state, since the cross section of the $H_L^{++}H_L^{--}$ production is 2.3 higher than that of $H_R^{++}H_R^{--}$ because of different couplings to $Z$ [14]. The study selected events

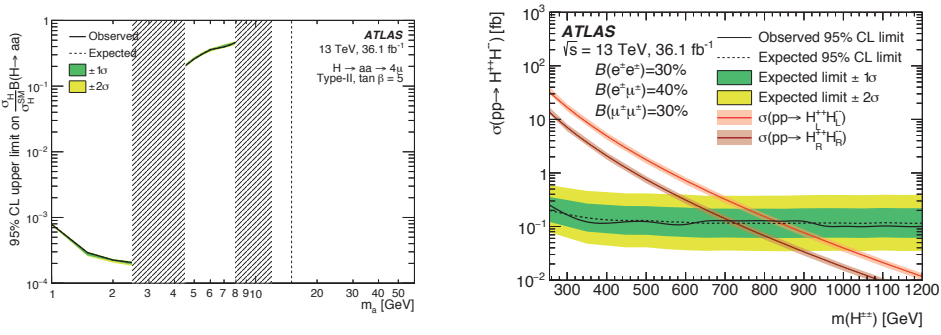


Figure 2 – Left: Upper 95% CL limit on $\frac{\sigma}{\sigma_{SM}}\mathcal{B}(H \to aa)$ as a function of $m_a$ obtained from the ATLAS search for $H \to aa \to 4\mu$. The interpretation is done within the 2HD+1S model of type-II with $\tan\beta = 5$. Right: Upper 95% CL limit on the cross section of the $H^{++}H^{--}$ production as a function of the probed $H^{\pm\pm}$ mass. Red curves show prediction of LRS models for $H_L^{\pm\pm}$ and $H_R^{\pm\pm}$ states.

into different signal regions, depending on the lepton multiplicity and lepton flavor composition. In the two- and three-lepton signal regions, the signal was searched for as a resonant peak in the distribution of the invariant mass of same-sign lepton pair. In the four-lepton region further rejection of background is obtained by requiring masses of same-sign lepton pairs to be consistent within the detector resolution. The search for a signal in the four-lepton region is performed in the distribution of the average mass of two same-sign lepton pairs. The analysis found no signal, and results of the search were used to set an upper limit on the production cross section as a function of the probed $H^{\pm\pm}$ mass for several benchmark assumptions on branching fractions of $H^{\pm\pm}$ decays into leptons. Figure 2 (right) shows as an example upper limits on the production cross section, assuming $\mathcal{B}(H^{\pm\pm} \to \mu^\pm\mu^\pm) = 0.3$, $\mathcal{B}(H^{\pm\pm} \to e^\pm e^\pm) = 0.3$ and $\mathcal{B}(H^{\pm\pm} \to e^\pm\mu^\pm) = 0.4$. Masses of $H_L^{\pm\pm}$ ($H_R^{\pm\pm}$) below 770 GeV (660 GeV) are excluded in LRS models under assumption that $\mathcal{B}(H^{\pm\pm} \to \ell^\pm\ell^\pm) = 100\%$ with $\ell = e, \mu$.

This note highlighted only few representative examples of analyses probing models with the exotic Higgs sector. A comprehensive physics program of searches for BSM Higgs bosons continues at the LHC. Experimental collaboration are constantly improving their analysis techniques, extending the scope of analyzed signatures and accumulating more data in hope to uncover hidden signs of a new physics.

## References


1. ATLAS Collaboration, *Phys. Lett.* B **716**, 1 (2012).
2. CMS Collaboration, *Phys. Lett.* B **716**, 30 (2012).
3. ATLAS and CMS Collaborations, *JHEP* **08**, 045 (2016).
4. P. Fayet, *Nucl. Phys.* B **90**, 104 (1975).
5. P. Fayet, *Phys. Lett.* B **69**, 489 (1977).
6. D. Curtin *et al*, *Phys. Rev.* D **90**, 075004 (2014).
7. CMS Collaboration, Physics Analysis Summary TAU-16-002.
8. CMS Collaboration, Physics Analysis Summary HIG-17-029.
9. CMS Collaboration, Physics Analysis Summary HIG-17-024.
10. ATLAS Collaboration, arXiv:1802.03388.
11. R. N. Mohapatra and J. C. Pati, *Phys. Rev.* D **11**, 566 (1975).
12. G. Senjanovic and R. N. Mohapatra, *Phys. Rev.* D **12**, 1502 (1975).
13. ATLAS Collaboration, *Eur. Phys. J.* C **78**, 199 (2018).
14. K. Huitu *et al*, *Nucl. Phys.* B **487**, 27 (1997).

# APPROXIMATE HIGGS ALIGNMENT WITHOUT DECOUPLING

HOWARD E. HABER
*Santa Cruz Institute for Particle Physics, University of California,*
*1156 High Street, Santa Cruz, CA 95064 USA*

The properties of the Higgs boson $h(125)$ observed in LHC data are consistent with Standard Model predictions. Consequently, if additional Higgs bosons are present, then the direction of $h(125)$ in field space must be approximately aligned with the direction of the Higgs vacuum expectation value. One way to achieve approximate Higgs alignment is in the decoupling limit, where all additional Higgs scalars are significantly heavier than the $h(125)$. In this presentation, the viability of approximate Higgs alignment *without* decoupling is addressed.

## 1 Introduction

With the discovery of the Higgs boson in 2012,[1,2] it appears that all the fundamental particles that comprise the Standard Model (SM) have been discovered. Of course, it is straightforward to add additional Higgs scalars to the SM. However, an extended Higgs sector is already highly constrained. For example, the electroweak $\rho$ parameter is very close to 1, which strongly suggests that additional Higgs multiplets consist of hypercharge one doublets and/or singlets under the electroweak gauge group.[3] Moreover, the extended Higgs sector must contain a SM-like $h(125)$,[4] whereas evidence for additional scalar states, either via direct production or by virtual exchange, must have (so far) escaped detection in LHC data.

## 2 The alignment limit of the 2HDM

In this presentation, we shall focus on the two-Higgs doublet model (2HDM) as a prototype for an extended Higgs sector. The 2HDM consists of two hypercharge one, doublet fields $\Phi_1$ and $\Phi_2$ After minimizing the scalar potential, $\langle \Phi_i^0 \rangle = v_i/\sqrt{2}$ (for $i = 1, 2$), with $v \equiv (|v_1|^2 + |v_2|^2)^{1/2} = 2m_W/g = 246$ GeV. It is convenient to introduce the Higgs basis fields,[5,6]

$$H_1 = \begin{pmatrix} H_1^+ \\ H_1^0 \end{pmatrix} \equiv \frac{v_1^* \Phi_1 + v_2^* \Phi_2}{v}\,, \qquad H_2 = \begin{pmatrix} H_2^+ \\ H_2^0 \end{pmatrix} \equiv \frac{-v_2 \Phi_1 + v_1 \Phi_2}{v}\,, \tag{1}$$

such that $\langle H_1^0 \rangle = v/\sqrt{2}$ and $\langle H_2^0 \rangle = 0$. The Higgs basis is uniquely defined up to an overall rephasing, $H_2 \to e^{i\chi} H_2$. In the Higgs basis, the scalar potential is given by,

$$\mathcal{V} = Y_1 H_1^\dagger H_1 + Y_2 H_2^\dagger H_2 + [Y_3 H_1^\dagger H_2 + \text{h.c.}] + \tfrac{1}{2} Z_1 (H_1^\dagger H_1)^2 + \tfrac{1}{2} Z_2 (H_2^\dagger H_2)^2 + Z_3 (H_1^\dagger H_1)(H_2^\dagger H_2) + Z_4 (H_1^\dagger H_2)(H_2^\dagger H_1) + \left\{ \tfrac{1}{2} Z_5 (H_1^\dagger H_2)^2 + \left[ Z_6 (H_1^\dagger H_1) + Z_7 (H_2^\dagger H_2) \right] H_1^\dagger H_2 + \text{h.c.} \right\} . \qquad (2)$$

The minimization of the scalar potential yields $Y_1 = -\frac{1}{2} Z_1 v^2$ and $Y_3 = -\frac{1}{2} Z_6 v^2$.

The neutral scalar field $H_1^0$ is *aligned* in field space with the Higgs vacuum expectation value. If $\sqrt{2}\,\text{Re}\, H_1^0 - v$ were a mass eigenstate, then its tree-level properties would coincide with the Higgs boson of the SM. For simplicity, we assume a CP-conserving scalar potential (where the scalar potential parameters are simultaneously real after an appropriate rephasing of $H_2$). The CP-even Higgs squared-mass matrix is,[5,7]

$$\mathcal{M}_H^2 = \begin{pmatrix} Z_1 v^2 & Z_6 v^2 \\ Z_6 v^2 & m_A^2 + Z_5 v^2 \end{pmatrix} .$$

where $m_A$ is the mass of the CP-odd Higgs scalar.

The CP-even Higgs bosons are $h$ and $H$ with $m_h \leq m_H$. Approximate alignment arises in two limiting cases:[8,9,10] Case 1: $m_A^2 \gg (Z_1 - Z_5) v^2$. This is the *decoupling limit*,[11] where $h$ is SM-like and $m_A^2 \sim m_H^2 \sim m_{H^\pm}^2 \gg m_h^2 \simeq Z_1 v^2$. Case 2: $|Z_6| \ll 1$. Then, $h$ is SM-like if $m_A^2 + (Z_5 - Z_1) v^2 > 0$; otherwise, $H$ is SM-like. This is alignment with or without decoupling, depending on how large $m_A$ is. In particular, the CP-even neutral scalar mass eigenstates are,

$$\begin{pmatrix} H \\ h \end{pmatrix} = \begin{pmatrix} c_{\beta-\alpha} & -s_{\beta-\alpha} \\ s_{\beta-\alpha} & c_{\beta-\alpha} \end{pmatrix} \begin{pmatrix} \sqrt{2}\ \text{Re}\, H_1^0 - v \\ \sqrt{2}\ \text{Re}\, H_2^0 \end{pmatrix} , \qquad (3)$$

where $c_{\beta-\alpha} \equiv \cos(\beta - \alpha)$ and $s_{\beta-\alpha} \equiv \sin(\beta - \alpha)$ are defined in terms of the mixing angle $\alpha$ that diagonalizes the CP-even Higgs squared-mass matrix when expressed in the $\Phi_1$–$\Phi_2$ basis of scalar fields, $\{\sqrt{2}\ \text{Re}\, \Phi_1^0 - v_1\,,\ \sqrt{2}\ \text{Re}\, \Phi_2^0 - v_2\}$, and $\tan\beta \equiv v_2/v_1$. Since the SM-like Higgs boson must be approximately $\sqrt{2}\ \text{Re}\, H_1^0 - v$, it follows that $h$ is SM-like if $|c_{\beta-\alpha}| \ll 1$ (corresponding to alignment with or without decoupling, depending on how large $m_A$ is). Likewise, $H$ is SM-like if $|s_{\beta-\alpha}| \ll 1$ (which is only possible in the case of alignment without decoupling).

Exact tree-level Higgs alignment corresponds to $Z_6 = 0$, which is satisfied in the inert doublet model (IDM).[12] This is a special case of the 2HDM in which there is an unbroken $\mathbb{Z}_2$ symmetry in the Higgs basis such that $H_2$ is the only $\mathbb{Z}_2$-odd field. In the IDM, the SM Higgs boson resides entirely in $H_1$. In contrast, approximate tree-level alignment without decoupling in a generic 2HDM would appear to depend on a judicious choice of model parameters. However, a more satisfying scenario would be one in which the latter is achieved as a consequence of an approximate symmetry. Thus, we now explore the possible symmetries of the 2HDM scalar potential that can lead naturally to tree-level Higgs alignment, and the symmetry-breaking mechanisms that can maintain approximate alignment, consistent with the LHC Higgs data.

## 3 A symmetry origin for Higgs alignment

One can reduce the number of 2HDM parameters by imposing additional symmetries on the scalar potential in the $\Phi_1$–$\Phi_2$ basis.[13,14] In this basis, the parameters of the scalar potential are three squared-mass parameters, $m_{11}^2$, $m_{22}^2$ and $m_{12}^2$ (the analogs of the $Y_i$ of eq. (2)), and seven quartic couplings, $\lambda_i$, $i = 1, 2, \ldots, 7$ (the analogs of the $Z_i$ of eq. (2)). The possible Higgs family symmetries are: (i) $\mathbb{Z}_2$: $\Phi_1 \to \Phi_1$ and $\Phi_2 \to -\Phi_2$; (ii) $\Pi_2$: $\Phi_1 \longleftrightarrow \Phi_2$; (iii) $\text{U}(1)_{\text{PQ}}$ [Peccei-Quinn[15]]: $\Phi_1 \to e^{-i\theta}\Phi_1$ and $\Phi_2 \to e^{i\theta}\Phi_2$; (iv) SO(3): $\Phi_i \to U_{ij}\Phi_j$, for $U \in \text{U}(2)/\text{U}(1)_{\text{Y}}$ (the scalar potential is automatically invariant with respect to the hypercharge $\text{U}(1)_{\text{Y}}$). In addition, one can also consider generalized CP symmetries: (i) CP1: $\Phi_i \to \Phi_i^*$, (ii) CP2: $\Phi_1 \to \Phi_2^*$ and $\Phi_2 \to -\Phi_1^*$; (iii) CP3: $\Phi_1 \to \Phi_1^* \cos\theta + \Phi_2^* \sin\theta$ and $\Phi_2 \to -\Phi_1^* \sin\theta + \Phi_2^* \cos\theta$ (for $0 < \theta < \frac{1}{2}\pi$). The constraints of each of these symmetries on the scalar potential parameters in the $\Phi_1$–$\Phi_2$

basis are easily obtained (see Table 1 of Ref. 13). Moreover, applying $\mathbb{Z}_2$ and $\Pi_2$ simultaneously is equivalent to a CP2-symmetric potential in a different basis. Similarly, applying $\mathrm{U}(1)_{\mathrm{PQ}}$ and $\Pi_2$ simultaneously is equivalent to a CP3-symmetric potential in a different basis.[14]

The parameters of the CP-conserving scalar potential in the $\Phi_1$–$\Phi_2$ basis are related to the corresponding Higgs basis parameters; e.g.,[16]

$$Y_3 = \tfrac{1}{2}(m_{22}^2 - m_{11}^2)s_{2\beta} - m_{12}^2 c_{2\beta}\,, \tag{4}$$

$$Z_6 = -\tfrac{1}{2}\big[\lambda_1 c_\beta^2 - \lambda_2 s_\beta^2 - \lambda_{345} c_{2\beta}\big] s_{2\beta} + \lambda_6 c_\beta c_{3\beta} + \lambda_7 s_\beta s_{3\beta}\,, \tag{5}$$

where $\lambda_{345} \equiv \lambda_3 + \lambda_4 + \lambda_5$, $s_\beta \equiv \sin\beta$, $c_\beta \equiv \cos\beta$, etc. Due to the scalar potential minimum condition, exact alignment (i.e., $Z_6 = 0$) implies that $Y_3 = 0$. The latter can be achieved if the scalar potential exhibits a CP2, CP3 or SO(3) symmetry, in which case $m_{11}^2 = m_{22}^2$ and $m_{12}^2 = 0$. In the case of CP2, setting $Z_6 = 0$ in eq. (5) determines the value of $\tan\beta$. In the CP3 and SO(3) cases, $\lambda_1 = \lambda_2 = \lambda_{345}$ and $\lambda_6 = \lambda_7 = 0$. Then, $Z_6 = 0$ is satisfied independently of $\tan\beta$, corresponding to the condition of natural alignment introduced by Bhupal Dev and Pilaftsis.[17]

In order to specify a complete model, one must also exhibit the Higgs–fermion Yukawa couplings. In the case of the IDM, the fermions are taken to be $\mathbb{Z}_2$-even states, which do not couple to the Higgs basis field $H_2$. In contrast, the extension of the CP2, CP3 or SO(3) symmetries to the Yukawa interactions is problematic, resulting in a massless quark or some other phenomenologically untenable feature.[18]

## 4 A model of approximate Higgs alignment

Consider the 2HDM with a CP2-symmetric scalar potential, which can be realized in another basis as a $\mathbb{Z}_2 \otimes \Pi_2$ discrete symmetry, where $m_{11}^2 = m_{22}^2$, $\lambda_1 = \lambda_2$, $m_{12}^2 = \lambda_6 = \lambda_7 = 0$, and $\lambda_5$ is real. To extend this symmetry to the Yukawa sector, we introduce mirror fermions.[19] The SM fermions are denoted by lower case letters (e.g. left-handed doublet fields $q$ and right-handed singlet fields $u$ and $d$), and mirror fermions by upper case letters. Under the discrete symmetries,

$$\begin{aligned}
&\Pi_2:\ \Phi_1 \longleftrightarrow \Phi_2\,, \quad q \longleftrightarrow q, \quad u \longleftrightarrow U, \qquad \overline{U} \longleftrightarrow \overline{U}\,,\\
&\mathbb{Z}_2:\ \Phi_1 \to \Phi_1\,, \quad \Phi_2 \to -\Phi_2\,, \quad q \to q, \quad u \to -u, \quad U \to U, \quad \overline{U} \to \overline{U}\,,
\end{aligned}$$

where $\overline{U}$ is in the representation conjugate to $U$ (to avoid anomalies). The Yukawa couplings consistent with the $\mathbb{Z}_2 \otimes \Pi_2$ discrete symmetry are,[a]

$$\mathscr{L}_{\mathrm{Yuk}} \supset y_t\,(q\Phi_2 u + q\Phi_1 U) + \mathrm{h.c.} \tag{6}$$

In addition, we introduce an explicit mass term, $\mathscr{L}_{\mathrm{mass}} = M_U U\overline{U} + \mathrm{h.c.}$ (with $M_U$ large enough to be consistent with the LHC experimental limits on mirror fermion masses), which preserves the $\mathbb{Z}_2$ but explicitly breaks the $\Pi_2$ discrete symmetry. This symmetry breaking is soft, so that $m_{22}^2 - m_{11}^2$ is protected from quadratic sensitivity to the cutoff scale $\Lambda$,

$$\Delta m^2 \equiv m_{22}^2 - m_{11}^2 \sim -\frac{3y_t^2 M_U^2}{4\pi^2}\ln(\Lambda/M_U)\,,$$

neglecting finite threshold corrections proportional to $M_U^2$. Due to the unbroken $\mathbb{Z}_2$ symmetry, a nonzero $m_{12}^2$ is not generated in this approximation. Integrating out the mirror fermions below the scale $M_U$, one also generates a splitting between $\lambda_1$ and $\lambda_2$. However, this is a small correction, which has a negligible impact on our analysis.

The important parameters of the scalar potential are: $m^2 \equiv \frac{1}{2}(m_{11}^2 + m_{22}^2)$, $\Delta m^2 \equiv m_{22}^2 - m_{11}^2$ and $R \equiv \lambda_{345}/\lambda$ (where $\lambda \equiv \lambda_1 = \lambda_2$). We impose $\lambda > 0$ and $R > -1$ to ensure that the vacuum is bounded from below. Solving for the scalar potential minimum, there are two possible phases:

[a] The down-type quarks and leptons can also be included by introducing the appropriate mirror fermions.

(i) the inert phase, where the $\mathbb{Z}_2$ is unbroken, corresponding to the IDM; and (ii) a mixed phase where both $v_1 \neq 0$ and $v_2 \neq 0$. In the case of the mixed phase, $m^2 = -\frac{1}{4}\lambda(1+R)v^2$ and

$$\tan\beta \equiv \frac{v_2}{v_1} = \sqrt{\frac{1-\epsilon}{1+\epsilon}}\,, \qquad \text{where} \quad \epsilon = \cos 2\beta = \frac{2\Delta m^2}{\lambda(1-R)v^2}\,. \tag{7}$$

The positivity of $v_1^2$ and $v_2^2$ and the curvature at the extremum requires $|R| < 1$ and $|\epsilon| < 1$.

The Higgs boson mass spectrum of the mixed phase is,

$$m^2_{h,H} = \tfrac{1}{2}\lambda v^2\big[1 \mp \sqrt{R^2 + (1-R^2)\epsilon^2}\,\big]\,, \qquad m^2_A = |\lambda_5|v^2\,, \qquad m^2_{H^\pm} = m^2_A - \tfrac{1}{2}(\lambda_4 - \lambda_5)v^2\,. \tag{8}$$

If $h$ is SM-like, then $-1 < R < -\epsilon^2/(1-\epsilon^2)$ and

$$c_{\beta-\alpha} \simeq \frac{\epsilon(1-R)}{2|R|} + \mathcal{O}(\epsilon^2)\,. \tag{9}$$

In particular, the alignment limit favors small $|\epsilon|$, which yields $\tan\beta \sim \mathcal{O}(1)$. In this parameter regime,

$$m^2_H \simeq m^2_h\left(\frac{1+|R|}{1-|R|} + \mathcal{O}(\epsilon^2)\right)\,, \tag{10}$$

corresponding to approximate alignment without decoupling as long as $|R|$ is not too close to 1.

One can also construct a model of approximate alignment without decoupling by employing a softly broken CP3 symmetry, augmented with the corresponding mirror fermions.[20] Further details on the phenomenology of the CP2 and CP3 models can be found in Refs. 19 and 20.


## Acknowledgments

This presentation is based on works in collaboration with Patrick Draper, Pedro Ferreira, João Silva, and Joshua Ruderman. H.E.H. is supported in part by the U.S. Department of Energy grant number DE-SC0010107.


## References


1. G. Aad *et al.* [ATLAS Collaboration], Phys. Lett. B **716** (2012) 1.
2. S. Chatrchyan *et al.* [CMS Collaboration], Phys. Lett. B **716** (2012) 30.
3. J.F. Gunion, H.E. Haber, G.L. Kane and S. Dawson, *The Higgs Hunter's Guide* (Westview Press, Boulder, CO, 2000).
4. G. Aad *et al.* [ATLAS and CMS Collaborations], JHEP **1608** (2016) 045.
5. G.C. Branco, L. Lavoura and J.P. Silva, *CP Violation* (Oxford University Press, 1999).
6. S. Davidson and H.E. Haber, Phys. Rev. D **72** (2005) 035004 [Erratum: **72** (2005) 099902].
7. H.E. Haber and D. O'Neil, Phys. Rev. D **74** (2006) 015018 [Erratum: **74** (2006) 059905].
8. N. Craig, J. Galloway and S. Thomas, arXiv:1305.2424 [hep-ph].
9. H.E. Haber, in Proceedings of the of the Toyama International Workshop on Higgs as a Probe of New Physics 2013 (HPNP2013), arXiv:1401.0152 [hep-ph].
10. M. Carena, I. Low, N.R. Shah and C.E.M. Wagner, *JHEP* **1404** (2014) 015.
11. J.F. Gunion and H.E. Haber, Phys. Rev. D **67** (2003) 075019.
12. R. Barbieri, L.J. Hall and V.S. Rychkov, Phys. Rev. D **74** (2006) 015007.
13. I.P. Ivanov, Phys. Rev. D **77** (2008) 015017.
14. P.M. Ferreira, H.E. Haber and J.P. Silva, Phys. Rev. D **79**, (2009) 116004.
15. R.D. Peccei and H.R. Quinn, Phys. Rev. D **16** (1977) 1791.
16. H.E. Haber and O. Stål, Eur. Phys. J. C **75** (2015) 491 [Erratum: **76** (2016) 312].
17. P.S. Bhupal Dev and A. Pilaftsis, JHEP **1412** (2014) 024 [Erratum: **1511** (2015) 147].
18. P.M. Ferreira and J.P. Silva, Eur. Phys. J. C **69** (2010) 45.
19. P. Draper, H.E. Haber and J.T. Ruderman, JHEP **1606** (2016) 124.
20. P. Draper and H.E. Haber, in preparation.

# SEARCHES FOR DARK MATTER AT ATLAS AND CMS

KATHARINA BIERWAGEN
on behalf of the ATLAS and CMS Collaboration
*Institut für Physik, Johannes Gutenberg-Universität, Mainz, Germany*

Cosmological and astrophysical observations indicate the presence of Dark Matter in the universe which cannot be explained by the Standard Model. Searches for Dark Matter are performed by both the ATLAS and CMS experiment at the LHC in events involving large missing transverse momentum in the final state. So far no signal for physics beyond the Standard Model has been found. An overview of the most recent results by both the ATLAS and CMS collaboration based on the full proton-proton collision dataset collected at a centre-of-mass energy of 13 TeV in 2015 and 2016 is presented.

## 1 Introduction

The search for Dark Matter (DM) is a fundamental part of the physics programme of the Large Hadron Collider (LHC). The LHC has the ability to produce DM in pp-collisions and will be able to probe all basic interactions. The simplest realistic models consist of a DM particle and a so-called mediator, which connects the Standard Model (SM) to the dark sector [1,2,3,4]. Recently, searches for these simplified models has become very popular at the LHC following two strategies. The first strategy looks for DM itself, while the second strategy searches for the mediator particle. Since in the first case the invisible DM particles will escape the dector undetected, the DM particles needs to be boosted opposite to the direction of visible particles, leading to the "mono-X" signatures. Therefore, all those signatures are characterized by a large amount of missing transverse momentum. At the LHC a wide range of final states can be investigated, reaching from mono-photon to mono-Higgs signatures.

In the following, the most recent searches by the ATLAS [5] and CMS [6] collaboration will be briefly summarized.

## 2 Searches for Dark Matter with jets

The search for DM in final states with an energetic jet and large missing transverse momentum has the largest $E_T^{miss} + X$ cross section and includes searches with jets from the hadronic decay of W and Z bosons.

The search has been performed using proton-proton collision data corresponding to an integrated luminosity of 36 fb$^{-1}$ at a centre-of-mass energy of 13 TeV collected in 2015 and 2016 [7,8].

Events are required to have at least one high momentum jet, large missing transverse energy and no leptons. The dominant background contributions originate from Z($\rightarrow \nu\nu$) and W+jets processes, which have been constrained using MC samples normalized using data in dedicated control regions (CR), seperately for the mono-jet and mono-V channel. The V+jets MC predictions are reweighted to account for higher-order QCD and electroweak corrections, following the recommendations described in Ref. [9].

Fig. 1 shows the missing transverse energy distribution in data and MC simulation in the signal region (SR).

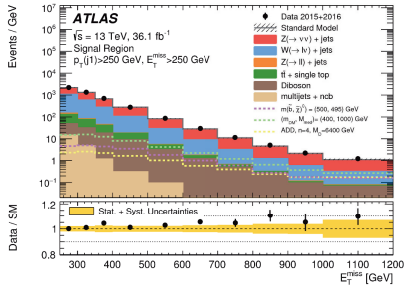


Figure 1 – Measured distributions of the $E_T^{miss}$ compared to the SM predictions. The error bands in the ratios shown in the lower panels include both the statistical and systematic uncertainties in the background predictions. The last bin of the $E_T^{miss}$ distribution contains overflows [7].

No significant deviation from SM has been observed. The results are therefore interpreted in terms of simplified models with an axial-vector, vector, pseudoscalar or scalar mediator. Fig. 2 and 3 exemplarily show the 95% CL exclusion contours for the axial-vector and vector mediator model.

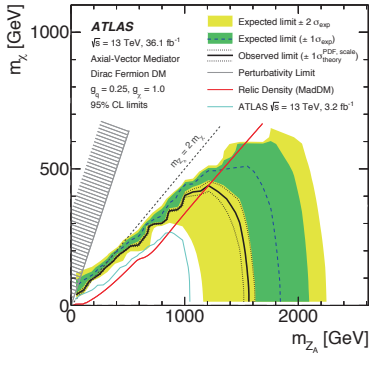


Figure 2 – Observed and expected 95% CL exclusion contours in the $m_{Z_A} - m_\chi$ parameter plane for a simplified model with an axial-vector mediator, Dirac DM particles and couplings $g_q = 0.25$ and $g_\chi = 1$ [7].

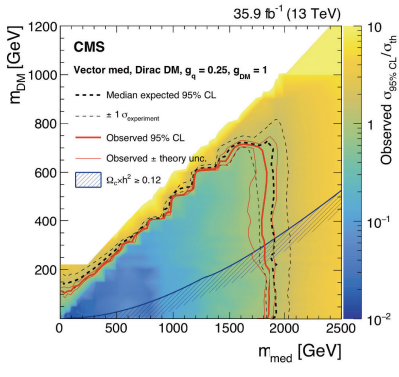


Figure 3 – Observed and expected 95% CL exclusion contours in the $m_{med} - m_{DM}$ parameter plane for a simplified model with a vector mediator, Dirac DM particles and couplings $g_q = 0.25$ and $g_{DM} = 1$ [8].

In addition, a model with the exchange of a coloured scalar mediator is considered [10,11,12]. Here, the jet can either originate from initial state radiation (ISR) or directly from the mediator decay. Fig. 4 shows the 95%CL exclusion limit for this model.

Mediator masses up to 1.7 TeV for very low DM masses are excluded.

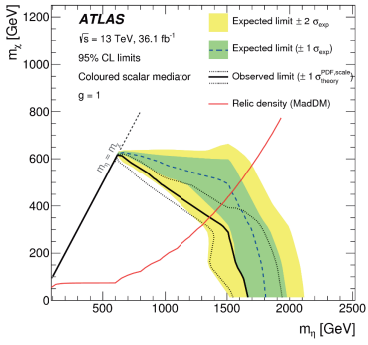


Figure 4 – Observed and expected 95% CL exclusion contours in the $m_\eta - m_\chi$ parameter plane for the coloured scalar mediator model, with minimal width and coupling set to $g = 1$ [7].

## 3 Searches for Dark Matter with Higgs bosons

Besides the conventional signatures, such as mono-photon or mono-jet, the Higgs boson can be used as a discovery tool. Searches have been performed in final states with large missing transverse momentum recoiling against a Higgs boson decaying to either a $b\bar{b}$ pair, a pair of tau leptons or a pair of photons using proton-proton collision data corresponding to an integrated luminosity of 36 fb$^{-1}$ at a centre-of-mass energy of 13 TeV collected in 2015 and 2016 [13,14]. No significant deviation from SM has been observed. The results are therefore interpreted in terms of two benchmark simplified models: a Z'-two-Higgs-doublet-model (Z'-2HDM) [15] and a barionic Z' model.

Fig. 5 shows the 95% CL exclusion contours for the Z'-2HDM model in the $m_{Z'} - m_A$ parameter plane and Fig. 6 shows the 95% CL upper limit on DM+h cross section for the barionic Z' model.

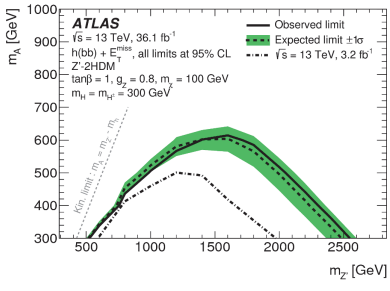


Figure 5 – Exclusion contours for the Z'-2HDM model in the $m_{Z'} - m_A$ parameter plane for $\tan\beta = 1$, $g_{Z'} = 0.8$, and $m_\chi = 100$ GeV [14].

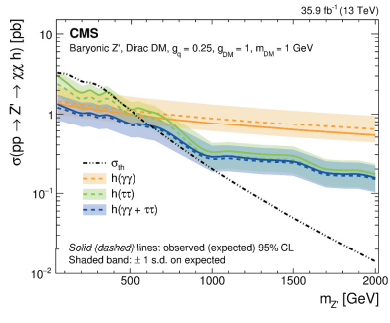


Figure 6 – Expected and observed 95% CL upper limits on the baryonic Z' cross section for dark matter associated production with a Higgs boson ($Z' \to \chi\chi h$), Dirac DM particles, couplings $g_q = 0.25$ and $g_{DM} = 1$, and $m_\chi = 1$ GeV [13].

For the Z'-2HDM model, $m_{Z'}$ is excluded up to 2.6 TeV and $m_A$ up to 0.6 TeV. For the barionic Z' model, Z' masses are excluded up to 615 GeV for $m_\chi = 1$ GeV.

## 4 Summary of Dark Matter Searches

A large number of mono-X and dijet searches have been performed by both the ATLAS and the CMS collaboration, already probing a large part of the parameter space. Fig. 7 shows the

95% CL excluded regions in a dark matter mass-mediator mass plane from a selection of dark matter searches for axial-vector models for both ATLAS and CMS.

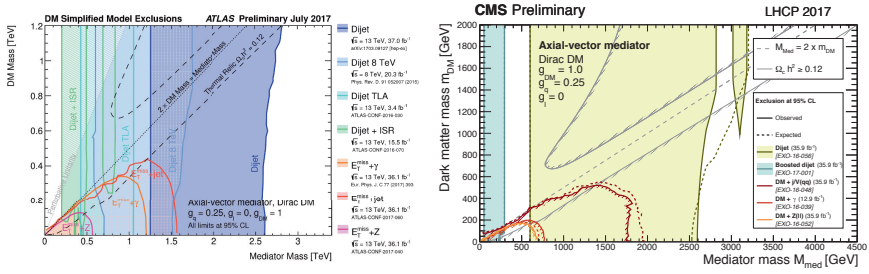


Figure 7 – 95% CL excluded regions in a dark matter mass-mediator mass plane from a selection of ATLAS [16] (left) and CMS [17] (right) dark matter searches in the leptophobic axial-vector mediator model. The exclusions are computed for a dark matter coupling $g_{DM} = 1.0$ and a quark coupling $g_q = 0.25$ universal to all flavors. The lepton coupling $g_l$ in this model is set to zero.

## 5 Conclusion

DM searches at the LHC remain a thrieving field of research. Results are reported from searches for DM in final states with an energetic jet and large missing transverse momentum, as well as from searches for DM in final states with large missing transverse momentum recoiling against a Higgs boson using proton-proton collision data corresponding to an integrated luminosity of 36 fb$^{-1}$ at a centre-of-mass energy of 13 TeV collected in 2015 and 2016. Unfortunately, so far no evidence for physics beyond the SM has been found. Therefore, the results are translated into 95%CL uper limits on WIMP-pair production.

## References


1. O. Buchmueller *et al.*, JHEP **1501** (2015) 037, arXiv:1407.8257 [hep-ph].
2. J. Abdallah *et al.*, Phys. Dark Univ. **9-10** (2015) 8, arXiv:1506.03116 [hep-ph].
3. D. Abercrombie *et al.*, arXiv:1507.00966 [hep-ex].
4. A. Albert *et al.*, arXiv:1703.05703 [hep-ex].
5. ATLAS Collaboration, 2008 JINST 3 S08003.
6. CMS Collaboration, 2008 JINST 3 S08004.
7. ATLAS Collaboration, JHEP **1801** (2018) 126, arXiv:1711.03301 [hep-ex].
8. CMS Collaboration, Phys. Rev. D **97** (2018) no.9, 092005, arXiv:1712.02345 [hep-ex].
9. J. M. Lindert *et al.*, arXiv:1705.04664 [hep-ph].
10. N. F. Bell *et al.*, Phys. Rev. D **86** (2012) 096011, arXiv:1209.0231 [hep-ph].
11. M. Papucci *et al.*, JHEP **1411** (2014) 024, arXiv:1402.2285 [hep-ph].
12. A. J. Brennan *et al.*, JHEP **1605** (2016) 112, arXiv:1603.01366 [hep-ph].
13. CMS Collaboration, arXiv:1806.04771 [hep-ex].
14. ATLAS Collaboration, Phys. Rev. Lett. **119** (2017) no.18, 181804, arXiv:1707.01302 [hep-ex].
15. A. Berlin, T. Lin and L. T. Wang, JHEP **1406** (2014) 078, arXiv:1402.7074 [hep-ph].
16. ATLAS Collaboration, https://twiki.cern.ch/twiki/bin/view/AtlasPublic/ExoticsPublicResults, 2018.
17. CMS Collaboration, https://twiki.cern.ch/twiki/pub/CMSPublic/PhysicsResultsEXO/DM-summary-plots-Jul17.pdf, 2018.

# Light dark sector at colliders and fixed target experiments

Luc Darmé,[1] Soumya Rao,[1] Leszek Roszkowski[1,2]
[1] *National Centre for Nuclear Research (NCBJ), 69 ul. Hoża, 00-681 WARSZAWA, POLAND*
[2] *Consortium for Fundamental Physics, Department of Physics and Astronomy, University of Sheffield, Sheffield S3 7RH, United Kingdom*

Minimal scenarios with light (sub-GeV) dark matter are usually accompanied by a correspondingly light "dark sector". Taking as an example a simple fermionic dark matter model, we will show that the presence of the dark sector plays a key role in constraining such scenarios at accelerators experiments. The effect of including in the light spectrum a dark Higgs boson is in particular investigated.

## 1 Light fermionic dark matter

Among the numerous solutions of the Dark Matter (DM) puzzle, the ones relying on the thermal freeze-out mechanism have been long considered among the most attractive. The prime example of a dark matter scenario based on this mechanism, the Weakly Interactive Massive Particle (WIMP), has been intensely searched for in the past decades. However, the absence so far of any uncontroversial signals from colliders, direct and indirect detection experiments has led the community to explore simultaneously numerous other possibilities. Among them the so-called thermal hidden sector scenarios are particularly attractive in that they closely resembled the WIMP while relaxing various experimental bounds and allowing for DM candidates with lighter, sub-GeV masses. The trade-off is that the DM annihilation needs to be generally mediated by a new light field since weak interaction-driven processes are typically too suppressed at this scale.

In this work we will focus on the case where the mediator is a new massive gauge boson $V$,[a] called henceforth the dark photon, corresponding to an abelian gauge group $U(1)_D$ spontaneously broken by the Vacuum Expectation Value (VEV) $v_S$ of a dark Higgs boson $S$. We will focus on the case of fermionic dark matter (the case of complex scalar DM is also viable even though more constrained [2]).

In order to keep the additional $U(1)_D$ anomaly-free, one minimally needs to introduce two Majorana fermions with opposite charges. We thus consider a Dirac fermion $\chi = (\chi_L, \bar{\chi}_R)$ with $U(1)_D$-charge $-1$ and choose the dark Higgs boson $U(1)_D$ charge to be $+2$ to allow for Yukawa couplings with the left and right-handed components. Writing $A_{\mu\nu}$ the electromagnetic field strength and $F'_{\mu\nu}$ the $U(1)_D$ one, the Lagrangian for the dark Higgs boson and dark photon contains:

$$\mathcal{L}_V \;=\; -\tfrac{1}{2}\varepsilon A_{\mu\nu}F'^{\mu\nu} + (D^\mu S)^*(D_\mu S) + \mu_S^2|S|^2 - \tfrac{\lambda_S}{2}|S|^4 \;, \tag{1}$$

where we have included a kinetic mixing term $\varepsilon$ and have neglected the quartic mixing between the dark Higgs boson and the Standard Model (SM) Higgs. [2] The DM part of the Lagrangian is

$$\mathcal{L}^{\rm DM} \;= \bar{\chi}\,(i\gamma_\mu D^\mu - m_\chi)\,\chi + y_{SL}S\bar{\chi}^c P_L\chi + y_{SR}S\bar{\chi}^c P_R\chi + \text{ h.c.}\,. \tag{2}$$

[a] The case of a light scalar is already strongly constrained by heavy meson decays. [1]

After the dark Higgs boson acquires its VEV, the dark matter mass matrix becomes

$$M_\chi = \begin{array}{c} \\ \bar{\chi}_L \\ \bar{\chi}_R \end{array} \begin{array}{c} \begin{array}{cc} \chi_L & \chi_R \end{array} \\ \begin{pmatrix} \sqrt{2} v_S y_{SL} & m_\chi \\ m_\chi & \sqrt{2} v_S y_{SR} \end{pmatrix} \end{array} , \tag{3}$$

and is diagonalised by introducing the two Majorana eigenstates $(\chi_1, \chi_2)$. Choosing to keep the rotation matrices $U_\chi$ real then implies that $\chi_1$ has a negative mass [b] when the off-diagonal contribution dominates but allows to write the $U(1)_D$ current in the simple form:

$$\mathcal{J}_D^\mu = \frac{1}{2} \bar{\chi}_i \gamma^\mu \gamma^5 \chi_j \left( U_\chi^{i2} U_\chi^{j2} - U_\chi^{i1} U_\chi^{j1} \right) . \tag{4}$$

In the rest of this work, we will note $M_{\chi_1}$ (respectively $M_{\chi_2}$) the absolute mass of the lightest (heaviest) eigenstate.

Overall the "dark sector" hence contains: a Majorana dark matter $\chi_1$, a heavier Majorana state $\chi_2$, a dark photon $V$ and a dark Higgs boson $S$. In the rest of this work, we will be interested in keeping generic values for the Yukawa couplings, departing from the standard (technically natural) choice $y_{SL} = y_{SR} \ll 1$. This very simple model leads to the correct relic density in three regimes with starkly different phenomenology: [2] the pseudo-Dirac regime (iDM), the Majorana DM case and finally a secluded regime where $\chi_1 \chi_1 \to SS$ dominates (even though the latter suffers from strong bounds from Big Bang Nucleosynthesis (BBN)-related observables). [c] In the following we will concentrate on accelerator-based analysis. All data points in scan-based plots are compatible with dark matter relic density at the $2\sigma$-level and satisfies the BBN constraints. [2]

## 2 Dark sector and search strategies at accelerators

For each fields of the dark sector, dedicated search strategies have been proposed over the last decade. We will present in the following the most relevant ones, focusing eventually on the particular role of the dark Higgs boson.

**Mediator/dark photon searches** Searches which focus directly on the dark photon are especially interesting in that they are largely model-independent. In all of our parameter space, the dark photon decays invisibly and the strongest bounds come from missing energy signature in BaBar [4] ($\varepsilon \lesssim 1 \times 10^{-3}$) and NA64 [5] (as low as $\varepsilon \lesssim 1.5 \times 10^{-4}$ for $M_V \sim 30$ MeV). In the future, the Belle II collaboration should expand these bounds [6] down to $\varepsilon \lesssim 0.8 \times 10^{-4}$. The sensitivity of these analysis scales as $\varepsilon^2$ so that these strategies have bright prospects on the long term. Indeed, as we show in Figure 1 they cover already a large portion of the parameter space compatible with the relic density constraint.

**Dark matter** Since in most of our parameter space the dark photon decays instantaneously into $\chi_1$ and $\chi_2$ any experiments producing it will generate effectively a "dark matter beam". Fixed target experiments designed originally for neutrinos studies are here particularly well-suited. Indeed, dark photons are abundantly produced either through dark bremsstrahlung or light meson decays in the beam dump, the dark matter particles then propagate through the shielding and subsequently scatter in the detector. This was first pointed out in [7,8] and a rich literature followed. The main drawback of this kind of analysis is the relatively large neutrino background and the fact that the expected number of events typically scales as $\varepsilon^4 \alpha_D$. Current bounds are mainly competitive against missing energy searches in the low dark matter mass region, where bounds from the LSND experiment [9] can be applied, due to the impressive accumulated dataset of $10^{22}$ light $\pi^0$ mesons.

[b] Note the different convention from the standard reference. [3]

[c] In this proceedings, we will keep $M_{\chi_1} < M_V/3$ and $M_S < M_V$, so that the usual "forbidden" setup in which dark matter annihilates into a pair of dark photons is not kinematically accessible.

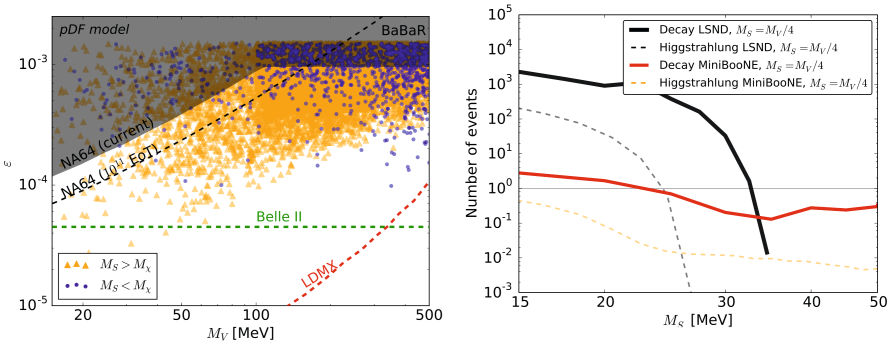


Figure 1 – (Left) Constraints on the dark photon mass $M_V$ and on the kinetic mixing parameter $\varepsilon$ from NA64, BaBaR, the projected Belle-II reach (50 ab$^{-1}$) and LDMX reach based on missing energy searches. (Right) Number of events expected at LSND and miniBooNE from dark Higgs boson decay, either produced through dark Higgsstrahlung (thin dashed) or through heavy sector particle decay (thick plain) as a function of the dark Higgs boson mass $M_S$ for $M_S = M_V/4$, $m_\chi = M_V/3$ (where $m_\chi$ is the bare DM Dirac mass), $\varepsilon = 0.001$, $y_{SR} = 0, y_{SL} = 0.2$ and $\alpha_D = 0.03$.

**Heavy dark sector state** These states are typically produced simultaneously with dark matter from the dark photon decay channels $V \to \chi_1\chi_2$ , $V \to \chi_2\chi_2$ whose branching ratios are determined by the dark gauge current from eq. (4). When the splitting between both states is smaller than the mass of other dark sector particles (and in particular of the dark Higgs boson mass, as we will see below) then the only decay channel is through an off-shell dark photon $\chi_2 \to \chi_1 V^* \to \chi_1 e^+ e^-$. Defining the splitting $\Delta_\chi \equiv M_{\chi_2} - M_{\chi_1}$, we have the approximate relation: [10]

$$c\tau_{\chi_2} \propto 100 \text{ m } \times \left(\frac{0.1}{\alpha_D}\right)\left(\frac{10^{-3}}{\varepsilon}\right)^2\left(\frac{0.2}{\Delta_\chi}\right)^5\left(\frac{25 \text{ MeV}}{M_S}\right)^5\left(\frac{M_V}{100 \text{ MeV}}\right)^4 . \tag{5}$$

Hence, in the optimal case large portion of the heavy dark states decay directly in the detector so that the expected of number of events can in theory scales as $\varepsilon^2$. Furthermore, the decay signature is an electron-positron pair which can be distinguished from the neutrino scattering events in experiments with basic track reconstructions capability. This approach typically leads to extremely strong bounds on the kinetic parameter, [10] probing values as low as $\epsilon \sim 10^{-6}$.

**Dark Higgs boson** Finally, when the dark Higgs boson is light enough not to decay into a pair of DM particle ($M_S < 2M_{\chi_1}$), its decay mainly proceeds through a loop-induced $\varepsilon^2$-suppressed diagram. This leads to an extremely long lifetime of typical order hundreds of seconds below the di-muon threshold:

$$\tau_S \propto 10 \text{ s} \times \left(\frac{\alpha_{\text{em}}}{q_S^2\alpha_D}\right)\left(\frac{10^{-3}}{\varepsilon}\right)^4\left(\frac{50 \text{ MeV}}{M_S}\right)\left(\frac{M_V}{100 \text{ MeV}}\right)^2 . \tag{6}$$

In principle dark Higgs bosons produced through dark-Higgsstrahlung and decaying into a electron-positron pair can be searched for in neutrino experiments, with signature similar to the one of a heavy state decay. [11] However, the very long lifetime implies that the expected number of events scales as $\varepsilon^6\alpha_D^2$ and current missing energy bounds outperformed such searches in all points of the parameter space realising the correct relic density. [2] The presence of the dark Higgs boson leads therefore to "blind spots" in the heavy dark sector decay signatures. Indeed, when the splitting between both $\chi_1$ and $\chi_2$ is large enough, $\Delta_\chi = M_{\chi_2} - M_{\chi_1} > M_S$ (and provided that $y_{SL}$ is not exactly equal to $y_{SR}$) then the heavy state will decay instantaneously by emitting a dark Higgs. As shown in Figure 1, this typically increases by an order of magnitude

the expected number of events from the dark Higgs boson decay signature described above. On the other hand, the heavy dark state is no longer long-lived so that the bound on $\varepsilon$ is reduced to values typically closer to the DM scattering ones.

To conclude, the presence of an accompanying dark sector is a key ingredient of accelerator-based searches for light thermal dark scenarios, potentially leading to bounds several orders of magnitude larger than the ones deduced from dark matter scattering alone. On the other hand, the high model-dependence of these bounds must be properly accounted for, as demonstrated by the presence of dark Higgs boson-induced "blind-spots" in the signature from heavy dark sector state decay.

**Acknowledgements**

LR is supported by the Lancaster-Manchester-Sheffield Consortium for Fundamental Physics under STFC Grant No. ST/L000520/1. LD, LR and SR are supported in part by the National Science Centre (NCN) research grant No. 2015-18-A-ST2-00748. The use of the CIS computer cluster at the National Centre for Nuclear Research in Warsaw is gratefully acknowledged.

**References**

1. Matthew J. Dolan, Felix Kahlhoefer, Christopher McCabe, and Kai Schmidt-Hoberg. A taste of dark matter: Flavour constraints on pseudoscalar mediators. *JHEP*, 03:171, 2015. [Erratum: JHEP07,103(2015)].
2. Luc Darmé, Soumya Rao, and Leszek Roszkowski. Light dark Higgs boson in minimal sub-GeV dark matter scenarios. *JHEP*, 03:084, 2018.
3. David Tucker-Smith and Neal Weiner. Inelastic dark matter. *Phys. Rev.*, D64:043502, 2001.
4. J. P. Lees et al. Search for Invisible Decays of a Dark Photon Produced in $e^+e^-$ Collisions at BaBar. *Phys. Rev. Lett.*, 119(13):131804, 2017.
5. D. Banerjee et al. Search for vector mediator of Dark Matter production in invisible decay mode. 2017.
6. Marco Battaglieri et al. US Cosmic Visions: New Ideas in Dark Matter 2017: Community Report. *FERMILAB-CONF-17-282-AE-PPD-T*, 2017.
7. Brian Batell, Maxim Pospelov, and Adam Ritz. Probing a Secluded U(1) at B-factories. *Phys. Rev.*, D79:115008, 2009.
8. Rouven Essig, Philip Schuster, and Natalia Toro. Probing Dark Forces and Light Hidden Sectors at Low-Energy e+e- Colliders. *Phys. Rev.*, D80:015003, 2009.
9. A. Aguilar-Arevalo et al. Evidence for neutrino oscillations from the observation of anti-neutrino(electron) appearance in a anti-neutrino(muon) beam. *Phys. Rev.*, D64:112007, 2001.
10. Eder Izaguirre, Yonatan Kahn, Gordan Krnjaic, and Matthew Moschella. Testing Light Dark Matter Coannihilation With Fixed-Target Experiments. *Phys. Rev.*, D96(5):055007, 2017.
11. Brian Batell, Maxim Pospelov, and Adam Ritz. Exploring Portals to a Hidden Sector Through Fixed Targets. *Phys. Rev.*, D80:095024, 2009.

# Searches with boosted objects at ATLAS and CMS

Dermot Moran, on behalf of the ATLAS and CMS Collaborations
*CIEMAT, Av. Complutense, 40, 28040 Madrid, Spain*

An overview of searches for beyond the standard model physics using boosted objects is presented. The searches are based on proton-proton collision data collected with the ATLAS and CMS detectors at the LHC during the 2015 and 2016 running periods.

## 1 Introduction

While the discovery of the Higgs boson[1,2] has consolidated the standard model (SM) its relatively light mass has also highlighted the so-called hierarchy problem, i.e. the large difference between the electroweak and Planck scales. Beyond standard model (BSM) mechanisms proposed to solve the hierarchy problem include models based on extra spatial dimensions [3], a composite Higgs boson [4] and supersymmetry (SUSY) [5]. Many of these models predict the existence of heavy resonances with large branching fractions for decays involving SM bosons and tops. Due to the high mass of the resonances these particles are given a large Lorentz boost, resulting in the collimation of their decay products. A single large-R jet may be used to reconstruct the hadronic decays of these boosted particles.

A variety of searches using large-R jets have been performed by the ATLAS [9] (R=1.0) and CMS [10] (R=0.8) experiments using proton-proton collision data collected at the LHC. The results presented here will focus on searches with boosted vector bosons (V), Higgs bosons (h), and $q\bar{q}$ pairs, using the 2015 and 2016 datasets. For these searches the signal jets will have substructure compatible with that of a highly-energetic quark pair which can be used to distinguish them from background QCD jets. The primary discriminating variable is the jet mass with grooming applied to remove soft and large angle radiation, the soft-drop [6] and trimming [7] grooming algorithms are used at CMS and ATLAS respectively. In addition CMS takes advantage of the pileup per particle identification (PUPPI) algorithm [8] to suppress contributions from pile-up interactions. ATLAS uses a track-assisted jet mass calculation, which complements the calorimeter measurement with track-based information. The N-subjettiness variable [11] quantifies to what extent the energy flow in the jet is aligned along N subjet axes. The ratio of 2-subjettiness over 1-subjettiness ($\tau_{21}$) is used to tag signal jets and suppress the contribution of QCD jets. Figure 1 shows the groomed mass of large-R jets near the W and Z boson masses for

a boosted $q\bar{q}$ resonance search at ATLAS [12] and the $\tau_{21}$ distribution of large-R jets for a high mass ZV resonance search at CMS [13].

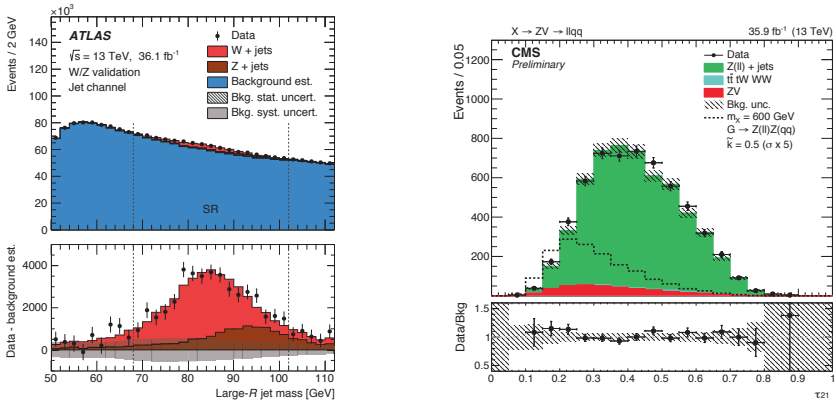


Figure 1 – Distribution of large-R jet groomed mass near the W and Z boson masses for a boosted $q\bar{q}$ resonance search at ATLAS [12] (left) and large-R jet $\tau_{21}$ for a high mass ZV resonance search at CMS [13] (right).

## 2 Diboson resonances

CMS has conducted a search for ZV resonances where the Z decays to two leptons and the V is reconstructed with a large-R jet or two narrow R=0.4 jets [13]. The analysis is sensitive to resonances in the mass region from 400 to 4500 GeV. To increase the signal sensitivity at low mass a categorization based on the b-tagging of jets is used while at high mass a categorization based on the $\tau_{21}$ variable is implemented. The main source of background arises from the Z+jets production process. It is estimated at low mass using NLO simulation with uncertainties based on data-simulation comparisons in the V mass sidebands. At high mass the alpha method, which takes the ratio of simulation to data in the V mass sideband and extrapolates to the signal region, is used to estimate this background. No significant excess over the SM expectation has been observed. The left hand plot of Figure 2 shows the invariant mass of the ZV resonance candidates for boosted events with 0 b-tags.

Both ATLAS and CMS have searched for a new resonance decaying to Wh or Zh where the vector boson decays leptonically and the Higgs boson decays to a $b\bar{b}$ pair [14,15]. A single large-R jet is used to reconstruct the Higgs boson decay. The ATLAS analysis also considers the resolved scenario where the Higgs boson decay is reconstructed with two narrow R=0.4 jets. Resonance mass ranges of 800 to 4500 GeV and 220 GeV up to 5000 GeV are covered by the CMS and ATLAS analyses respectively. To increase the signal sensitivity a categorization based on the b-tagging of the Higgs boson candidate is implemented. In the case of the ATLAS analysis an additional categorization based on the number of associated jets with b-tags is included, giving sensitivity to b-quark associated production of a CP-odd Higgs boson ($b\bar{b}A$). The dominant W/Z+jets background processes are estimated using the alpha-method at CMS and from simulation at ATLAS. A mild excess of events, with a $3.6\sigma$ local and $2.4\sigma$ global significance, is observed around 440 GeV in the b-quark associated production category of the ATLAS analysis. The right hand plot of Figure 2 shows the invariant mass of the Wh resonance candidates for boosted events with 2 b-tags at ATLAS.

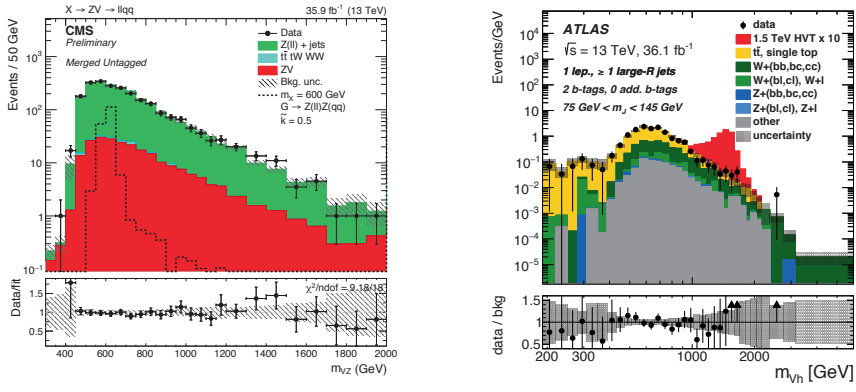


Figure 2 – Invariant mass distributions of the ZV resonance candidates for boosted events with 0 b-tags at CMS [13] (left) and the Wh resonance candidates for boosted events with 2 b-tags at ATLAS [14] (right).

## 3 $q\bar{q}$ resonances

The ATLAS experiment has searched for a light resonance decaying to a $q\bar{q}$ pair and produced in association with a high-$p_T$ initial-state radiation (ISR) photon or jet [12]. The analysis is sensitive to resonance masses from 100 GeV up to 220 GeV, a range in which the resonance is boosted from the recoil with the ISR and so may be reconstructed with a single large-R jet. For this analysis a linearly corrected version of $\tau_{21}$, which decorrelates $\tau_{21}$ from the jet mass, is implemented. This approach avoids modifying the final jet mass distribution in a way that makes it difficult to model. The dominant backgrounds in the jet and photon channels are due to multi-jet production and inclusive $\gamma$-production, respectively. A data-driven technique is used to model these backgrounds in the signal region via a transfer-factor, measured in the jet mass sidebands, which extrapolates from a $\tau_{21}$-fail control region. The largest deviation observed in this analysis is for a 140 GeV signal hypothesis, corresponding to a $2.4\sigma$ local and $1.2\sigma$ global significance.

## 4 Gluino pair production

CMS has searched for pair-produced gluinos, with the gluinos decaying to quark pairs and the next-to-lightest SUSY particle, NLSP, which then decays to the lightest SUSY particle, LSP, and a Higgs boson [16]. Given a small mass splitting between the gluino and the NLSP, and a light LSP, the events are characterized by a boosted Higgs boson, large missing transverse momentum, and soft quark jets. The analysis utilizes a b-quark tagging technique based on jet substructure to identify large-R jets from $h \to b\bar{b}$. Events are categorized by the multiplicity of h-tagged jets, the jet mass, and the missing transverse momentum. Dominant SM backgrounds arise from events containing jets misidentified as Higgs bosons in conjunction with W or Z bosons. The backgrounds are estimated by simultaneously extrapolating yields from the h-tag multiplicity and jet mass sidebands to the signal region. No significant excess above the expected SM background is observed. Assuming large mass splitting between the NLSP and LSP, and 100% NLSP branching fraction to h, the lower limit on the gluino mass is found to be 2010 GeV.

A search for gluino pair production with subsequent R-parity-violating (RPV) decays to quarks has been conducted by the ATLAS experiment [17]. Each gluino may decay directly into three quarks via RPV coupling, leading to six quarks in the final state, or in the cascade decay model each gluino may decay into two quarks and a neutralino, which in turn decays into three quarks via RPV coupling, resulting in ten quarks in the final state. Events produced in

these processes typically have a high multiplicity of reconstructed jets, with significant portion containing at least one bottom or top quark jet. The analysis is performed using requirements on the number of jets and the number of b-tagged jets as well as a topological observable formed by the scalar sum of masses of large-R jets in the event. Multijet events constitute the dominant background, a fully data-driven jet mass template method[18] is used to estimate its contribution. No significant excess is seen in any of the signal regions. In the cascade decay model gluinos with masses between 1000 GeV and 1875 GeV are excluded, depending on the neutralino mass.

## 5 Majorana neutrinos

A search for the direct production of a heavy Majorana neutrino (N), from the leptonic decay of a W boson where the SM neutrino oscillates into N, in the mass range between 20 and 1600 GeV has been conducted at CMS [19]. In this search N decays into a W boson, which decays hadronically, and a lepton giving a final state of two leptons and at least one jet. Same-sign dilepton events are selected giving very low SM backgrounds. To preserve sensitivity at high masses the hadronic W candidate may be reconstructed using a single large-R jet and tagged using the $\tau_{21}$ variable. Backgrounds with prompt leptons are estimated using simulation while the background from misidentified leptons is estimated using a dijet tag and probe method. The observed data yields in the signal regions are found to be in good agreement with the estimated backgrounds. Upper limits are set on the mixing matrix elements between SM neutrinos and Majorana neutrinos as a function of the N mass, the limits range between 2.3 x $10^{-5}$ and unity.

## 6 Conclusion

An extensive range of BSM searches has been conducted at ATLAS and CMS using boosted signatures, so far no new physics has been discovered. However many more final states are being explored and work is ongoing to refine and improve the analyses with the 2017 and 2018 datasets.

## References


1. ATLAS Collaboration, Phys. Lett. B **716:129** (2012)
2. CMS Collaboration, Phys. Lett. B **716:30** (2012)
3. A. L. Fitzpatrick, J. Kaplan, L. Randall and L. T. Wang, JHEP **0709** (2007) 013
4. K. Lane and L. Pritchett, JHEP **1706** (2017) 140
5. H. P. Nilles, Phys. Rep. **110** (1984) 1
6. A. J. Larkoski, S. Marzani, G. Soyez and J. Thaler, JHEP **1405** (2014) 14
7. D. Krohn, J. Thaler and L.-T. Wang, JHEP **02** (2010) 084
8. D. Bertolini, P. Harris, M. Low and N. Tran, JHEP **1410** (2014) 059
9. ATLAS Collaboration, JINST **3:S08003** (2008)
10. CMS Collaboration, JINST **3:S08004** (2008)
11. J. Thaler and K. Van Tilburg, JHEP **1103** (2011) 015.
12. ATLAS Collaboration, ATLAS-EXOT-2017-01, CDS Record 2302092
13. CMS Collaboration, CMS-PAS-B2G-17-013, CDS Record 2296238
14. ATLAS Collaboration, JHEP **03** (2018) 174
15. CMS Collaboration, CMS-PAS-B2G-17-004, CDS Record 2309980
16. CMS Collaboration, CMS-SUS-17-006, CERN-EP-2017-322
17. ATLAS Collaboration, SUSY-2016-22, CERN-EP-2017-298
18. T. Cohen, M. Jankowiak, M. Lisanti, H. K. Lou and J. G. Wacker, JHEP **05** (2014) 005
19. CMS Collaboration, CMS-PAS-EXO-17-028, CDS Record 2308273

# Global analyses of supersymmetry with GAMBIT

Pat Scott for the GAMBIT Collaboration
*Fundamental Physics Section, Department of Physics, Imperial College London, Blackett Laboratory, Prince Consort Road, London SW7 2AZ, UK*

I provide a brief summary of the status of supersymmetric models with parameters defined at either the unification or weak scale, based on global fits using the GAMBIT framework.

Supersymmetry (SUSY) realised at the weak scale remains one of the most popular scenarios for new physics, as it can solve many problems of the Standard Model (SM). SUSY is constrained by many complementary probes, ranging from direct searches at the LHC and LEP to flavour physics, precision measurements, direct and indirect searches for the lightest neutralino as dark matter (DM), and its thermal relic abundance.

We have analysed a number of SUSY scenarios [1,2] using the new global-fitting framework GAMBIT [3,4,5,6,7,8,9], producing the most advanced and comprehensive assessment of SUSY to date. The Minimal Supersymmetric SM (MSSM) may be described in terms of Lagrangian parameters defined directly at the weak scale, or at some other higher scale, where it is typically postulated that some of the parameters unify. We carried out global fits of the Constrained MSSM (CMSSM) and the first and second non-universal Higgs mass (NUHM1/2) models, which respectively have 4, 5, and 6 parameters defined at the scale of grand unification [1]. We also carried out a 7-parameter scan of a version of the MSSM with the parameters defined at the weak scale [2].

In each case, we also varied 5 nuisance parameters in the fits: the strong coupling $\alpha_s$, the top mass $m_t$, two nuclear matrix elements $\sigma_s$ and $\sigma_l$ (relevant for direct detection of DM), and the local density of DM $\rho_0$. For these fits, we employed the differential evolution sampler Diver [8] to efficiently and accurately map the likelihood function. The full set of likelihood functions that we included in these fits can be found in the relevant publications [1,2] (Tables 5 and 3, respectively). One particular point of note is that we treat the observed abundance of DM [10] as an upper limit on the relic density of neutralinos, rather than demanding that they constitute the entirety of DM.

Results of the CMSSM fits can be seen in Fig. 1. Here we see three distinct solutions, corresponding to three different mechanisms for obtaining an acceptable relic density: Higgsino DM (with chargino co-annihilation), stop co-annihilation, and annihilation through a heavy Higgs resonance. The final row shows current and projected limits on spin-independent DM-nucleon scattering from direct detection. Here we show rescaled spin-independent scattering cross-sections, which include a factor to account for the suppression of the local DM density due to the fraction $f = \Omega_\chi/\Omega_{\rm DM}$ of DM in neutralinos. These panels can be compared with Fig. 2, which shows the same quantity in the NUHM1 and NUHM2 models, illustrating the presence of an additional stau co-annihilation solution in the latter two cases, leading to a large volume of the parameter space with extremely small scattering cross-sections.

The status of the 7 parameter weak-scale MSSM is summarised in Fig. 3, where 5 different

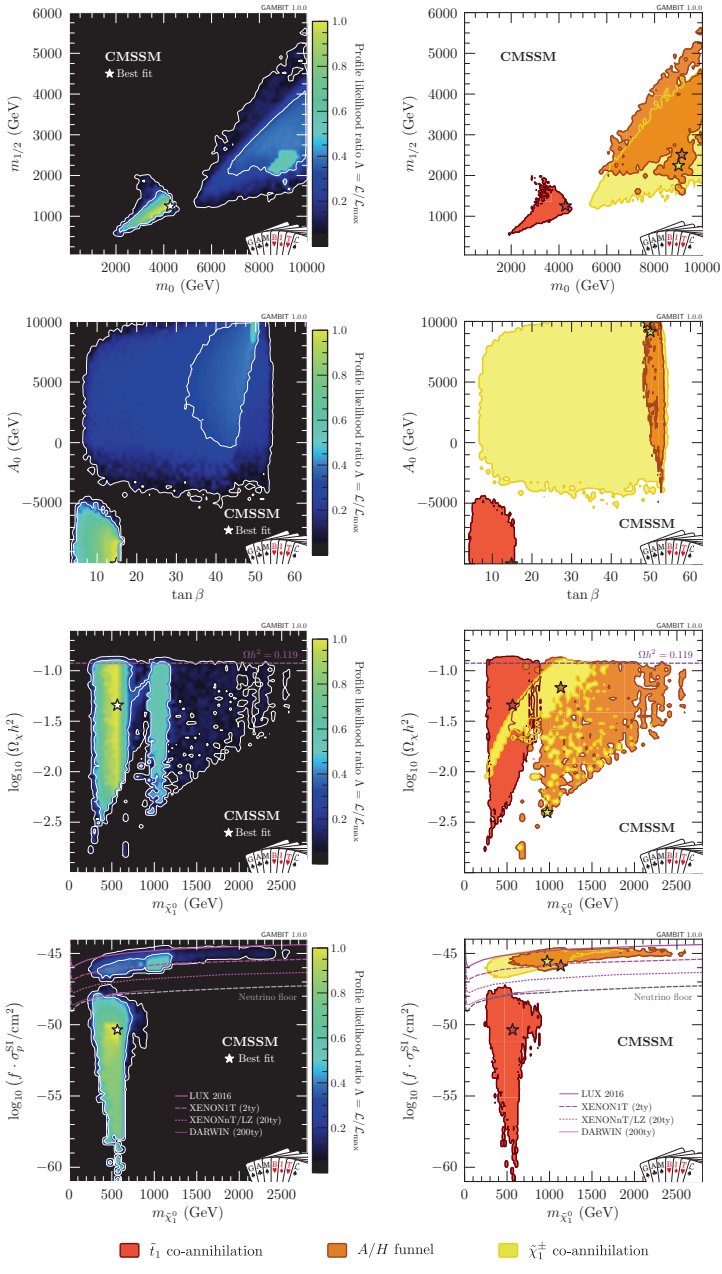


Figure 1 – Global fits of the CMSSM [1], showing pairs of fundamental parameters, the relic density, the lightest neutralino mass and the spin-independent nuclear scattering cross-section, rescaled for the fraction $f$ of DM made up by neutralinos. Left panels show profile likelihoods; white contours correspond to 1 and $2\sigma$ confidence regions. Right panels show $2\sigma$ regions colour-coded according to the most active mechanisms involved in determining the relic density of the lightest neutralino.

mechanisms can be distinguished: stop and sbottom co-annihilation, Higgsino DM (chargino co-annihilation), and both light and heavy Higgs resonances. The lowermost panels compare the preferred stop co-annihilation region to the current reach of the CMS Run II simplified model limit from stop pair production [11]. Although such compressed spectra are going to prove mostly impossible to probe with direct and indirect detection, this figure indicates that the LHC is within striking reach of some of the most interesting solutions in this model, and may be able to probe this region in Run III.

## Acknowledgments

I am supported by STFC (ST/K00414X/1, ST/P000762/1, ST/L00044X/1), and thank my collaborators in GAMBIT for their contributions to the results discussed here.

## References

1. GAMBIT Collaboration: P. Athron, C. Balázs, *et. al.*, *Global fits of GUT-scale SUSY models with GAMBIT*, *Eur. Phys. J. C* **77** (2017) 824, [arXiv:1705.07935].
2. GAMBIT Collaboration: P. Athron, C. Balázs, *et. al.*, *A global fit of the MSSM with GAMBIT*, *Eur. Phys. J. C* **77** (2017) 879, [arXiv:1705.07917].
3. GAMBIT Collaboration: P. Athron, C. Balázs, *et. al.*, *GAMBIT: The Global and Modular Beyond-the-Standard-Model Inference Tool*, *Eur. Phys. J. C* **77** (2017) 784, [arXiv:1705.07908].
4. GAMBIT Dark Matter Workgroup: T. Bringmann, J. Conrad, *et. al.*, *DarkBit: A GAMBIT module for computing dark matter observables and likelihoods*, *Eur. Phys. J. C* **77** (2017) 831, [arXiv:1705.07920].
5. GAMBIT Collider Workgroup: C. Balázs, A. Buckley, *et. al.*, *ColliderBit: a GAMBIT module for the calculation of high-energy collider observables and likelihoods*, *Eur. Phys. J. C* **77** (2017) 795, [arXiv:1705.07919].
6. GAMBIT Flavour Workgroup: F. U. Bernlochner, M. Chrząszcz, *et. al.*, *FlavBit: A GAMBIT module for computing flavour observables and likelihoods*, *Eur. Phys. J. C* **77** (2017) 786, [arXiv:1705.07933].
7. GAMBIT Models Workgroup: P. Athron, C. Balázs, *et. al.*, *SpecBit, DecayBit and PrecisionBit: GAMBIT modules for computing mass spectra, particle decay rates and precision observables*, *Eur. Phys. J. C* **78** (2018) 22, [arXiv:1705.07936].
8. GAMBIT Scanner Workgroup: G. D. Martinez, J. McKay, *et. al.*, *Comparison of statistical sampling methods with ScannerBit, the GAMBIT scanning module*, *Eur. Phys. J. C in press* **77** (2017) 761, [arXiv:1705.07959].
9. GAMBIT Collaboration: P. Athron, C. Balázs, *et. al.*, *Status of the scalar singlet dark matter model*, *Eur. Phys. J. C* **77** (2017) 568, [arXiv:1705.07931].
10. Planck Collaboration, P. A. R. Ade, *et. al.*, *Planck 2015 results. XIII. Cosmological parameters*, *A&A* **594** (2016) A13, [arXiv:1502.01589].
11. CMS Collaboration, *CMS Moriond 2017 EW Summary Plot*. https://twiki.cern.ch/twiki/pub/CMSPublic/PhysicsResultsSUS/T2tt_limits_summary_cms_Moriond17.pdf.

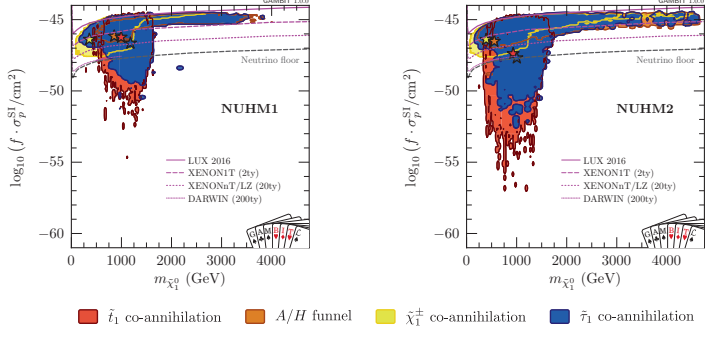


Figure 2 – Global fits of the NUHM1 and NUHM2 models [1], showing spin-independent nuclear scattering cross-sections, rescaled for the fraction $f$ of DM made up by neutralinos.

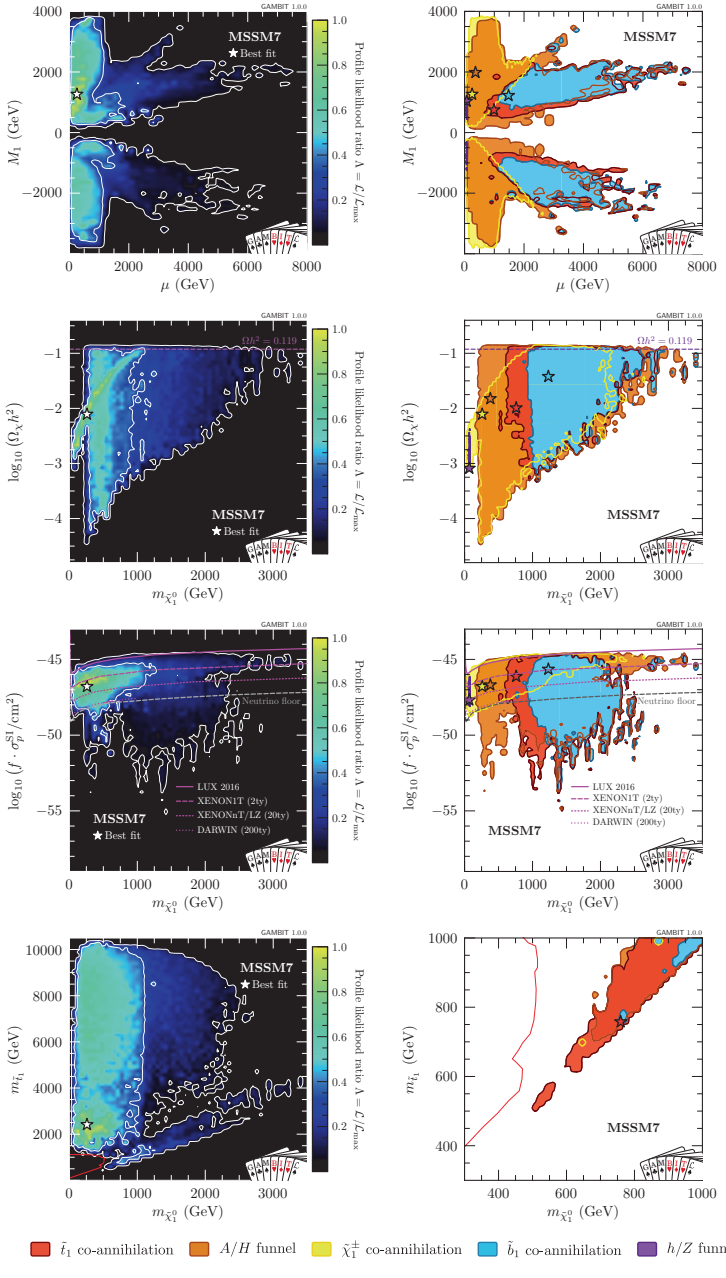


Figure 3 – Global fits of the MSSM-7 [2], showing fundamental parameters, the relic density, the spin-independent nuclear scattering cross-section (rescaled for the fraction $f$ of DM made up by neutralinos), and stop and neutralino masses. Left and right panels as per Fig. 1. Bottom panels include a red line corresponding to the sensitivity of the CMS Run II simplified model limit from stop pair production [11].

# The doubly charged scalar: current status and perspectives

MARGHERITA GHEZZI
*Paul Scherrer Institut, CH-5232 Villigen PSI, Switzerland*

The minimal extension of the Standard Model consisting in a doubly charged SU(2)-singlet scalar is theoretically well motivated by a mechanism of generation of the neutrino masses. As this particle allows for lepton flavour violation, the model is partially constrained by low energy flavour physics. Limits on the mass are also set by direct searches at LHC. Future $e^+e^-$ colliders could have a great sensitivity in exploring the t-channel exchange of this particle. Moreover, its resonance production in the single-production channel would be possible.

Doubly charged scalars (DCSs) are included in the spectrum of many Beyond-the Standard-Model (BSM) scenarios, often in connection with the leptonic sector and motivated by neutrino mass generation mechanisms [1,2,3]. The DCS phenomenology can show interesting features, both at low- and high-energy, characterized by lepton number violating (LNV) and lepton flavour violating (LFV) decays, as well as same-sign boosted lepton pairs in the production channels at high-energy colliders. A minimal setup is realized by adding to the SM field content only a $SU(2)_L$-singlet DCS, that couples to the right-handed fermions of the lepton sector:

$$\Delta\mathcal{L}_S = \mathcal{L}_{\rm SM} + \left(D_\mu S^{++}\right)^\dagger \left(D^\mu S^{++}\right) + \left(\lambda_{ab}\, \overline{(\ell_R)_a}^{\,c}\, (\ell_R)_b\; S^{++} + \text{h.c.}\right) \tag{1}$$

where $a$ and $b$ are flavour indices and $\lambda_{ab}$ are six complex couplings that have to be meant as input parameters of the model. The scalar potential of the new particle includes a quartic self-interaction and a quartic interaction with the Higgs field:

$$\Delta V_S = -\lambda_2 \left(H^\dagger H\right) \left(S^{--} S^{++}\right) - \lambda_4 \left(S^{--} S^{++}\right)^2 \tag{2}$$

However, the phenomenology of the DCS in the Higgs sector can be completely separated by the the phenomenology in the leptonic sector, by means of the independent parameter $\lambda_2$. No specific assumption on the origin of the DCS mass $m_S$ is made, therefore $\lambda_2$ and $m_S$ are understood to be unconstrained by the electroweak-symmetry-breaking mechanism. In the following, the focus will be on the effects of this particle in the leptonic sector.

## 1 Limits from low-energy flavour experiments

Thanks to the off-diagonal terms of the coupling matrix $\lambda_{ij}$ in Eq. 1, the DCS breaks explicitly the lepton number and the lepton flavour conservation. For this reason its phenomenology is strongly connected with the measurements at low-energy facilities of charged LFV processes. The current experimental limits are reported in Table 1. DCSs contribute at tree-level to three-body decays of charged leptons: the limits on the branching ratios for such decays are listed in the left column of the table. Among them, the results for the $\tau$ decays [6] are based on the measurements of the B-factories BELLE[9] and BaBar[10], as well as LHCb[11] and ATLAS results[12].

Table 1: Current experimental limits on charged LFV processes.

| | | | |
|---|---|---|---|
| $\mathrm{Br}[\mu^\mp \to e^\mp e^\pm e^\mp] \leq 1.0 \times 10^{-12}$ | [4] | $\mathrm{Br}[\mu \to e\gamma] \leq 4.2 \times 10^{-13}$ | [5] |
| $\mathrm{Br}[\tau^\mp \to \mu^\mp \mu^\pm \mu^\mp] \leq 1.2 \times 10^{-8}$ | [6] | $\mathrm{Br}[\tau \to \mu\gamma] \leq 4.4 \times 10^{-8}$ | [7] |
| $\mathrm{Br}[\tau^\mp \to e^\mp e^\pm e^\mp] \leq 1.4 \times 10^{-8}$ | [6] | $\mathrm{Br}[\tau \to e\gamma] \leq 3.3 \times 10^{-8}$ | [7] |
| $\mathrm{Br}[\tau^\mp \to e^\mp \mu^\pm \mu^\mp] \leq 1.6 \times 10^{-8}$ | [6] | | |
| $\mathrm{Br}[\tau^\mp \to \mu^\mp e^\pm \mu^\mp] \leq 9.8 \times 10^{-9}$ | [6] | $\mathrm{Br}^{\mathrm{Au}}_{\mu\to e} \leq 7 \times 10^{-13}$ | [8] |
| $\mathrm{Br}[\tau^\mp \to \mu^\mp e^\pm e^\mp] \leq 1.1 \times 10^{-8}$ | [6] | | |
| $\mathrm{Br}[\tau^\mp \to e^\mp \mu^\pm e^\mp] \leq 8.4 \times 10^{-9}$ | [6] | | |

Moreover, DCSs contribute to LFV decays at the one-loop level: the limits of these processes are given in the right column of the table, together with the limit on $\mu \to e$ conversion, that receives additional contribution from operators involving quarks that are generated by the QED renormalization group evolution from the scale $m_S$ down to experimental scale. For most of the processes mentioned above there are planned experiments that are going to increase the sensitivity by one or more orders of magnitude. [13,14,15,16]

## 2 Direct searches at the LHC

Dedicated searches of the DCS have been performed at the LHC, both with the 7 TeV [17,18] and the 13 TeV [19,20] data sets. The ATLAS search [19] was performed at 13 TeV with 36.1 $\mathrm{fb}^{-1}$ of integrated luminosity and considered both the cases in which the DCS couples to the left-handed leptons and to the right-handed leptons. Pairs of DCSs were searched at high values of the same-charge dilepton invariant mass, using electron and muon final states. Lower limits on the mass of the DCS were set: for a scalar decaying to light charged leptons only, the lower mass limit ranges in [770, 870] GeV if the particle couples to left-handed fermions, and in [660,760] GeV if it couples to right-handed fermions. Relaxing the assumption on the DCS branching ratios to $\mathrm{Br}(S^{\pm\pm} \to \ell^\pm\ell^\pm) > 10\%$ (with $\ell = e, \mu$), the bounds decrease to $m_S > 320$ GeV. The CMS search [20] at 13 TeV was performed with 12.9 $\mathrm{fb}^{-1}$ of integrated luminosity and focuses on a DCS that is part of a $SU(2)_L$ triplet. Therefore, it comes together with a neutral and a singly charged scalar. The analysis separates two possible production channels: pair production ($S^{++}, S^{--}$) and associate production ($S^{\pm\pm}, S^\mp$). The bounds that were set from the pair production search range within 400 GeV and 700 GeV, depending on the considered decay channel and the assumptions on the branching ratios.

On the phenomenological side, a comprehensive analysis of different production channels of doubly-charged scalars at the LHC has been performed [3], where the cross-sections for the processes of pair production through Drell-Yan, Z boson fusion and single production through W boson fusion were computed for different values of $m_S$ and the $WWS^{++}$ coupling. A recasting of experimental searches at 7 TeV was performed as well [21] for an extrapolated recasting at 13 TeV using 7 TeV data. A new recasting of the 13 TeV data to generalize to scenarios where the DCS can have a large width is in preparation, together with projections for the High Luminosity (HL) phase of the LHC [22].

## 3 Searches at future leptonic colliders

Future electron-positron colliders will have a great potential to study BSM physics in the leptonic sector. In particular, advanced operational stages of the International Linear Collider (ILC) [23,24] and the Compact Linear Collider (CLIC) [25,26] can play a central role both in indirect and in direct searches, superseeding the production threshold limits set by the HL phase of the LHC.

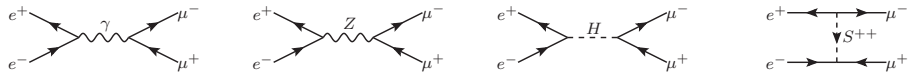


Figure 1 – Feynman diagrams for $e^+e^- \to \mu^+\mu^-$. The first three diagrams correspond to the SM contribution, while the last one contains the DCS in the t-channel.

According to the ILC Technical Design Report [23], three phases are currently under scrutiny, provinding energy in the centre of mass of 250 GeV, 500 GeV and 1 TeV and reaching, at the end of the phase, the integrated luminosity of 250 fb$^{-1}$, 500 fb$^{-1}$ and 1 ab$^{-1}$ respectively. For CLIC the planned phases are, after a phase zero with 100 fb$^{-1}$ at the $t\bar{t}$ threshold, three phases with 500 fb$^{-1}$, 1.5 ab$^{-1}$ and 3 ab$^{-1}$ of integrated luminosity at 380 GeV, 1.5 TeV and 3 TeV in the centre of mass, respectively, as stated in the CLIC Conceptual Design Report. [25]

In this section some phenomenological results on the discovery potential of these future prototypes in the context of the DCS described by Eqs. 1-2 are presented. The numerical simulations have been performed with CalcHEP [27], that provides options to automatically take into account the Initial State Radiation and the Beamstrahlung effects, determined by the beam parameters as given in the ILC Technical Design Report and in the CLIC Conceptual Design Report. Moreover, standard acceptance cuts for a linear collider have been applied to the final-state charged leptons:

$$E_\ell > 10\,\text{GeV}, \qquad |\cos(\theta_\ell)| < 0.95\,, \tag{3}$$

where $E_\ell$ are the energies of the charged leptons ($\ell = e^\pm, \mu^\pm, \tau^\pm$) and $\theta_\ell$ are their angles with respect to the beam direction.

### *3.1 Indirect searches and coupling measurement*

The charged-lepton pair production at $e^+e^-$ colliders can be sensitive to the couplings $\lambda_{ij}$ of the DCS to the charged leptons. In this kind of process a DCS can be exchanged via t-channel, as can be seen for example in the last Feynman diagram of Figure 1 for the muon pair production, possibly resulting in an enhancement of the cross section. In particular, when the produced charged leptons have the same flavour, these processes are sensitive to single couplings, namely $\lambda_{11}$, $\lambda_{12}$ and $\lambda_{13}$. On the other hand, when the produced leptons have different flavours, the resulting LFV processes are background free, but sensitive only to a combination of couplings.

In the most popular BSM models, the DCS couples only to the left-handed or to the right-handed leptons. For this reason, partial polarization of the collider beams can result in an increase/decrease of the cross section and can be used as a powerful tool to distinguish between the two options and reach a better sensitivity to the couplings [28]. Both the ILC and the CLIC prototypes are desiged with the option to polarize the beams. In particular, ILC will have the option to polarize the electron beam up to $P_{e^-} = \pm 0.4$ and the positron beam up to $P_{e^+} = \mp 0.15$ [23], while the CLIC will have the option to polarize the electron beam up to $P_{e^-} = \pm 0.4$ [25].

Figure 2 shows the contours of cross sections with $\Sigma = 5$, where $\Sigma$ is the significance defined as

$$\Sigma = \frac{N_s}{\sqrt{N_s + N_b}}\,, \tag{4}$$

with $N_s$ the number of signal events and $N_b$ the number of background events. The cross sections are given as functions of the mass and the coupling of the DCS involved in the process, both for the ILC and the CLIC, for the pair production of light charged leptons with right-polarized collider beams. In the case of $e^+e^- \to e^+e^-$ also a stronger cut on the angle $\theta$, namely $|\cos\theta| < 0.5$, has been applied beside the acceptance cuts of Eq. 3. Such a cut allows to better cope with the large SM background, enhancing the significance [28]. The plots are shown for the

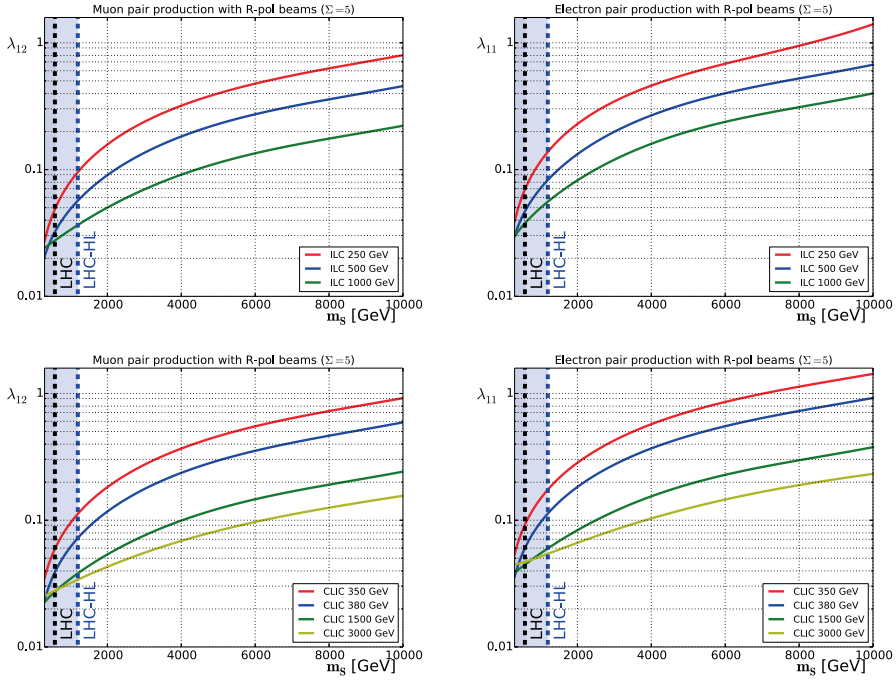


Figure 2 – Countours of the cross section of $e^+e^- \to \mu^+\mu^-$ (left) and $e^+e^- \to e^+e^-$ (right) with significance equal to 5 for different values of the coupling end the mass of the DCS, at ILC with R-polarized beams (upper row) and CLIC with R-polarized electron beam (lower row). For the electron-positron pair production, the restriction $|\cos\theta| < 0.5$ is also applied.

electron and muon pair production only, but the second case can be easily extended to cover also the $\tau$ leptons, by simply rescaling by the tau reconstruction efficiencies expected for the ILC and the CLIC detectors.

To complete the picture, the actual sensitivity of low-energy experiments has to be included in the previous analysis. A combined limit on $\lambda_{11}$ and $\lambda_{12}$ comes from the SINDRUM experiment [4] and will be improved by the Mu3e experiment [13]. Instead, the $e^+e^-$ colliders could explore $\lambda_{11}$ and $\lambda_{12}$ independently. The combined analysis is shown in Figure 5, that highlights the strong complementarity between the low- and high-energy investigations.

### *3.2 Single production*

The leptonic colliders offer the opportunity to explore a new production channel, that is absent at the LHC: a single DCS, in association with two same-sign uncorrelated leptons, can be produced when the collider energy is compatible with the mass of the particle. The production takes place via boson fusion and via radiation of the DCS from initial or final leptonic states (see Figure 3 for diagrammatic examples). The different sub-channels strongly interfere and cannot be separated at the level of the total cross section. The production cross sections are given in Figure 4 for the stage 2 (1.5 TeV) and the stage 3 (3 TeV) of CLIC. For illustrative purposes, the case in which the DCS couples only to the electrons is considered. The cross sections for $e^+e^- \to S^{++}e^-e^-$ are then given as a function of the coupling $\lambda_{11}$ and the mass $m_S$ of the DCS.

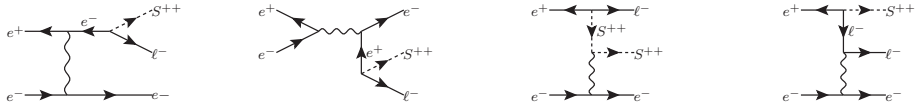

Figure 3 – Examples of Feynman diagrams for the single DCS production $e^+e^- \to S^{++}e^-e^-$.

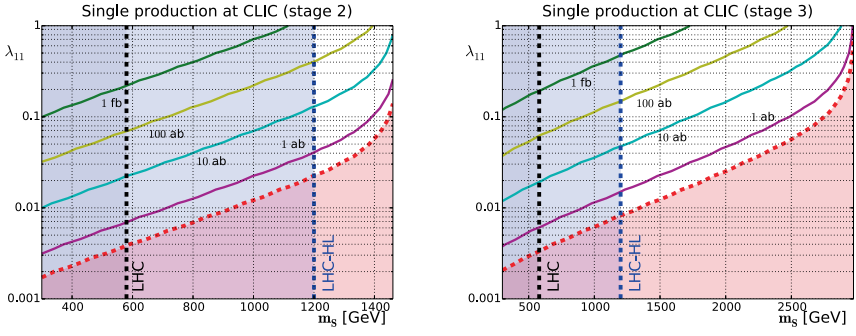


Figure 4 – Countours for $e^+e^- \to S^{++}e^-e^-$ cross section in the plane $m_s - \lambda_{11}$ for CLIC stage 2 (1.5TeV) and stage 3 (3 TeV). The red dashed line marks the threshold for the production af a single event. The expected bounds from LHC and HL-LHC are also reported.

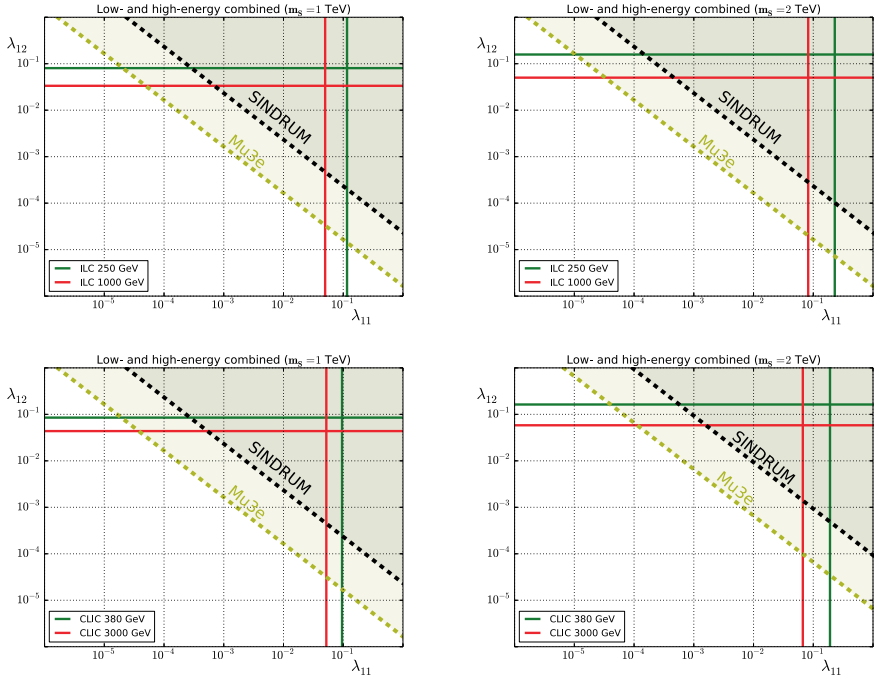


Figure 5 – Limits from SINDRUM and discovery power at ILC and CLIC prototypes and at the Mu3e experiment.

**Acknowledgments**

These results are selected from a work [22] done in collaboration with Andreas Crivellin, Luca Panizzi, Giovanni Marco Pruna and Adrian Signer. This work has been partially supported by the SNSF contract 200021_160156.

**References**

1. W. Konetschny and W. Kummer, Phys. Lett. **70B**, 433 (1977).
   T. P. Cheng and L. F. Li, Phys. Rev. D **22**, 2860 (1980).
   M. Magg and C. Wetterich, Phys. Lett. **94B**, 61 (1980).
   J. Schechter and J. W. F. Valle, Phys. Rev. D **22**, 2227 (1980).
   R. N. Mohapatra and J. D. Vergados, Phys. Rev. Lett. **47**, 1713 (1981).
   A. Halprin, Phys. Rev. Lett. **48**, 1313 (1982).
2. A. Zee, Nucl. Phys. B **264**, 99 (1986).
   E. Ma, Phys. Rev. D **73**, 077301 (2006) [hep-ph/0601225]. K. S. Babu, Phys. Lett. B **203**, 132 (1988).
   K. S. Babu and C. Macesanu, Phys. Rev. D **67**, 073010 (2003) [hep-ph/0212058].
   F. del Aguila, A. Aparici, S. Bhattacharya, A. Santamaria and J. Wudka, JHEP **1206**, 146 (2012) [arXiv:1204.5986 [hep-ph]].
   M. Gustafsson, J. M. No and M. A. Rivera, Phys. Rev. Lett. **110**, no. 21, 211802 (2013) Erratum: [Phys. Rev. Lett. **112**, no. 25, 259902 (2014)] [arXiv:1212.4806 [hep-ph]].
   M. Gustafsson, J. M. No and M. A. Rivera, Phys. Rev. D **90**, no. 1, 013012 (2014) [arXiv:1402.0515 [hep-ph]].
   Y. Cai, J. Herrero-Garca, M. A. Schmidt, A. Vicente and R. R. Volkas, Front. in Phys. **5**, 63 (2017) [arXiv:1706.08524 [hep-ph]].
3. S. F. King, A. Merle and L. Panizzi, JHEP **1411**, 124 (2014) [arXiv:1406.4137 [hep-ph]].
4. U. Bellgardt *et al.* [SINDRUM Collaboration], Nucl. Phys. B **299**, 1 (1988).
5. A. M. Baldini *et al.* [MEG Collaboration], Eur. Phys. J. C **76**, no. 8, 434 (2016) [arXiv:1605.05081 [hep-ex]].
6. Y. Amhis *et al.* [HFLAV Collaboration], Eur. Phys. J. C **77**, no. 12, 895 (2017) [arXiv:1612.07233 [hep-ex]].
7. B. Aubert *et al.* [BaBar Collaboration], Phys. Rev. Lett. **104**, 021802 (2010) doi:10.1103/PhysRevLett.104.021802 [arXiv:0908.2381 [hep-ex]].
8. W. H. Bertl *et al.* [SINDRUM II Collaboration], Eur. Phys. J. C **47**, 337 (2006).
9. K. Hayasaka *et al.*, Phys. Lett. B **687**, 139 (2010) [arXiv:1001.3221 [hep-ex]].
10. J. P. Lees *et al.* [BaBar Collaboration], Phys. Rev. D **81**, 111101 (2010) [arXiv:1002.4550 [hep-ex]].
11. R. Aaij *et al.* [LHCb Collaboration], JHEP **1502**, 121 (2015) [arXiv:1409.8548 [hep-ex]].
12. G. Aad *et al.* [ATLAS Collaboration], Eur. Phys. J. C **76**, no. 5, 232 (2016) [arXiv:1601.03567 [hep-ex]].
13. N. Berger [Mu3e Collaboration], Nucl. Phys. Proc. Suppl. **248-250**, 35 (2014).
14. R. M. Carey *et al.* [Mu2e Collaboration], doi:10.2172/952028
15. Y. G. Cui *et al.* [COMET Collaboration], KEK-2009-10.
16. A. M. Baldini *et al.* [MEG II Collaboration], Eur. Phys. J. C **78**, no. 5, 380 (2018) [arXiv:1801.04688 [physics.ins-det]].
17. G. Aad *et al.* [ATLAS Collaboration], Eur. Phys. J. C **72**, 2244 (2012) [arXiv:1210.5070 [hep-ex]].
18. S. Chatrchyan *et al.* [CMS Collaboration], Eur. Phys. J. C **72**, 2189 (2012) [arXiv:1207.2666 [hep-ex]].
19. M. Aaboud *et al.* [ATLAS Collaboration], Eur. Phys. J. C **78**, no. 3, 199 (2018) [arXiv:1710.09748 [hep-ex]].

20. CMS Collaboration, CMS-PAS-HIG-16-036.
21. T. Geib, S. F. King, A. Merle, J. M. No and L. Panizzi, Phys. Rev. D **93**, no. 7, 073007 (2016) [arXiv:1512.04391 [hep-ph]].
22. A. Crivellin, M. Ghezzi, L. Panizzi, G. M. Pruna and A. Signer, arXiv:1807.10224 [hep-ph].
23. T. Behnke *et al.*, arXiv:1306.6327 [physics.acc-ph].
24. H. Baer *et al.*, arXiv:1306.6352 [hep-ph].
25. M. Aicheler *et al.*, doi:10.5170/CERN-2012-007.
26. L. Linssen, A. Miyamoto, M. Stanitzki and H. Weerts, arXiv:1202.5940 [physics.ins-det].
27. A. Belyaev, N. D. Christensen and A. Pukhov, Comput. Phys. Commun. **184**, 1729 (2013) [arXiv:1207.6082 [hep-ph]].
28. T. Nomura, H. Okada and H. Yokoya, Nucl. Phys. B **929**, 193 (2018) [arXiv:1702.03396 [hep-ph]].


CHAMPAGNE
CHAMPAGNE

# GENUINE EXTRA YUKAWAS FROM EXTRA HIGGS, IMPLICATIONS

GEORGE WEI-SHU HOU
*Department of Physics, National Taiwan University, Taipei 10617, Taiwan*

With a second Higgs doublet, extra Yukawa couplings $\rho_{ij}$ generally exist. Baryon Asymmetry of the Universe (BAU) can be accounted for by $\rho_{tt} \sim \mathcal{O}(1)$, with first order electroweak phase transition (EWPT) arising from $\mathcal{O}(1)$ Higgs quartic couplings. The latter can explain why the observed $h(125)$ boson so resembles the Standard Model (SM) Higgs: with coupling $\eta_6 \sim \mathcal{O}(1)$ for two-doublet mixing, the $H$–$h$ mixing angle $\cos\gamma \cong -\eta_6 v^2/(m_H^2 - m_h^2)$ is suppressed by the $CP$-even boson mass splitting $m_H^2 - m_h^2 >$ few $v^2$. The approximate alignment, together with the fermion mass-mixing pattern, controls FCNC Higgs effects at low energy. The picture can be probed by $pp \to tt\bar{c}$, $tt\bar{t}$, i.e. same-sign top and triple-top processes at the LHC.

## 1 Introduction: Whither Extra Yukawas?

Though accounting for all observed $CP$ violation (CPV), the unique phase in CKM matrix falls far short of BAU. Considering the origin of this phase, *could there be extra Yukawa couplings?* In general, a second Higgs doublet (2HDM) — quite plausible — should imply extra Yukawas, but these were killed [1] by the *Natural* Flavor Conservation (NFC) condition: as $u$- and $d$-type quark masses each arise from a single doublet, the Yukawa couplings are basically the same as in SM. It was later noted that the fermion mass-mixing pattern could soften the need for NFC, and the best probe [2] may be $t \to ch$ or $h \to t\bar{c}$, as the top quark is the heaviest fermion.

With the case for 2HDM elevated by the discovery of 125 GeV boson in 2012, we emphasized [3] the need to probe the $2 \times 2$ *extra Yukawa couplings* $\rho_{ij}$ $(i,\, j = c,\, t)$. It also became understood that the flavor changing neutral Higgs (FCNH) couplings of the form

$$\rho_{tc} \cos(\beta - \alpha)\, \bar{t}_L c_R h, \tag{1}$$

are modulated by $H$–$h$ mixing, where $H$ is the second $CP$-even Higgs boson. The two doublets $\Phi_1$ and $\Phi_2$ give rise to Yukawa matrices $Y_1$ and $Y_2$. The combination $Y^{\rm SM} = Y_1 v_1 + Y_2 v_2$ is diagonalized as usual, but the orthogonal combination gives rise to Yukawa matrix $\boldsymbol{\rho}$ that cannot be simultaneous diagonalized. In the limit that $\cos(\beta - \alpha)$ is small, called *alignment* limit, [4] couplings of $h$ are diagonal, just as the SM Higgs, while $H$ couples with the Yukawa matrix $\boldsymbol{\rho}$. As Yukawa couplings, $\rho_{ij}$ should be complex,

$$\rho_{ij} \equiv |\rho_{ij}| e^{i\phi_{ij}}. \tag{2}$$

In place of NFC, we see that alignment $(\cos(\beta - \alpha) \to 0)$ removes FCNH couplings for $h$, while the mass-mixing pattern, shared by $Y_{1,2}$, further suppresses $\rho_{ij}$ involving light(er) quarks.

## 2 Bonus 1: EWBG from Extra Top Yukawa $\rho_{tt}$

Given that $Y^{\rm SM}$ for $u$-type quarks is dominated by Yukawa coupling $\lambda_t \cong 1$, together with the observed quark mass-mixing pattern, it is rather plausible that the orthogonal combination to

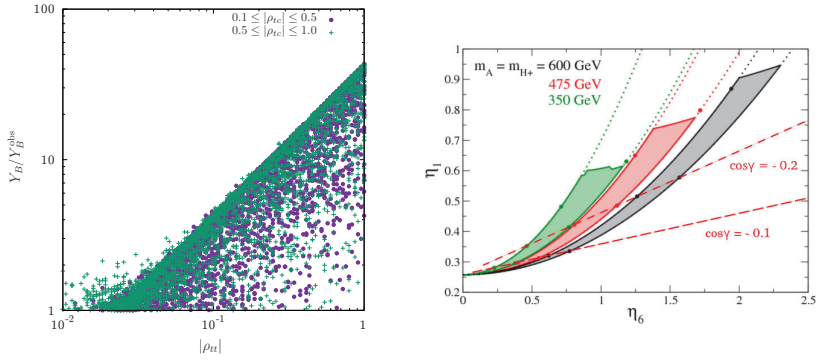


Figure 1 – [left] $Y_B/Y_B^{\rm obs}$ vs $|\rho_{tt}|$, and [right] $\Delta T$-allowed $\eta_1$ vs $\eta_6$ for $m_A = m_{H^+}$, varying $\eta_4 = \eta_5 \in (0.5, 2)$.

$Y^{\rm SM}$ should also have a dominant $\mathcal{O}(1)$ eigenvalue, with phase arbitrary. This motivates us [5] to consider its possible role in baryogenesis. It is known that [6] thermal loops involving extra Higgs bosons with $\mathcal{O}(1)$ Higgs quartic couplings can give rise to 1st order EWPT. It is of interest to explore whether $\mathrm{Im}\,\rho_{tt}$ could then lead to electroweak baryogenesis (EWBG).

The main issue is to generate sufficient $Y_B \equiv n_B/s$ (ratio of baryon and entropy densities) at the observed level of $Y_B^{\rm obs} \sim 0.86 \times 10^{-10}$ or higher. Putting aside the complicated transport problem, [5] which requires an actual 1st order EWPT, this boils down to producing enough left-handed top density at the expanding bubble wall of broken phase that accumulates inside the bubble, i.e. our Universe. This depends on CPV top interactions at the bubble wall, which boils down further to the CPV source term that arises from the extra top Yukawas, [5]

$$\mathrm{Im}[(Y_1)_{ij}(Y_2)^*_{ij}] = \mathrm{Im}[(V_L^u Y_{\rm diag} V_R^{u\dagger})_{ij}(V_L^u \rho V_R^{u\dagger})^*_{ij}], \tag{3}$$

where $V_L^u$, $V_R^u$ forms the biunitary transform that diagonalizes $Y^{\rm SM}$ to $Y_{\rm diag}$ for $u$-type quarks.

Flavor constraints from $B_d$ and $B_s$ mixing and chiral enhancement in $b \to s\gamma$ demand [3,7] $\rho_{ct}$ to be rather small, while $\rho_{cc} \sim \mathcal{O}(\lambda_c) \ll 1$ without fine tuning, hence the two main parameters are $\rho_{tt}$ and $\rho_{tc}$. Scanning over $|\rho_{tc}|$, $\phi_{tc}$ and $\phi_{tt}$, we find robust and large parameter space for EWBG. Fig. 1[left] plots $Y_B/Y_B^{\rm obs}$ vs $|\rho_{tt}| \in (0.01, 1)$, with higher $0.5 \le |\rho_{tc}| \le 1.0$ (lower $0.1 \le |\rho_{tc}| \le 0.5$) plotted as green + (purple $\cdot$). Little difference is seen between the two plots, hence $\rho_{tt}$ is the driver. However, for $|\rho_{tt}| < 0.05$ or so, the green +'s that populate $Y_B/Y_B^{\rm obs} > 1$ suggest $\rho_{tc} > 0.5$, with phase $\phi_{tc}$ near maximal, could be a backup to $\rho_{tt}$ for EWBG. In making this plot, the simplifying assumption of $m_H = m_A = m_{H^+} = 500$ GeV is taken. Much higher values would either run into issues of perturbativity, or damping by decoupling.

Fig. 1[left] scanned through realistic Yukawa matrices, but a simplified texture can help elucidate the driving effect. Suppose $(Y_1)_{tc} \neq 0$, $(Y_2)_{tc} \neq 0$ and $(Y_1)_{tt} = (Y_2)_{tt} \neq 0$, while all other extra Yukawas vanish, i.e. altogether 3 complex parameters. If one assumes $\sqrt{2}Y^{\rm SM}$ is the linear sum of $Y_1$ and $Y_2$, one can solve for $V_R^u$, while there is no need for $V_L^u$. One can then arrive at the combination of $Y_1$ and $Y_2$ that is orthogonal to $Y^{\rm SM}$. In this way, one finds [5]

$$\mathrm{Im}[(Y_1)_{tc}(Y_2)^*_{tc}] = -\lambda_t\,\mathrm{Im}\,\rho_{tt}, \quad \rho_{ct} = 0, \tag{4}$$

with $\rho_{tc}$ remaining basically a free parameter. We see from Eq. (4) that *both* doublets participate in the CPV source for EWBG in 2HDM, which is reminiscent to the Jarlskog invariant for SM. We can also see how 2HDM with extra Yukawas overcomes the suppression factors in the Jarlskog invariant, given that $\lambda_t$, $|\mathrm{Im}\,\rho_{tt}|$ are both $\mathcal{O}(1)$.

## 3 Bonus 2: : Alignment from $\mathcal{O}(1)$ Higgs Quartics

*It is remarkable that the extra Yukawa coupling $\rho_{tt}$ could account for BAU!*

Note that such mechanism does not exist in 2HDM-I or 2HDM-II, the 2HDMs that satisfy NFC, since NFC means there are essentially no new Yukawa couplings, despite having a second Higgs doublet. We now show [8] that the prerequisite for 1st order EWPT, that extra Higgs quartic couplings are $\mathcal{O}(1)$, could be behind the observed approximate alignment.

The general $CP$-conserving Higgs potential [9] of 2HDM is,

$$\begin{aligned} V(\Phi,\,\Phi') \;&= \mu_{11}^2|\Phi|^2 + \mu_{22}^2|\Phi'|^2 - \left(\mu_{12}^2\Phi^\dagger\Phi' + \text{h.c.}\right) \;+\tfrac{1}{2}\eta_1|\Phi|^4 + \tfrac{1}{2}\eta_2|\Phi'|^4 + \eta_3|\Phi|^2|\Phi'|^2 \\ &\quad + \eta_4|\Phi^\dagger\Phi'|^2 + \left\{\tfrac{1}{2}\eta_5(\Phi^\dagger\Phi')^2 + \left[\eta_6|\Phi|^2 + \eta_7|\Phi'|^2\right]\Phi^\dagger\Phi' + \text{h.c.}\right\}, \end{aligned} \tag{5}$$

where we take Higgs basis, i.e. $\mu_{11}^2 < 0$ but $\mu_{22}^2 > 0$. With the two minimization conditions

$$\mu_{11}^2 = -\frac{1}{2}\eta_1 v^2, \quad \mu_{12}^2 = \frac{1}{2}\eta_6 v^2, \tag{6}$$

$\mu_{11}^2 < 0$ is exchanged for $v$, the usual "soft breaking parameter" $\mu_{12}^2$ is removed, and the quartic coupling $\eta_6$ is solely responsible for $\Phi$–$\Phi'$ mixing. The $CP$-even Higgs mass matrix

$$M_{\text{even}}^2 = \begin{bmatrix} \eta_1 v^2 & \eta_6 v^2 \\ \eta_6 v^2 & \mu_{22}^2 + \frac{1}{2}(\eta_3+\eta_4+\eta_5)v^2 \end{bmatrix}, \qquad R_\gamma = \begin{bmatrix} c_\gamma & -s_\gamma \\ s_\gamma & c_\gamma \end{bmatrix}, \tag{7}$$

is diagonalized by $R_\gamma$, i.e. $R_\gamma^T M_{\text{even}}^2 R_\gamma$ is diagonal with elements $m_H^2$, $m_h^2$. In Eq. (7), our $c_\gamma \equiv \cos\gamma$ corresponds to $\cos(\beta-\alpha)$ in the 2HDM-II notation, and is the relative angle (mod. $\pi/2$) between the Higgs basis and the neutral Higgs mass basis.

Rather than give the formula for $m_H^2$, we note the mixing angle $c_\gamma$ satisfies two relations,

$$c_\gamma^2 = \frac{\eta_1 v^2 - m_h^2}{m_H^2 - m_h^2}, \qquad \sin 2\gamma = \frac{2\eta_6 v^2}{m_H^2 - m_h^2}. \tag{8}$$

In alignment *limit* of $c_\gamma \to 0$, $s_\gamma \to -1$, one has $\eta_1 \to m_h^2/v^2 \simeq 0.26$ in numerator of first term, where $m_h \simeq 125$ GeV is used. For $c_\gamma$ small but nonvanishing, $m_H^2 - m_h^2 >$ several $v^2$ can weigh down $|\eta_1 v^2 - m_h^2| < v^2$. Since $s_\gamma \to -1$ holds better than $c_\gamma \to 0$, the second relation gives

$$c_\gamma \simeq \frac{-\eta_6 v^2}{m_H^2 - m_h^2}. \qquad \text{(near alignment)} \tag{9}$$

Although the result exists [10] in the literature, $|\eta_6| \ll 1$ is generally assumed, as it arises through loop effects in MSSM. But we see that $c_\gamma$ can be small for

$$|\eta_6| \sim \mathcal{O}(1) \text{ (or smaller)}, \quad m_H^2 - m_h^2 > \textit{several}\ v^2. \tag{10}$$

Note that a low $m_h^2/v^2 \simeq 0.26$ is *not* required, i.e. $c_\gamma$ can be small even if $m_h \sim 300$ GeV.

What drives alignment in 2HDM? For $\eta_{1,3,4,5}$, $\mu_{22}^2/v^2 \sim \mathcal{O}(1)$, $[M_{\text{even}}^2]_{22}$ has four $\mathcal{O}(v^2)$ terms while $[M_{\text{even}}^2]_{11}$ has only one, hence $m_H^2 - m_h^2 >$ several $v^2$ is likely. However, $\mu_{22}^2/v^2 > 1$ would damp the 1st order EWPT, hence sub-TeV exotic Higgs masses are preferred. Second, $\eta_6 \sim \mathcal{O}(1)$ increases $m_H^2 - m_h^2$ by level repulsion, pushing $m_h^2/v^2$ down from $\eta_1 \sim \mathcal{O}(1)$. Finally, tuning $\eta_6 < 1/4 \sim m_h^2/v^2$ would give *extreme* alignment ($c_\gamma \to 0$) hence $\eta_1 \to 0.26$. These observations are illustrated in Fig. 1[right] for allowed $\eta_1$ vs $\eta_6$ range, where custodial SU(2) is assumed to evade $\Delta T$ constraint, i.e. $m_A^2 = m_{H^+}^2 = \mu_{22}^2 + \eta_3 v^2/2$. We vary $\eta_4 = \eta_5 \in (0.5,\, 2)$, so $m_H$ could be up to 100 GeV higher. High values of $\eta_1$ are cut off by $\Delta T$ (via scalar–vector loop), and the two dashed lines mark $-c_\gamma = 0.1$ and 0.2, which are quite close to alignment; even $-c_\gamma = 0.3$, close to the bound from $\Delta T$, is still allowed by observed approximate alignment at LHC.

$\mathcal{O}(1)$ *Higgs quartics could be behind approximate alignment*, or small $c_\gamma$, regardless of whether a $Z_2$ symmetry is used to enforce NFC or not, as our discussion is general. But we have advocated that $\rho_{tt} \sim \mathcal{O}(1)$ could explain BAU. It is then intriguing to comment that sizable $\rho_{tt}$ could possibly [11] help "protect" alignment: with $\mathcal{O}(1)$ Higgs quartics, bosonic loops would reduce $\Gamma_{h\to ZZ^*}$, but the top loop can bring $\Gamma_{h\to ZZ^*}$ back to SM value for $\rho_{tt}\, c_\gamma > 0$, consistent with what is observed. This was our original motivation to understand the mechanism of alignment.

## 4 Same-sign Top and Triple-top Signatures: $pp \to tH/A \to tt\bar{c}$, $tt\bar{t}$

The process $cg \to tA$ was suggested long time ago as a direct probe [12] of the $ctA$ FCNH coupling, restricting to $m_A < 2m_t$ such that $A \to t\bar{c}$ (and $\bar{t}c$) is at 100%. We recently studied [13] the $cg \to tH/A$ associated production through the $\rho_{tc}$ coupling, followed by subsequent decay $H/A \to t\bar{c}$, $\bar{t}c$ and $t\bar{t}$ final states involving $\rho_{tc}$ and $\rho_{tt}$ couplings, advocating the signatures of same-sign top, $tt\bar{c}$, and triple-top, $tt\bar{t}$. The same-sign top signature involves same-sign dileptons, together with two $b$-jets, missing energy, and additional jets. We find that, for $\rho_{tc} \sim 1$, the second case for EWBG can be probed with 300 fb$^{-1}$, but signature does not improve for higher luminosity, unless background can be further controlled. Given that $\rho_{tt}$ is the favored driver for EWBG, triple-top search at HL-LHC may be more interesting, and possesses more exquisite signatures: three leptons, three $b$-jets, missing energy. The backdrop of SM cross section at only fb level makes the case strong, where full HL-LHC data can cover up to 700 GeV mass range for $\rho_{tt} \sim 1$, but $\rho_{tc}$ needs to be not much smaller than 0.5 for signal cross section.

## 5 Conclusion: $H^0$, $A^0$, $H^\pm$ in Our Time

With $\mathcal{O}(1)$ Higgs quartics for 1st order EWPT, the extra Yukawa $\rho_{tt}$ (or $\rho_{tc}$) $\sim \mathcal{O}(1)$ in general 2HDM is remarkably efficient for EWBG. The $\mathcal{O}(1)$ Higgs quartics support approximate alignment, and together with quark mass-mixing hierarchy control low energy FCNH effect, without need for NFC. Having $H$, $A$ and $H^\pm$ sub-TeV in mass would be a boon to LHC search, the discovery of which in $tt\bar{c}$, $tt\bar{t}$ final states would touch upon Matter Asymmetry of the Universe.


### Acknowledgments

We thank our collaborators on three consecutive papers presented here for an enjoyable 2017, and we are grateful to illuminating discussions with Howie Haber at Moriond QCD 2018.


### References


1. S.L. Glashow and S. Weinberg, *Phys. Rev.* D **15**, 1958 (1977).
2. W.-S. Hou, *Phys. Lett.* B **296**, 179 (1992), and references therein.
3. K.-F. Chen, W.-S. Hou, C. Kao and M. Kohda, *Phys. Lett.* B **725**, 378 (2013).
4. J.F. Gunion and H.E. Haber, *Phys. Rev.* D **67**, 075019 (2003).
5. K. Fuyuto, W.-S. Hou and E. Senaha,, *Phys. Lett.* B **776**, 402 (2018).
6. See e.g. S. Kanemura, Y. Okada and E. Senaha, *Phys. Lett.* B **606**, 361 (2005).
7. B. Altunkaynak *et al.*, *Phys. Lett.* B **751**, 135 (2015).
8. W.-S. Hou and M. Kikuchi, arXiv:1706.07694 [hep-ph].
9. S. Davidson and H.E. Haber, *Phys. Rev.* D **72**, 035004 (2005); H.E. Haber and D. O'Neil, *ibid.* D **74**, 015018 (2006); and *ibid.* D **83**, 055017 (2011).
10. See e.g. P. Bechtle *et al.*, *Eur. Phys. J.* C **77**, 67 (2017).
11. W.-S. Hou and M. Kikuchi, *Phys. Rev.* D **96**, 015033 (2017).
12. W.-S. Hou, G.-L. Lin, C.-Y. Ma and C.-P. Yuan, *Phys. Lett.* B **409**, 344 (1997).
13. M. Kohda, T. Modak and W.-S. Hou, *Phys. Lett.* B **776**, 379 (2018).

# The Hyperbolic Higgs

Matthew McCullough
*CERN, Theoretical Physics Department, Geneva, Switzerland*

In this talk I briefly review the hierarchy problem and the Hyperbolic Higgs model.

## 1 The Hierarchy Problem

The hierarchy problem has been a driving puzzle in fundamental physics for decades. This problem may be briefly outlined by considering an analogy with superconductors. Together, Ginzburg and Landau developed a phenomenological model to describe the macroscopic physics of superconductivity [1]. Unsurprisingly, this model is referred to as the 'Ginzburg-Landau' model (GL). The details of this model are not necessary for the purpose of analogy considered here, other than the expression for the free energy of the scalar sector in their model, which is

$$F = \frac{1}{2m}|(-i\hbar\nabla - 2\mathbf{A})\phi|^2 + \alpha|\phi|^2 + \frac{\beta}{2}|\phi|^4 \quad . \tag{1}$$

The analogy with the scalar sector of the Standard Model (SM) is clear. The GL model contains a complex scalar field, with a mass, quartic interaction, and an interaction with the gauge field which, in this non-relativistic model, is the electromagnetic vector potential. The parameters of the theory are temperature dependent and, when the temperature falls below the critical value, the mass-squared becomes negative, $\phi$ condenses and obtains an expectation value throughout the superconductor. As a result, the photon obtains an effective mass due to this condensate.

I refer to the GL model as 'phenomenological' as the model is not intended to provide an explanation as to the true microscopic origins of superconductivity, but does adequately describe the physics at the relevant length scale. To understand the fundamental nature of superconductivity a microscopic model, relevant at smaller distance scales, was needed. This was delivered by Bardeen, Cooper, and Shrieffer, in the celebrated BCS model of superconductivity [2,3].

With the Higgs sector we are in a very different situation. We have an extraordinarily successful phenomenological model, unmistakably analogous to the GL model, however we do not yet have the 'BCS Theory' of the SM. The origin of the Higgs sector and the microscopic nature of the Higgs boson are unknown. While the LHC continues to explore the Higgs sector

we face a further puzzle. Not only is the microscopic origin of the Higgs sector unknown, but in the presence of the SM Yukawa and gauge interactions, there is no way to protect the Higgs mass from quantum corrections arising at a similar scale to the underlying scale of the UV completion. This is the essence of the hierarchy problem. In this proceeding I will discuss some exotic models with exotic experimental signatures that could give a clue as to the microscopic origins of the Higgs sector, explaining this apparent hierarchy.

## 2 The Hyperbolic Higgs

The weak scale can be protected from large quantum corrections by additional symmetries, such as a spacetime symmetry (Supersymmetry) or by continuous non-linearly realised global symmetries, of which the Higgs boson would correspond to a pseudo-Nambu Goldstone boson. The SM itself does not exhibit such symmetries, thus in any such scenario the field content must be extended to allow the symmetry to act on the full set of fields. In practise this leads to partners for SM particles. In particular, at the least one expects to have 'top partner' particles. These states allow the full action for the SM+partners to respect the desired symmetry, and the protection of the Higgs boson can be observed by noticing that quadratic sensitivity to the cutoff is ameliorated in such theories, if the cutoff also respects the symmetry. We are familiar with the stop squark top partners in Supersymmetry, and with the fermionic top partners of composite Higgs models. These top partners are coloured and would be produced in abundance at the LHC. However, there are alternative classes of models, known as 'Neutral Naturalness' models, in which the top partners are uncoloured.

A zoo of novel top partner states [4,5,6] have arisen through theoretical explorations of neutral naturalness models. The Twin Higgs approach demonstrated the possibility of fermionic top partners that are fully neutral under the Standard Model (SM) symmetries. However, the state-of-the-art for scalar top partners has not changed since the introduction of Folded Supersymmetry (SUSY) [6], where the folded stops must be charged under the visible $\mathrm{SU}(2)_W \times \mathrm{U}(1)_Y$ in order for them to couple to the Higgs via the fundamental superpotential. In [7], we introduced a new paradigm for neutral naturalness – the *Hyperbolic Higgs* – which realises the so-far elusive goal (see *e.g.* Table 1 of [7]) of fully SM neutral scalar top partners.

The Hyperbolic Higgs mechanism relies on a low-energy scalar potential that exhibits an *accidental* flat direction. This results from a $\mathrm{U}(2,2)$ non-compact global symmetry of the scalar potential, in contrast to the $\mathrm{U}(4)$ symmetry of the Twin Higgs theory. Note that $\mathrm{U}(2,2)$ is *not* an accidental symmetry of the low-energy theory: although the scalar potential respects it, the kinetic terms do not.

Explicitly, the scalar potential for the Higgs $H$ (charged under the SM gauge group) and the Hyperbolic Higgs $H_{\mathcal{H}}$ (charged under an identical copy of the SM gauge group) takes the form

$$V_{\mathcal{H}} = m^2\Big(\big|H\big|^2 - \big|H_{\mathcal{H}}\big|^2\Big) + \frac{\lambda}{2}\Big(\big|H\big|^2 - \big|H_{\mathcal{H}}\big|^2\Big)^2 . \tag{2}$$

The classical vacuum manifold is described by a hyperbola (with $f^2 \equiv m^2/\lambda$),

$$\big|H_{\mathcal{H}}\big|^2 - \big|H\big|^2 = f^2 . \tag{3}$$

This explains the moniker "Hyperbolic Higgs."

The flat direction $H_{\rm flat}$ is manifest after the field redefinition

$$H = H_0 \sinh\frac{H_{\rm flat}}{f} , \qquad H_{\mathcal{H}} = H_0 \cosh\frac{H_{\rm flat}}{f} , \tag{4}$$

as the potential $V_{\mathcal{H}}$ depends only on $H_0$ but not on $H_{\rm flat}$. Since eq. (4) corresponds to a hyperbolic rotation but not to a unitary transformation, the form of the kinetic terms is not preserved, signaling that $\mathrm{U}(2,2)$ is not a symmetry of the full theory. On the other hand, we

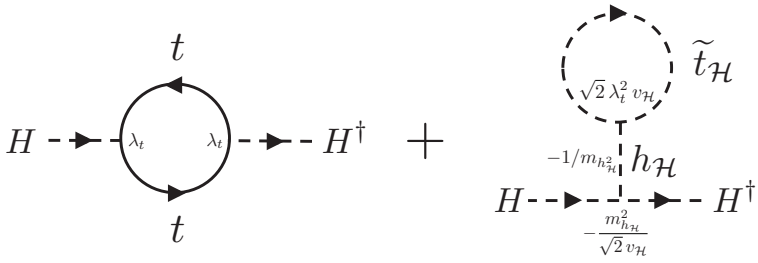


Figure 1 – The one-loop fixed order corrections to the SM-like Higgs boson mass squared parameter, where $t$ is a SM top quark, and $\widetilde{t}_{\mathcal{H}}$ is a Hyperbolic stop. Vertex factors and propagator follow from Eq. (2) and Eq. (6).

can identify a massless neutral scalar state by expanding the Higgs and Hyperbolic Higgs about their vacuum expectation values using $H = (0, v + h/\sqrt{2})$ and $H_{\mathcal{H}} = (0, v_{\mathcal{H}} + h_{\mathcal{H}}/\sqrt{2})$. We find two propagating scalar radial modes, $h$ and $h_{\mathcal{H}}$, while the remaining degrees of freedom are eaten by the SM gauge fields and by their Hyperbolic $\mathrm{SU}(2)_{\mathcal{H}} \times \mathrm{U}(1)_{\mathcal{H}}$ counterparts. The SM-like Higgs scalar $h_{\mathrm{SM}}$ emerges as the massless state

$$h_{\mathrm{SM}} = h\cos\theta + h_{\mathcal{H}}\sin\theta\,, \qquad\qquad \tan\theta = \frac{v}{v_{\mathcal{H}}}\quad . \tag{5}$$

While the detailed Hyperbolic phenomenology is sensitive to the UV completion, the above mixing leads to two universal features relevant for Higgs phenomenology: $\cos\theta$ measures the size of an overall modification of SM Higgs couplings, while $\sin\theta$ provides a portal into the Hyperbolic sector contributing to invisible Higgs decays. These features will be described in more detail in Sec. 2.1.

To illustrate the comparison between the Twin and Hyperbolic Higgs models, it is useful to abuse the physics jargon and think of the Higgs as a pseudo-Goldstone of a spontaneously broken non-compact $\mathrm{U}(2,2)$ symmetry (as emphasized above, the analogy holds for the scalar potential, but not for the kinetic terms, implying that some of the usual relations are violated at loop level).

If we are going to solve the little hierarchy problem, we must couple the Higgs sector to matter. The SM sector has Yukawa couplings involving *fermions* while the Hyperbolic sector contains quartic interactions with *scalars*

$$\mathcal{L} = (\lambda_t\, H\, \psi_Q\, \psi_{U^c} + \mathrm{h.c.}) + \lambda_t^2 \left( \left| H_{\mathcal{H}} \cdot \widetilde{Q}_{\mathcal{H}} \right|^2 + \left| H_{\mathcal{H}} \right|^2 \left| \widetilde{U}^c_{\mathcal{H}} \right|^2 \right)\,, \tag{6}$$

where $\lambda_t$ is the top quark Yukawa coupling, $\psi_Q$ and $\psi_{U^c}$ comprise the SM top quark, and $\widetilde{Q}_{\mathcal{H}}$ and $\widetilde{U}^c_{\mathcal{H}}$ are the scalar top partners, in a notation reminiscent of SUSY. An exchange symmetry guarantees the equality of $\lambda_t$ in the two sectors. Note that in the low-energy effective theory there are no SM charged top partner states. The field $H$ couples as a SM Higgs, while $H_{\mathcal{H}}$ participates in an interaction analogous to the SUSY Higgs-squark couplings. Since the UV regulator is equal for both fields due to the exchange symmetry, the one-loop quadratic corrections from these interactions also respect the accidental global $\mathrm{U}(2,2)$ symmetry, $\delta V \propto (\lambda_t/4\pi)^2\, \Lambda^2 \big( \left| H_{\mathcal{H}} \right|^2 - \left| H \right|^2 \big)$, where $\Lambda$ is the UV cutoff. The opposite sign in the loop corrections for Higgs and Hyperbolic Higgs comes from the replacement of virtual fermions with scalars. This is the central observation of this paper, as this fact guarantees that the one-loop top contributions to the SM Higgs mass squared parameter are insensitive to the UV: the contributions quadratic in the cutoff that result from top quark loops are cancelled by those involving gauge neutral top partner fields.

This UV insensitivity may equivalently be seen by integrating out the heavy radial mode $h_{\mathcal{H}}$ to yield the low energy effective theory

$$\mathcal{L} = (\lambda_t \, H \, \psi_Q \, \psi_{U^c} + \text{h.c.}) + \, \lambda_t^2 \, |H|^2 \Big( \big| \, \widetilde{t}_{\mathcal{H}}^{\,L} \, \big|^2 + \big| \, \widetilde{t}_{\mathcal{H}}^{\,R} \, \big|^2 \Big) \, . \tag{7}$$

The procedure is illustrated by the diagrams in Fig. 1 with the $h_{\mathcal{H}}$ line integrated out. The cancellation of divergences is now manifest, as it works in the same way as in ordinary low-energy SUSY.

The key to the Hyperbolic Higgs framework is that, by moving from a scalar potential with an approximate compact global symmetry U(4) to an approximate non-compact one U(2, 2), the gauge singlet *fermionic* top partners of the Twin Higgs theory may be replaced by gauge singlet *scalar* top partners. In other words, the extra minus sign due to the loop of fermions becoming a loop of scalars is compensated by the minus sign due to $\text{U}(4) \to \text{U}(2,2)$.

The way we formulated the basic ingredients of the Hyperbolic mechanism makes clear that its most natural realization relies on a SUSY setup. Indeed, in [7] we introduced a realistic example that utilizes a modification of the mirror structure developed for both SUSY Twin Higgs and Folded SUSY [6]: the UV theory contains two copies of identical matter content, with a $Z_2$ exchange symmetry relating their couplings. Specifically, the top sector of the model relies on 5D SUSY and a particular choice of Scherk-Schwarz boundary conditions [8,9] to lift the unwanted states from the low energy spectrum. We will refer the reader to [7] for discussion of the model details, and here focus on the phenomenological possibilities.

### *2.1 Phenomenology*

The phenomenological possibilities for Hyperbolic Higgs models are broad. As with other models of neutral naturalness, the principal signatures involve the Higgs sector. Much as in Twin Higgs models, there is tree-level mixing between the SM and Hyperbolic Higgs doublets, which leads to a universal reduction in Higgs couplings ($y_{hPP}$) compared to SM predictions ($y_{hPP}^{\text{SM}}$)

$$\frac{y_{hPP}}{y_{hPP}^{\text{SM}}} - 1 = \cos\theta - 1 \simeq -\frac{\omega^2 \, v^2}{2 \, v_{\mathcal{H}}^2} \simeq -\omega^2 \left( \frac{\text{TeV}}{v_{\mathcal{H}}} \right)^2 1.5\% \, , \tag{8}$$

where $\omega$ is a model-dependent coefficient, equal to one in the Hyperbolic limit and whose expression in our proposed model is given in [7].

Such a universal reduction in Higgs couplings drops out of Higgs branching ratios, but can be detected in measurements of the Higgs width and, more importantly, of Higgs production rates. Current Higgs coupling measurements (namely the combined ATLAS + CMS 7+8 TeV $2\sigma$ bounds on modifications to Higgs production rates [10]) require $v_{\mathcal{H}} \gtrsim 500$ GeV. This is ultimately a weaker constraint on the natural parameter space of the Hyperbolic Higgs than that imposed by precision electroweak limits on $\text{U}(1)_X$. As larger values of $v_{\mathcal{H}}$ are allowed without significantly increasing fine-tuning, future LHC Higgs coupling measurements are unlikely to place strong limits on the model.

The modification of the Higgs coupling to the top receives additional non-universal corrections. Taking the first derivative of $m_t(H)$ around $H = v + h_{\text{SM}} \cos\theta/\sqrt{2}$, we find

$$\begin{aligned} \frac{y_{htt}}{y_{htt}^{\text{SM}}} - 1 \;\; &= \;\; \frac{\cos\theta}{1 + \tan^2 \alpha_t} - 1 \simeq -\frac{\omega^2 \, v^2}{2 \, v_{\mathcal{H}}^2} - \pi^2 \, R^2 \, \lambda_t^2 \, v^2 \\ &\simeq \;\; -\omega^2 \left( \frac{\text{TeV}}{v_{\mathcal{H}}} \right)^2 1.5\% - \left( \frac{5 \text{ TeV}}{1/R} \right)^2 1.2\% \, . \end{aligned} \tag{9}$$

Mixing between the SM and Hyperbolic Higgs doublets also induces corrections to the Higgs self-coupling ($y_{h^3}$) relative to SM predictions ($y_{h^3}^{\text{SM}}$)

$$\frac{y_{h^3}}{y_{h^3}^{\text{SM}}} - 1 \;\; = \;\; \cos^3\theta + \frac{v}{v_{\mathcal{H}}} \sin^3\theta - 1 \simeq -\frac{3 \, \omega^2 \, v^2}{2 \, v_{\mathcal{H}}^2} \simeq -\omega^2 \left( \frac{\text{TeV}}{v_{\mathcal{H}}} \right)^2 4.5\% \, . \tag{10}$$

This analytic expression is exact, once we neglect the tower of higher-dimensional operators in the CW potential.

Mixing between the SM and Hyperbolic Higgs also imbues the SM-like Higgs with couplings to light states in the Hyperbolic sector. In contrast to the Twin Higgs, there are no light chiral fermions in the Hyperbolic sector, while the Hyperbolic scalars all acquire soft masses greater than, or comparable to, the electroweak scale. Consequently, the only possible light Hyperbolic degrees of freedom beneath the electroweak scale are the Hyperbolic photon and gluon. The effective coupling to Hyperbolic photons leads to a vanishingly small contribution to the Higgs invisible decay rate, at least an order of magnitude smaller than the SM contribution from $h \to 4\,\nu$. The coupling to Hyperbolic gluons, on the other hand, is more promising due to the effects of Hyperbolic confinement. Neglecting SUSY breaking corrections to Hyperbolic stop masses and their possible mixing, we find

$$\mathrm{BR}(h_{\mathrm{SM}} \to g_{\mathcal{H}}\, g_{\mathcal{H}}) = \frac{\sin^2\theta}{4} \frac{\alpha_{s,\mathcal{H}}^2}{\alpha_s^2} \frac{v^2}{v_{\mathcal{H}}^2}\, \mathrm{BR}(h_{\mathrm{SM}} \to g\, g) \simeq \omega^2 \left(\frac{\mathrm{TeV}}{v_{\mathcal{H}}}\right)^4 2 \times 10^{-5}\,, \qquad (11)$$

where the factor $1/4$ comes from the ratio of the loop functions (fermionic top for the SM and scalar stops for the Hyperbolic sector) and the factor $v^2/v_{\mathcal{H}}^2$ comes from the ratio between the scales of the dimension-5 operators mediating the decay. We have also kept explicitly the factor $\alpha_{s,\mathcal{H}}^2/\alpha_s^2$ to account for different renormalisation effects in the SM and Hyperbolic sectors.

Assuming that there is no additional spontaneous symmetry breaking in the Hyperbolic sector, the phenomenology of these Hyperbolic gluons is much like those in Folded SUSY [?] or the fraternal Twin Higgs [?]. Once produced, the Hyperbolic gluons form Hyperbolic glueballs, the lightest of which have $J^{PC} = 0^{++}$ and decay back to the SM via Higgs mixing, with a proper length on the order of meters to kilometers. In contrast to Folded SUSY and the fraternal Twin Higgs, this is the only process leading to the production of Hyperbolic glueballs from SM states, as there are no open Higgs decay modes or Drell-Yan production channels involving additional states charged under Hyperbolic color. In this respect, the Hyperbolic Higgs is the most predictive model of neutral naturalness in terms of the SM production rate for dark glueball states. As with the fraternal Twin Higgs, however, the radial Hyperbolic Higgs mode provides an additional portal into the Hyperbolic sector.

The above glueball phenomenology assumes no additional spontaneous symmetry breaking in the Hyperbolic sector. However, the Hyperbolic stops may obtain a vacuum expectation value if the vacuum structure favors it. In this case Hyperbolic QCD and electromagnetism can be spontaneously broken, removing the light gauge bosons to leave no new light states below the weak scale. Not only does this significantly reduce collider and cosmological signatures, but it also raises the intriguing prospect that $2/3$ of the top partner degrees of freedom would be eaten, hence the longitudinal modes of the Hyperbolic gluons would also be top partners in this picture. The other $1/3$ of the top partner degrees of freedom would also mix with the Higgs boson, implying that *the Higgs is partially its own top partner*.

The phenomenology of the gauge neutral Hyperbolic sfermions may be varied. They may be stable, due to an unbroken $Z_{2R}$ symmetry. In this case the top partners may make up some part of the dark matter, as suggested in [11]. In the event that some Hyperbolic sfermions obtain vacuum expectation values, they are rendered unstable and decay back to the visible sector through the Higgs portal. This concludes our discussion of the Hyperbolic Higgs and the associated phenomenology.

**Acknowledgments**

I would like to thank Timothy Cohen, Nathaniel Craig, and Gian Giudice for their collaboration.

## References


1. V. L. Ginzburg and L. D. Landau, Zh. Eksp. Teor. Fiz. **20** (1950) 1064.
2. J. Bardeen, L. N. Cooper and J. R. Schrieffer, Phys. Rev. **106** (1957) 162. doi:10.1103/PhysRev.106.162
3. J. Bardeen, L. N. Cooper and J. R. Schrieffer, Phys. Rev. **108** (1957) 1175. doi:10.1103/PhysRev.108.1175
4. Z. Chacko, H. S. Goh and R. Harnik, Phys. Rev. Lett. **96** (2006) 231802 doi:10.1103/PhysRevLett.96.231802 [hep-ph/0506256].
5. Z. Chacko, H. S. Goh and R. Harnik, JHEP **0601** (2006) 108 doi:10.1088/1126-6708/2006/01/108 [hep-ph/0512088].
6. G. Burdman, Z. Chacko, H. S. Goh and R. Harnik, JHEP **0702** (2007) 009 doi:10.1088/1126-6708/2007/02/009 [hep-ph/0609152].
7. T. Cohen, N. Craig, G. F. Giudice and M. Mccullough, JHEP **1805** (2018) 091 doi:10.1007/JHEP05(2018)091 [arXiv:1803.03647 [hep-ph]].
8. J. Scherk and J. H. Schwarz, Nucl. Phys. B **153** (1979) 61. doi:10.1016/0550-3213(79)90592-3
9. J. Scherk and J. H. Schwarz, Phys. Lett. **82B** (1979) 60. doi:10.1016/0370-2693(79)90425-8
10. G. Aad *et al.* [ATLAS and CMS Collaborations], JHEP **1608** (2016) 045 doi:10.1007/JHEP08(2016)045 [arXiv:1606.02266 [hep-ex]].
11. D. Poland and J. Thaler, JHEP **0811** (2008) 083 doi:10.1088/1126-6708/2008/11/083 [arXiv:0808.1290 [hep-ph]].

# Searches for new resonances in dijet and dilepton final states with the ATLAS and CMS detectors

R. Goldouzian on behalf of the ATLAS and CMS Collaborations
*Interuniversity Institute for High Energies (IIHE), Physique des particules élémentaires, Université Libre de Bruxelles, ULB, 1050, Brussels, Belgium*

Searches for new massive resonances in final states with a pair of leptons or jets have always been a powerful tool for discovery in high energy physics. We review here the latest results from the ATLAS and CMS experiments, based on proton-proton collision data collected at the centre-of-mass energy of 8 and 13 TeV at the LHC. The LHC dijet searches explore both the low-mass range and the high mass end of the spectrum by employing several novel search strategies. The results are interpreted in a range of theories beyond the standard model of particle physics.

## 1 Introduction

One of the most striking signatures of physics beyond the standard model (SM) would be the observation of a narrow resonance in the invariant mass spectrum of lepton or jet pairs. Such resonances are predicted by many models designed to address the shortcomings of the SM, as for example models with dark matter (DM), the Z′ spin-1 boson from Grand Unified Theory (GUT) or the spin-2 Kaluza-Klein graviton (Randall-Sundrum model) [1,2].

At the CERN LHC, the searches for new resonances performed by the ATLAS and CMS Collaborations [3,4] have mostly focused on the production of high mass particles at the end of the spectrum. Searches at the low mass range are challenging because of the very large backgrounds. In the dijet final state, overwhelming event rates from QCD multijet events at low masses are beyond the trigger bandwidth of the CMS and ATLAS experiments, which limit the statistical power of the dijet resonance searches below 1 TeV. These difficulties are avoided by applying various new techniques like reducing event size, looking at boosted dijet events or selecting dijet events originated from the fragmentation of a b-quark. In this report we review the results of recent searches for high mass resonances in dijet and dilepton final states performed by the ATLAS and CMS Collaborations.

## 2 Dijet resonance searches

### *2.1 High mass dijet resonance searches*

Searches for high mass resonances decaying to dijet final states in proton-proton collisions at $\sqrt{s}$ = 13 TeV are performed by both ATLAS and CMS Collaborations [5,6]. Collision events are recorded by single-jet trigger with a $p_{\mathrm{T}}$ greater than 380 (500) GeV by the ATLAS (CMS) experiment. In addition, events are triggered if the scalar sum of jet $p_{\mathrm{T}}$ for all reconstructed jets with $p_{\mathrm{T}}$ >30 GeV and $|\eta|$ <3.0 is greater than 800 GeV by the CMS experiment. Events

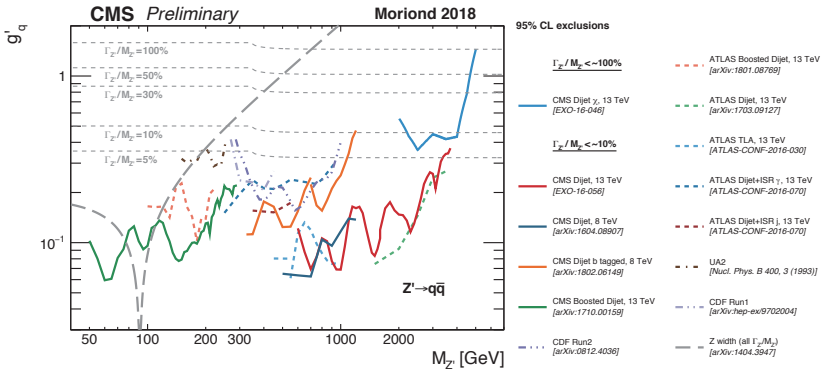


Figure 1 – Limits on the universal coupling $g'_q$ between a leptophobic Z′ boson and quarks from various dijet analyses from CMS, ATLAS, CDF, and UA2 [7].

are selected offline if at least two jets with $m_{jj}$ >1.1 TeV and $m_{jj}$ >1.25 TeV in the ATLAS and CMS analysis respectively for which the trigger is fully efficient.

The dominant background for this analysis is the QCD production of two or more jets which are simulated by Pythia8 Monte Carlo generator. The QCD background, mostly from t-channel dijet events, peaks at the large value of the rapidity/pseudorapidity separation of the two jets. On the other hand, new physics processes, mostly in the s-channel mode, have isotropic distribution for the mentioned variable. Therefore, the rapidity/pseudorapidity separation of the two jets are used in the ATLAS and CMS analyses to suppress the QCD background. After the selection, the observed number of dijet events falls smoothly as a function of mass and are very similar to the QCD prediction from Pythia8. Due to the challenging uncertainties on the prediction of the QCD background, the observed dijet mass spectra is fitted to estimate the SM background.

The dijet mass spectrum obtained in the ATLAS and CMS analyses are well described by the smooth falling data-driven distribution predicted by SM and no significance evidence for a high mass resonance is observed. Upper limits at 95% confidence level are set on the production cross section times the branching ratio for a narrow or wide heavy resonance. These results are interpreted to constrain a range of new physics scenarios as new heavy vector bosons (Z′,W′), excited quarks (q⋆), excited chiral bosons (W⋆), quantum black holes (QBH), Randall-Sundrum, etc. In figure 1, limits obtained by the ATLAS (dashed green line) and CMS (red line) Collaborations on the universal quark coupling $g'_q$ as a function of the resonance mass for a leptophobic Z′ resonance are shown.

### *2.2 Low mass dijet resonance searches*

Due to the high $p_T$ threshold of the single jet trigger (∼400 GeV), a large fraction of dijet events with an invariant mass below 1 TeV are not recorded by the trigger system. Recently, the ATLAS and CMS Collaborations employed an innovative data-taking approach, in which only a reduced set of trigger level information is recorded and analyzed [6,8]. Thus, by reducing the event size, the trigger acceptance rate is increased and the invariant mass region below 1 TeV becomes accessible. This approach is called "data scouting" and "trigger-object-level analysis" in CMS and ATLAS, respectively. The low mass resonance searches are performed by the ATLAS and CMS collaboration at $\sqrt{s} = 13$ TeV using 29.9 and 27 fb$^{-1}$ of data, respectively [6,8]. No significant local excess is observed compared to the SM prediction and upper limits are set at 95% CL on the signal cross section as a function of the resonance mass. The sensitivity

to the coupling to quarks, $g'_q$ is comparable between the ATLAS and CMS results, as shown in figure 1 with dashed blue line and red line, respectively.

### *2.3 Boosted dijet resonance searches*

Another approach for lowering the dijet mass range search is to trigger events where at least one high $p_T$ jet or photon from initial state radiation (ISR) is produced in association with a light dijet resonance. The high $p_T$ requirement on the ISR jet or photon leads to a boosted light resonance and its decay product become collimated. Therefore, the resonance mass is calculated from the mass of a large radius jet. The ATLAS and CMS Collaborations reported results of applying this technique to search for low mass resonances [9,10]. For the first time the mass range below 100 GeV is probed. In figure 1, excluded region for a light Z′ mass versus coupling values are shown from the ATLAS and CMS analyses.

### *2.4 Di-bjet resonance searches*

Another way for probing low dijet mass range is based on identifying b-jets at the trigger level. The background rate for $b\bar{b}$ final state is much lower compared to the inclusive dijet final states. The ATLAS and CMS collaboration, using this technique, could reach down to 570 and 325 GeV in dijet mass respectively [11,12]. No significant deviations from the SM expectation have been observed and limits at the 95% CL are set on the signal cross section.

## 3 Dilepton resonance searches

Both ATLAS and CMS Collaborations have searched for a heavy neutral particle decaying into an electron or muon pair at 13 TeV [13,14]. The CMS collaboration has updated the search for high mass resonance in dielectron final state using 41.6 $fb^{-1}$ of data recorded in 2017 [15]. Dilepton channels benefit from simple final state with low backgrounds from Drell-Yan, $t\bar{t}$, WW and multijets processes. No significant excess is observed in the measured dilepton mass spectra. The limits obtained by the ATLAS and CMS Collaborations are shown in figure 2. The limits exclude a $Z'_{SSM}$ boson with mass less than 4.7 TeV.

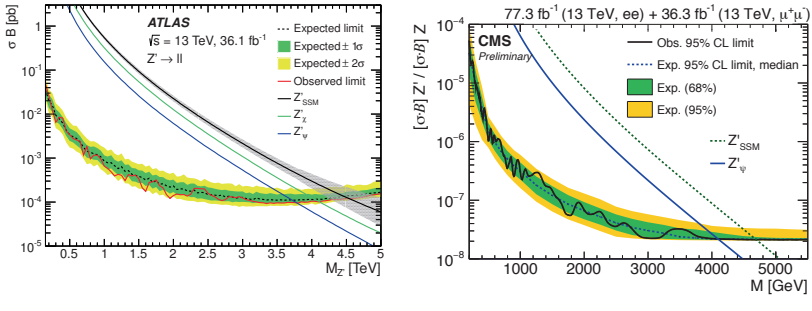


Figure 2 – The 95% CL upper limits on the production cross section times branching fraction for a spin-1 resonance using the ATLAS [11] (left) and CMS [15] (right) dilepton mass spectra. The CMS limits are relative to the production cross section times branching fraction for a Z boson

## 4 Dark matter interpretation

Searches for dijet and dilepton resonances exploit the fact that any mediator produced from quarks in the initial state can decay into quarks or leptons, which would lead to an excess over

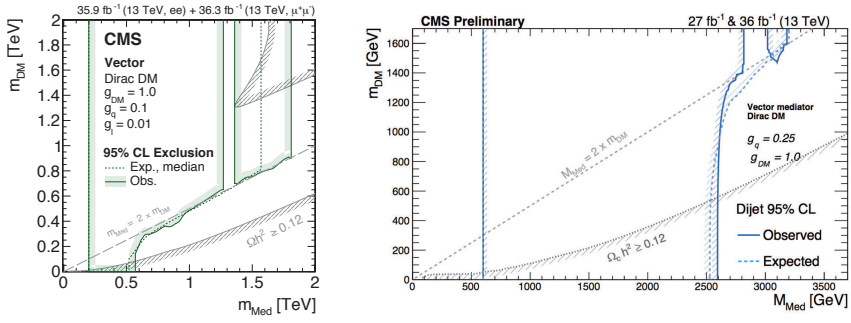


Figure 3 – The 95% CL observed (solid) and expected (dashed) excluded regions in the plane of dark matter mass versus mediator mass, for a vector mediator obtained from dilepton (left) and dijet (right) analyses. The constrain obtained from the cosmological relic density of DM is shown with light gray color.

the distribution of the invariant mass. Therefore, limits obtained from these searches can be reinterpreted to constrain simplified models of DM, with vector or axial vector mediators that couple to quarks and leptons. In figure 3, excluded region in the plane of dark matter mass versus mediator mass obtained from the CMS high mass dilepton and dijet resonance searches are shown [6,14] and compared to constraints from the cosmological relic density of DM.

## 5 Summary

The ATLAS and CMS Collaborations have searched for several types of new heavy resonances using dilepton and dijet final states in a wide range of mass. No significant excess has been observed and limits at the 95% confidence level have been set on a variety of models. Searches for new heavy resonances with the full run II dataset are underway and legacy results are expected to be released in the coming year.

## References


1. R. M. Harris and K. Kousouris, Int. J. Mod. Phys. A **26**, 5005 (2011).
2. E. Accomando, *et al*, Phys. Rev. D **83**, 075012 (2011).
3. ATLAS Collaboration, JINST 3:S08003 (2008).
4. CMS Collaboration, JINST 3:S08004 (2008).
5. ATLAS Collaboration, Phys. Rev. D **96**, no. 5, 052004 (2017)
6. CMS Collaboration, CMS-PAS-EXO-16-056.
7. https://twiki.cern.ch/twiki/bin/view/CMSPublic/SummaryPlotsEXO13TeV#Dijet_summary_plots.
8. ATLAS Collaboration, arXiv:1804.03496.
9. CMS Collaboration, JHEP **1801**, 097 (2018).
10. ATLAS Collaboration, arXiv:1801.08769.
11. ATLAS Collaboration, ATLAS-CONF-2016-031.
12. CMS Collaboration, arXiv:1802.06149.
13. ATLAS Collaboration, JHEP **1710**, 182 (2017).
14. CMS Collaboration, arXiv:1803.06292.
15. CMS Collaboration, CMS-PAS-EXO-18-006.

# Search for leptoquarks at CMS

David M. Morse on behalf of the CMS Collaboration
*Northeastern University, Boston, USA*

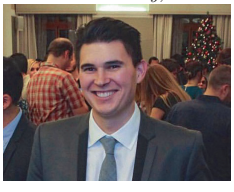

A summary of the current experimental searches for leptoquarks with the CMS detector at the CERN LHC is presented, along with updates of new results from analyses performed using the full 2016 proton-proton dataset, corresponding to 35.9 $\text{fb}^{-1}$.

## 1 Introduction

Leptoquarks (LQs) are new scalar or vector particles that carry both lepton and baryon number, and have fractional electric charge $\pm(1/3, 2/3, 4/3, 5/3)$e. They appear in a number of theories of physics beyond the standard model (SM) such as grand unified theories, technicolor, composite models, and R-parity violating supersymmetry (RPV SUSY). The free parameters of the theory include the mass of the leptoquark $\text{M}_{\text{LQ}}$; the LQ$\rightarrow \ell$q coupling $\lambda_{\text{LQ}}$; and $\beta$, the branching fraction of the LQ to a charged lepton and a quark, $\beta = \text{BF}(\text{LQ} \rightarrow \ell^{\pm}\text{q}) = 1 - \text{BF}(\text{LQ} \rightarrow \nu\text{q})$.

At the LHC, LQs can be singly or pair produced. Single LQ production cross section depends on $\lambda_{\text{LQ}}$, while pair production does not. For high values of $\text{M}_{\text{LQ}}$, single LQ becomes the dominant production mode, depending on the choice of the coupling $\lambda_{\text{LQ}}$, shown in Fig. 1 (left). Historically, and in the analyses presented here, searches for LQ assume no inter-generational mixing, in order to avoid tension with current bounds on flavor changing neutral currents and prompt proton decay. This leads to searches for LQs decaying to leptons and quarks of the same family, with final states $\ell^{\pm}\ell^{\mp}$qq, $\ell^{\pm}\nu$qq, and $\nu\nu$qq.

Interest in LQs has increased recently with the measurement of possible anomalies in the decays of B mesons seen at BaBar, Belle, and LHCb, which hint at possible lepton flavor non-universality. Leptoquarks are candidates to explain these anomalies at tree level, with particular emphasis on the second and third generations.

## 2 The CMS Detector

The central feature of the CMS apparatus is a superconducting solenoid of $6m$ internal diameter, providing a magnetic field of $3.8T$. Within the solenoid volume are a silicon pixel and strip tracker, a lead tungstate crystal electromagnetic calorimeter, and a brass and scintillator hadron calorimeter, each composed of a barrel and two endcap sections. Forward calorimeters extend

the pseudorapidity coverage provided by the barrel and endcap detectors. Muons are detected in gas-ionization chambers embedded in the steel flux-return yoke outside the solenoid.

A more detailed description of the CMS detector, together with a definition of the coordinate system used and the relevant kinematic variables, can be found in Ref. [1].

## 3 New CMS searches for leptoquarks

The new searches described here are performed with the full 35.9 fb$^{-1}$ CMS 2016 p-p dataset.

### *3.1 Third generation single LQ in the ττb channel*

This search represents the first search for third generation single LQ production [2]. This analysis selects at least one b-tagged jet and two $\tau$ mesons, separated into the $2\tau_{\rm had}$ and $\tau_{\rm had}$+lep (e,$\mu$) categories, where $\tau_{\rm had}$ represents a $\tau$ meson decaying hadronically. Limits at 95% confidence level (CL) are extracted through a simultaneous fit to the scalar sum $p_T$ distribution of the 3 channels. The $2\tau_{\rm had}$ channel drives the analysis sensitivity. Leptoquark masses below 744 GeV are excluded at 95% CL for $\beta$=1., $\lambda_{\rm LQ}$=1, shown in Fig. 1 (center). A two-dimensional scan is also performed in the $M_{LQ}$-$\lambda_{LQ}$ plane, for $0 < \lambda_{LQ} < 2.5$., shown in Fig. 1 (right).

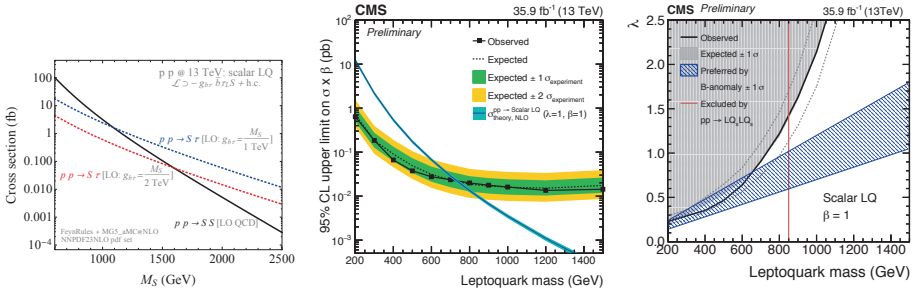


Figure 1 – Third generation single LQ in the ττb channel [2]. Left: LQ single and pair production cross sections for different values of $\lambda_{\rm LQ}$, from Ref. [6]. Center: 95% CL limits on the LQ mass. Right: 95% CL limits in the two-dimensional $M_{LQ}$-$\lambda_{LQ}$ plane.

### *3.2 First, second, third generation pair production in the νν+qq/bb/tt channel*

This analysis arises from a reinterpretation of SUSY searches for squark pair production decaying to a quark and neutralino $\tilde{q} \to q+\tilde{\chi}$ [3]. In the $\tilde{\chi} \to 0$ limit, this final state is equivalent to LQ→q+$\nu$. The search is performed for all flavors of quarks: light jets, b jets, t jets. A large number of categories are created, with different sensitivities in different channels. The most sensitive categories for the $\nu\nu$ tt channel for example requires large $M_{T2}$ >1500 GeV, 4-6 jets, and 1 or 2 b tagged jets. Squark signal sample acceptance and kinematics were shown to be consistent with LQ signal for both scalar and vector LQ. Limits are set at 95% CL in the $\nu\nu$+qq, $\nu\nu$+bb, and $\nu\nu$+tt channels for $\beta = 0$ and $\lambda_{\rm LQ} = 1$. Limits are also set in the $\nu\nu$+tt channel for $\beta = 1/2$ and $\lambda_{\rm LQ} = 1$, motivated by a model proposed in Ref. [6]. The limits are shown in Fig. 2.

### *3.3 Second generation pair production in the μμjj and μνjj channels*

This search looks for second generation LQs in two channels ($\mu\mu$jj and $\mu\nu$jj) with similar search strategies [4].One or two high momentum muons are selected, and 2 jets are required, with no jet flavor requirement. Candidate LQs are constructed from the $\ell^{\pm}$–LQ or $p_T^{miss}$–LQ pairs that minimize $|M_{LQ1}-M_{LQ2}|$. Final selections are optimized using 3 independent sensitive variables

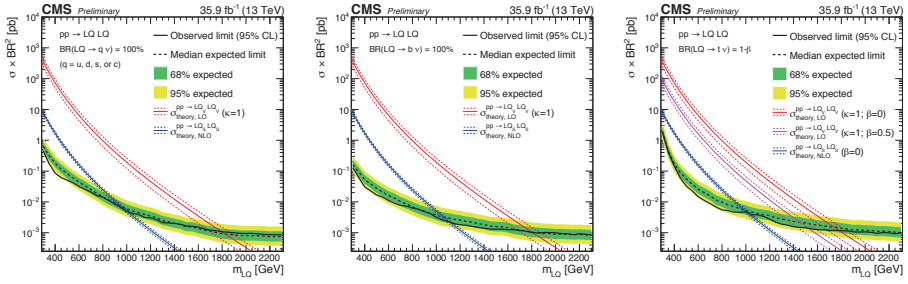


Figure 2 – First, second, third generation pair production in the $\nu\nu$+qq/bb/tt channel [3]. 95% CL limits on scalar and vector LQ masses in the $\nu\nu$+qq (left), $\nu\nu$+bb (center), and $\nu\nu$+tt (right) channels. The parameter $\kappa$ represents the coupling $\lambda_{LQ}$.

for each LQ mass hypothesis from 200-2000 GeV, and 95% CL limits are via a counting experiment. The limits are expressed as a function of $M_{LQ}$, shown for the $\mu\mu$jj ($\mu\nu$jj) channel in Fig. 3 left (center). These limits are also expressed in the two-dimensional $\beta-M_{LQ}$ plane, shown in Fig. 3 (right) for both channels as well as the combination of the two channels, for $0< \beta <1$. Both the $\beta =1$ and $\beta =1/2$ limits extend the LQ mass exclusion by more than 300 GeV.

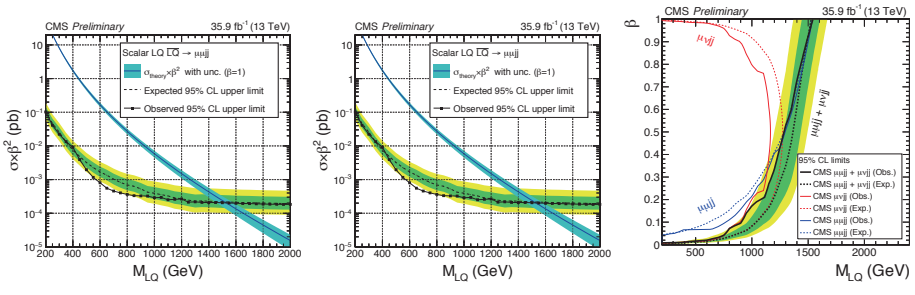


Figure 3 – Second generation pair production in the $\mu\mu$jj and $\mu\nu$jj channels [4]. 95% CL limits on scalar LQ masses in the $\mu\mu$jj (left) and $\mu\nu$jj (center) channels. Right: 95% CL limits in the two-dimensional $\beta-M_{LQ}$ plane for both channels as well as the combination of the two channels, for $0< \beta <1$.

### *3.4 Pair production of 3rd generation leptoquarks decaying to ττtt*

This analysis searches for pair production of 3rd generation leptoquarks decaying to $\tau\tau tt$ [5]. Categories are built from the $2\tau$+$2b$+$2W$ decay products: opposite-sign $(e/\mu + \tau_{had})$ + b tagged jet, and same-sign $(e/\mu + \tau_{had})$ + b-tagged jet. These two categories are further split into low and high scalar sum $p_T$ regions. The top candidate is reconstructed by choosing the three-jet combination closest to the top mass. A data control region with inverted $\tau_{had}$ isolation is used to estimate the $t\bar{t}$ and W+jets backgrounds, after being corrected for kinematical differences. The top $p_T$ spectrum is then used to extract 95% CL limits. A third category is built in the $e/\mu$ + 2 $\tau_{had}$ channel. Here the main backgrounds arise from jets faking hadronic taus. Multiple data control regions are used to estimate the backgrounds, and 95% CL limits are set via a counting experiment. In the end all categories are recombined, and limits are set as a function of $M_{LQ}$ for $\beta = 1$ and in the 2-dimensional $\beta$ vs $M_{LQ}$ plane, shown in Fig. 4 left and right, respectively.

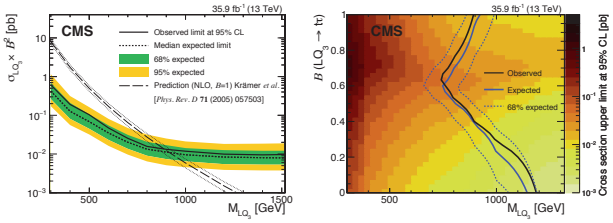


Figure 4 – 95% confidence level limits on pair production of 3rd generation leptoquarks decaying to $\tau\tau tt$ as a function of $M_{\mathrm{LQ}}$ for $\beta = 1$ (left) and in the 2-dimensional $\beta$ vs $M_{\mathrm{LQ}}$ plane (right) [5].

## 4 Summary

CMS has a large and expanding program of leptoquark searches. A summary of all the CMS leptoquark current exclusion limits is presented in Fig. 5 as a function of LQ mass. New results with the full 2016 proton-proton dataset have been presented for leptoquark single and pair production, in all three generations, in scalar and vector LQ models, and for multiple model parameters. Many channels push the sensitivity to LQ masses above the TeV scale. Intriguing hints of new physics in B meson decays have recently increased interest in leptoquarks, particularly associated with decays to third generation quarks and leptons, and may warrant investigation into final states or model phase space not previously considered.

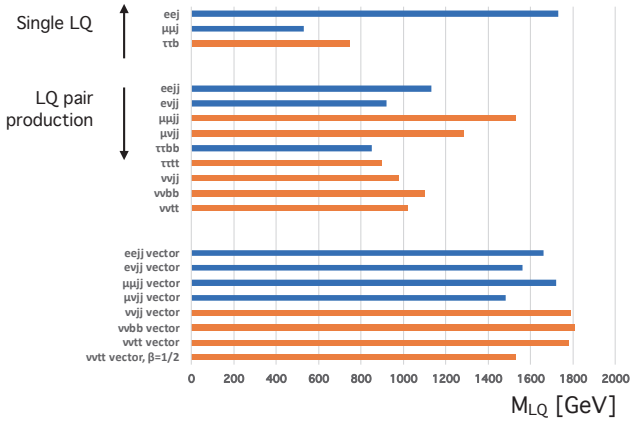


Figure 5 – Summary of CMS leptoquark results.

## References


1. CMS Collaboration, JINST **3**, S08004 (2008) doi:10.1088/1748-0221/3/08/S08004
2. CMS Collaboration, CMS-PAS-EXO-17-029. **https://cds.cern.ch/record/2308274**.
3. CMS Collaboration, CMS-PAS-SUS-18-001. **https://cds.cern.ch/record/2308307**.
4. CMS Collaboration, CMS-PAS-EXO-17-003. **https://cds.cern.ch/record/2308268**.
5. CMS Collaboration, CMS-PAS-B2G-16-028 [arXiv:1803.02864 [hep-ex]], Submitted to EPJC. **https://cds.cern.ch/record/2307701**.
6. D. Buttazzo, A. Greljo, G. Isidori and D. Marzocca, JHEP **1711**, 044 (2017) doi:10.1007/JHEP11(2017)044 [arXiv:1706.07808 [hep-ph]].
7. I. Dorner and A. Greljo, arXiv:1801.07641 [hep-ph].

# SEARCH FOR DARK PHOTONS AT NA62

Marco Mirra [a]
*Department of Physics "Ettore Pancini" of Università degli Studi di Napoli Federico II*

Fixed target experiments are a particularly useful tool in the search of very weakly coupled particles in the MeV-GeV range that could represent the mediators of a number of portals to a hidden sector, an example being the dark photon. The NA62 experiment at the CERN SPS is currently taking data. High-intensity setup and detector performance make NA62 particularly suited for searching new-physics in the hidden sector. We will report the status and prospects of the dark photon searches in the NA62 framework.

## 1 Introduction

The widely believed and presently well-established presence of a cosmic dark matter (DM) suggests us a clear evidence for physics beyond the Standard Model (SM): no SM particle satisfies the dark-matter properties deduced from observational cosmology. The dominance of DM on ordinary matter in the universe might suggest the existence of an entirely new dark sector with specific forces and particles, fleebly coupled to the SM. The link between the two worlds might lie in certain portal states, which we can classify according to the related transformation laws of the effective interactions lagrangian. In a rather general set of hidden sector models with an extra U(1) gauge symmetry [1], the interaction of a dark photons (denoted A') with the visible sector proceeds through kinetic mixing with the SM hypercharge. Such scenarios with GeV-

[a] On behalf of the NA62 Collaboration: R. Aliberti, F. Ambrosino, R. Ammendola, B. Angelucci, A. Antonelli, G. Anzivino, R. Arcidiacono, M. Barbanera, A. Biagioni, L. Bician, C. Biino, A. Bizzeti, T. Blazek, B. Bloch-Devaux, V. Bonaiuto, M. Boretto, M. Bragadireanu, D. Britton, F. Brizioli, M.B. Brunetti, D. Bryman, F. Bucci, T. Capussela, A. Ceccucci, P. Cenci, V. Cerny, C. Cerri, B. Checcucci, A. Conovaloff, P. Cooper, E. Cortina Gil, M. Corvino, F. Costantini, A. Cotta Ramusino, D. Coward, G. D'Agostini, J. Dainton, P. Dalpiaz, H. Danielsson, N. De Simone, D. Di Filippo, L. Di Lella, N. Doble, B. Dobrich, F. Duval, V. Duk, J. Engelfried, T. Enik, N. Estrada-Tristan, V. Falaleev, R. Fantechi, V. Fascianelli, L. Federici, S. Fedotov, A. Filippi, M. Fiorini, J. Fry, J. Fu, A. Fucci, L. Fulton, E. Gamberini, L. Gatignon, G. Georgiev, S. Ghinescu, A. Gianoli, M. Giorgi, S. Giudici, F. Gonnella, E. Goudzovski, C. Graham, R. Guida, E. Gushchin, F. Hahn, H. Heath, T. Husek, O. Hutanu, D. Hutchcroft, L. Iacobuzio, E. Iacopini, E. Imbergamo, B. Jenninger, K. Kampf, V. Kekelidze, S. Kholodenko, G. Khoriauli, A. Khotyantsev, A. Kleimenova, A. Korotkova, M. Koval, V. Kozhuharov, Z. Kucerova, Y. Kudenko, J. Kunze, V. Kurochka, V.Kurshetsov, G. Lanfranchi, G. Lamanna, G. Latino, P. Laycock, C. Lazzeroni, M. Lenti, G. Lehmann Miotto, E. Leonardi, P. Lichard, L. Litov, R. Lollini, D. Lomidze, A. Lonardo, P. Lubrano, M. Lupi, N. Lurkin, D. Madigozhin, I. Mannelli, G. Mannocchi, A. Mapelli, F. Marchetto, R. Marchevski, S. Martellotti, P. Massarotti, K. Massri, E. Maurice, M. Medvedeva, A. Mefodev, E. Menichetti, E. Migliore, E. Minucci, M. Mirra, M. Misheva, N. Molokanova, M. Moulson, S. Movchan, M. Napolitano, I. Neri, F. Newson, A. Norton, M. Noy, T. Numao, V. Obraztsov, A. Ostankov, S. Padolski, R. Page, V. Palladino, C. Parkinson, E. Pedreschi, M. Pepe, M. Perrin-Terrin, L. Peruzzo, P. Petrov, F. Petrucci, R. Piandani, M. Piccini, J. Pinzino, I. Polenkevich, L. Pontisso, Yu. Potrebenikov, D. Protopopescu, M. Raggi, A. Romano, P. Rubin, G. Ruggiero, V. Ryjov, A. Salamon, C. Santoni, G. Saracino, F. Sargeni, V. Semenov, A. Sergi, A. Shaikhiev, S. Shkarovskiy, D. Soldi, V. Sougonyaev, M. Sozzi, T. Spadaro, F. Spinella, A. Sturgess, J. Swallow, S. Trilov, P. Valente, B. Velghe, S. Venditti, P. Vicini, R. Volpe, M. Vormstein, H. Wahl, R. Wanke, B. Wrona, O. Yushchenko, M. Zamkovsky, A. Zinchenko

scale dark matter provide possible explanations to the observed rise in the cosmic-ray positron fraction with energy and the muon gyromagnetic ratio (g-2) measurement [2].
A plaethora of searches have been performed for dark photons, that can be divided into:

- short-lived: searches where the dark photon decays soon after production in the final state, such as in the decay chain $\pi^0 \to \gamma A', A' \to e^+e^-$.

- long-lived: searches where dark photon moves in the experimental apparatus before decaying to a visible final state.

NA62 [3] is a fixed target experiment at CERN using 400 GeV protons from the Super-Proton-Synchrotron (SPS) facility hitting a beryllium target to produce a 75 GeV momentum selected intense secondary beam of positive particles, 6% of which are charged kaons. NA62 has been designed and built requiring high intensity, full particle identification, hermetic coverage and low material badget, high rate tracking. Such setup might be suited for both dark photon searches listed above.

## 2 NA62 experimental apparatus

The NA62 experiment aims to measure the BR($K^+ \to \pi^+\nu\bar{\nu}$) with 10% precision. Since the SM predicts [4] a BR($K^+ \to \pi^+\nu\bar{\nu}$) $= (8.4 \pm 1.0) \times 10^{-11}$, it needs to collect about $10^{13}$ $K^+$ decays for a 10% signal acceptance. Keeping the background to signal ratio about 10% requires the use of redundant experimental techniques to suppress unwanted final states. Fig. 1 shows a schematic view of the NA62 experimental apparatus [3]. Primary SPS protons ($3.3 \times 10^{12}$

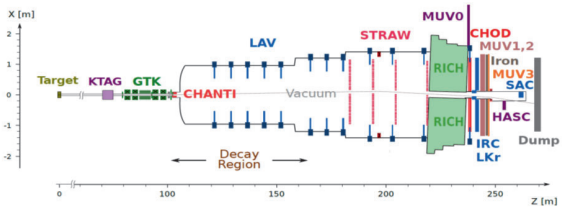


Figure 1 – NA62 experimental apparatus

protons per pulse at full intensity) strike a berillium target from which a secondary charged hadron beam of 75 GeV/c is selected and transported to the decay region. The incoming kaon is positively identified by a differential Cerenkov counter (KTAG) and its momentum and direction are measured by three stations of Si pixel detectors (GTK). A decay tank, holding a $10^{-6}$ mbar vacuum, is surrounded by lead-glass annular calorimeters (LAV) designed to efficiently detect photons up to 50 mrad. Four stations of straw chambers (STRAW) in vacuum trace downstream charged particles. A RICH identifies the secondary charged pion foreseen in signal events; plastic scintillators (CHOD) are used for triggering and timing. Photon rejection in the forward region is provided by an electromagnetic calorimeter based on liquid krypton (LKr) and two small angle calorimeters (IRC and SAC). Hadron calorimeters (MUV1,2) and a plastic scintillator detector (MUV3) placed downstream an iron-based absorber are used to detect hadrons and muons. Information from CHOD, RICH, MUV3 and LKr are hardware processed to issue level zero trigger conditions. Software-based algorithms from KTAG, CHOD, LAV and STRAW information provide higher level trigger requirements. Low intensity data have been taken in 2015 to study detector performances and to perform physics analysis. Since 2016 NA62 is collecting data for the measurement of the BR($K^+ \to \pi^+\nu\bar{\nu}$) and other physics cases.

## 3 Search for dark photons in NA62 apparatus

A large variety of searches for hidden sector particles can be performed at NA62 using kaon decays. Examples are: search for a axion-like particle ($a$) from the decay $K^+ \to \pi^+ a$, search for heavy neutral leptons ($N$) in the decays $K^+ \to \mu^+/e^+ N_{\mu/e}$, search for a dark photon in the decay $K^+ \to \pi^+\pi^0, \pi^0 \to \gamma A'$, with $A'$ decaying to invisible final states. The latter has been performed using $1.5 \times 10^{10}$ $K^+$ decays, corresponding to about 5% of the dataset collected in 2016. Events with a single downstream track reconstructed in the STRAW spectrometer are selected. The downstream track is required to match in time and space a GTK track, forming a vertex in the fiducial volume of the experimental apparatus. The GTK track is identified as a $K^+$ by the KTAG detector. The RICH and the calorimeters system identify the downstream track as a pion. The missing mass obtained from the momentum of the downstream and GTK tracks is required to be around the $\pi^0$ mass peak. Events with a single photon cluster in the LKr calorimeter are selected. No activity in time with the selected events in LAV, IRC and SAC detectors is required. Given the kaon, pion and photon momenta, the squared missing mass $M^2_{mass} = (P_K - P_\pi - P_\gamma)^2$ is expected to peak around the $A'$ mass for the $\pi^0 \to \gamma A'$ decay and around zero for the background process $\pi^0 \to \gamma\gamma$ decays with one photon undetected. A data-driven background estimate, based on the tail with negative missing mass values, is used. For each $A'$ mass, the signal region is defined as a 1.5-standard deviation range around the expected invariant mass peak. Frequentistic 90% CL intervals have been determined, taking into account the uncertainties of signal efficiency from MC determination, and the statistical uncertainties of data counts and background expectations. No statistically significant excess has been detected and upper limits have been computed on the number of signal events. The 90% confidence level exclusion limit on the kinetic mixing parameter versus the mass of the dark photon is shown in Fig. 2 together with the limits from BaBar [5], NA64 [6] and E949 [7] experiments.

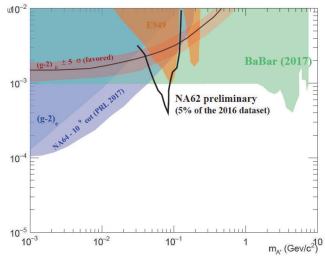


Figure 2 – 90% CL exclusion limit in the $\epsilon$ versun $m_{A'}$ plane for $\pi^0 \to \gamma A'$ events with $A'$ decaying into invisible final states. The limits from BaBar [5], NA64 [6] and E949 [7] are also shown together with the region of the parameters that could explain (g-2)$_\mu$ anomaly (red band) and the region excluded by the agreement of the anomalous magnetic moment of the electron (g-2)$_e$ with the expectations (dark blue shaded area).

## 4 Search for dark photons in NA62 beam-dump mode

Feebly-interacting exotic particles can be originated also by the decay of beauty and charm hadrons, and by virtual photons produced in the interaction of protons with a dump. Their couplings to SM particles are very suppressed leading to expected production rates of $10^{-10}$ or less. Since in this energy range the charm and beauty cross-sections steeply increase with the energy, a high-intensity, high-energy proton beam is required: the 400 GeV/c primary proton beam line serving the NA62 experiment can produce high intensity fluxes of beauty and charm hadrons. The Beryllium target used by NA62 is followed by two 1.6m long, water-cooled, beam-defining copper collimators (TAX) which can act also as a dump ($\sim 10.7\lambda_I$ ). In the standard NA62 operation, roughly 50% of the beam protons punch through the beryllium target and

are absorbed by the TAX collimators. The experimental signature of hidden sector decays into SM particles is two or more tracks or two photons originating from the same point of the decay volume and nothing else. For example dark photons can be produced in decays of mesons created in the beam dump, assuming $A'$ is coupled to quarks, or in hard Bremsstrahlung from the beam protons. NA62 can search for visible decays of $A'$ to $e^+e^-$ and $\mu^+\mu^-$ pairs. Fig. 3 shows the expected sensitivities assuming $10^{18}$ protons on target (equivalent of 1 year of running) and zero background, taking into account the trigger efficiency and detector acceptance.

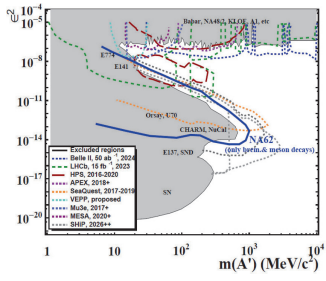


Figure 3 – NA62 sensitivity (90% CL exclusion limit) for $10^{18}$ proton on target in the coupling versus mass plane for dark photon (blue solid line) originated by the dump.

NA62 could be sensitive to even larger phase space since, in the estimate in fig. 3, only production in the Beryllium target is considered and not in the TAX. During the 2016 run NA62 collected several hours of data at different intensities with the Beryllium target lifted from the beam and closed TAX. The collected data is used for feasibility studies and tests of the zero background hypothesis. A preliminary analysis indicates that zero background might be achievable [8].

## 5 Conclusion

NA62 is successfully running in the North Area of the CERN SPS. Owing to the high beam energy and high beam intensity, the long decay volume and the hermetic detector coverage, NA62 has the opportunity to directly search for a plethora of hidden-sector particles, both in visible or invisible final states. Before the LS2 (2018) many searches in the hidden sector will be performed using the kaon beam and preliminary results concerning dark photon, based on 5% of 2016 data sample, were shown. The NA62 collaboration is currently discussing the possibility to use a fraction of the beam time during Run 3 (2021-2023) to operate NA62 in beam-dump mode: this would open a window of opportunity to search for hidden particles from charm and beauty meson decays. The current NA62 run can be exploited to evaluate background rejection capability up to $10^{17} - 10^{18}$ proton on target.

## References


1. B. Holdom, Phys. Lett. B 166 (1986) 196.
2. M. Pospelov, Phys. Rev. D 80 (2009) 095002.
3. The NA62 Collaboration, JINST12, P05025 (2017).
4. A.J. Buras, D. Buttazzo, J. Girrbach-Noe and R. Knegjens, JHEP 1511, 33 (2015).
5. BaBar collaboration (J. P. Lees et al.), arXiv:1702.03327.
6. NA64 collaboration (D. Banerjee et al.), Phys. Rev. Lett. 118 (2017) no.1, 011082.
7. E949 collaboration (A. V. Artamonov et al.), Phys. Rev. D79 (2009) 092004.
8. T. Spadaro, 2016 Physics beyond colliders workshop @ CERN (7 Sep 2016)

# Status and Prospects from the Fermilab Muon $g$–2 Experiment

M. W. Smith
*Instituto Nazionale di Fisica Nucleare*
*Edificio C - Polo Fibonacci Largo B. Pontecorvo, 3*
*56127 Pisa, Italy*

The anomalous magnetic moment of the muon is a quantity which arises from fundamental interactions in all sectors: Weak, QED, and QCD. As such, a high precision measurement of the quantity is also a high precision probe into the Standard Model of particle physics, and currently there exists statistical tension greater than three sigma between the experimentally measured and theoretically predicted values for anomaly, $a_\mu$. The tension makes the anomaly a valuable window into possible effects beyond the standard model, and calls for the need to measure it to even higher precision. The Fermilab Muon $g$–2 Experiment aims to do just that. The experiment endeavors to improve on the precision previous measurements of the muon anomalous magnetic moment by a factor of four, reaching an overall relative accuracy of 140 ppb. Currently the experiment has undergone a commissioning phase and has begun to the initial production of physics data.

## 1 Introduction

The Fermilab (FNAL) Muon $g$–2 experiment uses similar techniques as previous iterations of the measurement at Brookhaven National Lab[1] and CERN. Improvement in precision is attained by leveraging hardware upgrades alongside statistical gains. In short, the experiment is represented by equation 1. The experiment combines data from various hardware systems to produce two frequencies. One of these frequencies represents the anomalous magnetic moment directly in the experiment setup, $\omega_a$, and the other is the free proton precession frequency in the magnetic field used to store muons, $\omega_p$. The extracted frequencies are combined with several other quantities measured in other experiments.

$$a_\mu = \frac{\omega_a}{\omega_p}\frac{\mu_p}{\mu_e}\frac{m_\mu}{m_e}\frac{g_e}{2} \tag{1}$$

## 2 Status of Theory

Alongside the aspirations of the Fermilab Muon $g$–2 Experiment, a parallel effort to improve uncertainty is being undertaken by the theory community. The largest source of uncertainty in

the theoretical calculation arises in the QCD sector, specifically hadronic light-by-light (HLbL) and hadronic vacuum polarization (HVP). Improvements to these calculation come from several approaches. The HVP calculation can be improved by incorporating more cross-section data of $e^+e^- \rightarrow hadrons$. As for the HLbL, one approach aims to perform the calculation using lattice QCD [4]. Another approach uses a data driven technique to perform the calculation in a new way [5]. The current status of the theoretical calculation is shown in figure 1, a persistent difference between theory and experiment of more than 3 sigma. In figure 1, DHMZ is from reference [6], HLMNT is from reference [7], and "SMXX" is central value of the two models with the predicted increase in precision from additional cross-section data [8]. A more detailed treatment of the theory can be found in the full review [8].

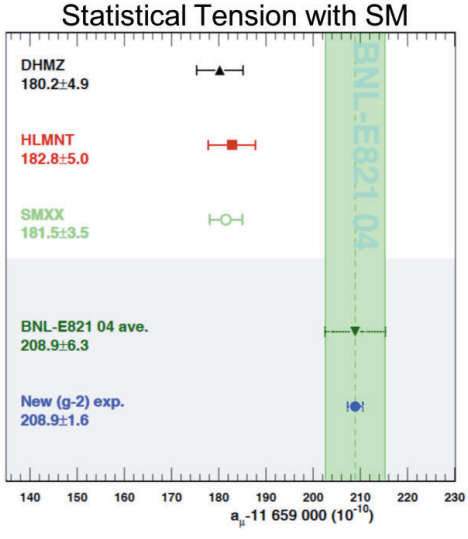


Figure 1 – The figure shows calculated theory values compiled by different groups as compared to the most recent measurement and the target precision for the current Fermilab $g$–2 experiment. A discrepency between the values of more than three sigma persists.

## 3 Status of Experiment

Over the past year, the $g$–2 experiment has come online. The process included a commissioning phase in summer 2017. During commissioning, many hardware systems were integrated together. Also importantly, the experiment tested data acquisition and analysis software with the first muon events. Beginning in January 2018, the experiment started collecting the first run of production physics data.

### *3.1 Experiment Principles*

The experiment can be broken down into four different phases. The muon production phase which is carried out by the Accelerator Division at Fermilab. In this phase, the spin polarized beam of muons is produced from pion decay. The muon injection phase in which the muons are transported from the beamline into the $g$–2 storage magnet. The muon storage phase is achieved through the experiment's magnetic storage ring. During the storage phase, the muon's spin vector phase advances on the muon's momentum vector at a rate directly proportional to $g$–2. And finally, the muon decay phase where the calorimetry system measures the decay positrons

(or electrons). Throughout all these phases asynchronous measurements are taken to monitor many hardware systems of the experiment. The overall design and many components are reused from the previous experiment at Brookhaven National Lab, but reaching the unprecedented precision goals of the experiment involves improvements across many of the hardware systems. Additionally, the experiment will need a 21-fold increase in event statistics. For more information about the experiment design see the experiment's technical design report [2].

### *3.2 Muon Production*

The Fermilab Accelerator Division manages the muon beamline, and they began delivering beam to the experiment in July 2017. After a break for upgrades, the Accelerator Division resumed muon production in Nov 2017. The muons arrive at the ring in 16 bunches of $\sim 10^6$ every 1.4 second supercycle. After months of beam upgrades, commissioning and tuning, the AD begin delivering physics quality beam to the experiment in February 2018.

### *3.3 Muon Injection*

The muon injection process in $g$–2 uses two main active hardware systems and three detector systems. The first step in injection is guiding the muons from the beamline through the outside of the muon storage magnet. The second step in the process of injection is adjusting the orbit mismatch by imparting a momentum deflection with an impulse from transient magnetic fields.

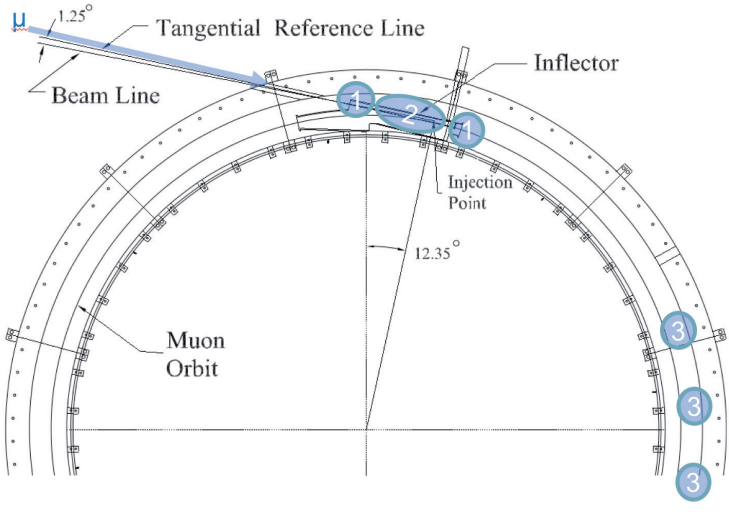


Figure 2 – The incoming muon beam and a portion of the storage magnet are shown in the image. The regions labeled 1 are the locations of the IBMS detectors. The region labeled 2 is the location of the inflector magnet. And, the region labeled 3 is the location of the fast kicker magnets. The inflector mitigates the effects of the fringe field from the storage region and the fast kicker magnets impart a momentum shift to the injected muons to the shift the orbit onto the central orbit of the storage magnet.

In the first stage, the inflector magnetic was reused from the previous g-2 experiment at Brookhaven. The superconducting magnetic is designed to cancel the fringe field of the main storage magnetic and facilitate a straight injection trajectory [3]. The device was installed and powered successfully at Fermilab. The kicker system was redesigned to improve upon the BNL system. The fast kicker magnet uses a transient magnetic field to shift the momentum of the muon beam by roughly 10 milliradians as the muons first pass. It must then turn the field off

very quickly to avoid re-kicking muons on the second pass, 149 ns later. The new kicker system uses a Blumlein circuit to create a magnetic field with a smaller temporal footprint and reduce the systematic effects of kicker magnetic fields on muons on subsequent orbits around the ring. The system is in use, and still being optimized.

The injection system also makes use of some detector systems. Near the interface between the beamline and the $g$–2 apparatus, there is a scintillating detector which is used for determining the timing of the muon bunches which are injected into the ring. Additionally, there are the IBMS detectors which measure the profile of the muon beam before and after traveling through the inflector magnet. Both systems are operational and have been used to optimize the number of muons stored in the main storage magnet.

### *3.4 Muon Storage*

After injection, the muons undergo cyclotron motion inside the main storage magnet. The cyclotron motion is maintained by the largest piece of hardware in the experiment, the main storage magnet which produces a highly uniform 1.4513 Tesla vertical magnetic field. The field uniformity is improved upon from the previous experiment by more than a factor of two which reduces the potential systematic uncertainty imparted by understanding the magnetic field experienced by the stored muons. The absolute field calibration system uses the NMR probes from BNL, as well as implementing new, high sensitivity NMR probes using $H_2O$ proton sample volumes and ongoing work to implement a new probe with a $^3He$ sample.

The beam dynamics of the injected muons are optimized using a few different hardware systems. There is a collimation system which consists of movable metal annuli at several points around the storage ring. The system removes muons which have aberrant orbit radii and heights as well as muons with large oscillations. After a few microseconds of beam scraping, the remaining muons are more normalized. The beam collimation system is installed and operational. In addition, the beam dynamics are affected by electrostatic focusing quads located at 4 locations around the ring. The quads were upgraded to be able to operate at higher voltages to provide a greater range of potential operating points that reduce the impact of resonances and coherent betatron oscillations.

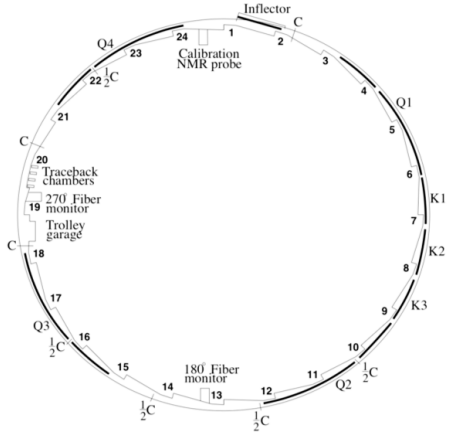


Figure 3 – The diagram above is an overview of the systems used in the muon storage volume. The collimators are labeled with the letter C. Some of these are prefixed with 1/2 as they are only semi-annuli instead of full. The fast kickers are labeled K1, K2, K3. The electrostatic focusing quads are labeled Q1, Q2, Q3, and Q4. Other systems are labeled clearly in the diagram.

The main detector system used to measure the muon beam dynamics in situ is the the fiber harp detectors. The detectors use a set of scintillating fibers aligned to the vertical plane at the storage volume in two locations in the magnetic storage ring. The detectors are able to reconstruct the radial profile of the beam and monitor beam dynamics.

### *3.5 Muon Decay*

The stored muons eventually decay into positrons which necessarily have a lower energy than the stored muon. As a consequence they have a smaller cyclotron radius, meaning they curl inwards where they are detected with the calorimetry system. The new calorimeter system improves upon the previous experiment by including segmentation and tighter pulse timing. The segmentation improves separability between multiple positrons which are near in spatial position, and the calorimeter uses only Cerenkov radiation to improve temporal pileup. Pileup was a large systematic error from the previous experiment that will be improved by the new calorimetry system. The calorimeter system has been commissioned and is fully operational.

Another large systematic from the previous experiment came from gain fluctuations of the calorimetry system. The Fermilab $g$–2 experiment adds a laser calibration system to measure and correct gain fluctuations in the calorimeter system. The system faciliates measuring short time scale gain fluctuations within a fill as well as long term drift in the calorimeter system with high precision. The gain changes must be corrected at a relative level of $10^{-4}$ within a fill. The laser system is installed an operational with study of the gain fluctuations and corrections underway.

On two of the calorimeter stations there is an additional detector system in place. The tracker system is comprised of a set of wire chamber planes as shown in figure 4. Measurements made by the tracker system can be used to reconstruct the trajectory of the decay positron and, with sufficient statistics, the beam profile of the stored muons. The tracker system has been installed at two locations which are fully operational. There is the possibility to install a third tracker in the future.

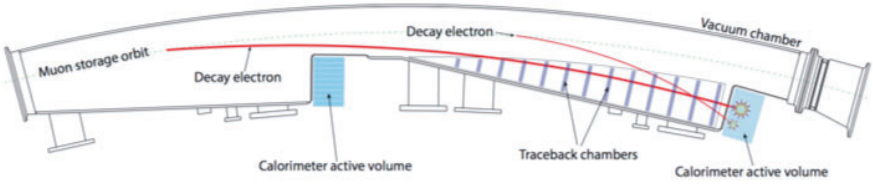


Figure 4 – The figure depicts typical trajectories of the decay positrons and the systems used to make measurements of those particles. The calorimeters shown are 2 of 24 around the storage ring, and they measure the energy of the positron to about 3% resolution. The traceback detector, one of two around the ring, is able to reconstruct the path of the positron and yield information about the muon profile in the storage volume.

## 4 Outlook and Conclusions

In summary, the Fermilab Muon $g$–2 Experiment is making its way forward. All major subsystems are commissioned and operational. The muons spins are precessing as evidenced in figure 5. Additionally the first production data run has started where we anticipate collecting events at similar statistical levels as the Brookhaven Experiment. The collaboration will be working hard on analysis and systematic studies to yield a measurement result as soon as reasonably possible.

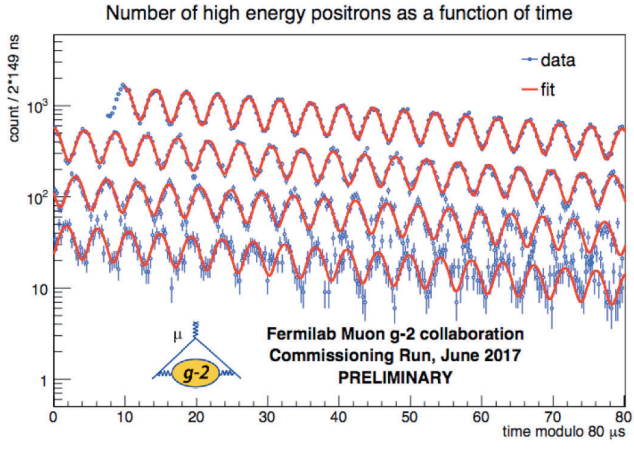


Figure 5 – The muon precession frequency as evidence from the commissioning data. Statistics are low but promise for the experiment is high.

## References


1. G. W. Bennett *et al.* [Muon g-2 Collaboration], Phys. Rev. D **73** (2006) 072003 doi:10.1103/PhysRevD.73.072003 [hep-ex/0602035].
2. J. Grange *et al.* [Muon g-2 Collaboration], arXiv:1501.06858 [physics.ins-det].
3. A. Yamamoto *et al.*, Nucl. Instrum. Meth. A **491** (2002) 23. doi:10.1016/S0168-9002(02)01232-9
4. T. Blum, N. Christ, M. Hayakawa, T. Izubuchi, L. Jin, C. Jung and C. Lehner, Phys. Rev. Lett. **118** (2017) no.2, 022005 doi:10.1103/PhysRevLett.118.022005 [arXiv:1610.04603 [hep-lat]].
5. M. Hoferichter, B. L. Hoid, B. Kubis, S. Leupold and S. P. Schneider, arXiv:1805.01471 [hep-ph].
6. M. Davier, A. Hoecker, B. Malaescu and Z. Zhang, Eur. Phys. J. C **71** (2011) 1515 Erratum: [Eur. Phys. J. C **72** (2012) 1874] doi:10.1140/epjc/s10052-012-1874-8, 10.1140/epjc/s10052-010-1515-z [arXiv:1010.4180 [hep-ph]].
7. K. Hagiwara, R. Liao, A. D. Martin, D. Nomura and T. Teubner, J. Phys. G **38** (2011) 085003 doi:10.1088/0954-3899/38/8/085003 [arXiv:1105.3149 [hep-ph]].
8. T. Blum, A. Denig, I. Logashenko, E. de Rafael, B. Lee Roberts, T. Teubner and G. Venanzoni, arXiv:1311.2198 [hep-ph].

# RECENT RESULTS FROM THE VEPP2000 $e^+e^-$ COLLIDER

E.P. SOLODOV
On behalf of CMD-3 and SND Collaborations

*Budker Institute of Nuclear Physics, 11 Lavrentieva ave., Novosibirsk, 630090, Russia*

The CMD-3 and SND detectors are taking data at the VEPP-2000 $e^+e^-$ collider (Budker INP, Novosibirsk, Russia). The main goal of experiments is the measurement of the cross-sections and dynamics of the exclusive modes of $e^+e^-$ annihilation to hadrons. In particular, these results provide an important input for calculations of the hadronic contribution to the muon anomalous magnetic moment. The first round of data taking was performed in 2011-2013 with about 60 1/pb integrated luminosity per detector in the center-of-mass (c.m.) energy range from 0.32 to 2.0 GeV. The collected data sample exceeds those in all previous experiments for this region. Here we present the survey of results of data taken in 2011-2013, including a precise measurement of the $e^+e^- \to \pi^+\pi^-$ reaction as well as other hadron final states with up to six pions or states including two kaons. At the end of 2016 the VEPP-2000 collider resumed operation after upgrade of the injection system, and performance approaching the project luminosity of $10^{32}\ cm^{-2}s^{-1}$ at 2 GeV has been demonstrated. Preliminary results of the new 2017 run are also presented.

## 1 Introduction

The electron-positron collider VEPP-2000 [1] has been operating at Budker Institute of Nuclear Physics since December 2010, and has been upgraded to the new injection system in December 2016. The collider is designed to provide luminosity up to $10^{32}\mathrm{cm}^{-2}\mathrm{s}^{-1}$ at the maximum c.m. energy $\sqrt{s} = 2$ GeV. Two detectors, CMD-3 [2] and SND [3], are installed in two interaction regions. The CMD-3 is the general-purpose particle magnetic (1.3 T) detector, equipped with the tracking system, two crystal (CSI and BGO) calorimeters, liquid Xe (LXe) calorimeter, TOF and muon systems. The CMD-3 detector has a high detection efficiency, good energy and angular resolution for charged particles as well as for photons. The SND is a non-magnetic detector based on the NaI crystals, arranged in three spherical layers, surrounding tracking system and Cherenkov aerogel counter: 1.05 and 1.13 refraction indexes can be used. The SND detector has very good energy resolutions for photons, and allows to separate particle types using energy deposition in three calorimeter layers and Cerenkov counter response. The integrated luminosity collected is about 60 $\mathrm{pb}^{-1}$ per detector in 2011-2013 runs with additional 80 $\mathrm{pb}^{-1}$ in 2017-2018 runs after the upgrade. The luminosity is measured with about 1% accuracy [4] using Bhabha events. Figure 1 (left) shows the integrated luminosity averaged over 10% of best runs: red points correspond to new 2017-2018 runs. Increase in the integrated luminosity vs experimental energy is shown in Fig. 1 by green color. The beam energy was continuously measured concurrently with the data taking using a Compton back scattering system [5].

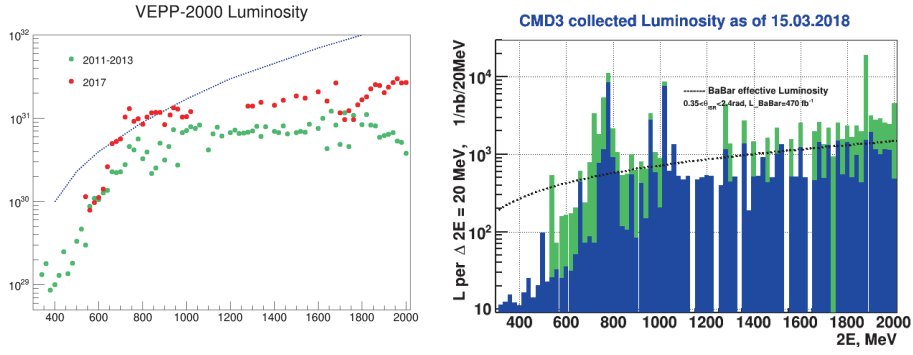


Figure 1 – (left) The integrated luminosity averaged over 10% of the best runs vs beam energy: 2017-2018 improvement is shown by red points. (right) The collected integrated luminosity vs energy at the CMD-3 detector. The luminosity collected in 2017-2018 is shown by green color.

## 2 Results from 2011-2013 runs

The analysis of data, collected in 2011-2013, is in process and a number of results on exclusive cross sections was published by the CMD-3 and SND Collaborations. All major channels are under analysis including channels with up to six pions or two kaons and two pions in the final state. Here we review the published results and show some of the recent preliminary results.

The CMD-3 collaboration has published several results with a few charged particles in the final state: $e^+e^- \to 3(\pi^+\pi^-)$ [6], $e^+e^- \to K^+K^-\pi^+\pi^-$ [7], $e^+e^- \to K_SK_L, K_S \to \pi^+\pi^-$ [8], $e^+e^- \to K^+K^-$ [9] and $e^+e^- \to 2(\pi^+\pi^-)$ [10] around the $\phi$-meson, $e^+e^- \to \pi^+\pi^-\pi^0\eta$ [11], and $e^+e^- \to p\bar{p}$ [12].

The SND group uses advantage of well granulated calorimeter and has published many results with only neutral particles in final state: $e^+e^- \to \pi^0\pi^0\gamma$ [14], $e^+e^- \to n\bar{n}$ [15], $e^+e^- \to \pi^0\gamma$ [16], $e^+e^- \to \eta\gamma$ [17], $e^+e^- \to \eta(958)$ [18], $e^+e^- \to K_SK_L\pi^0, K_S \to \pi^0\pi^0$ [20] . With the help of tracking system and Cherenkov counter many reactions with charged particles are also studies: $e^+e^- \to K^+K^-$ [19], $e^+e^- \to \omega\eta$ [21], $e^+e^- \to \pi^+\pi^-\eta$ [22].

Preliminary results for the pion form factor from the $e^+e^- \to \pi^+\pi^-$ cross section measurement are shown in Fig. 2.

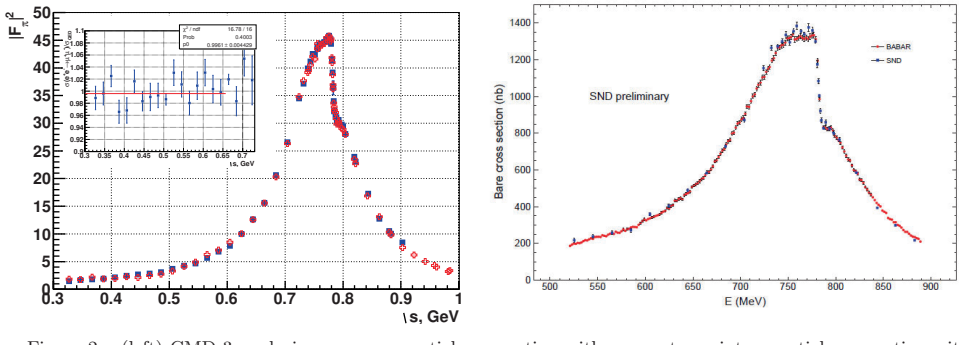


Figure 2 – (left) CMD-3 analysis: squares - particle separation with momenta, points - particle separation with energy deposition in calorimeter. insert box: Results of the measurement of muon pair production in comparison with the QED prediction. (right) SND first measurements of the $e^+e^- \to \omega\pi^0\eta$ cross section: intermediate state $\omega a_0$ has been identified (shown as inserted boxes).

CMD-3 uses two independent methods for separation of two-pion events from the $e^+e^-$ and $\mu^+\mu^-$ pairs: using only DC information or using only calorimeter response, shown in Fig. 2 (left). We already estimate the DC selection accuracy below or close to 1%, which is cross checked with the cross section of the $e^+e^- \to \mu^+\mu^-$ process, shown as inserted box with respect to the QED prediction: it provides an important overall systematic test of the measurement. A study of the systematic uncertainties of the calorimeter response is in progress, and we plan to "open the box" and present final result soon. SND detector uses energy deposition in three layers of the calorimeter and response of the Cherenkov counter. The separation also allows to obtain about 1% systematic error and preliminary results are shown in Fig. 2 (right) in comparison with BaBar data.

Many other exclusive cross sections like $e^+e^- \to \pi^+\pi^-\pi^0$, $e^+e^- \to \pi^+\pi^-\omega$, $e^+e^- \to \pi^+\pi^-\phi$, $e^+e^- \to K^+K^-\pi^0$, $e^+e^- \to K^+K^-\eta$, $e^+e^- \to 2(\pi^+\pi^-)$, $e^+e^- \to \pi^+\pi^-\pi^0\pi^0$ etc. in the VEPP2000 energy range are under study and results will be published soon.

Both, CMD-3 and SND detectors performed the measurements of the reactions, which never were studied before. Figure 3 (left) shows the cross section for the reaction $e^+e^- \to \pi^+\pi^-\pi^0\eta$ measured by CMD-3 detector for the first time [23]. Only part of the reaction with the $\omega\eta$ final state (signal from $\omega$ very well seen in data - see inserted box) was known before. SND has discovered the $e^+e^- \to \omega\pi^0\eta$ reaction (Fig. 3 (right)), and established the $\omega a_0$ intermediate state (shown in inserted boxes). These two measurements show that our knowledge in this energy range is incomplete, and we should continue search for new reactions, contributed to the total hadronic cross section.

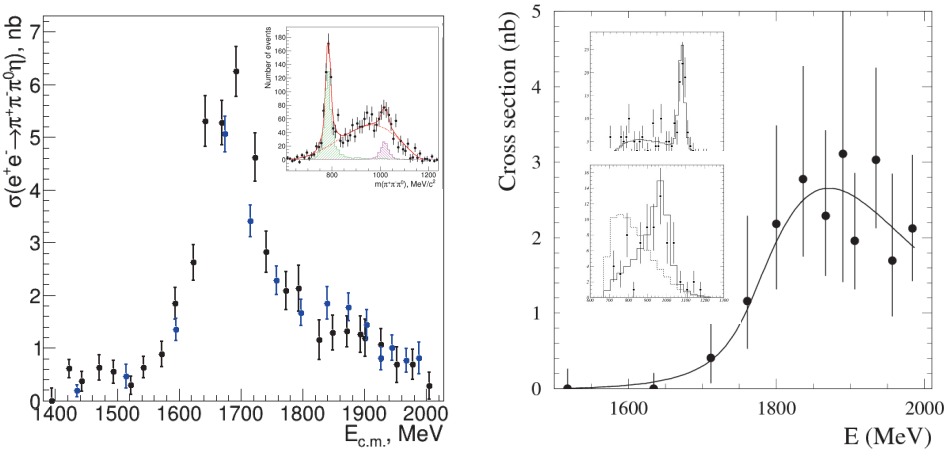


Figure 3 – (left) Preliminary results of the pion form factor measurement; squares - particle separation with momenta, points - particle separation with energy deposition in calorimeter; (right) Results of the measurement of muon pair production in comparison with the QED prediction.

## 3 Preliminary results from 2017 run

In 2017 the VEPP2000 collider has resumed operation with the new injection complex. We have no limitation with the number of positrons any longer. We have collected about 50 pb$^{-1}$ in 5 months of operation in the c.m. energy scan from 1680 to 2007 MeV. About 4 pb$^{-1}$ has been collected at $E_{c.m.}$=2007 MeV to to search for direct production of $D^*(2007)^0$ in the $e^+e^-$ annihilation. An observation of such production at any level above the SM prediction $B(D^{*0} \to e^+e^-) \sim O(10^{-19})$ would be a clear signal of physics beyond SM [13].

Another $\approx 10\text{pb}^{-1}$ has been collected in the $N\bar{N}$ threshold scan with a step comparable with the beam energy spread of 1.2 MeV. Figure 4 (left) shows our preliminary results for the $e^+e^- \to p\bar{p}$. Very sharp cross section behavior has been observe at the threshold, consistent with 1 MeV exponential rise (shown in inserted box). Figure 4 (right) shows our preliminary results for the $e^+e^- \to 3(\pi^+\pi^-)$ cross section measurement. All analysis procedures are the same as in our publication [6], and we confirm our previous observation of a very sharp cross section drop at the $N\bar{N}$ threshold. Moreover, an energy scan with a small step allows to investigate a structure of this drop, which is also in the scale of $p\bar{p}$-$n\bar{n}$ threshold energy difference .

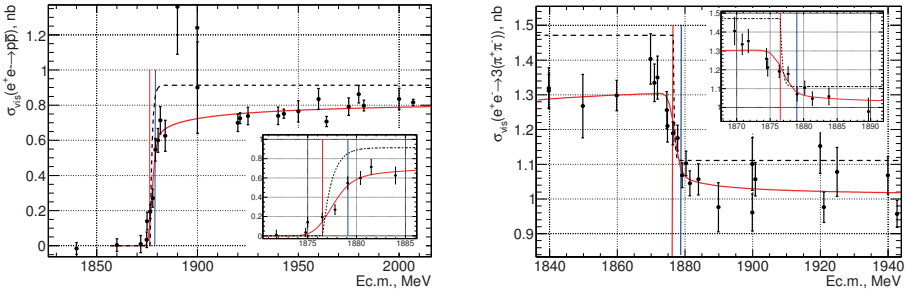


Figure 4 – (left) The $e^+e^- \to p\bar{p}$ visible cross section measured with the CMD-3 detector. Solid curve shows result of the fit by the exponentially-saturated function (dashed curve) convoluted with the 1.2 MeV energy spread and radiation functions. The vertical lines show the $p\bar{p}$ and $n\bar{n}$ thresholds. (right) The $e^+e^- \to 3(\pi^+\pi^-)$ visible cross section measured with the CMD-3 detector. Solid curve shows fit with Born cross section (dashed curve) convoluted with 1.2 MeV energy spread and radiation function. The vertical lines show the $p\bar{p}$ and $n\bar{n}$ thresholds.

## References


1. I. A. Koop, Nucl. Phys. B (Proc. Suppl.) **181-182**, 371 (2008). P. Yu. Shatunov *et al.*, Phys.Part.Nucl.Lett. **13** no.7 (2016). D. Shwartz *et al.*, PoS ICHEP2016 054 (2016).
2. B.I.Khazin *et al.*, Nucl.Phys.B, Proc. Suppl. **181-182**, 376 (2008).
3. M.N.Achasov *et al.*, Nucl.Instrum.Meth. **A598**, 31 (2009).
4. R.R.Akhmetshin *et al.*, JINST **9** C09003 (2014).
5. E.V.Abakumova *et al.*, Phys.Rev.Lett. **110**, 140402 (2013).
6. R. R. Akhmetshin *et al.*, Phys. Lett. B **723**, 82 (2013).
7. D. N. Shemyakin *et al.*, Phys. Lett. B **756**, 153 (2016).
8. E. A. Kozyrev *et al.*, Phys. Lett. B **760**, 314 (2016).
9. E. A. Kozyrev *et al.*, Phys. Lett. B **760**, 314 (2017).
10. R. R. Akhmetshin *et al.*, Phys. Lett. B **768**, 345 (2017).
11. R. R. Akhmetshin *et al.*, Phys. Lett. B **773**, 150 (2017).
12. R. R. Akhmetshin *et al.*, Phys. Lett. B **759**, 634 (2016).
13. A. Khodjamirian, T. Mannel, A. Petrov, JHEP **1511** 142 (2015).
14. M.N.Achasov *et al.*, Phys. Rev. D **94** 112001 (2016).
15. M.N.Achasov *et al.*, Phys. Rev. D **90** 112007 (2014).
16. M.N.Achasov *et al.*, Phys. Rev. D **93** 092001 (2016).
17. M.N.Achasov *et al.*, Phys. Rev. D **90** 032002 (2014).
18. M.N.Achasov *et al.*, Phys. Rev. D **91** 092010 (2015).
19. M.N.Achasov *et al.*, Phys. Rev. D **94** 112006 (2016).
20. M.N.Achasov *et al.*, Phys. Rev. D **97** 032011 (2018).
21. M.N.Achasov *et al.*, Phys. Rev. D **94** 092002 (2016).
22. M.N.Achasov *et al.*, Phys. Rev. D **97** 012008 (2018).
23. M.N.Achasov *et al.*, Phys. Rev. D **94** 092010 (2016).

# News on the CLIC Physics Potential

Nigel Watson, on behalf of the CLICdp Collaboration
*School of Physics and Astronomy, The University of Birmingham, Birmingham B15 2TT, U.K.*

Recent studies exploring the physics potential of the CLIC project are presented, with particular emphasis on $t$ quark and Higgs measurements.

## 1 Introduction: Motivation for CLIC

There are four high energy $e^+e^-$ collider projects considered worldwide. Two are synchrotrons, in the relatively early stages of development: the 100 km cirumference, $\sqrt{s}$ =90–240 GeV, Circular Electron Positron Collider (CEPC) in China; and the 98 km, $\sqrt{s}$ =90–365 GeV, Future Circular Collider (FCC-ee) at CERN. Two are linear accelerators and have been under development for a longer period of time: the 17–50 km, $\sqrt{s}$ =250–1000 GeV International Linear Collider (ILC) in Japan; and the 11–50 km, $\sqrt{s}$ =380–3000 GeV Compact Linear Collider (CLIC)[1] at CERN. We present highlights of the latter, which is based on a novel, twin-beam scheme with accelerating gradients of 100 MV/m and is unique in offering the only route to multi- TeV $e^+e^-$ collisions.

## 2 Top Quark Physics

The CLIC physics programme will be staged in energy [1] and has $t\bar{t}$ production accessible from the outset, with a scan of the $t\bar{t}$ threshold region as an early goal [2], progressing to large samples at higher energies that further enhance sensitivity to physics beyond the Standard Model (SM).

At threshold, the baseline strategy anticipates recording samples of approx. 10 $fb^{-1}$ at each of ten collision energies at 1 GeV intervals around the $t\bar{t}$ production threshold, as shown in Fig. 1(a), giving a statistical precision on the measured $t$ quark mass (PS scheme), $\Delta m_t \sim 20$ MeV. A dedicated tune of machine parameters with lower than nominal charge per bunch reduces beam-

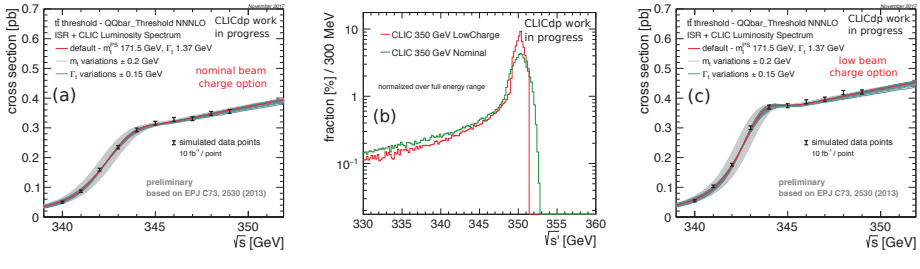


Figure 1 – (a) Cross-section for $t\bar{t}$ production near threshold for nominal beam parameters [2], (b) compares the luminosity spectra [2] for nominal and reduced bunch charge schemes, (c) as for (a) in reduced bunch charge scheme [2]

strahlung and narrows the main luminosity peak (Fig. 1(b)), enhancing dependence of the measured cross-section on the beam energy (Fig. 1(c)) and improving the uncertainty on $m_t$ for a fixed integrated luminosity. To achieve this requires twice the running time and the largest benefit would be expected for measurements of $t$ quark width and Yukawa couplings. The combined theoretical and parametric uncertainties on $m_t$ are expected to be ∼30–50 MeV, dominated by QCD scale, while the experimental systematics are estimated at ∼25–50 MeV. This improves significantly the precision expected at HL-LHC and, with sufficient luminosity, outperforms measurements of $m_t$ from "direct" kinematic reconstruction of observed four-momenta.

Above threshold, a further 500 $\text{fb}^{-1}$ would be recorded near to the $t\bar{t}$ production cross-section maximum, shown in Fig. 2(a), and the ∼350k $t\bar{t}$ events produced allow decay modes that are not straightforward at the LHC, such as $t \to c +$ missing energy, $t \to cH(H \to b\bar{b})$ or $t \to c\gamma$, to be studied. The reconstructed $m_t$ in a full simulation study of $t \to c\gamma$, shown in Fig. 2(b), illustrates how analyses at CLIC rise to the experimental challenges such as separation of $b$ from $c$ decays and control of multi-jet SM backgrounds.

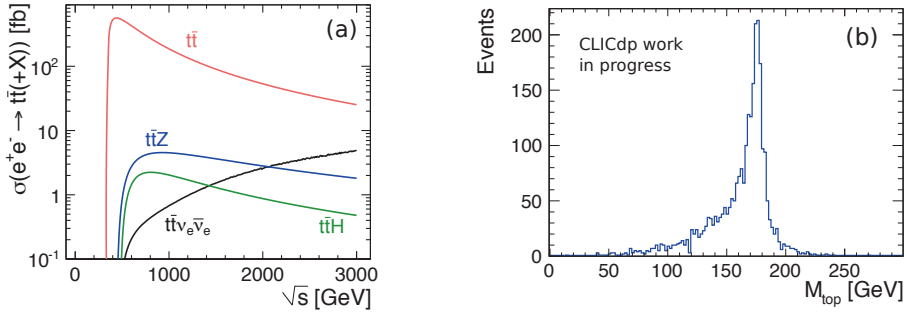


Figure 2 – (a) Leading-order cross-sections for the main $t\bar{t}$ production processes [2] ($m_t$ =174 GeV, $m_H$ =125 GeV, unpolarised beams, with ISR, without beamstrahlung), (b) reconstructed $m_t$ in the $t \to c\gamma$ decay mode [2].

At higher energies, the $e^+e^- \to t\bar{t}H$ cross-section peaks at $\sqrt{s} \sim 800$ GeV, where CLIC is the only machine for which this is accessible in the baseline plan. For the vector boson fusion process, $e^+e^- \to t\bar{t}\nu\bar{\nu}$, the higher the $\sqrt{s}$ the better, making CLIC uniquely placed.

At the higher energies that distinguish CLIC, the hadronic jets in a $t$ quark decay are less distinct from one another due to the Lorentz boost and, as shown in Fig. 3(a), may be initially characterised as broad, large-$R$ jets. To improve separation from background, jet substructure methods popularised at LHC are an important ingredient of the multivariate selections developed. Figure 3(b) shows the $p_T$ of subjets in a single, successfully tagged $t$ quark decay (without

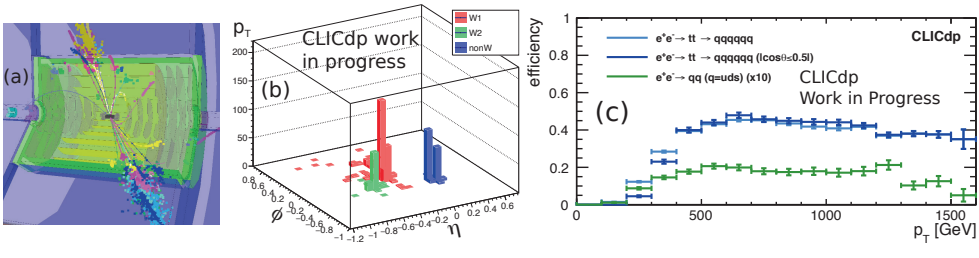


Figure 3 – (a) Typical $t\bar{t} \to b\bar{b}q\bar{q}\ell\nu_\ell$ decay [2] at $\sqrt{s} = 3$ TeV, (b) $p_T$ of subjets in a $t \to$ jets decay [2], harder (softer) subjet in red (green), $b$-quark jet in blue, (c) $t$ tagging efficiency in $t\bar{t} \to$ hadrons vs. $p_T$ of the large-$R$ jet [2].

use of vertexing information) vs. their azimuthal angle ($\phi$) and pseudorapidity ($\eta$), while Figure 3(c) gives the efficiency of the tagger as a function of the $p_T$ of the large-$R$ jet; the lower efficiency for $p_T < 500\,\text{GeV}$ is caused by incomplete containment of $t$ decay products within a single large-$R$ jet.

As the $t$ quark electroweak couplings are well-determined in the SM and have values that may change substantially in new physics scenarios, their precise measurement constitutes a stringent test of the validity of the SM itself. Measurements of the cross-section ($\sigma^{t\bar{t}}$), forward-backward asymmetry ($A_{FB}^{t\bar{t}}$) and the lepton helicity angle in $t\bar{t}$ decays are robust experimental observables and can be used to extract both CP-conserving and CP-violating form factors [1,4]. Beam polarisation, which is present for $e^-$ in the CLIC baseline and as an option for $e^+$, simplifies disentangling the $Z$ and $\gamma$ contributions, while measurements at higher $\sqrt{s}$ increase sensitivity to physics beyond the SM such as contact interactions.

To evaluate the precision with which the experimental observables can be determined, detailed studies of $t\bar{t}$ events using full simulation of the CLIC detector, including beam-related backgrounds, have been carried out. Due to the variation in the luminosity spectrum with the collision energy, as shown in Fig. 4(a), and the impact that this has on the topology of the final state, selection and reconstruction of $t\bar{t}$ events is optimised separately for each of $\sqrt{s}$ of 0.38, 1.4 and 3.0 TeV. The use of boosted reconstruction techniques is particularly relevant far above threshold. To ensure reliable separation of $t$ from $\bar{t}$, events are selected in the $bbq\bar{q}\ell\nu_\ell$ final state, where the sign of the charged lepton is used to infer the flavour of the fully hadronic $t$ decay, from which the polar angle in the $t\bar{t}$ centre-of-mass system is determined. For the two higher collision energies, events close to the nominal $\sqrt{s}$ are selected. In addition, at 1.4 TeV a constrained kinematic fit is used to estimate the effective centre-of-mass energy ($\sqrt{s'}$) of events having significant initial-state photon radiation (ISR) and/or energy loss due to beamstrahlung, from which $\sigma^{t\bar{t}}$ and $A_{FB}^{t\bar{t}}$ are reconstructed differential in $\sqrt{s'}$. The performance of this reconstruction method, which in full simulation with overlay of beam-related background has a resolution on $\sqrt{s'} \sim 75\,\text{GeV}$, is illustrated in Fig. 4(b).

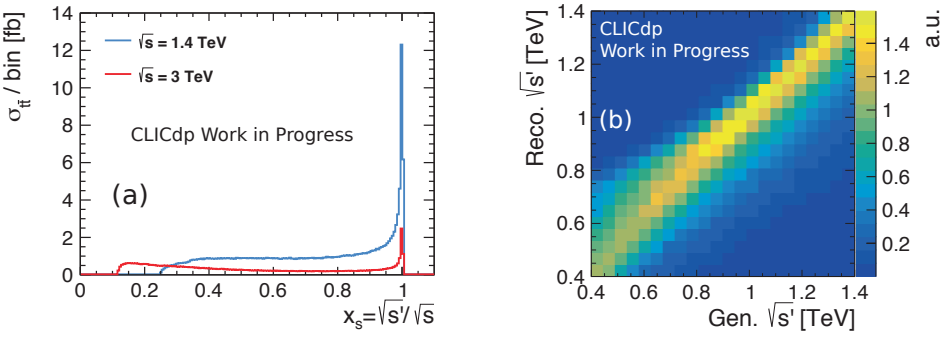


Figure 4 – (a) $\sigma^{t\bar{t}}$, including the effects of ISR, electroweak corrections and the CLIC luminosity spectrum [2], (b) comparison of reconstructed vs. true $\sqrt{s'}$ in $t\bar{t}$ events with a nominal collision energy of 1.4 TeV [2].

## 3 Higgs Physics

The impact that CLIC will have on our understanding of the nature of the Higgs boson has been studied in detail [3]. Figure 5(a) shows the $\sqrt{s}$-dependence of the cross-section for the main $H$ production processes. The cross-section for $H\nu\overline{\nu}$ has the largest sensitivity to beam polarisation, a factor $\sim 2$ enhancement for $-80\%$ $e^-$ beam polarisation. In the dominant Higgstrahlung

process at $\sqrt{s} \sim 350\,\text{GeV}$, $m_H$ can be reconstructed event-by-event via the $Z$ boson recoil mass, regardless of the decay mode of the $H$. For the case of $Z \to \mu^+\mu^-$ or $e^+e^-$, these allow effectively model-independent measurements, combining to give a statistical uncertainty on $\sigma(ZH)$ of 3.8% for an integrated luminosity of $500\,\text{fb}^{-1}$. A significantly better statistical precision of 1.8% is obtained for the case where $Z \to q\bar{q}$, although some small model dependence arises due to the ambiguity of pairing jets of hadrons to either the $Z$ or the $H$. Figure 5(b) shows reconstructed $Z \to q\bar{q}$ invariant mass vs. the recoil mass ($\sim m_H$). The combination of all Higgstrahlung channels leads to a relative uncertainty on the coupling $g_{HZZ}$ of 0.8%. This uncertainty was substantially larger at two alternative $\sqrt{s}$ (250 and 420 GeV) considered; $\sqrt{s} \sim 350\,\text{GeV}$ appears to be the best compromise between detector resolution and physics backgrounds.

Taking advantage of the higher branching fraction in the $Z \to q\bar{q}$ channel, $H$ decays to "invisible" (undetectable, for whatever reason) decays can be measured, with an estimated sensitivity to branching fractions $H \to \text{invisible} < 1\%$ at 90%CL (with $0.5\,\text{ab}^{-1}$, $\sqrt{s} = 350\,\text{GeV}$). At energies above 1 TeV, vector boson fusion processes become increasingly significant due to the $\log(s)$ cross-section dependence and improved luminosity performance, allowing access to rare $H$ decay modes. Above $\sqrt{s} \sim 700\,\text{GeV}$ the $t\bar{t}H$ production rates allows the Yukawa coupling to be extracted and, by combining eight-jet and six-jet plus $\ell\nu_\ell$ final states, a statistical precision on $g_{Ht\bar{t}}$ of 4.4% can be obtained after five years of data taking at $\sqrt{s} = 1.4\,\text{TeV}$ ($1.5\,\text{ab}^{-1}$). The precision with which the Higgs couplings can be determined [3] in a model-independent analysis are summarised in Fig. 5(c).

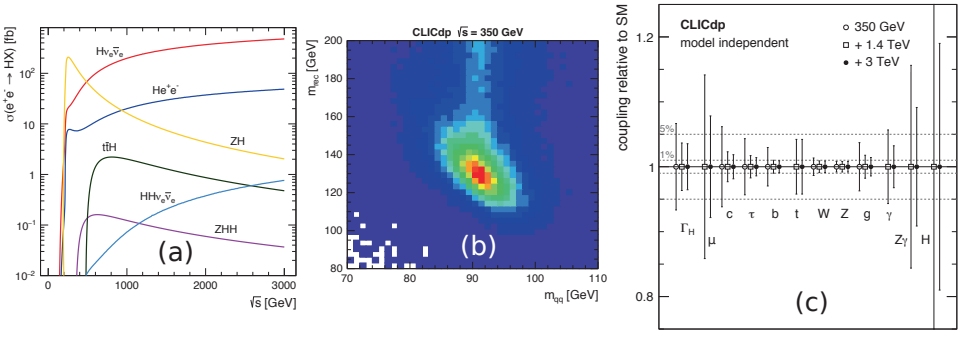


Figure 5 – (a) Cross-section vs. $\sqrt{s}$ for main $H$ production processes [3] ($m_H = 126\,\text{GeV}$, unpolarised beams, no beamstrahlung), (b) reconstructed di-jet invariant mass vs. recoil mass [3] for $e^+e^- \to Z(\to q\bar{q})H(\to \text{any})$, (c) statistical precision of $H$ couplings determined in the three-stage CLIC programme from model-independent fits [3].

## Summary

The expected precisons for selected $t$ quark [2] and Higgs physics [3] measurements at the CLIC facility are described. These are characterised as having greater precision and lower model dependence than measurements at HL-LHC. The first stage of CLIC at $\sqrt{s} \sim 380\,\text{GeV}$ will study Higgs production via the Higgstrahlung and vector-boson fusion modes, and measure $t$ quark production in the threshold and continuum regions, allowing rare decay modes to be investigated. At higher energies, the collider has enhanced potential to discover physics beyond the SM, with direct detection up to kinematic limits, indirect discovery potential though precise electroweak measurements up to a few tens of TeV, and a sensitivity in general that rises steeply with centre-of-mass energy. The combination of these factors makes CLIC unique among the proposed future $e^+e^-$ machines.

**Acknowledgments**

I would like to thank the organisers for the exciting programme, many colleagues in the CLICdp Collaboration for the opportunity to present our work and the UK STFC for funding.

**References**

1. M. J. Boland *et al.* [CLIC and CLICdp Collaborations], CERN-2016-004
2. CLICdp Collaboration,"Top-Quark Physics at the CLIC Electron-Positron Linear Collider", in preparation.
3. H. Abramowicz *et al.*, Eur. Phys. J. C **77** (2017) no.7, 475
4. W. Bernreuther *et al.*, Eur. Phys. J. C **78** (2018) no.2, 155

# 7.
# PDF

# Parton densities with Parton Branching method and applications

A. Bermudez Martinez[1], P. Connor[1], F. Hautmann[2,3,4], H. Jung[1],
A. Lelek[1], V. Radescu[3,5c], R. Žlebčík[1]
[1] *DESY, Hamburg, FRG*
[2] *Rutherford Appleton Laboratory, Chilton OX11 0QX*
[3] *University of Oxford, Oxford OX1 3NP*
[4] *Elementary Particle Physics, University of Antwerp, B 2020 Antwerp*
[5] *CERN, CH-1211 Geneva 23*

We present results from a parton branching solution of the QCD evolution equations which includes the transverse momentum distributions for all parton flavours. The transverse momentum dependent (TMD) parton densities were extracted by fitting inclusive HERA DIS data with two alternative evolution scenarios. In both cases the same ordering variable is used, but as $\alpha_S$ argument in the branching we use either the evolution scale or $p_T$. The resulting distributions differ mainly in the gluon component at low scales and/or small $k_T$ region. This was demonstrated by two phenomenological applications from LHC – the $Z$ boson $p_T$ spectrum and the azimuthal decorrelation of two leading jets.

## 1 Introduction

The Parton Branching evolution method is described in [1,2,3]. This formalism can be compared, on one hand, with DGLAP evolution equations [4] for ordinary (collinear) parton densities, and, on the other hand, with existing evolution equations for TMD parton densities [5] working in special regions of the phase space: CSS at low transverse momentum [6] and/or CCFM at high energy and low-x region [7].

## 2 Method description

In our approach, we use the evolution equation which deals with the resolvable branchings. Denoting $z$ as the fraction of the light-cone momentum of the parton after the branching with respect to the original one we introduce the resolution parameter $z_m < 1$ such that the emissions with $z < z_m$ are considered as resolvable. The amount of non-resolvable emissions with $z > z_m$ is then dictated by the unitarity of the evolution. Technically, this is done by Sudakov form factor $\Delta_a$

$$\Delta_a(\mu^2) = \exp\left(-\int_{\mu_0^2}^{\mu^2} \frac{\mathrm{d}\mu'^2}{\mu'^2} \sum_b \int_0^{z_m} \mathrm{d}z\, z\, \mathcal{P}_{ba}(\mu'^2, z)\right) \tag{1}$$

which can be interpreted as a probability that the parton $a$ does not undergo any resolvable branching between scales $\mu_0^2$ and $\mu^2$. The splitting function $\mathcal{P}_{ba}(\mu'^2, z)$ describes the probability density that parton $a$ splits into parton $b$ at scale $\mu'^2$ and momentum fraction $z$.

[c] Now at IBM Germany

The evolution equation for the momentum weighted PDF $\tilde{f}_a(x,\mu^2) = x f_a(x,\mu^2)$ is then given as:

$$\frac{\mathrm{d}}{\mathrm{d}\ln\mu^2}\frac{\tilde{f}_a(x,\mu^2)}{\Delta_a(\mu^2)} = \sum_b \int_x^{z_m} \frac{\mathrm{d}z}{z} z\,\mathcal{P}_{ab}(\mu^2,z)\frac{\tilde{f}_b(x/z,\mu^2)}{\Delta_a(\mu^2)}. \tag{2}$$

With $\mathcal{P}_{ab}$ being the standard DGLAP splitting functions, the evolution (2) converges to the DGLAP equation if $z_m$ is large enough[2]. The non-necessity to know the virtual terms of the splittings makes equation (2) a good candidate for possible extensions beyond standard DGLAP. In this text we focus on the effect from using a different functional form of the renormalisation scale which is the argument of $\alpha_S$ in $\mathcal{P}_{ab}$. In future, we plan to extend the splittings for the CCFM terms which are important in low-$x$ limit.

We solve the equation by the Monte Carlo technique which employs Markov chain of the branchings. Within this method the $\Delta_a(\mu_2^2)/\Delta_a(\mu_1^2)$ is a non-branching probability between two consecutive scales $\mu_1^2$ and $\mu_2^2$ and the splitting function integrated over $z < z_m$ represents the branching probability. The method is described in more detail in [2].

In [1,2,8] we demonstrated that at LO, NLO and NNLO the PDFs from the Parton Branching method are within 1% identical with the corresponding semi-analytical solution of the DGLAP evolution as implemented in QCDNUM [9]. Such precision was achieved with $z_m = 1 - 10^{-3}$ and higher $z_m$ gives even better agreement. To be noticed, the individual splitting functions $\mathcal{P}_{ab}$ at higher orders can be negative and cannot be interpreted in terms of probability. However, the Sudakov factor (1) is still well defined, i.e. it is a decreasing function of the scale $\mu$ for any $\mu > \mu_0$, which is the key property for the applicability of the Parton Branching method.

## 3 The evolution equation for the TMD densities

The main motivation for the Parton Branching method is to have PDFs dependent not only on $x$ but also on the transverse momentum $k_T$ for all parton flavours. For each branching in the evolution we generate the relative transverse momentum $q_T$ of the parton and consequently estimate the final $k_T$ value. The evolution scale $\mu$ can be identified either with virtuality, then $\mu \overset{\text{def}}{=\!=} q_T/\sqrt{1-z}$, or with the rescaled transverse momentum, $\mu \overset{\text{def}}{=\!=} q_T/(1-z)$. It can be shown, that in the second case the emissions are also ordered in the angle. Therefore, it includes the color coherence effects between the emissions and we use this kind of ordering in our fits. The complete evolution equation for TMD density $A_a$ has the following form:

$$\begin{aligned} A_a(x,\boldsymbol{k_T},\mu^2) &= \Delta_a(\mu^2)A_a(x,\boldsymbol{k_T},\mu_0^2) + \\ &+ \sum_b \int_{\mu_0^2}^{\mu^2} \frac{\mathrm{d}^2\boldsymbol{\mu'}}{\pi\mu'^2}\frac{\Delta_a(\mu^2)}{\Delta_a(\mu'^2)}\int_x^{z_m(\mu'^2)}\frac{\mathrm{d}z}{z}zP_{ab}\left(\alpha_s(\mu_r'^2),z\right)A_b\left(\frac{x}{z},\frac{\boldsymbol{k_T}+F(z)\boldsymbol{\mu'}}{z},\mu'^2\right), \end{aligned} \tag{3}$$

where $\mu' = |\boldsymbol{\mu'}|$ and the 2D integration over $\boldsymbol{\mu'}$ is performed in domain $\mu_0^2 < |\boldsymbol{\mu'}|^2 < \mu^2$. The TMD density $A_a$ is normalized in such a way that $\int_0^\infty \frac{\mathrm{d}^2\boldsymbol{k_T}}{\pi} A_a(x,\boldsymbol{k_T},\mu^2) = \tilde{f}_a(x,\mu^2)$.

In this evolution equation, one can choose the ordering condition, for angular ordering $F = 1-z$, the renormalisation scale denoted as $\mu_r'$, and the limit for the resolvable branchings $z_m$.

## 4 The extraction of TMDs from HERA DIS data

The fit is performed within `xFitter` package [10] where the Parton Branching method is implemented. We fitted precision measurements in neutral and charged current interactions at various beam energies from HERA 1+2 of $\sigma_{red} = \mathrm{d}^2\sigma^{ep}/\mathrm{d}x\mathrm{d}Q^2 \cdot Q^4 x/(2\pi\alpha^2(1+(1-y)^2))$ (which is the DIS cross section where the photon flux is removed) in the range $3.5 < Q^2 < 50000$ GeV$^2$ and $4\cdot 10^{-5} < x < 0.65$.

The TMD parton densities at NLO were extracted using two alternative evolution scenarios. In both cases the rescaled transverse momentum $q_T/(1-z)$ was used as an evolution variable,

but as $\alpha_S$ argument in the branchings in eq. (4) we use either the evolution scale, $\mu'_r = \mu'$, or $q_T$, $\mu'_r = (1-z)\mu'$. These are denoted as Set 1 and Set 2, respectively. A similar $\chi^2/ndf \approx 1.21$ is obtained for both sets[3]. However the sets differ in the gluon component at small scales, both in longitudinal component $x$ and in transverse momentum $k_T$.

## 5 Drell-Yan $p_T$ spectrum

The $k_T$ spectrum of the TMD densities is mainly determined by the evolution itself rather than the starting parametrisation. One of the classical ways to probe the transverse momenta of the partons is the $p_T$ spectrum of the Drell-Yan pair in $pp$ collisions.

To predict the cross sections, we convoluted the LO matrix element squared with the TMDs obtained in the previous section. Since EW branchings are not included in the evolution equation (4) the lepton pair can be produced only in the hard subprocess. In contrast to the classical approach, the partons entering the hard process have $k_T$ from the beginning generated according to TMDs and it is not affected by the initial-state parton shower.

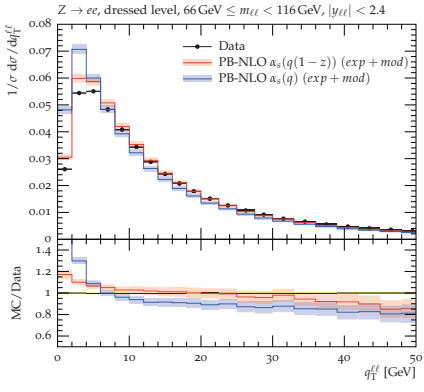


Figure 1 – The $p_T$ spectrum of the di-lepton pair as measured by ATLAS compared with the predictions based on Set 1, $\alpha_S(q)$, and Set 2, $\alpha_S(q(1-z))$, TMD densities.

In figure 1 we compare the $p_T$-spectrum of the ATLAS measurement[11] Drell-Yan production at $\sqrt{s} = 8\,\text{TeV}$ with our calculations. It can be seen that the renormalisation scale of the evolution affects small $p_T$ region, where the Set 2 agrees better with the data.

## 6 Dijet $\Delta\phi$ decorrelation

As the second application we show the prediction for the difference $\Delta\phi$ between azimuthal angles of two leading jets. In contrast to the previous case, the partons radiated by the parton shower can be clustered into the leading jets. The parton shower is generated according to the TMD densities by CASCADE MC [12]. In contrast to the classical approach, the parton shower does not change the kinematics of the hard process but still can change the measured distribution.

The predictions are based on the hard-subprocess generated at NLO using POWHEG 2-jets convoluted with the TMD densities and dressed by the parton shower from CASCADE.

In figure 2 we compare the $\Delta\phi$ distribution of the jets measured by CMS[13] at $\sqrt{s} = 13\,\text{TeV}$ with our predictions. It can be seen that there is no substantial difference between predictions based on Set 1 and Set 2 TMD densities. For the reference, the prediction based on collinear PDFs, i.e. POWHEG 2-jets matched with Pythia 8 MC, is also included.

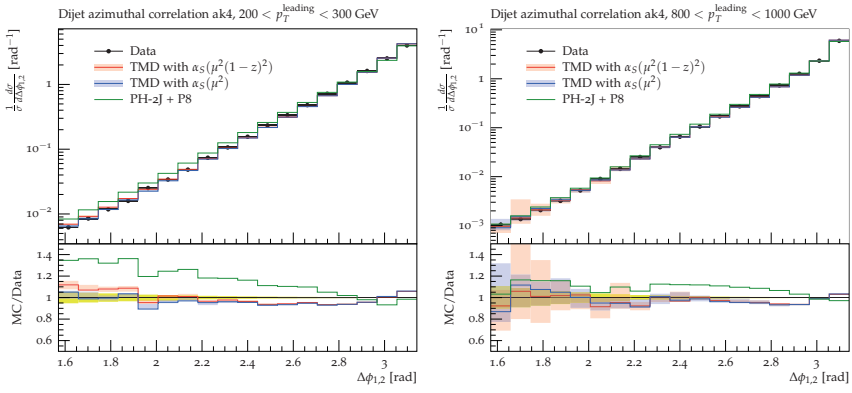


Figure 2 – The angle $\Delta\phi$ between two leading jets as measured by CMS compared with NLO predictions based on Set 1 and Set 2 densities. In addition the predictions from POWHEG 2jets matched with Pythia 8 is plotted.

## 7 Conclusion

For the first time, precision DIS measurements have been used to obtain both collinear and TMD parton densities, including uncertainties, over a wide range in $x$ and $\mu$ values, which are relevant for LHC and future collider phenomenology as well as for low-energy and small-$k_t$ physics. The renormalisation scale in the evolution has been chosen to be either the evolution scale $\mu_i$ (Set 1) or the transverse momentum $q_{ti}$ (Set 2). These TMD variants give similar $\chi^2/ndf = 1.21$ with respect to the fitted HERA data but differ in the gluon component at small scales.

The obtained TMDs are applied to calculate the transverse momentum spectrum of the $Z$-boson in DY production at LHC energies. This observable was found to be sensitive to the form of the renormalisation scale of the evolution, the choice used in Set 2 gives better agreement with data. On the other hand, for the second studied process, the azymtutal decorrelation in the dijet system at LHC, both TMD variants give identical predictions.

## References


1. F. Hautmann, H. Jung, A. Lelek, V. Radescu, and R. Zlebcik. *Phys. Lett.* B **772** 446–451 (2017), arXiv:1704.01757.
2. F. Hautmann, H. Jung, A. Lelek, V. Radescu, and R. Zlebcik. *JHEP* **01** 070 (2018), arXiv:1708.03279.
3. A. Bermudez Martinez, P. Connor, F. Hautmann, H. Jung, A. Lelek, V. Radescu, and R. Zlebcik. DESY 18-042 (2018), arXiv:1804.11152.
4. V. N. Gribov, and L.N. Lipatov. *Sov.J.Nuc.Phys.* **15** 438 (1972).
   Yu. L. Dokshitzer. *Sov.Phys. JETP* **46** 641 (1977).
   G. Altarelli., and G. Parisi *Nucl.Phys. B* **126** 298 (1977).
5. R. Angeles-Martinez *et al. Acta Phys. Polon. B* **46** no.12 2501 (2015), arXiv:1507.05267.
6. John Collins. *Foundations of perturbative QCD.* Cambridge University Press (2013).
7. S. Catani, F. Fiorani, and G. Marchesini. *Nucl. Phys.*, B **336** 18–85 (1990).
8. Radek Zlebcik. *PoS*, DIS2017 078 (2018).
9. M. Botje. *Comput. Phys. Commun.* **182** 490–532 (2011), arXiv:1005.1481.
10. S. Alekhin et al. *Eur. Phys. J.* C **75(7)** 304 (2015), arXiv:1410.4412.
11. Georges Aad et al. [ATLAS coll.] *Eur. Phys. J.*, C **76(5)** 291 (2016), arXiv:1512.02192.
12. M. Bury, A. van Hameren, H. Jung, K. Kutak, S. Sapeta, and M. Serino. *Eur. Phys. J.*, C **78(2)** 137 (2018), arXiv:1712.05932.
13. Albert M Sirunyan et al. [CMS coll.] CMS-SMP-16-014 (2017), arXiv:1712.05471.

# Constraining PDFs from neutral current Drell-Yan measurements and effects of resummation in slepton pair production [a]

Juri Fiaschi[1], Elena Accomando[2], Francesco Hautmann[3], Michael Klasen[1] and Stefano Moretti[2]

[1] *Institut für Theoretische Physik, Westfälische Wilhelms-Universität Münster, Wilhelm-Klemm-Straße 9, D-48149 Münster, Germany*

[2] *School of Physics & Astronomy, University of Southampton, Highfield, Southampton SO17 1BJ, UK*

[3] *Theoretical Physics Department, University of Oxford, Oxford OX1 3NP, UK*

The high statistics that will be collected during the LHC Run-II (and beyond) open the path to precision measurements at the TeV scale, where the PDFs will play a crucial role in BSM searches. In the di-lepton final state accurate measurements of the Forward-Backward Asymmetry (AFB) will be available, particularly in the invariant mass region around the Z peak. We show that this observable displays a statistical error which is competitive with that assigned to the existing PDF sets and which will rapidly become smaller than the latter as the integrated luminosity grows, thereby offering a means of constraining the (anti)quark PDFs over a sizeable $(x, Q^2)$ range. In the context of SUSY searches we consider the effects of employing threshold-improved PDFs in a consistent calculation at NLO+NLL of slepton pair production cross sections. The calculations featuring a consistent resummation procedure both at PDF and partonic matrix element level are accompanied by PDF and scale uncertainties, and they provide a reliable and updated theoretical estimation for experimental data analyses at the LHC Run-II.

## 1 Introduction

The LHC programme has recently entered in the Run-II stage, featuring an upgraded c.o.m. energy of 13 TeV and aiming to achieve a high integrated luminosity in the next years and furthermore during the following High Luminosity (HL) stage. In order to keep up with the increasing statistical precision of experimental measurements, an impressive effort has been made on the theoretical side to provide higher order calculations, often including also the resummation of large logarithmic contributions that appear in the perturbative expansion, such that in many cases the remaining uncertainty is dominated by the determination of the Parton Distribution Functions (PDFs). In this context, a precise determination of the PDFs will be a crucial point for LHC physics, as well as their consistent employment in the theoretical calculations of cross sections at next-to-leading order (NLO) and next-to-leading logarithmic (NLL) accuracy.

These two main points are considered in this work. In Sect. 2, we propose the inclusion of the di-lepton final state Forward-Backward Asymmetry (AFB) pertaining to the Neutral Current (NC) Drell-Yan (DY) production channel, in the fit of the PDFs. In Sect. 3 we consider a SUSY BSM scenario and we study the effect of adopting threshold-resummed improved PDFs in a consistent calculation of the slepton pair production cross section at NLO+NLL.

[a] MS-TP-18-14

## 2 The Forward-Backward Asymmetry in the fit of PDFs

In this section we consider the possibility of including the Forward-Backward Asymmetry (AFB) observable in future fits of the PDFs [2]. In Fig. 1 we compare the statistical and PDF errors on the AFB and we recognise that when the former is smaller than the latter, a precise experimental measurement of the observable can improve the fit of the PDFs, thus reducing its PDF uncertainty. In the plot on the left are shown the two sources of uncertainties in the Run-I setup. As visible the statistical indetermination is always of the same order or larger than the PDF error, thus no improvement in the PDF fit is to be expected due to the inclusion of this data. In the plot on the right the same exercise is repeated for the Run-II c.o.m. energy and for various stages of achieved integrated luminosity. In this scenario it is possible to define an invariant mass interval where the statistical precision overcomes the PDF error.

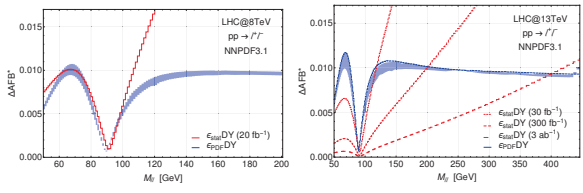


Figure 1 – Statistical and PDF uncertainties on the reconstructed $A_{\rm FB}^*$ distribution for the LHC with c.o.m. energy of 8 TeV (left) and 13 TeV (right). The blue band refers to the PDF uncertainty evaluated varying the factorisation scale in the interval $0.5M_{\ell\ell} < Q < 2M_{\ell\ell}$, while the dashed blue line (right plot only) represent the choice $Q = p_T$. The statistical error is obtained for different integrated luminosities as specified in the legend.

Another interesting feature of the AFB resides in its sensitivity on the partonic content of the proton which is parametrised differently in each PDF set. The AFB indeed depends on the relative size of the $u$ and $d$ quarks contribution to the DY process. The differences in the parametrisation of the quarks PDFs between the various sets is augmented in the high-$x$ region. Imposing a rapidity cut on the sample we select the di-lepton events arising with a large boost, thus originating from the interaction between a valence quark with a large-$x$ and a sea anti-quarks with small-$x$.

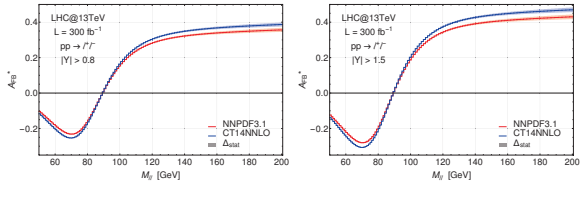


Figure 2 – $A_{\rm FB}^*$ distribution in the invariant mass region around the $Z$ peak at the LHC with c.o.m. energy of 13 TeV computed with the CT14NNLO and the NNPDF3.1 PDF sets. The error band represent the statistical uncertainty computed for an integrated luminosity $L = 300$ fb$^{-1}$. A rapidity cut of $|Y_{\ell\ell}| > 0.8$ (left) and $|Y_{\ell\ell}| > 1.5$ (right) is imposed on the di-lepton system.

In Fig. 2 we are showing the predictions for the AFB obtained with the NNPDF3.1 [1] and the CT14NNLO [3] PDF sets. From left to right, we have applied a rapidity cut $|Y| > 0.8$ and $|Y| > 1.5$ on the observable, while the statistical uncertainty bands have been computed for an integrated luminosity $L = 300$ fb$^{-1}$. As visible the separation between the predictions of the two PDF sets grows with the rapidity cut, thus an experimental measurement of the AFB in these conditions can be used to resolve the correct parametrisation of the quark (anti-quarks) PDFs in the high-$x$ (low-$x$) region and to extract information on the $u$ and $d$ quarks content in the proton.

## 3 Threshold-resummed improved PDFs in slepton pair production cross sections

Searches for BSM physics will reach considerably higher sensitivity as the LHC machine will operate at higher c.o.m. energy and luminosity. Impressive theoretical efforts have been spent to keep up with the increasing precision of experimental measurements, with the aim of providing reliable predictions for the relevant processes in the experimental analysis. This holds also in the context of SUSY searches since nowadays the cross sections for many processes have been calculated at NLO and beyond [4]. Also special resummation techniques have been established in order to take into account the contribution of logarithmic terms that appear in the perturbative expansions of the cross sections to all orders. In this work we make use the public code RESUMMINO [5], which has been developed specifically for the calculation of resummed cross sections at NLL precision for several SUSY processes, with the purpose of updating the theoretical predictions for slepton pair production cross sections with NLO+NLL accuracy for the c.o.m. energy of the LHC Run-II [6].

A consistent calculation of the cross sections requires that the order in the perturbation expansion of the partonic matrix element of the hard process matches the one of the fit of the PDFs which are employed in the computation. For this reason we will adopt the threshold-resummation improved PDFs provided by the NNPDF collaboration [7]. This particular set includes grids that have been obtained using matrix elements calculated at NLO (NNPDF30_nlo_disdytop) and NLO+NLL (NNPDF30_nll_disdytop) in the fit of a reduced experimental data set, including only Deep Inelastic Scattering (DIS), Drell-Yan and top pair production data. Consequently to this reduction these PDF sets are generally affected by a larger error with respect to the case of globally fitted PDFs.

We present our results in the form of a $K$-factor, following the prescription of Ref. [8], which is defined as:

$$K = \frac{\sigma(\mathrm{NLO}+\mathrm{NLL})_{\mathrm{NLO\ global}}}{\sigma(\mathrm{NLO})_{\mathrm{NLO\ global}}} \cdot \frac{\sigma(\mathrm{NLO}+\mathrm{NLL})_{\mathrm{NLO+NLL\ reduced}}}{\sigma(\mathrm{NLO}+\mathrm{NLL})_{\mathrm{NLO\ reduced}}}, \tag{1}$$

The purpose of this choice is two-fold. On one hand this definition allows to obtain (approximate) central total NLO+NLL cross sections with NLO+NLL PDFs via

$$\sigma(\mathrm{NLO}+\mathrm{NLL})_{\mathrm{NLL+NLO\ global}} = K \cdot \sigma(\mathrm{NLO})_{\mathrm{NLO\ global}}. \tag{2}$$

On the other hand we can rescale the (smaller) PDF error obtained from the global PDF set directly on the $K$-factor such that it will be straightforward to estimate the uncertainty on the consistent result at NLO+NLL. However in order to keep an important benefit of the resummation we will transfer on the $K$-factor the relative size of the scale uncertainty calculated on the NLO+NLL result. We will also sum in quadrature the two (independent) sources of uncertainty in order to obtain an overall theoretical error band.

In Fig. 3 we show the results for the differential (left) and integrated (right) cross section of first and second generation slepton pair production. The differential cross section has been evaluated for one choice of the SUSY parameters which predicts a slepton mass of 564 GeV, while the total cross section has been obtained for a range of slepton masses within the sensitivity of the LHC by the end of the Run-II [9]. In the lower plots we show the $K$-factor as defined in Eq. 1 (red curve) and the ratio of the central values obtained with the reduced PDF sets fitted at NLO and NLO+NLL (blue dashed line). The latter highlights the effect of the resummation in the sole PDF fit. Comparing these two curves we notice a partial compensation between the effect of the resummation within the PDFs and the partonic matrix element.

In Fig. 4 we repeat the same analysis for the case of third generation sleptons. The experimental searches for stau pair production yield less stringent limits on the mass of the SUSY particles since they also require the reconstruction of the taus in the final state [10]. Moreover since in the stau sector large mixing is allowed, the experimental limits have been determined

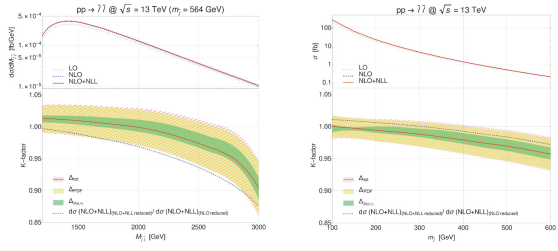


Figure 3 – Invariant-mass (left) and integrated cross section (right) distributions with their $K$-factors (lower panels) according to Eq.(1) using the full expression (full red) and only its second, PDF-dependent part (dashed blue line) for the pair production of left-handed selectrons/smuons at the LHC with $\sqrt{s} = 13$ TeV.

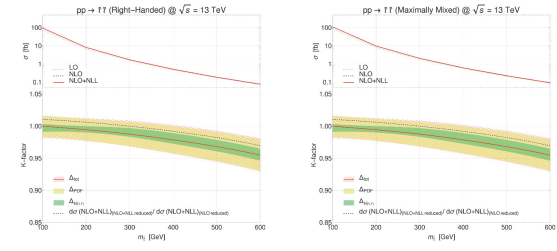


Figure 4 – Same as in the right plot of Fig. 3 for the integrated cross section of stau pair production for two mixing scenarios: totally right-handed (left) and maximally mixed (right).

assuming different compositions of the mass eigenstates. We show our results assuming purely right-handed staus and a maximal mixing respectively in the left and right plots of Fig. 4, since the case of purely left-handed staus can be directly related to the results obtained above. For what concerns the resulting $K$-factor we obtain similar results regardless of the stau mixing because the QCD corrections turn out to be largely independent on the weak coupling structure of the underlying partonic cross section and the dependence on the weak couplings cancels in the ratios of Eq. 1. Similarly to the previous case, we observe a compensation between the effect of the resummation within the PDFs and the partonic matrix element.

## Acknowledgments

This work is supported by the Science and Technology Facilities Council (STFC), grant number ST/P000711/1, and by the BMBF under contract 05H15PMCCA, and the DFG through the Research Training Network 2149 “Strong and weak interactions from hadrons to dark matter”.

## References

1. NNPDF Collaboration, Eur. Phys. J. **C77**, 10 (2017).
2. E. Accomando, J. Fiaschi, F. Hautmann, S. Moretti, arXiv:1712.06318 [hep-ph]
3. S. Dulat *et al*, *Phys. Rev.* D **93**, 3 (2016).
4. W. Beenakker *et al*, *Phys. Rev. Lett.* **83**, 3780-3783 (1999).
5. B. Fuks, M. Klasen, D.R. Lamprea, M. Rothering, Eur. Phys. J. **C73**, 2480 (2013).
6. J. Fiaschi, M. Klasen, JHEP **1803**, 094 (2018).
7. M. Bonvini *et al*, JHEP **1509**, 191 (2015).
8. W. Beenakker *et al*, Eur. Phys. J. **C76**, 2 (2016).
9. CMS Collaboration, CMS-PAS-SUS-17-009 (2017).
10. CMS Collaboration, CMS-PAS-SUS-17-003 (2017).

# Parton pseudo-distribution functions as a new approach for the ab-initio study of hadron structure

Joseph Karpie[1,2], Kostas Orginos [1,2], Anatoly Radyushkin [2,3] Savvas Zafeiropoulos[4a]
[1] *Department of Physics, The College of William & Mary, Williamsburg, VA 23187, USA*
[2] *Thomas Jefferson National Accelerator Facility, Newport News, VA 23606, USA*
[3] *Physics Department, Old Dominion University, Norfolk, VA 23529, USA*
[4] *Institute for Theoretical Physics, Universität Heidelberg, Philosophenweg 12, D-69120 Germany*

In this presentation we show the first results of the study of parton pseudo-distribution functions on the lattice which is a novel method that can be used to extract parton distribution functions employing ab-initio methods.

## 1 Introduction

A precise knowledge of Parton Distribution Functions (PDFs) is of utmost importance in order to capitalize all the information collected by hadron colliders and to transform it into predictions for Standard Model and beyond the Standard Model Physics. Factorization theorems, dictate that the cross-sections of different processes can be cast as the convolution of a part that can be calculated within QCD perturbation theory and a PDF, that characterizes the hadronic target involved, and thus is naturally non-perturbative. However PDFs, are defined through matrix elements of some bilocal operators on the light cone $z^2 = 0$ and therefore seem to be naturally inaccessible for lattice simulations that are performed in Euclidean space. An important step forward out of this deadlock was performed by X. Ji [1] who proposed the use of purely space-like separations and introduced the concept of quasi-PDF that can be matched to the PDF with the use of Large Momentum Effective Theory. Quasi-PDFs have been studied extensively in the literature [2]. Despite the promising first results, some of the tantalizing issues that the quasi-PDF approach faces is the fact that matrix elements with very large momentum need to be computed and that the non-perturbative renormalization program is relatively complicated. A related and very promising approach [3] was proposed by one of us (AR), and its first lattice implementation has been already performed [4]. Both previous approaches can be employed for the construction of lattice cross sections to study partonic structure from lattice QCD simulations [5].

## 2 Formalism

The starting point of our calculation is the equal time hadronic matrix element where the quark and anti-quark fields are separated by a finite distance. The pertinent matrix element

$$\mathcal{M}^{\alpha}(z,p) \equiv \langle p|\bar{\psi}(0)\,\gamma^{\alpha}\,\hat{E}(0,z;A)\tau_3\psi(z)|p\rangle\,, \tag{1}$$

[a] Speaker.

contains the $0 \to z$ straight-line gauge link $\hat{E}(0,z;A)$ in the fundamental representation, the flavor Pauli matrix $\tau_3$, and an appropriate gamma matrix $\gamma^a$ . One can decompose the matrix element as $\mathcal{M}^\alpha(z,p) = 2p^\alpha \mathcal{M}_p(-(zp),-z^2) + z^\alpha \mathcal{M}_z(-(zp),-z^2)$ . The twist-2 contribution can be obtained in the limit $z^2 \to 0$ from the $\mathcal{M}_p(-(zp),-z^2)$ part. When considering $z=(0,0,0,z_3)$, $\alpha$ in the temporal direction, and the hadron momentum $p=(p^0,0,0,p)$ the $z^\alpha$-part drops out. The Lorentz invariant quantity $\nu = -(zp)$, is coined as the Ioffe time [6,7]. With these definitions

$$\langle p|\bar{\psi}(0)\,\gamma^0\,\hat{E}(0,z;A)\tau_3\psi(z)|p\rangle \;= 2p^0 \mathcal{M}_p(\nu,z_3^2)\,. \tag{2}$$

We introduce the Ioffe time pseudo-PDF $\mathcal{M}(\nu,z_3^2)$ which can be matched to the regular PDF $f(x,\mu^2)$ at a scale $\mu^2 = 4e^{-2\gamma_E}/z_3^2$. One can derive the scale dependence of the Ioffe time pseudo-PDF from the DGLAP evolution of the regular PDFs. The evolution equation for the Ioffe time pseudo-PDF reads

$$\frac{d}{d\ln z_3^2}\,\mathcal{M}(\nu,z_3^2) = -\frac{\alpha_s}{2\pi}\,C_F \int_0^1 du\, B(u)\mathcal{M}(u\nu,z_3^2)\;,\quad \text{with}\;\; B(u) = \left[\frac{1+u^2}{1-u}\right]_+\,, \tag{3}$$

where $C_F = 4/3$, and $B(u)$ is the LO evolution kernel for the non-singlet quark PDF [7]. In principle one can use the matrix element of Eq. (2) in the small $z_3$ limit in order to extract the $\overline{\text{MS}}$ Ioffe time PDF $\mathcal{I}(\nu,\mu^2)$, the Fourier transform of the PDF, according to $\mathcal{M}(\nu,z_3^2) = C(\nu,\mu^2 z_3^2,\alpha)\otimes\mathcal{I}(\nu,\mu^2)+\mathcal{O}(z_3^2)$.[3] Unfortunately, large $\mathcal{O}(z_3^2)$ corrections forbid such an extraction.

It has been posited [3] that $z_3^2$ corrections which are related to the transverse structure of the hadron will hopefully cancel approximately if one constructs an appropriate ratio. One can argue that $\mathfrak{M}(\nu,z_3^2) \equiv \mathcal{M}_p(\nu,z_3^2)/\mathcal{M}_p(0,z_3^2)$ will have smaller $\mathcal{O}(z_3^2)$ corrections and we will use it to extract the Ioffe time pseudo-PDFs. This ratio is expected to have a well defined continuum limit and does not require renormalization.

## 3 Numerical Implementation

Our first study was performed employing 500 quenched gauge configurations with a volume of $32^3 \times 64$ and a lattice spacing of 0.093 fm. The maximum nucleon momentum of our study was 2.5 GeV. We calculate the relevant matrix elements by employing the methodology [8] using an operator insertion given by Eq. (1). We calculate a nucleon two point function given by $C_p(t) = \langle \mathcal{N}_p(t)\overline{\mathcal{N}}_p(0)\rangle$, where by $\mathcal{N}_p(t)$ we denote the helicity averaged, non-relativistic nucleon interpolating field of momentum $p$. Additionally, we calculate the correlator given by

$$C_p^{\mathcal{O}^0(z)}(t) = \sum_\tau \langle \mathcal{N}_p(t)\mathcal{O}^0(z,\tau)\overline{\mathcal{N}}_p(0)\rangle \quad \text{with} \quad \mathcal{O}^0(z,t) = \overline{\psi}(0,t)\gamma^0\tau_3\hat{E}(0,z;A)\psi(z,t)\,. \tag{4}$$

Then the effective bare matrix element

$$\mathcal{M}_{\text{eff}}(z_3 p, z_3^2; t) = \frac{C_p^{\mathcal{O}^0(z)}(t+1)}{C_p(t+1)} - \frac{C_p^{\mathcal{O}^0(z)}(t)}{C_p(t)}\,, \tag{5}$$

is defined. It was shown [8], that the desired matrix element $\mathcal{J}$ of Eq. (1) can be obtained considering the limit of large Euclidean time separation.

In Fig. 1, we plot the ratio $\mathfrak{M}(\nu,z_3^2)$ as a function of the Ioffe time $\nu$. It is interesting to observe that the data collapse approximately on the same curve (similarly for the imaginary part). One plausible explanation of this phenomenon is an approximate factorization of the transverse and longitudinal structure of the hadron. By considering the cosine Fourier transform of the quark minus the antiquark distributions (denoted as $q_v(x)$) one can obtain the real part $\mathfrak{M}_R(\nu)$ of the Ioffe-time distribution while the imaginary part of this distribution can be obtained by the sine Fourier transform of the function $q_+(x) = q(x) + \bar{q}(x)$.

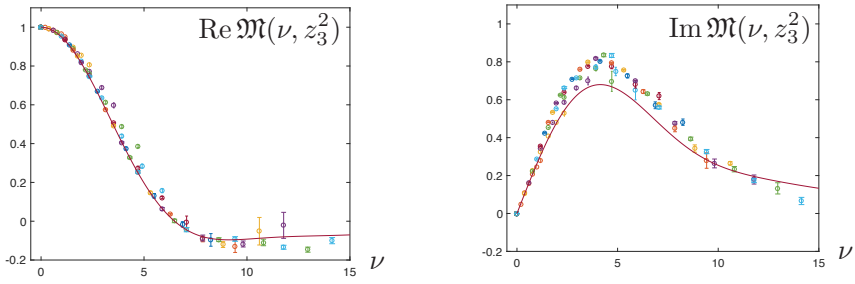


Figure 1 – Real and Imaginary parts of $\mathfrak{M}(\nu, z_3^2)$. The curves plotted for comparison are discussed in the text.

For eye-guidance and neglecting the anti-quark distribution, the Ioffe time distribution that one obtains from the model PDF given by $q_v(x) = \frac{315}{32}\sqrt{x}(1-x)^3$ is plotted. Despite the good agreement between the data plotted as a function of $\nu$ and the model curve there is still some lingering $z_3$-dependence. It was argued [4] that one can expect that since different values of $z_3^2$ for the same $\nu$ correspond to the Ioffe time distribution at different scales. Next, we check whether evolution can diminish or even get rid of this residual scatter, by solving the evolution equation at leading order and checking how it affects our data for energy scales larger than 500 MeV. More specifically, we fix the point $z_3'$ at the value $z_0 = 2a$ corresponding, at the leading logarithm level, to the $\overline{\text{MS}}$-scheme scale $\mu_0 \sim 0.8$ GeV and evolve the rest of the points to that scale. In Fig. 2 we plot the data for the reduced Ioffe time distribution before and after evolution and we observe a significant reduction of the residual scatter.

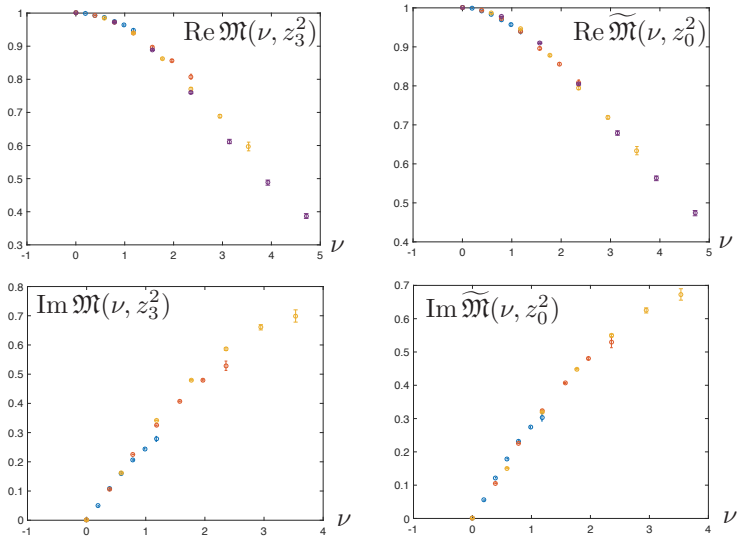


Figure 2 – The ratio $\mathfrak{M}(\nu, z_3^2)$ for for $z_3/a = 1, 2, 3$, and 4. **: Top:** Real part. **Bottom:** Imaginary part. **LHS:** Data before evolution. **RHS:** Data after evolution. Evolution collapses all data to the same universal curve.

Finally, as a proof of concept we attempted a first comparison of the evolved data for Re $\mathfrak{M}$ and compare them to recent results obtained from phenomenological studies performed by the global fitting community. In Fig. 3 we show the evolved data at the LHS and the comparison

with the phenomenological curves on the RHS.

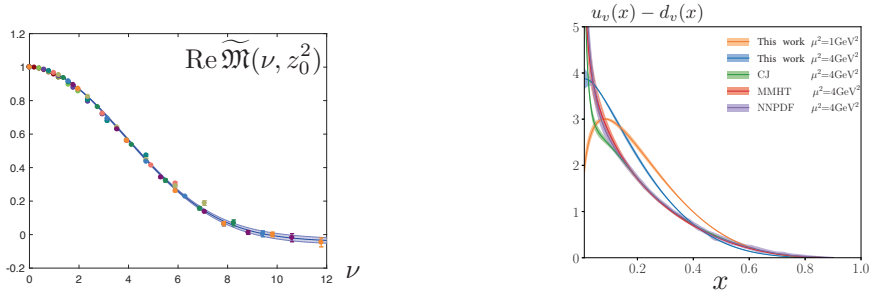


Figure 3 – LHS: Data points for Re $\mathfrak{M}(\nu, z_3^2)$ with $z_3 \leq 10a$ evolved to $z_3 = 2a$. RHS: $u_v(x) - d_v(x)$ built from the evolved data corresponding to the $\mu^2 = 1$ GeV$^2$ scale; evolved to $\mu^2 = 4$ GeV$^2$.

## 4 Conclusions

We presented the first results of the parton-pseudo distribution method as a means to extract PDFs from lattice QCD. A particular ratio of the pertinent matrix element leads to a practical method that one can adopt in order to obtain the PDFs in a lattice QCD computation. This method has expedited convergence to the light-cone limit and a well defined continuum limit. The first feasibility tests were carried out in the quenched approximation with relatively heavy pions but despite the limitations of the first study we demonstrated that already these data are in a reasonable agreement with the phenomenological extractions of the PDFs and additionally are consistent with the scale evolution of the PDFs. Having shown that a priori there are no conceptual obstacles for the lattice community to deliver a PDF employing this method we plan to address all the different sources of systematic errors in our forthcoming publications.

## Acknowledgments

This work is supported by Jefferson Science Associates, LLC under U.S. DOE Contract #DE-AC05-06OR23177. KO and JK were supported by U.S. DOE grant #DE-FG02-04ER41302, and by STFC consolidated grant ST/P000681/1. AR was supported by U.S. DOE Grant #DE-FG02-97ER41028. SZ acknowledges support by the NSF (USA) under grant PHY-1516509 and by the DFG CRC SFB 1225 (ISOQUANT). JK was supported by a DOE SCGSR fellowship at JLab. Simulations were run on computing facilities at the College of William and Mary, provided by contributions from the NSF (MRI grant PHY-1626177), the COVAETF and the Office of Naval Research. In addition resources at NERSC, a DOE Office of Science User Facility supported by the Office of Science of the U.S. DOE under Contract #DE-AC02-05CH11231, were used.

## References

1. X. Ji, Phys. Rev. Lett. **110**, 262002 (2013)
2. J. W. Chen *et al.*, Phys. Rev. D **97**, no. 1, 014505 (2018); C. Alexandrou *et al.*, arXiv:1803.02685 [hep-lat].
3. A. V. Radyushkin, Phys. Rev. D **96**, no. 3, 034025 (2017); A. Radyushkin, arXiv:1801.02427 [hep-ph].
4. K. Orginos *et al.*, Phys. Rev. D **96**, no. 9, 094503 (2017); J. Karpie *et al.*, EPJ Web Conf. **175**, 06032 (2018)
5. Y. Q. Ma and J. W. Qiu, Phys. Rev. Lett. **120**, no. 2, 022003 (2018)
6. B. L. Ioffe, Phys. Lett. **30B**, 123 (1969).
7. V. Braun *et al.*, Phys. Rev. D **51**, 6036 (1995)
8. C. Bouchard *et al.*, Phys. Rev. D **96**, no. 1, 014504 (2017)

# The importance of ln(1/x) resummation: a new QCD analysis of HERA data

Francesco Giuli
*Particle Physics, Denys Wilkinson Buildingg, Keble Road, University of Oxford, OX1 3RH Oxford, UK*

Fits to the final combined HERA deep-inelastic scattering cross-section data within the conventional DGLAP framework of QCD have shown some tension at low-$x$ and low-$Q^2$. A resolution of this tension incorporating $\ln(1/x)$-resummation terms into the HERAPDF fits is investigated using the `xFitter` program. The kinematic region where this resummation is important is delineated. Such high-energy resummation not only gives a better description of the data, particularly of the longitudinal structure function $F_L$, it also results in a gluon PDF which is steeply rising at low x for low scales, $Q^2 \simeq 2.7$ GeV$^2$, contrary to the fixed-order (FO) NLO and NNLO gluon PDF. This contribution is based on the results presented in Ref. 1 [1].

## 1 Input data sets

The input datasets in use are the final combined $e^{\pm}p$ cross-section measurements of H1 and ZEUS [2] (both from neutral-current (NC) and charged-current (CC) processes and for $e^+p$ and $e^-p$ scattering) and the HERA combined charm [3] from ZEUS and H1. The inclusion of charm data in the fit is useful to determine the optimal charm pole mass. Additionally, since they extend to rather small values of $x$, they may be sensitive to $\ln(1/x)$ resummation effects.

## 2 Fit strategy

The present QCD analysis uses the `xFitter` program [4,5] and is based on the HERAPDF2.0 setup. The quark distributions at the initial scale $Q_0^2$ were represented by the generic form:

$$xq_i(x, Q_0) = A_i x^{B_i}(1-x)^{C_i} P_i(x), \tag{1}$$

where $P_i(x) = 1 + \mathcal{O}(x)$ defines a polynomial in powers of $x$. The parametrised quark distributions $q_i$ were chosen to be the valence quark distributions ($xu_v$, $xd_v$) and the light anti-quark distributions ($x\bar{U} = x\bar{u}$, $x\bar{D} = x\bar{d} + x\bar{s}$). The gluon distribution was parametrised with the more flexible form:

$$xg(x) = A_g x^{B_g}(1-x)^{C_g} P_g(x) - A'_g x^{B'_g}(1-x)^{C'_g}\,. \tag{2}$$

The normalisation parameters $A_{u_v}$ and $A_{d_v}$ were fixed using the quark counting rules and $A_g$ using the momentum sum rule. The normalisation and slope parameters, $A$ and $B$, of $\bar{u}$ and $\bar{d}$ were set equal such that $x\bar{u} = x\bar{d}$ at very small $x$. The strange PDFs $xs$ and $x\bar{s}$ were parametrised as $xs = x\bar{s} = 0.4x\bar{D}$, representing a suppression of strangness with respect to the light down-type sea quarks, but the input data are not sensitive to the fraction of strangeness. The $\ln(1/x)$ resummation corrections are avaiable in the `HELL` code, which is a standalone code that implements the resummation corrections to the DGLAP splitting functions $P$ and to the DIS coefficient functions $C$ (both massless and massive) up to next-to-leading-log accuracy in $\ln(1/x)$ (NLL$x$). The scale at which PDFs are parameterised have been chosen to be $Q_0^2 = 2.56$ GeV$^2$

as compared to 1.9 GeV$^2$ of HERAPDF2.0. The reason is that the numerical computation of $\ln(1/x)$-resummation corrections may become unreliable at low scales due to the large value of the strong coupling $\alpha_S$.

## 3 Results

The effect of $\ln(1/x)$ resummation on splitting functions and DIS coefficient functions is more dramatic at NNLO than at NLO[6]. In fact, the full calculation with NNLO+NLL$x$ resummation is closer to the NLO result than it is to the NNLO result. This is not accidental and is mostly due to the perturbative instability of the NNLO correction to the splitting functions generated by small-$x$ logarithms[7]. Thus, to better assess the impact of the $\ln(1/x)$ resummation on the original HERAPDF analysis, we only focus on NNLO fits.

As well as evaluating uncertainties due to the experimental statistical and systematic errors we have perfomed an exploration of model and parametrisation uncertainties as follows. We have varied the charm mass ($m_c$ = 1.41, 1.51 GeV), the bottom mass ($m_b$ = 4.25, 4.75 GeV), the strong coupling $\alpha_S(m_Z^2)$ ($\Delta\alpha_S = \pm 0.002$), the strangeness fraction ($f_s = 0.3$, $f0.5$), the initial scale ($Q_0^2 = 2.88$ GeV$^2$), and the $Q^2$ cut on the data ($Q^2_{\rm min} = 2.7$ GeV$^2$, 5 GeV$^2$).

Furthermore, parametrisation uncertainties have been explored by adding extra terms to the polynomials $P_i(x)$ of Eq. 1. The only noticeable difference comes from the addition of a linear term to the polynomial $P_{u_V}(x)$ of the valence up quark PDF. The largest contribution to the uncertainty on the gluon distribution arises from the variation of the $Q^2_{\rm min}$ cut to 5 GeV$^2$. Interestingly, this uncertainty is reduced for the fit with $\ln(1/x)$ resummation, due to reduced tensions with the data.

Fig. 1 shows a comparison of PDFs with and without $\ln(1/x)$ resummation at $Q^2 = 3$ GeV$^2$. This figure displays also the full uncertainty bands. When resummation is included, both the gluon and the total singlet PDFs rise towards low $x$, in contrast to the behaviour of the gluon when resummation is not included.

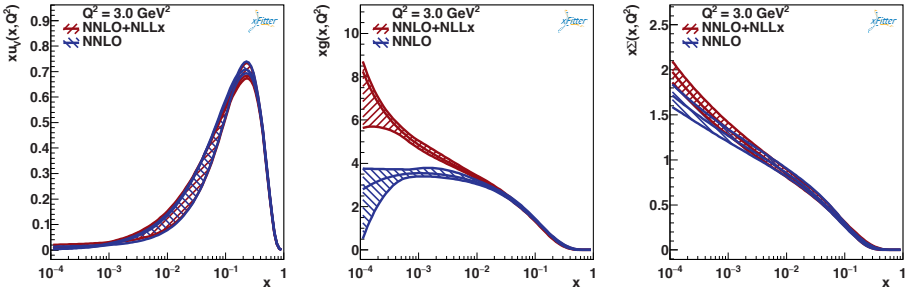


Figure 1 – The up valence PDF $xu_v$, the gluon PDF $xg$ and the total singlet PDF $x\Sigma$ for the final fits with (NNLO+NLL$x$) and without (NNLO) $\ln(1/x)$ resummation.

The $\chi^2$ values for the fits are summarised in Tab. 1. There is a decrease of 73 units in $\chi^2$ when the $\ln(1/x)$ resummation is used. Most of this difference is coming from the highly accurate NC $E_p = 920$ GeV data which probe the low-$x$ and low-$Q^2$ region and are thus most sensitive to $\ln(1/x)$ resummation (413/377 to be compared to 446/377). As expected, a decrease in $\chi^2$ has been also observed in the NC $E_p = 820$ GeV (65/70 for the NNLO+NLLx fit vs. 70/70 for the FO NNLO fit) and in the charm data (49/47 vs. 48/47), which are also expected to have some sensitivity. Other data sets entering the fit probe higher $x$ and $Q^2$ and their $\chi^2$ are not significantly changed. In Fig. 2 the fit results are compared to the NC $E_p = 920$ GeV inclusive reduced cross-section data in the lowest $Q^2$ bins included in the fits. It is evident that for the fit including $\ln(1/x)$-resummation effects, not only the initial description of the data is better,

Table 1: Total $\chi^2$ per d.o.f. for the PDF fits to HERA inclusive and charm data with the new settings. Also shown are the contributions to the $\tilde{\chi}^2$/n.d.p from the correlated shifts and the log terms.

| | NNLO fit with new settings | NNLO+NLL$x$ fit with new settings |
|---|---|---|
| Total $\chi^2$/d.o.f | 1446/1178 | 1373/1178 |
| correlated $\tilde{\chi}^2$/n.d.p inclusive | 102 | 77 |
| correlated $\tilde{\chi}^2$/n.d.p charm | 15 | 11 |
| log $\tilde{\chi}^2$/n.d.p inclusive | 20 | −3 |
| log $\tilde{\chi}^2$/n.d.p charm | −2 | −1 |

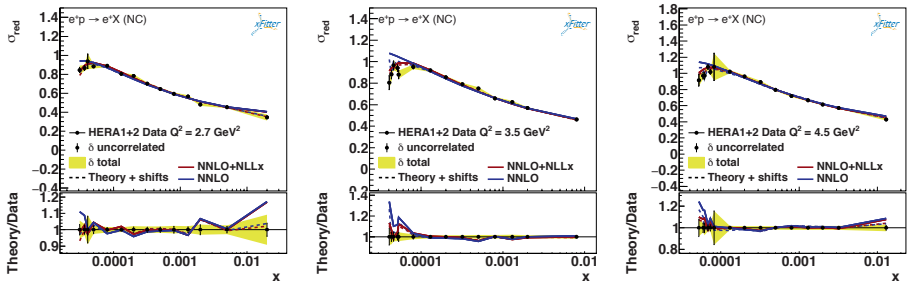


Figure 2 – The HERA NC $E_p = 920$ GeV data compared to the fits with and without $\ln(1/x)$ resummation for the $Q^2 = 3.5$, $Q^2 = 3.5$ and 4.5 GeV$^2$ bins.

but also the correlated shifts are smaller and this is one of the reasons why the $\chi^2$ of the fit is significantly smaller. In particular, it is evident that the low-$x$ turn-over of the measurements is better reproduced by the fit that includes $\ln(1/x)$ resummation, which in turn explains the big reduction of the $\chi^2$. This is a direct consequence of the steeper gluon at low $x$ (see Fig. 1) which makes $F_L$ larger at low $x$ causing a more pronounced turn-over of the reduced cross section, defined as follows:

$$\sigma_{\rm red} = F_2 - \frac{y^2}{Y_+} F_L \,, \tag{3}$$

where $F_2$ and $F_L$ are the structure functions related to the parton distributions[8], $Y_+ = 1+(1-y)^2$ and $y = Q^2/(sx)$.

This point is also illustrated in Fig. 3 where the H1 $F_L$ measurement is compared to the theoretical predictions of $F_L$ with and without $\ln(1/x)$. It is clearly visible that the description of this data set is improved in the former case thanks to the fact that $\ln(1/x)$-resummed predictions for $F_L$ are larger at low $x$.

The results presented so far indicate that the improvement of the description of the HERA data when including $\ln(1/x)$ resummation is driven by the low-$x$ and low-$Q^2$ data. We can also delineate the kinematic region responsible for the improvement more precisely. To do so, we have performed $\chi^2$ scans in $Q^2_{\rm min}$ with no cut in $x$, and in $x_{\rm min}$ (where $x_{\rm min}$ is the minimum value of Bjorken $x$ allowed in the fit) fixing $Q^2_{\rm min} = 2.7$ GeV$^2$. Furthermore, an additional $\chi^2$ scan in $y_{\rm max}$ has been done, excluding from the fit data with $y > y_{\rm max}$. The $\chi^2$ scans as a function of $Q_{\rm min}$, $x_{\rm min}$ and $y_{\rm max}$ allow us to delineate the region of the $(x, Q^2)$-plane in which $\ln(1/x)$ resummation is important.[a] Fig. 3 displays a zoom of the low-$x$ and low-$Q^2$ kinematic region covered by the HERA1+2 inclusive and charm data at $E_p = 920$ GeV. The green shaded area indicates the region such that $x < 5 \cdot 10^{-4}$, 2.7 GeV$^2$ $< Q^2 <$ 15 GeV$^2$, and $0.4 < y < 1$

[a] The actual plane over which the constraint acts is the $(x, Q^2/s)$-plane. However, for simplicity in the following we will only consider the $E_p = 920$ GeV inclusive and the charm datasets that were both taken at $\sqrt{s} = 318$ GeV.

(assuming $\sqrt{s} = 318$ GeV) determined by combining the results of the scans discussed above.[b] This provides an estimate of the region where $\ln(1/x)$ resummation provides a significantly better description of the HERA data as compared to FO predictions.

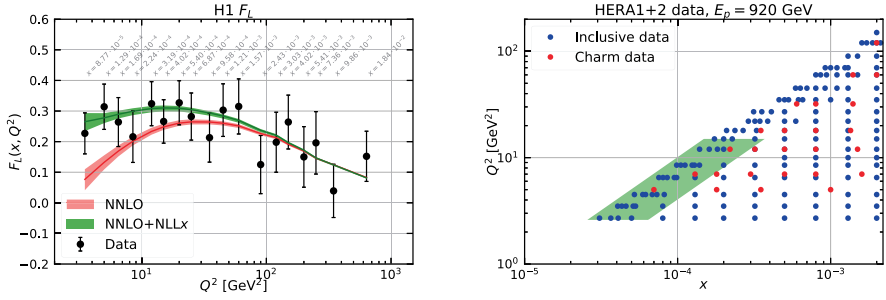


Figure 3 – Left: The H1 measurement of $F_L$ compared to the predictions with and without $\ln(1/x)$ resummation; Right: Scatter plot of the low-$x$ and low-$Q^2$ kinematic region covered by the HERA1+2 inclusive data and charm data at $E_p = 920$ GeV. The green shaded area indicates the region in which $\ln(1/x)$ resummation has a significant effect.

## 4 Conclusion

In conclusion, $\ln(1/x)$ resummation provides a substantial improvement in the description of the precise HERA1+2 combined data and it overcomes a major disadvantage of the FO analyses, namely a decreasing gluon PDF at low $x$ and $Q^2$. It represents an alternative to the addition of higher-twist terms [9,10,11] and does not suffer from the pathological features of some of these analyses [9].

## References


1. Abdolmaleki, H. et al, *Impact of low-x resummation on QCD analysis of HERA data*, arXiv:1802.00064 (2018).
2. Abramowicz, H. et al, *Combination of measurements of inclusive deep inelastic $e^{\pm}p$ scattering cross sections and QCD analysis of HERA data*, Eur. Phys. J. C75, 580 (2015).
3. Abramowicz, H. et al, *Combination and QCD Analysis of Charm Production Cross Section Measurements in Deep-Inelastic ep Scattering at HERA*, Eur. Phys. J. C73, 2311 (2013).
4. Alekhin, S. et al, *HERAFitter*, Eur. Phys. J. C75, 304 (2015).
5. Aaron, F.D. et al, *Combined Measurement and QCD Analysis of the Inclusive $e^{\pm}p$ Scattering Cross Sections at HERA*, JHEP 1001, 109 (2010).
6. Bonvini, M. et al, *Towards parton distribution functions with small-x resummation: HELL 2.0*, JHEP 12, 117 (2017).
7. Ball, R. et al, *Parton distributions with small-x resummation: evidence for BFKL dynamics in HERA data*, arXiv:1710.05935 (2017).
8. Gao, J. et al, *The Structure of the Proton in the LHC Precision Era*, arXiv:1709.04922 (2017).
9. Abt, I. et al, *Study of HERA ep data at low $Q^2$ and low $x_{Bj}$ and the need for higher-twist corrections to standard perturbative QCD fits*, Phys. Rev. D94 3, 034032 (2016).
10. Harland-Lang, L. A. et al, *The impact of the final HERA combined data on PDFs obtained from a global fit*, Eur. Phys. J. C76, 186 (2016).
11. Motyka, L. et al, *Evidence of quasi-partonic higher-twist effects in deep inelastic scattering at HERA at moderate $Q^2$*, arXiv:1707.05992 (2017).


[b] In fact, given the range in $y$, the constraint on $x$ has no effect on the shaded area.

# 8.
# QCD

# QCD Results from the Tevatron

Christina Mesropian
on behalf of the CDF and D0 collaborations
*The Rockefeller University,*
*New York, NY USA*

We present results from soft and hard QCD studies at the Tevatron. The recent study of central exclusive $\pi^+\pi^-$ production at $\sqrt{s} = 900$ and 1960 GeV is discussed, as well as results on multi-parton interaction (MPI) for different final states, including final states consisting of heavy flavor mesons, $J/\psi$ and/or $\Upsilon$. Finally, the measurement of $Z \to bb$ jets is presented.

## 1 Introduction

The Fermilab Tevatron, $p\bar{p}$ collider with superconducting magnets operated from 2001 to 2011 at a center of mass energy of 1.96 TeV (Run II). The CDF and D0 detectors each recorded approximately 10 fb$^{-1}$ of collision data in Run II. QCD studies at the Tevatron contributed significantly to the major progress in understanding the strong interactions. Almost 7 years after the Tevatrons final shutdown in September 2011, new interesting results from both collaborations address various aspects of QCD theory, providing rigorous tests of predictions for hadron colliders and reducing uncertainties for the most problematic parts of the theory.

## 2 Central Exclusive Production

Central exclusive production is defined as the class of reactions $p + \bar{p} \to p + X + \bar{p}$, where the colliding particles emerge intact and a produced state $X$ is separated from the leading particles by large rapidity gaps. These processes have been the subject of much interest in the recent years, particularly for large $\sqrt{s}$, where the rapidity range $\Delta y_{total} = 2 \times \ln \sqrt{s}/m_p$=15.3 at the Tevatron allows the possibility of large rapidity gaps produced between state X and proton and antiproton. The CDF experiment previously published results on the first observations of exclusive dijet production, exclusive di-photon production, photon-pomeron interactions[a] ($\gamma + pomeron \to J/\psi, \psi(2S)$) as well as exclusive productions of $\chi_c$ by double pomeron exchange (DPE), see review[1] for additional information. One can consider DPE as a quantum number filter, favoring

[a] the *pomeron* is a hypothetical object with the quantum numbers of the vacuum

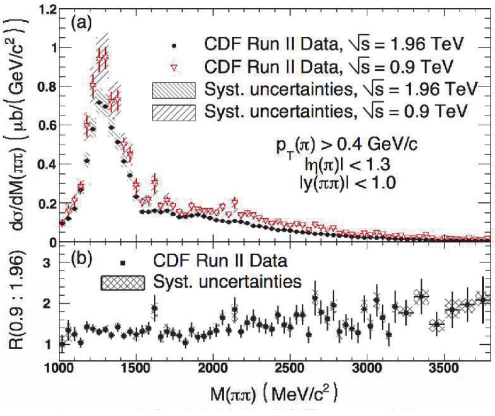


Figure 1 – (a) Differential cross section $d\sigma/dM(\pi\pi)$ for two charged particles, assumed to be $\pi^+\pi^-$, with $p_T >$ 0.4 GeV/c, $|\ \eta\ |$<1.3 and $|\ y(\pi\pi)\ |$<1.0 between two rapidity gaps 1.3<$|\ \eta\ |$< 5.9. Red(black) points correspond to 0.9(1.96) TeV data; (b) Ratio of cross sections at $\sqrt{s}$=0.9 and 1.96 TeV.

states having valence gluons, such as *glueballs*, i.e., hadrons with no valence quarks. Such states are expected in QCD, but their existence is not established.

The results [2] discussed here use the CDF data from 2 different $\sqrt{s}$ (900 and 1960 GeV), comprised from events with two charged particles, each with $|\ \eta\ |$<1.3 and $p_T$ >0.4 GeV/c, and no other activity above noise levels in the full detector up to $|\ \eta\ |$=5.9. The noise levels are determined for each sub-detector using bunch-crossing (zero-bias) triggers in which no tracks or CLC[b] hits are detected. The cross section 1 at $\sqrt{s} = 1.96$ TeV shows a sharp decrease at 1000 MeV/c$^2$ (for $p_T(\pi\pi) > 1$ GeV/c), a strong $f_2(1270)$ resonance, and indications of other features of uncertain origin at higher mass. The cross section at 0.9 TeV is similar in shape but higher by a factor of 1.21.6. As the production is expected to be dominated by double pomeron exchange, selecting isospin $I$ =0 and spin $J$ =0 or 2 states, the data can be used to further our knowledge of the isoscalar mesons.

## 3 Studies of Multiple Parton Interactions (MPI)

The CDF and D0 collaborations comprehensively studied the phenomenon of MPI. These studies become increasingly important at higher center of mass energies. The events with double parton scattering (DPS) provide insight into spatial distribution of partons in the colliding hadrons. They also can be a background to many rare processes. DPS results are usually interpreted in terms of a formula $\sigma^{AB}_{DPS} = \frac{m}{2}\frac{\sigma^{A}_{SPS}\sigma^{B}_{SPS}}{\sigma_{eff}}$, where $m$ is the combinatorial factor and equal 1 for identical states $A$ and $B$ and equal 2, when $A \neq B$. $\sigma_{eff}$ is related to the parton spatial distribution. Experimentally, the determination of $\sigma_{eff}$ is based on the percentage of identified DPS events. The latter is extracted based on topological considerations which involve a proper understanding of topologies expected in SPS.

The D0 collaboration has studied [3] DP events in $\gamma\gamma + 2jets$ final state in which two pairs of partons undergo two hard interactions in a single $p\bar{p}$ collision, see Figure 2(left) for depiction of key discriminant $\Delta S$, an azimuthal angle between diphotons and dijets, and Figure 2(right) representing $\Delta S$ distribution in the data in comparison with DP and SP models. The result, $\sigma_{eff} = 19.3 \pm 1.4(stat) \pm 7.8(syst)$mb, is compatible with previous CDF and D0 results for DPS events in 4 jets, photon+3 jets final states.

[b] Gas Cherenkov luminosity counters providing rapidity coverage from 3.7 to 4.7

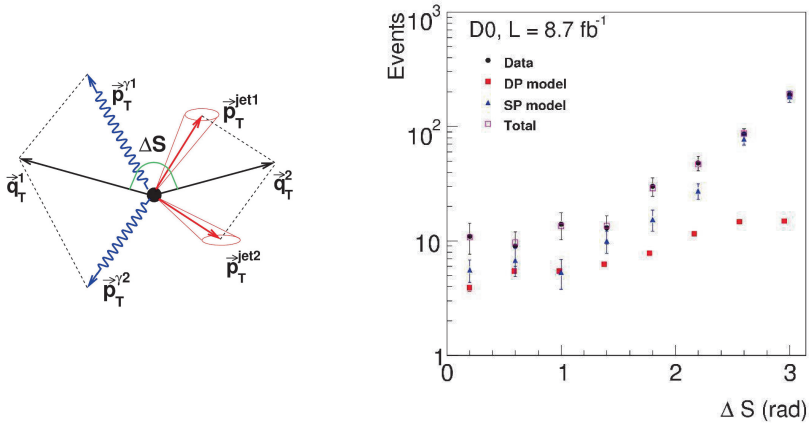


Figure 2 – (left) Pictorial representation of the key discriminant $\Delta S$, relative to orientation of photon and jet transverse momenta vectors in $\gamma\gamma + dijet$ events. Vectors $\vec{q}_T^{\,1}$ and $\vec{q}_T^{\,2}$ are the $p_T$ imbalance vectors of diphoton and dijet pairs respectively. (right) The fit of data $\Delta S$ distribution with SP and DP templates to extract the DP fraction. The black points correspond to data, red boxes correspond to the DP signal model normalized to the DP fraction obtained from the fit, and the blue triangles are the SP background template normalized to its fraction $(1 - f_{DP})$. The pink open boxes correspond to the sum of the signal and background (total).

The D0 collaboration also measured [4] for the first time the simultaneous production of $J/\psi$ and $\Upsilon\,(1S, 2S, 3S)$ in $p\bar{p}$ collisions at $\sqrt{s}$=1.96 TeV. This production is expected to be dominated by DP interactions, with production through SP being suppressed by additional powers of $\alpha_s$. Because of the dominance of $gg$ interactions in producing heavy quarkonium states, the spatial distribution of gluons in a proton is directly probed by the DP scattering rate. In contrast, the DP studies involving vector bosons and jets probe the spatial distributions of quark-quark or quark-gluon initial states. The result of $\sigma_{eff} = 2.2 \pm 0.7(stat) \pm 0.9(syst)$mb is in good agreement with the previous D0 result for double $J/\psi$ final state and lower than results for the final states that are produced predominantly by $q\bar{q}$, and $qg$ processes.

## 4 Studies of $Z \to b\bar{b}$ jets

CDF has collected 5.4 fb$^{-1}$ of $p\bar{p}$ events using the dedicated trigger path which required a displaced vertex compatible with a $b$-hadron decay. This unique dataset [5] is used to search for Standard Model $Z$ and Higgs resonances decaying into a pair of $b$-jets. The $Z$ production cross section times the $b\bar{b}$ branching ratio is measured by extracting $Z \to b\bar{b}$ events from a fit to the dijet invariant mass distribution, where the dominant QCD $b$-jet background is estimated by a data-driven technique to minimize the dependence of the analysis on the Monte Carlo simulation. The measured cross section is $\sigma(p\bar{p} \to Z) \times B(Z \to b\bar{b}) = 1.11 \pm 0.08(stat) \pm 0.13(sys)$ nb. The analysis technique is used on the same dataset to search for $H \to b\bar{b}$. No signal is found and an upper limit on the $p\bar{p} \to H \to b\bar{b}$ cross section is set at 95% C.L. resulting on 33 times the expected Standard Model value, see Figure 3.

In addition, CDF performed a search [6] for a narrow neutral scalar particle $\phi$ decaying into $b$-quark jets in multi $b$-quark jets final states. Since an inclusive search is difficult due to large multi-jet backgrounds, the analysis relies on the case where the $\phi$ boson is produced in association with one or more $b$-quarks. Final states with at least three $b$-quark jets represents a powerful search channel, with the third $b$-quark jet providing additional suppression of the large multi-jet background. The different initial production state and the lower center of mass energy with

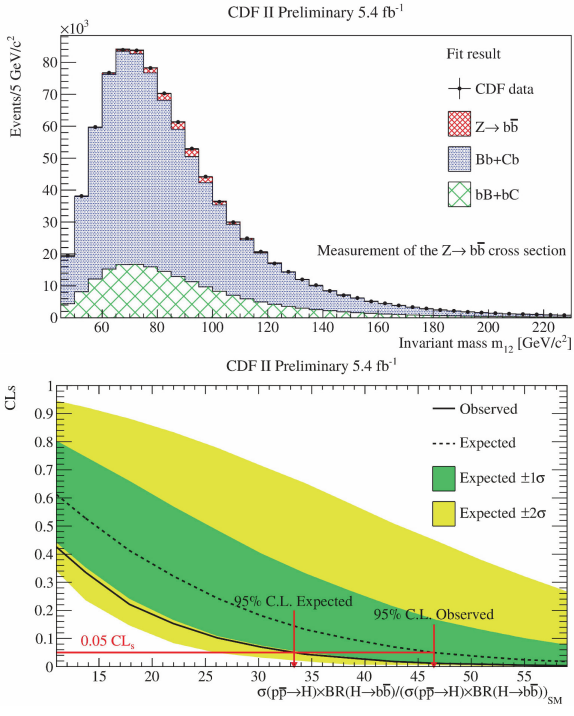


Figure 3 – (top) Invariant mass distribution of the double tagged data sample with the result of the fit In red the fitted $Z \to b\bar{b}$, in blue the $Bb + Cb$, and in green the $bB + bC$ background. Capital letter indicates the b-tag trigger jet. (bottom) Observed (black solid line) and expected (black dashed line) $CL_s$ as function of the cross section times the branching ratio normalized to SM $H \to b\bar{b}$.

respect to LHC makes this search competitive with the LHC measurements especially in the low b-quark jets invariant mass region. No hint of deviation from the SM background expectations has been observed.

## Acknowledgments

I would like to thank the organizers of the $53^{rd}$ Rencontres de Moriond for their warm hospitality and for an exciting conference.

## References

1. C. Mesropian and D. Bandurin, *Int. Journal of Modern Physics A*, Vol. **30**, 06 (2015).
2. T. Aaltonen *et al*, *Phys. Rev.* D **91**, 091101(R) (2015).
3. V.M. Abazov *et al*, *Phys. Rev.* D **93**, 052008 (2016).
4. V.M. Abazov *et al*, *Phys. Rev. Lett.* **116**, 082002 (2016).
5. CDF Public Note 11228
6. CDF Public Note 11229

# SOFT QCD AT ATLAS AND CMS

P. Starovoitov on behalf of the ATLAS and CMS Collaborations
*Kirchhoff Institute for Physics, Heidelberg University, Im Neuenheimer Feld 227, 69120 Heidelberg, Germany*

A short overview of the recent soft QCD measurements in proton-proton collisions at the Large Hadron Collider from the ATLAS and CMS collaborations is presented. The inelastic cross section measurement by CMS at 13 TeV is summarised. The contribution of the diffractive processes to the very forward photon spectra studied by ATLAS and LHCf is discussed. The ATLAS measurements of the exclusive two-photon production of the muon pairs is presented and compared to the previous ATLAS and CMS results.

## 1 Introduction

Study of proton-proton ($pp$) scattering at the high centre-of-mass energy is the main goal of LHC[3] experiments. Both ATLAS[1] and CMS[2] Collaborations perform measurements of Standard Model processes and conduct searches for new physics phenomena at the new energy frontier. Furthermore, LHC experiments are preparing the detectors upgrades for the high-luminosity LHC, where up to 200 simultaneous proton-proton collisions are foreseen. All these rely on the precise description of the non-perturbative effects in Monte Carlo simulations of detectors. Therefore, measurements of the soft QCD processes are an important ingredient of the success of Run-2 physics programs as well as the future studies towards the Phase-1 and Phase-2 upgrades.

## 2 Inelastic cross section measurement

Inclusive hadron-hadron cross sections are fundamental observables in high-energy particle, nuclear, and cosmic ray physics, and have been measured in experiments covering many orders of magnitude in center-of-mass energy, $\sqrt{s}$. The CMS measurement [4] based on $pp$ collision data collected, during several running periods with low pileup in 2015 at $\sqrt{s} = 13$ TeV with CMS forward calorimeters HF and CASTOR, covering pseudorapidities $-6.6 < \eta < -3.0$ and $+3.0 < \eta < +5.2$, is summarised in Fig. 1. These detectors provide sensitivity to a large part of the total inelastic cross section, including diffractive events with dissociated protons that produce particles only at forward rapidity. The presence of the CASTOR calorimeter in the $B = 0$ T data sample allows a larger coverage of the phase space for inelastic $pp$ collisions.

The CMS data acquisition system was triggered by the presence of both beams in the interaction point ("zero bias"). Additional triggers requiring the presence of only one beam or no beams were used to study beam-gas, electronic noise, and other backgrounds.

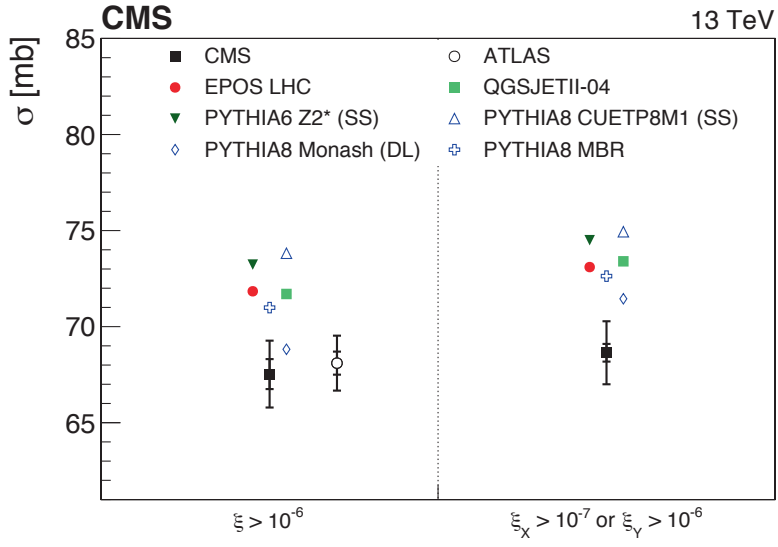


Figure 1 – Proton-proton inelastic cross section at $\sqrt{s} = 13$ TeV in two phase space regions [4], where $\xi = M^2/s$, compared to different models and to the ATLAS result [5].

An inelastic cross section of $67.5 \pm 0.8(\text{syst}) \pm 1.6(\text{lumi})$ mb is obtained for $\xi = M^2/s > 10^{-6}$ (corresponding to $M > 13$ GeV), with $M$ the larger of $M_X$ and $M_Y$, where $M_X$ and $M_Y$ are the masses of the diffractive dissociation systems with negative and positive pseudorapidities, respectively, consistent with a previous measurement in the same phase space [5]. In addition, an inelastic cross section of $68.6 \pm 0.5(\text{syst}) \pm 1.6(\text{lumi})$ mb is obtained in the enlarged phase space $\xi_X > 10^{-7}$ or $\xi_Y > 10^{-6}$ (corresponding to $M_X > 4.1$ GeV or $M_Y > 13$ GeV). The measured cross sections are smaller than those predicted by the majority of models for hadron-hadron scattering. In contrast, the same models generally describe reasonably well the measurements of the total inelastic cross section at $\sqrt{s} = 13$ TeV [5,6]. Given that the difference between the two sets of measurements is dominated by the contribution from low-mass diffractive processes, the data-model discrepancies observed here suggest a theoretical underestimation of the cross section for such events.

## 3 Diffractive processes contribution to the photon production

The LHCf [7] experiment consists of two independent detectors, called Arm1 and Arm2, installed at ±140 m from the ATLAS IP. The combined data-taking of the ATLAS and LHCf experiments, where ATLAS inner tracker is used to veto central charged-particle activity and LHCf detector is used to measure photons in the high rapidity range allows to study the diffractive events and provide precision constraints on the modelling of these processes [8].

The forward photon energy spectra measured by the LHCf-Arm1 detector are shown in Fig. 2, separately for region A ($\eta > 10.94, \phi < 180°$) and region B ($8.81 < \eta < 8.99, \phi < 20°$), and both for the $N_{\text{ch}}$-inclusive and $N_{\text{ch}} = 0$ regions. In region A, the $N_\gamma^{N_{\text{ch}}=0}$ photon energy spectrum observed in data is much harder than the inclusive-photon spectrum at the photon

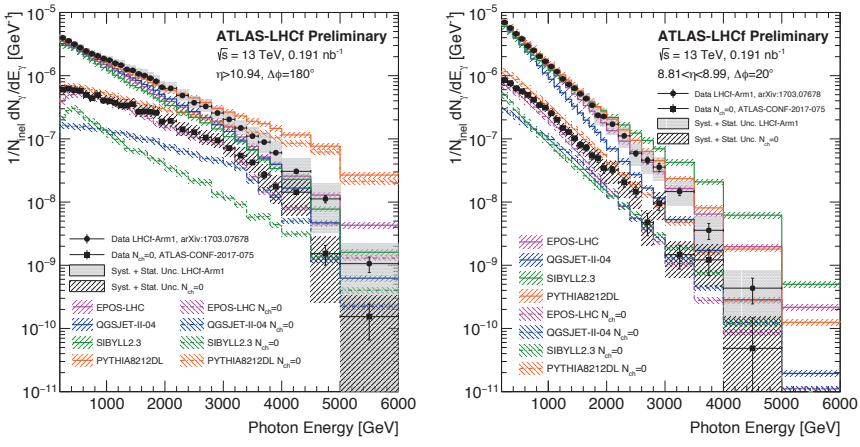


Figure 2 – Forward photon energy spectra [8] measured by the LHCf-Arm1 detector in the regions (left) A and (right) B. Filled circles show the inclusive-photon spectra [9]. Filled squares indicate the spectra for $N_{\rm ch} = 0$ events. Coloured lines indicate model predictions with (dashed lines) and without (solid lines) the $N_{\rm ch} = 0$ requirement.

energies below 3 TeV, whereas the $N_\gamma^{N_{\rm ch}=0}$ and inclusive photon spectra have similar slopes in region B.

The results are compared to predictions based on several hadronic interaction models: EPOS-LHC, QGSJET-II-04, SYBILL 2.3, and PYTHIA 8.212DL. Predictions from EPOS-LHC generally show best agreement with data. At photon energies above 2 TeV, the PYTHIA 8 predicts significantly higher ratio than observed in data. This indicates that the large discrepancy between PYTHIA 8 and data in the high-energy photon region [9] can be due to overestimation of the diffractive dissociation process in PYTHIA 8. The QGSJET-II-04 and SYBILL 2.3 models predict a relative rate of inclusive and $N_\gamma^{N_{\rm ch}=0}$ productions that is much lower than observed in data in both A and B regions. This suggests that QGSJET-II-04 and SYBILL 2.3 predict a too small contribution of low-mass diffractive events to the forward photon energy spectrum.

## 4 Exclusive $\gamma\gamma \to \mu^+\mu^-$ production

Rare photon–photon induced ($\gamma\gamma$) interactions in $pp$ collisions can be studied at the LHC with sufficient precision due to high centre-of-mass energy and high integrated luminosity.

The exclusive production process competes with the two-photon interactions involving single- or double-proton dissociation. The electromagnetic break-up of the proton typically results in a production of particles at small angles to the beam direction, which can mimic the exclusive process. However, the proton-dissociative processes have significantly different kinematic distributions compared to the exclusive reaction, allowing an effective separation of the different production mechanisms.

The exclusive $\gamma\gamma \to \mu^+\mu^-$ contribution is extracted from data by performing a binned maximum-likelihood fit to the measured dimuon acoplanarity $(1-|\phi_{\mu^+\mu}|/\pi)$ distribution [10]. The acoplanarity variable is not affected by the muon momentum scale and resolution uncertainties and provides a good separation of signal from background.

The fiducial cross section is measured to be $\sigma^{\rm excl.fid.}_{\gamma\gamma\to\mu^+\mu^-} = 3.12 \pm 0.07({\rm stat.}) \pm 0.14({\rm syst.})$ pb. This value can be compared to the bare EPA predictions from Herwig, $\sigma^{\rm EPA}_{\gamma\gamma\to\mu^+\mu^-} = 3.56 \pm 0.05$ pb, to the EPA predictions corrected for absorptive effects using the finite-size parameterisation, $\sigma^{\rm EPA,corr}_{\gamma\gamma\to\mu^+\mu^-} = 3.06 \pm 0.05$ pb.

The comparison between the measured differential cross sections and the theoretical predictions is shown in Fig. 3. The EPA predictions corrected for absorptive effects are in good agreement with the measured cross sections.

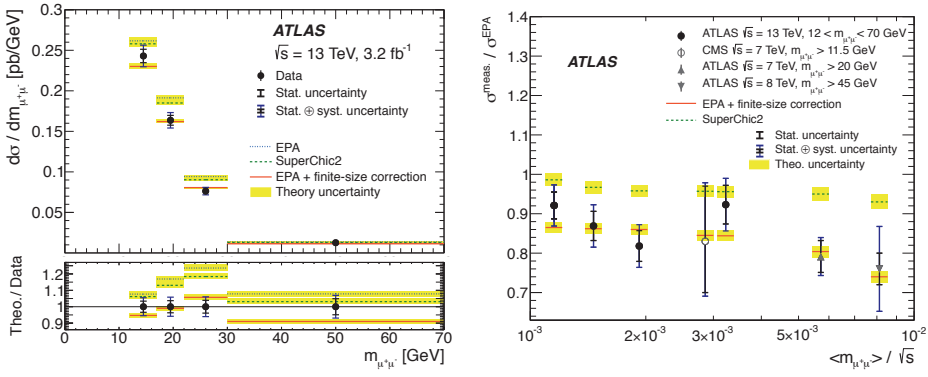


Figure 3 – (left) The exclusive $\gamma\gamma \to \mu^+\mu^-$ differential fiducial cross section measurements [10] as a function of dimuon invariant mass $m_{\mu^+\mu^-}$. (right) Comparison of the ratios of measured and predicted cross sections to the bare EPA calculations as a function of the average dimuon invariant mass scaled to the proton-proton centre-of-mass energy used. Full circle [10], open circle [11], up-triangle [12] and down-triangle [13] represent the mass points from several exclusive muon pair production measurements with different requirements on the dimuon invariant mass.

It is expected that absorptive effects in two-photon interactions in $pp$-collisions depend on the proton energy fractions passed to the quasi-real photons. Therefore, it is interesting to study the evolution of the ratio of the measured cross section to the bare EPA predictions, as a function of the average dimuon invariant mass, as shown in Fig. 3. The $\langle m_{\mu^+\mu^-} \rangle$ for different measurements is calculated using the Herwig generator and corresponding fiducial region definitions. The deviations from unity of the ratios of measured cross sections to the bare EPA-based predictions from Herwig increase slightly with the energy scale $\langle m_{\mu^+\mu^-} \rangle / \sqrt{s}$, indicating the increase of the size of the absorptive corrections with increasing energy scale. The measurements are also compared to two model predictions that differ in the implementation of the absorptive corrections. While the finite-size parameterisation of absorptive effects describes the data reasonably well, mismodelling at the level of 10–20% is observed with SuperChic2 [14].

## References


1. ATLAS Collaboration, 2008 JINST 3 S08003
2. CMS Collaboration, 2008 JINST 3 S08004
3. L. Evans and P. Bryant (editors) 2008 JINST 3 S08001
4. CMS Collaboration, arXiv:1802.02613 [hep-ex]
5. ATLAS Collaboration, Phys. Rev. Lett. **117**, no. 18, 182002 (2016)
6. TOTEM Collaboration, arXiv:1712.06153 [hep-ex]
7. LHCf Collaboration, CERN-LHCC-2006-004
8. ATLAS and LHCf Collaboration, ATLAS-CONF-2017-075, `https://cds.cern.ch/record/2291387`
9. LHCf Collaboration, Phys. Lett. **B 780** (2018) 233
10. ATLAS Collaboration, Phys. Lett. B **777** (2018) 303
11. CMS Collaboration, JHEP **1201** (2012) 052
12. ATLAS Collaboration, Phys. Lett. B **749** (2015) 242
13. ATLAS Collaboration, Phys. Rev. D **94** (2016) no.3, 03201
14. L. A. Harland-Lang, V. A. Khoze and M. G. Ryskin, Eur. Phys. J. C **76**, no. 1, 9 (2016)

# MULTIPLICITY AND UNDERLYING EVENT IN ALICE: AS MEASUREMENTS AND AS TOOLS TO PROBE QCD

V. ZACCOLO, ON BEHALF OF THE ALICE COLLABORATION
*INFN - Sezione di Torino*
*Via Pietro Giuria 1, 10125 Torino, Italy*

With the high collision energies at the LHC, the contributions to particle production from hard-QCD processes increase, but it remains dominated by soft-QCD processes. Such processes challenge the theoretical models, since they are described by non-perturbative phenomenology. A selection of the most recent ALICE measurements of charged-particle multiplicities and the Underlying Event will be presented, focusing on model comparisons. A summary of the current understanding of soft-QCD processes will be discussed, evaluating possible ways to further constrain theory.

## 1 Introduction

For the majority of the processes observed at the LHC non-perturbative aspects are involved. Of specific interest are Multiple Parton Interactions (MPI) that refer to the presence of more than one hard collision, with high transverse momentum $p_{\mathrm{T}}$. In the following, measurements of charged-particle multiplicities and the Underlying Event (UE), constituted by semi-hard and soft events, will be presented and discussed, highlighting model comparisons. ALICE is constituted by 18 different detector systems and has good momentum resolution and excellent particle identification. The experiment is described elsewhere [1].

## 2 Underlying Event

The measurement of the UE observables is crucial to separate soft and hard processes as a function of the leading track, i.e. the track with highest transverse momentum. Measurements from ALICE exist for pp collisions at $\sqrt{s} = 0.9$, 7 TeV and 13 TeV [2]. Figure 1 shows the results for the average charged-particle density as a function of the $p_{\mathrm{T}}$ of the leading track for toward (left) and transverse (right) regions. For the toward and away regions with respect to the leading track, where the fragmentation products from hard scattering are accumulated, the average particle density increases monotonically. The UE is probed in the transverse region, in which the particle density grows up to a few GeV and then flattens forming a plateau. This flattening can be attributed to the insignificance of the hard processes to the particle density at high leading-track $p_{\mathrm{T}}$, while at low leading-track $p_{\mathrm{T}}$ the particle density is influenced by hard processes (and eventually by MPI).

## 3 Particle multiplicities

Particle multiplicities are essential as a reference for other measurements and for tuning theoretical models. Both the pseudorapidity density $\mathrm{d}N_{\mathrm{ch}}/\mathrm{d}\eta$ and the probability $\mathrm{P}(N_{\mathrm{ch}})$ of charged

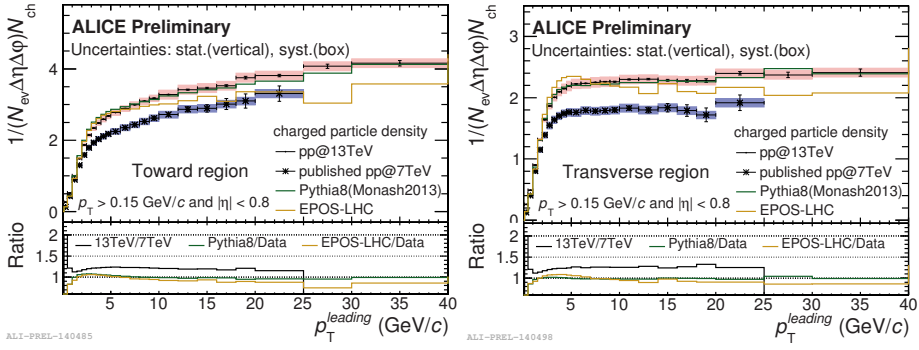


Figure 1 – Left: Number density in the toward region in pp collisions at $\sqrt{s} = 13$ TeV. Right: Number density in the transverse region.

particles have been measured by ALICE in proton–proton, pp, collisions at $\sqrt{s} = 0.9$ to 8 TeV [3] and at 13 TeV [4]. Figure 2 top left shows the $\mathrm{d}N_{\mathrm{ch}}/\mathrm{d}\eta$ as a function of the pseudorapidity in multiplicity slices derived from the V0 detector amplitude for high-multiplicity triggered data. On the top right plot, a comparison with Monte Carlo models is performed, PYTHIA 8 [5] with Colour Reconnection, PYTHIA 6 Perugia 2011 [6] and EPOS LHC [7] agree well with the data. On the bottom right panel of Fig. 2, the $\mathrm{d}N_{\mathrm{ch}}/\mathrm{d}\eta$ distribution as a function of the pseudorapidity $\eta$ in the laboratory system is shown for proton–lead, p–Pb, collisions at $\sqrt{s_{\mathrm{NN}}} = 8.16$ TeV. The number of charged particles is higher in the Pb-going side, at positive $\eta$. In general, models show a good agreement in the Pb-fragmentation side [8,9,7]. In the p-going side, theoretical calculations that assume gluon saturation, MC-rkBK [10] and KLN [11], reproduce the distribution better. On the bottom left, $\mathrm{d}N_{\mathrm{ch}}/\mathrm{d}\eta$ at midrapidity is scaled by half the average number of participants calculated with a Glauber model as a function of $\sqrt{s_{\mathrm{NN}}}$. Since the contribution from diffractive processes is negligible, the pA points agree with the pp inelastic event class. The rise of AA points is much steeper with respect to pp and pA. ALICE has measured the pseudorapidity density also for lead–lead [12] and xenon–xenon collisions [13], probing different system sizes and collision species, showing that the centrality-dependence distribution for the two different systems agrees up to the 10% most central collisions.

## 4 Multiplicity-dependence studies

Strangeness enhancement has been used as an observable to test the formation of the Quark–Gluon Plasma in heavy-ion collisions [14]. Nevertheless, ALICE has observed an enhancement also in high-multiplicity pp collisions when measuring the yields of strange particles [15]. While theoretical models are successfully describing particle multiplicity and the UE, they fail in the description of the multiplicity dependence of strange hadrons, as can be seen in Fig. 3 left. The DIPSY model [18], which contains the colour ropes formalism, reproduces better the data. In Fig. 3 right, instead, the J/Ψ yields are presented as a function of multiplicity for p–Pb collisions [17]. One can observe that the yields grow faster than the diagonal for the midrapidity region (hint of multiplicity and MPI saturation), while for the forward rapidity region, where the interaction is softer, there is a hint of saturation in the J/Ψ relative yield.

## 5 Summary

The charged-particle multiplicities and UE observables are described by models up to 10-20%. This is a good achievement given the complexity of non-perturbative soft-QCD description. Several measurements, like the UE and the J/Ψ meson yields as a function of the multiplicity, hint

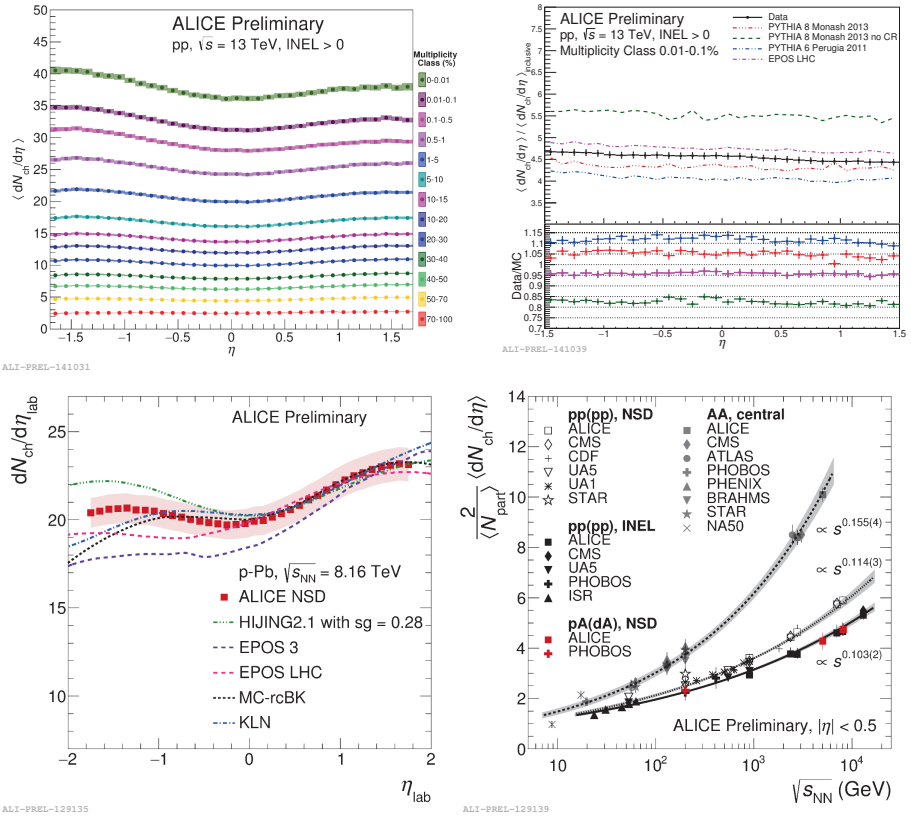


Figure 2 – Top left: Pseudorapidity density of charged particles measured for pp collisions at $\sqrt{s} = 13$ TeV in forward multiplicity slices. Top right: Monte Carlo comparisons to relative pseudorapidity density. Bottom left: $\mathrm{d}N_{\mathrm{ch}}/\mathrm{d}\eta_{\mathrm{lab}}$ in p–Pb collisions at $\sqrt{s_{\mathrm{NN}}}$=8.16 TeV. Bottom right: $\mathrm{d}N_{\mathrm{ch}}/\mathrm{d}\eta$ at midrapidity as a function of $\sqrt{s_{\mathrm{NN}}}$.

to saturation of MPI at high multiplicity and high $p_{\mathrm{T}}$. Progress has been made in the description of the multiplicity dependence of strange hadron production, but the models are still challenged. The multiplicity and UE measurements have significantly improved our phenomenological understanding of high-energy collisions. Nevertheless, further constraints can still be posed, e.g. probing QCD using the UE to test non-perturbative dynamics excluding the hard sector.

## References


1. K. Aamodt *et al.* [ALICE Collaboration], *JINST* **3**, S08002 (2008).
2. B. Abelev *et al.* [ALICE Collaboration], *JHEP* **1207**, 116 (2012).
3. K. Aamodt *et al.* [ALICE Collaboration], *Eur. Phys. J.* C **65**, 111 (2010); K. Aamodt *et al.* [ALICE Collaboration], *Eur. Phys. J.* C **68**, 89 (2010); K. Aamodt *et al.* [ALICE Collaboration], *Eur. Phys. J.* C **68**, 345 (2010); J. Adam*et al.* [ALICE Collaboration], *Eur. Phys. J.* C **77**, no.1, 33 (2017); S. Acharya *et al.* [ALICE Collaboration], *Eur. Phys. J.* C **77**, no.12, 852 (2017).
4. J. Adam*et al.* [ALICE Collaboration], *Phys. Lett.* B **753**, 319 (2016).
5. T. Sjostrand, S. Mrenna and P. Z. Skands, *Comput. Phys. Commun.* **178**, 852 (2008).

6. P. Z. Skands, *Phys. Rev.* D **82**, 074018 (2010).
7. T. Pierog, I. Karpenko, J. M. Katzy, E. Yatsenko and K. Werner, *Phys. Rev.* C **92**, no.3, 034906 (2015).
8. W. T. Deng, X. N. Wang and R. Xu, *Phys. Rev.* C **83**, 014915 (2011).
9. K. Werner, B. Guiot, I. Karpenko and T. Pierog, *Phys. Rev.* C **93**, no.6, 064903 (2014).
10. J. L. Albacete, A. Dumitru, H. Fujii and Y. Nara, *Nucl. Phys.* A **897**, 1 (2013).
11. A. Dumitru, D. E. Kharzeev, E. M. Levin and Y. Nara, *Phys. Rev.* C **85**, 044920 (2012).
12. J. Adam *et al.* [ALICE Collaboration], *Phys. Rev. Lett.* **116**, no.22, 222302 (2016); K. Aamodt *et al.* [ALICE Collaboration], *Phys. Rev. Lett.* **106**, 032301 (2011); K. Aamodt *et al.* [ALICE Collaboration], *Phys. Rev. Lett.* **105**, 252301 (2010).
13. S. Acharya *et al.* [ALICE Collaboration], `arXiv:1805.04432 [nucl-ex]`.
14. P. Koch, B. Muller, and J. Rafelski, *Phys. Rept* **142**, 167-262 (1986).
15. J. Adam*et al.* [ALICE Collaboration], *Nature Phys.* **13**, 535-539 (2017).
16. B. Abelev *et al.* [ALICE Collaboration], *Phys. Lett.* B **728**, 25-38 (2014).
17. D. Adamova *et al.* [ALICE Collaboration], *Phys. Lett.* B **776**, 91-104 (2018).
18. C. Bierlich and J.R. Christiansen, *Phys. Rev.* D **93**, no.9, 094010 (2015).


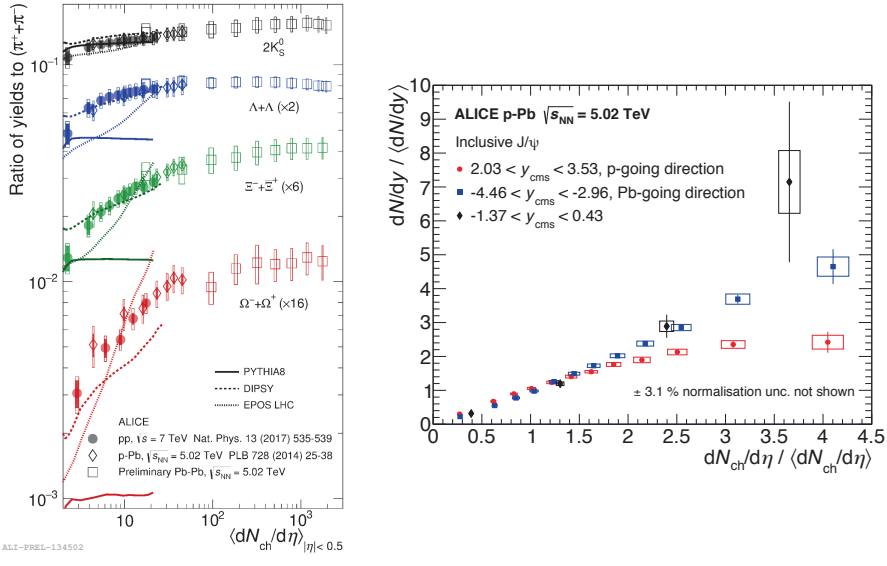


Figure 3 – Left: Momentum-integrated yield ratios to pions as a function of multiplicity for pp [15], p–Pb [16] and Pb–Pb collisions. Right: Relative yield of inclusive J/Ψ mesons as a function of relative multiplicity [17].

# QCD with jets and photons at ATLAS and CMS

Ralf Ulrich for the ATLAS and CMS Collaborations
*Institute for Nuclear Physics, Karlsruhe Institute of Technology, 76131 Karlsruhe, Germany*

Jets and photons are abundant messengers sensitive to QCD interactions and the structure of hadrons at the LHC. In this note recent results from the ATLAS and CMS Collaborations in proton-proton and proton-lead collisions are summarized. Major progress is being made in the observations and the understanding of those objects. Detailed QCD interpretations are possible today to an accuracy of about 5%. With full NNLO prediction becoming available in the close future another step in precision is getting in reach. Further work is also needed in improving the understanding of non-perturbative and soft effects in particular for multi-final states, and to keep up with the significant experimental and theoretical progress.

## 1 Introduction

The precision of measurements of jets and photons at the CERN LHC makes tremendous progress, and the complexity of observables and final states is more and more increased. The current status of jet and photon measurements by the ATLAS [1] and CMS [2] Collaborations is presented here. The comparison to theory predictions and modelling can in some cases already make statements on the order of 5% accuracy. Further improvements are expected with upcoming full NNLO event generation, combined with simultaneous better understanding of soft and non-perturbative contributions.

## 2 Review of measurements

In particular for the measurement of inclusive jet and photon production the data can typically be well described by NLO model predictions when they are combined with electroweak and non-perturbative corrections. A powerful demonstration of this are the double-differential inclusive jet cross section measured at 8 TeV [3], see Fig. 1. In the detailed analysis of inclusive jet and di-jet production [4] it is found that NLO predictions describe individual distributions well, with quantitative p-values on the order of $\approx 1\%$, while on a global level there remains tension. For the same data it is found that the NNLO predictions simulated with scale $p_{\mathrm{T}}^{\mathrm{jet}}$ are better compared to the ones simulated with scale $p_{\mathrm{T}}^{\mathrm{max}}$. However, these NNLO modelling uncertainties can not yet be fully determined, making a quantitative analysis not feasible at the moment on this level.

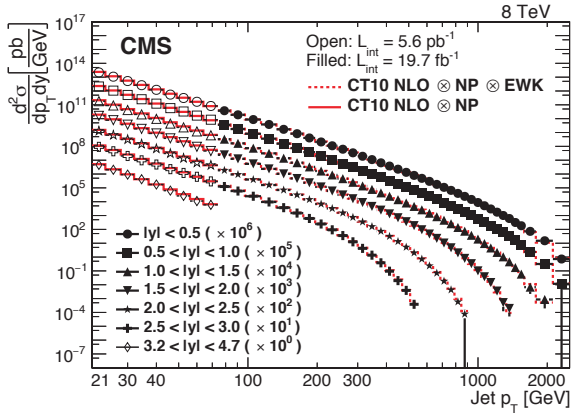


Figure 1 – The double differential jet distributions over a very wide $p_{\mathrm{T}}$−range measured by CMS [3].

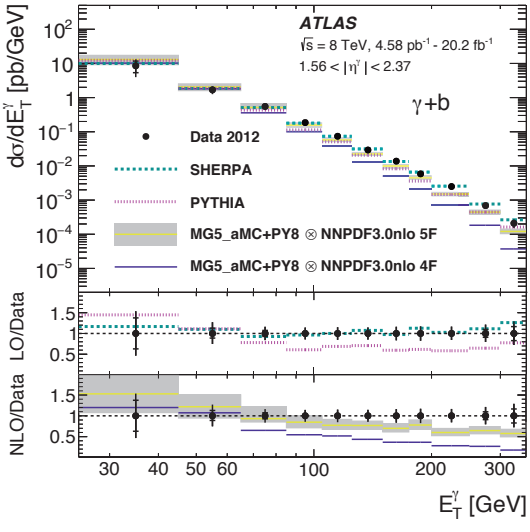


Figure 2 – Photon+heavy flavor jet production with photon in forward direction measured by ATLAS [6].

Furthermore, the analysis of photons+jet events illustrates good agreement with NLO predictions [5], whereas already the measurement of a photon plus one heavy-flavor jet illustrates obvious shortcomings of the NLO predictions [6], since the models systematically underestimate the cross sections at higher $E_{\mathrm{T}}^{\gamma}$ values, see Fig. 2. This becomes more obvious in the tri-photon final state, where the NLO predictions consistently remain about a factor of 2 below the measurements [7]. Also the study of correlations in multi-jet final states, with up to four jets, clearly reveals the various shortcomings of existing event generators [8]. Here the HERWIG7 NLO predictions are overall best, but none of the generators describe the data to a reasonable level. It is shown that this result is in particular sensitive to the modeling of parton showers.

If the measurements are analysed on inclusive level, fundamental conclusions can be derived from this on the level 5% accuracy. This has been exploited by various determinations of the strong coupling constant $\alpha_{\mathrm{S}}$ using different methods [11,3]. But also impressive constraints on the

parton density functions in the proton have been obtained [12]. The parton density of gluons at high values of x can be considerably better understood when LHC jet data is included in the analysis together with HERA data.

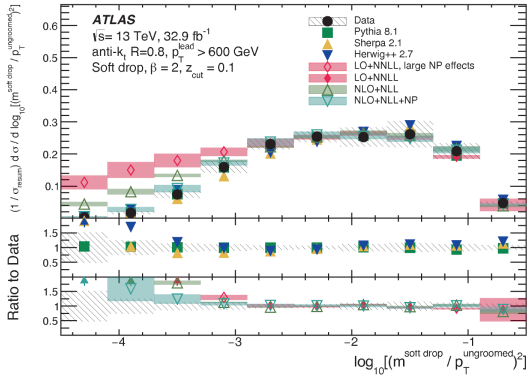


Figure 3 – The groomed jet structure measured by ATLAS [9] showing a mismatch of NLO predictions in the soft region.

Dedicated measurements with increased sensitivity to non-pQCD effects indicate the need to also better understand non-perturbative and soft effects. The analysis of jet sub structure reveals the need for non-perturbative contributions in the domain more sensitive to soft physics [9]. However, otherwise these data are well described by NNLL predictions, c.f. Fig. 3. Also the measurement of the jet charge is an interesting probe [10]. Finally, also the measurement of very-forward directed jets is in particular sensitive to soft QCD and low-x effects. A measurement of the inclusive jet cross section in $-6.6 < \eta < -5.2$ in proton-lead collisions (see Fig. 4) illustrates a major opportunity to significantly improve model predictions [13] and learn about the very low-x QCD dynamics as well as soft contributions in this phase-space.

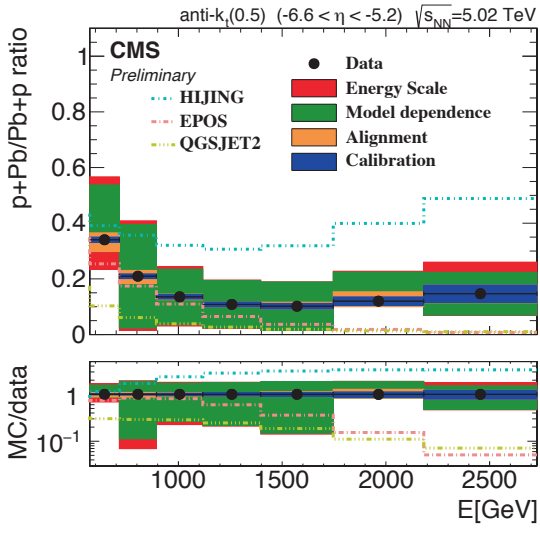


Figure 4 – Inclusive very-forward jet production in proton-lead collisions. Shown is the ratio between jet production in proton-lead relative to lead-proton in CMS/CASTOR [13].

## 3 Conclusion

NLO predictions with non-perturbative and EW corrections are able to well describe data in huge phase-space regions. Detailed QCD interpretations are possible to an accuracy of about 5%. NNLO predictions with full uncertainties are needed to make the next step, and this will have a huge potential to enter true precision QCD interpretation at LHC.

Soft and non-perturbative effects are typically described better by event generators compared to NLO model predictions. Some work is needed in non-perturbative physics to keep up with the increased level of precision in particular for multi-final states, and other more complex observables.


## Acknowledgments

I thank very much the CMS and ATLAS Collaborations for the pleasure of giving this review talk on behalf of them, and profiting from the excellent work performed in the research of jets and photons at LHC. It is amazing to work in such an outstanding environment with so many brilliant colleagues.




## References


1. G. Aad *et al.* [ATLAS Collaboration], `The ATLAS Experiment at the CERN Large Hadron Collider`. JINST **3** (2008) S08003 doi:10.1088/1748-0221/3/08/S08003.
2. S. Chatrchyan *et al.* [CMS Collaboration], `The CMS Experiment at the CERN LHC`, JINST **3** (2008) S08004 doi:10.1088/1748-0221/3/08/S08004/
3. V. Khachatryan *et al.* [CMS Collaboration], *Measurement and QCD analysis of double-differential inclusive jet cross sections in pp collisions at* $\sqrt{s} = 8$ *TeV and cross section ratios to 2.76 and 7 TeV*, JHEP **03** (2017) 156 doi:10.1007/JHEP03(2017)156 [arXiv:1609.05331 [hep-ex]].
4. M. Aaboud *et al.* [ATLAS Collaboration], *Measurement of inclusive jet and dijet cross-sections in proton-proton collisions at* $\sqrt{s} = 13$ *TeV with the ATLAS detector*, JHEP **05** (2018) 195 doi:10.1007/JHEP05(2018)195 [arXiv:1711.02692 [hep-ex]].
5. M. Aaboud *et al.* [ATLAS Collaboration], *Measurement of the cross section for isolated-photon plus jet production in pp collisions at* $\sqrt{s} = 13$ *TeV using the ATLAS detector*, Phys. Lett. B **780** (2018) 578 doi:10.1016/j.physletb.2018.03.035 [arXiv:1801.00112 [hep-ex]].
6. M. Aaboud *et al.* [ATLAS Collaboration], *Measurement of differential cross sections of isolated-photon plus heavy-flavour jet production in pp collisions at* $\sqrt{s} = 8$ *TeV using the ATLAS detector*, Phys. Lett. B **776** (2018) 370 doi:10.1016/j.physletb.2017.11.054.
7. M. Aaboud *et al.* [ATLAS Collaboration], *Measurement of the production cross section of three isolated photons in pp collisions at* $\sqrt{s}$*=8 TeV using the ATLAS detector*, Phys. Lett. B **781** (2018) 55 doi:10.1016/j.physletb.2018.03.057 [arXiv:1712.07291 [hep-ex]].
8. A. M. Sirunyan *et al.* [CMS Collaboration], *Azimuthal correlations for inclusive 2-jet, 3-jet, and 4-jet events in pp collisions at* $\sqrt{s}$ *=13 TeV*, arXiv:1712.05471 [hep-ex].
9. M. Aaboud *et al.* [ATLAS Collaboration], *A measurement of the soft-drop jet mass in pp collisions at* $\sqrt{s} = 13$ *TeV with the ATLAS detector*, arXiv:1711.08341 [hep-ex].
10. A. M. Sirunyan *et al.* [CMS Collaboration], *Measurements of jet charge with dijet events in pp collisions at* $\sqrt{s} = 8$ *TeV*, JHEP **1710** (2017) 131 doi:10.1007/JHEP10(2017)131 [arXiv:1706.05868 [hep-ex]].
11. M. Aaboud *et al.* [ATLAS Collaboration], *Determination of the strong coupling constant* $\alpha_s$ *from transverse energyenergy correlations in multijet events at* $\sqrt{s} = 8$ *TeV using the ATLAS detector*, Eur. Phys. J. C **77** (2017) 872 doi:10.1140/epjc/s10052-017-5442-0 [arXiv:1707.02562 [hep-ex]].
12. A. M. Sirunyan *et al.* [CMS Collaboration], *Measurement of the triple-differential dijet cross section in proton-proton collisions at* $\sqrt{s} = 8$ *TeV and constraints on parton distribution functions*, Eur. Phys. J. C **77** (2017) 746 doi:10.1140/epjc/s10052-017-5286-7 [arXiv:1705.02628 [hep-ex]].
13. CMS Collaboration, *Very forward inclusive jet cross sections in pPb collisions at* $\sqrt{s_{\rm NN}} = 5.02$ *TeV*, CMS-PAS-FSQ-17-001 (2017) [cds.cern.ch/record/2258273].

# Computing Planar Five-Gluon Amplitudes with Numerical Unitarity

Samuel Abreu[a], Fernando Febres Cordero[a], Harald Ita[a], Ben Page[a], Mao Zeng[b]

[a] *Physikalisches Institut, Albert-Ludwigs Universität Freiburg, D-79104 Freiburg, Germany*
[b] *Mani L. Bhaumik Institute for Theoretical Physics, UCLA Department of Physics and Astronomy, Los Angeles, CA 90095, USA*

We discuss the numerical unitarity method for the computation of two-loop scattering amplitudes relevant for LHC phenomenology. We extend one-loop technologies by making use of novel ideas such as a geometric construction of surface terms and finite field numerics. Recently the method has been employed to perform the first reduction of the leading-colour two-loop five-gluon scattering amplitudes to master integrals.

## 1 Introduction

Experiments at the LHC have entered a new phase of measurement where the Standard Model will be probed with an unprecedented level of precision. The success of this program requires theoretical predictions that match these experimental precision targets - at the percent level for many observables. In practice, this means an increasing number of QCD processes must be evaluated at NNLO accuracy. In recent years, significant progress in the handling of real radiation has led to the calculation of several 2-to-2 processes at NNLO. For processes with more particles or jets in the final state, one of the bottlenecks is the evaluation of the virtual contributions, which requires the evaluation of complex multi-scale two-loop scattering amplitudes. Modern amplitude calculations are based on the reduction of an amplitude into a linear combination of so-called master integrals. At one loop, the basis of master integrals is known for generic processes and the reduction for high-multiplicity one-loop matrix elements is now largely automated. At higher loops, the reduction to master integrals is still an obstacle for high-multiplicity processes. In this talk, we discuss a method for the reduction of two-loop multi-leg amplitudes, numerical unitarity, which builds on the successes of the one-loop programme. We will discuss its recent application in obtaining the first complete reduction of a five-point two-loop QCD amplitude to a minimal set of master integrals [1].

## 2 Numerical Unitarity

### *2.1 Principles of numerical unitarity*

The starting point of a numerical unitarity algorithm is to consider the integrand of the scattering amplitude, denoted $\mathcal{A}$, as a rational function of the loop momenta. It can be organised by the possible set of propagator structures $\Gamma$ determined from the natural decomposition of the amplitude in different topologies. The next key idea is to construct a convenient ansatz for the numerator of each propagator structure, where each term behaves in a well defined manner under integration—more specifically where every term either corresponds to a master integral

or to a surface term (i.e. it integrates to zero). Taking $\rho_j$ to be the inverse propagators, the ansatz is written as

$$\mathcal{A}(\ell_l) = \sum_{\Gamma} \sum_{i \in M_\Gamma \cup S_\Gamma} \frac{c_{\Gamma,i}\, m_{\Gamma,i}(\ell_l)}{\prod_{\text{props } j} \rho_j}\,, \tag{1}$$

where $\ell_l$ denotes the loop momenta, $M_\Gamma$ and $S_\Gamma$ the set of master integrals and surface terms associated with $\Gamma$, and dependence on external kinematics is implicit. Finally, this ansatz can be constrained by exploiting the unitarity of the theory which dictates that leading residues at multi-propagator poles of the integrand (denoted $\ell^\Gamma$) factorise into a product of tree amplitudes $\mathcal{A}_i^{\text{tree}}$ summed over the physical states of the theory,

$$\sum_{\text{states}} \prod_i \mathcal{A}_i^{\text{tree}}(\ell_l^\Gamma) = \sum_{\substack{\Gamma' \geq \Gamma, \\ i \in M_{\Gamma'} \cup S_{\Gamma'}}} \frac{c_{\Gamma',i}\, m_{\Gamma',i}(\ell_l^\Gamma)}{\prod_{\text{props } j} \rho_j}\,, \tag{2}$$

where the sum is over propagator structures $\Gamma'$ which contain a subset of the propagators in $\Gamma$. Starting at two-loops subleading poles can also appear[3]. We thus obtain a system of equations for the unknown coefficients in the ansatz of the numerator. Using powerful numerical techniques, the system is solved to obtain a decomposition of the amplitude as a linear combination of master integrals. Combining the decomposition with the results for the integrals we can evaluate the amplitude at a given kinematic point. These ideas have been extensively used at one-loop, but their extension to higher orders require new improvements which we shall now review.

### *2.2 Two-loop numerical unitarity*

A main obstacle to numerical unitarity at higher loops is the generation of an ansatz for the numerator with good properties under integration [2]. The generation of surface terms can be achieved with integration-by-parts (IBP) relations [4],

$$0 = \int \prod_{l=1,2} d^D \ell_l \frac{\partial}{\partial \ell_j^\nu} \left[ \frac{u_j^\nu}{\prod_{\text{props } k} \rho_k} \right], \tag{3}$$

where $u_j^\nu$ is called an IBP-generating vector. Arbitrary vectors will generate relations between integrals that do not fit naturally in our integrand parametrisation, such as integrals with other propagator structures. This can be avoided by using vectors which satisfy [5]

$$u_i^\nu \frac{\partial}{\partial \ell_i^\nu} \rho_j = f_j \rho_j. \tag{4}$$

As the vectors are polynomials in loop momenta, this is a so-called syzygy equation, the solution of which can be formulated as a problem in algebraic geometry. We aim to construct a generating set of solutions to insert into eq. (3) to build a complete set of surface terms. The function space of the integrand that is not filled by surface terms corresponds to the master integrals.

Having constructed a master/surface parametrisation of the integrand, we must now solve eq. (2) and numerically obtain the coefficients of the master integrals. We have implemented the linear function system in a C++ code where, given a set of external momenta, we sample the many systems of equations over a sufficient number of on-shell loop momenta. This allows us to build a numerical linear system which can be solved with standard linear algebra techniques such as PLU factorisation. At two loops, the size of the linear system may lead to loss of precision. While floating point calculations are possible [6], this issue can be avoided altogether by formulating numerical unitarity in terms of finite fields [7,8]. Importantly, because we allow the surface terms to depend on the dimensional regulator $D$, the coefficients of the master integrals are $D$ dependent. To be able to perform a Laurent expansion of the amplitude in $\epsilon = (4 - D)/2$, we must obtain the full functional dependence on $\epsilon$. This dependence can be recovered numerically by evaluating the coefficients for multiple values of $D$ in an extension of the one-loop procedure [9] combined with Thiele's formula [7].

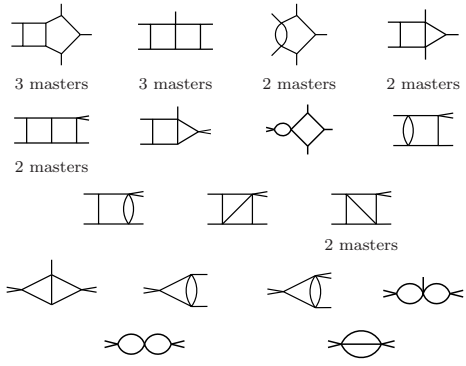


Figure 1 – Propagator structures with master integrals for 5-point two-loop massless kinematics.

## 3 Five-Gluon QCD Amplitudes

We now discuss how the method described above was used for the first complete reduction to master integrals of all independent helicity configurations of the five-gluon two-loop QCD amplitudes in the leading-colour approximation [1]. The parametrisation of the integrand function-space was performed using a combination of standard tensor-reduction techniques and IBP relations constructed from vectors generated with the computational algebraic geometry package Singular. All surface terms constructed in this way were validated on a numerical kinematic point using IBP relations generated with Fire [11]. For this process, there are 155 master integrals corresponding to all the permutation of the topologies listed in fig. 1. Standard numerical unitarity was modified to compute with finite fields (we use the implementation of the Givaro library [12]) which removes any issues related to precision loss, at the expense of requiring a completely rational parametrisation of the external kinematics and on-shell phase space. The external kinematics are guaranteed to be rational by starting from a parametrisation based on momentum twistors [7], and for the on-shell phase space we constructed a convenient set of variables that guarantees all manipulations can be done with rational operations. The reduction to master integrals can then be done with finite fields, and the coefficients subsequently promoted to rational numbers. In this way we compute exact numerical values for the coefficients of the master integrals. Finally, combining these with the available expressions for the master integrals [13], which can be evaluated to arbitrary precision, we obtain exact benchmark values for all four independent helicity configurations of the planar two-loop five-gluon QCD amplitudes.

In table 1 we present the results we obtained at the point $s_{12} = -1$, $s_{23} = -8$, $s_{34} = -10$, $s_{45} = -7$, $s_{15} = -3$ with $s_{ij} = (p_i + p_j)^2$. The results, corresponding to the coefficient of $\alpha_0^2/(4\pi)^2$, were computed in the 't Hooft-Veltman scheme with the master integrals normalised to $(2\pi)^{4\epsilon-8}$. We verified that we reproduce the expected universal pole structure [14], and the known analytic results for the all-plus helicity configuration [15]. Furthermore, using our code we validate an independent set of benchmark results [16] within their error bounds.

## 4 Conclusions

We have discussed the numerical unitarity method for the calculation of phenomenologically relevant two-loop scattering amplitudes. This approach is based on a generic organisation of the amplitude's integrand which opens the door to the automation of the calculation of two-loop amplitudes. We have applied it to perform the first complete numerical reduction of the leading-colour five-point two-loop gluonic amplitudes in QCD. We employ cutting-edge techniques such

Table 1: Numerical results for the 4 independent helicity configurations of the 5-point 2-loop gluonic QCD amplitudes in the HV scheme, truncated to 6 digits. The MHV helicity amplitudes are normalised to tree-level, and the all-plus and single-minus to the leading order of the one-loop result.

| $\mathcal{A}/(\mathcal{A}_0 N_c^2)(4\pi)^4$ | $\epsilon^{-4}$ | $\epsilon^{-3}$ | $\epsilon^{-2}$ | $\epsilon^{-1}$ | $\epsilon^0$ |
|---|---|---|---|---|---|
| $(+,+,+,+,+)$ | 0 | 0 | -5.00000 | -3.89318 | 5.98109 |
| $(-,+,+,+,+)$ | 0 | 0 | -5.00000 | -16.3220 | -10.3838 |
| $(-,-,+,+,+)$ | 12.5000 | 25.46247 | -1152.84 | -4072.94 | -3637.25 |
| $(-,+,-,+,+)$ | 12.5000 | 25.46247 | -6.12163 | -90.2218 | -115.784 |

as the geometrical constructions of surface terms and finite fields. Use of the latter paves the way to future analytic reconstruction of the result. We expect that this promising method can be used to compute new multi-scale scattering amplitudes at two loops in the near future.

## Acknowledgments

The work of S.A., F.F.C. and B.P. is supported by the Alexander von Humboldt Foundation, in the framework of the Sofja Kovalevskaja Award 2014, endowed by the German Federal Ministry of Education and Research. The work of M.Z. is supported by the U.S. Department of Energy under Award NumberDE-SC0009937.

## References

1. S. Abreu, F. Febres Cordero, H. Ita, B. Page and M. Zeng, arXiv:1712.03946 [hep-ph].
2. H. Ita, Phys. Rev. D **94**, no. 11, 116015 (2016) [arXiv:1510.05626 [hep-th]].
3. S. Abreu, F. Febres Cordero, H. Ita, M. Jaquier and B. Page, Phys. Rev. D **95** (2017) no.9, 096011 [arXiv:1703.05255 [hep-ph]].
4. K. G. Chetyrkin and F. V. Tkachov, Nucl. Phys. B **192** (1981) 159.
5. J. Gluza, K. Kajda and D. A. Kosower, Phys. Rev. D **83** (2011) 045012, [arXiv:1009.0472 [hep-th]].
6. S. Abreu, F. Febres Cordero, H. Ita, M. Jaquier, B. Page and M. Zeng, Phys. Rev. Lett. **119** (2017) no.14, 142001 [arXiv:1703.05273 [hep-ph]].
7. T. Peraro, JHEP **1612**, 030 (2016) [arXiv:1608.01902 [hep-ph]].
8. A. von Manteuffel and R. M. Schabinger, Phys. Lett. B **744** (2015) 101 [arXiv:1406.4513 [hep-ph]].
9. W. T. Giele, Z. Kunszt and K. Melnikov, JHEP **0804** (2008) 049 [arXiv:0801.2237 [hep-ph]].
10. W. Decker, G.-M. Greuel, G. Pfister, H. Schönemann. 2015. "Singular 4-0-2. A computer algebra system for polynomial computations." http://www.singular.uni-kl.de
11. A. V. Smirnov, Comput. Phys. Commun. **189** (2015) 182 [arXiv:1408.2372 [hep-ph]].
12. Thierry Gautier, Jean-Louis Roch, and Gilles Villard, "Givaro", `http://givaro.forge.imag.fr`, accessed 2017-12-09.
13. C. G. Papadopoulos, D. Tommasini and C. Wever, JHEP **1604** (2016) 078 [arXiv:1511.09404 [hep-ph]].
14. S. Catani, Phys. Lett. B **427** (1998) 161 [hep-ph/9802439].
15. T. Gehrmann, J. M. Henn and N. A. Lo Presti, Phys. Rev. Lett. **116** (2016) no.6, 062001 Erratum: [Phys. Rev. Lett. **116** (2016) no.18, 189903] [arXiv:1511.05409 [hep-ph]].
16. S. Badger, H. Frellesvig and Y. Zhang, JHEP **1312** (2013) 045 [arXiv:1310.1051 [hep-ph]] ; S. Badger, C. Brønnum-Hansen, H. B. Hartanto and T. Peraro, Phys. Rev. Lett. **120** (2018) no.9, 092001 [arXiv:1712.02229 [hep-ph]].

# Including higher-order mixed QCD-QED effects in hadronic calculations

Germán F. R. Sborlini
*Tif lab, Dipartimento di Fisica, Università di Milano and INFN, Sezione di Milano, I-20133 Milan, Italy.*

We review some recent results about the computation of mixed QCD-QED corrections beyond the leading order in perturbation theory. We start by considering the effects induced in the Altarelli-Parisi equations and the partonic distributions. In particular, we describe the computation of one-loop mixed QCD-QED and two-loop QED terms in the splitting kernels, which are relevant to account for the presence of photon distributions. In the last part, we briefly talk about the implementation of these corrections in the context of the $q_T$-subtraction/resummation formalism.

## 1 Introduction and motivation

The study of hadronic collisions in the high-energy and high-luminosity regime is pushing the theoretical predictions to the precision frontier. The experimental analysis require accurate simulations which should include most of the effects predicted by the theoretical framework. With more data becoming available, the experimental uncertainties rapidly reduce and this increases the sensitivity to tiny deviations from the dominant QCD background. In particular, the QED and electroweak contributions are turning into crucial components of the full predictions since they could provide percent-level modifications, now detectable by the experiments.

The purpose of this work is to briefly summarize some recent developments concerning the precision program in QCD-QED computations. In Sec. 2, we describe the extension of the DGLAP equations to include mixed $\mathcal{O}(\alpha\alpha_S)$ corrections. In Sec. 2.1, we comment on a technique that allows to recover these QED and mixed QCD-QED contributions from the well-known QCD calculations. After that, in Sec. 3, we apply the Abelianization algorithm to a particular collider process, namely diphoton production, and we show that the Abelianized $q_T$-subtraction framework successfully deals with the singularities due to the presence of soft/collinear gluons and photons. Finally, we present the conclusions in Sec. 4.

## 2 Extended DGLAP equations

The DGLAP equations control the perturbative evolution of the parton distribution functions, through the well-known splitting kernels. These objects can be computed within perturbation theory, by studying the collinear limits of scattering amplitudes. Higher-order corrections to the splitting functions for QCD partons have been computed, both in the multi-loop and in the multiple-collinear case. In particular, we have explored the double and triple collinear limits at one-loop level for processes including photons[1].

The formalism can be extended to include leptons and photons, as well as QCD partons. This leads to a more complicated system of integro-differential coupled equations which can be

partially simplified by changing the PDF basis. Explicitly, by using the canonical basis, i.e. $\mathcal{B} = \{u, \bar{u}, d, \bar{d}, \ldots, e^-, e^+, \ldots, \gamma, g\}$, the system is written as

$$\frac{df_i}{dt} = \sum_{j \in \mathcal{B}} P_{f_i f_j} \otimes f_j \,, \tag{1}$$

with $t = \log(Q^2/\mu^2)$ the evolution variable and $\otimes$ denotes a convolution among distributions ($f_i$) and splitting kernels ($P_{f_i f_j}$). The last ones are expanded in a perturbative series according to

$$P_{ij} = \sum_{k,l} a_{\rm S}^k a^l \, P_{ij}^{(k,l)} \,, \tag{2}$$

with $\alpha \equiv 2\pi\, a$ and $\alpha_{\rm S} \equiv 2\pi\, a_{\rm S}$. In general, the evolution kernels are not diagonal, thus conducing to a highly non-trivial mixing of the different distributions. However, by using an optimized basis[2], we get

$$\frac{d\{\Delta_2^l, \Delta_3^l\}}{dt} = P_l^+ \otimes \{\Delta_2^l, \Delta_3^l\} \,, \quad \frac{d\{\Delta_U\}}{dt} = P_u^+ \otimes \{\Delta_U\} \,, \quad \frac{d\{\Delta_D\}}{dt} = P_d^+ \otimes \{\Delta_D\} \,, \tag{3}$$

with $\Delta_i^l$, $\Delta_U$ and $\Delta_D$ some specific linear combinations of leptons, up and down quarks PDFs, respectively[3,4]. Moreover, up to $\mathcal{O}(\alpha\, \alpha_{\rm S}^n)$, the kernels relating different quark and/or lepton flavors vanish, which allows to write the equations for the valence distributions as

$$\frac{dq_{v_i}}{dt} = P_{q_i}^- \otimes q_{v_i} \,, \qquad \frac{dl_{v_i}}{dt} = P_l^- \otimes l_{v_i} \,, \qquad u_v = u - \bar{u}, \ldots, e_v = e^- - e^+, \ldots \tag{4}$$

besides highly simplifying the singlet equations[3,4].

The full set of evolution equations must fulfill physical constraints in the end-point region (i.e. $x = 1$), which are related to the conservation of the proton total momentum and its fermionic composition (i.e. the fermion number conservation). These conditions are used to derive the terms proportional to $\delta(1-x)$ in the splitting functions, besides imposing strong restrictions on the functional dependence of the different kernels for $0 \leq x < 1$.

### *2.1 Abelianization of splitting kernels*

The key idea of our work is related with the possibility of extracting the mixed QCD-QED corrections from previous computations performed within pure QCD. The algorithmic approach is based on the Abelianization of the different contributions to the QCD computation, which accounts for the replacement of *gluons by photons*[3]. If the computation is available on a diagram-by-diagram decomposition, then the Abelianization is trivial: we can strip the color factor and multiply the kinematic part by the recomputed factor, including the charge dependence. But, the interesting fact is the possibility of recovering the QCD-QED corrections from *analytic results* provided that we keep track of the color factors (i.e. $C_A$, $C_F$) and contributions proportional to $n_F$. Then, we can derive explicit rules to transform the results. For instance, starting from the $\mathcal{O}(\alpha_{\rm S}^2)$ splitting functions, the $\mathcal{O}(\alpha\, \alpha_{\rm S})$ terms are obtained by:

- removing the color average over the initial states, writing the color factors as functions of $N_C$ and expanding around $N_C = 0$;
- keeping the leading terms and recomputing the color structure (inserting the electric charges where it corresponds).

There are some subtleties related with the presence of symmetry factors and the treatment the closed fermion loops: we need to consider the replacement $n_F \to \sum_q e_q^2$. In an analogous way, well-defined transition rules to extract the $\mathcal{O}(\alpha^2)$ contributions can be defined[4].

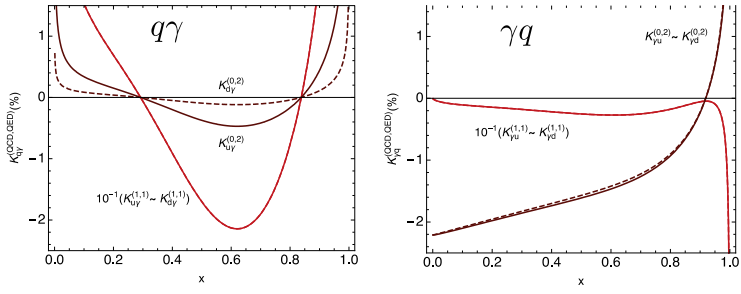


Figure 1 – Corrections due to the inclusion of QED contributions in the $P_{q\gamma}$ (left) and $P_{\gamma q}$ splitting kernels. We include both $\mathcal{O}(\alpha^2)$ (brown) and $\mathcal{O}(\alpha\,\alpha_S)$ (red) terms.

To quantify the impact of the QED corrections, we define the $K$-ratios according to

$$K_{ab}^{(i,j)} = a_S^i\, a^j\, P_{ab}^{(i,j)}(x)/P_{ab}^{\rm LO}(x)\,, \qquad P_{ab}^{\rm LO} = a_S\, P_{ab}^{(1,0)} + a\, P_{ab}^{(0,1)}\,, \tag{5}$$

where the lowest-order kernel contains both the lowest QED and QCD contributions. It is important to notice that these corrections allow to connect the quark and photon PDFs, thus leading to a non-trivial evolution of the last distribution. In Fig. 1, we plot the $K$-ratios for the $P_{q\gamma}$ and $P_{\gamma q}$ splitting kernels. The $\mathcal{O}(\alpha^2)$ (brown) contributions are suppressed by a factor 10 in comparison to the dominant $\mathcal{O}(\alpha\,\alpha_S)$ ones (red). A non-trivial charge separation effect is present in the middle-$x$ region, in particular for the $P_{q\gamma}$ kernel.

## 3 Application to diphoton production

By applying the Abelianization algorithm to the public code `2gNNLO`[5], we modified the structure of the NLO QCD terms to recover the corresponding NLO QED contributions. In this procedure, we obtained the NLO QED extension of the $q_T$-subtraction formalism[6,7], which allows to consistently deal with the fixed-order calculation beyond the LO in QCD-QED. Moreover, we checked the behavior of the different pieces of the calculation and found a complete cancellation of IR singularities in the $q_T \to 0$ limit.

In Fig. 2, we present the NLO QED corrections to the transverse momentum (left) and invariant mass (right) distributions for the diphoton production at LHC. We used the typical ATLAS cuts, with 14 TeV c.m. energy and `NNPDF3.1QED` [8,9] PDFs (which implements the `LUXqed` approach[10] to reduce the uncertainties in the determination of the photon PDF). In the invariant-mass spectrum, the momentum ordering of the triple-photon system leads to a dynamical cut, which is a novel feature of the QED corrections. Also, we notice that the $q\gamma$-channel (green line) dominates the NLO QED contribution in the high-transverse momentum region, thus showing the importance of a precise determination of the photon PDF.

## 4 Conclusions and outlook

In this article, we summarized some recent developments in the computation of mixed QCD-QED corrections. We provided an algorithmic technique to recover these contributions from the higher-order QCD computations. By applying the Abelianization procedure, we managed to obtain the $\mathcal{O}(\alpha\,\alpha_S)^3$ and $\mathcal{O}(\alpha^2)^4$ corrections to the Altarelli-Parisi splitting functions. This knowledge is crucial for the proper treatment of the PDF evolution beyond LO QED.

Besides that, the Abelianization proved to be useful for obtaining corrections to physical cross-sections. We applied it through the $q_T$-subtraction method, and obtained the universal

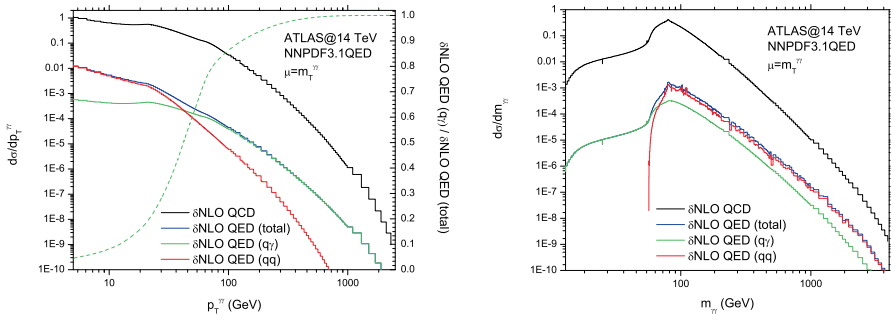


Figure 2 – Transverse momentum (left) and invariant mass (right) distributions for the diphoton production at LHC. The black (blue) curve shows the total NLO QCD (QED) prediction, without including the LO. The dashed green line indicates the relative contribution of the $q\gamma$-channel to the total NLO QED correction.

coefficients to compute the NLO QED corrections to the production of neutral colorless particles. As a proof-of-concept, we included $\mathcal{O}(\alpha^3)$ terms to the diphoton production cross-section[7,11]. We discussed the phenomenology for hadron colliders (LHC at 14 TeV), and we found non-negligible corrections in the high-energy region.

Further considerations on the development of a framework to deal with mixed QCD-QED is needed to achieve precise predictions for current experiments[11]. In this direction, we have managed to successfully extend the $q_T$-resummation formalism to compute mixed QCD-QED corrections, using on-shell $Z$ production as benchmark process[12].

## Acknowledgments

This work has been done in collaboration with D. de Florian, G. Rodrigo, L. Cieri and G. Ferrera. The research project was supported by CONICET, ANPCyT, the Spanish Government, EU ERDF funds (grants FPA2014-53631-C2-1-P and SEV-2014-0398) and Fondazione Cariplo under the grant number 2015-0761. This article is based upon work from COST Action CA16201 PARTICLEFACE supported by COST (European Cooperation in Science and Technology).

## References

1. G. F. R. Sborlini, D. de Florian and G. Rodrigo, JHEP **1401** (2014) 018; JHEP **1410** (2014) 161; JHEP **1503** (2015) 021.
2. M. Roth and S. Weinzierl, Phys. Lett. B **590** (2004) 190.
3. D. de Florian, G. F. R. Sborlini and G. Rodrigo, Eur. Phys. J. C **76** (2016) no.5, 282.
4. D. de Florian, G. F. R. Sborlini and G. Rodrigo, JHEP **1610** (2016) 056.
5. S. Catani, L. Cieri, D. de Florian, G. Ferrera and M. Grazzini, Phys. Rev. Lett. **108** (2012) 072001; Erratum: [Phys. Rev. Lett. **117** (2016) no.8, 089901].
6. S. Catani and M. Grazzini, Phys. Rev. Lett. **98** (2007) 222002.
7. G. F. R. Sborlini, PoS **EPS-HEP2017** (2017) 398.
8. R. D. Ball *et al.* [NNPDF Collaboration], Eur. Phys. J. C **77** (2017) no.10, 663.
9. V. Bertone *et al.* [NNPDF Collaboration], arXiv:1712.07053 [hep-ph].
10. A. Manohar, P. Nason, G. P. Salam and G. Zanderighi, Phys. Rev. Lett. **117** (2016) no.24, 242002; JHEP **1712** (2017) 046.
11. L. Cieri, G. Ferrera and G. Sborlini, *in preparation.*
12. L. Cieri, G. Ferrera and G. Sborlini, TIF-UNIMI-2018-4.

# Modeling of quantum effects in the hadronization

Šárka Todorova-Nová
*LAPP, Annecy-le-Vieux, France*

A recent observation of a threshold momentum difference in the production of adjacent hadrons is implemented in the fragmentation model of a three-dimensional QCD string, with the aim to investigate the common origin of the azimuthal ordering of hadrons and of the correlations commonly attributed to the Bose-Einstein effect. The role of particle decays and their polarization in the measurement of two-particle correlations is evaluated. A comparison with the available data is presented and further measurements suggested. The impact of the hadronization on the long range angular correlations is discussed.

## 1 Introduction

The aim of the study [1] is to translate the observation of a distinct correlation pattern between close hadrons [3] into a MC description of quantized fragmentation of a helical QCD string [4]. The hadronization effects are expected to be universal and their MC implementation plays an important role in the interpretation of measurements of the hadron production.

## 2 String fragmentation with helical string

In the first approximation, the helical structure of the string can be implemented as a modulation on top of the default longitudinal string fragmentation (two degrees of freedom describing the generation of the intrinsic transverse momentum of hadrons are nevertheless suppressed as the transverse momentum of hadrons is obtained from the transverse shape of the string). Such a study can be performed by doing modifications in the Pythia generator [5]. In practice, all hadrons are assigned a quantized transverse mass (the nearest multiple of $\kappa R \Delta\Phi \simeq 0.192$ GeV which is bigger than the tabulated mass). The size of the intrinsic transverse momentum being thus defined, its direction follows the rotation of the phase of the helical field. It is argued that it is the correlation introduced by the helical winding which is responsable for various observable correlation phenomena such as the azimuthal ordering of hadrons [2] and the Bose-Einstein (BE) effect [3]. Since the data suggest the BE correlations stems from part of string with approximately homogeneous helix field, or from a decay of heavier object (such as $\eta'$ meson), the ordered chains are injected into the fragmentation chains as triplets of pions with

identical longitudinal momentum, correlated in the transverse plane, according to the observed production rate of ordered triplets (about 1% per final charged track). Fig. 1 illustrates the properties of the simulation using the difference between pairs of particles with the opposite-sign(OS) charge and with the like-sign(LS) charge, normalized to the number of charged particles in the sample: $\Delta(Q) = \frac{1}{N_{\rm ch}}$ [ $N(Q)^{\rm OS} - N(Q)^{\rm LS}$ ], where $Q = \sqrt{-(p_i - p_j)^2}$ stands for the 4-momentum difference. This observable is particularly sensitive to the properties of pairs of adjacent hadrons.

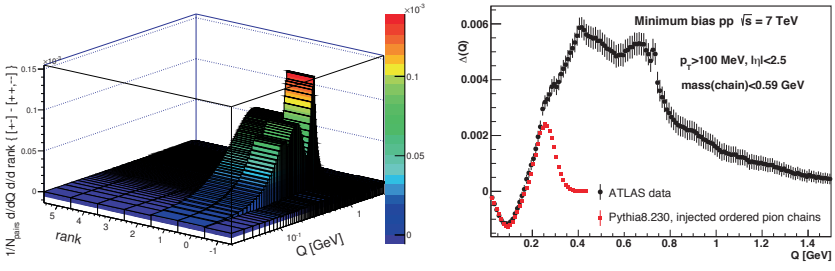


Figure 1 – Left: The rank dependence of the subtraction between opposite-sign and like-sign pairs in the default PYTHIA simulation; pairs of hadrons originating from different strings (color-disconnected chains) are assigned rank=-1. Rank 0 designs pairs of hadrons from the decay of a direct common resonance. Right: The measured $\Delta(Q)$ and the shape generated by ordered charged pion triplet chains injected into simulation with rate of $\sim 1\%$ per charged hadron produced.

For a proper description of the correlation pattern predicted by the model of helical QCD string, it is not sufficient to inject the source of correlations into simulation. The model predicts a threshold momentum difference for the production of adjacent hadrons at $Q \simeq$0.26 GeV and effectively, looking at the Fig. 1, there is no place left for additional adjacent hadrons in the region $Q <$0.25 GeV. The implementation of the polarized $\eta$ decay measured by [?] (Fig. 2), the enhancement of the longitudinal polarization for $\rho$ and $K^*$ decay, and the explicit veto on pairs of adjacent hadrons produced in the "forbidden" low-$Q$ region allows to reproduce (roughly) the measured data. The aim of the exercise is to identify the simulation components which need a further experimental cross-check : for example, there is an excess in the simulation in the region of the $\eta$/chain decay, and it is possible that the excess appears as the result of double counting of $\pi^+\pi^-$ pairs in the chain and $\eta$ decay contributions.

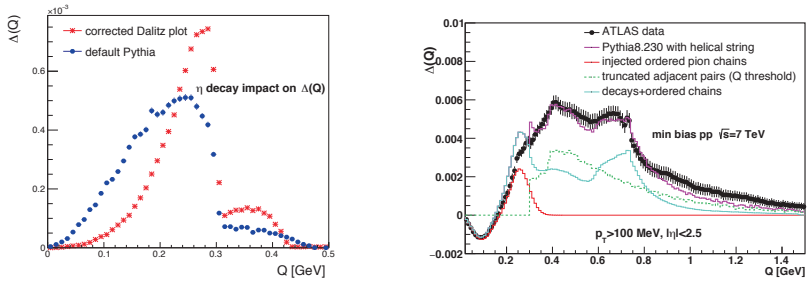


Figure 2 – Left: The $\eta$ decay contribution to the $\Delta(Q)$. Right: The contributions of direct and adjacent hadron pairs to the shape of $\Delta(Q)$ in Pythia8.230. The default $\rho^0$ production rate has been reduced by 20%, the production rate of $K^{0*}$ has been increased by 50%, and $\rho^{+-}$ and $K^{+-*}$ decay plane has been rotated to the string transverse plane, in order to reproduce the overall shape of the data.

## 3 Bose-Einstein correlations, azimuthal ordering - the same source?

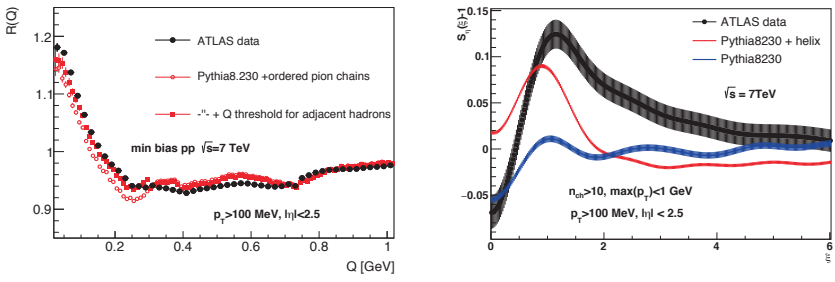


Figure 3 – Left: The injection of ordered pion chains translates into enhanced production of like-sign hadron pairs. $R(Q)$ is the ratio of the like-sign and opposite-sign inclusive Q distribution. Right: The injection of ordered pion chains translates into an azimuthal ordering signal. The simulation is not corrected for the pairs of adjacent hadrons in the "forbidden" region below Q-threshold.

Figure 3(left) shows the traditional correlation function, defined as the ratio of like-sign pair Q distribution and the unlike-sign pair Q distribution [3]. The simulation based on the injection of correlated adjacent pion triplets describes the data well, in particular when the Q-threshold is enforced for all the adjacent hadrons. The role of the adjacent hadrons is primordial in the model and in the simulation, and it is not compatible with the picture of BE interference in the incoherent particle production the physicists usually work with. The assumptions made about the nature of the correlations have a large impact on the focus and interpretation of the experimental data : from the point of view of the hadronization studies, the ratio does not allow to extract the quantized properties of the hadron production (the gaussian shape of the excess of correlated like-sign pairs is completely invisible in the ratio of inclusive Q distributions). The ratio also retains a dependence on the shape of the uncorrelated combinatorial background, contrary to the subtraction, which removes the background efficiently.

Figure 3(right) shows the appearance of the azimuthal ordering (positive correlations in the power spectrum measuring correlations between the azimuthal opening angle and the pseudorapidity difference is observed) [2]. The data are not as well reproduced as the Bose-Einstein effect, but the hypothesis of the common origin of both effects seems plausible. The measurement of the azimuthal ordering therefore provides a useful complementary input which should help to to adjust various components of the simulation.

## 4 Long range correlations

The presence of narrow strings may have been one of factors facilitating the emergence of the so-called "ridge" effect observed both in HI and pp collisions, where azimuthal correlations spanning over a larger intervals of pseudorapidity appear in the data.

The ridge-like structure can be easily generated by a laterally boosted helical string: the pions produced in the string fragmentation have instrinsic transverse momentum of only $\sim 140$ MeV, w.r.t. the string axis, and are therefore likely to be measured in the direction of the boost. As an example, a simple string with the mass of 20 GeV has been generated, fragmented into set of pions within the helix string scenario, and boosted laterally (with $\gamma$ =1.2). Fig. 4 shows the angular correlations of the produced pions, with significant signal at large pseudorapidity difference. It is interesting to look at the rank dependence of these correlations (the bottom plot): the side peaks are dominated by larger rank differences, but adjacent pairs can be nevertheless observed at large pseudorapidity difference, extending up to 4.

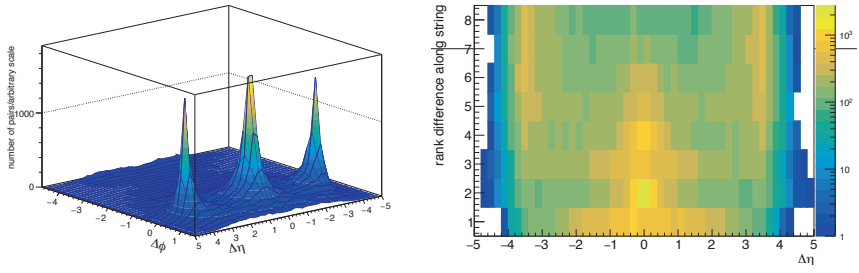


Figure 4 – Top: The emergence of a ridge-like structure in the fragmentation of a helical string with a lateral boost. The narrow helix radius (0.07 fm) implies a small intrinsic momentum (∼140 MeV) of hadrons and thus smaller smearing in the boosted direction. The recoiling system is not shown. Bottom: The rank dependence of the ridge structure shown above. Higher eta difference is effectively dominated by pairs with larger rank distance (the distribution is truncated) but the adjacent hadrons may have a large pseudorapidity difference as well.

## 5 Further experimental input

The model of the helical QCD string is rather successful in terms of the reduction of the number of independent parameters entering the simulation. For the validation and further development, it can be compared with a large variety of measurements (single particle spectra, particle correlations). The data used so far do not contain all the information which is necessary: the correlation measurements shown here do not identify the charged particles, and therefore do not see a difference between pions and kaons, for example. The properties of an ordered chain of kaons cannot be predicted easily within the model : kaons are expected to contain a string loop, and the properties of the string knotting are not known. The measurement of the $\Delta(Q)$ for pairs of identified hadrons (pions,kaons,..) is therefore of utmost interest. The model predicts the bulk of correlations should be carried by particles with (intrinsic) transverse momentum of ∼140 MeV, which is a value very close to, or even below, the acceptance of the LHC experiments. A dedicated measurement of the very low $p_T$ region would be very welcome indeed.

## 6 Conclusions

The simulation strategy for the quantum properties of the string fragmentation is outlined and the first simulation of the so-called Bose-Einstein effect is performed, successfully reproducing the data. The correlation of like-sign pairs of hadrons is a consequence of non-trivial properties of the production of adjacent hadrons, which are themselves correlated, too. The building blocks of the simulation contributing to the description of the Q spectra are identified and the uncertainties discussed. The simulation marks an additional success by obtaining a signal of the azimuthal ordering of hadrons, even though the measurement is not reproduced in sufficient detail yet. From the initial studies it seems the long range correlations can be modelled by the fragmentation of boosted helical strings. A presence of adjacent hadron pairs in the long range correlation signal is not excluded.

## References

1. Š.Todorova-Nová, arXiv:1801.10232 [hep-ph].
2. ATLAS Collaboration, *Phys. Rev.* D **86**, 052005 (2012).
3. ATLAS Collaboration, *Phys. Rev.* D **96**, 092008 (2017).
4. Š.Todorova-Nová, *Phys. Rev.* D **89**, 015002 (2014).
5. T. Sjöstrand, S. Mrenna, and P. Z. Skands, *J. High Energy Phys.* **05**, 026 (2006).

# Forward-backward $b$-quark asymmetry at the Z pole: QCD uncertainties redux

David d'Enterria[1], and Cynthia Yan[1,2]
[1] *CERN, EP Department, CH-1211 Geneva 23, Switzerland*
[2] *Harvey Mudd College, Department of Physics, Claremont CA91711, USA*

The forward-backward asymmetry of $b$-quarks measured at LEP in $e^+e^-$ collisions at the Z pole, $A_{\rm FB}^{0,b}|^{\rm exp} = 0.0992 \pm 0.0016$, remains today the electroweak precision observable with the largest disagreement ($2.8\sigma$) with the Standard Model theoretical prediction, $A_{\rm FB}^{0,b}|^{\rm th} = 0.1037 \pm 0.0008$. The dominant systematic uncertainties are due to QCD effects — $b,c$-quark showering and fragmentation, and $B, D$ meson decay models — which have not been revisited in the last 20 years. We reassess the QCD uncertainties of the eight original LEP measurements of $A_{\rm FB}^{0,b}$, using modern parton shower simulations based on PYTHIA 8 and PYTHIA 8 + VINCIA with different tunes of soft and collinear radiation as well as of hadronization. Our analysis indicates QCD uncertainties, of order $\pm 0.4\%$ and $\pm 1\%$ for the jet-charge and lepton-charge based analyses, that are overall slightly smaller but still consistent with the original ones. Using the updated QCD systematic uncertainties, we obtain $A_{\rm FB}^{0,b} = 0.0996 \pm 0.0016$.

## 1 Introduction

In the Standard Model (SM), the Z boson mediates weak neutral currents between fermions of the same generation. The Z couples to both left- and right-handed chiral states with different strengths depending on weak-isospin and electromagnetic charges. The vector and axial-vector Z couplings for a fermion of type $f$ are $g_V^f = (g_L^f + g_R^f) = I_3^f - 2Q^f \sin^2\theta_{\rm W}$ and $g_A^f = (g_L^f - g_R^f) = I_3^f$ respectively, where $I_3$ is the third component of the weak isospin of the fermion, $Q^f$ its charge (related to the former via the hypercharge $Y^f$: $Q^f = I_3^f + Y^f/2$), and $\sin^2\theta_{\rm W} \approx 0.23$ is the weak mixing angle that controls the $\gamma$–Z mixing and provides a relationship between the coupling constants of the electroweak theory: $g\sin\theta_W = g'\cos\theta_W = e$. From the expressions above, the varying strengths of the Z-fermion couplings for the $(\nu_e, \nu_\mu, \nu_\tau)$, $(e, \mu, \tau)$, $(u, c, t)$, and $(d, s, b)$ lepton/quark groups are explained. The mixed Z vector and axial-vector couplings not only affect the total $e^+e^- \to f\overline{f}$ cross section but induce asymmetries in the angular distributions of the final-state fermions produced in the process. Angular asymmetries in the $e^+e^- \to f\overline{f}$ final-state are ultimately driven by the fermions' charge $Q$ and the weak mixing angle:

$$\mathcal{A}_f = \frac{(g_L^f)^2 - (g_R^f)^2}{(g_L^f)^2 + (g_R^f)^2} = 2\frac{g_V^f/g_A^f}{1 + (g_V^f/g_A^f)^2}\,, \text{ with } \quad \frac{g_V^f}{g_A^f} = 1 - 4|Q_f|\sin^2\theta_{\rm eff}^f\,. \tag{1}$$

Experimentally, forward-backward asymmetries in $e^+e^- \to f\overline{f}$ are determined from the ratio of the number of forward- (backward-)going (anti)fermions measured in the hemisphere defined by the direction of the $e^+$ ($e^-$) beams:

$$A_{\rm FB}^f = \frac{N_F - N_B}{N_F + N_B}, \quad \text{where} \;\; F = \int_0^1 \frac{d\sigma}{d\Omega} d\Omega, \;\; B = \int_{-1}^0 \frac{d\sigma}{d\Omega} d\Omega, \tag{2}$$

The forward-backward asymmetry of $b$ quarks ($A_{\rm FB}^{0,b}$) in the process $e^+e^- \to Z \to b\bar{b}$ at $\sqrt{\rm s} = m_Z$ is the one most accurately measured among all quarks at LEP, given that $b$-quarks are the easiest jets to identify. The value $A_{\rm FB}^{0,b}|^{\rm exp} = 0.0992 \pm 0.0016$, obtained from the combination of eight measurements at $\sqrt{\rm s} = 91.21$–$91.26$ GeV using two different (lepton- and jet-charge based) methods, shows today the largest discrepancy ($2.8\sigma$) with respect to the theoretical SM prediction, $A_{\rm FB}^{0,b}|^{\rm th} = 0.1037 \pm 0.0008$ (and so does the value of $\sin^2\theta_{\rm W}$ derived from them) [1]. We reanalyze here the original studies to see if such a discrepancy could be explained by a potential underestimation of the associated systematic uncertainties.

## 2 LEP $b$-quark forward-backward asymmetry data

Table 1 lists the eight $A_{\rm FB}^{0,b}$ measurements with the breakdown of their uncertainties. In four measurements, the original $b$, $\bar{b}$ quarks are identified from the charge of the leading lepton $\ell$ inside each $b$-jet (through the fragmentation $b \to B, b \to c \to D$ and subsequent $B, D \to \ell$ decay), whereas in the other four, the $b$ charge is reconstructed from the jet constituent particles. The statistical uncertainties of $A_{\rm FB}^{0,b}$ dominate, being twice bigger than the systematic ones, while the QCD uncertainties account for about half of the latter (and are assumed to be fully-correlated among measurements). The QCD-related biases on $A_{\rm FB}^{0,b}$ depend strongly on the experimental selection procedure and are related to: (i) hard gluon radiation, and (ii) smearing of the $b$-jet (thrust) axis due to $b$ and ($b \to$)$c$ soft radiation and hadronization, and subsequent $B$ and $D$ hadron decay models. Whereas the first bias is theoretically well controlled through next-to-next-to-leading-order perturbative QCD (plus massive $b$-quark) corrections [2], the uncertainties of the latter were estimated using Monte Carlo (MC) parton shower simulations [3] that have not been revisited in 20 years.

Table 1: LEP measurements of $A_{\rm FB}^{0,b}$ and associated statistical, total systematic, and QCD-systematic uncertainties (with the newly-computed QCD systematics quoted in parentheses).

| Measurement | $A_{\rm FB}^{0,b}$ | uncertainties | | |
|---|---|---|---|---|
| | | stat. | total syst. | QCD syst. (new) |
| ALEPH lepton (2002) [4] | $0.1003 \pm 0.0038 \pm 0.0017$ | 4.1% | 1.7% | 0.6% (0.8%) |
| DELPHI lepton (2004-5) [5] | $0.1025 \pm 0.0051 \pm 0.0024$ | 6.4% | 2.4% | 1.5% (1.3%) |
| L3 lepton (1999) [6] | $0.1001 \pm 0.0060 \pm 0.0035$ | 6.9% | 3.4% | 1.8% (0.8%) |
| OPAL lepton (2003) [7] | $0.0977 \pm 0.0038 \pm 0.0018$ | 4.3% | 1.5% | 1.1% (1.4%) |
| ALEPH jet-charge (2001) [8] | $0.1010 \pm 0.0025 \pm 0.0012$ | 2.7% | 1.1% | 0.5% (0.5%) |
| DELPHI jet-charge (2005) [9] | $0.0978 \pm 0.0030 \pm 0.0015$ | 3.3% | 1.5% | 0.5% (0.4%) |
| L3 jet-charge (1998) [10] | $0.0948 \pm 0.0101 \pm 0.0056$ | 10.8% | 5.9% | 4.1% (0.4%) |
| OPAL jet-charge (2002) [11] | $0.0994 \pm 0.0034 \pm 0.0018$ | 3.7% | 1.8% | 1.5% (0.3%) |

At future high-luminosity $e^+e^-$ machines, such as the FCC-ee with $10^5$ times more data collected at the Z pole than at LEP [12], statistical uncertainties will be totally negligible, and the latter QCD effects will dominate the systematics of the $A_{\rm FB}^{0,b}$ measurement.

## 3 Simulation of the LEP $b$-quark forward-backward asymmetry measurements

The eight original LEP measurements of $A_{\rm FB}^{0,b}$ have been implemented in a MC event simulation based on PYTHIA 8.226 [13] with seven different parton-shower and hadronization tunes, as well as based on two alternative (dipole antenna) shower approaches from PYTHIA 8.210 combined with VINCIA 1.1 and 2.2 (with uncertainties given by 12 variations of the VINCIA parameter set) [14]. Ten million $e^+e^- \to Z(b\bar{b})$ events are thereby generated at $\sqrt{\rm s} = 92.4$ GeV with QED radiation on, and analysed as done in the original experiments. The whole MC setup effectively corresponds to nine different modelings of the underlying QCD effects (bottom- and charm-quark gluon radiation and fragmentation functions, and $B, D$ semileptonic decays). Tune-7 and VINCIA 2.2 include proton-proton data whereas all other models are based on LEP data alone. For all analyses, the $b$-jets are first reconstructed with the JADE algorithm from the list of final-state particles and the thrust axis of the event is computed as a proxy of the $b\bar{b}$ direction. Each original $y_{\rm cut}$ and $M_{\rm jet}$ jet selection criteria, and (transverse) momenta ($p_T$) $p$ cuts on the final electron and muons, are applied. On the one hand, the lepton-based analyses determine the $b$-quark charge from that of the hardest charged lepton in the event, and then extract $A_{\rm FB}^{obs,b}$ by fitting the corresponding distribution of polar angles $\theta$ between the $e^-$ and the thrust axis, $dN/d\cos\theta = 3/8\ [1 + \cos^2\theta + 8/3\, A_{\rm FB}^{obs,b}(1 - 2\chi_B)\cos\theta]$, where $\chi_B \approx 0.12$ is the $B^0\overline{B^0}$ effective mixing parameter. On the other, in the jet-charge-based analyses, $b, \bar{b}$-quarks are identified via their measured jet charge $Q_{\rm jet} = \sum p_L^\kappa\, Q / \sum p_L^\kappa$ (where $p_L$ is the longitudinal momentum of the final-state particles, with charge $Q$, with respect to the thrust axis, and the power $\kappa$ varies between 0.4 and 0.6), and $A_{\rm FB}^{obs,b}$ is derived by fitting the distribution $\langle Q_F - Q_B\rangle \,/\, \langle Q_b - Q_{\bar{b}}\rangle = 8/3\, A_{\rm FB}^{obs,b}(1+C)\cos\theta/(1+\cos^2\theta)$, where $Q_F$ ($Q_B$) are the jet charges in the forward (backward) hemisphere, and the $C$ factor is a $\sim$3.5% correction for missing higher-order QCD terms and for the difference between the thrust axis and the $b$-quark direction [1,3].

## 4 Results and conclusions

Through the procedure describe above, we extract 9 different MC values of $A_{\rm FB}^{obs,b}$ for each one of the eight experimental setups, which we compare among themselves and against the experimental data in Fig. 1 and 2 for lepton- and jet-charge analyses. The central $A_{\rm FB}^{obs,b}$ values plotted differ slightly from the $A_{\rm FB}^{0,b}$ values quoted in Table 1, since the latter are obtained correcting for radiative effects, $\gamma$ exchange, Z-$\gamma$ interference, and shifted to the pole $m_Z = 91.187$ GeV mass. The first (leftmost) MC point corresponds to the PYTHIA 8 tune-1 result obtained with the 1990 JETSET parameter set, very similar to the one used to obtain the original LEP QCD uncertainties [3]. The red band around the MC points is the standard deviation of the predictions, which we take as indicative of the associated QCD systematic uncertainty for each measurement. It amounts to about 1% (0.4%) for the lepton (jet) charge-based measurements, and is found to be overall slightly smaller but still fully consistent with the original QCD uncertainties (last column of Table 1). Using the updated QCD systematics, we obtain [15] a new weighted-average $b$-quark forward-backward asymmetry, $A_{\rm FB}^{0,b} = 0.0996 \pm 0.0016$, very similar to the current one.

## References


1. S. Schael *et al.* [LEP/SLD Electroweak Working Group], Phys. Rept. **427** (2006) 257
2. W. Bernreuther, L. Chen, O. Dekkers, T. Gehrmann, and D. Heisler, JHEP **01** (2017) 053
3. D. Abbaneo *et al.* [LEP Heavy Flavor Working Group], Eur. Phys. J. C **4** (1998) 185
4. A. Heister *et al.* [ALEPH Collaboration], Eur. Phys. J. C **24** (2002) 177
5. P. Abreu *et al.* [DELPHI Collaboration], Z. Phys. C **65** (1995) 569; J. Abdallah *et al.* [DELPHI Collaboration], Eur. Phys. J. C **34** (2004) 109

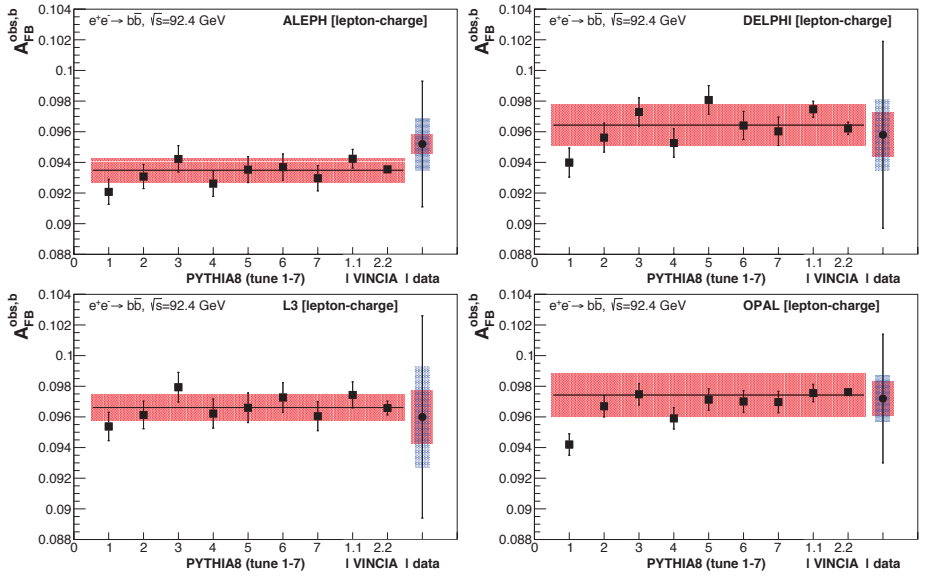


Figure 1 – $b$-quark forward-backward asymmetry extracted from lepton-charge analyses of $e^+e^- \to b\bar{b}$ simulations based on seven PYTHIA 8 and two PYTHIA 8+VINCIA tunes (squares with red band), compared to the corresponding experimental results (rightmost data point, with QCD, in red, and uncorrelated, in blue, systematic uncertainty bands) measured by ALEPH (top left) [4], DELPHI (top right) [5], L3 (bottom left) [6], and OPAL (bottom right) [7].

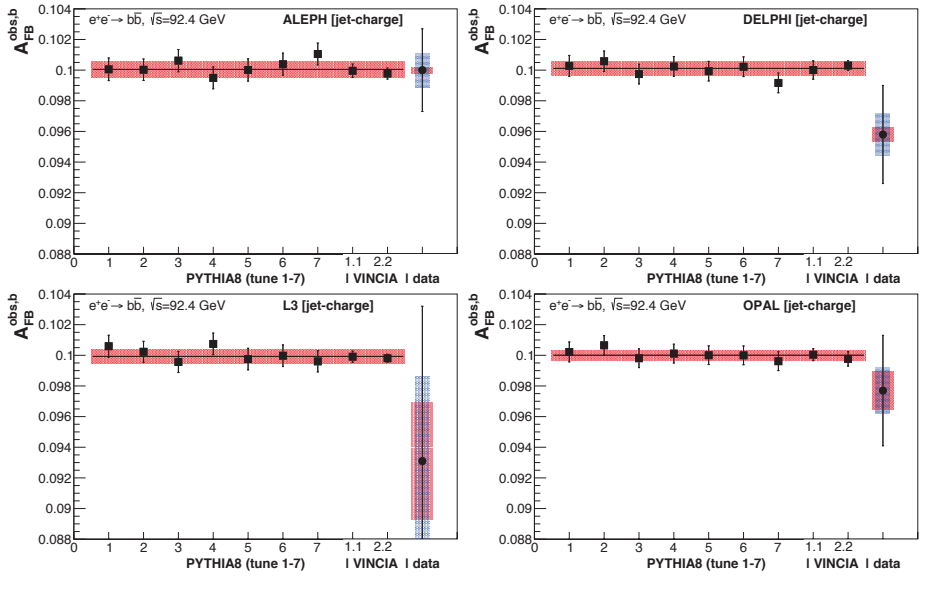


Figure 2 – $b$-quark forward-backward asymmetry extracted from jet-charge analyses of $e^+e^- \to b\bar{b}$ simulations based on seven PYTHIA 8 and two PYTHIA 8+VINCIA tunes (squares with red band), compared to the corresponding experimental results (rightmost data point, with QCD, in red, and uncorrelated, in blue, systematic uncertainty bands) measured by ALEPH (top left) [8], DELPHI (top right) [9], L3 (bottom left) [10], and OPAL (bottom right) [11].

6. O. Adriani *et al.* [L3 Collaboration], Phys. Lett. B **292** (1992) 454; M. Acciarri *et al.* [L3 Collaboration], Phys. Lett. B **448** (1999) 152
7. G. Abbiendi *et al.* [OPAL Collaboration], Phys. Lett. B **577** (2003) 18
8. A. Heister *et al.* [ALEPH Collaboration], Eur. Phys. J. C **22** (2001) 201
9. J. Abdallah *et al.* [DELPHI Collaboration], Eur. Phys. J. C **40** (2005) 1
10. M. Acciarri *et al.* [L3 Collaboration], Phys. Lett. B **439** (1998) 225
11. G. Abbiendi *et al.* [OPAL Collaboration], Phys. Lett. B **546** (2002) 29; K. Ackerstaff *et al.* [OPAL Collaboration], Z. Phys. C **75** (1997) 385
12. M. Bicer *et al.* [TLEP Design Study Working Group], JHEP **01** (2014) 164; and D. d'Enterria, doi:10.1142/9789813224568_0028; arXiv:1602.05043 [hep-ex]
13. T. Sjöstrand *et al.*, Comput. Phys. Commun. **191** (2015) 159
14. N. Fischer, S. Prestel, M. Ritzmann and P. Skands, Eur. Phys. J. C **76** (2016) 589
15. D. d'Enterria and C. Yan, in preparation

# FIRST MEASUREMENT OF ELASTIC, INELASTIC AND TOTAL CROSS-SECTION, DETERMINATION OF THE $\rho$ PARAMETER AT $\sqrt{s} = 13$ TEV BY TOTEM AND AN EVIDENCE FOR ODDERON

J. KAŠPAR
*INFN, Sezione di Pisa, Italy*
*and CERN, Geneva, Switzerland*
*and Institute of Physics of the ASCR, Prague, Czech Republic*

(on behalf of the TOTEM Collaboration)

The TOTEM experiment has performed the first 13 TeV measurements of the total cross-section and the $\rho$ parameter, i.e. the real-to-imaginary ratio of the nuclear elastic scattering amplitude at $t = 0$. The obtained $\rho$ value is significantly lower than expected and together with the total cross-section the new TOTEM measurements rule out most of the pre-LHC models and indicate a strong role of a crossing-odd scattering amplitude even at high energies. A similar conclusion is made from comparison of proton-proton and proton-antiproton elastic differential cross-section in the dip region. Theory offers several candidates for the crossing-odd scattering amplitude. In particular, in perturbative QCD it could be realised as $t$-channel exchange of a colourless bound state of 3 gluons.

## 1 Introduction

This contribution presents two recent measurements [1,2] by the TOTEM experiment [3]. Both are related to proton-proton scattering at 13 TeV, the first determines the value of the total cross-section, the second of the parameter

$$\rho = \left.\frac{\Re\mathcal{A}_{\rm el}}{\Im\mathcal{A}_{\rm el}}\right|_{t=0} , \tag{1}$$

where $\mathcal{A}_{\rm el}$ stands for the nuclear elastic-scattering amplitude and $t$ for four-momentum transfer squared. The two measured observables are related by dispersion relations and thus discussing them together allows to draw stronger physics conclusions.

The article is organised as follows. Section 2 presents the total cross-section measurement, Section 3 the $\rho$ measurement. Section 4 shows that these measurements indicate a strong role of a crossing-odd amplitude, which could be realised in QCD as an exchange of a colourless bound state of 3 gluons. A similar conclusion can be drawn from the dip region of the elastic differential cross-section as shown in Section 5. Section 6 gives a short review of theoretical concepts that introduce crossing-odd amplitudes.

## 2 Total cross-section measurement

At 13 TeV, TOTEM determined the total cross-section using data from a special LHC fill with $\beta^* = 90$ m optics [1]. The measurements of the inelastic rate, $N_{\rm inel}$, of the elastic rate, $N_{\rm el}$, and

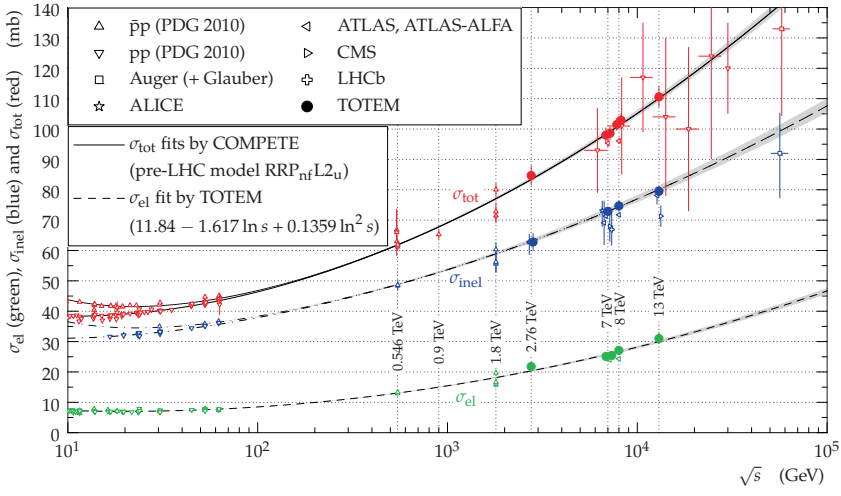


Figure 1 – Total (red), inelastic (blue) and elastic (green) cross-section measurements plotted as function of collision energy, $\sqrt{s}$. The black lines with grey bands correspond to data fits and associated uncertainties.

its extrapolation to the forward direction, $\mathrm{d}N_{\mathrm{el}}/\mathrm{d}t|_{t=0}$, were combined via the optical theorem to determine the total cross section in a luminosity-independent way:

$$\sigma_{\mathrm{tot}} = \frac{16\pi(\hbar c)^2}{1+\rho^2}\frac{\mathrm{d}N_{\mathrm{el}}/\mathrm{d}t|_{t=0}}{N_{\mathrm{el}}+N_{\mathrm{inel}}} \ . \tag{2}$$

Using $\rho = 0.10$ (see Section 3), the following results were obtained:

$$\sigma_{\mathrm{tot}} = (110.6 \pm 3.4)\,\mathrm{mb} \ , \quad \sigma_{\mathrm{inel}} = (79.5 \pm 1.8)\,\mathrm{mb} \ , \quad \sigma_{\mathrm{el}} = (31.0 \pm 1.7)\,\mathrm{mb} \ . \tag{3}$$

Figure 1 compares total, inelastic and elastic cross-section measurements by TOTEM to the results of other experiments. The TOTEM measurements at 13 TeV confirm the trend of cross-section growth with energy – the data are compatible with asymptotic $\log^2 s$ dependence. The continuous growth is an important aspect for physics implications discussed in Section 4. Also, it is worth noting the remarkable agreement of the total cross-section data with the pre-LHC prediction by COMPETE [4] (solid black line).

## 3 $\rho$ measurement

Elastic scattering of protons is a process mediated by strong ("nuclear") and electromagnetic ("Coulomb") interactions. At LHC energies, the interference of the associated scattering amplitudes gives a significant effect at $|t| = \mathcal{O}(10^{-4}\,\mathrm{GeV}^2)$. Since the Coulomb amplitude is known from QED, the interference exposes the phase of the nuclear amplitude in the measurable differential cross-section. Consequently, this provides a tool to determine the $\rho$ parameter.

In order to reach the very low $|t|$, special experimental arrangement was needed, including an LHC optics with very high $\beta^* = 2500\,\mathrm{m}$ and very close approach of the forward-proton detectors to the beam requiring a dedicated scheme for the LHC collimators. In this way, $|t|$ values as low as $8 \cdot 10^{-4}\,\mathrm{GeV}^2$ were reached.

The $\rho$ parameter was determined by means of differential cross-section fits. Following the empirical observation, the modulus of the nuclear amplitude was parametrised by an exponential form: $a\exp(\sum_{n=1}^{N_b} b_n t^n)$. The coefficients $b_2$, $b_3$, etc. can account for small deviations from the

Table 1: Summary of $\rho$-fit results for various fit configurations.

| | $\lvert t\rvert_{\max} = 0.07\,\mathrm{GeV}^2$ | | $\lvert t\rvert_{\max} = 0.15\,\mathrm{GeV}^2$ | |
|---|---|---|---|---|
| $N_b$ | $\chi^2$/ndf | $\rho$ | $\chi^2$/ndf | $\rho$ |
| 1 | 0.7 | $0.09 \pm 0.01$ | 2.6 | - |
| 2 | 0.6 | $0.10 \pm 0.01$ | 1.0 | $0.09 \pm 0.01$ |
| 3 | 0.6 | $0.09 \pm 0.01$ | 0.9 | $0.10 \pm 0.01$ |

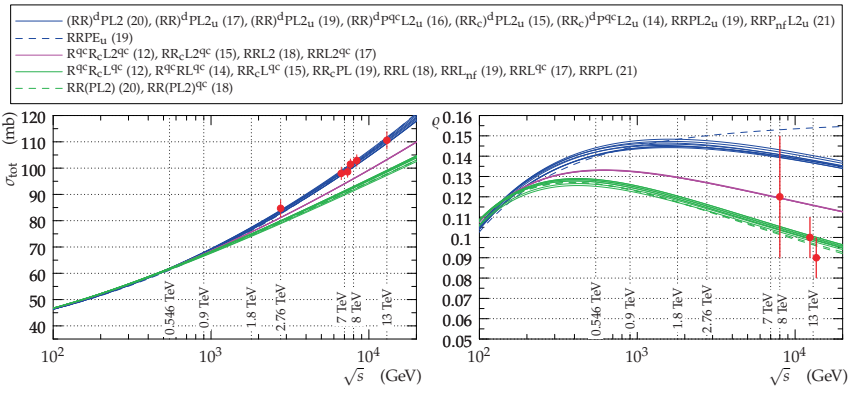


Figure 2 – Selected TOTEM measurements (red) of total cross-section (left) and $\rho$ (right) compared to pre-LHC models by COMPETE.

leading exponential behaviour of the data reflected in the coefficient $b_1$. Table 1 summarises the fit results for several degrees of the polynomial in the exponent (rows) and two values of the upper $|t|$ bound (columns). For the latter, the value of $0.07\,\mathrm{GeV}^2$ corresponds to a $|t|$ region where a purely-exponential nuclear amplitude is sufficient, the value of $0.15\,\mathrm{GeV}^2$ includes all the data usable for $\rho$ extraction. The combination of $N_b = 1$ and $|t| < 0.15\,\mathrm{GeV}^2$ gives a bad fit quality and indicates "non-exponentiality" of the differential cross-section on the full $|t|$ range at 13 TeV, as previously observed by TOTEM at 8 TeV [5]. Consequently, the $\rho$ value for this combination is not given. All other combinations give reasonable fit quality and $\rho$ constrained to a narrow range from 0.09 to 0.10 – significantly lower than extrapolations from lower energies [4].

The fit combination $N_b = 1$ and $|t| < 0.07\,\mathrm{GeV}^2$ has another important meaning: it is the closest fit configuration to the UA4/2 analysis [6] and other past $\rho$ determinations. Due to the phenomenon of "forward-cone shrinkage", many lower-energy experiments could only probe the low-$|t|$ end of the differential spectrum where a purely-exponential description is appropriate. From this point of view, this fit combination corresponds to the most fair comparison to models and extrapolations based on lower-energy data.

## 4 Physics implications

Figure 2 confronts selected TOTEM measurements with pre-LHC models represented by the comprehensive study by the COMPETE collaboration [4]. The colourful curves correspond to 23 models which were found to give reasonable description of pre-LHC data. While the TOTEM measurements of total cross-section are only compatible with the COMPETE models in the blue band, the measurements of $\rho$ only with the green models. In summary, there is no model which can describe the TOTEM total cross-section and $\rho$ measurements simultaneously.

Another, even less model-dependent, relation between $\sigma_{\mathrm{tot}}$ and $\rho$ can be obtained from

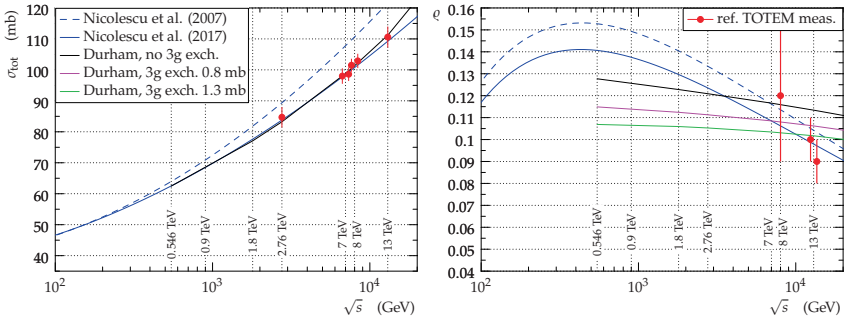


Figure 3 – Example of models including a crossing-odd component that can describe the TOTEM measurements.

dispersion relations [7]. If only the crossing-even component of the amplitude is considered, it can be shown that $\rho$ is proportional to the rate of growth of $\sigma_{\text{tot}}$ with energy. Therefore, the low value of $\rho$ presented in Section 3 indicates that either the total cross-section growth should slow down at higher energies or that there is a need for an odd-signature object being exchanged by the protons. While at lower energies such contributions may naturally come from secondary Reggeons, their contribution is generally considered negligible at LHC energies due to their Regge trajectory intercept lower than unity.

Since the total cross-section measurement presented in Section 2 does not indicate slowing down of the $\sigma_{\text{tot}}$ growth, the interpretation based on a crossing-odd amplitude is favoured. Consequently, Figure 3 shows two examples of models including such a contribution and being compatible with TOTEM data. For both, the model by Nicolescu et al. [8] and the Durham model [9], the inclusion of a crossing-odd component was essential for reaching the good agreement with data.

## 5 Indications for crossing-odd contribution from non-forward region

The interpretation presented in Section 4 and indicating a strong role of a crossing-odd amplitude component was based on measurements related to elastic scattering at $t = 0$. However, a similar conclusion can be drawn also from non-forward elastic differential cross-section. In particular, the dip region is a sensitive area, since the crossing-even component is expected to be suppressed and thus crossing-odd components can make an appreciable effect: shallower dip in proton-antiproton and more pronounced dip in proton-proton collisions [10].

Figure 4 provides a comparison of pp and $\mathrm{p\bar{p}}$ differential cross-section in the dip region. The left plot shows the only available direct comparison at the same energy [11]. It gives a significant confirmation of the expected pp vs. $\mathrm{p\bar{p}}$ difference, however, at the low energy of $\sqrt{s} = 53\,\text{GeV}$ the difference might be attributed to secondary (mesonic) Reggeons. The effect of the latter is expected to vanish at gluon-dominated regime at higher energies (TeV scale), thus the very shallow dips in the middle plot ($\mathrm{p\bar{p}}$) [12] together with the pronounced dips in the right plot (pp) indicate an exchange of a standalone odd-signature object.

## 6 Odd-signature objects in theory

Sections 4 and 5 presented experimental arguments for a strong role of odd-signature objects as mediators in high-energy proton scattering. This section briefly summaries theoretical studies of such objects, following the reviews by Ewerz [10] and Braun [13].

In axiomatic field theory, an odd-signature object was first introduced by Nicolescu et al. under the name Odderon [14]. The maximal Odderon follows from the assumption of maximal

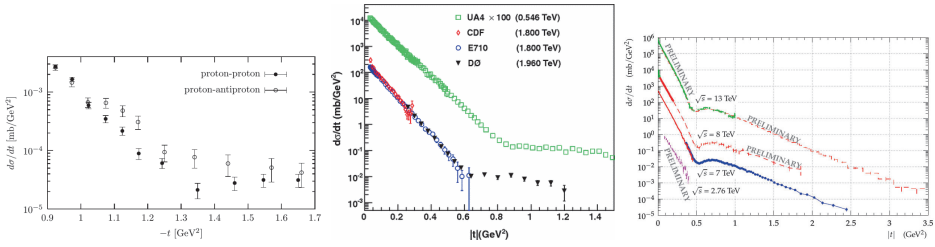


Figure 4 – Elastic differential cross-section from ISR (left, $\sqrt{s} = 53\,\text{GeV}$), Tevatron (middle) and TOTEM at LHC (right).

strength of strong interactions and is constructed as a double pole at $J = 1$ when $t = 0$. This leads to a number of distinct predictions such as $\sigma_{\text{tot}}^{\text{pp}}, \sigma_{\text{tot}}^{\text{p}\bar{\text{p}}} \propto \log^2(s)$ and $\sigma_{\text{tot}}^{\text{pp}} - \sigma_{\text{tot}}^{\text{p}\bar{\text{p}}} \propto \log(s)$, which is compatible with the generalised Pomeranchuk theorem stating that $\sigma_{\text{tot}}^{\text{pp}}/\sigma_{\text{tot}}^{\text{p}\bar{\text{p}}} \to 1$ for $s \to \infty$. The concept of maximal Odderon was argued generally consistent with quantum field theory [15], while other authors claims that it violates unitarity [16].

In Regge theory, the Odderon is often introduced as a partner of the Pomeron, typically constructed as a Regge pole or cut with quantum numbers $C = P = -1$.

In perturbative QCD, the Odderon corresponds to a colourless $C = -1$ bound state of 3 reggeised gluons. It emerges similarly as the Pomeron from BFKL: via (generalised) LLA resummation which leads to the Bartels-Kwiecinski-Praszalovicz (BKP) equation [17,18]. Several solutions have been found, all having Regge-like energy dependence $s^\alpha$. The Janik-Wosiek solutions [19] lead to Odderon intercept $\approx 0.96$ and have some phenomenologically relevant couplings missing. The Bartels-Lipatov-Vacca solutions [20] give intercept 1. The physics relevance of different solutions is not yet quite clear.

There have been attempts to include the Odderon in (semi-)non-perturbative QCD models, following the approaches developed for the Pomeron. A notable example can be the combination of the framework by Nachtman [21], Stochastic Vacuum Model [22] and modified gluon propagators that reflect non-perturbative properties [23]. This model predicts the Odderon intercept to be 1.

Another non-perturbative approach is based on the AdS/CFT correspondence, where the Odderon emerges on equally firm footing as the Pomeron [24].

In lattice-QCD calculations the $J^{PC} = 1^{--}$ state is typically called vector glueball and is a confirmed part of the glueball spectrum [25], typically with a mass between 3 and 4 GeV.

## 7 Summary

The TOTEM collaboration has published the first 13 TeV measurements of proton-proton total cross-section and the $\rho$ parameter. The latter has been found to be significantly lower than the pre-LHC expectations.

None of the COMPETE models, which can be regarded as representative of pre-LHC physics modelling, can describe simultaneously the total cross-section and $\rho$ measurements by TOTEM.

Two models have been found to be compatible with TOTEM measurements, in both cases the inclusion of a crossing-odd component was essential for reaching the good agreement.

The consistent pattern of shallow dips in $\text{p}\bar{\text{p}}$ and pronounced dips in pp elastic elastic scattering provides an independent strong indication for the importance of a crossing-odd component.

A crossing-odd component is naturally present in many theoretical frameworks. In particular, it emerges from various treatments of QCD and is thus its unavoidable consequence. In perturbative QCD the crossing-odd amplitude is realised by an exchange of a colourless bound state of 3 gluons.

If the role of the crossing-odd contribution is shown to be negligible for elastic proton-proton

scattering in the future, the presented $\rho$ measurement predicts via dispersion relations that the growth of the total cross-section should slow down at higher energies.

**Acknowledgements**

We are grateful to Chung-I Tan for pointing out the Odderon studies within the AdS/CFT correspondence.

**References**

1. G. Antchev et al. (TOTEM Collaboration), First measurement of elastic, inelastic and total cross-section at $\sqrt{s} = 13$ TeV by TOTEM and overview of cross-section data at LHC energies, CERN-EP-2017-321.
2. G. Antchev et al. (TOTEM Collaboration), First determination of the $\rho$ parameter at $\sqrt{s} = 13$ TeV – probing the existence of a colourless three-gluon bound state, CERN-EP-2017-335.
3. G. Anelli et al. (TOTEM Collaboration), JINST **3**, S08007 (2008).
4. COMPETE Collaboration, J. Cudell et al., Phys. Rev. Lett. 89 (2002) 201801.
5. TOTEM Collaboration, Nucl. Phys. B 899 (2015) 527-546.
6. C. Augier et al. (UA4/2 Collaboration), Phys. Lett. B316 (1993) 448.
7. V. Barone and E. Predazzi, High-Energy Particle Diffraction (Springer Berlin Heidelberg, 2002).
8. E. Martynov and B. Nicolescu, Phys. Lett. B 778 (2018) 414.
9. V.A. Khoze, A.D. Martin and M.G. Ryskin, Phys. Rev. D 97 (2018) 034019.
10. C. Ewerz, The Odderon in quantum chromodynamics, (2003), arXiv:hep-ph/0306137.
11. A. Breakstone et al., Phys. Rev. Lett. 54 (1985) 2180.
12. V.M. Abazov et al. (D0 Collaboration), Phys. Rev. D 86 (2012) 012009.
13. M.A. Braun, Odderon and QCD, (1998), arXiv:hep-ph/9805394.
14. L. Lukaszuk and B. Nicolescu, Lett. Nuovo Cim. 8 (1973) 405.
15. P. Gauron, L. Lukaszuk and B. Nicolescu, Phys. Lett. B 294 (1992) 298.
16. V.A. Khoze, A.D. Martin, M.G. Ryskin, (2018), arXiv: 1801.07065v1.
17. J. Bartels, Nucl. Phys. B 175 (1980) 365.
18. J. Kwiecinski and M. Praszalowicz, Phys. Lett. B 94 (1980) 413.
19. R.A. Janik and J. Wosiek, Phys. Rev. Lett. 82 (1999) 1092.
20. J. Bartels, L.N. Lipatov and G.P. Vacca, Phys. Lett. B 477 (2000) 178.
21. O. Nachtmann, Annals Phys. 209 (1991) 436.
22. H.G. Dosch, Phys. Lett. B 190 (1987) 177.
23. P.V. Landshoff and O. Nachtmann, Z. Phys. C 35 (1987) 405.
24. R.C. Brower and M. Djuric and Chung-I Tan, JHEP 0907:063 (2009).
25. C.J. Morningstar and M. Peardon, Phys. Rev. D 60 (1999) 034509.

# 9.
# Heavy Ion

# MEASUREMENT OF JETS AND PHOTONS WITH THE ALICE EXPERIMENT AT THE LHC

L. LEARDINI
*Physikalisches Institut, Heidelberg University, Im Neuenheimer Feld 226, 69120 Heidelberg, Germany*

Jets and direct photons are used to probe the formation and the properties of the Quark-Gluon Plasma (QGP) by the ALICE Collaboration. The results shown here will present the measurements obtained from Pb–Pb and p–Pb collisions. It is observed that in Pb–Pb collisions jets are collimated and hadron yields ($\pi^0$ and $\eta$) at high transverse momentum undergo strong suppression due to the interaction of the patrons with the QGP. On the other hand, photons do not show any suppression in this region, and, in addition, an excess attributed to a thermal emission is observed at low transverse momentum. No hints of medium modifications are observed for the p–Pb results, for which a jet quenching limit of $-0.4$ GeV/$c$ is calculated.

## 1 Introduction

The main focus of the ALICE experiment is the study of the ultra-relativistic heavy-ion collisions and of the subsequent hot and dense phase of the matter, the Quark-Gluon Plasma (QGP). The understanding and characterisation of the properties of the created medium is accomplished using, among others, hard probes: the prompt component of the direct photons and jets from parton fragmentation. Prompt photons and jets have a common origin in the hard scatterings in the initial phase of the system evolution after the initial nucleus-nucleus collision. The partons created in the initial hard collisions scatter and lose energy while moving in the QCD medium. The modification of the hadron yields originating from these partons as a function of momentum gives information on the medium. This quantity is studied for several particle species, where the comparison to pp and p–Pb results contributes to the characterisation of the parton energy loss and QGP evolution. While for jet measurements the attention is focused on the modifications induced by the medium, a key feature of the direct photon (*i.e.* not coming from hadron decays) measurement is that its information is unaffected by the passage through the QCD matter. However, the medium itself will be a source of thermal emission and will lead to additional contribution of direct photons at low transverse momentum. Thus, the early stages are accessible in the form of the direct photon emission temperature and collective flow measurements. Considering that most of the photons are created in hadron decays, the direct photon measurement

requires a good knowledge of the decay photon contribution to the inclusive photon yields.

## 2 Jet measurements

In ALICE, jets can be measured via charged-particle tracking, using the central barrel detectors, and via clusters in the EMCal, one of the electromagnetic calorimeters [1]. Jets are reconstructed using FastJet: the anti-$k_{\mathrm{T}}$ algorithm is used for signal jets while the $k_{\mathrm{T}}$ algorithm is used for the average background estimation. The typical resolution parameters are $R = 0.2$ and 0.4. The ALICE Collaboration already measured jet quenching in Pb–Pb collisions [2] but to better characterise the medium properties, detailed studies on jet shapes are carried out.

In Fig. 1 (left), the fully-corrected mean jet mass as a function of the charged jet $p_{\mathrm{T}}$ measured in 0–10% most central Pb–Pb collisions at $\sqrt{s_{\mathrm{NN}}} = 2.76$ TeV centre-of-mass energy [3] is shown. The jet mass is directly related to the leading parton virtuality and it can be used as a measure of the jet broadening: soft splittings within the jet cone will increase the jet mass while large angle radiation outside the jet cone will reduce the jet mass. The measurement points to a collimated jet structure, with the mean value of the jet mass increasing for increasing jet transverse momentum, as expected from NLO pQCD calculations. Moreover, the comparison to models with and without jet quenching indicates that competing effects, energy loss in the medium and medium response, enter this measurement and that further efforts are needed in order to isolate them.

The study of p–Pb collisions, that started out as a way to disentangle initial and final state and cold nuclear matter effects, became of relevance by itself to verify whether QGP formation takes place also in small systems. As mentioned above, the jet quenching has already been measured in central Pb–Pb in ALICE, setting the lower limit at $-8$ GeV/$c$ of jet spectrum shift [4]. The same measurement has been carried out in p–Pb collisions using semi-inclusive hadron-jet coincidence [5]. This method allows for an unbiased measurement, independent of the collision geometry. The observable considered is the ratio of the recoil distributions ($\Delta_{\mathrm{recoil}}$) in high (0–20%) and low (50–100%) multiplicity collisions, shown in Fig. 1, (right). In the presence of jet quenching, the ratio should be below unity. As no suppression is observed, the limit for jet quenching in small systems is set as a $-0.4$ GeV/$c$ shift in the jet spectrum, indicated by the red line in the figure.

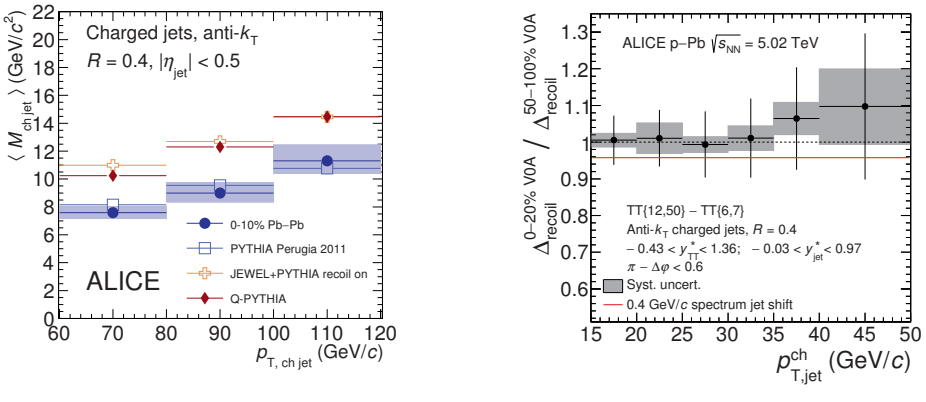


Figure 1 – Left: Fully-corrected mean jet mass compared to Pythia and to event generators with jet quenching (JEWEL and Q-PYTHIA) for jets with $R = 0.4$ in the 10% most central Pb–Pb collisions at $\sqrt{s_{\mathrm{NN}}} = 2.76$ TeV [3]. Right: Ratio of $\Delta_{\mathrm{recoil}}$ distributions measured with $R = 0.4$ for 0–20%/50–100% in p–Pb collisions at $\sqrt{s_{\mathrm{NN}}} = 5.02$ TeV [5]. The grey boxes show the systematic uncertainty of the ratio, including the correlated uncertainty of numerator and denominator. The red line indicates the jet quenching limit as a $p_{\mathrm{T}}$-shift of $-0.4$ GeV/$c$.

## 3 Neutral mesons and photon measurements

Photons are measured in ALICE with the electromagnetic calorimeters (EMCal, PHOS) or reconstructing electron-positron pairs coming from photon conversions in the detector material (PCM) [1]. Neutral meson and direct photon measurements are closely connected: the main background for the direct photon measurement are the photons from hadron decays, the largest contributions are given by the neutral pion and $\eta$ meson decays in two photons. Therefore, for a good direct photon measurement, a very precise knowledge of the decay photon background and therefore an accurate measurement of the neutral meson contribution is necessary.
Neutral pions and $\eta$ mesons have been measured in pp collisions at $\sqrt{s} = 0.9$, 2.76, 7 and 8 TeV, in non-single diffractive (NSD) p–Pb collisions at $\sqrt{s_{\rm NN}} = 5.02$ TeV and in Pb–Pb collisions at $\sqrt{s_{\rm NN}} = 2.76$ TeV. Fig. 2 shows only the most recent results for pp collisions at $\sqrt{s} = 8$ TeV (left) [6], p–Pb (middle) [7] and Pb–Pb collisions (right) [8].

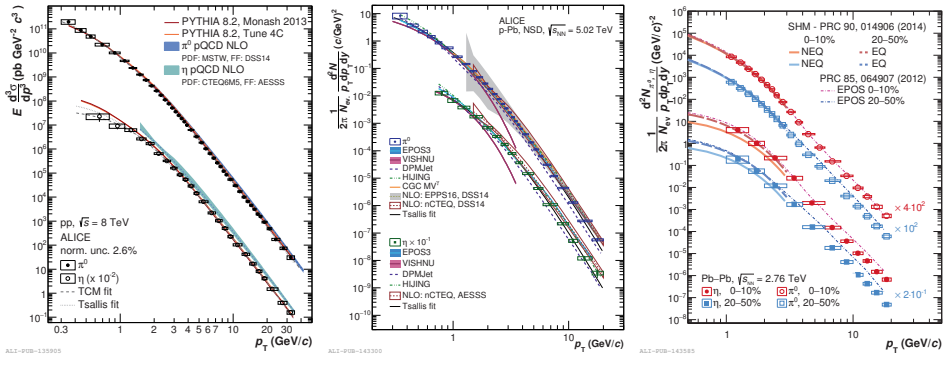


Figure 2 – Neutral meson $p_{\rm T}$-differential spectra measured in pp collisions at $\sqrt{s} = 8$ TeV (left), in NSD p–Pb collisions at $\sqrt{s_{\rm NN}} = 5.02$ TeV (middle) and Pb–Pb collisions at $\sqrt{s_{\rm NN}} = 2.76$ TeV (right). The ALICE data are compared to several theory predictions, detailed and referenced in the respective papers [6,7,8].

These results illustrate ALICE capabilities of measuring identified particles over a large transverse momentum range, combining the different reconstruction methods. In Fig. 2, the comparison to several theoretical predictions is also shown (detailed descriptions and references are given in the respective ALICE papers). While the model description of the neutral pion spectra is overall good, the agreement is worse for the $\eta$ meson. Thus, the ALICE measurements could help in improving the theory if, for example, they are included in the global parameterization of the $\eta$ fragmentation function.
Once the neutral mesons have been measured, the spectra are used to estimate the total decay photon contribution. This contribution will be then subtracted from the inclusive photons to obtain the direct photon signal. The direct photon spectra are composed of two types of photons: photon from hard scattering (originating from the same environment as jets), dominant at high-$p_{\rm T}$ and described by NLO pQCD, and photon from thermal emission of the QGP and hadronic phase, dominant at low-$p_{\rm T}$. This second component is used to extract the medium characteristics, *e.g.* the emission temperature [9].
Fig. 3 shows the neutral meson (in p–Pb and Pb–Pb) and direct photon (in Pb–Pb) nuclear modification factors, $R_{\rm AA}$, as a function of the transverse momentum. The $R_{\rm AA}$ is calculated as the ratio of the yields measured in Pb–Pb (p–Pb) collisions over the yields measured in pp collisions, scaled by the number of binary collisions. Since no precise pp reference exists for the direct photons, a theoretical calculation is used instead, as illustrated in the figure. Focusing on the low-$p_{\rm T}$ direct photon measurement, a large excess above unity can be observed. This is the thermal photon component, characteristic of heavy-ion collisions, where the QGP forms, which is absent in minimum bias pp collisions. Considering the high-$p_{\rm T}$ region instead, we ob-

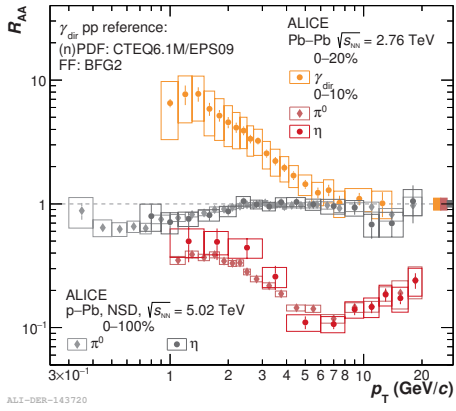


Figure 3 – Nuclear modification factor of direct photons in 0–20% Pb–Pb collisions at $\sqrt{s_{\rm NN}} = 2.76$ TeV [9] and of neutral mesons in 0–10% Pb–Pb collisions at $\sqrt{s_{\rm NN}} = 2.76$ TeV [8] and NSD p–Pb collisions at $\sqrt{s_{\rm NN}} = 5.02$ TeV [7].

serve the expected behaviour as mentioned in the introduction. Direct photons are expected to be unaffected by the QGP, and in fact the $R_{\rm AA}$ agrees with unity within uncertainties. On the other hand, the hadron yields show a strong suppression, reflecting the energy loss of the parton from which they originate in the strongly interacting medium. Moreover, we have the confirmation from the p–Pb measurement that the suppression is indeed a final state effect: no such suppression is observed for the neutral mesons measured in p–Pb collisions.

## 4 Summary

Jets and photons are complementary probes that can be used to study the characteristics of the QGP in Pb–Pb collisions and to judge whether or not this medium is formed in small systems as produced in p–Pb collisions. Concerning the latter, no evidence of medium induced effects has been found neither in the jet nor in the high-$p_{\rm T}$ hadron measurements, which are therefore used to set a limit for jet quenching in small systems and disentangle initial and final state effects. Conversely, the presence of QGP is suggested by the strong suppression of jet and hadron yields at intermediate and high-$p_{\rm T}$ in Pb–Pb collisions and by the excess of direct photons at low-$p_{\rm T}$, consistent with the emission from a hot medium.

## Acknowledgments

I would like to thank the Heidelberg Graduate School for Fundamental Physics (HGSFP) for providing the funding that allowed me to give my contribution to the conference.

## References

1. (ALICE Collaboration) B. Abelev *et al.*, *Int. J. Mod. Phys.* A **29**, 1430044 (2014).
2. (ALICE Collaboration) J. Adam *et al.*, *Phys. Lett.* B **746**, 1 (2015).
3. (ALICE Collaboration) S. Acharya *et al.*, *Phys. Lett.* B **776**, 249 (2018).
4. (ALICE Collaboration) J. Adam *et al.*, *JHEP* **09**, 170 (2015).
5. (ALICE Collaboration) S. Acharya *et al.*, arXiv/nucl-ex:1712.05603.
6. (ALICE Collaboration) S. Acharya *et al.*, *Eur. Phys. J.* C **78**, 263 (2018).
7. (ALICE Collaboration) S. Acharya *et al.*, arXiv/nucl-ex:1801.07051.
8. (ALICE Collaboration) S. Acharya *et al.*, arXiv/nucl-ex:1803.05490.
9. (ALICE Collaboration) J. Adam *et al.*, *Phys. Lett.* B **754**, 235 (2016).

# Measuring hydrodynamical expansion via the production of identified hadrons in Pb–Pb collisions with ALICE

Nicolò Jacazio for the ALICE Collaboration
*Bologna University and INFN*

During the LHC Run-2, ALICE has collected data from Pb–Pb collisions at $\sqrt{s_{\rm NN}} = 5.02$ TeV. The centrality dependence of identified particle production, including elliptic ($v_2$) and higher harmonic flow coefficients ($v_3, v_4$), has been measured. The high-precision measurement of transverse momentum ($p_{\rm T}$) differential elliptic flow of the $\phi$-meson (whose mass is close to that of the proton) allows for a unique testing of mass ordering at low $p_{\rm T}$ as well as baryon and meson grouping at intermediate $p_{\rm T}$. The $p_{\rm T}$-differential hadron spectra are presented and, together with flow coefficients, compared with state-of-the-art calculations from models based on relativistic hydrodynamics coupled with UrQMD. The added transport code is to describe rescattering in the hadronic phase, which has been successful in describing the $p_{\rm T}$-spectra of identified particles up to a few GeV/$c$. Moreover, results from the simultaneous Blast-Wave fit to the $p_{\rm T}$ distributions are compared across multiple collisions energies and system sizes in order to address the evolution of collective behaviour from small systems to large systems.

## 1 Introduction

The ultimate goal of heavy-ion physics is the study of the properties of the Quark-Gluon Plasma (QGP), a de-confined state of matter in which chiral symmetry is restored. The presence of a de-confined phase manifests with typical signatures that can be quantified by studying the particle production. In particular the measurement of identified particles provides a unique way to gain insight into the physical quantities at play. The latest Pb–Pb runs at the LHC, concluded in 2015, recorded Pb–Pb collisions at the highest energy ever achieved in the laboratory, allowing the quantitative comparison with collisions at lower energy. The ALICE experiment [1,2], thanks to its excellent tracking performance coupled with extensive particle identification (PID) capabilities, is particularly well suited for the study of identified hadron production over a wide range of transverse momentum. This is achieved by combining multiple techniques that allow, at mid-rapidity, to perform hadron identification starting from 100 MeV/$c$ and up to $\sim$ 20 GeV/$c$.

## 2 Data analysis and results

We report results on the production of identified $\pi$, K, p and $\phi$-meson production measured in Pb–Pb collisions at $\sqrt{s_{\rm NN}} = 5.02$ TeV as a function of centrality. The data sample was recorded in 2015 with a minimum-bias trigger. The total charge collected in the V0 detectors (V0M amplitude), a set of two scintillator hodoscopes located in the pseudorapidity region $2.8 < \eta < 5.1$ (V0A) and $-3.7 < \eta < -1.7$ (V0C) and covering the full azimuth, was used to determine the centrality of each Pb–Pb collision defined as percentiles of the total hadronic cross section. Further details on the centrality determination can be found in [3,4]. The amount of pile-up per event was reduced by selecting runs with low interaction rate and by rejecting events with more than one reconstructed vertex, resulting in a negligible contamination effect.

The $p_{\mathrm{T}}$ spectra of identified $\pi$, K and p are shown for two centrality classes in Figs. 1(a) and 1(c). This measurement refers to primary particles [5] only, i.e. the contributions from weak decays of strange particles and from particle knock-out in the material were removed with the data driven approach described in [6]. The systematic uncertainties were estimated by varying the PID techniques and the selection criteria used to define the track sample. The evaluation of the efficiencies and acceptance corrections was performed by using events simulated with the HIJING [7] event generator and embedded into a detailed description of the ALICE detector through which tracks are propagated with the GEANT3 [8] transport code.

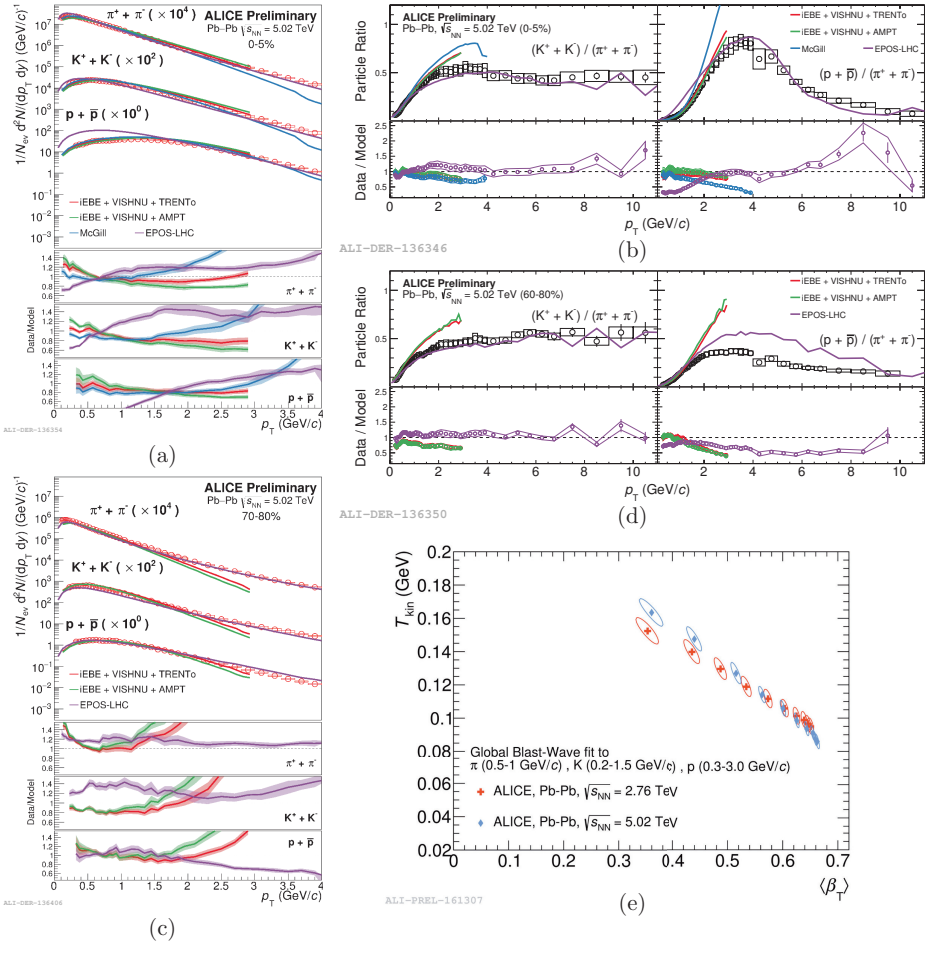


Figure 1 – Spectra of identified charged pions, kaons and protons for $0-5\%$ (a) and $70-80\%$ (c) as a function of $p_{\mathrm{T}}$ as measured in Pb–Pb collisions at $\sqrt{s_{\mathrm{NN}}} = 5.02$ TeV and compared to model predictions (iEBE + VISHNU, McGill, EPOS-LHC). (b) and (d) show particle ratios compared to the predictions from the same models. In figure (e) are reported the values of the Blast-Wave parameters obtained by performing a combined fit to the $\pi$, K, p spectra for each centrality class across different collision energy.

A direct comparison of the spectral shapes between the two centralities reveals steeper falling spectra for the peripheral case, while for the central one particles are boosted towards higher $p_{\mathrm{T}}$ following the mass hierarchy typical of radial flow. The spectral shapes are compared to the predictions from different models such as iEBE-VISHNU with TRENTo and AMPT initial con-

ditions [9,10], IP-Glasma + Music + UrQMD (McGill) [11] and EPOS-LHC [12]. In central collisions, the description of the data is qualitatively good especially at low $p_{\mathrm{T}}$ where hydrodynamics is expected to work the best. EPOS-LHC is found to give a better description of the peripheral collisions. The particle ratios p/$\pi$ and K/$\pi$ are computed and compared to the predictions of the same models in Figs. 1(b) and 1(d). In central collisions the agreement is remarkably good at low $p_{\mathrm{T}}$ (below 2 GeV/$c$) for the K/$\pi$ ratio (meson/meson), the ratio is also well reproduced by EPOS-LHC up to high $p_{\mathrm{T}}$; on the contrary in peripheral collisions only EPOS-LHC is able to reproduce the data well. The p/$\pi$ ratio (baryon/meson) is well described at low $p_{\mathrm{T}}$ by the iEBE-VISHNU model, while McGill shows increasing discrepancies and EPOS-LHC agreement is good only above 2 GeV/$c$. In peripheral collisions the iEBE-VISHNU model describes the data below 1 GeV/$c$ and EPOS-LHC generally overestimates the value of the p/$\pi$ ratio. The picture depicted by the models indicates that hydrodynamics is at work in central heavy ion collisions and is able to describe the data, while in peripheral collisions the description is more difficult and a core-corona such as EPOS-LHC is able to better describe the data. These observations advocate the creation of a fireball subject to larger flow in central heavy-ion collisions while in peripheral collisions hydrodynamical models have more difficulty to describe the data. Similar conclusions can be drawn from the analysis of the spectral shape in the framework of the Blast-Wave model [13], shown in Fig. 1(e), which yields a larger transverse expansion velocity for the most central events.

In a complementary way, particle production can be studied more differentially by measuring the flow coefficients obtained studying the particle azimuthal distribution with respect to the common symmetry plane. In Figs. 2 and 3, the results of the flow coefficients $v_2$, $v_3$ and $v_4$ as a function of $p_{\mathrm{T}}$ as measured with the scalar product method in Pb–Pb collisions at $\sqrt{s_{\mathrm{NN}}} = 5.02$ TeV are shown. More details can be found in [14].

The conclusions drawn from Figs. 2 and 3 complete the ones on the spectral shape. At low

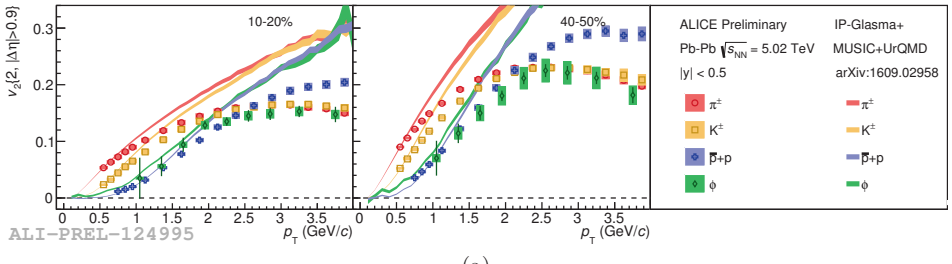


(a)

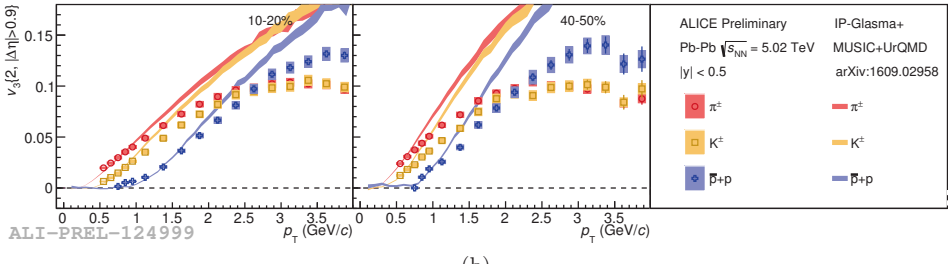


(b)

Figure 2 – $v_2$ (a) and $v_3$ (b) of identified pions, kaons, protons, and $\phi$-mesons for semi-central (10 − 20%) and semi-peripheral (40 − 50%) centrality classes, measured with the scalar product method. The measured flow coefficients are compared with the IP-Glasma + Music + UrQMD (McGill) model predictions [11].

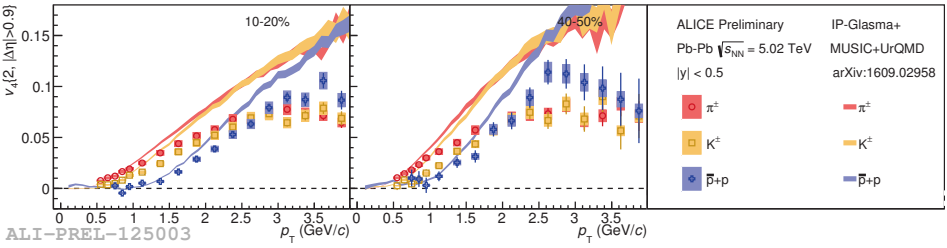


Figure 3 – $v_4$ of identified pions, kaons, protons for semi-central ($10-20\%$) and semi-peripheral ($40-50\%$) centrality classes, measured with the scalar product method. The measured flow coefficients are compared with the IP-Glasma + Music + UrQMD (McGill) model predictions [11].

$p_T$, $v_2$ shows a clear mass ordering which can be once more explained in terms of strong radial flow, for $p_T > 3$ GeV/$c$ the $v_2$ shows a separation of baryons from mesons suggesting that the production of hadrons may happen via quark coalescence. The McGill [11] IP-Glasma model prediction (viscous hydrodynamics with $\eta/s = 0.095$ and temperature-dependent $\zeta/s(T)$ coupled to a hadronic cascade) of the $v_n$ are also shown in Figs. 2 and 3. As for the comparison to the measured particle spectra the model seems to describe flow coefficients better in central collisions for $p_T < 1$, while an overestimation is observed in the same $p_T$ range in more peripheral ones. When performing this comparison it is important to note that in the theoretical models the breaking of the mass ordering for the $\phi$-meson occurs during the hadronic re-scattering phase.

## 3 Conclusions

The ALICE Collaboration has presented the results on the production of identified pions, kaons, protons and $\phi$-mesons measured as a function of the event centrality in Pb–Pb collisions at $\sqrt{s_{NN}} = 5.02$ TeV. Particle flow was quantified thanks to the analysis of the spectral shape in the Blast-Wave framework and the direct comparison to models as well as the measurement of $v_2$, $v_3$ and $v_4$ coefficients and their comparison to the model predictions.

## References


1. K. Aamodt et al. (ALICE Collaboration). *Journal of Instrumentation*, 3:S08002, 2008.
2. B. Abelevet al. (ALICE Collaboration). *Int. J. Mod. Phys.*, 29:1430044, 2014.
3. J. Adam et al. (ALICE Collaboration). *ALICE-PUBLIC-2015-008*, 2015.
4. B. Abelev et al. (ALICE Collaboration). *Phys. Rev. C*, 88:044909, 2013.
5. J. Adam et al. (ALICE Collaboration). *ALICE-PUBLIC-2017-005*, 2017.
6. B. Abelevet al. (ALICE Collaboration). *Phys. Rev. Lett.*, 109:252301, 2012.
7. Xin-Nian Wang and Miklos Gyulassy. *Phys. Rev. D*, 44:3501, 1991.
8. R. Brun et al. *CERN Program Library Long Write-up*, page No. W5013, 1994.
9. Wenbin Zhao, Hao-jie Xu, and Huichao Song. *Eur. Phys. J. C*, 77:645, 2017.
10. Rajeev S. Bhalerao, Amaresh Jaiswal, and Subrata Pal. *Phys. Rev. C*, 92:014903, 2015.
11. S. McDonald et al. *Phys. Rev. C*, 95:064913, 2017.
12. T. Pierog et al. *Phys. Rev. C*, 92:034906, 2015.
13. E. Schnedermann, J. Sollfrank, and U. W. Heinz. *Phys. Rev. C*, 48:2462–2475, 1993.
14. S. Acharya al. (ALICE Collaboration). *arXiv:1805.04390*, 2018.

# Heavy ion measurements at CMS and ATLAS

E. Chapon, on behalf of the ATLAS and CMS Collaborations
*Experimental Physics Department, CERN, CH-1211 Geneva 23, Switzerland*

We present an overview of recent results from the ATLAS and CMS collaborations on heavy ion physics. Using data from proton-proton, proton-lead and lead-lead collisions at the LHC, these results help to shed light on the properties of hot and dense nuclear matter.

Relativistic heavy ion collisions (HIC) are probing a wide variety of physics phenomena. The main motivation for PbPb collisions is to study hot medium effects, related in particular to the creation of a quark-gluon plasma (QGP). Cold nuclear matter effects, such as a realistic description of the initial state and its fluctuations, nuclear absorption, or energy loss, are also important and better studied in pPb collisions. Finally, it is important to simultaneously perform the measurements in pp collisions at the same centre-of-mass energy, which serve as a reference of "nucleons colliding in vacuum". We present an overview of recent heavy-ion results from the ATLAS [1] and CMS [2] Collaborations.

Electroweak bosons and photons are good probes of the initial state of the collisions, including nuclear modifications to parton distribution functions (nPDFs). They interact weakly with the medium, and they are expected to scale with the number of binary collisions, without medium suppression. The Z boson nuclear modification factor ($R_{\mathrm{AA}}$), for instance, has been measured to be compatible with unity at all centralities by ATLAS in PbPb collisions at $\sqrt{s_{\mathrm{NN}}} = 5.02\,\mathrm{TeV}$ [3], as shown in Fig. 1. Top quarks are another probe to gluon nPDFs, recently observed by CMS in the $\ell$+jets channel for the first time in HIC [4]. The mass of the hadronically decaying W bosons is used for signal extraction, fitted in categories of the number of b-tagged jets (0, 1, or $\leq 2$) and lepton flavour (electron or muon). The measurement is shown in Fig. 1 and is consistent with expectations from pQCD calculations including nPDF effects.

Though nPDFs play an important role in the understanding of quarkonia in HIC, more phenomena come into play, already in pPb collisions where the ratio of the $\Upsilon$(2S) and $\Upsilon$(3S) to the $\Upsilon$(1S) is found to be smaller in pPb than in pp collisions at the same energy, as well as the ratio of $\psi$(2S) to J/$\psi$ [5]. Such a different modification of the excited quarkonium states compared to the ground states could point to the importance of final-state interactions after the quarkonium state has been produced. Further, in PbPb collisions, colour screening further suppresses the production of the more weakly bound states (as seen in the $\Upsilon$ meson system [6] in Fig. 1), regeneration may be relevant especially for low-$p_{\mathrm{T}}$ charmonia, and a hint for energy loss effects, similar to other hadrons, has been found in the slight increase of the prompt J/$\psi$ $R_{\mathrm{AA}}$ at high $p_{\mathrm{T}}$ [7].

The production of open heavy flavour has been studied by ATLAS and CMS via the measurements of both charm ($\mathrm{D}^0$ and $\mathrm{D}^*$) and beauty ($\mathrm{B}^{\pm}$ and nonprompt J/$\psi$). In PbPb collisions, a similar suppression is found for the different measured hadrons at high $p_{\mathrm{T}}$: $\mathrm{D}^0$, $\mathrm{B}^{\pm}$ and nonprompt J/$\psi$ feature a similar $R_{\mathrm{AA}}$ compared to that of charged hadrons [8], as can be seen in Fig. 2. Such universality of the high-$p_{\mathrm{T}}$ $R_{\mathrm{AA}}$ would be expected from a flavour independence of

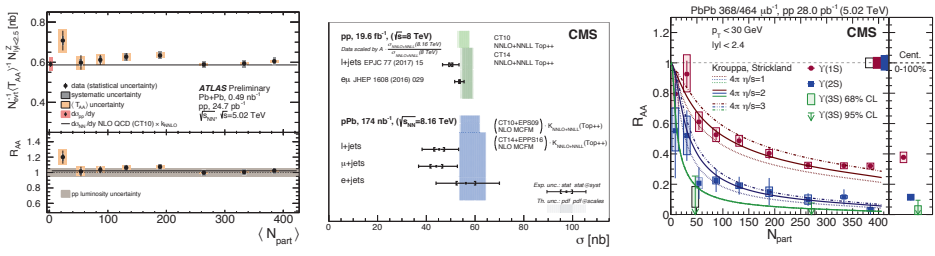


Figure 1 – Left: scale production yield and nuclear modification factor of Z bosons as a function of centrality, using pp and PbPb data at $\sqrt{s_{NN}} = 5.02\,\text{TeV}$ [3]. Center: measured $t\bar{t}$ cross section in pPb collisions, compared to the expectation from pQCD calculations and measurements in pp collisions [4]. Right: nuclear modification factor of $\Upsilon$(1S,2S,3S) as a function of centrality [6].

the path-length dependence of energy loss. In addition CMS has measured the $v_2$ and $v_3$ flow coefficients of $D^0$ mesons in PbPb collisions [9] (Fig. 2), and found them to be significantly non zero at low $p_T$, with $v_2$ staying positive up to 40 GeV and compatible with the $v_2$ of charged particles: this apparent universality at high $p_T$ is consistent with the $R_{AA}$ picture. In pPb collisions, ATLAS has found the forward-backward ratio of both $D^0$ and $D^*$ mesons to be consistent with unity [10], in the explored kinematic range ($|y_{CM}| < 0.5$, $5 < p_T < 30\,\text{GeV}$). CMS has also measured a significant $v_2$ of $D^0$ mesons in pPb collisions [11]. Smaller $D^0$ $v_2$ values are found at a given $p_T$ compared to strange hadrons. However, in PbPb collisions, approximate scaling of $v_2$ with the number of constituent quarks is found for both strange and charm mesons. This could be interpreted as a weaker coupling between heavy quarks and the medium in pPb than PbPb collisions.

Detailed studies of jets allow for better understand the interactions of the partons with the medium. CMS has compared the correlation between reconstructed jets and hadrons in pp and PbPb collisions [12], showing that fewer high $p_T$ and more low $p_T$ hadrons are found at large angle from the jet, compared to pp data, which could indicate additional in-medium gluon radiation and / or a medium backreaction, i.e., a wake-like response of the QGP to the propagating parton. The dijet asymmetry [13], defined as the ratio of the transverse momenta of the two jets, $x_J = \frac{p_{T,2}}{p_{T,1}}$, and unfolded for detector resolution effects, is shown in Fig. 2. A larger asymmetry is found in PbPb (smaller $x_J$ values) compared to pp data, showing that one of the two jets loses more energy than the other in the medium, consistent with expectations from medium energy loss due to jet quenching.

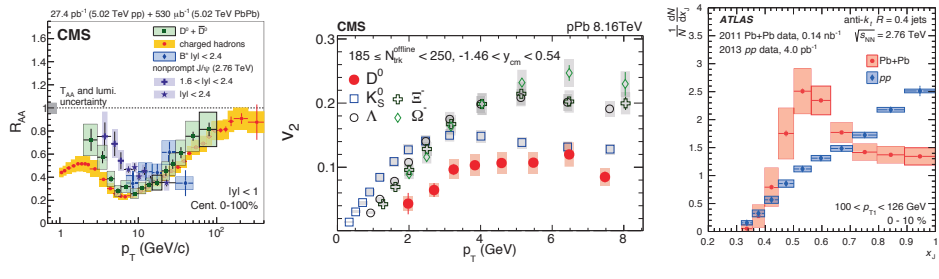


Figure 2 – Left: Nuclear modification factors of prompt $D^0$, charged hadrons, and nonprompt $J/\psi$, as a function of $p_T$ [8]. Center: Elliptic flow of prompt $D^0$ mesons in pPb collisions, compared to several strange hadrons[9]. Right: Dijet asymmetry $x_J$ in pp and PbPb collisions at 2.76 TeV [13].

Such jet modifications also depend on the flavour of the parton that initiated the jets. Using

photon-tagged jets [14], one favours quark jets over gluon jets, compared to inclusive jets. ATLAS reports a different modification of the jet fragmentation for photon-tagged and inclusive jets, in PbPb compared to pp collisions, but such an observation (illustrated in Fig. 3) may also arise from the different underlying jet $p_{\mathrm{T}}$ spectra. CMS has studied b jet pairs in pp and PbPb collisions, measuring their mean dijet asymmetry $\langle x_{\mathrm{J}} \rangle$ [15]. Such a selection enhances the contribution of primary b quarks, compared to an inclusive b jet selection which is contaminated by gluon splitting. The higher transverse momentum imbalance (smaller $\langle x_{\mathrm{J}} \rangle$ values) found in PbPb compared to pp events is compatible for light and b jets.

CMS is also probing the substructure of jets in pp and PbPb collisions, allowing for an even finer understanding of the medium modification of the parton shower evolution. The grooming techniques allow for the removal of soft wide-angle radiation from the jet, revealing the underlying hard structure via the identification of two subjets. The splitting function, measured as a function of the momentum imbalance between the two subjets, $z_g = p_{\mathrm{T},2}/(p_{\mathrm{T},1} + p_{\mathrm{T},2})$, is found to be steeper in central PbPb collisions than in pp [16]. These two leading subjets are also used to build the groomed jet mass [17] $M_g$. When the soft drop grooming parameters are chosen to be independent from the subjet $\Delta R$, a hint for an increased probability to produce jets at large $M_g/p_{\mathrm{T,\,jet}}$ is found in central PbPb events, compared to pp, as shown in Fig. 3. The dependence of these results with the grooming settings indicates that the region of phase space where modifications are most significant corresponds to splittings with large angular separation and low-to-moderate momentum sharing.

The very strong electromagnetic fields in PbPb collisions allow for the use of these beams as a photon-photon collider, in ultra-peripheral events (when the impact parameter of the collision is larger than twice the radius of the Pb nucleus). ATLAS has used this data sample to directly measure a novel process: light-by-light scattering [18] (see Fig. 3), with a significance over a background-only hypothesis of 4.4 standard deviations (3.8 expected). CMS has also used ultra-peripheral pPb collisions as a photon-proton collider, measuring $\Upsilon(1S)$ photoproduction [19] in photon-proton energies $W_{\gamma p}$ bridging the gap between previous HERA and LHCb measurements, and providing new constraints for the evolution of the gluon density at low values of fractional momenta $x$ in the proton.

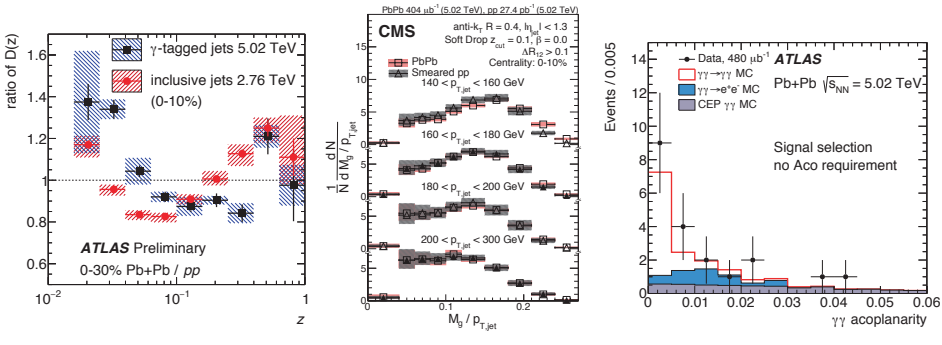


Figure 3 – Left: ratio of the fragmentation functions $D(z)$ ($z = p_{\mathrm{T,had}}/p_{\mathrm{T,jet}}$) in pp and central PbPb collisions at 5.02 TeV, for photon-tagged and inclusive jets [14]. Center: distribution of the ratio of the groomed jet mass $M_g$ to the jet $p_{\mathrm{T}}$, compared in pp and PbPb collisions at 5.02 TeV and in several jet $p_{\mathrm{T}}$ bins [17]. Right: diphoton acoplanarity $(1 - \Delta\phi(\gamma\gamma)/\pi)$ distribution in ultraperipheral PbPb collisions, consistent with the expectation from light-by-light scattering [18].

The collective behaviour of charged particle production in hadronic collisions can teach us about fluctuations in the initial stage of the collisions, as well as about properties of the medium created in the collision. Collectivity in small systems (pp and pPb collisions) is more difficult to understand and has been the focus of several recent studies. ATLAS has analysed a large sample

of pp collisions at $\sqrt{s} = 8$ TeV, selecting events associated to a Z boson, i.e. corresponding to a high-$Q^2$ hard-scattering process [20]. The elliptic flow coefficient $v_2$ is found to be $8 \pm 6\%$ larger than in inclusive pp events, with at most a weak dependence on the multiplicity. A major experimental difficulty in the study of collectivity in small systems is to avoid the contribution from non-flow, i.e. from dijet-like topologies. One way is to divide the event into subevents [21], to suppress such contributions, allowing one to obtain a negative 4-particle cumulant $c_2\{4\}$ and a well-defined $v_2\{4\} = (-c_2\{4\})^{1/4}$. CMS has measured symmetric cumulants, probing the event-by-event correlation between $v_n$ harmonics. It was found that, at high multiplicity, $v_2$ and $v_3$ are anti-correlated, while $v_2$ and $v_4$ are positively correlated, in a similar way in pp, pPb and, PbPb collisions [22]. The study of particle correlations also allows one to look for the chiral magnetic effect, predicted to arise in heavy ion collisions because of chiral symmetry restoration and the strong magnetic fields induced by the nuclei. Observations made by CMS so far in pPb and PbPb collisions [23,24] are consistent with the expectation from local charge conservation and allow one to set stringent limits on the maximum amount of signal present.

In short, we have reported recent results from the ATLAS and CMS Collaborations at the LHC allowing to get a better picture of QCD in a dense and hot medium. The studies help improve our understanding of the initial state and its fluctuations, the hydrodynamic evolution of the medium, parton interactions and their flavour dependence, etc. The increasing size of the datasets gives access to new processes, such as top quark production or light-by-light scattering.

## References


1. ATLAS Collaboration, JINST **3**, S08003 (2008).
2. CMS Collaboration, JINST **3**, S08004 (2008).
3. ATLAS Collaboration, ATLAS-CONF-2017-010, `https://cds.cern.ch/record/2244821` (2017).
4. CMS Collaboration, PRL **119**, 242001 (2017).
5. ATLAS Collaboration, EPJC **78**, 171 (2018).
6. CMS Collaboration, arXiv:1805:09215.
7. CMS Collaboration, arXiv:1712.08959.
8. CMS Collaboration, PRL **120**, 202301 (2018).
9. CMS Collaboration, arXiv:1708.03497.
10. ATLAS Collaboration, ATLAS-CONF-2017-073, `http://cds.cern.ch/record/2285811` (2017).
11. CMS Collaboration, arXiv:1804.09767.
12. CMS Collaboration, JHEP **1805**, 006 (2018).
13. ATLAS Collaboration, PLB **774**, 379 (2017).
14. ATLAS Collaboration, ATLAS-CONF-2017-074, `https://cds.cern.ch/record/2285812/` (2017).
15. CMS Collaboration, JHEP **1803**, 181 (2018).
16. CMS Collaboration, PRL **120**, 142302 (2018).
17. CMS Collaboration, arXiv:1805.05145.
18. ATLAS Collaboration, Nature Physics **13**, 852 (2017).
19. CMS Collaboration, CMS-PAS-FSQ-13-009, `https://cds.cern.ch/record/2147428` (2016).
20. ATLAS Collaboration, ATLAS-CONF-2017-068, `http://cds.cern.ch/record/2285806` (2017).
21. ATLAS Collaboration, PRC **97**, 024904 (2018).
22. CMS Collaboration, PRL **120**, 092301 (2018).
23. CMS Collaboration, arXiv:1708.08901.
24. CMS Collaboration, PRC **97**, 044912 (2018).

# Hard probes with $p$-Pb and Pb-Pb collisions and fixed target results at LHCb

F. Fleuret on behalf of the LHCb Collaboration
*Laboratoire Leprince-Ringuet (LLR),*
*École polytechnique, CNRS/IN2P3,*
*Palaiseau, France*

Since 2013, the LHCb collaboration extended its physics programme to the study of ion collisions. Thanks to the unique tracking and PID capabilities of the detector in the forward rapidity region, LHCb can provide important results on heavy flavour production in proton-Pb and Pb-Pb collisions at LHC. Moreover, LHCb has the unique capability to operate in a fixed target configuration and study proton and ion-beam induced reactions on gaseous targets. In the following, we report on the results and performances on open and hidden heavy-flavour hadron production in pPb and PbPb collisions, recorded in collider mode, and in pAr collisions, recorded in fixed target mode.

## Introduction

Heavy quarks and quarkonia are recognized to be privileged probes of Quantum ChromoDynamics (QCD). Because of their mass - significantly larger than the QCD scale - they are excellent tools to investigate the rich interface between the perturbative and non-perturbative domain of QCD. Moreover, in the high density/temperature regime of QCD, they are decisive probes of the deconfined state of matter, the Quark Gluon Plasma (QGP) which can experimentally be studied in nucleus-nucleus collisions. Besides, the study of heavy flavour production in proton-induced reactions on various nuclear targets, which are insensitive to effects due to deconfinement, is needed for a correct interpretation of the results obtained in nucleus-nucleus collisions. This is crucial to establish a robust baseline in order to clearly identify phenomena specifically related to QGP. Several effects can be studied in proton-nucleus collisions, such as parton shadowing or anti-shadowing (nPDF) in the target nucleus [1], saturation effects [2], interaction with comoving hadrons [3], and parton energy loss [4,5].

In the recent years, the LHCb collaboration extended its physics programme to the study of ion collisions. The LHCb detector [6] is a single-arm forward spectrometer covering the pseudorapidity range $2 < \eta < 5$, designed for the study of particles containing $b$ or $c$ quarks. The detector includes a high-precision tracking system consisting of a silicon-strip vertex detector surrounding the interaction region, a large-area silicon-strip detector located upstream of a dipole magnet with a bending power of about 4 Tm, and three stations of silicon-strip detectors and straw drift tubes placed downstream of the magnet. Different types of charged hadrons are distinguished using information of two ring-imaging Cherenkov detectors and muons are identified by a system composed of alternating layers of iron and multiwire proportional chambers. The online event selection is performed by a trigger which consists of a hardware stage, based on information from the calorimeter and muon systems, followed by a two stage software stage trigger, which full event reconstruction in the second step.

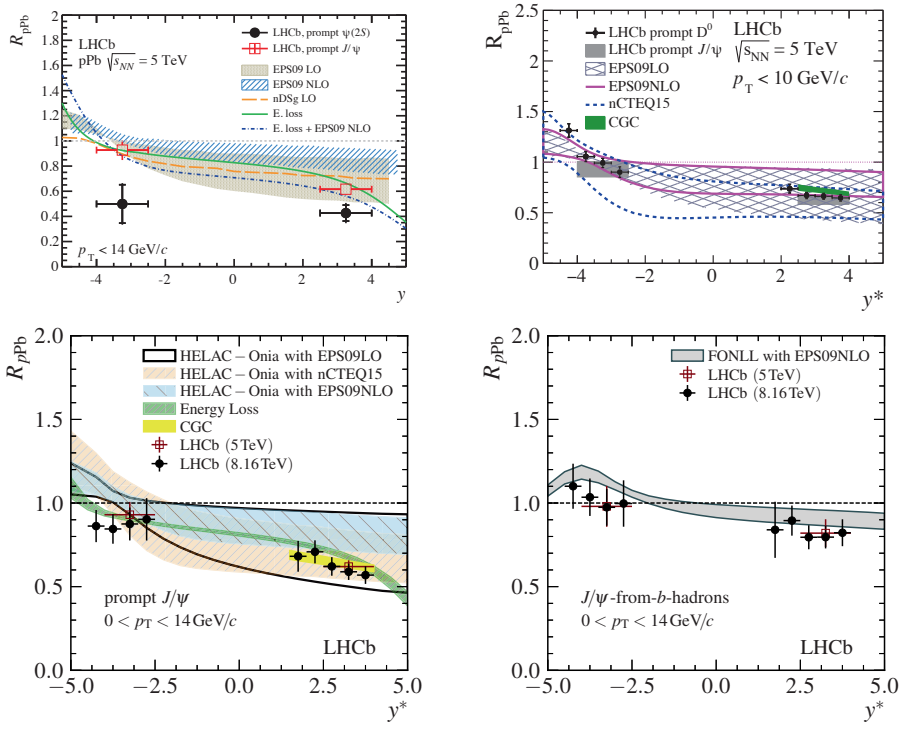


Figure 1 – Nuclear modification factors in $p$Pb collisions as a function of the rapidity in the centre-of-mass system. Top left: prompt J/ψ and prompt ψ(2$S$) $R_{pPb}$ in $\sqrt{s_{NN}}$ = 5 TeV data. Top right: prompt $D^0$ $R_{pPb}$ in $\sqrt{s_{NN}}$ =5 TeV data. Bottom left: prompt J/ψ $R_{pPb}$ in $\sqrt{s_{NN}}$ = 8.16 TeV data. Bottom right: $R_{pPb}$ of J/ψ from $b$-hadron decay at $\sqrt{s_{NN}}$ = 5 TeV and $\sqrt{s_{NN}}$ = 8.16 TeV.

## Heavy flavour production in $p$Pb and Pb$p$ collisions

In early 2013, the LHCb detector collected two data samples of $p$Pb and Pb$p$ [a] collisions at $\sqrt{s_{NN}}$ = 5 TeV, corresponding to an integrated luminosity of 1.6 nb$^{-1}$. In 2016, two other samples of $p$Pb and Pb$p$ collisions have been recorded at $\sqrt{s_{NN}}$ = 8.16 TeV corresponding to an integrated luminosity of about 30 nb$^{-1}$. Thanks to the inversion of the beams, LHCb covers the rapidity ranges -4 < $y^*$ < -2.5 in Pb$p$ collisions, 2.5 < $y^*$ < 4 in $p$Pb collisions. Fig. 1 (top, left) shows the nuclear modification factor $R_{pPb}$ of prompt J/ψ and prompt ψ(2$S$) as a function of the rapidity in the nucleon-nucleon centre-of-mass system [7,8]. Prompt J/ψ results are in fair agreement with nPDF, coherent energy loss [9] and CGC [10] predictions. On the other hand, the ψ(2$S$) results show, in the backward region, a much larger suppression than expected by nPDF and coherent energy loss predictions. This additionnal suppression may be due to the interaction of the lightly-bound ψ(2$S$) state with the outcoming hadrons or partons produced in the collision [3]. Prompt $D^0$ mesons, measured in their hadronic decay channel, show a similar behavior as

[a] Either the proton beam or the lead beam is pointing along the beamline from the interaction point towards the LHCb detector, referred respectively as forward or backward configuration.

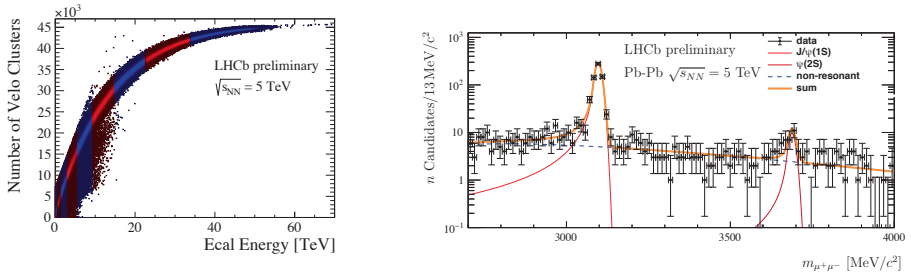


Figure 2 – PbPb collisions at $\sqrt{s_{NN}}$ = 5.02 TeV. Left: correlation between the number of hits in the VELO detector and the energy measured in the electromagnetic calorimeter. Each band corresponds to a 10% centrality interval. Right: Dimuon invariant mass distribution for Ultra-Peripheral Collisions (UPC).

J/ψ and are in good agreement with nPDF and CGC predictions, as shown on Fig. 1 (top, right).

Thanks to the much larger samples obtained with the 2016 data, more precise results on prompt J/ψ production have been obtained [11]. Those results confirm the pattern observed at lower energy and are in good agreement with nPDF, coherent energy loss and CGC expectations, as shown on Fig. 1 (bottom, right). Thanks to the very good precision achieved, these results put strong constraints on the nPDF parametrizations. Finally, it is interesting to note that non-prompt J/ψ coming form the decay of $b$-hadrons show smaller nuclear matter effects, in good agreement with expectations (Fig. 1, bottom right plot).

### Heavy flavour production in Pb-Pb collisions

LHCb participated for the first time in PbPb data taking in December 2015 collecting about 50 millions events at $\sqrt{s_{NN}}$ =5.02 TeV. In its current design, the detector performances are limited to peripheral collisions. As shown in Fig. 2, for central events (large energy deposited in the electromagnetic calorimeter tracking detectors show very high occupancy preventing event reconstruction. However, the detector is very well suited for ultra-peripheral collisions where one ion interacts with the electromagnetic field of the other and where therefore a small number of tracks reach the detector.

### Heavy Flavour production at low energy

Lattice QCD predictions imply that, at sufficiently high temperature, the production of charmonium bound states, in a hot and dense medium, decreases due to the modification of their binding. Heavy quarks are then assumed to move freely inside the medium until they hadronize as open heavy mesons. To each $c\bar{c}$ bound state there corresponds a dissociation temperature (larger than the QGP critical temperature) related to its radius. Hence, it is expected that the produced ground states such as J/ψ, due to the feed-down from $\chi_c$ and $\psi(2S)$ decays exhibit a step-by-step suppression with increasing density of the medium, also called sequential suppression. Experimentally, the sequential suppression of charmonium bound states must be tested and studied in nucleus-nucleus collisions at "low" energy (typically at a centre-of-mass energy per nucleon-nucleon collisions of $\sqrt{s_{NN}}$ ∼100 GeV). In contrast, at "high" energy (typically $\sqrt{s_{NN}}$ ∼1 TeV), because of the large number of $c\bar{c}$ pairs produced, secondary charmonium production via statistical recombination is expected to occur and offset the thermal suppression of primary production.
Fig. 3 shows the preliminary results obtained with proton beam induced reactions on a gaseous

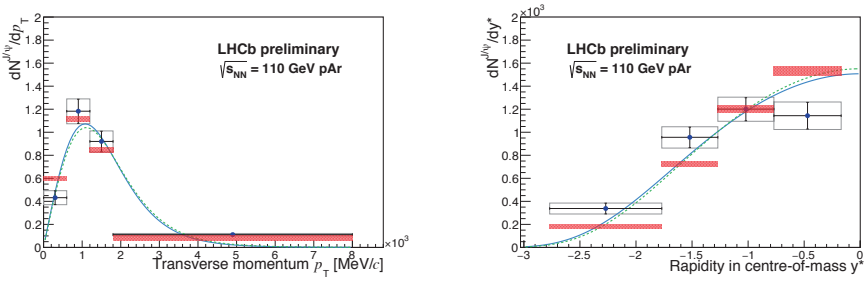


Figure 3 – J/ψ yields measured in $p$Ar collisions at $\sqrt{s_{NN}}$ =110 GeV. Left: J/ψ yield as a function of its transverse momentum. Right: J/ψ yield as a function of its rapidity in the centre-of-mass frame of the reaction.

Ar target at $\sqrt{s_{NN}} = 110$ GeV [12]. The J/ψ transverse momentum and rapidity (in the centre-of-mass system) distributions show reasonable agreement with phenomenological predictions and PYTHIA distributions (see Ref. [12] for more details). These results demonstrate the feasibility of the LHCb fixed target program. In 2016, a $p$He data sample at $\sqrt{s_{NN}} = 86.8$ GeV has been recorded, and a $\sqrt{s_{NN}} = 69$ GeV $p$Ne sample in 2017. A first PbNe run at $\sqrt{s_{NN}} = 69$ GeV is foreseen in 2018. Besides heavy flavour studies, the measurement of anti-proton production in $p$He collisions at $\sqrt{s_{NN}}$ =110 GeV, of key interest for cosmic rays physics, has also been performed [13].

## Conclusion

The LHCb experiment has recently provided very important results in heavy-ion collisions, providing in particular new constraints on nuclear matter effects in Heavy Flavour production. Moreover, the LHCb experiment has the unique capability to perform a thorough heavy-ion program in a fixed target mode to disentangle charmonium suppression in heavy-ion collisions. In PbPb collisions, the detector performances are currently limited to peripheral collisions, but its performances should be improved after the upgrade of the tracking system which will occur during the next LHC Long Shutdown (LS2). Further improvements are envisioned for a longer term future.

## References


1. de Florian, D. and Sassot, R., Phys. Rev. D **69** (2004)
2. J. L. Albacete and C. Marquet, Progress in Particle and Nuclear Physics **76** (2014) 1-42
3. E. G. Ferreiro, Phys. Lett. B **749** (2015) 98
4. Arleo, F. and Peigné, S., Phys. Rev. Lett. **109** (2012) 122301
5. Arleo, F. and Peigné, S. and Sami, T., Phys. Rev. D **83** (2011) 114036
6. LHCb collaboration, A. A. Alves Jr. *et al.*, JINST **3** (2008) S08005
7. LHCb collaboration, R. Aaij *et al.*, JHEP **02** (2014) 072
8. LHCb collaboration, R. Aaij *et al.*, JHEP **03** (2016) 133
9. Arleo, F. and Peigné, S., JHEP **03** (2013) 122
10. B. Ducloué, T. Lappi and H. Mantysaari, Phys. Rev. D **91**, 114005
11. LHCb collaboration, Phys. Lett. B 774 (2017) 159178
12. LHCb collaboration, LHCb-CONF-2017-001, https://cds.cern.ch/record/2255650
13. LHCb collaboration, LHCb-CONF-2017-002, https://cds.cern.ch/record/2260835

# Heavy Flavor Results from PHENIX

K. Nagashima for the PHENIX collaboration
*Hiroshima University, Kagamiyama, Higashi-Hiroshima 739-8526 ,Japan*

Heavy quarks are a sensitive probe of the quark-gluon plasma created in heavy-ion collisions because the modification of their phase-space distribution in the QGP reflects the medium dynamics. The PHENIX collaboration at the Relativistic Heavy Ion Collider has measured the cross-section and the nuclear modification factor of open and hidden heavy flavor in a variety of collision systems to understand the full-time evolution of heavy-ion collisions. We present the cross-section of open heavy flavor pairs as a function of the azimuthal opening angle in $p+p$ collisions, the system size dependence of charmonium nuclear modifications in $p$+Au, $p$+Al, and $^3$He+Au, $R_{\rm AA}$ of $B \rightarrow$J/$\psi$ in Cu+Au collisions and the $R_{\rm AA}$ of electrons from charm and bottom hadron decays in Au+Au collisions. All these analyses used data collected in collisions at $\sqrt{S_{NN}} = 200$ GeV. The interpretation of these results is discussed in the view of the production mechanism and the quarkonia breaking in medium, and the quark mass dependent energy loss in the QGP.

## 1 Introduction

Heavy quarks are produced at the initial stage of heavy-ion collisions and subsequently propagate through the quark-gluon plasma (QGP) because heavy quark masses are larger than the QGP temperature. Therefore, the modification of the heavy flavor phase-space distribution in the QGP strongly reflects the medium dynamics. Transport properties, such as the diffusion coefficient $D \propto \eta/(sT)$, and the quark-mass-dependent energy loss in the QGP can be studied by the measured nuclear modification factor $R_{\rm AA}$ [1,2].

The PHENIX collaboration at the Relativistic Heavy Ion Collider (RHIC) has measured the cross-section and the nuclear modification factor of open and hidden heavy flavor in a variety of collision systems to understand the full-time evolution of heavy-ion collisions. PHENIX silicon vertex detectors allow measuring the distance of closest approach (DCA) for an extraction of charm and bottom quark yields and a greater mass resolution for a separation of $\psi$(2S) from $\psi$(1S). We present the cross section of open heavy flavor pairs as a function of the azimuthal opening angle in $p$+$p$ collisions, the system size dependence of charmonium nuclear modifications in $p$+Au, $p$+Al, and $^3$He+Au, $R_{\rm AA}$ of $B \rightarrow$J/$\psi$ in Cu+Au collisions and the $R_{\rm AA}$ of electrons from charm and bottom hadron decays.

## 2 Results

### *2.1 Production Mechanism of Heavy Flavor*

The heavy flavor measurement in p+p collisions is important for an understanding of the production mechanism and a baseline measurement of heavy-ion collisions. The PHENIX has measured the invariant yield of $\mu\mu$ pairs from $c\bar{c}$ and $b\bar{b}$ as a function of $\Delta\phi$ and $p_{\rm T}$ with like- and unlike-sign $\mu\mu$ mass distributions in $p$+$p$ collisions[3] at $\sqrt{S_{NN}} = 200$ GeV as shown in Fig. 1. The high

mass like-sign $\mu\mu$ provides a strong constraint to the $b\bar{b}$ cross-section. The azimuthal opening angle distribution of $b\bar{b}$ pairs is well described by PYTHIA and POWHEG, which provides the understanding of the production mechanism of heavy flavor pairs.

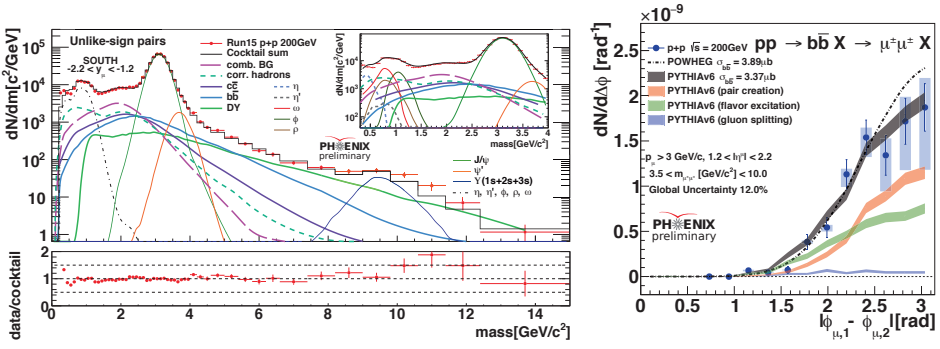


Figure 1 – Left: The inclusive $\mu\mu$ pair mass distribution from $p+p$ collisions at $\sqrt{s_{\rm NN}} = 200$ GeV. The cocktail calculation of expected sources describe well the measured $\mu\mu$ pair mass distribution. Right: The azimuthal opening angle distribution from $b\bar{b}$. PYTHIA and POWHEG models describe well the data.

### *2.2 Charmonium suppression in Small Collision Systems*

The measurement of charmonium suppression due to interactions with comoving hadrons [4] is necessary to correctly interpret the quarkonia suppression in heavy-ion collisions. We measured the dimuon mass distribution and the relative production ratio of $\psi(2S)$ and $\psi(1S)$ mesons at forward rapidity in $p+p$, $p$+Al, $p$+Au and $^3$He+Au collisions [5] as shown in Fig. 2. These double ratios are also measured in different energy and collision system at ALICE [6] and LHCb [7]. For the study of suppression due to comoving particles, the double ratio is measured as a function of the comoving particle density which is defined as the particle multiplicity $\mathrm{d}N/\mathrm{d}\eta$ divided by the nuclear overlap $< S_T >$. Fig. 2 (right) shows the dependence of the comoving particle density of $\psi(2S)$ suppression which favors the charmonium suppression due to interactions of the fully formed color-neutral meson with comovig particles. This breakup mechanism is likely important for the interpretation of sequential screening of quarkonia in A+A collisions.

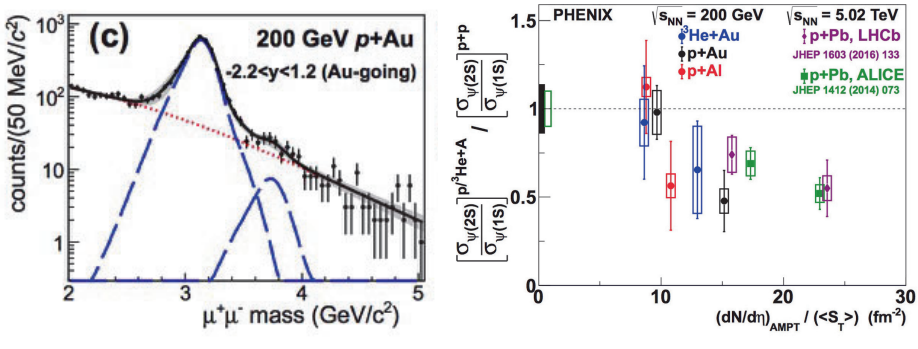


Figure 2 – Left: The measured dimuon mass spectrum for $p$+Au collisions at $\sqrt{s_{\rm NN}} = 200$ GeV. Right: The double ratio of $\psi(2S)$ and $\psi(1S)$ mesons measured in $p/^3$He+Au collisions to that same ratio in $p+p$ collisions as a function of the comoving particle density.

### 2.3 *Nuclear Modification of B→J/ψ and prompt J/ψ in Cu+Au Collisions*

The PHENIX has measured the fraction of B-meson decays in the inclusive J/$\psi$ yield in p+p and Cu+Au collisions at $\sqrt{s_{\rm NN}}$ = 200 GeV for integrated $p_{\rm T}$ and centrality [8]. The fraction of B-meson decays in Cu+Au collisions is systematically larger than in p+p collisions, which indicates a smaller suppression of B mesons than that prompt J/$\psi$ in Cu+Au collisions. The nuclear modification factor $R_{\rm CuAu}$ is calculated by the fractions in Cu+Au and p+p collisions and the measured $R_{\rm CuAu}$ of inclusive J/$\psi$ as shown in Fig. 3. The $R_{\rm CuAu}$ of B→$J/\psi$ indicates no significant nuclear modification of B-meson for $p_{\rm T} > 0$. On the other hands, prompt $J/\psi$ is strongly suppressed in Cu+Au collisions, which indicates that $c\bar{c}$ binding is broken in the medium. There is no significant difference between the positive (Au-going) and negative (Cu-going) rapidity within uncertainties. However, the systematically yield enhancement at negative rapidity (Cu-going) is shown in both $R_{\rm CuAu}$ of B→$J/\psi$ and prompt $J/\psi$, which favors the cold-nuclear-matter effects.

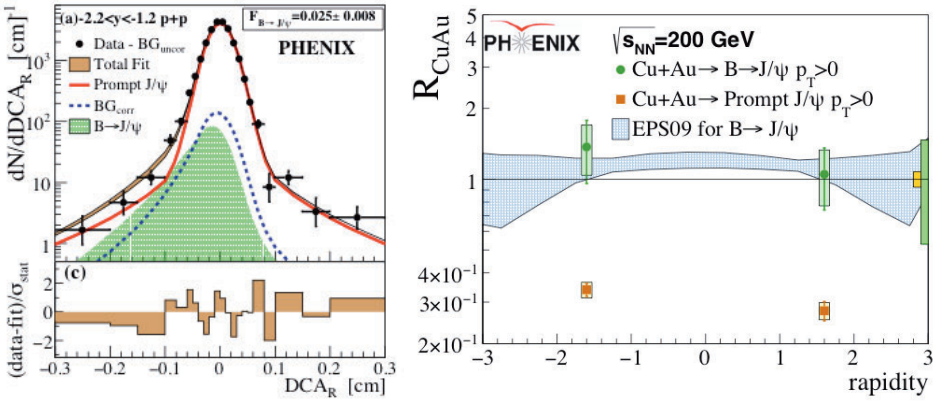


Figure 3 – Left: The $\rm DCA_R$ distribution and the fitting function for prompt J/$\psi$ and B→$J/\psi$. Right: Nuclear modification factors $R_{\rm CuAu}$ of prompt J/$\psi$ and B→J/$\psi$.

### 2.4 *Nuclear Modification of $c \to e$ and $b \to e$ in Au+Au Collisions*

The PHENIX has measured the invariant yield of separated charm and bottom hadron decay electrons and the bottom electron fraction in 0-10% central Au+Au collisions via applying the Bayesian inference techniques [9] simultaneously to the invariant yield of $c + b \to e$ and $\rm DCA_T$ distributions. Nuclear modification factors, $R_{\rm AA}$, of electrons from charm and bottom hadron decays are calculated with the inclusive $R_{\rm AA}$ and the bottom electron fraction in $p + p$ [10] and Au+Au collisions as shown in Fig. 4. We found that a quark mass dependence of $R_{\rm AA}$, $R_{\rm AA}$(c→e) < $R_{\rm AA}$(b→e), for $3.0 < p_{\rm T} < 8.0$ GeV/c , which indicates the quark mass ordering of the energy loss in the QGP. A T-Matrix model [11] parametrized as the diffusion constant $D(2\pi T) = 4$ is in good agreement with the measured bottom electron fraction in 0-10% central Au+Au collisions [12], which favors that heavy quarks are strongly coupled in the QGP.

## 3 Summary

The PHENIX has measured open and hidden heavy flavor in a variety of collision systems to study the production mechanism, the cold-nuclear-matter effects, and the QGP dynamics. The cross-section of $c\bar{c}$ and $b\bar{b}$ as a function of $\Delta\phi$ and $p_{\rm T}$ in $p + p$ collisions is measured a like- and unlike-sign $\mu\mu$ pairs. PYTHIA model well describes the azimuthal opening angle distribution

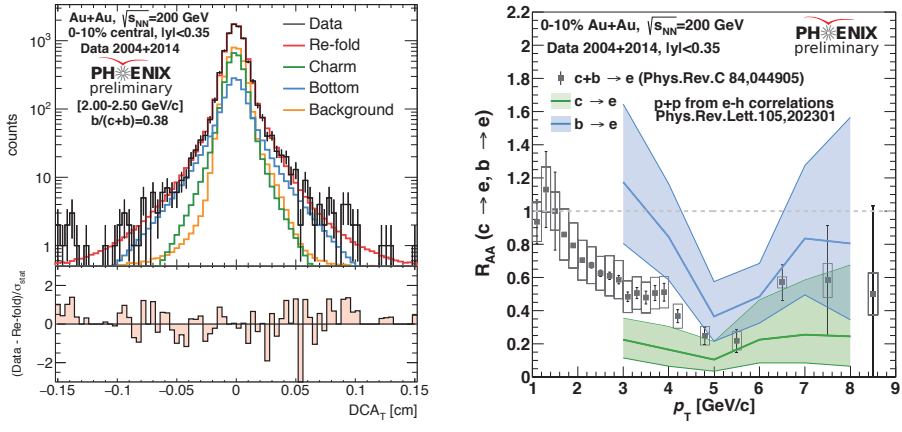


Figure 4 – Left: The $DCA_T$ distribution of electrons from charm and bottom hadron decays. Right: The nuclear modification factor of electrons from charm (green line) and bottom (blue line) hadron decays in 0-10% central Au+Au collisions.

of both $c\bar{c}$ and $b\bar{b}$ which provides the understanding of the production mechanism of heavy flavor pairs. The double ratio of $\psi(2S)/\psi(1S)$ mesons measured in $p/^3$He+A collisions to that same ratio in p+p collisions is measured as a function of comoving particle density to study the breakup mechanism of charmonium in small system collisions, which favors the interactions of the fully formed color-neutral meson with comovig particles. This breakup mechanism is likely important for the interpretation of sequential screening of quarkonia in A+A collisions. $J/\psi$ production is measured separately for prompt $J/\psi$ and B$\rightarrow$J/$\psi$ in $p+p$ and Cu+Au collisions at forward rapidity. We found no significant modification of B$\rightarrow$J/$\psi$ and a strong suppression of prompt J/$\psi$ for $p_T > 0$. Invariant yields of electrons from charm and bottom hadron decays are measured in Au+Au collisions via applying the Bayesian inference technique simultaneously to the inclusive invariant yield and $DCA_T$ distributions. We found that the quark mass dependence of $R_{AA}$, $R_{AA}$(c$\rightarrow$e) $< R_{AA}$(b$\rightarrow$e). It indicates the quark mass ordering of the energy loss in the QGP. The model comparison favors that the heavy quark diffusion constant is $D(2\pi T) = 4$ which indicates that heavy quarks are strongly coupled in the QGP.

## References


1. A. Adare *et al.* (PHENIX collaboration), *Phys. Rev. Lett.* **96**, 032301 (2006).
2. A. Adare *et al.* (PHENIX collaboration), *Phys. Rev.* C **84**, 044905 (2011).
3. C. Aidala *et al.* (PHENIX collaboration), arXiv:1805.02448.
4. E. G. Ferreiro, *Phys. Lett.* B **749**, 98 (2015)
5. A. Adare *et al.* (PHENIX collaboration), *Phys. Rev.* C **95**, 034904 (2017).
6. B. Abelev *et al.* (ALICE collaboration), *Phys. Rev. Lett.* **110**, 032301 (2013).
7. R. Aaij *et al.* (LHCb collaboration), Journal of High Energy Physics **03**, 133 (2016).
8. C. Aidala *et al.* (PHENIX collaboration), *Phys. Rev.* C **96**, 064901 (2017).
9. A. Adare *et al.* (PHENIX collaboration), *Phys. Rev.* C **93**, 034904 (2016).
10. M. Aggarwal *et al.* (STAR collaboration), *Phys. Rev. Lett.* **105**, 202301 (2010).
11. H. van Hees, M. Mannarelli, V. Greco, and R. Rapp , *Phys. Rev. Lett.* **100**, 192301 (2008)
12. K.Nagashima (PHENIX collaboration), *Nucl. Phys.* A **967**, 644 (2017).

# Systematic measurements of low $p_T$ direct photons at PHENIX

Y. Yamaguchi for the PHENIX collaboration
*RIKEN, Hirosawa 2-1, Wako, Saitama, Japan*

The low $p_T$ direct photons are of keen interest since thermal photons from a hot and dense medium are supposed to be dominant. PHENIX has conducted new measurements of the low $p_T$ direct photons in $\sqrt{s_{NN}} = 200$ GeV Cu+Cu and 39, 62.4 GeV Au+Au collisions to study the system size and collision energy dependence on direct photon production. While the integrated yields of the direct photons, $dN/dy$, have separate scalings with different collision energies for $p_T > 5$ GeV/$c$, a unique scaling of $dN/dy$ for $p_T > 1$ GeV/$c$ with respect to the charged particle multiplicity is observed across a wide range of the collision energies from 39 GeV to 2.76 TeV. A possible explanation of this unique scaling for $p_T > 1$ GeV/$c$ is that most of photons are produced near the phase transition from QGP to hadron gas around a critical temperature.

## 1 Introduction

Direct photons are one of the most important probes to understand the time evolution of a hot and dense QCD medium [1]. The definition of direct photons is photons not originating from hadron decays. They are produced at every stage of the collision until freeze-out of the medium. Particularly thermal photons from the medium are of keen interest because they pass through the medium without strong interaction, then carry the thermodynamic information of the medium at the point of their production. The contribution of the thermal photons from the medium is expected to be dominant at the low $p_T$ region, typically $1 < p_T < 4$ GeV/$c$ [2]. However a large amount of photons from hadron decays, particularly $\pi^0$, make the direct photon measurements challenging due to a small significance level of the direct photon signal over the background photons.

## 2 Direct photon puzzle

The PHENIX experiment has reported the first observation of the excess yield of the direct photons over the scaled $p + p$ data, which is considered as the hard photon contribution from initial parton scatterings, for $p_T < 4$ GeV/$c$ [3] in Au+Au collisions at $\sqrt{s_{NN}} = 200$ GeV. Then, the low $p_T$ direct photon result in $d$+Au has shown no significant modification of the direct photon $p_T$ distribution [4], encouraging the observed excess yield of the direct photons by medium effects.

An azimuthal anisotropy of the direct photons, which results from an elliptic flow with a conversion of an initial spacial anisotropy to a final momentum anisotropy, is another key observable sensitive to a production time for direct photons. At first, the azimuthal anisotropy of the direct photons was expected to be small due to a large contribution from the hotter medium at an early stage where an elliptic flow is not fully developed. However, the measured azimuthal

anisotropy of the direct photons in Au+Au collisions at $\sqrt{s_{NN}} = 200$ GeV is surprisingly large, comparable to those for hadrons [5,6].

Figure 1 shows the comparison results with several model calculations for both $p_T$ spectrum and azimuthal anisotropies ($v_{2,3}$) for 20-40% most central Au+Au collisions at $\sqrt{s_{NN}} =$ 200 GeV [5]. Any model calculations can not make a consistent description for both large excess yield and large azimuthal anisotropy of the direct photons in $p_T < 4$ GeV/$c$. Thus, it is challenging to understand the mechanism simultaneously producing a large yield and a large azimuthal anisotropy as observed.

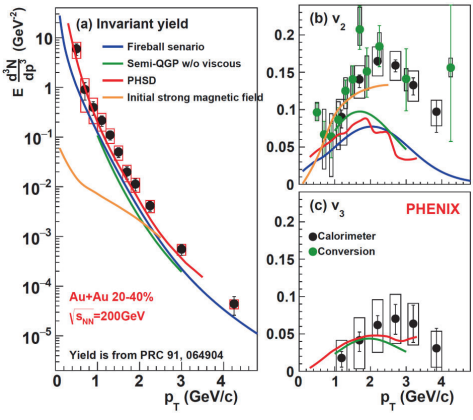


Figure 1 – The comparison results with several model calculations for both $p_T$ spectrum and azimuthal anisotropies ($v_{2,3}$) for 20-40% most central Au+Au collisions at $\sqrt{s_{NN}} = 200$ GeV.

## 3 New PHENIX results on direct photons

PHENIX has newly conducted the low $p_T$ direct photon measurements in $\sqrt{s_{NN}} = 200$ GeV Cu+Cu and 62.4, 39 GeV Au+Au collisions. They allow us to further study the system size and energy dependences on low $p_T$ direct photon production. Figures 4 and 2 show the new PHENIX results of the low $p_T$ direct photon measurements for $\sqrt{s_{NN}} = 200$ GeV Cu+Cu [7] and 62.4, 39 GeV Au+Au collisions, respectively.

Clear excess yields over the binary-scaled $p + p$ result are seen in MB and 0-40% most central Cu+Cu collisions as we have seen in Au+Au collisions at the same energy. While neither $p+p$ data nor reliable theoretical calculations on primordial photon production are available for Au+Au results with lower energies, the $p_T$ spectra look exponential as same as other heavy ion data.

An inverse slope, $T_{eff}$, of the exponential fit is related to an averaged temperature of the medium. Figure 3 shows the collision energy dependence of $T_{eff}$ of the exponential fit to the heavy ion data including the ALICE data [8]. It is seen that $T_{eff}$ monotonically increases as a function of $\sqrt{s_{NN}}$. However, the direct photons have a blue-shift effect, making $T_{eff}$ larger by a radial flow than as it is. In general, a radial flow velocity gets larger at a higher collision energy and its development with time evolution of the medium is non-trivial. Considering the blue-shift effect on the direct photon $p_T$ spectrum, an increasing trend of $T_{eff}$ should become more modest.

An integrated yield of the direct photons, $dN/dy$, can give a further insight on the mechanism of the direct photon production. Figure 5 shows integrated yields of the direct photons for different collision energy data in different $p_T$ integrated ranges, $p_T > 1$ GeV/$c$ (left) and $p_T >$ 5 GeV/$c$ (right), as a function of the charged particle multiplicity, $dN_{ch}/d\eta$, at mid-rapidity [9].

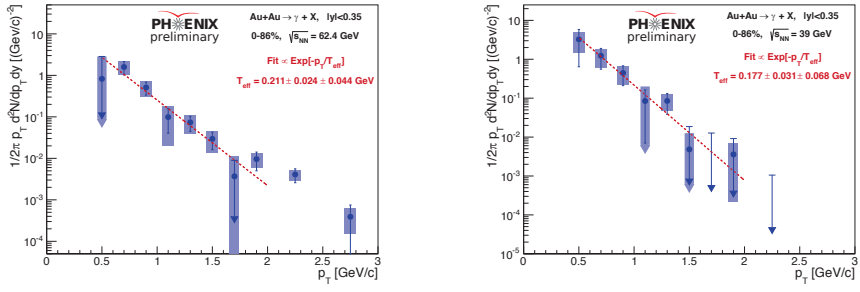


Figure 2 – The low $p_T$ direct photon results for $\sqrt{s_{NN}} = 62.4$ GeV (left) and 39 GeV (right) Au+Au collisions.

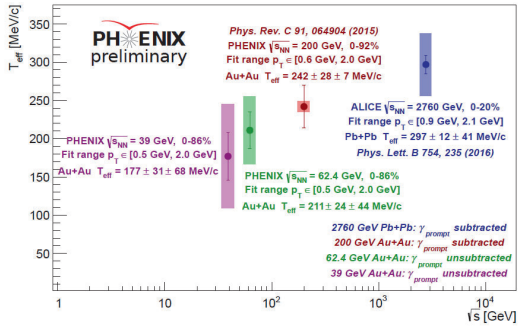


Figure 3 – The collision energy dependence of an inverse slope, $T_{eff}$, of the exponential fit to the $\sqrt{s_{NN}} = 39 - 200$ GeV Au+Au data at RHIC as well as $\sqrt{s_{NN}} = 2.76$ TeV Pb+Pb data at LHC.

Surprisingly, a unique scaling of $dN/dy$ with $(dN_{ch}/d\eta)^{1.25}$ is observed independent of the collision energies for $p_T > 1$ GeV/$c$, where the excess yield over the scaled $p+p$ data is seen. The expected $dN_{ch}/d\eta$ dependence from the scaled $p+p$ data is shown together as a band, locating below the heavy ion data. A possible interpretation of this unique scaling is that the main contributor in the low $p_T$ region is similar across a wide range of the collision energies from 39 GeV to 2.76 TeV. It is natural if most of the low $p_T$ direct photons are produced near the phase transition from QGP to hadron gas around a critical temperature. In addition, the observed large azimuthal anisotropy can reasonably be explained with this interpretation. On the other hand, different energy data are separately scaled for $p_T > 5$ GeV/$c$. The same scaling for $p+p$ and heavy ion data with the same collision energy supports that the hard photons from initial parton scatterings are dominant in $p_T > 5$ GeV/$c$.

## 4 Summary

The measurements of the low $p_T$ direct photons have been newly performed for 200 GeV Cu+Cu and 39, 62.4 GeV Au+Au collisions at PHENIX to study the system size and collision energy dependences on direct photon production. A unique scaling of $dN/dy$ with respect to $dN_{ch}/d\eta$ is observed across a wide range of the collision energies for $p_T > 1$ GeV/$c$, where the excess yield over the scaled $p+p$ data is expected due to thermal radiations from the medium. If most of the photons making the excess yield over the scaled $p+p$ data are produced near the phase transition from QGP to hadron gas around a critical temperature, this unique scaling of $dN/dy$ with respect to $dN_{ch}/d\eta$ is possibly reasonable and the observed azimuthal anisotropy of the low $p_T$ direct photons can be explained as well.

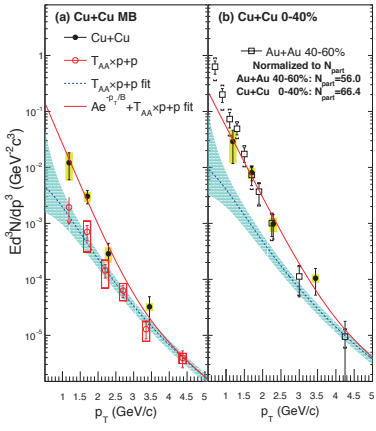


Figure 4 – The low $p_T$ direct photon results with $\sqrt{s_{NN}} = 200$ GeV Cu+Cu data for MB and 0-40% most central collisions.

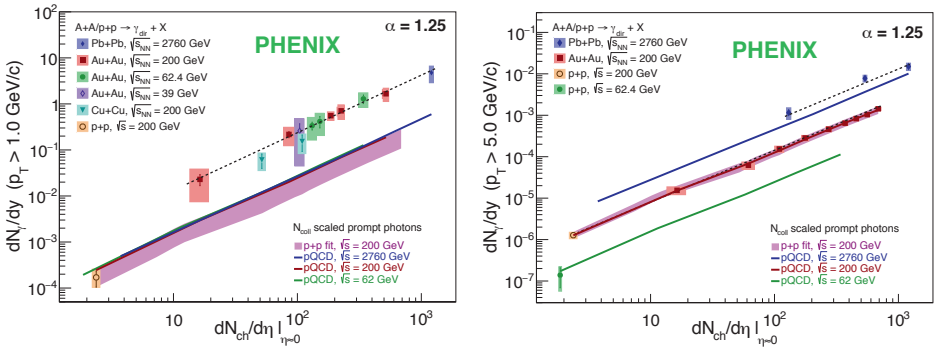


Figure 5 – Integrated yields of the direct photons for different collision energy data in different $p_T$ integrated ranges, $p_T > 1$ GeV/$c$ (left) and $p_T > 5$ GeV/$c$ (right), as a function of the charged particle multiplicity, $dN_{ch}/d\eta$, at mid-rapidity.

## References


1. K. Adcox *et al*, *Nucl. Phys.* A **757**, 184 (2005).
2. S. Turbide, R. Rapp, and C. Gale, *Phys. Rev.* C **69**, 014903 (2004).
3. A. Adare *et al*, *Phys. Rev. Lett.* **104**, 132301 (2010).
4. A. Adare *et al*, *Phys. Rev.* C **87**, 054907 (2013).
5. A. Adare *et al*, *Phys. Rev.* C **91**, 064904 (2015).
6. A. Adare *et al*, *Phys. Rev. Lett.* **109**, 122302 (2012).
7. A. Adare *et al*, arXiv:1805.04066 [hep-ex].
8. J. Adam *et al*, *Phys. Lett.* B **754**, 235 (2016).
9. A. Adare *et al*, arXiv:1805.04084 [hep-ex].

# CRITICAL ACOUSTICS AND SINGULAR BULK VISCOSITY OF QUARK MATTER

Boris O. Kerbikov
*Alikhanov Institute for Theoretical and Experimental Physics, B. Cheremushkinskya 25, 117218 Moscow, Russia* [a]

We examine the behavior of sound attenuation and bulk viscosity near the 2'nd order QCD phase transition at finite density. A dynamical model is presented describing the coupled evolution of sound mode and a slow mode of fluctuations.

## 1 Introduction

The main result of heavy ion experiments performed over almost two last decades at RHIC and at RHIC and LHC is a discovery of a new form of matter with properties markedly different from the pre-RHIC era predictions. Theoretical efforts accompanying the experimental discoveries added a lot to our understanding of the quark matter properties. There is, however, an unfortunate aspect in the theoretical studies. Only zero, or very small $\mu_B$ domain of the QCD phase diagram in the $(\mu_B, T)$ plane is accessible to lattice Monte-Carlo simulations since for $\mu \neq 0$ the fermion determinant is no longer real.

The analysis of the quark matter properties can be carried out testing its response to external exitations. Transport coefficients characterize how small perturbations from equilibrium are transmitted through the medium. Shortly after the collision and until hadronization the created matter is in the form of an almost ideal liquid. Sound is the only long-lived propagating mode in a near-ideal fluid. Viscosity leads to the dissipation of the sound wave energy. Shear viscosity $\eta$ dominates the sound attenuation in the regime of weak interaction when the system is approximately scale invariant (Stokes absorption). If the medium is compressible and close to deconfiment/confinement transition the bulk viscisity $\zeta$ is responsible for the sound absorption. Close to the critical temperature $T_c$ the sound attenuation is anomalously strong [1,2,3,4,5]. The bulk viscosity $\zeta$ sharply rises towards singularity near $T_c$ [6,7,8,9,10]. The speed of sound which is by the fluctuation-dissipation theorem related to the sound absorption attains its minimum near $T_c$. This is the softest point of EoS. In ultra-relativistic and ultra-nonrelativistic limits when the trace of the energy-momentum tensor depends only on the energy and particle densities $\zeta = 0$ [11].

As shown by Mandelshtam and Leontovich (ML) long ago [12] and later confirmed by Tisza [13] the anomalous behavior of the sound absorption coefficient $\gamma$ near $T_c$ is caused by the contribution from the slow mode with a large relaxation time $\tau = \Gamma^{-1}$. The divergent bulk viscosity has the same origin. The essence of ML theory is the following [1,2,12,14]. Propagation of the sound wave changes the temperature in compression-rarefaction regions. The slow mode (chemical reactions in the original ML work [12]) can not keep up with this process. During the slow equilibration energy dissipation takes place resulting in anomalous sound absorption and enhanced bulk viscosity. In [14] the sound attenuation near the 2'nd order transition point has been investigated along the lines of the ML theory.

[a] e-mail: bkerbikov@gmail.com

In this case the slow mode corresponds to the relaxation of the order parameter which exhibits fluctuations near $T_c$. Let us present a compendium of the results of the ML theory for the low frequency $\omega\tau \lesssim 1$ region [1,2,9,14]

$$\gamma(\omega) = \frac{\omega^2\tau}{2c_0^3}\frac{(c_\infty^2 - c_0^2)}{1+\omega^2\tau^2}, \tag{1}$$

$$\zeta(\omega) = \frac{\zeta(0)}{1+\omega^2\tau^2} = \frac{\varepsilon\tau(c_\infty^2 - c_0^2)}{1+\omega^2\tau^2}, \tag{2}$$

$$c^2(\omega) = c_0^2 + \frac{\omega^2\tau^2}{1+\omega^2\tau^2}(c_\infty^2 - c_0^2) - i\frac{\omega\tau}{1+\omega^2\tau^2}(c_\infty^2 - c_0^2). \tag{3}$$

Here $c_0^2 = \left(\frac{\partial p}{\partial \varepsilon}\right)_s$ is the ordinary hydrodynamic speed of sound, $c_\infty^2 = \left(\frac{\partial p}{\partial \varepsilon}\right)_\varphi$ – the speed of sound at a given value of the order parameter $\varphi$, $c_\infty > c_0$. Expression for $\zeta(0)$ in (2) is the known Landau-Khalatnikov formula [14]. In order to equilize the short and long waves distortions caused by the attenuation one introduces the dimensionless attenuation per wavelength $\alpha_\lambda = \lambda\gamma$. According to (1)-(2)

$$\alpha_\lambda = \omega\frac{\pi\zeta(0)}{\varepsilon c_0^2}, \tag{4}$$

This relation is used to determine the bulk viscosity of conventional materials from the sound absorption. From (1) it follows that $\omega\tau \ll 1$ means $\alpha_\lambda \ll \pi$, i.e., weak absorption. The clear-cut picture of the high frequency $\omega\tau \gg 1$ transport coefficients is far from being complete. According to [5] with $\omega\tau$ increasing $\alpha_\lambda(\omega)$ slowly approaches the constant value defined by the critical indices.

The most difficult problem within the slow relaxation ML theory is the behavior of $\zeta$ and $\alpha_\lambda$ in the immediate vicinity of the 2'nd order transition temperature, i.e., at $|t| \lesssim Gi$, where $t = (T - T_c)/T_c$, and $Gi$ is the Ginzburg-Levanyuk number. The subtle point is the distinction between hydrodynamic and non-hydrodynamic sectors [2,9,15]. Following [7,8,10] we consider $\omega \to 0$, $T \to T_c$. In various approaches, like $d = 4 - \varepsilon$ renormalization, modes coupling theory, or isomorphism between the fluid and 3d Ising system the bulk viscosity $\zeta(\omega \to 0, T \to T_c)$ shows a power divergence

$$\zeta \sim \xi^{z-\alpha/\nu} \sim t^{-z\nu+\alpha}, \tag{5}$$

Here $\xi$ is the correlation length, $z \simeq 3$ is the dynamical critical exponent, $\nu \simeq 0.6$ is the correlation length critical exponent, $\xi(t) \simeq t^{-\nu}$, $\alpha \simeq 0.11$ is the critical exponent of the heat capacity. According to (4) $\alpha_\lambda$ diverges near $T_c$ as $\alpha_\lambda \sim t^{-1.69}$. The above anomalies of $\zeta$ and $\alpha_\lambda$ arise as a result of coupling between the hydrodynamical modes and the slow order parameter mode. Below we present a dynamical model [16] which explicitly contains the slow mode and gives the critical behavior of $\zeta(T)$ very close to (5). Consider a region of the QCD phase diagram corresponding to the onset of the 2SC superconductivity. For the orientation purposes one can take $T_c \simeq 40$ MeV, $\mu(\text{quark}) \simeq 400$ MeV. In color superconductor the exceedingly narrow BCS fluctuation region is replaced by a wide and physically important one $\delta T/T \simeq 10^{-4}$ instead of $(10^{-12} - 10^{-14})$ in BCS. When the temperature approaches $T_c$ from above precursor quark pairing takes place. Fluctuations of the pair field are described by a collective mode propagator, or the fluctuation propagator (FP) $L(\mathbf{q}, \omega)$ [4].

In [16,17] the FP was derived for the relativistic quark system using either Dyson equation, or the time-dependent Landau-Ginzburg equation with stochastic Langevin forces. The FP reads

$$L(\mathbf{q},\omega) = -\frac{1}{\nu}\cdot\frac{1}{t+\frac{\pi}{8T_c}(-i\omega+Dq^2)}, \tag{6}$$

where $\nu = p_0\mu/2\pi^2$, $p_0$ is the Fermi momentum, $D$ is the diffusion coefficient. At small $\omega$ and $q$ the FP $L(\mathbf{q},\omega)$ can be arbitrary large in the $t\to 0$ limit. Within the Kubo formalism $\zeta$ and $\alpha_\lambda$ are expressed in terms of the pressure-pressure correlation function. In the diagrammatic expansion of the correlation function close to $T_c$ diagrams containing $L(\mathbf{q},\omega)$ bring the dominant contribution. Based on the experience gained in condensed matter physics [4] we assume that the Aslamazov-Larkin (AL) diagram shown in Fig.1 plays the leading role. In the short presentation we leave out the detailed evaluation of this diagram which may be found in [16,17].

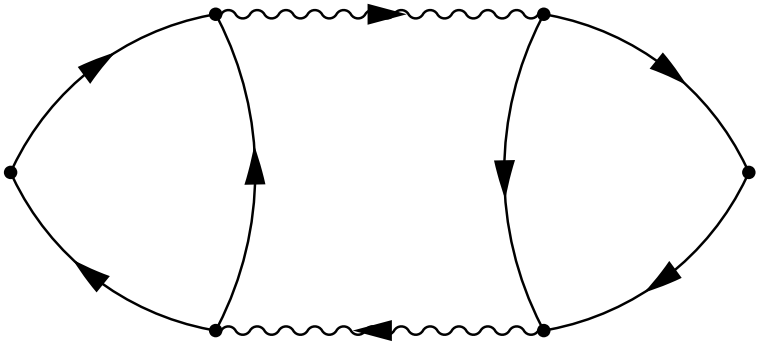

Figure 1 – Feynman diagram for the AL polarization operator. The way lines correspond to $L(\mathbf{q},\omega)$.

The important point is that the imaginary part of the polarization operator corresponding to the AL diagram is proportional to $t^{-3/2}$. Then the Dyson equation yields

$$\alpha_\lambda \simeq R\cdot\omega\cdot t^{-3/2}\cdot\ln^2\frac{\Lambda}{2\pi T_c}, \tag{7}$$

where $R$ has a dimension $\mathrm{m}^{-1}$ and depends on the critical temperature, Fermi momentum and the quark mean free path [16,17], $\Lambda$ is the UV cut-off equal to the Debye frequency in BCS. The bulk viscosity is

$$\zeta \simeq R\cdot\frac{\varepsilon c^2}{\pi}\cdot t^{-3/2}\cdot\ln^2\frac{\Lambda}{2\pi T_c}. \tag{8}$$

The temperature dependence $t^{-3/2}$ is rather close to the scaling law (5). Finally, we note that the electrical conductivity given by the AL diagram has the $t^{-1/2}$ dependence [17]. We also note that a broad range of acoustic problems in QGP has been examined in [18].

The author was supported by a grant from the Russian Science Foundation project number 16-12-10414. The author expresses his gratitude to M.S. Lukashov who participated in the early stage of this work.

**References**


1. L. D. Landau and E. M. Lifshitz,"Fluid Mechanics" 2nd ed. (Pergamon Press, Oxford, 1987).
2. A. Z. Patashinskii, V. L. Pokrovskii, "Fluctuation Theory of Phase Transitions" (Pergamon Press, Oxford, 1979).
3. K. Kawasaki, Phys. Rev. **150**, 291 (1966).
4. L. G. Aslamazov and A. I. Larkin, Sov. Phys. Solid State **10**, 875 (1968);
   L. G. Aslamazov and A. A. Varlamov, Sov. Phys. JETP **50**, 1164 (1979).
5. A. Onuki, Phys. Rev. **E 55**, 403 (1997);
   J. Phys. Soc. Jpn. **66**, 511 (1997).
6. D. Kharzeev, K. Tuchin, JHEP **0809**, 093 (2008);
   F. Karsch, D. Kharzeev, K. Tuchin, Phys. Lett. **B 663**, 217 (2008).
7. Guy D. Moore and Omid Saremi, JHEP **0809**, 015 (2008).
8. N. Antoniou, F. K. Diakonos, A. S.Kapoyannis, Nucl. Phys. **A 967**, 816 (2017).
9. M. Stephanov anv Y. Yin, arXiv:1712.10305.
10. Y. Akamatsu, M. Mazeliauskas, D. Teaney, Phys. Rev. **C 97**, 024902 (2018).
11. S. Weinberg, "Gravitation and Cosmology" (John Wiley and Sons, New York, 1972).
12. L. L. Mandelshtam and M. A. Leontovich, Zh. Eksp. Teor. Fiz. **7**, 438 (1937).
13. L. Tisza, Phys. Rev. **61**, 531 (1942).
14. L. D. Landau and I. M. Khalatnikov, Dokl. Akad. Nauk USSR **96**, 469 (1954).
15. A. Kurkela and Urs. A. Wiedemann, arXiv:1712.0437.
16. B. O. Kerbikov, EPJ Web of Conferences **125**, 04013 (2016);
    B. O. Kerbikov and M. S. Lukashov, Vod. Phys. Lett. **A 31**, 1650179 (2016).
17. B. O. Kerbikov and M. A. Andreichkov, Phys. Rev. **D 91**, 074010 (2015).
18. E. Shuryak, Nucl. Phys. **A 904-905**, 349c (2013);
    E. Shuryak and P. Staig, Phys. Rev. **C 88**, 064905 (2013);
    **C88**, 054903 (2013).

# 10.
# Electroweak Physics

# Precise predictions for the angular coefficients in $Z$-boson production

R. Gauld, A. Gehrmann–De Ridder
*Institute for Theoretical Physics, ETH, CH-8093 Zürich, Switzerland*

T. Gehrmann
*Department of Physics, University of Zürich, CH-8057 Zürich, Switzerland*

E. W. N. Glover
*Institute for Particle Physics Phenomenology, Durham University, Durham DH1 3LE, UK*

A. Huss
*CERN, Theory Division, CH-1211 Geneva 23, Switzerland*

The angular distributions of lepton pairs in the Drell–Yan process can provide a wealth of information on the underlying QCD production mechanisms. It is possible to parameterise these dynamics in terms of a set of frame dependent angular coefficients, $A_{i=0,\ldots,7}$, which depend on the invariant mass, transverse momentum, and rapidity of the final-state lepton pair. Motivated by recent measurements of these coefficients by both ATLAS and CMS, we perform a precision study of the angular coefficients at $\mathcal{O}(\alpha_s^3)$ in perturbative QCD. We make predictions relevant for pp collisions at $\sqrt{s} = 8$ TeV, and perform comparisons with the available ATLAS and CMS data. The compatibility of this data is assessed by performing a partial $\chi^2$ test with respect to the central theoretical prediction which shows that $\chi^2/N_{\rm data}$ is significantly reduced by going from $O(\alpha_s^2)$ to $O(\alpha_s^3)$.

## 1 Introduction

The production of Z bosons followed by subsequent leptonic decay is a benchmark process at hadron colliders. The production rate for this process is extremely large, and, combined with the fact that the final state is experimentally clean, it has allowed precise differential Z-boson cross section measurements to be performed at the LHC. Typically, these measurements are performed inclusively with respect to the kinematic information of the gauge boson decay and have many phenomenological applications, including PDF and luminosity determinations.

However, additional tests of the QCD dynamics for Z-boson production may also be performed by explicitly studying the angular distribution of the final-state leptons [1,2,3,4,5,6,7]. Under the assumption that the lepton pair is produced through the exchange of a gauge boson, the reconstructed leptons provide a direct probe of the polarisation of the intermediate gauge boson, which in turn exposes the underlying QCD production mechanism. The QCD dynamics of this process can be expressed in terms of a set of eight frame dependent angular coefficients $A_{i=0,\ldots,7}$, which depend on the invariant mass, transverse momentum, and rapidity of the lepton pair and describe the production of the intermediate gauge boson. Distributions for the angular coefficients can be extracted experimentally through fits to the measured final-state lepton kinematics, which in turn can be compared to the corresponding predictions obtained in pQCD.

The CMS [8] and ATLAS [9] collaborations have recently performed a measurement of these angular coefficients in pp collisions at $\sqrt{s} = 8$ TeV. These analyses have been performed in the

Collins–Soper reference frame [1], with an invariant-mass selection around the Z-boson resonance. Most notably, both ATLAS and CMS observe clear evidence of non-vanishing distributions for the difference of the angular coefficients $A_0$ and $A_2$. These results are interesting as they demonstrate a violation of the Lam–Tung relation [2,3,4], $A_0 - A_2 = 0$.

The purpose of this work is to reassess the compatibility of the LHC data to theory by providing predictions for the phenomenologically most important angular coefficients in high-mass lepton pair production at $O(\alpha_s^3)$.

## 2 Theoretical and numerical setup

Consider the inclusive production of lepton pairs through the decay of an intermediate gauge boson, $\mathrm{p}(\mathrm{p}_1) + \mathrm{p}(\mathrm{p}_2) \to \mathrm{V}(\mathrm{q}) + \mathrm{X} \to \ell(\mathrm{k}_1) + \bar{\ell}(\mathrm{k}_2) + \mathrm{X}$. In the lepton-pair rest frame, we define the final-state lepton momenta in terms of the angles $\theta$ and $\phi$ according to

$$k^\mu_{1,2} = \frac{Q}{2}\,(1, \pm\sin\theta\cos\phi, \pm\sin\theta\sin\phi, \pm\cos\theta)^T, \qquad Q = \sqrt{q^2}\,. \tag{1}$$

The differential cross-section for lepton-pair production may be written as an expansion in spherical harmonics of the lepton kinematics of up to degree two according to

$$\begin{aligned}\frac{\mathrm{d}\sigma}{\mathrm{d}^4q\;\mathrm{d}\cos\theta\;\mathrm{d}\phi} = \frac{3}{16\pi}\,\frac{\mathrm{d}\sigma^{\text{unpol.}}}{\mathrm{d}^4q}\,\Big\{&(1+\cos^2\theta) + \frac{1}{2}\,A_0\,(1-3\cos^2\theta)\\ &+ A_1\;\sin(2\theta)\cos\phi + \frac{1}{2}\,A_2\;\sin^2\theta\;\cos(2\phi)\\ &+ A_3\;\sin\theta\;\cos\phi + A_4\;\cos\theta + A_5\;\sin^2\theta\;\sin(2\phi)\\ &+ A_6\;\sin(2\theta)\;\sin\phi + A_7\;\sin\theta\;\sin\phi\Big\},\end{aligned} \tag{2}$$

where $\mathrm{d}\sigma^{\text{unpol.}}$ is the unpolarised cross section. We note that the first term inside the parenthesis equal to $(1+\cos^2\theta)$ is not accompanied by a separate angular coefficient, as its normalisation is described by $\mathrm{d}\sigma^{\text{unpol.}}$ that has been extracted as a pre-factor in Eq. (2).

To provide theoretical predictions for these angular coefficients, one can make use completeness of the spherical harmonics and extract the angular coefficients appearing in Eq. (2) with the use of the projectors

$$\begin{aligned}&A_0 = 4 - 10\,\left\langle\cos^2\theta\right\rangle, && A_1 = 5\,\left\langle\sin(2\theta)\,\cos\phi\right\rangle, && A_2 = 10\,\left\langle\sin^2\theta\,\cos(2\phi)\right\rangle,\\ &A_3 = 4\,\left\langle\sin\theta\,\cos\phi\right\rangle, && A_4 = 4\,\left\langle\cos\theta\right\rangle, && A_5 = 5\,\left\langle\sin^2\theta\,\sin(2\phi)\right\rangle,\\ &A_6 = 5\,\left\langle\sin(2\theta)\,\sin\phi\right\rangle, && A_7 = 4\,\left\langle\sin\theta\,\sin\phi\right\rangle,\end{aligned} \tag{3}$$

where $\langle\ldots\rangle$ denotes taking the (normalised) weighted average over the angular variables $\theta$, $\phi$ and is defined as

$$\left\langle f(\theta,\phi)\right\rangle \equiv \frac{\int_{-1}^{1}\mathrm{d}\cos\theta\int_0^{2\pi}\mathrm{d}\phi\;\mathrm{d}\sigma(\theta,\phi)\;f(\theta,\phi)}{\int_{-1}^{1}\mathrm{d}\cos\theta\int_0^{2\pi}\mathrm{d}\phi\;\mathrm{d}\sigma(\theta,\phi)}. \tag{4}$$

In this way, one can use a general implementation of the differential cross-section for the process $\mathrm{p}(\mathrm{p}_1)+\mathrm{p}(\mathrm{p}_2) \to \mathrm{V}(\mathrm{q})+\mathrm{X} \to \ell(\mathrm{k}_1)+\bar{\ell}(\mathrm{k}_2)+\mathrm{X}$ to reconstruct the differential cross-section according to the expansion given in Eq. (2). Our predictions are obtained with the calculation of Ref. [10], to provide NNLO-accurate QCD predictions for the $p_{T,\mathrm{Z}}$ distributions of the angular coefficients. This process is implemented in the flexible parton-level Monte Carlo generator NNLOJET. The shown predictions have been obtained with the central member of the `PDF4LHC15_nnlo_30` PDF set, and an uncertainty due to independent variation of factorisation and renormalisation scales is included. In fact, when performing the projection according to Eq. (4) we chose to

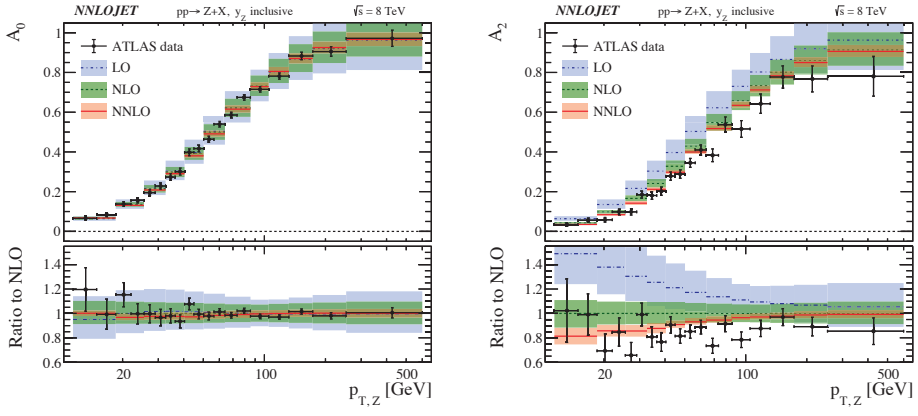


Figure 1 – The $p_{T,Z}$ distribution for the angular coefficients $A_0$ (left) and $A_2$ (right), in pp collisions at $\sqrt{s} = 8$ TeV. The ATLAS data (black points) are compared to the LO (blue fill), NLO (green fill), and NNLO (red fill) theoretical predictions. In the lower panel, each distribution is shown normalised with respect to the central NLO prediction.

partially un-correlate the scales choices in the numerator and denominator of the expression. We provide predictions in the $G_\mu$-scheme, where we additionally include the dominant corrections to the $\rho$-parameter to define effective values for both the sine of the weak mixing angle and electromagnetic coupling. For more detail we direct the reader to [11].

## 3 Phenomenological results

In this Section we provide predictions for the phenomenologically most relevant angular coefficients $A_{0,1,2}$, as well as the difference $(A_0 - A_2)$. We do not discuss the angular coefficients $A_3$ and $A_4$ in what follows. The experimental precision of the extracted values of these coefficients is relatively poor, and the corresponding QCD corrections for these distributions are also small [11].

A comparison of the ATLAS data and corresponding theoretical predictions is provided for the angular coefficients $A_0$ (left) and $A_2$ (right) as a function of $p_{T,Z}$ in Fig. 1. The corresponding distributions for $A_1$ (left) as well as the difference $(A_0 - A_2)$ (right) are provided in Fig 2. Each distribution is obtained with the kinematic selection of $80 < m_{\ell\ell} < 100$ GeV on the lepton-pair final state. The ATLAS data is indicated by black points and compared to the LO (blue fill), NLO (green fill), and NNLO (red fill) theoretical predictions. In the lower panel of each plot, the distributions are provided normalised with respect to the central NLO prediction.

It is found that the NNLO corrections are important for improving the precision of each theoretical predictions, and that the shapes of the $A_1$ and $A_2$ distributions are altered at NNLO. The importance of these corrections is most apparent for the $A_2$ distribution, where large negative corrections are observed, resulting in an improved description of the data.

In Fig. 2 (right), the data for the difference of the angular coefficients $A_0$ and $A_2$ is shown, which provides clear evidence for violation of the Lam–Tung relation, $A_0 - A_2 = 0$. In the framework of perturbative QCD (pQCD), this relation can be shown to hold up to $O(\alpha_s)$ and is violated only at $O(\alpha_s^2)$ and higher[a]. Consequently, the NLO predictions for this observable are the first non-trivial predictions (the LO predictions being zero), and the first correction to this distribution being provided by the NNLO calculation. A visual comparison between the data and the corresponding predictions for this observable indicate that the NNLO predictions

[a] Note that for the Z-boson $p_{T,Z}$ distribution, the $O(\alpha_s^2)$ calculation is labelled as NLO.

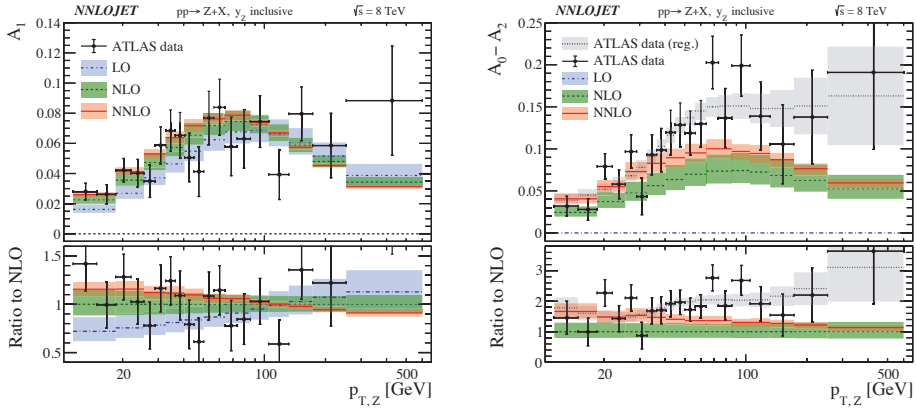


Figure 2 – As in Fig. 1, now for the angular coefficients $A_1$ (left), and the difference $(A_0 - A_2)$ (right). For the distribution of $(A_0 - A_2)$, the regularised ATLAS data is also shown.

provide an improved description of the data as compared to NLO. To better quantify this comparison, we perform a $\chi^2$ test for this data with respect to the central theory prediction. We consider the unregularised ATLAS data for the angular coefficients $A_0$ and $A_2$ (and their correlations, as provided through the covariance matrix) within the range of $p_{T,\mathrm{Z}} \in [11.4, 600]$ GeV, corresponding to a total of 38 data points. The results are: $\chi^2_{\mathrm{NLO}}/\mathrm{N_{data}} = 185.8/38 = 4.89$ at NLO; and $\chi^2_{\mathrm{NNLO}}/\mathrm{N_{data}} = 68.3/38 = 1.80$ at NNLO. Similar conclusions are drawn when the CMS data is similarly analysed [11].

## 4 Conclusions

We have provided NNLO predictions for the $p_{T,\mathrm{Z}}$ distributions of the angular coefficients in pp collisions at $\sqrt{s} = 8$ TeV. It is found that the NNLO corrections reduce the overall theoretical uncertainty of the predictions, and result in an improved description of the data. Of particular note are the large (and negative) corrections to the $A_2$ distribution, which are seemingly necessary to adequately describe the observed distributions for $A_2$ as well as the difference $(A_0 - A_2)$.

Current approaches to performing an extraction of the W-boson mass in hadron-hadron collisions rely upon an accurate modelling of the angular coefficients in vector-boson production [12]. The Monte Carlo samples used in such an analysis are in part obtained from a reweighting based upon the fixed-order calculation of the angular coefficients in vector-boson production at $O(\alpha_s^2)$ accuracy. The $O(\alpha_s^3)$ corrections to the decay lepton distributions in vector-boson production computed in this work provide an important step towards improving the theoretical description of reference quantities necessary for the precise measurement of $M_{\mathrm{W}}$. Upon request, predictions for the angular coefficients in W-boson production at $O(\alpha_s^3)$ will be obtainable with the calculation of Ref. [13].


## Acknowledgments

We acknowledge the computing resources provided to us by the Swiss National Supercomputing Centre (CSCS) under the project ID p501b. This research was supported in part by the UK Science and Technology Facilities Council, by the Swiss National Science Foundation (SNF) under contracts 200020-162487 and CRSII2-160814, by the Research Executive Agency (REA) of the European Union under the Grant Agreement PITN-GA-2012-316704 ("HiggsTools") and the ERC Advanced Grant MC@NNLO (340983).

## References


1. J. C. Collins and D. E. Soper, Phys. Rev. D **16** (1977) 2219. doi:10.1103/PhysRevD.16.2219
2. C. S. Lam and W. K. Tung, Phys. Rev. D **18** (1978) 2447. doi:10.1103/PhysRevD.18.2447
3. C. S. Lam and W. K. Tung, Phys. Lett. **80B** (1979) 228. doi:10.1016/0370-2693(79)90204-1
4. C. S. Lam and W. K. Tung, Phys. Rev. D **21** (1980) 2712. doi:10.1103/PhysRevD.21.2712
5. E. Mirkes, Nucl. Phys. B **387** (1992) 3. doi:10.1016/0550-3213(92)90046-E
6. E. Mirkes and J. Ohnemus, Phys. Rev. D **50** (1994) 5692 doi:10.1103/PhysRevD.50.5692 [hep-ph/9406381].
7. E. Mirkes and J. Ohnemus, Phys. Rev. D **51** (1995) 4891 doi:10.1103/PhysRevD.51.4891 [hep-ph/9412289].
8. V. Khachatryan *et al.* [CMS Collaboration], Phys. Lett. B **750** (2015) 154 doi:10.1016/j.physletb.2015.08.061 [arXiv:1504.03512 [hep-ex]].
9. G. Aad *et al.* [ATLAS Collaboration], JHEP **1608** (2016) 159 doi:10.1007/JHEP08(2016)159 [arXiv:1606.00689 [hep-ex]].
10. A. Gehrmann-De Ridder, T. Gehrmann, E. W. N. Glover, A. Huss and T. A. Morgan, Phys. Rev. Lett. **117** (2016) no.2, 022001 doi:10.1103/PhysRevLett.117.022001 [arXiv:1507.02850 [hep-ph]].
11. R. Gauld, A. Gehrmann-De Ridder, T. Gehrmann, E. W. N. Glover and A. Huss, JHEP **1711** (2017) 003 doi:10.1007/JHEP11(2017)003 [arXiv:1708.00008 [hep-ph]].
12. M. Aaboud *et al.* [ATLAS Collaboration], Eur. Phys. J. C **78** (2018) no.2, 110 doi:10.1140/epjc/s10052-017-5475-4 [arXiv:1701.07240 [hep-ex]].
13. A. Gehrmann-De Ridder, T. Gehrmann, E. W. N. Glover, A. Huss and D. M. Walker, Phys. Rev. Lett. **120** (2018) no.12, 122001 doi:10.1103/PhysRevLett.120.122001 [arXiv:1712.07543 [hep-ph]].


LA THUILE
33
39
37
34
10
6
22
3
4
21
12
15
17

# Electroweak scale physics & exotic searches at LHCb

O. Lupton on behalf of the LHCb collaboration
*European Organization for Nuclear Research (CERN), Meyrin, Switzerland*

The LHCb experiment has a broad and varied physics programme, extending far beyond its core set of flavour physics measurements. This contribution summarises recent electroweak scale measurements and searches for exotic states in the dimuon final state.

## 1 Introduction

The LHCb detector is a single-arm forward spectrometer covering the pseudorapidity range 2–5 that is principally designed for the study of $b$- and $c$-hadrons, but which is well-suited to a wide variety of electroweak scale measurements and exotic searches that are highly complementary to other experiments at the LHC and elsewhere. Several features of the detector that are crucial for the core flavour physics programme, such as excellent vertex and momentum resolution, and a powerful trigger system, contribute to excellent jet tagging performance and sensitivity to low mass exotic states. LHCb operates at a substantially lower instantaneous luminosity than the general purpose detectors at the LHC, ATLAS and CMS, which results in a clean, low pile-up environment in which to search for physics beyond the Standard Model (SM).

## 2 Searches for exotic dimuon resonances

The excellent mass resolution and muon identification performance of the detector over a wide range of momenta make searches for exotic dimuon resonances an attractive prospect in LHCb data. Two results are presented in this section, one covering a wide mass range and another focused on the region in the immediate vicinity of the $\Upsilon$ resonances.

### *2.1 Dark photons*

Several theories of physics beyond the SM propose new particles that could explain the nature of dark matter. Such theories typically include additional particles and dark boson-mediated forces, with a massive dark photon $A'$ being a popular feature. These dark photons typically do not couple directly to charged SM particles, but they can gain a weak coupling to the SM electromagnetic current via kinetic mixing. The strength of this coupling is suppressed by a factor $\varepsilon$ with respect to the SM photon. There is, therefore, a 2D parameter space to be probed.

The LHCb measurement[1] presented here uses the dimuon final state and is based on a dataset corresponding to an integrated luminosity of $\mathcal{L} = 1.6\,\text{fb}^{-1}$ recorded at $\sqrt{s} = 13$ TeV during 2016. The flexible nature of the LHCb software trigger[2] allows the full rate of prompt, *i.e.* consistent with originating at the primary $pp$ interaction vertex, dimuon candidates to be recorded for analysis, from the dimuon mass threshold up to the $Z^0$. The prompt-like dimuon spectrum is shown in Fig. 1. Backgrounds due to semileptonic decays of heavy-flavour hadrons,

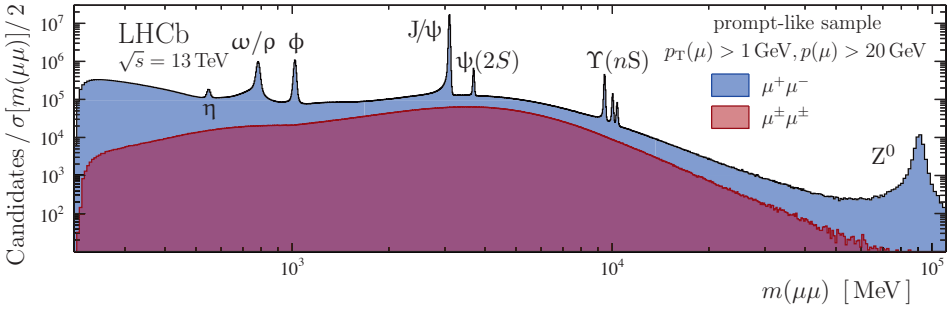


Figure 1 – Prompt-like dimuon spectrum used in the dark photon search with various resonance peaks labelled.[1]

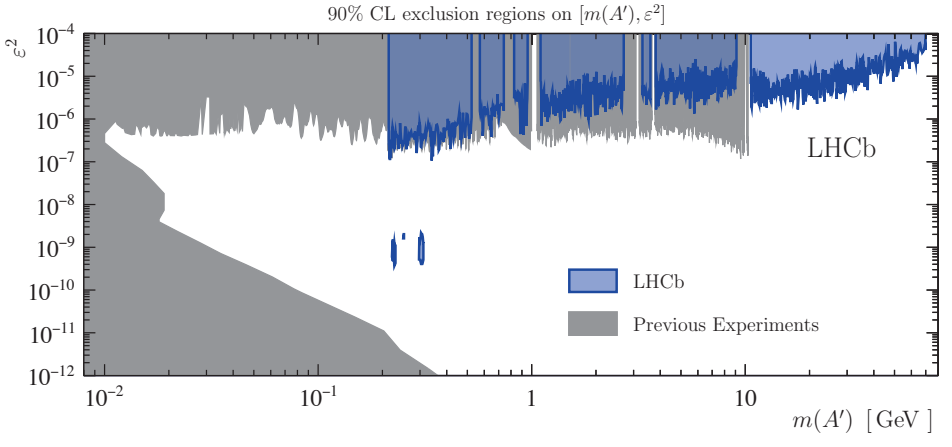


Figure 2 – Results of the dark photon search. Both prompt-like (top) and displaced (centre) exclusions are shown.[1]

and misidentified hadrons, are determined using fits to $\chi^2$-like variables relating to the dimuon vertex quality. Background due to off-shell photon decays $\gamma^* \to \mu^+\mu^-$ is irreducible and used to normalise the dark photon search in a data-driven manner. The various well-known quarkonia peaks labelled in Fig. 1 are excluded from the prompt-like search, which extends up to 70 GeV/$c^2$.

A search is performed for displaced dimuon vertices in the mass range $[214, 350]$ MeV/$c^2$, in this case the background composition is somewhat different. At radii of more than 5 mm and low mass the background is dominated by real photon conversions in the vertex locator material. Such conversions are vetoed using a new method based on a large dataset of secondary hadronic interaction vertices[3]. At smaller radii the background is dominated by heavy flavour decays.

No significant excess is found, and the limits set are shown in Fig. 2. The prompt-like search sets world-best limits in the mass region $[10.7, 70]$ GeV/$c^2$, while the displaced search probes a world-first region of parameter space. Future updates to these searches are expected to take advantage of the novel all-software trigger in the LHCb experiment upgrade for Run 3 of the LHC, and to extend to lower values of $m(A')$ by exploiting the dielectron channel.[4,5]

### *2.2 Search in vicinity of the ϒ resonances*

A dedicated search for dimuon resonances in the vicinity of the $\Upsilon(n\mathrm{S})$ resonances has also been performed, probing closer to, and in between, these peaks than the dark photon search.[6] The mass region that is probed in this analysis is illustrated in Fig. 3. No significant excess is seen,

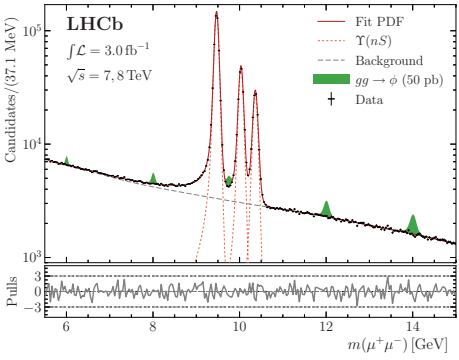


Figure 3 – Dimuon spectrum in the vicinity of the $\Upsilon(n\text{S})$ resonances[6]. Peaks corresponding to scalar resonances $\phi$ are also shown, where it has been assumed that $\sigma(pp \to \phi)\mathcal{B}(\phi \to \mu^+\mu^-) = 50\,\text{pb}$.[6]

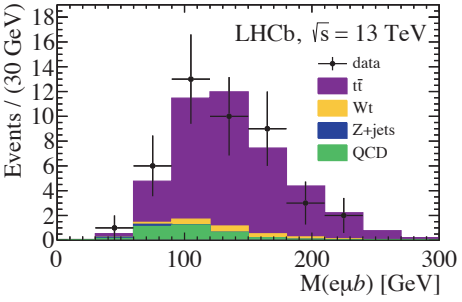


Figure 4 – $e\mu b$ invariant mass for all 44 selected candidates in the $t\bar{t}$ measurement[9]. No fit is performed to this distribution, it is presented simply to illustrate the signal purity.

but the first limits are set in the mass range $[8.7, 11.5]\,\text{GeV}/c^2$. Limits are set assuming that the produced resonance is either a scalar or a vector boson.

## 3 $t\bar{t}$ production

Top quark physics forms an important part of the electroweak scale physics programme at LHCb, and is an excellent example of an area of study where the forward acceptance of the LHCb detector has several advantages with respect to the central region instrumented by ATLAS and CMS. For example, top quark cross-sections can provide important constraints on the large-$x$ gluon PDF, with the forward kinematic region being particularly sensitive. The forward region also provides a greater fraction of events with quark-initiated production than central detectors, enhancing the size of $t\bar{t}$ asymmetries visible at LHCb.

Carrying out such measurements at LHCb presents several challenges relating to the small acceptance, low luminosity and lack of missing energy measurement. Despite these challenges, $t$ and $t\bar{t}$ production[7,8] have previously been observed at LHCb using data recorded at $\sqrt{s} = 7\,\text{TeV}$ and 8 TeV.

The step to $\sqrt{s} = 13\,\text{TeV}$ for Run 2 of the LHC has increased the LHCb-visible cross sections for top quark processes by an order of magnitude, bringing new channels into statistical reach. The new result presented here is a measurement of $t\bar{t}$ production at $\sqrt{s} = 13\,\text{TeV}$ using the $e\mu b$ final state[9] and an integrated luminosity of $\mathcal{L} = 2\,\text{fb}^{-1}$. This is a very pure final state, as the second lepton suppresses $W + b\bar{b}$ production and the opposite-flavour leptons suppress $Z^0 + b\bar{b}$. The signal purity is illustrated in Fig. 4, and the fiducial cross section is calculated as

$$\sigma_{t\bar{t}} = \frac{N - N_{\text{bkg}}}{\mathcal{L} \cdot \epsilon} \cdot \mathcal{F}_{\text{res}} = 126 \pm 19\,(\text{stat}) \pm 16\,(\text{syst}) \pm 5\,(\text{lumi})\,\text{fb}^{-1}. \quad (1)$$

Figure 5 compares this result, and an extrapolation to the full cross section, with SM predictions at next-to-leading order. The measured cross sections are compatible with these predictions.

## 4 $Z^0 \to b\bar{b}$

The final measurement discussed in these proceedings is the first observation of $Z^0 \to b\bar{b}$ production in the forward region[10]. This measurement is an important validation of the LHCb jet reconstruction and $b$-tagging performance. Two $b$-tagged jets are reconstructed, with a third balancing jet also reconstructed to help control the QCD background and define signal and

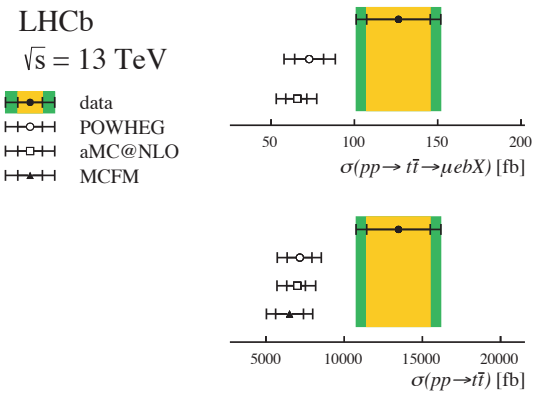


Figure 5 – Fiducial (top) and extrapolated (bottom) $t\bar{t}$ cross sections, compared to SM predictions at next-to-leading order[9].

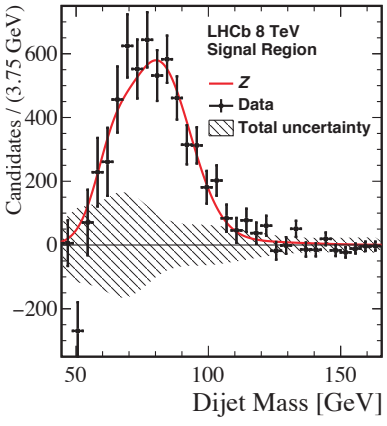


Figure 6 – Background subtracted dijet mass spectrum showing the $Z^0 \to b\bar{b}$ signal[10].

control regions using a multivariate technique. The background-subtracted signal distribution is shown in Fig. 6. The signal is observed with a statistical significance of $6\sigma$ and the measured cross section is found to be compatible with SM predictions at next-to-leading order.

## 5 Conclusions

LHCb has a broad and exciting programme of electroweak and exotic measurements, which are typically still statistically limited and will benefit significantly from further Run 2 updates and, crucially, from the LHCb upgrade ahead of Run 3 of the LHC.

## References


1. LHCb collaboration, *Search for dark photons produced in 13 TeV pp collisions*, Phys. Rev. Lett. **120** (2018) 061801, arXiv:1710.02867
2. R. Aaij, *Tesla: an application for real-time data analysis in High Energy Physics*, Comput. Phys. Commun. **208** (2016) 35, arXiv:1604.05596
3. M. Alexander *et al.*, *Mapping the material in the LHCb vertex locator using secondary hadronic interactions*, arXiv:1803.07466
4. P. Ilten, J. Thaler, M. Williams, and W. Xue, *Dark photons from charm mesons at LHCb* Phys. Rev. **D92** (2015) 115017, arXiv:1509.06765
5. P. Ilten *et al.*, *Proposed inclusive dark photon search at LHCb*, Phys. Rev. Lett. **116** (2016) 251803, arXiv:1603.08926
6. LHCb collaboration, *Search for a dimuon resonance in the $\Upsilon$ mass region*, arXiv:1805.09820, submitted to JHEP
7. LHCb collaboration, *First observation of top quark production in the forward region*, Phys. Rev. Lett. **115** (2015) 112001, arXiv:1506.00903
8. LHCb collaboration, *Measurement of the $t\bar{t}$, $W + b\bar{b}$ and $W + c\bar{c}$ production cross sections in pp collisions at $\sqrt{s}$ = 8 TeV*, Phys. Lett. **B767** (2017) 110, arXiv:1610.08142
9. LHCb collaboration, *Measurement of forward top pair production in the dilepton channel in pp collisions at $\sqrt{s}$ = 13 TeV*, arXiv:1803.05188, submitted to JHEP
10. LHCb collaboration, *First observation of forward $Z \to b\bar{b}$ production in pp collisions at $\sqrt{s}$ = 8 TeV*, Phys. Lett. **B776** (2017) 430, arXiv:1709.03458

# SEARCHES FOR ELECTROWEAK SIGNATURES OF SUPERSYMMETRY AT ATLAS AND CMS

T.J. KHOO
ON BEHALF OF THE ATLAS AND CMS COLLABORATIONS [a]
*Département de Physique Nucléaire et Corpusculaire,*
*Université de Genève, Quai Ernest-Ansermet, 1211 Genève 4*

Searches for strongly-produced superparticles at the Large Hadron Collider have excluded gluinos and squarks of all generations up to the TeV scale. While limited by statistics, electroweak signatures remain less thoroughly explored, and in particular the Higgsino sector has proven challenging. Conventional searches for leptons associated with missing transverse momentum do not fully cover the phase space, requiring new approaches to extend experimental sensitivity. Dedicated reconstruction techniques address the challenge posed by mass-degenerate spectra. By looking beyond the assumption of leptonic signatures, searches for gauge-mediated supersymmetry have broken new ground.

## 1 Introduction

Supersymmetry (SUSY)[1–6] at low scales has long been considered a leading candidate for new physics within reach of the Large Hadron Collider[7] (LHC). To date, experimental searches have disfavoured the existence of strongly-produced sparticles up to the TeV scale. Sparticles produced via electroweak (EW) processes are less tightly constrained due to various challenges, not least their generally lower production cross-sections.

With naturalness arguments not having delivered their promised bounty, the present goal of the experimental search programme is to "leave no piste unskied". Therefore, this talk reviews the status of conventional searches for electroweak signatures, and describes the approaches used by the ATLAS[8] and CMS[9] collaborations to extend sensitivity where these searches are limited, such as by mass-degenerate SUSY spectra or by reduced decay rates to leptons. Emphasis is placed on new results showing sensitivity to Higgsino production.

### *1.1 Phenomenology of the SUSY electroweak sector*

EW signatures are primarily defined by the phenomenology of the lightest supersymmetric particle (LSP), and the next-to-lightest supersymmetric particle (NLSP). Assuming R-parity conservation,[10] the LSP (typically the lightest neutralino, $\tilde{\chi}_1^0$) is stable and holds neither electric nor colour charge, and is therefore a dark matter candidate. EW NLSPs include the chargino ($\tilde{\chi}_1^\pm$) and neutralino ($\tilde{\chi}_2^0$), respectively electrically charged or neutral mass eigenstates of mixtures between the superpartners of the Standard Model (SM) gauge bosons and the five Higgs bosons expected from a 2-Higgs-doublet model.[11] Alternatively, the NLSP could be a slepton ($\tilde{\ell}$), partnered with the electron, muon or tau lepton.

For EW sparticle masses of a few hundred GeV, the cross-sections are around $\mathcal{O}(0.1) - \mathcal{O}(10)$ fb, comparable to Higgs production cross-sections, and therefore orders of magnitude below significant background sources such as SM diboson production. The specific example of $M_{\mathrm{NLSP}} = 500$ GeV implies cross-sections of 22fb for pair-producing charginos that are pure Wino admixtures, but only 6fb for pure Higgsinos.[12,13] Left- (right-)handed sleptons of the same mass have cross-sections of 0.5fb (0.2fb).

## 2 Conventional searches: multileptons

The traditional signature of at least two high transverse momentum ($p_{\mathrm{T}}$) leptons [b] mitigates the drawbacks of a small production cross-section in comparison with the strong processes dominating proton-proton collisions. This motivates the classic strategy of selecting two or more leptons, in conjunction with missing transverse momentum ($\not{E}_{\mathrm{T}}$) from the invisible LSPs. The most recent analyses of this nature from ATLAS and CMS have been carried out using 36 fb$^{-1}$ of LHC proton-proton collision data collected at a centre-of-mass energy of 13 TeV.[14–17]

In all cases, these searches deal mainly with irreducible backgrounds from SM diboson production, and implement vetos on hadronic jets to mitigate jetty backgrounds such as top-quark pair-production ($t\bar{t}$), where no jets are expected from the signal decay processes. Searches for $\geq 3$ leptons may suffer from a high rate of non-prompt or misidentified leptons.

### *2.1 Searches for slepton production*

Searches for slepton production by ATLAS and CMS highlight various interesting experimental methods.[16,18] Besides selecting events with two opposite-sign, same flavour leptons and no jets, a veto is applied to events whose dilepton mass $M_{\ell\ell}$ falls within the Z mass window. A minimum $M_{\ell\ell}$ cut is also applied to remove dileptons from light hadronic resonances. Further sensitivity is achieved by utilising the "stransverse mass" or $M_{\mathrm{T2}}$ variable.[19,20] This observable effectively separates signal from background by assuming that the event arises from the pair-production of two heavy objects that each decay to a visible (lepton) and an invisible (neutrino or neutralino) particle, and uses the $\not{E}_{\mathrm{T}}$ constraint to place a lower bound on the parent particle mass. The CMS analysis applies a simple cut at 90 GeV to substantially reduce the dominant WW background, as a kinematic endpoint in $M_{\mathrm{T2}}$ exists for this process at the W mass, then defines signal regions (SRs) in $\not{E}_{\mathrm{T}}$. ATLAS, in contrast, uses bins at large $M_{\mathrm{T2}}$.

For many of the background processes, background estimation is possible using Monte Carlo simulated events, whose normalisation is constrained by auxiliary measurements of data in control regions. CMS utilises a data-driven "flavour symmetry" method for the two major residual background components of $t\bar{t}$ and WW production. In these processes, the rate of $ee$ and $\mu\mu$ events with the selected kinematics is identical to that of $e\mu$ events, up to corrections for different reconstruction and particle identification efficiencies for the two lepton flavours.

In Figure 1, the flavour symmetry approach is shown to accurately reproduce the data in the signal region, demonstrating the effectiveness of the method, albeit also revealing the lack of any supersymmetric signal. The same figure shows the constraints placed by this search on the masses of sleptons and the LSP, in a simplified model scenario where only production of mass-degenerate left- and right-handed selectrons and smuons is assumed. For light LSPs, the expected (observed) exclusion reach is 500 (450) GeV. Slepton production may be excluded for LSP masses up to 220 GeV. Similar sensitivity is shown by the ATLAS dilepton search channels.[16]

Searches for staus occupy a particular niche within the slepton analyses. While many of the same approaches apply to defining the searches, the dominant hadronic tau decay modes are more difficult to differentiate from other hadronic jets, reducing the signal purity. To address

[b] Typically, "lepton" is used to refer only to the electron and muon, with tau leptons being mentioned explicitly.

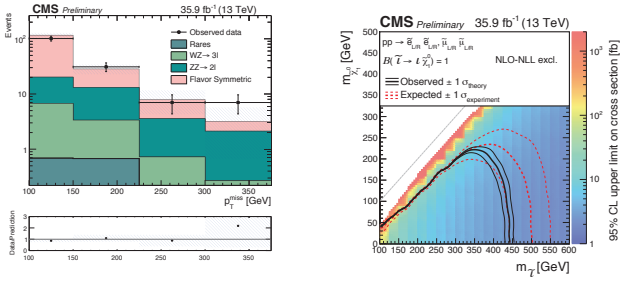


Figure 1 – Left: Signal region $\not{E}_T$ distribution for the CMS slepton search,[18] showing the use of the "flavour symmetry" method to estimate the dominant backgrounds. Right: Limits placed on the slepton and LSP masses, in a simplified model assuming mass-degenerate left- and right-handed selectrons and smuons.

this, both ATLAS and CMS have invested significantly in optimising tau reconstruction and identification for LHC Run 2.[21,22] CMS has searched for stau production in channels considering all decay modes of the two taus.[23,24] Due to the low purity, exclusion sensitivity to the nominal stau production cross section has not yet been reached, as shown in Figure 2, but overall, the doubly hadronic decay channel is seen to be more sensitive.

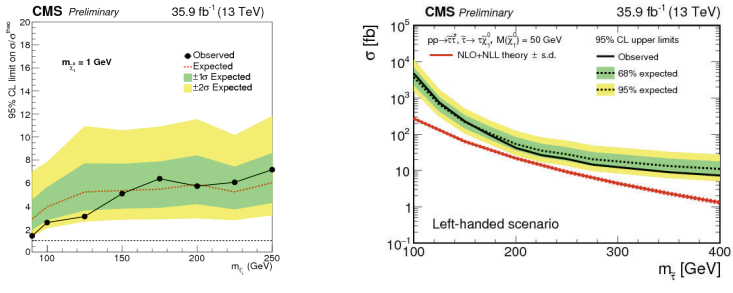


Figure 2 – Limits placed on stau production cross-sections by CMS analyses in channels considering at least one leptonic decay of the taus[23] (left) or doubly hadronic tau decays[24] (right).

### *2.2 Searches for charginos and neutralinos*

Chargino/neutralino decay modes are less constrained than those of sleptons. Different-flavour dileptons or more than two leptons can be produced. The decay chain may feature on-shell Z bosons, allowing a very clean signature to be identified. However, the rates of purely leptonic final states are diluted due to the propensity of SM bosons to decay to hadrons.

It is possible to carry out searches for chargino pair-production with a very similar approach to the slepton analyses, as exemplified by a recent CMS result.[25] This strategy is effective when assuming 100% chargino decays to leptons via an intermediate slepton or sneutrino, but sensitivity to W-mediated decays is more modest.

Surveying the searches for a wide range of chargino/neutralino decays depicted in Figure 3,[26,27] a few observations are possible. Firstly, for slepton-mediated decays, exclusion sensitivity is achieved for NLSP masses up to nearly 1150 GeV in the limit of massless LSPs. However,the lack of coverage at large LSP masses illustrates how "compression" of the SUSY mass spectrum poses a challenge for experimental sensitivity due to the limited visible final state energy. Constraints are also much weakened when allowing the electroweakino NLSPs to decay

via SM bosons. These observations have motivated new analyses that address the challenge of compressed signal scenarios and challenge the assumption of leptonic signatures.

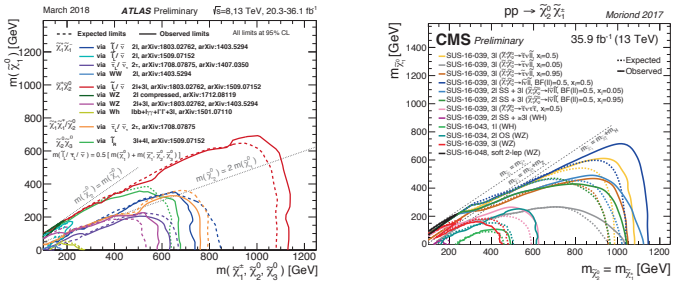


Figure 3 – Overview of current exclusion limits on production of charginos and neutralinos in different search channels using LHC data, shown in the plane of the parent and LSP masses. Left: ATLAS limits on pair-production of charginos or neutralinos, or associated chargino-neutralino production using 8 and 13 TeV data.[26] Right: CMS limits on associated chargino-neutralino production using 13 TeV data.[27]

## 3 Searches for compressed supersymmetric states

In EW SUSY signal scenarios with compressed mass spectra, leptonic signatures may still be present, but the phase space available to the leptons is severely reduced, as illustrated in Figure 4. This has necessitated special procedures for reconstructing and calibrating soft leptons in both ATLAS and CMS.[28–31]

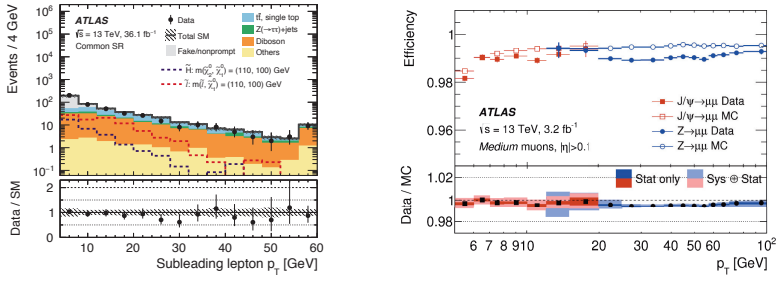


Figure 4 – Left: Subleading lepton transverse momentum spectrum for SM processes and Higgsino or slepton NLSPs with a mass of 110 GeV decaying to a 100 GeV LSP.[32] Right: Efficiency as a function of transverse momentum for reconstructing and identifying muons in ATLAS, measured in simulation and in data using $Z \to \mu\mu$ and $J/\psi \to \mu\mu$ decays.[29]

Searches using soft leptons have been published by both collaborations.[32,33] Leptons with transverse momenta as low as 4-5 GeV can be reconstructed offline, but triggering on these soft leptons is a challenge, although soft dimuon triggers are employed in the CMS search. Due to the large NSLP mass scale, hard ISR jets can be emitted, boosting the entire sparticle system. The heavy LSPs carry away most of the momentum, facilitating a $\not{E}_{\mathrm{T}}$ trigger selection as an alternative to lepton triggers. Other analysis techniques common to ATLAS and CMS include vetos on b-tagged jets, as a major source of soft leptons.

For the final signal-background discriminants, a variety of observables are used: $M_{\mathrm{T2}}$ for sleptons, a large ratio of the $\not{E}_{\mathrm{T}}$ to the total visible transverse momentum, or finally structures in the $M_{\ell\ell}$ spectrum, as demonstrated in Figure 5.

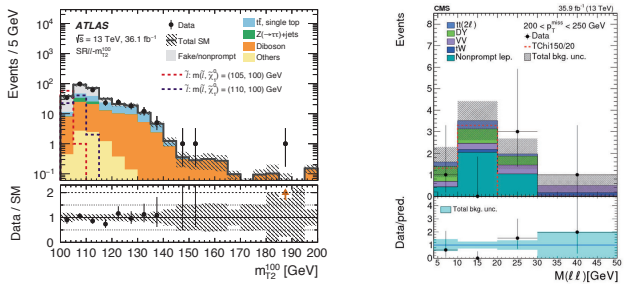


Figure 5 – Discriminating variable distributions used in searches for compressed electroweak SUSY by ATLAS and CMS. Left: Stransverse mass $M_{\mathrm{T2}}$ distribution in ATLAS compressed slepton signal regions.[32] Right: Dilepton invariant mass distribution in CMS signal regions in a search with soft leptons.[33]

Analysis of the $M_{\ell\ell}$ spectrum in these signal regions requires vetos on the mass ranges associated with light hadronic resonances such as $J/\psi$ and $\Upsilon$. Unlike in conventional searches, the signal inhabits ranges well below those typical for the SM background processes. Another important aspect of these analyses is that non-prompt and misidentified leptons make up a major background component, necessitating careful estimation using data-driven methods. These specialised searches extend the limits on slepton, Wino and Higgsino production to NLSP-LSP mass splittings of $\mathcal{O}(10$ GeV), for NLSP masses below 150-200 GeV as shown in Figure 6.

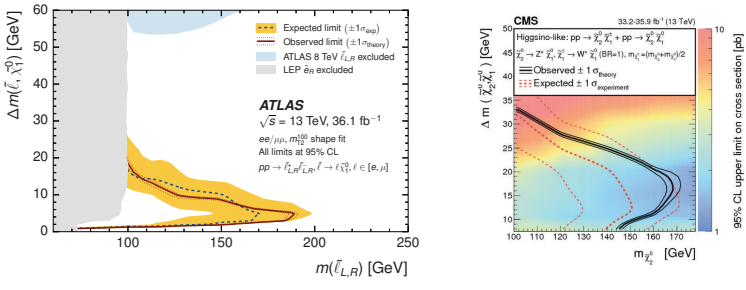


Figure 6 – Limits placed on compressed electroweak SUSY models by using searches with soft leptons, shown in the plane of the NLSP mass and the NLSP-LSP mass splitting.[32,33] Left: ATLAS limits on compressed sleptons. Right: CMS limits on compressed Higgsinos.

Even more unconventional reconstruction is needed for the extremely compressed spectra that can arise in models of Anomaly-Mediated Supersymmetry Breaking (AMSB).[34,35] In such scenarios, a general expectation is that the chargino NLSP is only separated by $\mathcal{O}(100$ MeV) from the LSP, and therefore undergoes a non-prompt decay to a soft pion and the LSP, with a typical lifetime of $\mathcal{O}(0.1$ns), implying that a chargino produced with some boost can travel several centimetres from the interaction point before decaying.[36] Searches have been carried out for this unique "disappearing track" signature by reconstructing "tracklets" with a series of hits in the inner tracking layers but none in the outer layers.[37,38]

These analyses rely on robust data-driven estimates of the rates of fake tracklets, which can originate from genuine hadron or lepton tracks that are bent by nuclear interactions or photon emission, or from random combinations of nearby hits. As in the searches with soft leptons, triggering is accomplished using $\not{E}_{\mathrm{T}}$ triggers benefiting from ISR jet emission. Both ATLAS and CMS produce limits on charginos in the AMSB scenario, featured in Figure 7. Due to different choices in the tracklet reconstruction, the CMS analysis has peak sensitivity for proper lifetimes

of a few nanoseconds, while the ATLAS analysis is better tuned for sub-nanosecond lifetimes, successfully excluding pure Higgsinos with masses below 152 GeV.[39]

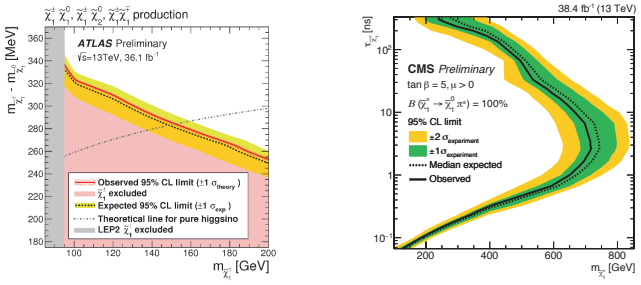


Figure 7 – Exclusion limits on long-lived charginos in AMSB scenarios from searches for disappearing tracks.[37–39] Left: Limits set by ATLAS, shown in the plane of the NLSP-LSP mass splitting versus the chargino mass. Right: CMS limits, shown in the plane of the sparticle lifetime versus the chargino mass.

## 4 Searches without leptons

New search channels have been realised by stepping beyond the boundaries of leptonic signatures. Gauge-Mediated Supersymmetry Breaking (GMSB) models in particular motivate the investigation of photonic or purely hadronic final states.[40,41] A characteristic feature of GMSB is a keV-scale gravitino LSP, which eliminates the possibility of a compressed mass spectrum. The lightest neutralino can then be the NLSP, its mixings determining the precise signature.

Pure Bino NLSPs typically decay producing a high $p_{\mathrm{T}}$ photon, the subject of searches by CMS and ATLAS.[42,43] Because both of the Bino decay products are massless, the combination of one or two energetic photons and large $\not{E}_{\mathrm{T}}$ suffices to extract a signal. This can be seen from the ATLAS and CMS limits in Figure 8, in which it is assumed that the production process features the heavier $\tilde{\chi}_1^{\pm}$ and/or $\tilde{\chi}_2^0$ due to the low rate of Bino direct production. The limits from both experiments are seen to be consistent, and are sensitive only to the production cross-section, but not to other mass scales that would affect the kinematics of additional jets and leptons in the final state.

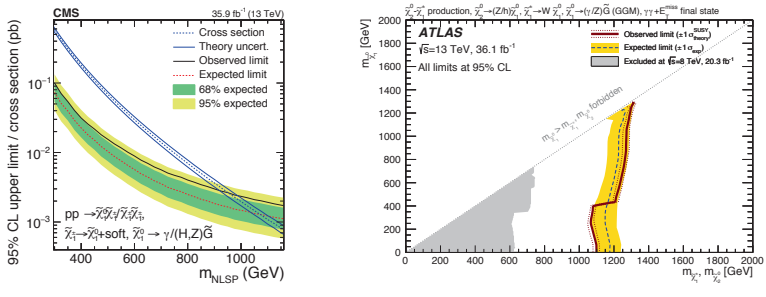


Figure 8 – Exclusion limits on GMSB models from searches in photonic final states, where the lightest neutralino is a pure Bino.[42,43] Left: CMS limits on the cross-section of chargino pair-production or associated chargino-neutralino production with the lightest neutralino and chargino being mass-degenerate. Right: ATLAS limits presented in the mass plane of the lightest neutralino versus the mass-degenerate lightest chargino and second-lightest neutralino.

Finally, all-hadronic final states have become of interest particularly in the context of Higgsino production. Both CMS and ATLAS have exploited the multi-b topology in searches that

reconstruct two Higgs bosons accompanied by large $\not{E}_{\mathrm{T}}$ from the light gravitino LSP.[44,45] Reconstruction of Higgs candidates from high-mass Higgsinos in the ATLAS analysis is done by pairing nearby b-tagged jets, based on the expectation that the Higgs bosons will be somewhat boosted, and hence their decay products will be collimated. In the CMS analysis, as well as in the ATLAS dedicated low-mass selection, the Higgs candidates are instead identified by minimising the mass difference between the candidate jet pairs. The ATLAS low-mass analysis further accounts for possible biases in the mass peak position. Top pair-production being the dominant source of background with multiple b-tagged jets, an explicit reconstruction of and veto on top pairs is executed in both searches. Remaining background contributions are assessed using side bands and control regions, with the ATLAS low-mass estimate employing a BDT reweighting of 2-b-tag data to the 4-b-tag signal region.

Figure 9 shows the resulting exclusion limits. Higgsinos with masses up to 890 GeV are excluded, with the ATLAS low-mass optimisation proving crucial for closing the gap at Higgsino masses below 200 GeV.

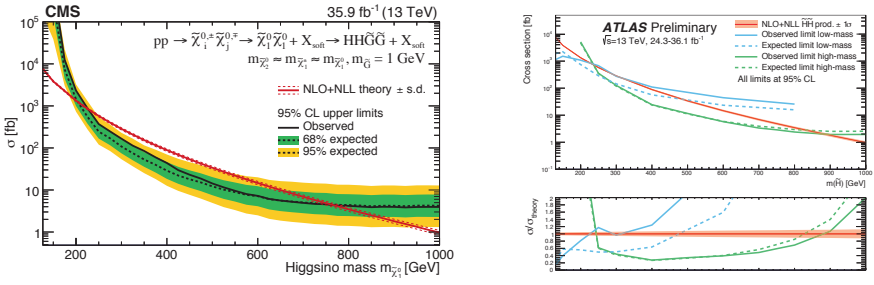


Figure 9 – Exclusion limits on Gauge-Mediated Supersymetry Breaking models from searches in fully hadronic final states, where the lightest neutralino is a pure Higgsino, using data from CMS[44] (left) and ATLAS[45] (right). Limits on the production cross-section are displayed, with the ATLAS plot showing the contributions of selections optimised for low and high Higgsino masses separately.

## 5 Conclusions

Having analysed up to 36 fb$^{-1}$ of LHC Run 2 data, the ATLAS and CMS collaborations have made substantial inroads in the search for electroweak signatures of supersymmetry. Conventional searches for multilepton signatures are well developed and provide some of the strongest bounds on chargino and neutralino production. More challenging searches for compressed mass spectra have been implemented thanks to refinements in soft electron and muon reconstruction, and more exotic methods have been employed to achieve sensitivity to sparticles with $\mathcal{O}$(100 MeV) degeneracies. Sensitivity to pure Higgsino production is beginning to be achieved, aided by the use of non-leptonic and in particular fully hadronic final states. Yet, weak-scale SUSY might still be hiding in the form of the stau.


## Acknowledgments

TJK is grateful for support under Swiss National Science Foundation grant SNF 200020_175597.


## References


1. Y. A. Golfand and E. P. Likhtman, JETP Lett. **13**, 323 (1971) [Pisma Zh. Eksp. Teor. Fiz. **13**, 452 (1971)

2. D. V. Volkov and V. P. Akulov, Phys. Lett. B **46**, 109 (1973).
3. J. Wess and B. Zumino, Phys. Lett. B **49**, 52 (1974).
4. J. Wess and B. Zumino, Nucl. Phys. **B 70**, 39 (1974).
5. S. Ferrara and B. Zumino, Nucl. Phys. B **79**, 413 (1974).
6. A. Salam and J. A. Strathdee, Phys. Lett. B **51**, 353 (1974).
7. L. Evans and P. Bryant, (editors), JINST **3**, S08001 (2008).
8. ATLAS Collaboration, JINST **3**, S08003 (2008).
9. CMS Collaboration, JINST **3**, S08004 (2008).
10. G. R. Farrar and P. Fayet, Phys. Lett. B **76**, 575 (1978).
11. T. D. Lee, Phys. Rev. D **8**, 1226 (1973).
12. B. Fuks and M. Klasen and D. R. Lamprea and Rothering, Marcel, JHEP **10**, 081 (2012).
13. B. Fuks and M. Klasen and D. R. Lamprea and Rothering, Marcel, Eur. Phys. J. C **73**, 2480 (2013).
14. CMS Collaboration, JHEP **076**, 03 (2018).
15. CMS Collaboration, JHEP **166**, 03 (2018).
16. ATLAS Collaboration, Submitted to Eur. Phys. J. C, arXiv:1803.02762.
17. ATLAS Collaboration, Submitted to Phys. Rev. D, arXiv:1804.03602.
18. CMS Collaboration, CMS-PAS-SUS-17-009, http://cds.cern.ch/record/2297116.
19. C. G. Lester and D. J. Summers, Phys. Lett. B **463**, 99 (1999).
20. A. J. Barr and C. G. Lester and P. Stephens, J. Phys. G **29**, 2343 (2003).
21. CMS Collaboration, CMS-DP-2017-006, http://cds.cern.ch/record/2255737.
22. ATLAS Collaboration, ATLAS-CONF-2017-029, http://cds.cern.ch/record/2261772.
23. CMS Collaboration, CMS-PAS-SUS-17-002, http://cds.cern.ch/record/2297162.
24. CMS Collaboration, CMS-PAS-SUS-17-003, http://cds.cern.ch/record/2273395.
25. CMS Collaboration, CMS-PAS-SUS-17-010, http://cds.cern.ch/record/2309556.
26. ATLAS Collaboration, http://atlas.web.cern.ch/Atlas/GROUPS/PHYSICS/CombinedSummaryPlots/SUSY/ATLAS_SUSY_EWSummary/ATLAS_SUSY_EWSummary.pdf, Accessed: 2018-05-01.
27. CMS Collaboration, http://twiki.cern.ch/twiki/pub/CMSPublic/PhysicsResultsSUS/EWK-slep_limits_summary_cms_Moriond17.pdf, Accessed: 2018-05-01.
28. ATLAS Collaboration, ATLAS-CONF-2016-024, http://cds.cern.ch/record/2157687.
29. ATLAS Collaboration, Eur. Phys. J. C **76**, 292 (2016).
30. CMS Collaboration, CMS-DP-2017-004, http://cds.cern.ch/record/2255497.
31. CMS Collaboration, Submitted to JINST, arXiv:1804.04528.
32. ATLAS Collaboration, Phys. Rev. D **97**, 052010 (2018).
33. CMS Collaboration, Submitted to Phys. Lett. B, arXiv:1801.01846.
34. L. Randall and R. Sundrum, Nucl. Phys. B **557**, 79 (1999).
35. G. F. Giudice and M. A. Luty and H. Murayama and R. Rattazzi, JHEP **12**, 027 (1998).
36. C. H. Chen and M. Drees and J. F. Gunion, Phys. Rev. D **55**, 330 (1997) [Erratum: Phys. Rev. D **60**, 039901 (1999)].
37. ATLAS Collaboration, Submitted to JHEP, arXiv:1712.02118.
38. CMS Collaboration, Submitted to JHEP, arXiv:1804.07321.
39. ATLAS Collaboration, ATL-PHYS-PUB-2017-019, http://atlas.web.cern.ch/Atlas/GROUPS/PHYSICS/PUBNOTES/ATL-PHYS-PUB-2017-019/.
40. C. Cheung and A. L. Fitzpatrick and D. Shih, JHEP **07**, 054 (2008).
41. P. Meade and N. Seiberg and D. Shih, Prog. Theor. Phys. Suppl. **177**, 143 (2009).
42. CMS Collaboration, Phys. Lett. B **780**, 118 (2018).
43. ATLAS Collaboration, Submitted to Phys. Rev. D, arXiv:1802.03158.
44. CMS Collaboration, Phys. Rev. D **97**, 032007 (2018).
45. ATLAS Collaboration, ATLAS-CONF-2017-081, http://cds.cern.ch/record/2297400.

# PRECISION MEASUREMENT OF THE FORM FACTORS OF SEMILEPTONIC CHARGED KAON DECAYS FROM NA48/2

S. SHKAROVSKIY [a]
*Joint Institute for Nuclear Research, Joliot-Curie, 6, Dubna, Moscow region 141980, Russia*

We present a measurement of the charged kaon semileptonic form factors based on 4.3 million $K^{\pm} \to \pi^0 e^{\pm} \nu_e$ and 2.9 million $K^{\pm} \to \pi^0 \mu^{\pm} \nu_\mu$ decays collected by the NA48/2 experiment. The single results for the semi-electronic and semi-muonic channel have better and similar precision, respectively, than previous measurements. The combination of both channels yields the most precise measurement of the form factors of semileptonic kaon decays.

## 1 Introduction

The main purpose of the NA48/2 experiment at the CERN SPS was a search for the direct CP violation in $K^{\pm}$ decay to three pions [1]. The experiment used simultaneous $K^+$ and $K^-$ beams with momenta of 60 GeV/c propagating through the detector along the same beam line.

The main components of the NA48/2 detector were a magnetic spectrometer, composed by four drift chambers and a dipole magnet deflecting the charged particles in the horizontal plane, and a liquid krypton electromagnetic calorimeter (LKr) with an energy resolution of about 1% for 20 GeV photons and electrons. For the selection of $K^{\pm}_{\mu 3}$ decays, a muon veto system (MUV) was essential to distinguish muons from pions.

The data used for the form factor (FF) analysis were collected in 2004 during a dedicated run with a special trigger setup which required one or more tracks in the magnetic spectrometer and an energy deposit of at least 10 GeV/c in the electromagnetic calorimeter.

## 2 $K_{l3}$ form factors

Semileptonic kaon decays $K^{\pm} \to \pi^0 l^{\pm} \nu$ ($K_{l3}$) offer the most precise determination of the CKM matrix element $|V_{US}|^2$, that require both a branching ratio and a FFs experimental measurement.

[a] for the NA48/2 Collaboration: G. Anzivino, R. Arcidiacono, W. Baldini, S. Balev, J.R. Batley, M. Behler, S. Bifani, C. Biino, A. Bizzeti, B. Bloch-Devaux, G. Bocquet, N. Cabibbo, M. Calvetti, N. Cartiglia, A. Ceccucci, E. Celeghini, P. Cenci, C. Cerri, C. Cheshkov, J.B. Chèze, M. Clemencic, G. Collazuol, F. Costantini, A. Cotta Ramusino, D. Coward, D. Cundy, A. Dabrowski, P. Dalpiaz, C. Damiani, M. De Beer, J. Derré, H. Dibon, L. DiLella, N. Doble, K. Eppard, V. Falaleev, R. Fantechi, M. Fidecaro, L. Fiorini, M. Fiorini, T. Fonseca Martin, P.L. Frabetti, L. Gatignon, E. Gersabeck, A. Gianoli, S. Giudici, A. Gonidec, E. Goudzovski, S. Goy Lopez, M. Hita-Hochgesand, M. Holder, P. Hristov, E. Iacopini, E. Imbergamo, M. Jeitler, G. Kalmus, V. Kekelidze, K. Kleinknecht, V. Kozhuharov, W. Kubischta, G. Lamanna, C. Lazzeroni, M. Lenti, L. Litov, D. Madigozhin, A. Maier, I. Mannelli, F. Marchetto, R. Marchevski, G. Marel, M. Markytan, P. Marouelli, M. Martini, L. Masetti, E. Mazzucato, A. Michetti, I. Mikulec, M. Misheva, N. Molokanova, E. Monnier, U. Moosbrugger, C. Morales Morales, D.J. Munday, A. Nappi, G. Neuhofer, A. Norton, M. Patel, M. Pepe, A. Peters, F. Petrucci, M.C. Petrucci, B. Peyaud, M. Piccini, G. Pierazzini, I. Polenkevich, Yu. Potrebenikov, M. Raggi, B. Renk, P. Rubin, G. Ruggiero, M. Savrié, M. Scarpa, M. Shieh, S. Shkarovskiy, M.W. Slater, M. Sozzi, S. Stoynev, E. Swallow, M. Szleper, M. Valdata-Nappi, B. Vallage, M. Velasco, M. Veltri, S. Venditti, M. Wache, H. Wahl, A. Walker, R. Wanke, L. Widhalm, A. Winhart, R. Winston, M.D. Wood, S.A. Wotton, A. Zinchenko, M. Ziolkowski.

$K_{l3}$ precision FFs measurement results based on the NA48/2 data analysis are presented in this paper.

The $K_{l3}$ decay width in the absence of electromagnetic effects can be represented by the Dalitz plot density depending on the lepton and pion energies in kaon rest frame $E_l$ and $E_\pi$ respectively [3]:

$$\frac{d^2\Gamma_0(K_{l3})}{dE_l dE_\pi} = N(Af_+^2(t) + Bf_+(t)f_-(t) + Cf_-^2(t)), \quad (1)$$

where $t = (P_K - P_\pi)^2 = m_K^2 + m_\pi^2 - 2m_K E_\pi$, $N$ is a normalization constant and $f_-(t) = (f_+(t) - f_0(t))(m_K^2 - m_{\pi+}^2)/t$. Here $f_+(t)$ and $f_0(t)$ are the so called vector and scalar $K_{l3}$ FFs, respectively. The $m_K$ is a mass of $K^+$, $m_\pi$ is a mass of $\pi^0$ and $m_{\pi^+}$ is a mass of $\pi^+$.

Table 1: Definitions of the FF parameterizations used in the analysis

| | $f_+(t)$ | $f_0(t)$ |
|---|---|---|
| Quadratic | $1 + \lambda'_+ t/m_\pi^2 + \frac{1}{2}\lambda''_+(t/m_\pi^2)^2$ | $1 + \lambda'_0 t/m_\pi^2$ |
| Pole | $\frac{M_V^2}{(M_V^2 - t)}$ | $\frac{M_S^2}{(M_S^2 - t)}$ |
| Dispersive | $\exp\left(\frac{(\Lambda_+ + H(t))t}{m_\pi^2}\right)$ | $\exp\left(\frac{(ln[C] - G(t))t}{(m_K^2 - m_\pi^2)}\right)$ |

Definitions of the implemented parameterizatios are shown in the Table 2: the Quadratic [4] parameterization (fit parameters $\lambda'_+, \lambda''_+, \lambda'_0$), the Pole [5] (fit parameters $M_V, M_S$) and the Dispersive [6] one (fit parameters $\Lambda_+, ln[C]$).

### *2.1 The $K_{l3}$ events reconstruction and selection*

The data selection requires one track in the magnetic spectrometer and a time coincidence with at least two clusters in the LKr from the $\pi^0$ decay. The track had to be inside the geometrical acceptance of the detector, and needed a good reconstructed decay vertex, proper timing and a momentum $p > 5GeV/c$ in case of electrons. For muons the momentum needed to be greater than $10GeV/c$ to ensure proper efficiency of the MUV system. To identify a track as the electron we require $2.0 > E/p > 0.9$, where $E$ is the energy deposited in the LKr and $p$ is the momentum measured in the spectrometer, and no signal in the MUV system. To identify the track as a muon we require an associated hit in the MUV system and $E/p < 0.9$.

Longitudinal $K_{l3}$ decay position $Z_n$ (neutral vertex Z coordinate) is defined as a longitudinal position of $\pi^0$ decay, reconstructed from LKr data assuming PDG [7] value for $\pi^0$ mass. The transverse neutral vertex coordinates $(X_n, Y_n)$ are calculated as the impact point position of the reconstructed charged track on the $Z_n$ plane.

For the kaon momentum ($P_K$) measurement we direct Z axis along the beam average position in space, measured from $3\pi^\pm$ data. In the assumptions of $m(\nu) = 0$ and kaon flight along the beam axis (that means availability of the measured $P_t(\nu) = -P_t$), two solutions of quadratic equation for $P_K$ exist: $P_K = P_{1,2} = (\phi P_Z \pm \sqrt{d})/(E^2 - P_Z^2)$, where $\phi = 0.5(M_K^2 + E^2 - P_t^2 - P_Z^2)$, $d = \phi^2 P_Z^2 - (E^2 - cxP_Z^2)(M_K^2 E^2 - \phi^2))$ and $E, P_t, P_Z$ are the total energy and total momentum of all the registered particles $\pi^0, l$.

The background contribution (see Table 2) has been estimated using the NA48/2 Monte Carlo. For $K_{e3}$ the background from $K^\pm \to \pi^\pm\pi^0$ ($2\pi$) significantly contributes to the signal. A cut in the $P_t(\nu) >= 0.03$ $GeV/c$ of the event reduced this background. For $K_{\mu 3}$ selection, essential background may come from $2\pi$ decays with a subsequent $\pi^\pm \to \mu^\pm\bar{\nu}$. The cuts in $m(\pi^\pm\pi^0)$ and $m(\mu\bar{\nu})$ reduced this background. For both $K_{\mu 3}$ and $K_{e3}$ samples the $K^\pm \to \pi^\pm\pi^0\pi^0$ decays can contribute to the background.

Additionally, the effect of $K_{\mu 3}$ misidentification as $K_{e3}$ (due to the $\mu \to e\nu$ decay) has been taken into account.

Inner bremsstrahlung part of $\pi^{\pm}\pi^0\gamma$ decay was simulated separately for the kaon rest frame kinetic energy of the charged pion $T^*_{\pi^{\pm}} < 90MeV$, its probability estimation is taken from [8].

Table 2: Simulated background processes, their probabilities $Br$ (in %), generated MC statistics $N_g$ (in $10^6$ events) and the estimated fractions $F_e$ and $F_\mu$ (both in units of per mill) in $K_{e3}$ and $K_{\mu 3}$ samples for the present selection.

| Process | Notation | $Br$ | $N_g$ | $F_e$ | $F_\mu$ |
|---|---|---|---|---|---|
| $K^{\pm} \to \pi^{\pm}(\pi^0 \to 2\gamma)$ | $2\pi$ | 20.66 | 393.2 | 0.270 | 0.264 |
| $K^{\pm} \to \pi^{\pm}2(\pi^0 \to 2\gamma)$ | $3\pi$ | 1.761 | 62.5 | 0.286 | 1.833 |
| $K^{\pm} \to \pi^{\pm}(\pi^0 \to e^+e^-\gamma)$ | $2\pi D$ | 1.174 | 1.5 | 0.049 | 0.000 |
| $K^{\pm} \to \pi^{\pm}\gamma(\pi^0 \to 2\gamma)$ | $2\pi\gamma$ | 0.0275 | 35.3 | 0.004 | 0.044 |
| $K^{\pm} \to \pi^0\mu^{\pm}\nu(\mu \to e\nu)$ | $K^e_{\mu 3}$ | 0.03353 | 174.3 | 0.004 | 0.000 |

The experimental two-dimensional Dalitz plot is corrected for background by subtracting of the estimated background contributions.

The total statistics of selected data is $4.28 \times 10^6$ events for $K_{e3}$, and $2.91 \times 10^6$ events for $K_{\mu 3}$ selection.

### *2.2 Preliminary results on the $K_{l3}$ form factors*

To extract the FF a events-weighting fit is performed in $5 \times 5MeV$ cells in the Dalitz plot of $E^*_{\pi^0}$ vs $E^*_l$ energies, computed in the kaon rest frame. The $K_{e3}$ and $K_{\mu 3}$ Dalitz plots were fitted simultaneously with a common set of the fit parameters MINUIT [9] package called from the ROOT [10] interface minimizes $\chi^2$ by means of parameters variation. The preliminary fit results and contributions to systematic uncertainty for Quadratic, Pole and Dispersive Parameterisation are shown in the Table 3.

Table 3: Fit results for the Quadratic ($\times 10^3$), Pole ($MeV/c^2$) and Dispersive ($\times 10^3$) Parameterisation

| Quadratic | $\lambda'_+$ | $\lambda''_+$ | $\lambda_0$ |
|---|---|---|---|
| $K_{\mu 3}$ | $23.32 \pm 3.08_{sta} \pm 3.50_{sys}$ | $2.14 \pm 1.06_{sta} \pm 0.96_{sys}$ | $14.33 \pm 1.11_{sta} \pm 1.25_{sys}$ |
| $K_{e3}$ | $23.52 \pm 0.78_{sta} \pm 1.29_{sys}$ | $1.60 \pm 0.30_{sta} \pm 0.39_{sys}$ | |
| $K_{l3}$ | $23.35 \pm 0.75_{sta} \pm 1.23_{sys}$ | $1.73 \pm 0.29_{sta} \pm 0.41_{sys}$ | $14.90 \pm 0.55_{sta} \pm 0.80_{sys}$ |
| Pole | $m_V$ | $m_S$ | |
| $K_{\mu 3}$ | $879.1 \pm 8.1_{sta} \pm 13.5_{sys}$ | $1196.4 \pm 18.1_{sta} \pm 28.8_{sys}$ | |
| $K_{e3}$ | $896.8 \pm 3.4_{sta} \pm 7.6_{sys}$ | | |
| $K_{l3}$ | $894.3 \pm 3.2_{sta} \pm 5.4_{sys}$ | $1185.5 \pm 16.6_{sta} \pm 35.5_{sys}$ | |
| Dispersive | $\Lambda_+$ | $ln[C]$ | |
| $K_{\mu 3}$ | $23.55 \pm 0.50_{sta} \pm 0.97_{sys}$ | $186.68 \pm 5.12_{sta} \pm 9.23_{sys}$ | |
| $K_{e3}$ | $22.54 \pm 0.20_{sta} \pm 0.62_{sys}$ | | |
| $K_{l3}$ | $22.67 \pm 0.18_{sta} \pm 0.55_{sys}$ | $189.12 \pm 4.91_{sta} \pm 11.09_{sys}$ | |

The NA48/2 is the first experiment measuring the FF using both $K^+$ and $K^-$. In $K_{\mu 3}$ the result is dominated by the statistical error, for $K_{e3}$ by the systematic (Fig. 1).

In order to avoid the problem of partially correlated systematic uncertainties in the $K_{e3}$ and $K_{\mu 3}$ results averaging, we just repeated the complete analysis considering the two decay modes information as the joint data set, containing two Dalitz plots that should be simultaneously fitted with a common form factor parameters.

The combined fit results for Quadratic, Pole and Dispersive parametrizations are also listed in Table 3. The comparison between $K_{l3}$ Quadratic fit results by recent experiments is shown in Fig. 2. The 68% confidence level contours are displayed for both $K^0_{l3}$ (KLOE, KTeV and NA48) and charged kaon decays (ISTRA+ studied $K^-_{l3}$ only). The preliminary NA48/2 results

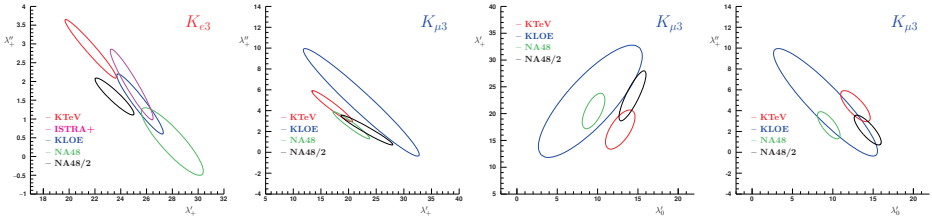


Figure 1 – (Color online) $1\sigma$ confidence contours for measurements of $K_{e3}$ vector form factor and of $K_{\mu3}$ $\lambda'_+, \lambda''_+$ and $\lambda'_0$ form factor parameters. NA48/2: result of the present work.

presented here are the first high precision measurements done with both $K^+$ and $K^-$ decays. All the measured parameters are in good agreement with the measurements done by the other experiments.

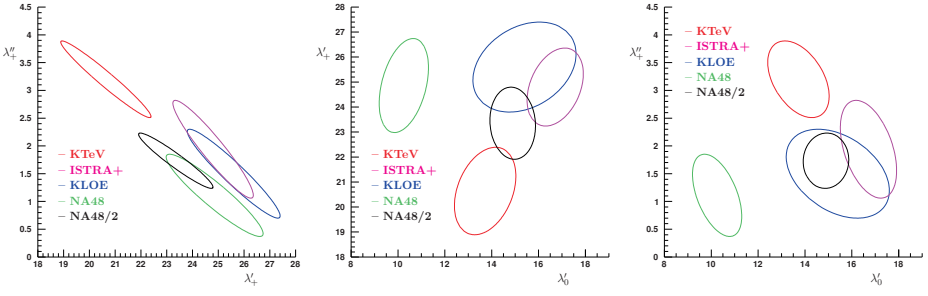


Figure 2 – Joint $K_{l3}$ results for the $\lambda'_+, \lambda''_+$ and $\lambda'_0$ form factor in comparison with the $K_{l3}$ from another experiments.

## Conclusion

$K_{l3}$ form factors measurement is performed by NA48/2 experiment on the basis of 2004 run data. Result is competetive with the other ones in $K^{\pm}_{\mu3}$, and a smallest error in $K^{\pm}_{e3}$ has been reached, that gives us also the combined result with the smallest error.

## References


1. J.R. Batley *et al*, Eur. Phys. J. C **52**, 875 (2007).
2. L. Cappiello, O. Cata, G. D'Ambrosio, D. Gao, Eur. Phys. J. C **72**, 1872 (2012).
3. L.M. Chounet, J.M. Gaillard, M.K. Gaillard, Phys.Rept. **4**, 199 (1972).
4. K.A. Olive *et al* (Particle Data Group), Chin.Phys. C **38**, 090001 (2014).
5. P. Lichard, *Phys. Rev.* D **55**, 5385 (1997).
6. V. Bernard, M. Oertel, E. Passemar, J. Stern, *Phys. Rev.* D **80**, 034034 (2009).
7. C. Patrignani *et al* (Particle Data Group), Chin.Phys. C **40**, 100001 (2016).
8. C. Amsler *et al* (Review of Particle Physics)*Phys. Lett.* B **667**, 1-1340 (2008).
9. F. James, and M. Roos, (Minuit: A System for Function Minimization and Analysis of the Parameter Errors and Correlations) Comput. Phys. Commun. **10**, 343-367 (1975)
10. R. Brun and F. Rademakers (ROOT: An object oriented data analysis framework), Nucl. Instrum. Meth. **A389**, 81-86 (1997)

# Theory of rare kaon decays

Giancarlo D'Ambrosio [a]
*Istituto Nazionale di Fisica Nucleare, Sezione di Napoli, Complesso Universitario di Monte S. Angelo, Via Cintia Edificio 6, 80126 Napoli, Italy*

I review rare kaon decays in the LHC era: we discuss interplay with B-anomalies and possible New Physics in direct CP violation in $K \to 2\pi$: very rare kaon decays like $K \to \pi\nu\bar{\nu}$ are very important to this purpose We discuss also the decays $K^0 \to \mu^+\mu^-$ due to the LHCB measurement

## 1 Introduction and $K \to \pi\nu\bar{\nu}$

Rare kaon decays furnish challenging MFV probes and will severely constrain additional flavor physics motivated by NP [1]. SM predicts the $V-A \otimes V-A$ effective hamiltonian (Fig. 1)

$$\mathcal{H} = \frac{G_F}{\sqrt{2}}\frac{\alpha}{2\pi \sin^2\theta_W}\Big( \underbrace{V_{cs}^* V_{cd}}_{\lambda} X_{NL} + \underbrace{V_{ts}^* V_{td}}_{A^2\lambda^5\,(1-\rho-i\eta)} X(x_t) \Big)\, \bar{s}_L\gamma_\mu d_L\, \bar{\nu}_L\gamma^\mu\nu_L, \qquad (1)$$

$x_q = m_q^2/M_W^2$, $\theta_W$ the Weak angle and $X$'s are the Inami-Lin functions with Wilson coefficients known at two-loop electroweak corrections and the main uncertainties is due to the strong corrections in the charm loop contribution. The structure in (1) leads to a pure CP violating contribution to $K_L \to \pi^0\nu\bar{\nu}$, induced only from the top loop contribution and thus proportional to $\Im m(\lambda_t)$ ($\lambda_t = V_{ts}^* V_{td}$) and free of hadronic uncertainties. This leads to the prediction

$$\mathcal{B}(K_L \to \pi^0\nu\bar{\nu})_{\rm SM} = (2.9 \pm 0.2) \times 10^{-11} \quad \mathcal{B}(K^+ \to \pi^+\nu\bar{\nu})_{\rm SM} = (8.3 \pm 0.9) \times 10^{-11}.$$

where the parametric uncertainty due to the error on $|V_{cb}|$, $\rho$ and $\eta$ is shown.

Typical BSM predict new flavor structure that might affect $K \to \pi\nu\bar{\nu}$ that now can be tested at NA62 and KOTO [2]; we describe two different BSM effects i) new flavor structures for $\epsilon'$ avoiding $\Delta S = 2$ constraints (Fig. 1) [3,1] and ii) attempts to describe B-anomalies [4], typically induce large flavor effects at O(1) TeV [5]. i) the recent lattice results for $K \to 2\pi$ leave open the possibility of BSM for $\epsilon'$; to isospin breaking terms in $\Im(A_2)$ have been studied [3] in Fig.1. We

[a] Supported by MIUR under Project No. 2015P5SBHT (PRIN 2015) and by INFN research initiative ENP

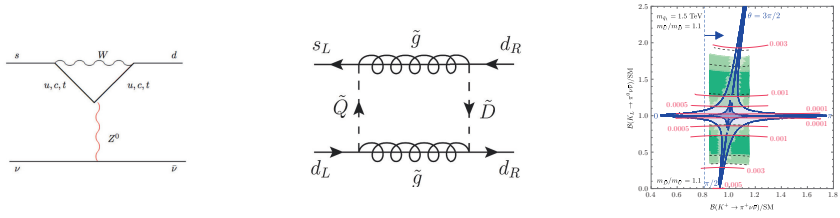


Figure 1 – $K \to \pi\nu\bar{\nu}$: SM (left), $K \to 2\pi$ isospin breaking terms ($\Im(A_2)$) and typical effects (right)

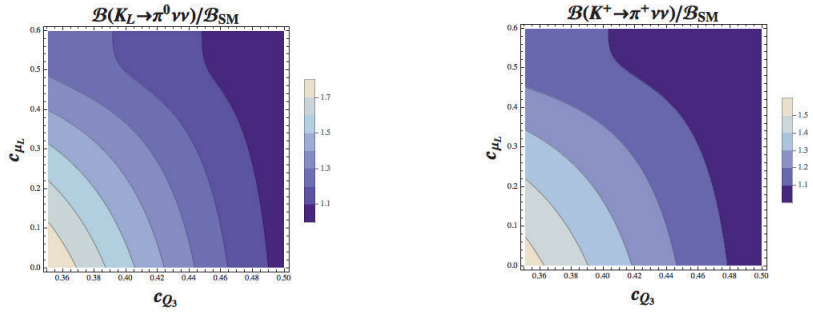


Figure 2 – RS scenario to explain B-anomalies: $B(K \to \pi\nu\bar{\nu})$ ranges as a function of fermion profiles ($c_i$'s)

expect effects at most 10% in $K^+ \to \pi^+\nu\bar{\nu}$ while are more sizable for $K_L \to \pi^0\nu\bar{\nu}$. Theoretically addressing flavor in Randall Sundrum models is more challenging: we have studied the so called flavor anarchy scenario with 5D MFV and custodial symmetry; the only sources of flavor breaking are two 5D anarchic Yukawa matrices. These matrices also generate also the bulk masses, which are responsible for the resulting flavor hierarchy. The theory flows to a next to minimal flavor violation model where flavor violation is dominantly coming from the 3rd generation. We show that it is possible to find a range of parameters for bulk masses satisfying experimental flavor constraints, but also we explain the neutral B-anomalies, requiring NP flavor scale at O(1) TeV. Then we address $K \to \pi\nu\bar{\nu}-$decays: we show the TH predictions as a function f the bulk fermion masses in Fig.2 [5]. A natural issue is to test O(1) TeV physics at LHC; we are trying to apply the technique of Ref. [6] to this purpose.

## 2 $K_{L,S} \to \mu^+\mu^-$

Recent $K_S \to \mu\overline{\mu}$ LHCB measurement is very interesting and unexpected

$$B(K_S \to \mu\overline{\mu})_{LHCB} < 9 \times 10^{-9} \text{ at } 90\ \%\ \text{CL} \qquad B(K_S \to \mu\overline{\mu})_{SM} = (5.0 \pm 1.5) \times 10^{-12}. \quad (2)$$

It represents an important milestone since it has improved the previous limit, $< 3.2{\times}10^{-7}$ at 90 % CL, lasted 40 years. It is based on a production of $10^{13}$ $K_S$ per fb$^{-1}$ inside the LHCB acceptance and it is obtained using 1.0 fb$^{-1}$ of pp collisions at $\sqrt{s} = 7$ TeV collected in 2011.

Two photon exchange generates the dominant contribution for both $K_L$ and $K_S$ decays to two muons [7]. The structure of weak and electromagnetic interactions entails a vanishing CP conserving short distance contribution to $K_S \to \mu^+\mu^-$. Indeed the SM short diagrams (similar to $K \to \pi\nu\bar{\nu}$ in Fig. 2) lead to the SM effective hamiltonian similar to eq. (1).

The LD contributions to $K_S \to \mu^+\mu^-$ Fig. (4) have been computed reliably in CHPT ($B = (5.0 \pm 1.5) \times 10^{-12}$). The relevant short distance contributions are

$$B(K_S \to \mu\overline{\mu})^{SD}_{SM} = 1 \times 10^{-5} |\Im(V^*_{ts}V_{td})|^2 \sim 10^{-13} \qquad \text{vs} \qquad B(K_S \to \mu\overline{\mu})_{NP} \leq 10^{-11} \quad (3)$$

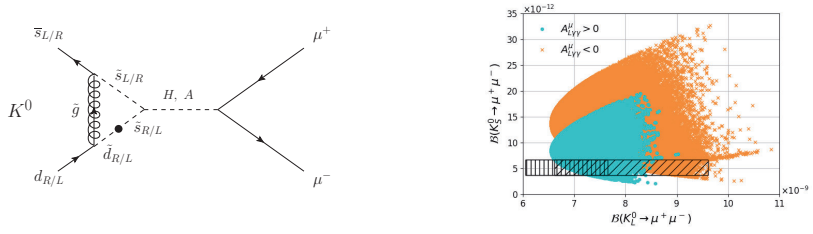


Figure 3 – Susy scenario: $K_S \to \mu\mu$ diagram (left), theory predictions: in dashed area no interference effects are considered (right)

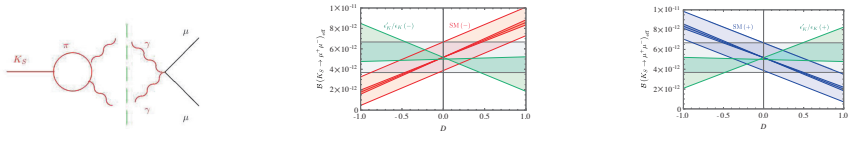


Figure 4 – $K_S$ LD diagram (left), interference effect from eq. 5 on $\mathcal{B}(K_S \to \mu^+\mu^-)$ depending on the $A_{L\gamma\gamma}$ sign: negative (center and in red SM while in green NP contributions) and positive (right and in blue SM while in green NP contributions).

We have shown that in some appealing susy scenario in Fig. (3) [8] large allowed new physics contributions (NP) can be substantially larger that SM SD contributions.

The short distance hamiltonian will contribute also to $K_L \to \mu\overline{\mu}$, through a CP conserving amplitude, $\Re(A_{\rm short})$, that has to be disentangled from the large LD two-photon exchange contributions, $A_{\gamma\gamma}$: the absorptive LD contribution is much larger than SD, in the rate respectively 25 times larger than dispersive; total ($B_{\rm expt} = (6.84 \pm 0.11) \times 10^{-9}$) To extract SD info the situation would be better if we would know the sign of $A_{\gamma\gamma}$, theoretically and experimentally unknown. While $K_L-$decays outside the LHCB fiducial volume the interference $A(K_L \to \mu\overline{\mu}^* A(K_S \to \mu\overline{\mu}$ may affect the LHCB $K_S-$rates: we can study the time interference $K_{S,L} \to \mu\mu$ ; this can be done by flavor tagging $K^0\bar{K}^0$ , specifically by detecting the associated $\pi^{\pm}$ and (or) $K^{\mp}$, determining the impurity parameter $D = \frac{K^0 - \bar{K}^0}{K^0 + \bar{K}^0}$. Then interference term will affect the measured branching [7]:

$$\mathcal{B}(K_S^0 \to \mu^+\mu^-)_{\rm eff} = \tau_S \left( \int_{t_{\rm min}}^{t_{\rm max}} dt e^{-\Gamma_S t} \varepsilon(t) \right)^{-1} \left[ \int_{t_{\rm min}}^{t_{\rm max}} dt \left\{ \Gamma(K_S^0 \to \mu^+\mu^-) e^{-\Gamma_S t} \right.\right.$$
$$\left.\left. + \frac{D f_K^2 M_K^3 \beta_\mu}{8\pi} {\rm Re}\left[ i \left( A_S A_L - \beta_\mu^2 B_S^* B_L \right) e^{-i\Delta M_K t} \right] e^{-\frac{\Gamma_S + \Gamma_L}{2} t} \right\} \varepsilon(t) \right], \tag{4}$$

Then we are i) increasing the sensitivity to short distance and ii) possibly determining the sign $A_{L\gamma\gamma}$

$$\sum_{\rm spin} \mathcal{A}(K_1 \to \mu^+\mu^-)^* \mathcal{A}(K_2 \to \mu^+\mu^-) \sim \underbrace{{\rm Im}[\lambda_t] y'_{7A}}_{SD} \left\{ \underbrace{A^{\mu}_{L\gamma\gamma}}_{LD} - 2\pi \sin^2\theta_W \left( {\rm Re}[\lambda_t] y'_{7A} + {\rm Re}[\lambda_c] y_c \right) \right\} \tag{5}$$

Experimentally, one can also access an *effective* branching ratio of $K_S^0 \to \mu^+\mu^-$ [7] which includes an interference contribution with $K_L^0 \to \mu^+\mu^-$ in the neutral kaon sample. LHCB has a beautiful

kaon physics program

| | PDG | Prospects | |
|---|---|---|---|
| $K_S \to \mu\mu$ | $< 9 \times 10^{-9}$ at 90% CL | (LD)$(5.0 \pm 1.5) \cdot 10^{-12}$ | NP $< 10^{-11}$ |
| $K_L \to \mu\mu$ | $(6.84 \pm 0.11) \times 10^{-9}$ | difficult : SD << LD | |
| $K_S \to \mu\mu\mu\mu$ | – | SM LD $\sim 2 \times 10^{-14}$ | (6) |
| $K_S \to ee\mu\mu$ | – | $\sim 10^{-11}$ | |
| $K_S \to eeee$ | – | $\sim 10^{-10}$ | |
| $K_S \to \pi^+\pi^-\mu^+\mu^-$ | – | SM LD $\sim 10^{-14}$ | |

## 3 The weak chiral lagrangian

In Ref. [9] we have studied how to determine the weak O($p^4$) chiral countertems in

$$\mathcal{L}_{\Delta S=1} = \mathcal{L}^2_{\Delta S=1} + \mathcal{L}^4_{\Delta S=1} + \cdots = G_8 F^4 \underbrace{\langle \lambda_6 D_\mu U^\dagger D^\mu U \rangle}_{K \to 2\pi/3\pi} + \underbrace{G_8 F^2 \sum_i N_i W_i}_{K^+ \to \pi^+\gamma\gamma, K \to \pi l^+ l^-} + \cdots .$$

Due to the accurate NA48/2 study of the decays $K^\pm \to \pi^\pm\pi^0\gamma$ and $K^\pm \to \pi^\pm\pi^0 e^+ e^-$ the subset of CT's in the table can be determined

| | | | |
|---|---|---|---|
| $K^\pm \to \pi^\pm\gamma^*$ | $N^r_{14} - N^r_{15}$ | $a_+ = -0.578 \pm 0.016$ | NA48/2 |
| $K_S \to \pi^0\gamma^*$ | $2N^r_{14} + N^r_{15}$ | $a_S = (1.06^{+0.26}_{-0.21} \pm 0.07)$ | NA48/1 |
| $K^\pm \to \pi^\pm\pi^0\gamma$ | $N^r_{14} - N^r_{15} - N^r_{16} - N_{17}$ | $X_E = (-24 \pm 4 \pm 4)$ GeV$^{-4}$ | NA48/2 |
| $K^+ \to \pi^+\gamma\gamma$ | $N^r_{14} - N^r_{15} - 2N^r_{18}$ | $\hat{c} = 1.56 \pm 0.23 \pm 0.11$ | NA48/2 |

(7)


### Acknowledgments

We thank the organizers for the invitation to *Moriond QCD* 2018, in particular Prof.ssa Nazila and the secretariat in particular Mrs. Vera de Sa-Varanda.


### References


1. A. Crivellin, G. D'Ambrosio, T. Kitahara and U. Nierste, Phys. Rev. D **96**, no. 1, 015023 (2017) doi:10.1103/PhysRevD.96.015023 [arXiv:1703.05786 [hep-ph]].
2. Marco Mirra, these Proceedings
3. T. Kitahara, U. Nierste and P. Tremper, Phys. Rev. Lett. **117**, no. 9, 091802 (2016) doi:10.1103/PhysRevLett.117.091802 [arXiv:1604.07400 [hep-ph]].
4. T. Hurth, C. Langenbruch and F. Mahmoudi, JHEP **1711**, 176 (2017) doi:10.1007/JHEP11(2017)176 [arXiv:1708.04474 [hep-ph]].
5. G. D'Ambrosio and A. M. Iyer, arXiv:1712.08122 [hep-ph].
6. A. Chakraborty, A. M. Iyer and T. S. Roy, arXiv:1707.07084 [hep-ph].
7. G. D'Ambrosio and T. Kitahara, *Phys. Rev. Lett.* **119**, 201802 (2017)
8. V. Chobanova, G. D'Ambrosio, T. Kitahara, M. Lucio Martinez, D. Martinez Santos, I. S. Fernandez and K. Yamamoto, JHEP **1805**, 024 (2018) doi.org/10.1007/JHEP05(2018)024 [arXiv:1708.04474 [hep-ph]] arXiv:1711.11030 [hep-ph].
9. L. Cappiello, O. Catà and G. D'Ambrosio, Eur. Phys. J. C **78**, no. 3, 265 (2018) doi:10.1140/epjc/s10052-018-5748-6 [arXiv:1712.10270 [hep-ph]].

# 11.
# Closing

# QCD AND HIGH ENERGY INTERACTIONS: MORIOND 2018 THEORY SUMMARY

Gudrun Heinrich
*Max Planck Institute for Physics, Föhringer Ring 6, 80805 Munich, Germany*

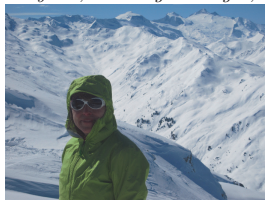

The highlights of the theory developments presented at the Rencontres de Moriond 2018 on QCD and High Energy Interactions are summarised and put into perspective.

## 1 Introduction

With the wealth of new experimental results presented at Moriond 2018 and still to come, theorists have to keep up with the increasing experimental precision, offer interpretations of the data, come up with new ideas how to probe the Standard Model and think ahead what could be beyond and how it could be tested. All these points have been addressed in may exciting talks, reflecting the current situation in particle physics from the QCD side, whose understanding in all aspects is of great importance, both in its own right and also in order to tell apart New Physics from QCD effects.

## 2 Higgs Physics and precision calculations

As the excitement about the Higgs boson discovery is ebbing away, we should not forget that we are just at the beginning of our exploration of the Higgs sector. The fact that the Higgs boson so far looks pretty Standard-Model-like means that higher order corrections in the Higgs sector are extremely important in order to establish that small deviations form the Standard Model (SM) predictions are indeed signs of New Physics. Therefore Higgs physics and precision calculations are closely related. As Keith Ellis [1] put it, new results in the Higgs sector are "guaranteed deliverables", and therefore it should be our primary goal to scrutinise the Higgs sector, in particular get a handle on the Higgs couplings to light SM particles, the total and partial widths, invisible decays and the trilinear Higgs coupling. He also presented a comparison of various future collider options and put it into perspective for the upcoming European Particle Physics Strategy document.

An update on available predictions and their uncertainties for Higgs boson production and decay was given by Michael Spira [2]. While for inclusive Higgs boson production the theoretical uncertainties nowadays are rather well under control [3,4,5], this was less the case for the Higgs

boson transverse momentum. Important progress on this subjet was presented at Moriond 2018. Luca Rottoli reported on results [6,7] based on momentum space resummation at N$^3$LL, matched to NNLO in the heavy top limit, for the Higgs boson $p_T$ spectrum, see Fig. 1(a). The same procedure also has been used to produce predictions at this level of precision for the Drell-Yan process, and the method allows to resum entire classes of observables. Results for the Higgs boson transverse momentum spectrum at N$^3$LL, matched to NNLO also have been presented very recently in Ref. [8]. However, the heavy top limit is not a good approximation in the $p_T$-range where the energy is sufficient to resolve the top quark loops. Therefore the prediction of the Higgs boson $p_T$-spectrum at NLO with full top quark mass dependence was much in demand, and has been presented by Matthias Kerner [9], showing that the full result differs from the NLO result in the heavy top approximation by about 9% at total cross section level [10]. The full top quark mass dependence significantly alters the tail of the $p_{T,H}$-distribution, as can be seen from Fig. 1(b). Note that the top-bottom interference effects for Higgs+jet at NLO are also available [11].

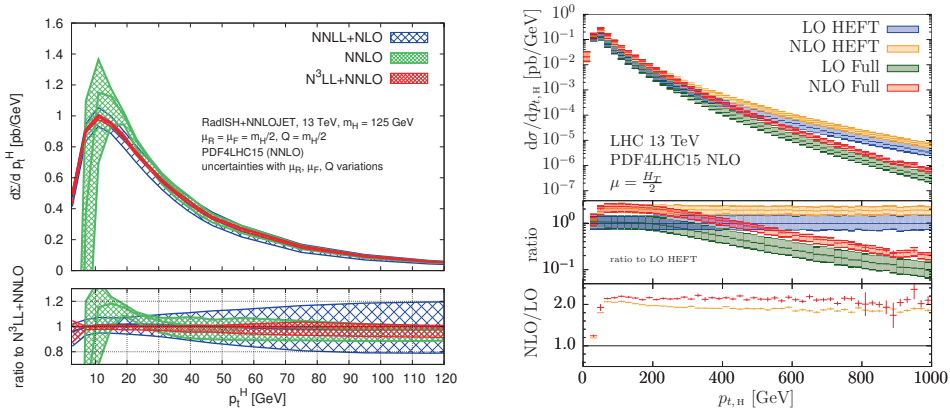


Figure 1 – Left: comparison of the transverse momentum distribution for Higgs boson production at NNLO and N$^3$LL+NNLO, NNLL+NLO, and NNLO for a central scale choice of $\mu_R = \mu_F = m_H/2$. Right: Higgs boson transverse momentum spectrum at LO and NLO QCD in the $m_t \to \infty$ limit (HEFT) and with full top-quark mass dependence. The upper panel shows the differential cross sections, the middle panel the ratio to the LO HEFT prediction, the lower panel the differential K-factors for both the HEFT (orange) and the full theory (red).

Precision calculations within models suggesting an extended Higgs sector, for example the Two-Higgs Doublet Model, are important for BSM searches. Stefan Dittmaier reported on a calculation of NLO electroweak and QCD corrections to the decay $h \to WW/ZZ \to 4$ fermions of the light CP-even Higgs boson within various types of Two-Higgs-Doublet Models, available in `PropHecy4f` [12,13], comparing also various renormalisation schemes.

Certainly, model independent approaches to the search for non-SM phenomena in the Higgs sector are also very important, and many creative ideas, also including deep learning algorithms, are emerging rapidly these days. For example, optimisations of measurements in the Higgs sector based on information geometry, was presented by Felix Kling [14,15].

## 3 Perturbative QCD at work

In the discussion session with the title "Where is New Physics?" the question was raised how well "QCD backgrounds" are under control. The answer is: better and better! At Moriond 2018, the record of loops+legs was held by Ben Ruijl (5 loops, 2 legs) and Ben Page (5 legs, 2 loops). Ben Page presented results for planar 2-loop 5-gluon amplitudes [16,17], obtained by numerical

unitarity and finite field reconstruction, thus using a method which may replace standard two-loop reduction methods at some point.

Ben Ruijl [18] presented a generalised $R^\star$ operation [19] to extract pole parts from multi-loop Feynman graphs with numerators, which has been worked out in order to calculate the 5-loop $\beta$-function [20]. He also showed results for Higgs decays to gluons at N$^4$LO [21], which reduce the scale uncertainties by almost a factor of 4 compared to N$^3$LO, such that the uncertainties due to the truncation of the perturbative series now play a sub-leading role in $\Gamma_{H\to gg}$ compared to other effects (e.g. top mass effects, $\alpha_s$).

Fabrizio Caola [22] reported about an efficient method to handle infrared divergent real radiation at NNLO, called "nested soft-collinear subtraction" [23], which has been used to calculate $pp \to WH, H \to b\bar{b}$ at NNLO [24]. Large corrections have been found at NNLO in regions which are not populated by LO, as well as interesting effects related to the fact that the $b$-quark is treated as massless.

Rhorry Gauld presented a study of the angular coefficients which parametrise the angular dependence of the decay to leptons in $Z$-boson production at NNLO [25,26], based on a calculation of $Z + X$ in the NNLOJET framework [27]. These coefficients have been measured and a tension with previous predictions has been observed for $A_0 - A_2$. It turned out that NNLO is necessary to describe the data.

David d'Enterria revisited the forward-backward asymmetry of $b$-quarks in $e^+e^- \to Z\,(\to b\bar{b})$, asking the question whether the large ($2.8\sigma$) discrepancy between data and theory predictions in $A_{FB}^{0,b}$, determined at LEP times, persists if the QCD uncertainties are re-assessed with modern simulation tools [28]. Interestingly it turns out that the QCD uncertainties are overall slightly smaller but still consistent with the original ones.

## 4 PDFs, non-perturbative QCD and Spectroscopy

Cranking up the orders in perturbative QCD is useful only if the gain in precision is not spoiled by non-perturbative effects. Major contributions to this subject concern PDF determinations and a better understanding of hadron physics.

### *4.1 New developments related to PDFs*

German Sborlini showed us that QED effects can compete with NNLO QCD effects and therefore it is important to take a photon content of the proton into account, as has been pointed out in [29]. He presented a calculation of the mixed QED-QCD splitting functions [30] and also showed a calculation of NLO QED corrections to diphoton production, pointing out that jet vetos can lead to enhanced QED effects [31].

R. Zlebcik presented a new method to calculate transverse momentum dependent parton distribution functions and its implementation into `xFitter` [32], together with applications to the $p_T$ distribution of the $Z$-boson and dijet decorrelations [33]. The version `xFitter-2.0.0` and its various functionalities has been presented by F. Giuli [34], focusing in particular on the inclusion of small-$x$ resummation. J. Fiaschi pointed out that the forward-backward asymmetry from Drell-Yan production could also be useful to be included in PDF fits [35]. Promising results have been shown from the Lattice community by S. Zafeiropoulos [36]. A new approach based on ratios of matrix elements leads to quark PDFs from first principles which are competitive with PDFs from global fits.

### *4.2 Non-perturbative QCD and hadron physics*

News about modelling quantum effects in hadronisation, in particular on a model which provides an explanation for the emergence of Bose-Einstein-like correlations without additional free

parameters, have been reported by S. Todorova-Nova [37,38]. B. Kerbikov proposed a dynamic model for sound absorption and bulk viscosity near the critical temperature [39,40].

Chris Quigg pointed out that stable heavy tetra-quark mesons of type $Q_i Q_j \bar{q}_k \bar{q}_l$ must exist in the limit of very heavy quarks $Q$. He predicts that double-beauty states will be stable against strong decays, while the double-charm states and mixed beauty-charm states will dissociate into pairs of heavy-light mesons. Observation of such states would establish the existence of tetra-quarks, and comparison with theoretical predictions for their production rate and lifetime would teach us about the role of heavy colour-antitriplet di-quarks as hadron constituents [41].

Shi-Yuan Li also pursued the deeper understanding of multi-quark states and emphasised the importance of studying hadron correlations in this context [42].

An explanation why the lifetimes of five $\Omega_c$ excited states – recently found by LHCb and confirmed by Belle – are so small, has been offered by M. Praszalowicz [43], based on an extension of the chiral quark-soliton model, where the two narrowest states are interpreted as penta-quarks belonging to the $\overline{\mathbf{15}}$ representation of $SU(3)$.

Cai-Dian Lu offered calculations of branching fractions for several doubly charmed baryon states [44], and in fact the $\Sigma_{cc}^{++}$ state has been discovered by LHCb in the decay channel $\Lambda_c^+ K^- \pi^+ \pi^+$, which has been calculated to have the largest branching fraction.

## 5 Flavour Physics

The flavour sessions started with a talk by Gudrun Hiller [45] stating the experimental facts and their possible theory implications: there are hints in semi-leptonic B-meson decays ($b \to sll$ transitions) pointing towards a violation of lepton-universality. The ratios

$$R_H = \frac{\int_{\mathrm{q}^2_{\min}}^{q^2_{\max}} dq^2 \, d\mathcal{B}/dq^2(\bar{B} \to \bar{H}\mu\mu)}{\int_{\mathrm{q}^2_{\min}}^{q^2_{\max}} dq^2 \, d\mathcal{B}/dq^2(\bar{B} \to \bar{H}ee)} \tag{1}$$

for $H = K$ and $K^*$ have been measured to deviate from unity at the $\sim 2.6\,\sigma$ level [46,47], while the radiative corrections do not exceed the percent level. The dimension six operators which can be responsible for a violation of lepton-universality can be clearly identified [48,49]. The measured ratios $R_D$ and $R_{D^*}$ ($b \to cl\nu$ transitions) also seem to indicate signs of lepton-non-universality (LNU). Rather minimal extensions of the Standard Model to account for LNU would be $U(1)$ extensions ($Z'$-models) with gauged lepton flavour [50] or leptoquarks, see Section 6. Collider searches for such states will certainly give important information complementary to the data from LHCb and Belle II.

Robert Fleischer [51] reported on a theoretical framework to study leptonic decays $B_q^0 \to l^+ l^-(q = s, d)$, which belong to the cleanest rare $B$ decays, and therefore offer an outstanding opportunity to explore the flavour sector. So far, only $B_s^0 \to \mu^+\mu^-$ has been observed, and agrees with the Standard Model expectation. On the other hand, another promising decay, $B_s^0 \to e^+e^-$, has received little attention so far because of its helicity suppressed Standard Model branching ratio, which however may be hugely enhanced through new (pseudo)-scalar contributions which lift the helicity suppression. He also pointed out that new sources of CP violation may enter the game, and presented observables which are well suited to explore in this direction, while not giving up flavour universality [51,52]. Utilising $B \to \pi K$ decays as a probe of new physics, in particular with regards to CP asymmetries, is another interesting subject. Ruben Jaarsma has presented a new state-of-the-art analysis, including also effects from electroweak penguin diagrams, which confirms the tension with current data [53,54].

Roman Zwicky explained that the contamination of right-handed currents in $B \to V\gamma$ (or $B \to V\,l\bar{l}$) decays due to long-distance effects can be controlled by considering in addition the corresponding decay $B \to A\gamma\,(l\bar{l})$, where $V/A$ are vector/axial vector mesons, exploiting the opposite relative sign of left- versus right-handed amplitudes [55,56].

Giancarlo D'Ambrosio gave us a broad overview on recent developments in Kaon physics [57], also listing models which address the $\epsilon'/\epsilon$ anomaly and discussing the interplay with B-anomalies. More details will be provided in the following section.

## 6 Beyond the Standard Model

The contributions about physics beyond the Standard Model can roughly be divided into two categories: the ones which address specifically the flavour anomalies, and the ones which don't.

In the first category (see also [58] for a small review) is a class of models presented by Andreas Crivellin [59,60], which is of Pati-Salam type, i.e. based on a gauge group where lepton number is the fourth colour. Implementing this gauge symmetry in a 5D Randall- Sundrum background, the mass scales of the Kaluza-Klein resonances, in particular the vector leptoquarks, can be in the few TeV range. The model naturally accommodates the $R_{K,K^*}$ anomalies, and in a non-minimal version also can offer an explanation of the tensions in the anomalous magnetic moment of the muon.

Abhishek Iyer also offered an explanation for the anomalies in $B$- and rare $K$-decays, in the context of custodial Randall-Sundrum models [61,62]. Two solutions are possible within such models, one where both muons and electrons play a role in lepton non-universality, and one where primarily muons play a role. More data on rare Kaon decays could serve to distinguish the two possibilities [57].

What is next if (some of) the indirect signs of New Physics in the flavour sector turn out to be firmly established? Tevong You addressed the interesting question whether we can reach the scale of New Physics which may be behind the flavour anomalies at future colliders [63,64]. Focusing on rather minimal $Z'$ and leptoquark models, the conclusion is that for narrow width $Z'$ models there is a good but not complete sensitivity at the HE-LHC, whereas FCC-hh would almost guarantee a discovery, see Fig. 2. If leptoquarks are responsible, the conclusion depends critically on the leptoquark masses, but for masses below 4.5 TeV a discovery at HE-LHC would be very likely.

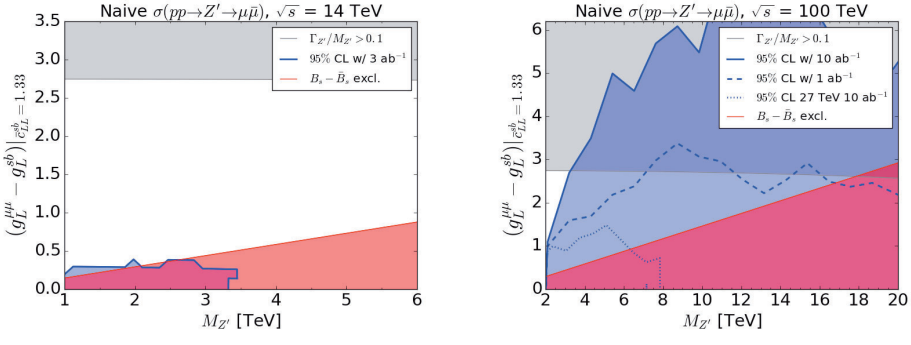


Figure 2 – Coverage of the parameter space for a minimal $Z'$-model that could explain the anomaly in $B \to K^{(*)}\mu^+\mu^-$. Left: HL-LHC, right: FCC at 100 TeV.

Extended Higgs sectors can offer solutions to open questions like the origin of dark matter, baryogenesis or unexplained hierarchies. Howie Haber gave a classification of extended Higgs sectors within the framework of two-Higgs doublet models (THDMs) [65,66]. In particular, he showed how alignment without decoupling can be achieved. George Hou presented models with extra Higgs bosons, where alignment emerges naturally, which should lead to distinctive signatures like triple top production [67,68]. Margherita Ghezzi talked about doubly charged scalars, which can arise in many BSM models, and pointed out the importance of taking finite

width effects into account [69]. Luc Darmé gave convincing arguments that scenarios with light thermal dark matter might be naturally accompanied by a corresponding light dark sector, offering prospects to detect a dark Higgs boson in the light spectrum [70,71]. Matthew McCullough offered two different solutions to the hierarchy problem [72], a linear dilaton model [73] which would lead to oscillatory signals in the $m_{\gamma\gamma}$ spectrum, and a "hyperbolic Higgs" model [74], where the Higgs boson becomes partially its own top partner.

How to compare a plethora of BSM models to data? GAMBIT [75,76] can help: it provides a general global fitting framework, including many statistical and scanning options, a fast likelihood calculator, and an extensive model database, which can be extended straightforwardly to additional models.

## 7 Conclusions

The Moriond QCD 2018 edition contained a discussion session with the title "Where is New Physics?", and one named "Heavy Flavour indirect search for New Physics". Should we combine this into the slogan "Heavy Flavour: here goes New Physics"? Even though the flavour anomalies seem to be intriguingly persistent and consistent with each other, it is certainly too early make a definite statement, but the good news is that we will have more information from the experimental side in the not too distant future, awaiting eagerly results from LHCb and Belle II.

In any case we have seen plenty of progress to improve the precision of Standard Model predictions in various aspects. Some results are showpieces of perturbation theory in QCD, others operate at the interface between QCD and electroweak corrections, or concern the deeper understanding of non-perturbative QCD. There is also much progress in providing convenient observables as well as tools to confront theory predictions with data and to identify interesting regions in the vast BSM parameter space. Some intriguing ideas about possible extensions of the Standard Model have been presented, and it is not unlikely that the model builders may soon get more hints about which direction to take.

## Acknowledgments

I am grateful to Andrzej Czarnecki for the kind invitation, and I would like to thank all the organisers of the "Rencontres de Moriond" for creating such a pleasant and fruitful environment. Thanks also to the participants for discussions about their talks (and for skiing company).

## References

1. Keith Ellis. These proceedings.
2. Michael Spira. These proceedings.
3. D. de Florian et al. Handbook of LHC Higgs Cross Sections: 4. Deciphering the Nature of the Higgs Sector. *1610.07922*.
4. Falko Dulat, Bernhard Mistlberger, and Andrea Pelloni. Differential Higgs production at $N^3LO$ beyond threshold. *JHEP*, 01:145, 2018.
5. Bernhard Mistlberger. Higgs Boson Production at Hadron Colliders at $N^3LO$ in QCD. *1802.00833*.
6. Wojciech Bizon, Xuan Chen, Aude Gehrmann-De Ridder, Thomas Gehrmann, Nigel Glover, Alexander Huss, Pier Francesco Monni, Emanuele Re, Luca Rottoli, and Paolo Torrielli. Fiducial distributions in Higgs and Drell-Yan production at $N^3LL$+NNLO. *1805.05916*.
7. Wojciech Bizon, Pier Francesco Monni, Emanuele Re, Luca Rottoli, and Paolo Torrielli. Momentum-space resummation for transverse observables and the Higgs $p_\perp$ at $N^3LL$+NNLO. *JHEP*, 02:108, 2018.
8. Xuan Chen, Thomas Gehrmann, E. W. Nigel Glover, Alexander Huss, Ye Li, Duff Neill, Markus Schulze, Iain W. Stewart, and Hua Xing Zhu. Precise QCD Description of the Higgs Boson Transverse Momentum Spectrum. *1805.00736*.

9. Matthias Kerner. These proceedings.
10. S. P. Jones, M. Kerner, and G. Luisoni. NLO QCD corrections to Higgs boson plus jet production with full top-quark mass dependence. *Phys. Rev. Lett.*, 120(16):162001, 2018.
11. Jonas M. Lindert, Kirill Melnikov, Lorenzo Tancredi, and Chris Wever. Top-bottom interference effects in Higgs plus jet production at the LHC. *Phys. Rev. Lett.*, 118(25):252002, 2017.
12. Stefan Dittmaier. These proceedings.
13. Lukas Altenkamp, Stefan Dittmaier, and Heidi Rzehak. Precision calculations for $h \to WW/ZZ \to 4$ fermions in the Two-Higgs-Doublet Model with Prophecy4f. *JHEP*, 03:110, 2018.
14. Felix Kling. These proceedings.
15. Johann Brehmer, Kyle Cranmer, Felix Kling, and Tilman Plehn. Better Higgs boson measurements through information geometry. *Phys. Rev.*, D95(7):073002, 2017.
16. Ben Page. These proceedings.
17. Samuel Abreu, Fernando Febres Cordero, Harald Ita, Ben Page, and Mao Zeng. Planar Two-Loop Five-Gluon Amplitudes from Numerical Unitarity. *1712.03946*.
18. Ben Ruijl. These proceedings.
19. Franz Herzog and Ben Ruijl. The R*-operation for Feynman graphs with generic numerators. *JHEP*, 05:037, 2017.
20. F. Herzog, B. Ruijl, T. Ueda, J. A. M. Vermaseren, and A. Vogt. The five-loop beta function of Yang-Mills theory with fermions. *JHEP*, 02:090, 2017.
21. F. Herzog, B. Ruijl, T. Ueda, J. A. M. Vermaseren, and A. Vogt. On Higgs decays to hadrons and the R-ratio at $N^4LO$. *JHEP*, 08:113, 2017.
22. Fabrizio Caola. These proceedings.
23. Fabrizio Caola, Kirill Melnikov, and Raoul Röntsch. Nested soft-collinear subtractions in NNLO QCD computations. *Eur. Phys. J.*, C77(4):248, 2017.
24. Fabrizio Caola, Gionata Luisoni, Kirill Melnikov, and Raoul Röntsch. NNLO QCD corrections to associated $WH$ production and $H \to b\bar{b}$ decay. *Phys. Rev.*, D97(7):074022, 2018.
25. Rhorry Gauld. These proceedings.
26. R. Gauld, A. Gehrmann-De Ridder, T. Gehrmann, E. W. N. Glover, and A. Huss. Precise predictions for the angular coefficients in Z-boson production at the LHC. *JHEP*, 11:003, 2017.
27. A. Gehrmann-De Ridder, T. Gehrmann, E. W. N. Glover, A. Huss, and T. A. Morgan. Precise QCD predictions for the production of a Z boson in association with a hadronic jet. *Phys. Rev. Lett.*, 117(2):022001, 2016.
28. David d'Enterria and Cynthia Yan. Forward-backward $b$-quark asymmetry at the Z pole: QCD uncertainties redux. *1806.00141*.
29. Aneesh Manohar, Paolo Nason, Gavin P. Salam, and Giulia Zanderighi. How bright is the proton? A precise determination of the photon parton distribution function. *Phys. Rev. Lett.*, 117(24):242002, 2016.
30. Daniel de Florian, Germn F. R. Sborlini, and Germn Rodrigo. Two-loop QED corrections to the Altarelli-Parisi splitting functions. *JHEP*, 10:056, 2016.
31. German Sborlini. These proceedings.
32. https://www.xfitter.org/xFitter/.
33. Radek Zlebcik. These proceedings.
34. Francesco Giuli. These proceedings.
35. Juri Fiaschi. These proceedings.
36. Kostas Orginos, Anatoly Radyushkin, Joseph Karpie, and Savvas Zafeiropoulos. Lattice QCD exploration of parton pseudo-distribution functions. *Phys. Rev.*, D96(9):094503, 2017.
37. Sarka Todorova-Nova. These proceedings.
38. Sarka Todorova-Nova. Modeling of quantum effects in the hadronization. *1801.10232*.
39. Boris Kerbikov. These proceedings.
40. Boris Kerbikov. Sound Attenuation in Quark Matter Due to Pairing Fluctuations. *EPJ Web Conf.*, 125:04013, 2016.
41. Chris Quigg. Stable Tetraquarks. *1804.04929*.
42. Shi-Yuan Li. These proceedings.
43. Michal Praszalowicz. Exotic interpretation of $\Omega_c$ excited states. *1805.03862*.
44. Cai-Dian Lu. These proceedings.
45. G. Hiller. Lepton nonuniversality anomalies and implications. *1804.02011*.
46. Andrew Crocombe. These proceedings.
47. Johannes Albrecht. These proceedings.

48. Gudrun Hiller and Martin Schmaltz. Diagnosing lepton-nonuniversality in $b \to s\ell\ell$. *JHEP*, 02:055, 2015.
49. Gudrun Hiller and Frank Krüger. More model-independent analysis of $b \to s$ processes. *Phys. Rev.*, D69:074020, 2004.
50. Wolfgang Altmannshofer, Stefania Gori, Maxim Pospelov, and Itay Yavin. Quark flavor transitions in $L_\mu - L_\tau$ models. *Phys. Rev.*, D89:095033, 2014.
51. Robert Fleischer. New Probes of New Physics with Leptonic Rare B Decays. *1805.05625*.
52. Robert Fleischer, Daniela Galrraga Espinosa, Ruben Jaarsma, and Gilberto Tetlalmatzi-Xolocotzi. CP Violation in Leptonic Rare $B_s^0$ Decays as a Probe of New Physics. *Eur. Phys. J.*, C78(1):1, 2018.
53. Ruben Jaarsma. These proceedings.
54. Robert Fleischer, Ruben Jaarsma, and K. Keri Vos. Towards New Frontiers with $B \to \pi K$ Decays. *1712.02323*.
55. Roman Zwicky. These proceedings.
56. James Gratrex and Roman Zwicky. Parity Doubling as a Tool for Right-handed Current Searches. *1804.09006*.
57. Giancarlo D'Ambrosio. These proceedings.
58. Andreas Crivellin et al. PSI/UZH Workshop: Impact of $B \to \mu^+\mu^-$ on New Physics Searches. *1803.10097*.
59. Andreas Crivellin. These proceedings.
60. Monika Blanke and Andreas Crivellin. $B$ Meson Anomalies in a Pati-Salam Model within the Randall-Sundrum Background. *1801.07256*.
61. Abhishek Iyer. These proceedings.
62. Giancarlo D'Ambrosio and Abhishek M. Iyer. Flavour issues in warped custodial models: $B$ anomalies and rare $K$ decays. *1712.08122*.
63. Tevong You. Can We Reach the Scale of New Physics Behind the $B$ Anomalies? 2018.
64. B. C. Allanach, Ben Gripaios, and Tevong You. The case for future hadron colliders from $B \to K^{(*)}\mu^+\mu^-$ decays. *JHEP*, 03:021, 2018.
65. Howard E. Haber. Approximate Higgs alignment without decoupling. *1805.05754*.
66. Patrick Draper, Howard E. Haber, and Joshua T. Ruderman. Partially Natural Two Higgs Doublet Models. *JHEP*, 06:124, 2016.
67. George Hou. These proceedings.
68. Masaya Kohda, Tanmoy Modak, and Wei-Shu Hou. Searching for new scalar bosons via triple-top signature in $cg \to tS^0 \to tt\bar{t}$. *Phys. Lett.*, B776:379–384, 2018.
69. Margherita Ghezzi. These proceedings.
70. Luc Darmé, Soumya Rao, and Leszek Roszkowski. Light dark sector at colliders and fixed target experiments. *1805.06179*.
71. Luc Darmé, Soumya Rao, and Leszek Roszkowski. Light dark Higgs boson in minimal sub-GeV dark matter scenarios. *JHEP*, 03:084, 2018.
72. Matthew McCullough. These proceedings.
73. Gian F. Giudice, Yevgeny Kats, Matthew McCullough, Riccardo Torre, and Alfredo Urbano. Clockwork / Linear Dilaton: Structure and Phenomenology. *1711.08437*.
74. Timothy Cohen, Nathaniel Craig, Gian F. Giudice, and Matthew Mccullough. The Hyperbolic Higgs. *1803.03647*.
75. Pat Scott. These proceedings.
76. https://gambit.hepforge.org.

# FROM QCD TO COSMOLOGY

TIM M.P. TAIT

*Department of Physics & Astronomy, University of California, Irvine, CA 92617 USA*

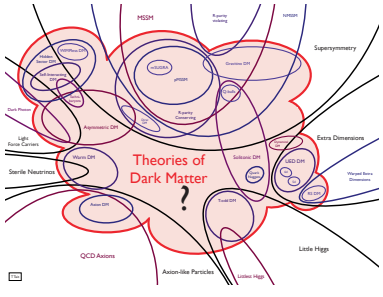


This summary of the talk "From QCD to Cosmology" was presented in the joint QCD and Cosmology session of the 53rd Rencontres de Moriond, held March 17-24, 2018 in La Thuile. It is a meditation on the connections between the wide array of interesting subjects taking place in both sessions of the conference.

## 1 Introduction

It was really a pleasure to prepare this talk for the joint session between QCD and Cosmology at Moriond. For many years, my work has been somewhere between these two subjects, and I have always felt in previous visits that I profited from the fact that they are held on the same week – this year was no different! In constructing this talk, I chose a few topics which I found to be particularly interesting which highlight the rich cross pollinization between the two areas. It is obviously very personalized and incomplete in that sense as far as the choice of topics is concerned, and the referencing will similarly be abbreviated.

## 2 Dark Matter

As is well known, the identity of the dark matter, which is required by observations of the cosmos on a wide variety of length scales, remains mysterious, and may represent a crucial piece of information necessary to extend the Standard Model (SM) of particle physics. While there are many theoretical ideas for how to extend the SM in order to incorporate dark matter, there is currently no clear incontrovertible experimental signs that any one is favored. There is rich interplay between our knowledge of QCD and the physics of many candidate ideas about dark matter.

### 2.1 WIMPs

For example, a large and popular class of dark matter theories invoke weakly-interacting massive particles (WIMPs), whose observed abundance in the Universe can be understood through a history in which they are originally in thermal equilibrium with the SM plasma, but eventually fall out of equilibrium due to the expansion of the Universe, at which point their abundance freezes out. For particles whose masses are around the weak scale, this typically takes place while the Universe is hot enough that the hadronic degrees of freedom are described by a weakly coupled plasma of quarks and gluons. For this reason, the nature of the interactions of WIMPs with quarks and/or gluons are often the key to understanding the WIMP relic density. In addition, two of the major searches for WIMP-like particles, their production at high energy accelerators and their scattering with heavy nuclei, reflect these same interactions.

Theories in which dark matter interacts primarily with quarks are well-trod theoretical ground, and have been extensively studied in the context of effective field theories[1,2] and simplified models[4,3]. Searches using mono-jet[5] or for dijet resonances at the LHC are quite mature and probing interesting regions of parameter space[6]. However, there are still interesting theoretical constructions which are not captured by these simplified models. For example, one can construct a model in which the dark matter is a scalar particle, which interacts with another colored scalar particle (through a renormalizable quartic interaction), and thereby at loop level with gluons[7,8]. In such a construction, the color and electroweak charges of the mediator scalar sweep out a family of related theories, and because they need not decay into a single dark particle, they typically do not contribute to missing momentum signals at the LHC. The mono-jet signal receives its leading order contribution at one loop, though the suppression may be compensated for large color representation of the mediator[9]. Such a theory serves as a guidepost to theories in which the dark matter interacts with the SM through loop processes, and theories for which the LHC searches for colored mediators can look very different from supersymmetric theories.

There are also potentially interesting lessons for the physics of dark matter from the techniques developed to understand QCD itself. A beautiful example are the calculations of dark matter annihilation for heavy, electroweakly charged particles. For heavy WIMPs, the $W$ and $Z$ bosons are effectively massless, and accurate estimates of the annihilation rate must re-sum multiple particle exchanges. A recent calculation[10] applying technology from soft collinear effective theory, finds that large corrections relative to more naive treatments are typical.

The QCD phase transition is an important event. Where it occurs relative to the period in which dark matter is produced may play an important factor in determining the resulting dark matter abundance. For a weak scale WIMP, freeze out is typically well before the phase transition. In the SM, the phase transition is predicted to be a cross-over, but for heavier or lighter $u$, $d$, and $s$ quarks, it would have been first order[11]. The fact that the transition region is close to the quark masses realized in nature is an indication that it is plausible that some kind of presently unknown physics could change the story while having so far escaped direction.

### 2.2 Sterile Neutrinos

Another motivated dark matter candidate is a sterile neutrino, often invoked as an ingredient in theories which modify the SM to explain the observation that active neutrino flavors oscillate over long distances. At the loop level, sterile neutrinos can decay into an active neutrino and a photon, but it can be long enough lived to play the role of dark matter provided its mass and mixing with the active neutrinos are both small enough. An interesting regime of mass is around a few keV, where it can have a sufficient lifetime, but is not so light that it would interfere with the formation of galaxies to a noticeable degree. There are intriguing (and controversial) $X$-ray signals which might provide hints that such particles exist and are slowly decaying today[12,13].

One mechanism to produce sterile neutrinos is through out-of-equilibrium scattering of the active neutrinos on the background plasma. For keV masses, this process is maximal at tem-

peratures around 130 MeV – right at the QCD phase transition! As a result, the nature of the phase transition can influence the resulting abundance of sterile neutrinos as dark matter, which affects the mapping from the particle physics parameters to their final density[14,15]. As a result, detailed measurements of both the parameters of sterile neutrinos and the QCD phase transition can assemble a picture of cosmology at temperatures of $\sim 100$ MeV.

### *2.3 Axions*

The axion is another light dark matter candidate, whose very existence is inspired by the strong CP problem, which contrasts the fact that the QCD Lagrangian admits a term which violates CP, and yet searches for an electric dipole moment of the neutron have so far yielded only null results, implying that the coefficient of this term must be less than about $10^{-10}$. Such a tiny value for a quantity that could have been $\mathcal{O}(1)$ begs for some kind of dynamical explanation. The leading candidate theory works by positing that this coefficient is itself a scalar field, which the QCD dynamics then adjusts to zero[16]. The quantum fluctuations in this field are usually referred to as "axions", and owing to their pseudo-Goldstone boson nature are extremely light, weakly coupled fields which can play the role of dark matter[17,18].

The axion abundance is often seeded by a primordial misalignment in the value of the field in the early Universe. When QCD confines, and the axion experiences a potential, it begins to oscillate, acting like nonrelativistic particles. The temperature dependence of the mass thus influences the mapping between the initial misalignment and the final density of dark matter, and so controls our understanding of the relationship between the particle physics and cosmology. As an intrinsically non-perturbative phenomenon, the axion mass is best studied via lattice gauge theory, which has recently made good progress toward providing accurate calculations[19,20].

## 3 QCD and Dark Energy

The QCD phase transition also poses a question for dark energy. The current observation of the acceleration of the expansion of the Universe points to a tiny but non-zero cosmological constant. At the same time, one generically expects that a phase transition will contribute a quantity of order the temperature at which it occurs to the effective cosmological constant. Bellazini et. al.[21] present this as a different way of parsing the famous cosmological constant problem which is more grounded in known physics than the usual framing. In particular, it suggests that the QCD phase transition contributed something of order $(100 \text{ MeV})^4$, which either had to be delicately cancelled against a bare contribution, or adjusted away by some dynamics.

An interesting way to explore this idea is furnished by the interiors of neutron stars, which are thought to be likely to exist in a different phase of QCD owing to the incredibly high baryon densities. A different phase is characterized by different expectation values of QCD condensates, which is likely to result in an order $(100 \text{ MeV})^4$ shift in the effective dark energy in cores of such stars. This in turn implies a shift in the equation of state of the stellar material, leading to a different and possibly observable mass-radius equilibrium condition, or visible modifications of the wave-form of gravitational waves produced in neutron star mergers[22].

## 4 QCD as a Metaphor

Finally, it may be that QCD provides a guide to the construction of a theory of dark matter. A new confined force leads to massive particles which may interact very weakly with the SM, while still experiencing strong self-interactions. For example, a dark SU(N) gauge theory without any matter at all has dark matter in the form of dark glueballs. If (mild) hints for scattering from small scale structure are taken seriously, they suggest a confinement scale of a few hundred MeV – amusingly close to $\Lambda_{\text{QCD}}$! – to explain the observations[23,24].

**Acknowledgments**

I am grateful to the organizers for organizing a delightful meeting filled with very interesting physics. My research is supported in part by the US NSF through grant No. PHY-1620638.

**References**

1. J. Goodman, M. Ibe, A. Rajaraman, W. Shepherd, T. M. P. Tait and H. B. Yu, Phys. Lett. B **695**, 185 (2011) doi:10.1016/j.physletb.2010.11.009 [arXiv:1005.1286 [hep-ph]].
2. J. Goodman, M. Ibe, A. Rajaraman, W. Shepherd, T. M. P. Tait and H. B. Yu, Phys. Rev. D **82**, 116010 (2010) doi:10.1103/PhysRevD.82.116010 [arXiv:1008.1783 [hep-ph]].
3. A. DiFranzo, K. I. Nagao, A. Rajaraman and T. M. P. Tait, JHEP **1311**, 014 (2013) Erratum: [JHEP **1401**, 162 (2014)] doi:10.1007/JHEP11(2013)014, [arXiv:1308.2679].
4. Y. Bai, P. J. Fox and R. Harnik, JHEP **1012**, 048 (2010) doi:10.1007/JHEP12(2010)048 [arXiv:1005.3797 [hep-ph]].
5. M. Beltran, D. Hooper, E. W. Kolb, Z. A. C. Krusberg and T. M. P. Tait, JHEP **1009**, 037 (2010) doi:10.1007/JHEP09(2010)037 [arXiv:1002.4137 [hep-ph]].
6. See e.g. the talks by Katharina Bierwagen and Carl Gwilliam at Moriond 2018 QCD.
7. R. M. Godbole, G. Mendiratta and T. M. P. Tait, JHEP **1508**, 064 (2015) doi:10.1007/JHEP08(2015)064 [arXiv:1506.01408 [hep-ph]].
8. Y. Bai and J. Osborne, JHEP **1511**, 036 (2015) doi:10.1007/JHEP11(2015)036 [arXiv:1506.07110 [hep-ph]].
9. R. M. Godbole, G. Mendiratta, A. Shivaji and T. M. P. Tait, Phys. Lett. B **772**, 93 (2017) doi:10.1016/j.physletb.2017.06.019 [arXiv:1605.04756 [hep-ph]].
10. M. Baumgart, T. Cohen, I. Moult, N. L. Rodd, T. R. Slatyer, M. P. Solon, I. W. Stewart and V. Vaidya, JHEP **1803**, 117 (2018) doi:10.1007/JHEP03(2018)117 [arXiv:1712.07656 [hep-ph]].
11. For a review: B. J. Schaefer and M. Wagner, Prog. Part. Nucl. Phys. **62**, 381 (2009) doi:10.1016/j.ppnp.2008.12.009 [arXiv:0812.2855 [hep-ph]].
12. E. Bulbul, M. Markevitch, A. Foster, R. K. Smith, M. Loewenstein and S. W. Randall, Astrophys. J. **789**, 13 (2014) doi:10.1088/0004-637X/789/1/13 [arXiv:1402.2301].
13. A. Boyarsky, O. Ruchayskiy, D. Iakubovskyi and J. Franse, Phys. Rev. Lett. **113**, 251301 (2014) doi:10.1103/PhysRevLett.113.251301 [arXiv:1402.4119 [astro-ph.CO]].
14. K. N. Abazajian and G. M. Fuller, Phys. Rev. D **66**, 023526 (2002) doi:10.1103/PhysRevD.66.023526 [astro-ph/0204293].
15. T. Venumadhav, F. Y. Cyr-Racine, K. N. Abazajian and C. M. Hirata, Phys. Rev. D **94**, no. 4, 043515 (2016) doi:10.1103/PhysRevD.94.043515 [arXiv:1507.06655 [astro-ph.CO]].
16. R. D. Peccei and H. R. Quinn, Phys. Rev. Lett. **38**, 1440 (1977). doi:10.1103/PhysRevLett.38.1440
17. S. Weinberg, Phys. Rev. Lett. **40**, 223 (1978). doi:10.1103/PhysRevLett.40.223
18. F. Wilczek, Phys. Rev. Lett. **40**, 279 (1978). doi:10.1103/PhysRevLett.40.279
19. E. Berkowitz, M. I. Buchoff and E. Rinaldi, Phys. Rev. D **92**, no. 3, 034507 (2015) doi:10.1103/PhysRevD.92.034507 [arXiv:1505.07455 [hep-ph]].
20. R. Kitano and N. Yamada, JHEP **1510**, 136 (2015) doi:10.1007/JHEP10(2015)136 [arXiv:1506.00370 [hep-ph]].
21. B. Bellazzini, C. Csaki, J. Hubisz, J. Serra and J. Terning, JHEP **1606**, 104 (2016) doi:10.1007/JHEP06(2016)104 [arXiv:1502.04702 [astro-ph.CO]].
22. C. Cski, C. Erncel, J. Hubisz, G. Rigo and J. Terning, arXiv:1802.04813 [astro-ph.HE].
23. K. K. Boddy, J. L. Feng, M. Kaplinghat and T. M. P. Tait, Phys. Rev. D **89**, no. 11, 115017 (2014) doi:10.1103/PhysRevD.89.115017 [arXiv:1402.3629 [hep-ph]].
24. K. K. Boddy, J. L. Feng, M. Kaplinghat, Y. Shadmi and T. M. P. Tait, Phys. Rev. D **90**, no. 9, 095016 (2014) doi:10.1103/PhysRevD.90.095016 [arXiv:1408.6532 [hep-ph]].

# Future Steps in CMB Cosmology

Jens Chluba
*Jodrell Bank Centre for Astrophysics, School of Physics and Astronomy, University of Manchester, Oxford Road, Manchester M13 9PL, UK*

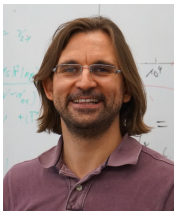

The cosmic microwave background (CMB) has proven itself to be an invaluable source of cosmological information. Since the early measurements with COBE in the 90's, we have greatly advanced our studies of the CMB temperature and polarization anisotropies. This helped us to establish the ΛCDM concordance model, with its key parameters being determined to (sub) percent-level precision today. The main next steps with CMB anisotropies are the cosmic-variance-limited extraction of cosmological information from the *E*-mode polarization patterns and the search for primordial *B*-modes predicted by inflation models. However, as highlighted in this contribution, in addition to the CMB anisotropies the CMB energy spectrum provides unique complementary cosmological information that is within reach of present-day technology. This will allow us to probe processes in the pre- and post-recombination Universe, shedding new light on inflation, reionization, recombination and early-universe particle physics, as outlined here.

## 1 Introduction and motivation

The standard ΛCDM cosmology has been shown to describe our Universe to extremely high accuracy [1,2,3,4]. This model is based upon a spatially flat, expanding Universe with dynamics governed by General Relativity and whose dominant constituents at late times are cold dark matter (CDM) and a cosmological constant ($\Lambda$). The primordial seeds of structures are furthermore Gaussian-distributed adiabatic fluctuations with an almost scale-invariant power spectrum thought to be created by inflation. We know the main cosmological parameters of the ΛCDM model (e.g., the total, CDM and baryon densities, the CMB photon temperature, expansion rate, etc.) to (sub) percent-level precision [4,5]. Assuming standard Big Bang Nucleosynthesis (BBN) and a standard thermal history, we can furthermore derive precise values for the helium abundance, $Y_{\rm p}$, and effective number of relativistic degrees of freedom, $N_{\rm eff}$ [6]. Also the physics of the recombination era, which determines the decoupling of photons and baryons around redshift $z \simeq 10^3$, is now believed to be well understood within ΛCDM [7,8].

Of the many cosmological data sets, measurements of the cosmic microwave background (CMB) temperature and polarization anisotropies, beyond doubt, have driven the development towards the era of precision cosmology over the past decades. We have exhausted practically all information about the primordial Universe contained in the primary CMB temperature power spectra. Sources of secondary CMB anisotropies related to the Sunyaev-Zeldovich effect [9] have been mapped in detail [10,11] and a beautiful

all-sky picture of the large-scale lensing potential has been constructed [12]. *WMAP* and *Planck* have also clearly seen the $E$-mode polarization signals [13,14,15], although there still is much more information left before reaching the cosmic variance limit on $E$-modes. And finally, from measurements of the $B$-mode polarization patterns we derived upper limits on the tensor-to-scalar ratio, which already rule out large classes of early-universe models [4,16].

We are now entering an exciting new chapter in cosmological studies using the CMB. The next steps with CMB anisotropies are pretty clear: several sub-orbital experiments and space-based missions/concepts (e.g., *BICEP3, CLASS, SPTpol, ACTpol, SPIDER, PIPER, LiteBird, PIXIE, COrE+, PICO, CMB-Bharat, PRISTINE*) are rushing to detect the primordial $B$-modes at large angular scales and to squeeze every last bit of information out of the $E$-mode signals, all to deliver the long-sought proof of inflation, refine our understanding of the late Universe (e.g., reionization, lensing science) and answer questions about extensions of the standard cosmological model [17,18,19,20,21].

However, it is well known that CMB *spectral distortions* – tiny departures of the average CMB energy spectrum from that of a perfect blackbody – deliver a new independent probe of different processes occurring in the early Universe. The case for spectral distortions has been made several times and the physics of their formation is well understood (for recent overview see [22,23,24,25,26,27]). The purpose of this contribution is to provide an overview of various distortion signals created within ΛCDM (Fig. 3) and to highlight a few new-physics examples (i.e., decaying particles or evaporating primordial black holes) that could cause additional interesting signals to look for. Thus far, no all-sky distortion has been found [28,29]; however, innovative experimental concepts, such as *PIXIE* [30,31], *PRISTINE* and *CMB-Bharat*, are being actively discussed and promise improvements of the earlier measurements with *COBE/FIRAS* by several orders of magnitude. Similarly, from the ground novel concepts are being considered (e.g., *APSERa* [32], *COSMO*). It is thus time to ask what information could be extracted from the CMB energy spectrum and how this could help us refine our understanding of the Universe.

## 2 CMB spectral distortion physics

This section provides a brief summary of CMB spectral distortion physics. The pioneering works on this topic are mainly due to Yakov Zeldovich and Rashid Sunyaev in the 60's and 70's [9,33,34,35]. These early works were later extended by [36,37], to include the effect of double Compton emission, and [38,39], with refined numerical and analytical treatments. Latest considerations of spectral distortion and their science can be found in [22,23,24,25,26,40] and [41,42,43] for the recombination radiation. For more in depth reading we refer to recent lecture notes [27].

Since the measurements of COBE/FIRAS in the mid-90's we know that the energy spectrum of the cosmic microwave background (CMB) is extremely close to that of a perfect blackbody at an average temperature $T_0 = (2.726 \pm 0.001)\,\mathrm{K}$ [28,29]. However, a number of early-universe processes are expected to create CMB spectral distortions at a level that is within reach of present-day technology. This provides strong motivation to study the physics of CMB spectral distortions and ask what these small signals might be able to tell us about the Universe we live in.

The physics going into the cosmological *thermalisation* calculation — the process that restores the pure blackbody spectrum after some departure from thermal equilibrium — are pretty simple and well understood, allowing us to make precise predictions for different thermal histories and energy release scenarios [22,24]. For primordial spectral distortions, we are mainly concerned with the average CMB spectrum, so that spatial perturbations can be neglected and the Universe can be described as uniformly expanding, thermal plasma consisting of free electrons, hydrogen and helium atoms and their corresponding ions inside a uniform bath of CMB photons. We shall also restrict ourselves to redshifts $z \lesssim \mathrm{few}\times 10^7$, when electron-positron pairs already completely disappeared, since earlier thermalisation is perfect from any practical point of view and no observable distortion remains.

Under these circumstances, any energy release or photon production inevitably causes a momentary distortion of the CMB spectrum. In the early Universe, the double Compton (DC) and Bremsstrahlung (BR) processes are controlling the number of CMB photons, while Compton scattering (CS) allows

photons to diffuse in energy/frequency. The interplay of these interactions between matter and radiation determines the precise shape of the CMB spectrum at any stage of its evolution. When studying different energy release mechanisms, one question thus is whether there was enough time between the energy release and our measurement of the spectrum to *produce* and *redistribute* those distortion photons [a], thereby completing the thermalisation process.

### 2.1 Distortion visibility function

The thermalisation problem has been studied thoroughly both analytically [9,33,35,37,45,44,46,47,48] and numerically [38,39,49,50,22,51,24]. From these studies, the following simplified picture can be drawn (Fig. 1): at $z \gtrsim 2\times10^6$, when the Universe is less than a few month old, the thermalisation process is extremely efficient and practically any distortion can be erased until today. At lower redshifts, the CMB spectrum becomes vulnerable to disturbances in the thermal history and only small amounts of energy or photons can be ingested without violating the tight experimental bounds from COBE/*FIRAS* [52,28,53] and other distortion measurements [54,55,56].

The transition from efficient to inefficient thermalisation is encoded by the *distortion visibility function*, $\mathcal{J}(z,z')$, which determines by how much the distortion amplitude (regardless of its shape) is suppressed between two redshifts $z$ and $z'<z$. Due to the huge entropy of the Universe (there are $\simeq 1.6\times10^9$ times more photons than baryons), the DC process [57,58,59,60] is the most important source of soft photons at high redshifts ($z \gtrsim 4\times10^5$), such that the distortion visibility function is roughly given by $\mathcal{J}(z,z') \approx \mathrm{e}^{-(z/z_{\rm dc})^{5/2}}\mathrm{e}^{(z'/z_{\rm dc})^{5/2}}$, with thermalisation redshift $z_{\rm dc}\approx 1.98\times10^6$, which is determined by the efficiency of DC photon production and Compton redistribution [37,38,39]. Improved approximations for the visibility function exist [46,48], but for simple estimates the above expression suffices. Since we are interested in the final distortion, for our purpose we set $z'=0$ and then use $\mathcal{J}(z)=\mathcal{J}(z,0)=\mathrm{e}^{-(z/z_{\rm dc})^{5/2}}$. The distortion visibility function thus cuts off exponentially for $z\gtrsim z_{\rm dc}$. How far into the *cosmic photosphere* [61] — the epoch of the Universe during which $\mathcal{J}\ll1$ — one could view, thus depends on the absolute sensitivity of the experiment and how much initial energy had to be thermalised. For instance, with a PIXIE-type experiment [30], one might be able to detect a distortion created as early as $z\simeq6\times10^6$ if $\Delta\rho_\gamma/\rho_\gamma\simeq0.01$ of energy were liberated by some process. At much later times ($z\lesssim$ few $\times10^5$), the distortion visibility is very close to unity ($\leftrightarrow$ basically all injected energy will still be visible as a distortion today) and the upper limits from COBE/*FIRAS* imply $\Delta\rho_\gamma/\rho_\gamma\lesssim6\times10^{-5}$ [28]. With a PIXIE-type experiment, this could be improved to $\Delta\rho_\gamma/\rho_\gamma\lesssim8\times10^{-9}$, allowing us to constrain tiny amounts of energy release due to (standard) processes occurring in our Universe.

### 2.2 Types of primordial distortions

While the distortion visibility tells us how much of the released energy will still be visible as a spectral distortion today, it does not fix the *shape* of the distortion. Here, three regimes are most important: at $z\gg2\times10^6$, thermalisation is extremely efficient (distortion visibility $\mathcal{J}\ll1$) and CS, DC and BR are able to adjust the initial blackbody spectrum, $B_\nu(T)$, at temperature $T$ to a new blackbody, $B_\nu(T+\Delta T)\approx B_\nu(T)+\partial_T B_\nu(T)\Delta T+\mathcal{O}(\Delta T^2/T^2)$, with $\Delta T/T\approx(1/4)\Delta\rho_\gamma/\rho_\gamma$ assuming that a total energy of $\Delta\rho_\gamma/\rho_\gamma\ll1$ was released (Fig. 1). In the next regime, valid until $z\simeq3\times10^5$, the efficiency of DC and BR gradually reduces while photons are still efficiently redistributed in energy by the Compton process. In this case, electrons and photons are in kinetic equilibrium with respect to CS, forming a *chemical potential* or $\mu$-distortion [33], but thermalisation stops being complete ($\leftrightarrow$ the distortion visibility function $\mathcal{J}$ approaches unity). Thus, the departure from the initial blackbody is given by the superposition of a temperature shift and a pure $\mu$-distortion. At $z\lesssim10^4$, up-scattering of photons by electrons also becomes inefficient and photons diffuse only a little in energy. In this era, a Compton-$y$ distortion is formed, also known in connection with the Sunyaev-Zeldovich effect of galaxy clusters [9]. The classical $\mu$- and $y$-distortion, have

[a] Energy release is the most common mechanism to produce distortions. However, the adiabatic cooling of matter in fact extracts energy from the CMB [44,22], so that an excess of photons is found in the CMB spectrum. In this case, the DC and BR processes absorb photons.

a slightly different shapes (Fig. 1). For a $\mu$-distortion, the deviation from the CMB blackbody vanishes at $\nu \simeq 124\,\mathrm{GHz}$, while the cross-over frequency for a $y$-distortion is $\nu \simeq 217\,\mathrm{GHz}$. With future experiments, one can thus hope to distinguish these two types of distortions, and since a $\mu$-distortion can only be formed in the very early stage of the Universe, its amplitude directly constrains episodes of early energy release at $z \gtrsim 5 \times 10^4$ or until about 100 years after the Big Bang.

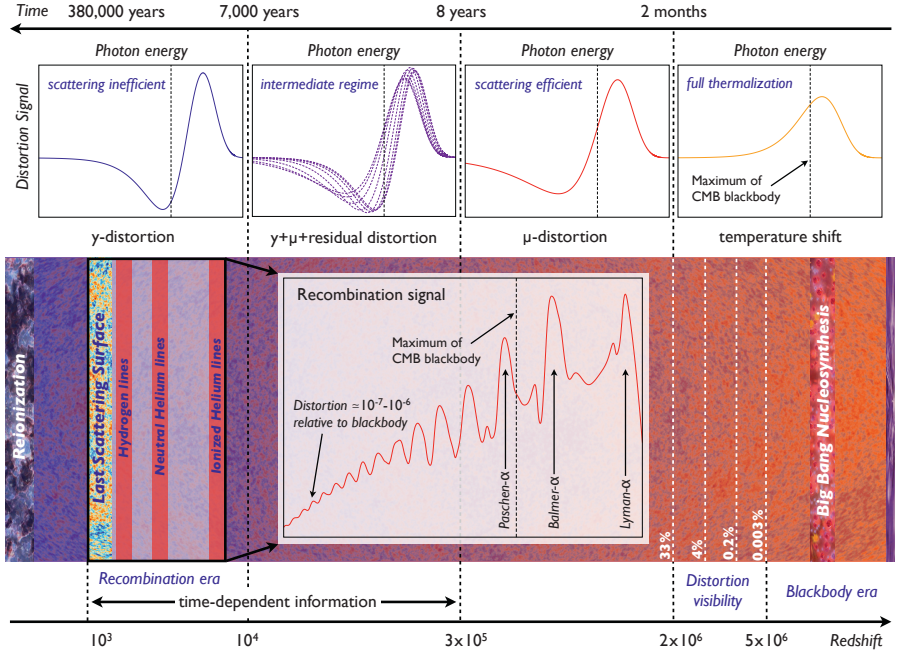


Figure 1 – Various phases for the evolution of CMB spectral distortions in the history of the Universe. At redshift $z_\mathrm{h} \gtrsim \mathrm{few} \times 10^6$, thermalisation is very rapid and a temperature shift is created. Around $z_\mathrm{h} \simeq 3\times10^5$ a pure $\mu$-distortion appears, while at $z_\mathrm{h} \lesssim 10^4$ a pure $y$-distortion is formed. At all intermediate stages, the signal is given by a superposition of these extreme cases with a small (non-$\mu$/non-$y$ or $r$-type) residual distortion that contains valuable information about the time-dependence of the energy-release process in particular at $z \simeq 10^4 - 3\times10^5$. At redshifts $z \simeq 10^3 - 10^4$, an additional rich distortion signal is created by the recombining hydrogen and helium atoms (Figure adapted from[62]).

The shape of primordial distortions caused by energy release is close to a superposition of the extreme cases described above. However, at $10^4 \lesssim z \lesssim 3\times10^5$, scattering becomes inefficient in redistributing photons over frequency and the distortion morphs between a $\mu$- and $y$-distortion, but the transition is non-linear in the energy exchange and a smaller residual (non-$\mu$/non-$y$ or $r$-type) distortion is formed in addition. The sum of $y$-, $\mu$- and $r$-distortion is sometimes called *intermediate* or *hybrid* distortion, but additional information is only gained from the *residual* distortion. Although in earlier numerical studies this regime was also mentioned [38,63], only in the past years it was stressed that the residual distortion contains valuable time-dependent information [22,47,51], which allows us to distinguish different energy release scenarios [24,64]. This adds another dimension to the CMB, delivering more than just two numbers related to the $\mu$- and $y$-distortion amplitudes. This is especially important since at late times ($z \lesssim 10-20$), the formation of structures reheats the medium to temperatures $T \simeq 10^4\,\mathrm{K} - 10^5\,\mathrm{K}$. In this era, a large uniform $y$-distortion is formed with $y \simeq 10^{-7} - 10^{-6}$ [65,66,67,68,69,70,71], which will swamp any primordial $y$-signal. Without the $r$-distortion we were left only with the amplitude of the $\mu$-distortion and thus could just constrain the overall energy release!

### 2.3 *Computing and characterising the distortion*

It is straightforward to calculate the distortion for any energy release history directly integrating the corresponding Boltzmann equations [35,38,39,50]. One flexible numerical approach is `CosmoTherm` [b] [22], which for the first time allowed direct integration of the thermalisation problem explicitly including full time-dependence for a wide range of energy-release scenarios. However, for case-by-case studies and parameter estimation full numerical approaches are currently too time-consuming. Fortunately, the problem can be simplified: generally we expect the distortion to be very small, so that the Boltzmann equations can be linearised. In this case, a Green's function approach can be used [51]. This allows us to precisely calculate the distortion for a wide range of energy release scenarios and perform parameter estimations, as first shown in [24].

For estimates, it is usually sufficient to compute the effective energy release within the different distortion eras, splitting $\mu$ and $y$-era at $z \simeq 5 \times 10^4$. For the $y$-type distortion, this yields the $y$-parameter $y \simeq (1/4)\Delta\rho_\gamma/\rho_\gamma$ [9] and for the $\mu$-distortion one has $\mu \approx 1.4\,\Delta\rho_\gamma/\rho_\gamma$ [33]. A detailed comparison of various analytic approximations was given in [40].

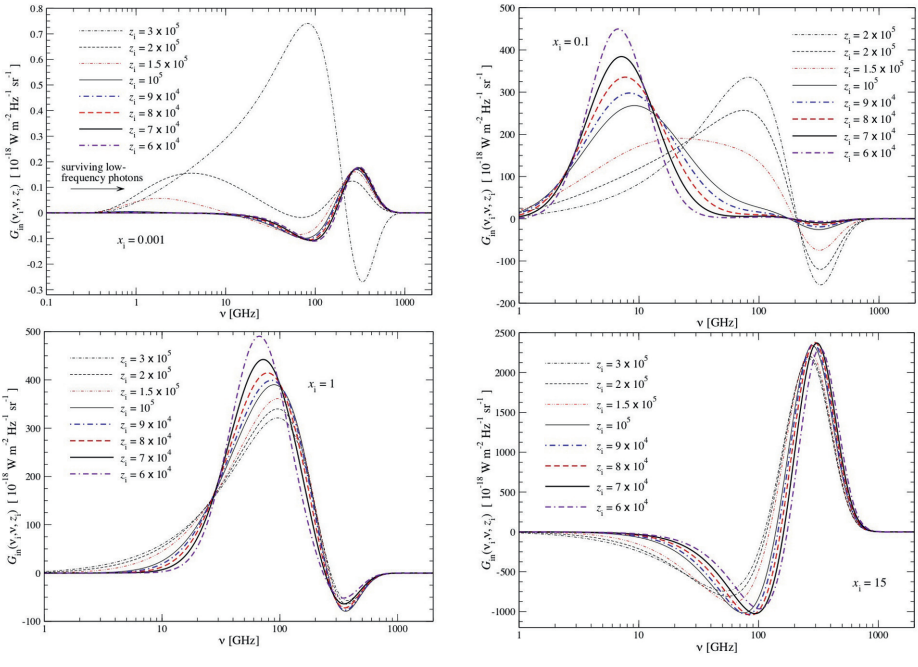


Figure 2 – Spectral distortions created by photon injection at different frequencies and initial redshifts. The signal shows a rich phenomenology, beyond the standard $\mu$ and $y$ distortion shapes. The Figure is taken from [72].

### 2.4 *Photon injection distortions*

In addition to distortions from energy release, we can also create distortions by photon injection. As shown by [72], these can have a much more rich phenomenology than just the broad $\mu$ and $y$-distortions created by energy release. This is illustrated in Fig. 2 for several cases, showing that the final distortion depends on both the injection time and frequency.

[b] `www.Chluba.de/CosmoTherm`

In terms of physics, distortions created by photon injection do not directly heat the electrons or baryons. Only once Comptonization becomes relevant do the electrons start heating or cooling. The net effect depends on the injection frequency of the photons. For frequencies $x_i = h\nu_i/kT_\gamma \gtrsim 3.6 - 3.8$, photons on average loose energy heating the matter. This causes a broad $\mu$- and $y$-type contribution to the total distortion signal, which for extremely high frequency injection, $x_i \gtrsim 10$, can dominate. At lower frequencies, cooling of the medium occurs since photons are on average up-scattered. This can create negative $\mu$ and $y$-type contributions[72]. In addition, for $x_i \gg 1$, a significant number of secondary particles can built up, leading to interesting new effects from the particle cascade[72].

Photon injection distortions are by no means exotic. For example, the cosmological recombination radiation[42], one of the standard ΛCDM distortions, is created by photon injection. Injection of photons can also occur in decaying or annihilating particle scenarios or evaporation of primordial black holes. In light of recent measurements of EDGES[73] and the ARCADE low-frequency excess[74,56,75], photon injection distortions of the CMB have become a very interesting possibility. This is because these observations potentially point towards a connection with photon injection (or absorption) from decaying or annihilating particles and their low energy by-products in form of non-thermal Bremsstrahlung or synchrotron emission[72,76,77,78].

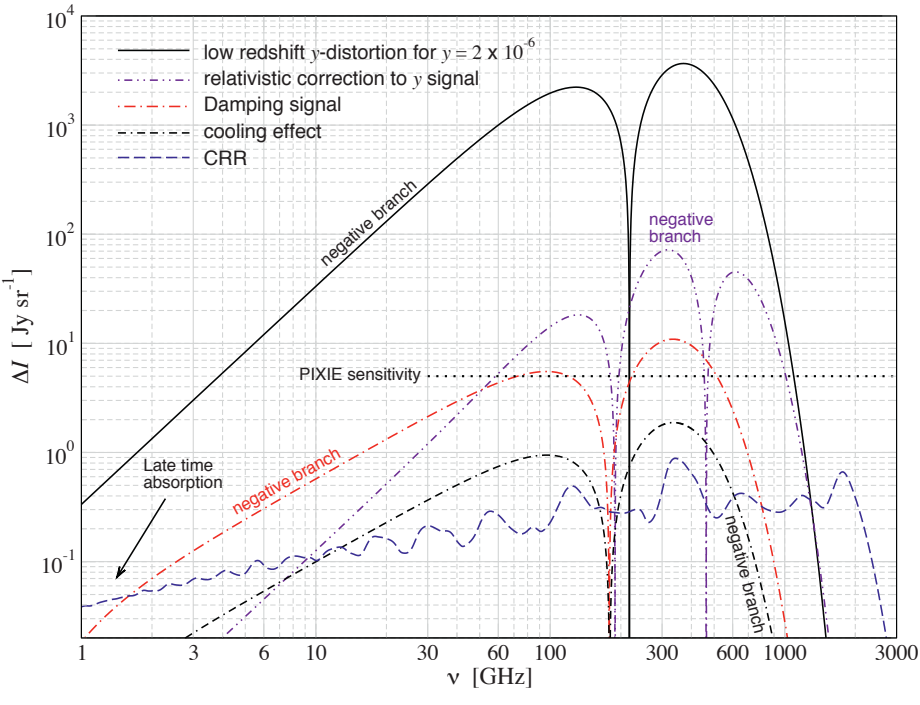


Figure 3 – Comparison of several CMB monopole distortion signals produced in the standard ΛCDM cosmology. The low-redshift distortion created by reionization and structure formation is close to a pure Compton-$y$ distortion with $y \simeq 2 \times 10^{-6}$. Contributions from the hot gas in low mass haloes give rise to a noticeable relativistic temperature correction, which is taken from[79]. The damping and adiabatic cooling signals were explicitly computed using `CosmoTherm`[22]. The cosmological recombination radiation (CRR) was obtained with `CosmoSpec`[43]. The estimated sensitivity ($\Delta I_\nu \approx 5\,\mathrm{Jy/sr}$) of PIXIE is shown for comparison (dotted line). The figure was taken from[40].

## 3 CMB spectral distortion signals from various scenarios

Several exhaustive reviews on various spectral distortion scenarios exist [22,23,24,25,26,40], covering both standard and non-standard processes. Here we highlight some of the main distortion signals expected within ΛCDM and only briefly mention more exotic sources of distortions. A summary of the relevant ΛCDM distortions is shown in Fig. 3.

The distortion templates are available at `www.Chluba.de/CosmoTherm`.

### *3.1 Reionization and structure formation*

The first sources of radiation during reionization [66,80], supernova feedback [70] and structure formation shocks [65,67,69,68] heat the intergalactic medium at low redshifts ($z \lesssim 10$), producing hot electrons (in a wide range of temperatures $T_{\rm e} \simeq 10^4\,{\rm K} - 10^6\,{\rm K}$) that partially up-scatter CMB photons, causing a Compton $y$-distortion. Although this is the *largest* expected average distortion of the CMB caused within ΛCDM, its amplitude is quite uncertain and depends on the detailed structure and temperature of the medium, as well as scaling relations (e.g., between halo mass and temperature). Several estimates for this contribution were obtained, yielding values for the total $y$-parameter at the level $y \simeq$ few $\times\, 10^{-6}$ [69,71,79,81,26].

Following [79], we use a fiducial value of $y = 2\times10^{-6}$ (see Fig. 3). This is dominated by the low-mass end of the halo function ($M \simeq 10^{13}\,M_\odot$) and the signal should be detectable with a PIXIE-type experiment at more than $10^3\,\sigma$. The detection significance reduces to a few hundred $\sigma$ when including estimates for the CMB foregrounds [82], but still this provide a sensitive probe of reionization and structure formation physics. Future CMB imagers (e.g., CORE and PICO) furthermore have the potential to separate the spatially varying signature caused by the warm hot intergalactic medium (often referred to as WHIM) and proto-clusters [69,71], if the challenge of accurate channel intercalibration can be overcome.

Because the signal is so easily detectable, small corrections due to the high gas temperature ($kT_{\rm e} \simeq 1\,{\rm keV}$) become noticeable [79]. The relativistic temperature correction can be computed using the temperature moment method of `SZpack` [83,84] and differs from the distortions produced in the early Universe (see Fig. 4). This correction should be detectable with PIXIE at $\simeq 10-20\,\sigma$ [79,82] and could teach us about the average temperature of the intergalactic medium, promising a way to solve the missing baryon problem [67]. Both distortion signals are illustrated in Fig. 3.

### *3.2 Damping of primordial small-scale perturbations*

The damping of small-scale fluctuations of the CMB temperature set up by inflation at wavelength $\lambda < 1\,{\rm Mpc}$ causes another inevitable distortion of the CMB spectrum [86,87,88,89,90]. The idea behind this mechanism is extremely simple and just based on the mixing of blackbodies with varying temperatures through Thomson scattering (see Fig. 5). However, the process was only recently described rigorously [91,92], allowing us to perform detailed computations of the associated distortion signal for different early-universe models [91,93,94,95,24,96,97]. The distortion is sensitive to the amplitude and shape of the power spectrum at very small scales (wavenumbers $1\,{\rm Mpc}^{-1} \lesssim k \lesssim 2\times10^4\,{\rm Mpc}^{-1}$ corresponding to multipoles $10^5 \lesssim \ell \lesssim 10^8$) and thus provides a promising new way for constraining inflation while modes are still evolving in the linear regime.

In the early days of CMB cosmology, this effect was already used to derive first upper limits on the spectral index of scalar perturbations, yielding $n_{\rm S} \lesssim 1.6$ from COBE/FIRAS [89]. Perturbation modes with $1\,{\rm Mpc}^{-1} \lesssim k \lesssim 50\,{\rm Mpc}^{-1}$ create $y$-distortions, while modes with $50\,{\rm Mpc}^{-1} \lesssim k \lesssim 2\times10^4\,{\rm Mpc}^{-1}$ yield $\mu$-distortions. These scales are hard to access by any other means but spectral distortions provide a new sensitive probe in this regime (Fig. 6).

For a given initial power spectrum of perturbations, the effective heating rate in general has to be computed numerically [91]. However, at high redshifts the tight coupling approximation can be used to simplify the calculation [91,98]. We can then directly compute the associated distortion using `CosmoTherm` [22]. The various isocurvature perturbations can be treated in a similar manner [98]; however, in the standard

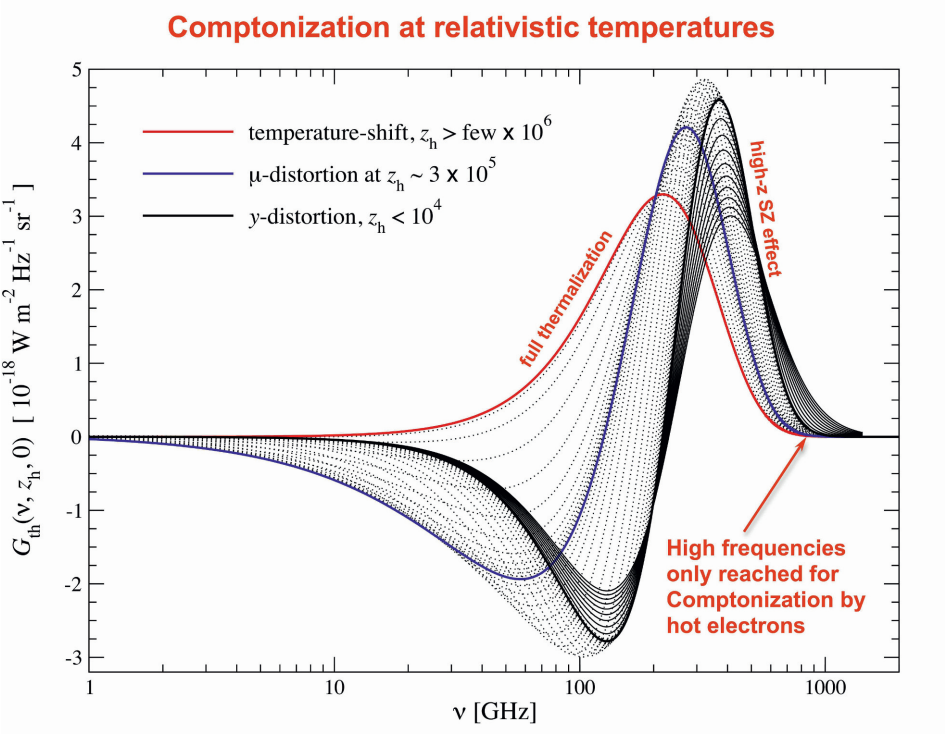


Figure 4 – Illustration for the effect of relativistic temperature corrections on the distortion signal. In the primordial Universe, electrons hardly reach temperatures $\simeq$ 1 keV during the thermalization era ($z \lesssim 10^6$). Therefore even repeated Compton scattering cannot push the distortion signals beyond the standard non-relativistic $y$-distortion signal. Inside clusters of galaxies, electrons can have temperatures $kT_e \gtrsim 1$ keV. In this case, the distortion signals can extend to much higher frequencies.

inflation model these should be small. Tensor perturbations also contribute to the dissipation process, but the associated heating rate is orders of magnitudes lower than for adiabatic modes even for very blue tensor power spectra and thus can be neglected[99,100].

For standard power spectrum parameters $A_s = 2.207 \times 10^{-9}$, $n_S = 0.9645$ and $n_{run} = 0^4$, we present the result in Fig. 3. The adiabatic cooling distortion (see Sect. 3.3) was simultaneously included. The signal is uncertain to within $\simeq$ 10% in ΛCDM, simply because of the remaining uncertainties in the measurement of $A_s$ and $n_S$. It is described by a sum of $\mu$- and $y$-distortion with $\mu \approx 2.0 \times 10^{-8}$ and $y \approx 3.6 \times 10^{-9}$ and a non-vanishing overall residual at the level of $\simeq 20\% - 30\%$[40]. In terms of raw sensitivity, this signal is close to the detection limit of a PIXIE-like experiment; however, foregrounds in particular at low frequencies make a detection more challenging [82]. Still, a PIXIE-like experiment could place interesting upper limits on the amplitude of scalar fluctuations around $k \simeq 10^3$ Mpc$^{-1}$ [93,64], potentially helping to shed light on the small-scale crisis [101] and rule out models of inflation with increased small-scale power[96,102].

The damping signal is also sensitive to primordial non-Gaussianity in the squeezed-limit, leading to a spatially varying spectral signal that correlates with CMB temperature anisotropies as large angular scales [103,104]. This effect therefore provides a unique way for studing the scale-dependence of $f_{NL}$ [105,106,107,108,109,110]. CMB spectral distortions hence deliver a complementary and independent probe of early-universe physics, which allows capitalizing on the synergies with large-scale $B$-mode polarization measurements.

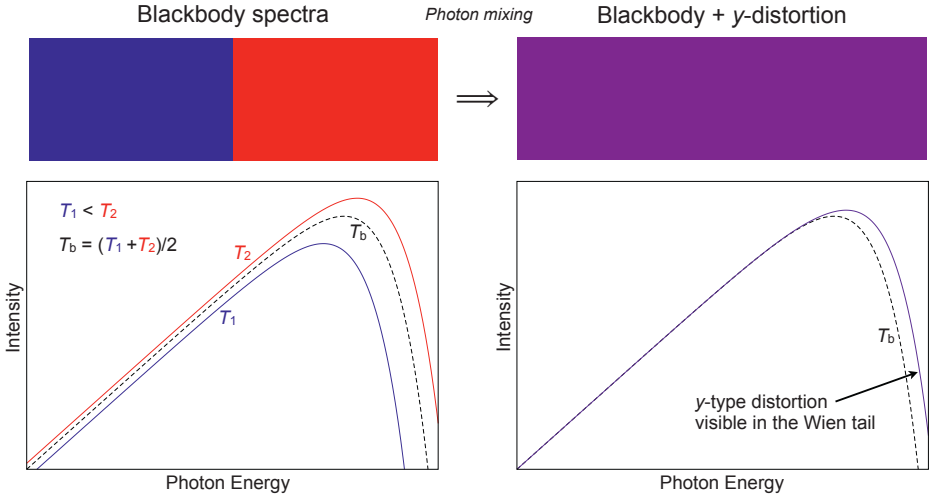


Figure 5 – Illustration for the superposition of blackbodies. We envision blackbody photons inside a box at two temperatures $T_1$ and $T_2$, and mean $T_b = \frac{1}{2}(T_1 + T_2)$ initially (left panel). Thomson scattering mixes the two photon distributions without changing the photon number or energy. The averaged distribution is not a pure blackbody but at second order in the temperature difference exhibits a $y$-type distortion in the Wien tail (right panel). This then starts the thermalization process and repeated Compton scattering slowly converts the distortion to a $\mu$-distortion.

### *3.3 Adiabatic cooling for baryons*

The adiabatic cooling of ordinary matter continuously extracts energy from the CMB photon bath by Compton scattering, leading to another small but guaranteed distortion that directly depends on the baryon density and helium abundance. The distortion is characterized by *negative* $\mu$- and $y$-parameters at the level of $\simeq$ few $\times\, 10^{-9}$ [44,22,111]. For *Planck* 2015 parameters, the signal is shown in Fig. 3. It is uncertain at the $\simeq 1\%$ level in $\Lambda$CDM and cancels part of the damping signal; however, it is roughly one order of magnitude weaker and cannot be separated at the currently expected level of sensitivity of next generation CMB spectrometers.

Additional interactions of dark matter with photons, electrons or protons could further increase the cooling distortion [112]. This allows placing interesting constraints on the nature of dark matter and its interactions with the standard sectors. The recent EDGES measurements [73] have spurred increased interest in this possibility [113,114,115].

### *3.4 The cosmological recombination radiation*

The cosmological recombination process is associated with the emission of photons in free-bound and bound-bound transitions of hydrogen and helium [116,117,118]. This causes a small distortion of the CMB and the redshifted recombination photons should still be visible as the cosmological recombination radiation (CRR), a tiny spectral distortion ($\simeq$ nK-$\mu$K level) present at mm to dm wavelength (for overview see [42]). The amplitude of the CRR depends directly on the number density of baryons in the Universe. The helium abundance furthermore affects the detailed shape of the recombination lines, while the number of neutrinos has a minor effect [43]. Finally, the line positions and widths depend on when and how fast the Universe recombined. The CRR thus provides an independent way to constrain cosmological parameters and map the recombination history [119].

Several computations of this CRR have been carried out in the past [120,121,122,123,41,124,125,126,127,128]. These calculations were very time-consuming, taking a few days of supercomputer time for one cosmology [125,128]. This big computational challenge was recently overcome [129,43], today allowing us to

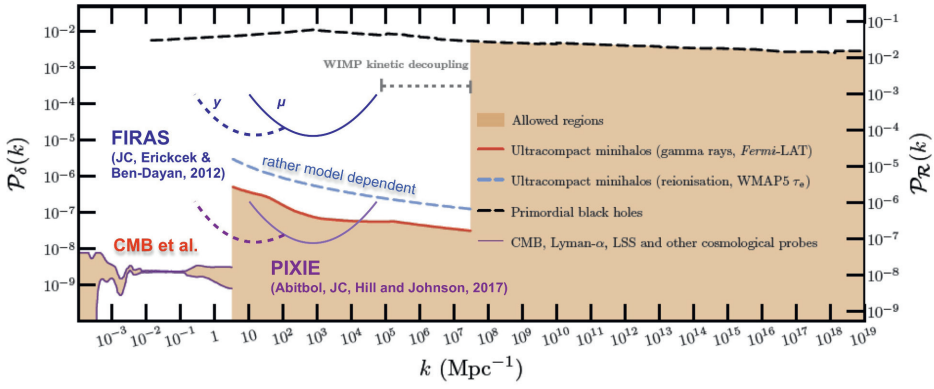


Figure 6 – Current constraints on the small-scale power spectrum. At large scales ($k \lesssim 3\,\mathrm{Mpc}^{-1}$), CMB anisotropies and large scale structure measurements provide very stringent limits on the amplitude and shape of the primordial power spectrum. At smaller scales, the situation is much more uncertain and at $3\,\mathrm{Mpc}^{-1} \lesssim k \lesssim 10^4\,\mathrm{Mpc}^{-1}$, which can be targeted with CMB spectral distortion measurements, wiggle room of at least two orders of magnitude is present. Future CMB distortion measurements could improve these limits to a level similar to the large-scale constraints. The figure is adapted from[85].

compute the CRR in about 15 seconds on a standard laptop using `CosmoSpec`[c 43]. The *fingerprint* from the recombination era shows several distinct spectral features that encode valuable information about the recombination process (Fig. 3). Many subtle radiative transfer and atomic physics processes [125,127,7,8] can now be included by `CosmoSpec`, yielding the most detailed and accurate predictions of the CRR in the standard ΛCDM model to date (see Fig. 7). In ΛCDM, the CRR is uncertain at the level of a few percent, with the error being dominated by atomic physics rather than cosmological parameter values[43].

The CRR is currently roughly $\simeq 6$ times below the estimated detection limit of PIXIE (cf. Fig. 3) and a detection from space will require several times higher sensitivity [130]. In the future, this could be achieved by experimental concepts similar to PRISM[17] or Millimetron[131]. At low frequencies ($1\,\mathrm{GHz} \lesssim \nu \lesssim 10\,\mathrm{GHz}$), the significant spectral variability of the CRR may also allow us to detect it from the ground with APSERa[32]. This could open a new way for directly studying the conditions of the Universe at $z \simeq 10^3$ (HI-recombination), $z \simeq 2000$ (HeI-recombination) and $z \simeq 6000$ (HeII-recombination). Furthermore, if something unexpected happened during different stages of the recombination epoch, atomic species will react to this [132] and produce additional distortion features that can exceed those of the normal recombination process. This will provide a unique way to distinguish pre- from post-recombination energy release [132,133].

To appreciate the importance of the cosmological recombination process at $z \simeq 10^3$ a little more, consider that today measurements of the CMB anisotropies are sensitive to uncertainties of the ionization history at a level of $\simeq 0.1\% - 1\%$ [134,135]. For a precise interpretation of CMB data, uncertainties present in the original recombination calculations had to be reduced by including several previously omitted atomic physics and radiative transfer effects [136,134]. This led to the development of the new recombination modules CosmoRec[7] and HyRec[8] which are used in the analysis of Planck data[3]. Without these improve treatments of the recombination calculation the value for $n_\mathrm{S}$ would be biased by $\Delta n_\mathrm{S} \simeq -0.01$ to $n_\mathrm{S} \simeq 0.95$ instead of $\simeq 0.96$ [135]. We would be discussing different inflation models [137] without these corrections taken into account! Conversely, this emphasizes how important it is to experimentally confirm the recombination process and CMB spectral distortions provide a way to do so.

[c] `www.Chluba.de/CosmoSpec`

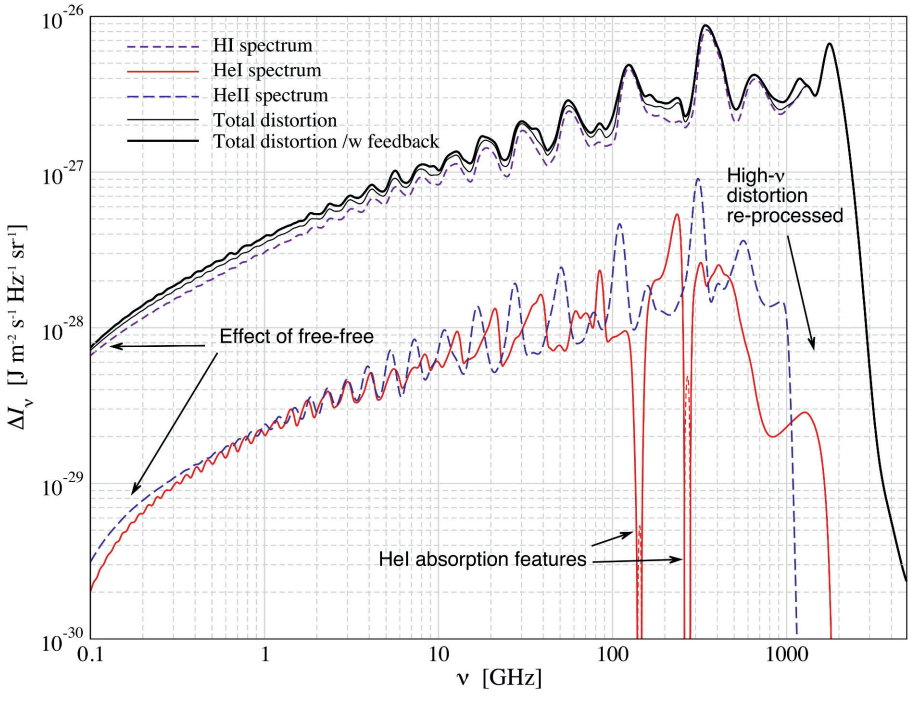


Figure 7 – CRR from hydrogen and helium for 500-shell calculations. The different curves show individual contributions (without feedback) as well as the total distortion with and without feedback processes. At low frequencies, free-free absorption becomes noticeable. The effect is stronger for the contributions from helium due to the larger free-free optical depth before recombination ends at $z \simeq 10^3$. In total, some $6.1\gamma$ are emitted per hydrogen atom when all emission and feedback are included. Hydrogen alone contributes about $5.4\gamma/N_{\rm H}$ and helium $\simeq 0.7\gamma/N_{\rm H}$ ($\simeq 8.9\gamma/N_{\rm He}$). The Figure was taken from[43].

### *3.5 Dark matter annihilation*

Today, cold dark matter is a well-established constituent of our Universe[2,3,4]. However, the nature of dark matter is still unclear and many groups are trying to gather any new clue to help unravel this big puzzle [138,139,140,141,142,85,143]. Similarly, it is unclear how dark matter was produced, however, within ΛCDM, the WIMP scenario provides one viable solution [144,145]. In this case, dark matter should annihilate at a low level throughout the history of the Universe and even today.

For specific dark matter models, the level of annihilation around the recombination epoch is tightly constrained with the CMB anisotropies [139,146,147,148,142,149,150,4]. The annihilation of dark matter can cause changes in the ionization history around last scattering ($z \simeq 10^3$), which in turn can lead to changes of the CMB temperature and polarization anisotropies [151,152,153,154]. Albeit significant dependence on the interaction of the annihilation products with the primordial plasma [155,148,156,157,158], the same process should lead to distortions of the CMB [159,133,22]. Sadly, it turns out that for the standard WIMP scenario with s-wave annihilation cross section, the expected signal is even smaller than the adiabatic cooling distortion[24]. We will thus not go into more details here.

### *3.6 Decaying particle scenarios*

The CMB spectrum also allows us to place stringent limits on decaying particles in the pre-recombination epoch [163,164,160,165,159,133,22]. This is especially interesting for decaying particles with lifetimes $t_{\rm X} \simeq$

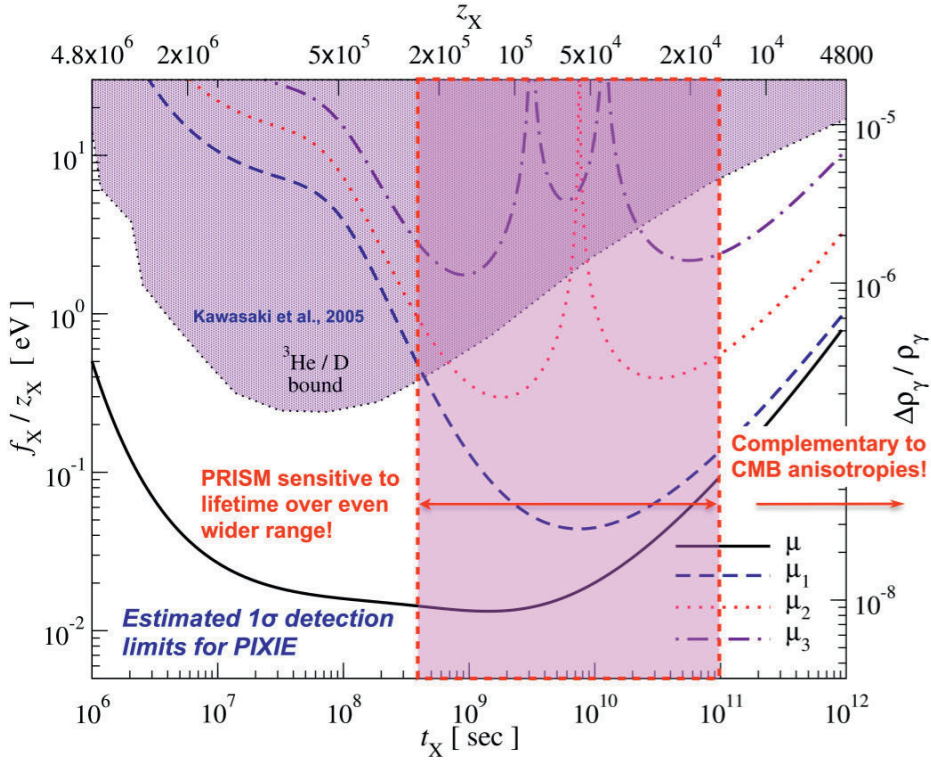


Figure 8 – Decaying particle detection limits ($1\sigma$) for a PIXIE-like experiment. The eigenamplitudes $\mu_i$ characterize the non-$\mu$/non-$y$ distortion signal [64], which provides time-dependent information of the energy release history. CMB distortion limits could be $\simeq$ 50 times tighter than those derived from light element abundances [160,?]. A separate determination of lifetime and particle abundance could be possible for lifetimes $t_X \simeq 10^8$ sec – $10^{11}$ sec, being complementary to constraints derived using the CMB anisotropies [151,152,162]. The figure is adapted from [64].

$10^8$ sec – $10^{11}$ sec [24,64], as the exact shape of the distortion encodes when the decay occurred. Decays associated with significant low-energy photon production could furthermore create a unique spectral signature that can be distinguished from simple energy release [72]. This would provide an unprecedented probe of early-universe particle physics (e.g., dark matter in excited states [166,167]), with many natural particle candidates found in supersymmetric models [168,169]. This could also shed light on gravitino physics [164,170], axions [171] and primordial black holes [172,173].

The expected $1\sigma$ detection limits for a PIXIE-like experiment are illustrated in Fig. 8. The bounds obtained from measurements of light-elements [160,161] could be superseded by more than one order of magnitude. Similar improvements from light-elements are not expected any time soon, and most recent updated only improved the limits by $\simeq 10\%$ [174]. Spectral distortions thus provide a powerful new probe of particle physics.

### *3.7 Anisotropic CMB distortions*

To close the discussion of different distortion signals, we briefly mention anisotropic ($\leftrightarrow$ *spectral-spatial*) CMB distortions. Even in the standard $\Lambda$CDM cosmology, anisotropies in the spectrum of the CMB are expected. The largest source of anisotropies is due to the Sunyaev-Zeldovich effect caused by the hot

plasma inside clusters of galaxies[9,175,176,177], as mentioned above. The $y$-distortion power spectrum has already been measured directly by Planck[10,11] and encodes valuable information about the atmospheres of clusters[69,178,179,180,181,182,81]. Similarly, the warm hot intergalactic medium contributes and should become visible[71,81].

In the primordial Universe, anisotropies in the $\mu$ and $y$ distortions are expected to be tiny (relative perturbations $\lesssim 10^{-4}$, e.g., see[183]) unless strong spatial variations in the primordial heating mechanism are expected[91]. As mentioned above, this could in principle be caused by non-Gaussianity of perturbations in the squeezed limit[103,104,105,106,107,108]; however, a present detectable levels of non-Gaussianity are beyond $\Lambda$CDM cosmology (see[109] for discussion of some of the foreground issues) and will not be considered further.

Another guaranteed anisotropic signal is due to Rayleigh scattering of CMB photons in the Lyman-series resonances of hydrogen around the recombination era[184,185]. The signal is strongly frequency dependent, can be modelled precisely and may be detectable with future CMB imagers (e.g., COrE+) or possibly PIXIE at large angular scales[185]. In a very similar manner, the resonant scattering of CMB photons by metals appearing in the dark ages[186,187,188,189] or scattering in the excited levels of hydrogen during recombination[190,?] can lead to anisotropic distortions. To measure these signals, precise channel intercalibration and foreground rejection is required.

Due to our motion relative to the CMB rest frame, the spectrum of the CMB dipole should also be distorted simply because the CMB monopole has a distortion[191,192]. The signal associated with the large late-time $y$-distortion could be detectable with PIXIE at the level of a few $\sigma$[192]. Since for these measurements no absolute calibration is required, this effect will allow us to check for systematics. In addition, the dipole spectrum can be used to constrain monopole foregrounds[192,26,193].

Finally, due to the superposition of blackbodies of different temperatures (caused by the spherical harmonic expansion of the intensity map), the CMB quadrupole spectrum is also distorted, exhibiting a $y$-distortion related to our motion[194,195]. The associated effective $y$-parameter is $y_{\rm Q} = \beta^2/6 \approx (2.525 \pm 0.012) \times 10^{-7}$ and should be noticeable with PIXIE and future CMB imagers[193].

## 4 Conclusions

CMB spectral distortion measurements provide a unique way for studying physical processes leading to energy release or photon injection in the pre- and post-recombination eras. In the future, this could open a new unexplored window to early-universe and particle physics, delivering independent and complementary pieces of information about the Universe we live in. We highlighted several processes that should lead to distortions at a level within reach of present-day technology. Different distortion signals can be computed precisely and efficiently for various scenarios using both analytical and numerical schemes. Time-dependent information, beyond the standard $\mu$- and $y$-type parametrization, may allow us to independently constrain lifetime and abundance of decaying relic particles, learn about the shape and amplitude of the small-scale power spectrum of primordial perturbations and shed light on dark matter. The cosmological recombination radiation will allow us to check our understanding of the recombination processes at redshifts of $z \simeq 10^3$. It furthermore should allow us to distinguish pre- from post-recombination $y$-distortions. All this emphasizes the immense potential of CMB spectroscopy, both in terms of *discovery* and *characterization* science, and we should make use of this invaluable source of information with the next CMB space mission and worldwide ground-based efforts.


## Acknowledgments

JC is supported by the Royal Society as a Royal Society University Research Fellow and an European Research Council Consolidator Grant (*CMBSPEC*, No. 725456) at the University of Manchester, UK.

**References**


1. G. F. Smoot et al. Structure in the COBE differential microwave radiometer first-year maps. *ApJL*, 396:L1–L5, September 1992.
2. C. L. Bennett et al. First-Year Wilkinson Microwave Anisotropy Probe (WMAP) Observations: Preliminary Maps and Basic Results. *ApJS*, 148:1–27, September 2003.
3. Planck Collaboration, P. A. R. Ade et al. Planck 2013 results. XVI. Cosmological parameters. *A&A*, 571:A16, November 2014.
4. Planck Collaboration, P. A. R. Ade et al. Planck 2015 results. XIII. Cosmological parameters. *A&A*, 594:A13, September 2016.
5. Planck Collaboration, N. Aghanim et al. Planck 2018 results. VI. Cosmological parameters. *ArXiv e-prints*, July 2018.
6. G. Steigman. Primordial Nucleosynthesis in the Precision Cosmology Era. *Annual Review of Nuclear and Particle Science*, 57:463–491, November 2007.
7. J. Chluba and R. M. Thomas. Towards a complete treatment of the cosmological recombination problem. *MNRAS*, 412:748–764, April 2011.
8. Y. Ali-Haïmoud and C. M. Hirata. HyRec: A fast and highly accurate primordial hydrogen and helium recombination code. *Phys.Rev.D*, 83(4):043513–+, February 2011.
9. Y. B. Zeldovich and R. A. Sunyaev. The Interaction of Matter and Radiation in a Hot-Model Universe. *ApSS*, 4:301–316, July 1969.
10. Planck Collaboration, P. A. R. Ade et al. Planck 2013 results. XXI. Power spectrum and high-order statistics of the Planck all-sky Compton parameter map. *A&A*, 571:A21, November 2014.
11. Planck Collaboration, N. Aghanim et al. Planck 2015 results. XXII. A map of the thermal Sunyaev-Zeldovich effect. *A&A*, 594:A22, September 2016.
12. Planck Collaboration, P. A. R. Ade et al. Planck 2015 results. XV. Gravitational lensing. *A&A*, 594:A15, September 2016.
13. L. Page et al. Three-Year Wilkinson Microwave Anisotropy Probe (WMAP) Observations: Polarization Analysis. *ApJS*, 170:335–376, June 2007.
14. Planck Collaboration, P. A. R. Ade et al. Planck 2013 results. XV. CMB power spectra and likelihood. *A&A*, 571:A15, November 2014.
15. Planck Collaboration, N. Aghanim et al. Planck 2015 results. XI. CMB power spectra, likelihoods, and robustness of parameters. *ArXiv:1507.02704*, July 2015.
16. BICEP2/Keck Collaboration, Planck Collaboration, P. A. R. Ade et al. Joint Analysis of BICEP2/Keck Array and Planck Data. *Physical Review Letters*, 114(10):101301, March 2015.
17. P. André et al. PRISM (Polarized Radiation Imaging and Spectroscopy Mission): an extended white paper. *JCAP*, 2:6, February 2014.
18. K. N. Abazajian et al. Inflation physics from the cosmic microwave background and large scale structure. *Astroparticle Physics*, 63:55–65, March 2015.
19. K. N. Abazajian et al. Neutrino physics from the cosmic microwave background and large scale structure. *Astroparticle Physics*, 63:66–80, March 2015.
20. K. N. Abazajian et al. CMB-S4 Science Book, First Edition. *ArXiv:1610.02743*, October 2016.
21. J. Delabrouille et al. Exploring cosmic origins with CORE: Survey requirements and mission design. *JCAP*, 4:014, April 2018.
22. J. Chluba and R. A. Sunyaev. The evolution of CMB spectral distortions in the early Universe. *MNRAS*, 419:1294–1314, January 2012.
23. R. A. Sunyaev and R. Khatri. Unavoidable CMB Spectral Features and Blackbody Photosphere of Our Universe. *International Journal of Modern Physics D*, 22:30014, June 2013.
24. J. Chluba. Distinguishing different scenarios of early energy release with spectral distortions of the cosmic microwave background. *MNRAS*, 436:2232–2243, December 2013.
25. H. Tashiro. CMB spectral distortions and energy release in the early universe. *Prog. of Theo. and Exp. Physics*, 2014(6):060000, June 2014.
26. G. De Zotti, M. Negrello, G. Castex, A. Lapi, and M. Bonato. Another look at distortions of the Cosmic Microwave Background spectrum. *JCAP*, 3:047, March 2016.
27. J. Chluba. Future Steps in Cosmology using Spectral Distortions of the Cosmic Microwave Background. *ArXiv:1806.02915*, June 2018.
28. D. J. Fixsen, E. S. Cheng, J. M. Gales, J. C. Mather, R. A. Shafer, and E. L. Wright. The Cosmic Microwave Background Spectrum from the Full COBE FIRAS Data Set. *ApJ*, 473:576–+, December 1996.
29. D. J. Fixsen. The Temperature of the Cosmic Microwave Background. *ApJ*, 707:916–920, December 2009.

30. A. Kogut et al. The Primordial Inflation Explorer (PIXIE): a nulling polarimeter for cosmic microwave background observations. *JCAP*, 7:25–+, July 2011.
31. A. Kogut, J. Chluba, D. J. Fixsen, S. Meyer, and D. Spergel. The Primordial Inflation Explorer (PIXIE). In *SPIE Conference Series*, volume 9904 of *Proc.SPIE*, page 99040W, July 2016.
32. M. Sathyanarayana Rao, R. Subrahmanyan, N. Udaya Shankar, and J. Chluba. On the Detection of Spectral Ripples from the Recombination Epoch. *ApJ*, 810:3, September 2015.
33. R. A. Sunyaev and Y. B. Zeldovich. The interaction of matter and radiation in the hot model of the Universe, II. *ApSS*, 7:20–30, April 1970.
34. A. F. Illarionov and R. A. Sunyaev. Comptonization, the spectrum of RELICT radiation, and the thermal history of the universe. *Astronomicheskii Zhurnal*, 51:1162–1176, December 1974.
35. A. F. Illarionov and R. A. Sunyaev. Comptonization, characteristic radiation spectra, and thermal balance of low-density plasma. *Soviet Astronomy*, 18:413–419, February 1975.
36. L. Danese and G. de Zotti. The relic radiation spectrum and the thermal history of the Universe. *Nuovo Cimento Rivista Serie*, 7:277–362, September 1977.
37. L. Danese and G. de Zotti. Double Compton process and the spectrum of the microwave background. *A&A*, 107:39–42, March 1982.
38. C. Burigana, L. Danese, and G. de Zotti. Formation and evolution of early distortions of the microwave background spectrum - A numerical study. *A&A*, 246:49–58, June 1991.
39. W. Hu and J. Silk. Thermalization and spectral distortions of the cosmic background radiation. *Phys.Rev.D*, 48:485–502, July 1993.
40. J. Chluba. Which spectral distortions does ΛCDM actually predict? *MNRAS*, 460:227–239, July 2016.
41. J. A. Rubiño-Martín, J. Chluba, and R. A. Sunyaev. Lines in the cosmic microwave background spectrum from the epoch of cosmological hydrogen recombination. *MNRAS*, 371:1939–1952, (RMCS06), October 2006.
42. R. A. Sunyaev and J. Chluba. Signals from the epoch of cosmological recombination (Karl Schwarzschild Award Lecture 2008). *Astronomische Nachrichten*, 330:657–+, 2009.
43. J. Chluba and Y. Ali-Haïmoud. COSMOSPEC: fast and detailed computation of the cosmological recombination radiation from hydrogen and helium. *MNRAS*, 456:3494–3508, March 2016.
44. J. Chluba. *Spectral Distortions of the Cosmic Microwave Background*. PhD thesis, LMU München, March 2005.
45. C. Burigana, G. de Zotti, and L. Danese. Analytical description of spectral distortions of the cosmic microwave background. *A&A*, 303:323–+, November 1995.
46. R. Khatri and R. A. Sunyaev. Creation of the CMB spectrum: precise analytic solutions for the blackbody photosphere. *JCAP*, 6:38, June 2012.
47. R. Khatri and R. A. Sunyaev. Beyond y and $\mu$: the shape of the CMB spectral distortions in the intermediate epoch, $1.5 \times 10^4$lesssimzlesssim$2 \times 10^5$. *JCAP*, 9:16, September 2012.
48. J. Chluba. Refined approximations for the distortion visibility function and $\mu$-type spectral distortions. *MNRAS*, 440:2544–2563, April 2014.
49. C. Burigana and R. Salvaterra. What can we learn on the thermal history of the Universe from future cosmic microwave background spectrum measurements at long wavelengths? *MNRAS*, 342:543–556, June 2003.
50. P. Procopio and C. Burigana. A numerical code for the solution of the Kompaneets equation in cosmological context. *A&A*, 507:1243–1256, December 2009.
51. J. Chluba. Green's function of the cosmological thermalization problem. *MNRAS*, 434:352–357, September 2013.
52. J. C. Mather et al. Measurement of the cosmic microwave background spectrum by the COBE FIRAS instrument. *ApJ*, 420:439–444, January 1994.
53. D. J. Fixsen and J. C. Mather. The Spectral Results of the Far-Infrared Absolute Spectrophotometer Instrument on COBE. *ApJ*, 581:817–822, December 2002.
54. A. Kogut et al. ARCADE: Absolute radiometer for cosmology, astrophysics, and diffuse emission. *New Astronomy Reviews*, 50:925–931, December 2006.
55. M. Zannoni et al. TRIS. I. Absolute Measurements of the Sky Brightness Temperature at 0.6, 0.82, and 2.5 GHz. *ApJ*, 688:12–23, November 2008.
56. M. Seiffert et al. Interpretation of the ARCADE 2 Absolute Sky Brightness Measurement. *ApJ*, 734:6, June 2011.
57. A. P. Lightman. Double Compton emission in radiation dominated thermal plasmas. *ApJ*, 244:392–405, March 1981.
58. K. S. Thorne. Relativistic radiative transfer - Moment formalisms. *MNRAS*, 194:439–473, February 1981.
59. R. J. Gould. The cross section for double Compton scattering. *ApJ*, 285:275–278, October 1984.

60. J. Chluba, S. Y. Sazonov, and R. A. Sunyaev. The double Compton emissivity in a mildly relativistic thermal plasma within the soft photon limit. *A&A*, 468:785–795, June 2007.
61. J. R. Bond. Theory and Observations of the Cosmic Background Radiation. In R. Schaeffer, J. Silk, M. Spiro, and J. Zinn-Justin, editors, *Cosmology and Large Scale Structure*, page 469, January 1996.
62. J. Silk and J. Chluba. Next Steps for Cosmology. *Science*, 344:586–588, May 2014.
63. W. Hu. Wandering in the Background: A CMB Explorer. *arXiv:astro-ph/9508126*, August 1995.
64. J. Chluba and D. Jeong. Teasing bits of information out of the CMB energy spectrum. *MNRAS*, 438:2065–2082, March 2014.
65. R. A. Sunyaev and Y. B. Zeldovich. Formation of Clusters of Galaxies; Protocluster Fragmentation and Intergalactic Gas Heating. *A&A*, 20:189–+, August 1972.
66. W. Hu, D. Scott, and J. Silk. Reionization and cosmic microwave background distortions: A complete treatment of second-order Compton scattering. *Phys.Rev.D*, 49:648–670, January 1994.
67. R. Cen and J. P. Ostriker. Where Are the Baryons? *ApJ*, 514:1–6, March 1999.
68. F. Miniati, D. Ryu, H. Kang, T. W. Jones, R. Cen, and J. P. Ostriker. Properties of Cosmic Shock Waves in Large-Scale Structure Formation. *ApJ*, 542:608–621, October 2000.
69. A. Refregier and et al. Power spectrum of the Sunyaev-Zel'dovich effect. *Phys.Rev.D*, 61(12):123001, June 2000.
70. S. P. Oh, A. Cooray, and M. Kamionkowski. Sunyaev-Zeldovich fluctuations from the first stars? *MNRAS*, 342:L20–L24, June 2003.
71. P. Zhang, U.-L. Pen, and H. Trac. The temperature of the intergalactic medium and the Compton y parameter. *MNRAS*, 355:451–460, December 2004.
72. J. Chluba. Green's function of the cosmological thermalization problem - II. Effect of photon injection and constraints. *MNRAS*, 454:4182–4196, December 2015.
73. J. D. Bowman, A. E. E. Rogers, R. A. Monsalve, T. J. Mozdzen, and N. Mahesh. An absorption profile centred at 78 megahertz in the sky-averaged spectrum. *Nature*, 555:67–70, March 2018.
74. D. J. Fixsen et al. The Temperature of the Cosmic Microwave Background at 10 GHz. *ApJ*, 612:86–95, September 2004.
75. D. J. Fixsen et al. ARCADE 2 Measurement of the Absolute Sky Brightness at 3-90 GHz. *ApJ*, 734:5–+, June 2011.
76. C. Feng and G. Holder. Enhanced Global Signal of Neutral Hydrogen Due to Excess Radiation at Cosmic Dawn. *ApJL*, 858:L17, May 2018.
77. A. Hektor, G. Hütsi, L. Marzola, M. Raidal, V. Vaskonen, and H. Veermäe. Constraining Primordial Black Holes with the EDGES 21-cm Absorption Signal. *ArXiv:1803.09697*, March 2018.
78. T. Moroi, K. Nakayama, and Y. Tang. Axion-Photon Conversion and Effects on 21cm Observation. *ArXiv:1804.10378*, April 2018.
79. J. C. Hill, N. Battaglia, J. Chluba, S. Ferraro, E. Schaan, and D. N. Spergel. Taking the Universe's Temperature with Spectral Distortions of the Cosmic Microwave Background. *Physical Review Letters*, 115(26):261301, December 2015.
80. R. Barkana and A. Loeb. In the beginning: the first sources of light and the reionization of the universe. *Physics Reports*, 349:125–238, July 2001.
81. K. Dolag, E. Komatsu, and R. Sunyaev. SZ effects in the Magneticum Pathfinder simulation: comparison with the Planck, SPT, and ACT results. *MNRAS*, 463:1797–1811, December 2016.
82. M. H. Abitbol, J. Chluba, J. C. Hill, and B. R. Johnson. Prospects for measuring cosmic microwave background spectral distortions in the presence of foregrounds. *MNRAS*, 471:1126–1140, October 2017.
83. J. Chluba, D. Nagai, S. Sazonov, and K. Nelson. A fast and accurate method for computing the Sunyaev-Zel'dovich signal of hot galaxy clusters. *MNRAS*, 426:510–530, October 2012.
84. J. Chluba, E. Switzer, K. Nelson, and D. Nagai. Sunyaev-Zeldovich signal processing and temperature-velocity moment method for individual clusters. *MNRAS*, 430:3054–3069, April 2013.
85. T. Bringmann, P. Scott, and Y. Akrami. Improved constraints on the primordial power spectrum at small scales from ultracompact minihalos. *Phys.Rev.D*, 85(12):125027, June 2012.
86. R. A. Sunyaev and Y. B. Zeldovich. Small scale entropy and adiabatic density perturbations – Antimatter in the Universe. *ApSS*, 9:368–382, December 1970.
87. R. A. Daly. Spectral distortions of the microwave background radiation resulting from the damping of pressure waves. *ApJ*, 371:14–28, April 1991.
88. J. D. Barrow and P. Coles. Primordial density fluctuations and the microwave background spectrum. *MNRAS*, 248:52–57, January 1991.
89. W. Hu, D. Scott, and J. Silk. Power spectrum constraints from spectral distortions in the cosmic microwave background. *ApJL*, 430:L5–L8, July 1994.

90. W. Hu and N. Sugiyama. Thermal history constraints on the isocurvature baryon model. *ApJ*, 436:456–466, December 1994.
91. J. Chluba, R. Khatri, and R. A. Sunyaev. CMB at $2 \times 2$ order: the dissipation of primordial acoustic waves and the observable part of the associated energy release. *MNRAS*, 425:1129–1169, September 2012.
92. E. Pajer and M. Zaldarriaga. A hydrodynamical approach to CMB $\mu$-distortion from primordial perturbations. *JCAP*, 2:36, February 2013.
93. J. Chluba, A. L. Erickcek, and I. Ben-Dayan. Probing the Inflaton: Small-scale Power Spectrum Constraints from Measurements of the Cosmic Microwave Background Energy Spectrum. *ApJ*, 758:76, October 2012.
94. J. B. Dent, D. A. Easson, and H. Tashiro. Cosmological constraints from CMB distortion. *Phys.Rev.D*, 86(2):023514, July 2012.
95. R. Khatri and R. A. Sunyaev. Forecasts for CMB $\mu$ and i-type spectral distortion constraints on the primordial power spectrum on scales $8¡k¡10^4$ Mpc$^{-1}$ with the future Pixie-like experiments. *JCAP*, 6:26, June 2013.
96. S. Clesse, B. Garbrecht, and Y. Zhu. Testing inflation and curvaton scenarios with CMB distortions. *JCAP*, 10:046, October 2014.
97. G. Cabass, A. Melchiorri, and E. Pajer. $\mu$ distortions or running: A guaranteed discovery from CMB spectrometry. *Phys.Rev.D*, 93(8):083515, April 2016.
98. J. Chluba and D. Grin. CMB spectral distortions from small-scale isocurvature fluctuations. *MNRAS*, 434:1619–1635, September 2013.
99. A. Ota, T. Takahashi, H. Tashiro, and M. Yamaguchi. CMB $\mu$ distortion from primordial gravitational waves. *JCAP*, 10:029, October 2014.
100. J. Chluba, L. Dai, D. Grin, M. A. Amin, and M. Kamionkowski. Spectral distortions from the dissipation of tensor perturbations. *MNRAS*, 446:2871–2886, January 2015.
101. T. Nakama, J. Chluba, and M. Kamionkowski. Shedding light on the small-scale crisis with CMB spectral distortions. *Phys.Rev.D*, 95(12):121302, June 2017.
102. S. Clesse and J. García-Bellido. Massive primordial black holes from hybrid inflation as dark matter and the seeds of galaxies. *Phys.Rev.D*, 92(2):023524, July 2015.
103. E. Pajer and M. Zaldarriaga. New Window on Primordial Non-Gaussianity. *Physical Review Letters*, 109(2):021302, July 2012.
104. J. Ganc and E. Komatsu. Scale-dependent bias of galaxies and $\mu$-type distortion of the cosmic microwave background spectrum from single-field inflation with a modified initial state. *Phys.Rev.D*, 86(2):023518, July 2012.
105. M. Biagetti, H. Perrier, A. Riotto, and V. Desjacques. Testing the running of non-Gaussianity through the CMB $\mu$-distortion and the halo bias. *Phys.Rev.D*, 87(6):063521, March 2013.
106. R. Emami, E. Dimastrogiovanni, J. Chluba, and M. Kamionkowski. Probing the scale dependence of non-Gaussianity with spectral distortions of the cosmic microwave background. *Phys.Rev.D*, 91(12):123531, June 2015.
107. J. Chluba, E. Dimastrogiovanni, M. A. Amin, and M. Kamionkowski. Evolution of CMB spectral distortion anisotropies and tests of primordial non-Gaussianity. *MNRAS*, 466:2390–2401, April 2017.
108. A. Ravenni, M. Liguori, N. Bartolo, and M. Shiraishi. Primordial non-Gaussianity with $\mu$-type and y-type spectral distortions: exploiting Cosmic Microwave Background polarization and dealing with secondary sources. *JCAP*, 9:042, September 2017.
109. M. Remazeilles and J. Chluba. Extracting foreground-obscured $\mu$-distortion anisotropies to constrain primordial non-Gaussianity. *MNRAS*, April 2018.
110. G. Cabass, E. Pajer, and D. van der Woude. Spectral distortion anisotropies from single-field inflation. *ArXiv e-prints*, May 2018.
111. R. Khatri, R. A. Sunyaev, and J. Chluba. Does Bose-Einstein condensation of CMB photons cancel $\mu$ distortions created by dissipation of sound waves in the early Universe? *A&A*, 540:A124, April 2012.
112. Y. Ali-Haïmoud, J. Chluba, and M. Kamionkowski. Constraints on Dark Matter Interactions with Standard Model Particles from Cosmic Microwave Background Spectral Distortions. *Physical Review Letters*, 115(7):071304, August 2015.
113. R. Barkana. Possible interaction between baryons and dark-matter particles revealed by the first stars. *Nature*, 555:71–74, March 2018.
114. J. B. Muñoz and A. Loeb. Insights on Dark Matter from Hydrogen during Cosmic Dawn. *ArXiv:1802.10094*, February 2018.
115. A. Berlin, D. Hooper, G. Krnjaic, and S. D. McDermott. Severely Constraining Dark Matter Interpretations of the 21-cm Anomaly. *ArXiv:1803.02804*, March 2018.
116. Y. B. Zeldovich, V. G. Kurt, and R. A. Syunyaev. Recombination of Hydrogen in the Hot Model of the

Universe. *ZETF*, 55:278–286, July 1968.
117. P. J. E. Peebles. Recombination of the Primeval Plasma. *ApJ*, 153:1–+, July 1968.
118. V. K. Dubrovich. Hydrogen recombination lines of cosmological origin. *Soviet Astronomy Letters*, 1:196–+, October 1975.
119. J. Chluba and R. A. Sunyaev. Is there a need and another way to measure the cosmic microwave background temperature more accurately? *A&A*, 478:L27–L30, February 2008.
120. G. B. Rybicki and I. P. dell'Antonio. Spectral Distortions in the CMB from Recombination. In G. L. Chincarini, A. Iovino, T. Maccacaro, and D. Maccagni, editors, *ASP Conf. Ser. 51: Observational Cosmology*, pages 548–+, January 1993.
121. V. K. Dubrovich and V. A. Stolyarov. Fossil radio lines of hydrogen in the cosmic background radiation at decimeter and meter wavelengths. *A&A*, 302:635–+, October 1995.
122. V. K. Dubrovich and V. A. Stolyarov. The spectrum of fossil He I and He II recombination lines. *Astronomy Letters*, 23:565–572, September 1997.
123. E. E. Kholupenko, A. V. Ivanchik, and D. A. Varshalovich. CMBR distortion concerned with recombination of the primordial hydrogen plasma. *Gravitation and Cosmology*, 11:161–165, June 2005.
124. J. Chluba and R. A. Sunyaev. Free-bound emission from cosmological hydrogen recombination. *A&A*, 458:L29–L32, November 2006.
125. J. Chluba, J. A. Rubiño-Martín, and R. A. Sunyaev. Cosmological hydrogen recombination: populations of the high-level substates. *MNRAS*, 374:1310–1320, February 2007.
126. J. A. Rubiño-Martín, J. Chluba, and R. A. Sunyaev. Lines in the cosmic microwave background spectrum from the epoch of cosmological helium recombination. *A&A*, 485:377–393, July 2008.
127. J. Chluba and R. A. Sunyaev. Cosmological recombination: feedback of helium photons and its effect on the recombination spectrum. *MNRAS*, 402:1221–1248, February 2010.
128. J. Chluba, G. M. Vasil, and L. J. Dursi. Recombinations to the Rydberg states of hydrogen and their effect during the cosmological recombination epoch. *MNRAS*, 407:599–612, September 2010.
129. Y. Ali-Haïmoud. Effective conductance method for the primordial recombination spectrum. *Phys.Rev.D*, 87(2):023526, January 2013.
130. V. Desjacques, J. Chluba, J. Silk, F. de Bernardis, and O. Doré. Detecting the cosmological recombination signal from space. *MNRAS*, 451:4460–4470, August 2015.
131. A. V. Smirnov et al. Space mission Millimetron for terahertz astronomy. In *SPIE Conference Series*, volume 8442, September 2012.
132. J. Chluba and R. A. Sunyaev. Pre-recombinational energy release and narrow features in the CMB spectrum. *A&A*, 501:29–47, July 2009.
133. J. Chluba. Could the cosmological recombination spectrum help us understand annihilating dark matter? *MNRAS*, 402:1195–1207, February 2010.
134. J. A. Rubiño-Martín, J. Chluba, W. A. Fendt, and B. D. Wandelt. Estimating the impact of recombination uncertainties on the cosmological parameter constraints from cosmic microwave background experiments. *MNRAS*, 403:439–452, March 2010.
135. J. R. Shaw and J. Chluba. Precise cosmological parameter estimation using COSMOREC. *MNRAS*, 415:1343–1354, August 2011.
136. W. A. Fendt, J. Chluba, J. A. Rubiño-Martín, and B. D. Wandelt. RICO: A New Approach for Fast and Accurate Representation of the Cosmological Recombination History. *ApJS*, 181:627–638, April 2009.
137. Planck Collaboration, P. A. R. Ade et al. Planck 2013 results. XXII. Constraints on inflation. *A&A*, 571:A22, November 2014.
138. O. Adriani et al. An anomalous positron abundance in cosmic rays with energies 1.5-100GeV. *Nature*, 458:607–609, April 2009.
139. S. Galli, F. Iocco, G. Bertone, and A. Melchiorri. CMB constraints on dark matter models with large annihilation cross section. *Phys.Rev.D*, 80(2):023505–+, July 2009.
140. CDMS II Collaboration, Z. Ahmed et al. Dark Matter Search Results from the CDMS II Experiment. *Science*, 327:1619, March 2010.
141. J. Zavala, M. Vogelsberger, T. R. Slatyer, A. Loeb, and V. Springel. Cosmic X-ray and gamma-ray background from dark matter annihilation. *Phys.Rev.D*, 83(12):123513–+, June 2011.
142. G. Hütsi, J. Chluba, A. Hektor, and M. Raidal. WMAP7 and future CMB constraints on annihilating dark matter: implications for GeV-scale WIMPs. *A&A*, 535:A26, November 2011.
143. G. Aslanyan et al. Ultracompact minihalos as probes of inflationary cosmology. *ArXiv:1512.04597*, December 2015.
144. G. Jungman, M. Kamionkowski, and K. Griest. Supersymmetric dark matter. *Physics Reports*, 267:195–373, March 1996.

145. G. Bertone, D. Hooper, and J. Silk. Particle dark matter: evidence, candidates and constraints. *Physics Reports*, 405:279–390, January 2005.
146. M. Cirelli, F. Iocco, and P. Panci. Constraints on Dark Matter annihilations from reionization and heating of the intergalactic gas. *JCAP*, 10:9–+, October 2009.
147. G. Hütsi, A. Hektor, and M. Raidal. Constraints on leptonically annihilating dark matter from reionization and extragalactic gamma background. *A&A*, 505:999–1005, October 2009.
148. Tracy R. Slatyer, Nikhil Padmanabhan, and Douglas P. Finkbeiner. Cmb constraints on wimp annihilation: Energy absorption during the recombination epoch. *Physical Review D (Particles, Fields, Gravitation, and Cosmology)*, 80(4):043526, 2009.
149. G. Giesen, J. Lesgourgues, B. Audren, and Y. Ali-Haïmoud. CMB photons shedding light on dark matter. *JCAP*, 12:8, December 2012.
150. R. Diamanti, L. Lopez-Honorez, O. Mena, S. Palomares-Ruiz, and A. C. Vincent. Constraining dark matter late-time energy injection: decays and p-wave annihilations. *JCAP*, 2:017, February 2014.
151. J. A. Adams, S. Sarkar, and D. W. Sciama. Cosmic microwave background anisotropy in the decaying neutrino cosmology. *MNRAS*, 301:210–214, November 1998.
152. X. Chen and M. Kamionkowski. Particle decays during the cosmic dark ages. *Phys.Rev.D*, 70(4):043502–+, August 2004.
153. N. Padmanabhan and D. P. Finkbeiner. Detecting dark matter annihilation with CMB polarization: Signatures and experimental prospects. *Phys.Rev.D*, 72(2):023508–+, July 2005.
154. L. Zhang, X. Chen, Y.-A. Lei, and Z.-G. Si. Impacts of dark matter particle annihilation on recombination and the anisotropies of the cosmic microwave background. *Phys.Rev.D*, 74(10):103519–+, November 2006.
155. J. M. Shull and M. E. van Steenberg. X-ray secondary heating and ionization in quasar emission-line clouds. *ApJ*, 298:268–274, November 1985.
156. M. Valdés, C. Evoli, and A. Ferrara. Particle energy cascade in the intergalactic medium. *MNRAS*, 404:1569–1582, May 2010.
157. S. Galli, T. R. Slatyer, M. Valdes, and F. Iocco. Systematic uncertainties in constraining dark matter annihilation from the cosmic microwave background. *Phys.Rev.D*, 88(6):063502, September 2013.
158. T. R. Slatyer. Indirect dark matter signatures in the cosmic dark ages. II. Ionization, heating, and photon production from arbitrary energy injections. *Phys.Rev.D*, 93(2):023521, January 2016.
159. P. McDonald, R. J. Scherrer, and T. P. Walker. Cosmic microwave background constraint on residual annihilations of relic particles. *Phys.Rev.D*, 63(2):023001–+, January 2001.
160. J. Ellis, G. B. Gelmini, J. L. Lopez, D. V. Nanopoulos, and S. Sarkar. Astrophysical constraints on massive unstable neutral relic particles. *Nuclear Physics B*, 373:399–437, April 1992.
161. M. Kawasaki, K. Kohri, and T. Moroi. Big-bang nucleosynthesis and hadronic decay of long-lived massive particles. *Phys.Rev.D*, 71(8):083502, April 2005.
162. L. Zhang, X. Chen, M. Kamionkowski, Z.-G. Si, and Z. Zheng. Constraints on radiative dark-matter decay from the cosmic microwave background. *Phys.Rev.D*, 76(6):061301–+, September 2007.
163. S. Sarkar and A. M. Cooper. Cosmological and experimental constraints on the tau neutrino. *Physics Letters B*, 148:347–354, November 1984.
164. J. Ellis, D. V. Nanopoulos, and S. Sarkar. The cosmology of decaying gravitinos. *Nuclear Physics B*, 259:175–188, September 1985.
165. W. Hu and J. Silk. Thermalization constraints and spectral distortions for massive unstable relic particles. *Physical Review Letters*, 70:2661–2664, May 1993.
166. M. Pospelov and A. Ritz. The galactic 511 keV line from electroweak scale WIMPs. *Physics Letters B*, 651:208–215, July 2007.
167. D. P. Finkbeiner and N. Weiner. Exciting dark matter and the INTEGRAL/SPI 511keV signal. *Phys.Rev.D*, 76(8):083519, October 2007.
168. J. L. Feng, A. Rajaraman, and F. Takayama. Superweakly interacting massive particle dark matter signals from the early Universe. *Phys.Rev.D*, 68(6):063504, September 2003.
169. J. L. Feng. Dark Matter Candidates from Particle Physics and Methods of Detection. *ARA&A*, 48:495–545, September 2010.
170. E. Dimastrogiovanni, L. M. Krauss, and J. Chluba. Constraints on gravitino decay and the scale of inflation using CMB spectral distortions. *Phys.Rev.D*, 94(2):023518, July 2016.
171. H. Tashiro, J. Silk, and D. J. E. Marsh. Constraints on primordial magnetic fields from CMB distortions in the axiverse. *Phys.Rev.D*, 88(12):125024, December 2013.
172. B. J. Carr, K. Kohri, Y. Sendouda, and J. Yokoyama. New cosmological constraints on primordial black holes. *Phys.Rev.D*, 81(10):104019–+, May 2010.
173. V. Poulin, P. D. Serpico, F. Calore, S. Clesse, and K. Kohri. CMB bounds on disk-accreting massive

primordial black holes. *Phys.Rev.D*, 96(8):083524, October 2017.
174. M. Kawasaki, K. Kohri, T. Moroi, and Y. Takaesu. Revisiting big-bang nucleosynthesis constraints on long-lived decaying particles. *Phys.Rev.D*, 97(2):023502, January 2018.
175. R. A. Sunyaev and I. B. Zeldovich. The velocity of clusters of galaxies relative to the microwave background - The possibility of its measurement. *MNRAS*, 190:413–420, February 1980.
176. M. Birkinshaw. The Sunyaev-Zel'dovich effect. *Phys. Reports*, 310:97–195, March 1999.
177. J. E. Carlstrom, G. P. Holder, and E. D. Reese. Cosmology with the Sunyaev-Zel'dovich Effect. *ARA&A*, 40:643–680, 2002.
178. E. Komatsu and U. Seljak. The Sunyaev-Zel'dovich angular power spectrum as a probe of cosmological parameters. *MNRAS*, 336:1256–1270, November 2002.
179. J. M. Diego and S. Majumdar. The hybrid SZ power spectrum: combining cluster counts and SZ fluctuations to probe gas physics. *MNRAS*, 352:993–1004, August 2004.
180. N. Battaglia, J. R. Bond, C. Pfrommer, J. L. Sievers, and D. Sijacki. Simulations of the Sunyaev-Zel'dovich Power Spectrum with Active Galactic Nucleus Feedback. *ApJ*, 725:91–99, December 2010.
181. L. D. Shaw, D. Nagai, S. Bhattacharya, and E. T. Lau. Impact of Cluster Physics on the Sunyaev-Zel'dovich Power Spectrum. *ApJ*, 725:1452–1465, December 2010.
182. D. Munshi, S. Joudaki, J. Smidt, P. Coles, and S. T. Kay. Statistical properties of thermal Sunyaev-Zel'dovich maps. *MNRAS*, 429:1564–1584, February 2013.
183. C. Pitrou, F. Bernardeau, and J.-P. Uzan. The y-sky: diffuse spectral distortions of the cosmic microwave background. *JCAP*, 7:19, July 2010.
184. Q. Yu, D. N. Spergel, and J. P. Ostriker. Rayleigh Scattering and Microwave Background Fluctuations. *ApJ*, 558:23–28, September 2001.
185. A. Lewis. Rayleigh scattering: blue sky thinking for future CMB observations. *JCAP*, 8:053, August 2013.
186. A. Loeb. Probing the Universe after Cosmological Recombination through the Effect of Neutral Lithium on the Microwave Background Anisotropies. *ApJL*, 555:L1–L5, July 2001.
187. M. Zaldarriaga and A. Loeb. The Imprint of Lithium Recombination on the Microwave Background Anisotropies. *ApJ*, 564:52–59, January 2002.
188. K. Basu, C. Hernández-Monteagudo, and R. A. Sunyaev. CMB observations and the production of chemical elements at the end of the dark ages. *A&A*, 416:447–466, March 2004.
189. C. Hernández-Monteagudo, J. A. Rubiño-Martín, and R. A. Sunyaev. On the influence of resonant scattering on cosmic microwave background polarization anisotropies. *MNRAS*, 380:1656–1668, October 2007.
190. J. A. Rubiño-Martín, C. Hernández-Monteagudo, and R. A. Sunyaev. The imprint of cosmological hydrogen recombination lines on the power spectrum of the CMB. *A&A*, 438:461–473, August 2005.
191. L. Danese and G. de Zotti. Dipole anisotropy and distortions of the spectrum of the cosmic microwave background. *A&A*, 94:L33, February 1981.
192. S. A. Balashev, E. E. Kholupenko, J. Chluba, A. V. Ivanchik, and D. A. Varshalovich. Spectral Distortions of the CMB Dipole. *ApJ*, 810:131, September 2015.
193. C. Burigana et al. Exploring cosmic origins with CORE: Effects of observer peculiar motion. *JCAP*, 4:021, April 2018.
194. M. Kamionkowski and L. Knox. Aspects of the cosmic microwave background dipole. *Phys.Rev.D*, 67(6):063001, March 2003.
195. J. Chluba and R. A. Sunyaev. Superposition of blackbodies and the dipole anisotropy: A possibility to calibrate CMB experiments. *A&A*, 424:389–408, September 2004.

# Authors Index

# Authors Index

# List of Participants

| Family name | First name | Home institution | Country | Email |
|---|---|---|---|---|
| Albrecht | Johannes | TU Dortmund | Germany | albrecht@cern.ch |
| Augé | Etienne | Université Paris-Sud | France | etienne.auge@u-psud.fr |
| Barton | Adam | Lancaster University | UK | abarton@cern.ch |
| Bierwagen | Katharina | Johannes Gutenberg University Mainz | Germany | kbierwag@uni-mainz.de |
| Bluj | Michal | National Centre for Nuclear Research | Poland | michal.bluj@cern.ch |
| Bordry | Frederick | CERN | Switzerland | frederick.bordry@cern.ch |
| Bose | Tulika | Boston University | USA | tulika@bu.edu |
| Caola | Fabrizio | IPPP Durham | UK | fabrizio.caola@cern.ch |
| Cavaliere | Viviana | Brookhaven National Lab | USA | viviana.cavaliere@cern.ch |
| Chapon | Emilien | CERN | Switzerland | emilien.chapon@cern.ch |
| Corrales Morales | Yasser | University of Turin | Italy | ycorrale@cern.ch |
| Crivellin | Andreas | PSI | Switzerland | andreas.crivellin@psi.ch |
| Crocombe | Andrew | Department of Physics | UK | andrew.christopher.crocombe@cern.ch |
| D'Ambrosio | GIancarlo | INFN | Italy | gdambros@na.infn.it |
| d'Enterria | David | CERN | Switzerland | dde@cern.ch |
| Darmé | Luc | National Centre for Nuclear Research | Poland | luc.darme@ncbj.gov.pl |
| Dittmaier | Stefan | University of Freiburg | Germany | stefan.dittmaier@physik.uni-freiburg.de |
| Duehrssen | Michael | CERN | Switzerland | michael.duehrssen@cern.ch |
| Ellis | Keith | IPPP, Durham | UK | keith.ellis@durham.ac.uk |
| Fiaschi | Juri | University of Münster | Germany | fiaschi@uni-muenster.de |
| Fleischer | Robert | Nikhef / VUA | Netherlands | Robert.Fleischer@nikhef.nl |
| Fleuret | Frédéric | Laboratoire Leprince-Ringuet | France | fleuret@in2p3.fr |
| Gauld | Rhorry | ETH | Switzerland | rggauld@gmail.com |
| Ghezzi | Margherita | Paul Scherrer Institut | Switzerland | margherita.ghezzi@psi.ch |
| Giani | Simone | CERN | Switzerland | Simone.Giani@cern.ch |
| Gibson | Adam | Valparaiso University | USA | adam.gibson-even@valpo.edu |
| Giuli | Francesco | University of Oxford | UK | francesco.giuli@cern.ch |
| Glatzer | Julian | IFAE - Barcelona | Spain | jglatzer@cern.ch |
| Goldouzian | Reza | Université libre de Bruxelles | Belgium | Reza.Goldouzian@cern.ch |
| Gwilliam | Carl | The University of Liverpool | UK | gwilliam@hep.ph.liv.ac.uk |
| Haber | Howard | University of California, Santa Cruz | USA | haber@scipp.ucsc.edu |
| Heinrich | Gudrun | Max Planck Institute for Physics | Germany | gudrun@mpp.mpg.de |
| Heintz | Ulrich | Brown University | USA | ulrich_heintz@brown.edu |
| Hiller | Gudrun | Theoretical Physics T IV, TU Dortmund | Germany | ghiller@physik.uni-dortmund.de |
| Hirosky | Bob | University of Virginia | USA | hirosky@virginia.edu |
| Hogan | Julie | Bethel University | USA | j.hogan@cern.ch |
| Hou | George W.S. | National Taiwan University | Taiwan | wshou@phys.ntu.edu.tw |
| Howarth | James | University of Manchester | UK | jhowarth@cern.ch |
| Iyer | Abhishek | INFN | Italy | iyera@na.infn.it |
| Jaarsma | Ruben | Nikhef | Netherlands | rjaarsma@nikhef.nl |
| Jacazio | Nicolo' | University of Bologna / INFN | Italy | nicolo.jacazio@cern.ch |
| Jung | Andy | Purdue University | USA | anjung@purdue.edu |
| Kaspar | Jan | INFN Sezione di Pisa | Italy | jan.kaspar@cern.ch |
| Kato | Yuji | Nagoya University | Japan | kato@hepl.phys.nagoya-u.ac.jp |
| Kerbikov | Boris | ITEP and Lebedev | Russia | bkerbikov@gmail.com |
| Kerner | Matthias | Max Planck Institute for Physics | Germany | kerner@mpp.mpg.de |
| Khoo | Teng Jian | Université de Genève (DPNC) | Switzerland | khoo@cern.ch |
| Klaver | Suzanne | INFN e Laboratori Nazionali di Frascati | Italy | sklaver@cern.ch |
| Klima | Boaz | Fermilab | USA | klima@fnal.gov |
| Kling | Felix | University of California, | USA | fkling@uci.edu |
| Komarov | Ilya | DESY | Germany | ilya.komarov@desy.de |
| Leardini | Lucia | Physikalisches Institut | Germany | lucia.leardini@cern.ch |
| Li | Shiyuan | Shandong University | China | lishy@sdu.edu.cn |
| Lontkovskyi | Denys | Vrije Universiteit Brussel | Belgium | denys.lontkovskyi@vub.be |

| | | | | |
|---|---|---|---|---|
| Lu | Cai-Dian | IHEP | China | lucd@ihep.ac.cn |
| Lupton | Oliver | CERN | Switzerland | oliver.lupton@cern.ch |
| Mahmoudi | Nazila | Lyon University | France | nazila@cern.ch |
| McCullough | Matthew | CERN | Switzerland | matthew.mccullough@cern.ch |
| Mesropian | Christina | The Rockefeller University | USA | christina.mesropian@rockefeller.edu |
| Mirra | Marco | Università Federico II - Napoli | Italy | marco.mirra@cern.ch |
| Moran | Dermot | CIEMAT | Spain | dermot.anthony.moran@cern.ch |
| Morse | David | Northeastern University | USA | dmorse@cern.ch |
| Nagashima | Kazuya | Hiroshima University | Japan | kazuyan@quark.hiroshima-u.ac.jp |
| Narain | Meenakshi | Brown University | USA | meenakshi_narain@brown.edu |
| Neumeister | Norbert | Purdue University | USA | neumeist@purdue.edu |
| Orginos | Kostas | College of William and Mary | USA | kostas@jlab.org |
| Page | Ben | Albert-Ludwigs-Universitaet Freiburg | Germany | ben.page@physik.uni-freiburg.de |
| Pietrzyk | Bolek | LAPP | France | bolek.pietrzyk@cern.ch |
| Praszalowicz | Michal | Uniwersytet Jagielloński | Poland | michal@if.uj.edu.pl |
| Quigg | Chris | Fermilab | USA | quigg@fnal.gov |
| Raspiareza | Aliaksei | DESY Hamburg | Germany | rasp@mail.desy.de |
| Rottoli | Luca | University of Oxford | UK | luca.rottoli@physics.ox.ac.uk |
| Ruijl | Ben | ETH Zurich | Switzerland | benruyl@gmail.com |
| Sborlini | German | Università degli Studi/ INFN Milano | Italy | german.sborlini@unimi.it |
| Schröder | Matthias | Karlsruhe Institute of Technology (KIT) | Germany | matthias.schroeder@kit.edu |
| Scott | Pat | Imperial College London | UK | p.scott@imperial.ac.uk |
| Shkarovskiy | Sergey | Joint Institute for Nuclear Research | Russia | Sergey.Shkarovskiy@cern.ch |
| Skands | Peter | Monash University | Australia | peter.skands@monash.edu |
| Smith | Matthias | INFN Pisa | Italy | matthias.smith@pi.infn.it |
| Soffer | Abner | Tel Aviv University | Israel | asoffer@tau.ac.il |
| Solodov | Evgeny | Budker INP | Russia | solodov@inp.nsk.su |
| Spira | Michael | Paul Scherrer Institut | Switzerland | michael.spira@psi.ch |
| Starovoitov | Pavel | Heidelberg University | Germany | pavel.starovoitov@cern.ch |
| Tait | Tim | University of California, Irvine | USA | ttait@uci.edu |
| Tan | Chung-I | Physics department, Brown University | USA | chung-i_tan@brown.edu |
| Tang | Zebo | University of Science and Technology | China | zbtang@ustc.edu.cn |
| Tellarini | Giulia | Istituto Nazionale Fisica Nucleare | Italy | tellarini@fe.infn.it |
| Thomas | Deepa | The University of Texas at Austin | USA | deepa.thomas@cern.ch |
| Todorova | Sarka | LAPP | France | sarka.todorova@cern.ch |
| Torró-Pastor | Emma | University of Washington - Seattle | Switzerland | Emma.Torro.Pastor@cern.ch |
| Tran Thanh | Son | department of Biology and Agrotechnic | Vietnam | |
| Tran Thanh Van | Jean | Rencontres de Moriond | France | jtrantv@gmail.com |
| Tuchming | Boris | CEA Irfu | France | boris.tuchming@cea.fr |
| Tuna | Alexander | Harvard University | USA | tuna@cern.ch |
| Ulrich | Ralf | Karlsruhe Institute of Technology | Germany | ralf.ulrich@kit.edu |
| Watson | Nigel | University of Birmingham | UK | Nigel.Watson@cern.ch |
| Wolke | Magnus | Uppsala University | Sweden | magnus.wolke@fysast.uu.se |
| Yamaguchi | Yorito | RIKEN | Japan | yorito.yamaguchi@riken.jp |
| Yan | Liang | University of Turin and INFN | Italy | yanliangustc@gmail.com |
| You | Tevong | University of Cambridge | UK | tty20@cam.ac.uk |
| Zaccolo | Valentina | INFN Torino | Italy | valentina.zaccolo@cern.ch |
| Zafeiropoulos | Savvas | Universität Heidelberg | Germany | savvaslz@gmail.com |
| Zanderighi | Giulia | CERN | Switzerland | giulia.zanderighi@cern.ch |
| Zenaiev | Oleksandr | DESY | Germany | oleksandr.zenaiev@desy.de |
| Zlebcik | Radek | DESY | Germany | radek.zlebcik@desy.de |
| Zwicky | Roman | Edinburgh University | UK | roman.zwicky@ed.ac.uk |

Dépôt légal : novembre 2018
Achevé d'imprimer : novembre 2018
COPYMEDIA
www.copy-media.net
Avenue de Guitayne - 33610 CANÉJAN